Optical studies of the vibrational properties of disordered solids

A. S. Barker, Jr.

Bell Laboratories, Murray Hill, New Jersey 07974

A. J. Sievers*

Laboratory of Atomic and Solid State Physics, Cornell University, Ithaca, New York 14850
(Received 11 June 1975)

Since approximately 1950 an increasing portion of experimental solid state physics research has been concerned with studying defects in crystals. This trend might appear to be a rather belated recognition that most of the materials we come into contact with have a random structure. In fact the theoretical understanding and controlled preparation of compounds with defects or random structure has been very slow in developing. The present paper examines and reviews our knowledge of the lattice vibrations associated with defects. The coverage is extremely broad, as shown by the table of contents. It includes localized and resonant modes of isolated defects as well as the modes in highly disordered mixed crystals and glasses. It is primarily a review of experimental work but theoretical results are included where the latter explain or predict significant features. In order to be self-contained several sections of the paper deal entirely with theoretical matters. There is a chapter on explicit solutions of the linear chain vibration problem and a short chapter on Green's function methods. The review emphasizes the infrared absorption and Raman scattering of defects. This is simply because other techniques have not yielded nearly so much information. Neutron scattering and electron tunneling are referred to only where they have shed light on certain systems. Extensive tables of defects and mode frequencies are included for each type of solid. The major solids which are reviewed include semiconductors, ionic compounds, organic compounds, and amorphous insulators.

We dedicate this review to the memory of Bernd Fritz who pioneered in this field and whose very productive efforts were cut short by his untimely death.

CONTENTS

*The contribution by A. J. Sievers has been supported by the U.S. Atomic Energy Commission under Contract No. At(11-1)—3151, Technical Report No. COO—1351—42. Additional support was received from the National Science Foundation under grant #CH-33637 through the Cornell Materials Science Center, Report # 2256.

I. INTRODUCTION

A. Historical background

Since approximately 1950 an increasing portion of experimental solid state physics research has been concerned with studying randomly spaced defects or irregularities in crystals. This trend might appear to be a rather belated recognition that most of our environment and most of the materials we come into contact with have a random structure. In fact the theoretical understanding of random systems has been very slow in developing. Where technology has needed new or improved materials it has had to proceed by mainly empirical or "cut and try" methods. Elliott, Krumhansl, and Leath (1974) have reviewed some of the background leading up to the recent growth in theoretical understanding. The major developments they list are the discovery of sophisticated perturbation techniques in many-body theory, particularly the use of Green's functions, and the development of computers powerful enough to calculate results for reasonably large models. Since these developments date from about 1950, it is apparent that the interplay between theory and experiment has been important in the growth of this field of disordered solids.

A count of the articles contained in various bibliographies shows that if we restrict our attention to optical studies of the vibrational properties of disordered solids, the publication rate has grown from about one paper per year in 1950 to about one hundred per year in 1974. Papers dealing with the related theory show about the same numbers; both groups exhibit a doubling time of four years. These numbers show the need for a broad review to survey the field. In no sense does this review close the field or present experiments which answer all questions one might ask about optical properties. This area of experimental research will remain active for many years. The authors hope, however, that this review will direct attention to areas that need deeper study.

The present paper examines and reviews our knowledge of the lattice vibrations associated with defects. Our viewpoint is that the lattice vibrations of perfect, pure crystals are reasonably well understood. In many, though not all cases, the introduction of defects can be viewed as causing shifts in the vibrational states of the pure crystal. This viewpoint is also used to some extent even when the crystal is one hundred percent defective, as, for example, in amorphous solids. The new vibrational states, whether they are in fact only slightly perturbed crystalline states or are completely new modes, serve as tools for examining both the defects and the host lattice. A wide range of defects have been studied and we use the broad term *disordered solid* in an attempt to cover the many situations which are encountered in practice.

The investigation of the electronic properties of defects in crystals has actually been an active field of research since Goldstein's original work on color centers in alkali halide crystals in 1896. One should note that even before this, man has shown strong interest in the optical properties of defects as evidenced by the high esteem he has had for gems. Colored jewels and "star" gems result from optical effects associated with localized defects.

In the nineteen twenties when the infrared region of the electromagnetic spectrum became readily accessible, the internal vibrational modes of molecular impurities in alkali halide crystals was investigated by Maslakowez (1928) and the first observation of defect-induced lattice absorption was obtained in type 1 diamond by Robertson *et al.* (1934). The correct interpretation of these spectra had to wait until the 1950s for the reasons mentioned above. The alkali halide crystal has proven to be a well-suited medium in which to study the vibrational properties of crystal defects because of its exceedingly simple electronic and lattice structure. In addition to this basic fact there are new impetuses to encourage an even better understanding of these materials. In recent years it has become possible to unidirectionally solidify combinations of metal halides under controlled growth conditions (Batt *et al.*, 1969). The most interesting optical properties of these eutectics stem from microstructures which contain periodic arrays of one component embedded in the other (Sievers, 1973). An interpretation of the vibrational properties of such superlattice structures requires a detailed knowledge of the defect-activated vibrations in each component in order to identify the vibrations associated with the interfaces.

Because of the need for windows and lenses for high-power CO_2 lasers, there has been a great deal of interest in the absorption processes of infrared radiation in alkali halides in the 10 μ wavelength region (Sparks and Sham, 1973; Deutsch, 1973). At the present time in the most pure material (KCl), bulk impurities and surface impurities provide equal contributions to the absorption coefficient at 10.6 μ. The relative contribution of different impurities to this absorption has not yet been determined. Since each alkali halide presents its own chemical purification problems this lack of information about specific impurity-induced absorption processes presents a serious drawback to any generalization of the KCl success to other window materials.

B. Localized and resonant vibrational modes

The effect of certain kinds of defect or disorder on the normal mode vibrational frequencies of a system of particles was first studied theoretically in the 1890s by Lord Rayleigh. One principal result of interest here was the finding that under the right circumstances a vibrational mode could split away from the band of modes and exist above the maximum frequency of the unperturbed system. This type of special mode was first observed experimentally by Schäfer in 1958. Figure 1 shows the mode due to a hydrogen ion impurity in potassium chloride. In addition to having a narrow width and high frequency this mode is "localized," that is, its eigenvector does not have a sinusoidal or wavelike dependence in space but is strongly peaked at the impurity atom and falls off rapidly one or two lattice sites away. Theoretical consideration of this type of defect situation shows that the unique property of localization is concomitant with the fact that the mode frequency is well away

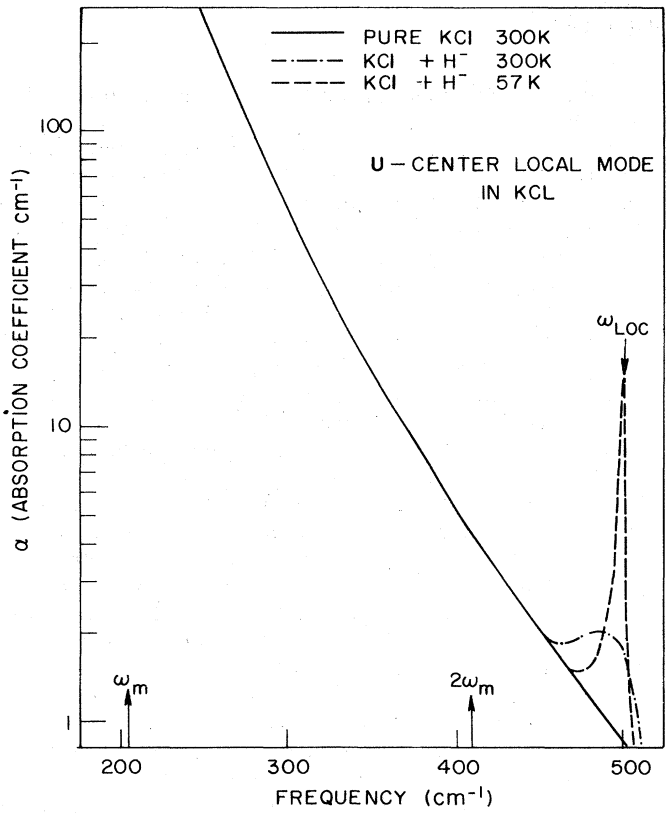

FIG. 1. Absorption spectrum of KCl at frequencies above the maximum phonon frequency ω_m. The addition of H^- (U centers) causes a sharp localized mode in the region of very low absorption near 500 cm^{-1}. ω_{loc} peak taken from Schäfer (1960).

from the band of normal frequencies of the host crystal. This result has led to the terminology *localized mode*. Since Schäfer's experimental observation, many kinds of localized modes associated with defects have been observed. These now include low-frequency localized modes which lie within the band of normal frequencies. Such modes were a somewhat unexpected development and they still cause difficulty in visualization for the beginner. They are called resonant modes. Resonant modes have recently been invoked in astrophysics. The temperature of interstellar grains is controlled by their emissivity in the far infrared. The presence of low-frequency resonant modes would increase the emissivity and control the formation of a frozen hydrogen mantle and the processes of molecule formation and ultimately the gravitational collapse (Aannestad and Purcell, 1973).

Localized modes of both the high-frequency type and the resonant type have an intrinsic interest, but in addition hold special promise as probes of the impurity atom or defect and its nearest-neighbor surroundings. Some localized mode studies have been used as a diagnostic method to identify the impurity, both its type and actual location in the lattice. As the concentration of impurities increases, new features appear which begin to bridge the gap between the case of the isolated impurity in a crystal and the case of disordered solids and alloys. A major part of this review deals with such studies of localized modes. Studies of nonlocalized modes, and of modes in highly disordered systems where the degree of localization has not been established are also reviewed. The modes in disordered solids are important to our basic understanding of these solids; however, the use of these modes as probes of the structure is still in its infancy.

C. Scope of review

It is clear that, in spite of the large body of work reviewed here, much more remains to be done in the field of defect vibrational modes. One viewpoint is that the method couples spectroscopic techniques to the dynamics of a solid at the microscopic level. While many cases of single defects have been delineated, the study of interacting pairs of defects, of more extended defect clusters, and of amorphous solids is just beginning. The present paper reviews experimental results up to early 1975. It is a review of experimental work and is written principally for experimentalists. In spite of this approach a sizeable fraction of the paper deals with theoretical matters. There is a chapter on explicit solutions of the linear chain vibration problem and a short chapter on Green's function methods. The reason for this is inherent in the subject itself. A full appreciation or even a full description of the results of an experimental study of the disordered solid depends on using theory beyond that normally employed for the evaluation of bulk properties of crystals. For example, the special property of localization is not apparent directly in a spectrum such as Fig. 1. The intuitive (and correct) argument can be made that a high-frequency mode such as that observed in Fig. 1, if it involves the impurity at all, must be localized, since there are no lattice modes up at this frequency to carry the energy away from the impurity. Such an argument is not quantitative, however, and detailed models are necessary to appreciate the localization of the mode and to allow prediction of the behavior as either the host crystal or the impurity is changed, as pressure is applied, or temperature or some other parameter is varied. The models presented in the theoretical sections are elementary, in the sense that they will provide an intuitive understanding without introducing excessive mathematics. They do not represent the state of the art in defect theory. They will allow the appreciation of more practical and detailed models which are used in the primary literature. These more detailed models will be referred to where appropriate in the various experimental sections.

Many short reviews of localized vibrations have appeared in the past ten years, principally in conference proceedings. These reviews will be referred to in subsequent sections. A major experimental review has been written by R. Newman (1969). Newman's review should be regarded as complementary to the present paper. He emphasizes the local anharmonic oscillator model of the impurity with a full treatment using group theory applied to the impurity and its nearest neighbors. He treats in detail hydrogen and deuterium impurities in the alkaline earth fluorides and impurities in semiconductors, most especially silicon and germanium. The present paper deals less fully with these topics since the review by Newman is quite complete and up to

II. MODEL CALCULATIONS

A. The one-dimensional diatomic chain with perfect regularity

In this section we calculate in detail the vibrational modes of a linear chain. Figure 2 shows the chain to be considered. We take all force constants k to be identical, but use alternating masses M and m. Using cyclic boundary conditions and taking the total number of atoms N to be even, the equations of motion are

$$\begin{aligned} M\ddot{x}_1 &= k(x_2 - x_1) + k(x_N - x_1) + F_1, \\ m\ddot{x}_2 &= k(x_3 - x_2) + k(x_1 - x_2) + F_2, \\ M\ddot{x}_3 &= k(x_4 - x_2) + k(x_2 - x_3) + F_2, \\ &\vdots \\ m\ddot{x}_N &= k(x_1 - x_N) + k(x_{N-1} - x_N) + F_N. \end{aligned} \tag{2.1}$$

Here F_j is an external force applied to the jth atom. While it is difficult in practice to apply a force such as F_1 to one particular atom, it is mathematically convenient to include the F_j for later discussions of response functions for the chain.

The above equation can be written in a very compact form using matrix notation. In this notation the lattice vibration problem can be written:

$$\mathsf{M}\ddot{\vec{x}} = -\mathsf{k}\vec{x} + \vec{F}. \tag{2.2}$$

For the diatomic chain shown in Fig. 2 the mass and force constant matrices are:

$$\mathsf{M} = \begin{bmatrix} M & 0 & 0 & & \\ 0 & m & 0 & \cdots & \\ 0 & 0 & M & & \\ \cdot & & & & \\ \cdot & & & & \\ \cdot & & & & \end{bmatrix},$$

$$\mathsf{k} = \begin{bmatrix} 2k & -k & 0 & 0 & \cdots & 0 & -k \\ -k & 2k & -k & 0 & & & \\ 0 & -k & 2k & -k & 0 & \cdots & 0 \\ 0 & 0 & -k & 2k & -k & & \\ \cdot & & & & & & \\ \cdot & & & & & & \\ -k & & & & & & \end{bmatrix}.$$

The mass matrix is of diagonal form and the force constant matrix has entries on the principal diagonal as well as on diagonals one above and one below the principal diagonal. Obviously, second-neighbor forces would put entries on the diagonals two above and two below, etc. The displacements and forces are simply column vectors with the jth entry describing the jth atom. Assuming simple harmonic time dependence for each variable, we now change notation and use x_j and F_j to describe the time-independent amplitudes; i.e., displacement of j atom $= x_j \cos(\omega t + \Phi)$, etc. The equations of motion become

$$-\omega^2 \mathsf{M}\vec{x} = -\mathsf{k}\vec{x} + \vec{F}. \tag{2.3}$$

In this section we use computer solutions of Eq. (2.3). Analytic solutions are easily obtained, however, for the pure chain by exploiting the periodicity and forming solutions of the type

$$x_n \sim \exp(iqna/2). \tag{2.4}$$

Here $na/2$ fixes the position along the chain, and q is the wave vector which is to be determined. Kittel (1968) has given examples of this type of solution for the monatomic and diatomic chains with no defects. Dean (1967) and Genzel (1969) have extended this type of solution to chains with defects.

Returning to (2.3), we now set $\vec{F} = \vec{0}$[1] and define the matrix

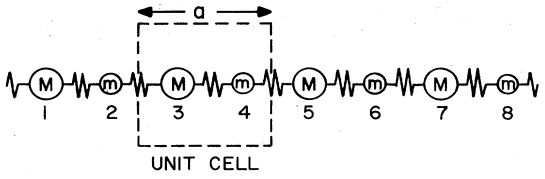

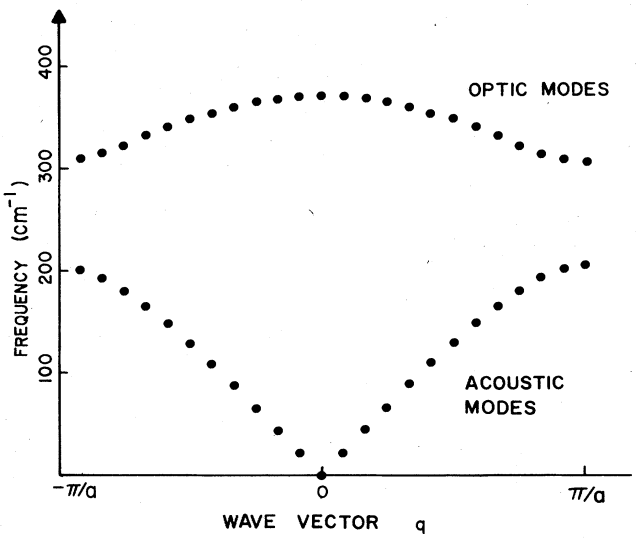

FIG. 2. Diatomic linear chain with nearest-neighbor force constants. The dispersion curves are shown in the lower part of the figure. These modes arise from a 48-atom chain with periodic boundary conditions (see Table II.1 under GaP for parameters). The 48 modes fall into acoustic and optic bands separated by a frequency gap. Here 44 of the modes occur as doubly degenerate pairs which are plotted here as left and right ($+q$ and $-q$) traveling waves.

[1] i.e., we solve for the free vibrations.

date in these matters.

The present review emphasizes the optical studies of defects simply because other techniques have not yielded nearly so much information. Neutron scattering does not yet possess the sensitivity to deal with very low concentrations of defects and also does not possess the resolution to study fine structure. Electron tunneling and luminescence studies have also had only limited usefulness in this area. All of these methods will be referred to where appropriate in succeeding sections in the cases where they have shed light on certain systems. The reader is assumed to have some knowledge of the optical properties of solids, including the concepts of oscillator strength, effective charge, and classical oscillator representation of modes. Such ubiquitous solid state physics concepts as phonon dispersion curves and the Debye model of a solid are also assumed. An outline of the paper may be seen in the list of contents above. In many cases the division into sections may appear arbitrary, which it is from the point of view of the theoretical development. However, the special crystal preparation requirements and methods of taking spectra dictate such a division of topics for the experimentalist. In Sec. II model linear chain calculations are used to illustrate in detail the local mode, both where it occurs well above all modes of the host lattice and where it occurs in a gap in the host crystal spectrum. The resonant mode, which is much more difficult for the beginner to grasp, is also treated in detail in the context of the linear chain model. Section III presents an introduction to Green's functions at a level sufficient to develop the basic equation which determines the new vibrational frequency when the mass of an atom is changed in a crystal (the mass defect or isotope model). The next five sections (IV–VIII) deal with localized vibrations in semiconductors, ionic crystals, van der Waals and special organic crystals. The last two sections deal with disorder of a different sort. Here, rather than having point imperfections, the entire crystal is involved in the disorder. Section IX deals with a crystal whose spacing is still more or less regular but in which the atomic species occupying each lattice site varies in a random way. The final section deals with the somewhat complementary situation of vibrations in systems (no longer called crystals) where the atomic spacing is random though the atomic composition may be fixed. The variable spacing can lead to some ion positions being occupied but unstable. This allows the possibility of low-frequency modes best described as tunneling transitions.

TABLE II.1. Standard data for linear chains.

Chain parameter	GaP	GaAs
M cation mass (amu)	70	70
m anion mass (amu)	31	75
Z cation charge (e)	2	2
z anion charge (e)	−2	−2
k force constant (dyne/cm)	0.87×10^5	0.87×10^5
a cell length (Å)	3.42	3.42
V cell volume (Å^3)	40.0	40.0
Highest frequency [a] optic mode (cm^{-1})	370	285
Gap in mode spectrum (cm^{-1})	205–308	198–205
Dielectric parameters for a solid composed of chains		
ϵ_∞	9.0	9.0
ω_{TO} [b] (cm^{-1})	370	285
ω_{LO} [b] (cm^{-1})	402.8	310.3
S mode strength	1.667	1.667
$\epsilon_0=\epsilon_\infty+S$	10.667	10.667

[a] We use wave number frequency units $\bar\nu=\omega/2\pi c$ where c is the velocity of light. 1 cm^{-1} $=3\times10^{10}$ Hz $=0.477\times10^{10}$ rad/sec.

[b] Real GaP (GaAs) has $\omega_{TO}=366$ (268) and $\omega_{LO}=402.8$ (291) cm^{-1} at room temperature.

$$\mathsf{M}^{-1/2}=\begin{bmatrix} M^{-1/2} & 0 & 0 & \cdot & \cdot \\ 0 & m^{-1/2} & 0 & & \\ 0 & 0 & M^{-1/2} & & \\ \cdot & \cdot & \cdot & & \end{bmatrix}.$$

Multiplying $\mathsf{M}^{-1/2}$ into (2.3) yields

$$-\omega^2\vec{u}=-M^{-1/2}\mathsf{k}\mathsf{M}^{-1/2}\vec{u}\equiv-\mathsf{D}\vec{u}, \tag{2.5}$$

where

$$\vec{u}=\mathsf{M}^{+1/2}\vec{x}. \tag{2.6}$$

Equation (2.5) shows that the problem of solving for u (or x) is simply a diagonalization problem

$$(\mathsf{D}-\omega^2\mathsf{I})\vec{u}=0, \tag{2.7}$$

where the eigenvalues are the allowed values of ω^2, and the eigenvectors are the displacements $\vec{u}$. The displacements $\vec{u}$ may be transformed to actual atom motions by making use of (2.6). Our procedure is to construct the matrix D from k, M, m and to insert D into a matrix diagonalization routine in a digital computer.

To illustrate the form of typical solutions, we have used the parameters given in Table II.1. The solutions are shown in the bottom part of Fig. 2 and several succeeding figures for the case of 48 atoms.

From Fig. 2 we note that there are 48 modes. The modes are grouped into two bands; 24 modes in the range 0 to 205[2] cm^{-1}, and 24 modes in the range 308 to 370[2] cm^{-1}. These groupings are called the acoustic and optic bands, respectively. Except for four special modes (including the highest and lowest frequency), the modes occur in doubly degenerate pairs. Dean (1967) has given a discussion of the effect of different boundary conditions which can lift the degeneracy.

The eigenvectors of each mode in this pure chain are found to have a sinusoidal spatial dependence, as was anticipated in the analytic approach [Eq. (2.4)], allowing a unique wave vector q to be associated with each mode frequency. In Fig. 2 we have plotted the 48 mode frequencies against their wave vectors in a dispersion plot. For the model used here we may choose standing waves, or left and right traveling waves for the solutions (Dean, 1967). Figure 2 displays the modes as traveling waves with each pair of degenerate solutions separated into a $+q$ and $-q$ mode and plotted separately. Figure 3 shows some of the mode eigenvectors. The displacement vector for each atom is drawn perpendicular to the chain, for clarity in Fig. 3 though the real displacements are along the chain for this model. From Fig. 3 we see that four modes stand out as having very simple eigenvectors. At $\omega=0$ all atoms move together. At the top of the acoustic band $q=\pi/a$ and only the heavy atoms move. At the bottom of the optic band $q=\pi/a$ with only the light atoms moving, and finally the highest-frequency mode has $q=0$ and the ion pairs move against each other with identical displacements in each cell.

Since we lose the sinusoidal spatial dependence [Eq. (2.4)] in many cases for the defect chain, it is desirable to display the modes of Fig. 2 in a q-independent way. This may be done using the density of states. The total number of modes is

$$N=\int_0^\infty g(\omega)\,d\omega=\int_0^\infty G(\omega^2)\,d\omega^2, \tag{2.8}$$

[2] Throughout this review we use the spectroscopists frequency units cm^{-1} (wave numbers). These units are sometimes given the symbol ν and the conversion is $\nu=\omega/2\pi c$. In many places, however, we lapse into the common practice of writing ω but giving wave number units.

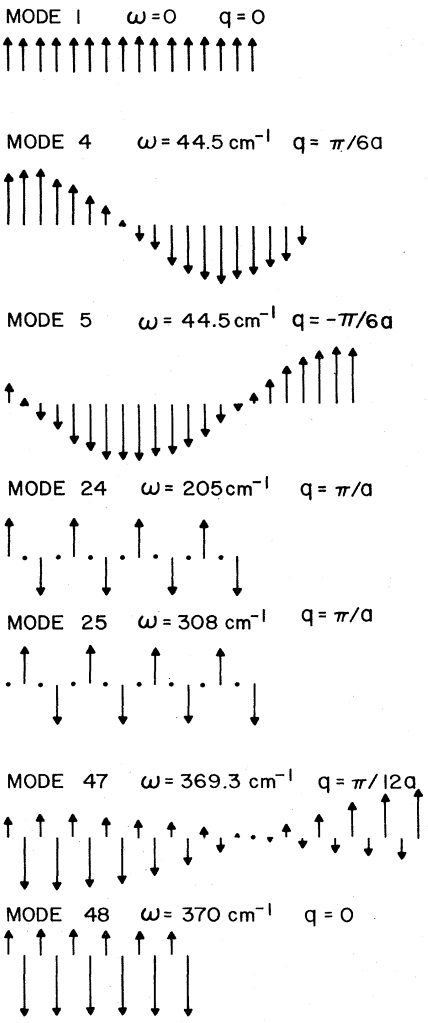

FIG. 3. Mode eigenvectors for the 48-atom chain described in the preceding figure. Position along the chain is plotted horizontally and ion displacement vertically. Modes 24 and 25 occur on either side of the gap between the acoustic and optic bands.

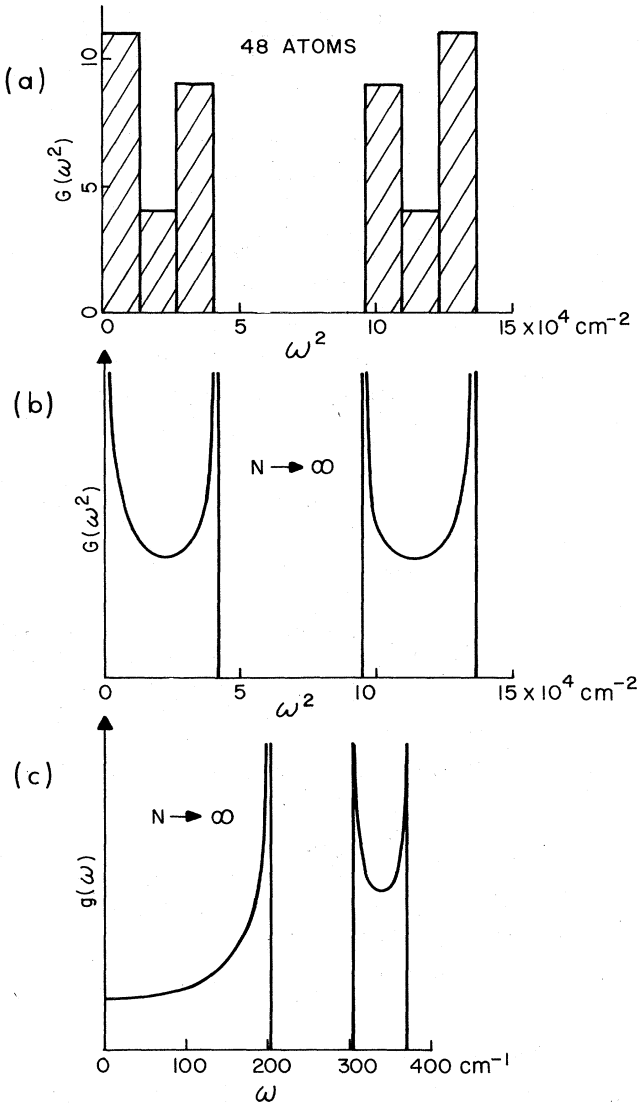

FIG. 4. (a) Density of states histogram for the $N=48$ atom chain of the preceding figures. In part (b) the analytic result for the same chain as N approaches infinity is shown. Part (c) shows the result of part (b) plotted in the linear frequency space.

where $g(\omega)d\omega$ is the total number of modes in the range $d\omega$, i.e., $g(\omega)$ is the density of states or frequency distribution function. In writing (2.8) we have gone over to the continuous variable ω. This is appropriate as $N\to\infty$ causing the modes to become infinitely closely spaced. Here $G(\omega^2)$ is often particularly useful, being the distribution of squared frequencies. Both $G(\omega^2)$ and $g(\omega)$ can be derived analytically for the perfect linear chain (Maradudin *et al.*, 1963; Dean, 1967). The problem with the finite chain is that $G(\omega^2)$ and $g(\omega)$ are really a series of delta function peaks. To get a useful picture of G which avoids the singular peaks we can use a histogram method. Figure 4 shows the histogram for the 48-atom diatomic chain. The histogram interval must be quite coarse for only 48 modes; however, it clearly shows the acoustic and optic bands (of Fig. 2), as well as the gap between them where there are no modes. The histogram also shows a peaking up of states at the edge of each band. In the bottom part of the figure sketches of $G(\omega^2)$ and $g(\omega)$ are shown in the limit $N\to\infty$ for the diatomic chain under discussion [see Dean (1967) for explicit formulas]. The analytic forms of the distribution function of Fig. 4 clearly show infinities or critical points at the band edges. Maradudin *et al.* (1963) and Bilz (1969) have given extensive discussions of critical points. Van Hove (1953) was the earliest worker to clarify the significance of these singularities in $G(\omega^2)$ or its derivatives, as well as to show they must always occur for a periodic lattice. We do not discuss critical points further here but merely note two of the ways they can be important in vibration spectra. First, the addition of an impurity can cause all modes of a crystal to become absorbing. The spectrum of an impure crystal may show a (possibly weighted) image of $g(\omega)$ and its critical points in absorption or in Raman scattering.

Second, the addition of a finite concentration of impurities modifies all modes and may remove sharp features such as critical points. This effect is well known in electron energy band structure where random impurities can remove a sharply defined band gap by causing tailing of states into the energy gap region, which is forbidden for the perfect crystal. Examples of both these types of behavior will be given below.

B. The TO-LO splitting and optical spectra

1. Infrared absorption

In this section we discuss the coupling of the optical probe to the chain model. Infrared absorption is considered first. Since power absorption is a bulk (volume) effect, some consideration must be given to representing a real three-dimensional solid. Many identical linear chains can be imagined to represent a solid with the sodium chloride structure shown in Fig. 5. This is, in fact, a poor model of the solid in certain respects since it is unstable (i.e., has zero restoring force) if one chain is moved parallel to its neighbors. This feature arises because we have used only stretching force constants. Bending force constants can be added (Barker, 1970); however, this takes us too far afield into three-dimensional modes and eigenvectors. Since the instabilities mentioned above do not occur in the modes responsible for optical absorption, we continue to use the chain model extended as shown in Fig. 5. The results obtained are valid for optical absorption and have the correct form for real crystals.

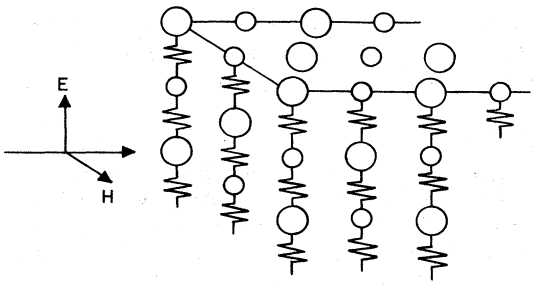

$$\epsilon = \epsilon_\infty + \frac{S\,\omega_{TO}^2}{\omega_{TO}^2 - \omega^2} = \frac{\epsilon_\infty(\omega_{LO}^2 - \omega^2)}{\omega_{TO}^2 - \omega^2}$$

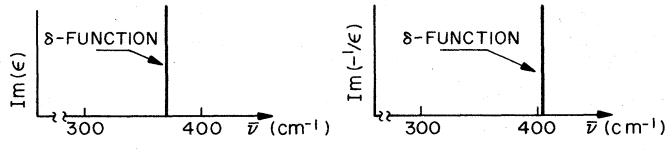

FIG. 5. A three-dimensional diatomic solid composed of chains. The chains are taken to lie along the direction of the electric vector of the infrared beam. Below are shown the dielectric function and the transverse and longitudinal mode spectra when the atoms are taken to be charged. The spectra are drawn for the GaP model parameters in Table II.1.

If a transverse-plane electromagnetic wave is applied to the crystal (Fig. 5), it can couple to modes which cause a dipole moment. From Fig. 3 we note that if the two kinds of atoms are oppositely charged, the $q=0$ optic mode at 370 cm^{-1} is the only mode which possesses such moments simultaneously in many unit cells. The optical absorption resulting from the coupling to the dipole moment is conveniently described by the dielectric function of the crystal. The reader is referred to standard texts on optical properties of solids (Born and Huang, 1954; Moss, 1959).

For the present linear diatomic chain, we find

$$\epsilon = S\omega_{TO}^2/(\omega_{TO}^2 - \omega^2), \tag{2.9}$$

where

$$S = 4\pi Z^2/(a^3\bar{m}\omega_{TO}^2) \tag{2.10}$$

is the dimensionless strength,[3]

$$\omega_{TO} = (2k/\bar{m})^{1/2} \tag{2.11}$$

is the transverse optic mode frequency (370 cm^{-1} in our example), and

$$\bar{m} = Mm/(M+m) \tag{2.12}$$

is the reduced mass of the ions.

The dielectric function has a pole at ω_{TO}, the optic mode frequency. As is usual in problems of frequency response functions, we must include real and imaginary parts, which we write

$$\epsilon = \epsilon' + i\epsilon'',$$

where ϵ' is understood to be the principal valued part of (2.9), and

$$\epsilon'' = \mathrm{Im}(\epsilon) = \pi/2\ \omega_{TO} S[\delta(\omega - \omega_{TO}) - \delta(\omega + \omega_{TO})]$$

describes the absorptive part of ϵ. Table II.2 relates ϵ to the index of refraction and to the power absorption coefficient α.

Since no damping has been put into the model, the mode spectrum $\mathrm{Im}(\epsilon)$ shows an absorptive line of zero width (a delta function) at $\pm\omega_{TO}$. The lower part of Fig. 5 illustrates the mode structure. In succeeding sections, the mode spectra ($\mathrm{Im}\epsilon$) are plotted for linear chains with defects. For defect chains, ϵ contains a sum of delta functions occurring at many frequencies in addition to ω_{TO}. We wish to study both the mode frequency and mode strength of these defect modes for several kinds of defect chains.

To complete the description of the infrared absorption some account must be taken of the polarizable electrons which surround each atom in a solid. This may be accomplished by adding a real, frequency-independent

[3] The present approach avoids explicit inclusion of local field effects which would cause factors like $(\epsilon_\infty+2)/3$ to appear. This in no way limits the usefulness of the model. The reader interested in pursuing these matters is referred to Lax and Nelson (1971).

TABLE II.2. Optical parameters, absorption strength, and Raman intensity.

Index of refraction	$n+ik$
Dielectric constant	$\epsilon=\epsilon'+i\epsilon''$ [$=(n+ik)^2$ in an isotropic material]
Power absorption coefficient	$\alpha=4\pi k/\lambda$ [λ infrared wavelength in cm]
Dimensionless mode strength [a]	$S=\frac{2}{\pi}\int_0^\infty \frac{\epsilon''d\omega}{\omega}=\frac{2c}{\pi}\int_0^\infty \frac{n\,\alpha d\omega}{\omega^2}$
For a weak absorption band at frequency ν_0 cm^{-1} [a]	$\alpha\simeq 2\pi\nu\epsilon''/n$; $S\simeq\frac{n}{\pi^2\nu_0^2}\int_{\text{band}}\alpha d\nu$
Absorption strength for N one-oscillator defects per cubic centimeter [b]	$\int_{\text{band}}\alpha d\nu=\frac{\pi N(ze)^2}{c^2\sqrt{\epsilon'}\,m}\left(\frac{\epsilon'+2}{3}\right)^2$
Absorption strength per defect (For $\epsilon'=1, m=16$ amu, $z=1$)	$\sigma_{\text{loc}}=\frac{1}{N}\int_{\text{band}}\alpha d\nu=0.30\times10^{-16}$ cm
Raman scattering intensity for Stoke's scattering with frequency shift ω	$I(\omega)\propto[n(\omega)+1]\,\text{Im}(\epsilon)$ for transverse modes; $I(\omega)\propto[n(\omega)+1]\,\text{Im}(-1/\epsilon)$ for longitudinal modes

[a] In these formulas ω and ν represent frequency in units of rad per sec and cm^{-1}, respectively.
[b] This formula assumes a fully localized charge of ze on the oscillator and the Lorentz local-field correction (given by the right-hand factor) appropriate to a cubic or random array of oscillators. The range of integration is over the defect band only.
[c] The Stoke's scattered light will emerge from the crystal with frequency $\omega_s=\omega_l-\omega$, where ω_l is the laser or pump frequency. These formulae depend on simplifying assumptions which are described by Barker and Loudon (1972). The Stoke's factor $n(\omega)+1$ contains the quantum mechanical thermal factor $n(\omega)=[\exp(\hbar\omega/k_BT)-1]^{-1}$.

term[4] ϵ_∞ to (2.9). Once ϵ_∞ has been added to the dielectric function, the solid shown in Fig. 5 has a second optical mode described by a peak in the function $\text{Im}(-1/\epsilon)$. This resonance is also shown at the bottom of Fig. 5 for $\epsilon_\infty=9$. This second mode corresponds to longitudinal plane waves in the crystal with E along the chain axis. The new frequency, designated ω_{LO} (for longitudinal optic mode), is higher than 370 cm^{-1} because of an electric stiffening effect. The electrostatic forces which the ions exert on each other add to the original spring constants when the ions are moved in a longitudinal-plane-wave pattern. Note that ω_{LO} does not exist or have meaning for a single linear chain. Our approach is to use the linear chain model to calculate ω_{TO}. Charges are then assumed for the ions and ϵ is constructed for the model solid using (2.9) with ϵ_∞ added.

To summarize the infrared effects, $\epsilon(\omega)$ may be inserted into standard formulas to predict transmission and reflection spectra (Moss, 1959). Table II.2 gives the interrelation of ϵ, the index of refraction, and the absorption coefficient α. The infrared absorption spectra of very thin crystals in special orientation can show peaks at ω_{TO} and ω_{LO}, allowing assignments of these modes. When additional impurity or defect resonances are present, infrared transmission is usually the best method of detecting the defect modes which appear as additional weak absorption peaks. The dielectric function contains all the information for determining the absorption. Its form in a defect crystal is discussed in succeeding sections.

[4] ϵ_∞ will be frequency dependent and have a significant imaginary part at optical frequencies where ω begins to approach the energy of electronic transitions or the band gap energy in a semiconductor. In the infrared region near ω_{TO} it is constant for most insulators and semiconductors.

2. Raman scattering

For the chain model illustrated in Fig. 2 to exhibit Raman scattering by the vibration modes, two new ingredients are needed. First, polarizable electrons must be included whose polarizability depends on the ion motions. Second, the center of symmetry, which exists at each atom in the chain model of Fig. 2 must be removed. Figure 6 shows a chain model which has the center of symmetry removed from each ion. This model may have two different force constants, k_1 and k_2, one for the short bond and one for the long bond. The diatomic chain now can serve as a model of a zinc blende structure crystal, such as gallium phosphide, which has no inversion center. If we set the charges equal to zero and the masses equal, it serves as a model of silicon, germanium, or diamond. The Raman effect arises from the lattice motion changing (i.e., modulating) the electronic polarizability and hence the optical index of refraction. This modulation produces sidebands at frequencies $\omega_l+\omega_{TO}$ and $\omega_l-\omega_{TO}$ when a laser beam of frequency ω_l passes through the medium (for a review see Barker and Loudon, 1972). In a three-dimensional zinc blende crystal (charges not equal to zero) there are two Raman-active modes, one at ω_{TO} and one at ω_{LO} because of the TO–LO splitting in these crystals. The Raman spectrum shows both these sidebands. A fairly simple model shows that the Raman spectrum depends essentially on the spectra $\text{Im}(\epsilon)$ and $\text{Im}(-1/\epsilon)$ shown in Fig. 5

(Barker and Loudon, 1972). The Raman spectrum contains, therefore, information on the normal modes of the crystal. In a crystal containing defects the Raman spectrum also contains peaks due to the defect vibrations. Because of the special symmetry requirements for Raman scattering, certain defect modes may show up only in Raman scattering, so that the Raman and infrared spectra for a defect crystal often contain complementary information. Table II.3 lists the optic modes and their activity for some common crystals. Note that there can be optic modes which are neither Raman nor infrared active in some crystal structures.

C. The case of one substitutional defect; the localized and resonant modes

1. The localized mode

We now turn our attention to the linear chain shown in Fig. 7. First, the single mass defect is introduced by replacing the light atom m by a new atom of mass m' bound to its neighbors by the same force constant as before. This is called an isotopic substitution. Some real isotope experiments are possible, e.g., LiH with some deuterium added in place of H. In practice many nonisotopic substitutions, e.g., P_{As} in GaAs,[5] Si_{Ge} in Ge, etc., are analyzed using the isotopic model. The justification is that the model is much simpler (there are not adjustable force constants to parametrize) and that it works fairly well in many cases. For $m' < m$, a new mode with frequency greater than 370 cm^{-1} appears when the linear chain equations (2.1) are solved. This mode is localized spatially. Its eigenvector shows the impurity ion moving with large amplitude, the neighbors of the impurity moving with considerably less amplitude, etc. Thus the eigenvector does *not* have simple harmonic spatial dependence as described by (2.4). Figure 7 shows some of the 48 eigenvectors for a chain containing one defect with $m' = 20$. Mode 1 is identical with mode 1 of the unperturbed chain (Fig. 2). Modes 2 and 3, and 4 and 5, etc. are no longer degenerate. In fact all the double degeneracies of the unperturbed chain are now lifted. The presence of the one impurity (m' at m) leaves only a single reflection plane at m' so that there must be even and odd (symmetric and antisymmetric) solutions. From Fig. 7 we see that for the even[6] solutions m' has no motion so that the mode has exactly the same frequency and wavelength as before (Fig. 3). The odd[6] solution (mode 5) now has a slightly higher frequency of 44.7 cm^{-1} and a slightly shorter wavelength. This mode is no longer pure sinusoidal right at m', as is discussed below. Mode 24 was an even-symmetry mode of the pure chain so it remains unperturbed with the impurity remaining stationary and not participating in the dynamics of the motion in any way. Note that the bonds attached to m' *do* participate in all modes. Thus for a force constant change, all modes (not just odd-symmetry modes) would have changed frequencies and

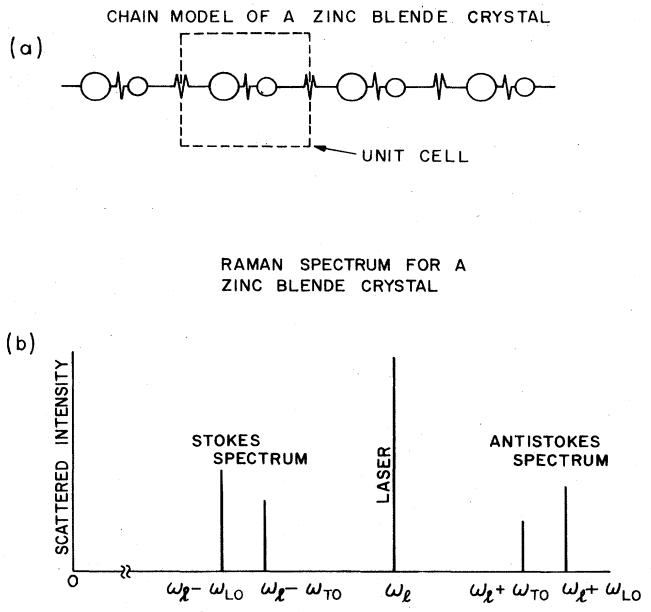

FIG. 6. (a) Diatomic chain with unequal spacing which leads to piezoelectricity and the Raman effect. (b) Because of the polarizability being modulated by TO and LO optic modes a laser beam of frequency ω_l is modulated and acquires side bands on passing through the crystal as shown.

eigenvectors for the defect chain. Mode 47 is the new long-wavelength optic mode ω_{TO}. It has low amplitude at the impurity but still has positive ions moving to the right and negative ions moving to the left in every unit cell. This mode still has the largest dipole moment. For an N-atom chain, as $N \to \infty$, this mode would asymptotically approach the same dipole moment and frequency as the perfect chain. Finally we come to the unique defect mode—the 48th mode at 416.4 cm^{-1}. This is the localized mode. It has a nonsinusoidal eigenvector with amplitude which falls towards zero far from m'. All other mode eigenvectors remain nonzero far from m'. Figure 8 shows schematically the density of states spectrum $G(\omega^2)$ for an N-atom chain with one isotopic defect $m' < m$. The local mode appears as a delta function well above the optic band of modes.

There are several points worth emphasizing regarding the local mode. First, one might question how the nonsinusoidal mode pattern arises. A rough argument which is often given is that the light particle m' wants to vibrate at a high frequency ω_{loc}. This frequency is in the stop band (forbidden band) of frequencies above the optic band so that sinusoidal (i.e., bandlike) motions of the neighbors of m' are not possible at frequency ω_{loc}. A more mathematical approach is to try solutions (2.4) $x_n \sim \exp(iqna/2)$ for the defect chain. One finds that the secular equation for the chain cannot be satisfied unless q is complex, indicating a damped wave solution whose amplitude approaches zero for large x (Kittel, 1966). A second property of the local mode is that it becomes more localized as $m' \to 0$. Figure 9 shows the local mode displacement pattern for $m' = 25$, 20, then 5 amu replacing the $m = 31$ amu atom in our linear chain. We introduce a quantitative measure of localization by spe-

[5]We use the subscript notation B_A to denote a B atom occupying an A site. B_i means a B atom at an interstitial site.

[6]For the reader puzzled by these even/odd designations it must be recalled that the vibrations are along the chain but are drawn perpendicular to the chain axis for clarity.

TABLE II.3. Zone center optic mode frequencies of some crystals with simple structures.

The Diamond Structure [O_h^7 $Fd3m$]

$\omega_{TO} = \omega_{LO} = \omega_R$ degenerate and Raman active only

	ω_R	References[b]
C	1332 cm^{-1}	1
Si	520	2
Ge	301	3

The Zincblende Structure [T_d^2 $F\bar{4}3m$]

Modes infrared and Raman active

	ω_{TO}	ω_{LO}	References[b]
AlSb	318	345	4
CdTe	140	167	5
GaAs	269	292	6
GaP	366	402	7
GaSb	225	236	8
InAs	219	243	4
InP	307	351	4
InSb	174	183	9
SiC	794	962	10
ZnS	271	352	11
ZnSe	209	250	4
ZnTe	190	210	4

The Wurtzite Structure [C_{6v}^4 $P63mc$]

4 Modes ir and R active, 2 modes R active, 2 modes inactive

	$E \parallel c$		$E \perp c$				
	ω_{TO}	ω_{LO}	ω_{TO}	ω_{LO}	ω_R	ω_R	References[b]
GaN	533	744	560	746	145	568	12, 13
CdS	228	305	235	305	44	252	14
CdSe	166	211	172	210	a	a	15
SiC	790	962	794	962	a	a	16
ZnO	380	574	407	583	101	437	17

The Rocksalt Structure [O_h^5 $Fm3m$]

	ω_{TO}	ω_{LO}	References[b]
LiH	590	1120	18
LiF	307	662	18
LiCl	191	398	18
LiBr	159	325	18
LiI	144	a	19
NaF	239	414	18
NaCl	164	264	18
NaBr	134	209	18
NaI	117	181	19
KF	192	330	19
KCl	142	214	18
KBr	113	165	18
KI	101	139	18
RbF	156	286	18
RbCl	116	173	18
RbBr	88	127	18
RbI	75	103	18
AgCl	106	196	20
AgBr	79	138	20
AgI	108	a	20
MgO	403	716	19
CaO	295	577	21
SrO	227	487	21
BaO	132	425	22
CoO	349	546	23
NiO	401	580	23
PbS	71	212	24

TABLE II.3. Zone center optic mode frequencies of some crystals with simple structures. *(Continued)*.

The CsCl Structure [O_h^1 $Pm3m$]

	ω_{TO}	ω_{LO}	References [b]
CsF	127	a	19
CsCl	99	165	18
CsBr	73	112	18
CsI	62	85	18
TlF	148	a	25
TlCl	63	158	18
TlBr	43	101	18
TlI	52	a	25

The Fluorite and Antifluorite Structures [O_h^5 $Fm3m$]

	ω_{TO}	ω_{LO}	ω_R	References [b]
CaF_2	257	463	321.5	26, 27
SrF_2	217	374	286	26, 27
BaF_2	184	326	241	26, 27
EuF_2	194	347	a	28
$GeMg_2$	207	~250	265	29
ThO_2	281	568	a	30
UO_2	281	556	445	30, 31

[a] Denotes modes whose frequency has not yet been measured or reported.

[b] The references for Table II.3 are the following:

1. Borer, W. J., S. S. Mitra, and K. V. Namjoshi (1971) Solid State Commun. **9**, 1377.
2. Parker, J. H., D. W. Feldman, and M. Ashkin (1967) Phys. Rev. **155**, 712.
3. Nilsson, G., and G. Nelin, (1971) Phys. Rev. B **3**, 364.
4. Mitra, S. S., and R. Marshall, (1964) Jour. Chem. Phys. **41**, 3158.
5. Vodopyanov, L. K., E. A. Vinogradov, and V. V. Kolotkov, (1974) Sov. Phys. Solid State **16**, 912.
6. Mooradian, A., and A. L. McWhorter, (1967) Phys. Rev. Lett. **19**, 849.
7. Barker, A. S., Jr., (1968) Phys. Rev. **165**, 917.
8. Skryabinskii, I. V., and Yu. I. Ukhanov, (1973) Sov. Phys. Solid State **15**, 886.
9. Hass, M. (1967) *Semiconductors and Semimetals*, edited by R. K. Willardson and A. C. Beer (Academic Press, New York), Vol. 3.
10. Spitzer, W. G., D. A. Kleinman, and C. J. Frosch, (1959) Phys. Rev. **113**, 133.
11. Nilsen, W. G. (1969) Phys. Rev. **182**, 838.
12. Barker, A. S., Jr., and M. Ilegems, (1973) Phys. Rev. B **7**, 743.
13. Manchon, D. D., Jr., A. S. Barker, Jr., P. J. Dean, and R. B. Zetterstrom, (1970) Solid State Commun. **8**, 1227.
14. Tell, B., T. C. Damen, and S. P. S. Porto, (1966) Phys. Rev. **144**, 771.
15. Geick, R., C. H. Perry, and S. S. Mitra, (1966) J. Appl. Phys. **37**, 1994.
16. Spitzer, W. G., D. Kleinman, D. Walsh, (1959) Phys. Rev. **113**, 127.
17. Damen, T. C., S. P. S. Porto, and B. Tell, (1966) Phys. Rev. **142**, 570.
18. Burstein, E., (1964) *Phonons and Phonon Interactions*, edited by T. Bak (W. A. Benjamin, New York), p. 296.
19. Martin, D. H., (1965) Adv. in Phys. **14**, 39.
20. Bottger, G. L., and A. L. Geddes, (1967) J. Chem. Phys. **46**, 3000.
21. Jacobson, J. L., and E. R. Nixon, (1968) J. Phys. Chem. Solids **29**, 967.
22. Galtier, M., A. Montaner, and G. Vidal, (1972) J. Phys. Chem. Solids **33**, 2295.
23. Gielisse, P. J., J. N. Plendl, L. C. Mansur, R. Marshall, S. S. Mitra, R. Mykolajewycz, and A. Smakula, (1965) J. Appl. Phys. **36**, 2446.
24. Geick, R., (1964) Phys. Lett. **10**, 51.
25. Houghton, J., and S. D. Smith, (1966) *Infrared Physics* (Oxford U. P., Oxford, England), p. 95.
26. Kaiser, W., W. G. Spitzer, R. H. Kaiser, and L. E. Howarth, (1962) Phys. Rev. **127**, 1950.
27. Chang, R. K., B. Lacina, and P. S. Pershan, (1966) Phys. Rev. Lett. **17**, 755.
28. Axe, J. D., and G. D. Pettit, (1966) J. Phys. Chem. Solids **27**, 621.
29. Buchenauer, C. J., and M. Cardona, (1971) Phys. Rev. B **3**, 2504.
30. Axe, J. D., and G. D. Pettit, (1966) Phys. Rev. **151**, 676.
31. Marlow, P. G., J. P. Russell, and J. R. Hardy, (1966) Phil. Mag. **14** (8th ser.) 409.

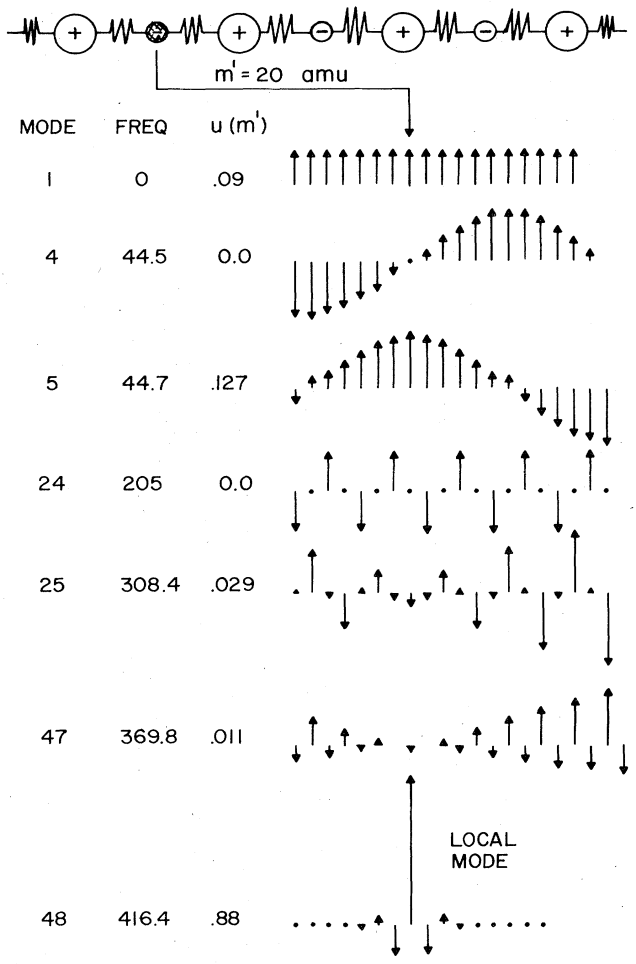

FIG. 7. 48-atom linear chain with a light-atom isotopic substitution. Many of the modes are perturbed very little. Compare for example modes 4 and 5 with Fig. 3. Note the new high-frequency mode (number 48) with its localized eigenvector.

cifying the component of the eigenvector of each mode at the site m'. The eigenvectors $\vec{u}$ (2.6) are normalized to 1 so that the component of $\vec{u}$ at a particular site is usually between zero and $1/\sqrt{N}$ for any band mode in an N-atom chain. If for some mode $u_j = 1$, then obviously all other components $u_k (k \neq j)$ are zero to preserve the normalization. In Figs. 7 and 9 the component $u_{m'}$ is shown. In Fig. 9 we note that $u_{m'}$ approaches 1 as the mode becomes more localized. In many figures below we specify the component of $\vec{u}$ at the impurity to save drawing the complicated and detailed displacement pattern for all the atoms.

We note from Fig. 9 that by the time $m' = 5$ there is practically no motion of any atoms but the impurity itself. This situation suggests the approximation

$$\omega_{\text{loc}} = \sqrt{2k/m'} \tag{2.13}$$

for the local mode frequency. We will call (2.13) the one-oscillator model of a localized vibration. Table II.2 gives the absorption strength for the one-oscillator resonance.

Figure 10 shows the local mode frequency for $m \to m'$ as a function of the dimensionless defect parameter

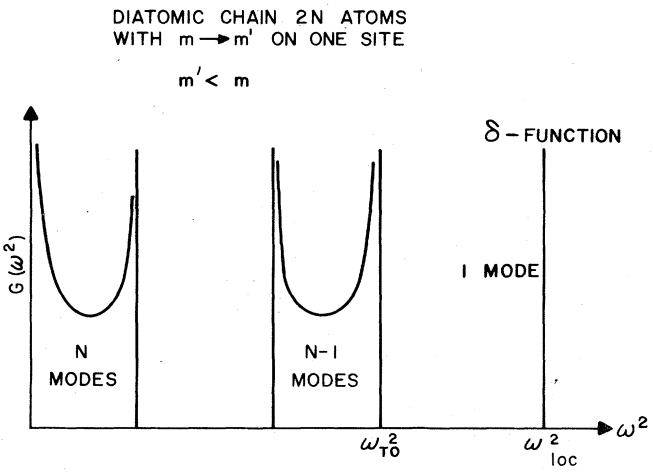

FIG. 8. Sketch of the density of states for the linear chain of $2N$ atoms, one of which is replaced by a light impurity.

$$\epsilon = 1 - m'/m.$$

$\epsilon = 0$ implies a perfect crystal. Finite positive values of ϵ result in a local mode whose frequency is shown by the solid curve above the optic band. The one-oscillator solution (2.13) shown as a dashed curve is obviously a very good approximation as ϵ approaches 1.

2. Band modes

Before leaving our first example of a chain with a mass defect we wish to examine the detailed nature of the band modes. For the linear chain, half of these modes are unchanged from the pure chain and the other half are slightly perturbed with new wavelengths. Figure 11 shows in detail two modes from a monatomic chain ($M = m$) when a light defect mass ($m' = 0.1m$) is introduced. The mode picked for detailed examination had the wavelength $\lambda = 3a$, before the impurity was intro-

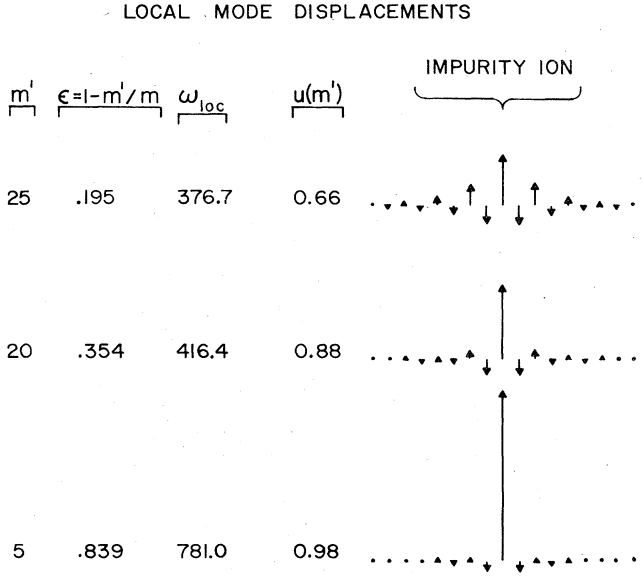

FIG. 9. Eigenvectors for the highest-frequency (localized) mode for three isotopic substitutions on the $m = 31$ site. Note the extreme localization for a substituent of mass 5.

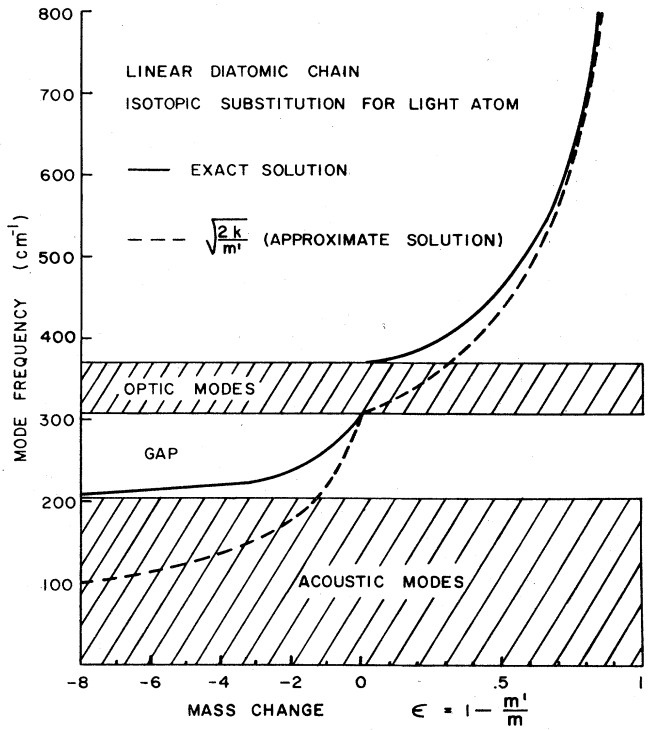

FIG. 10. Local mode frequencies for the diatomic linear chain for both light and heavy isotopic substitutions on the $m=31$ site. Note that the approximate formula breaks down quite badly for negative mass defect parameter.

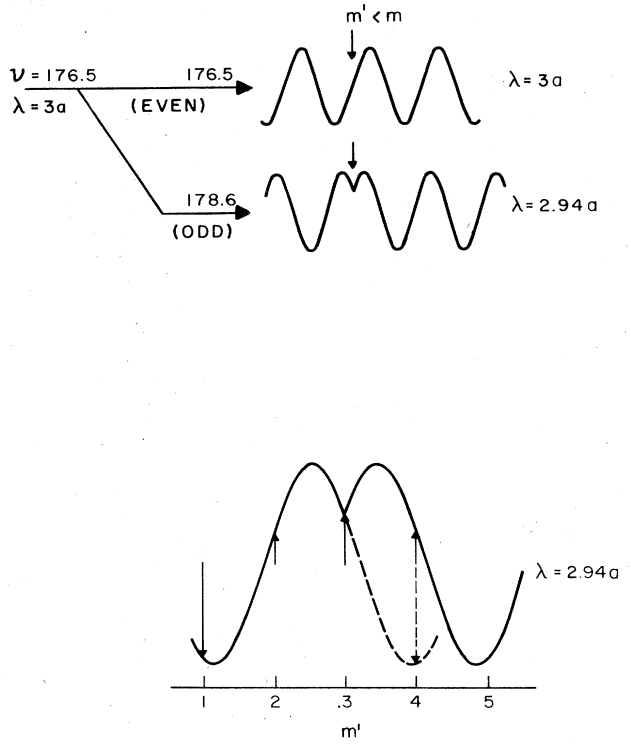

FIG. 11. Eigenvector of two low-frequency acoustic modes which were formerly degenerate. A light impurity m' has been substituted for atom 3 in the lattice. The odd mode is perturbed by acquiring a phase shift in its spatial wave pattern at atom 3. Because of the phase shift its wavelength is no longer $3a$ as in the pure lattice. The lower part of the figure shows by a dashed line the displacement atom 4 would have had if the impurity were not present.

duced. A monatomic chain was used so that only one amplitude function is needed for the description of all particle motions. We draw this function rather than plot its value at each atom as is done in other figures. For the defect chain the even mode has unchanged frequency since m' does not move. The odd mode has a slightly increased frequency and an abrupt change in phase (of the spatial sinusoidal function) at the impurity. Note that this mode pattern is exactly what is needed to balance the forces on the neighboring atoms. Atom 4, the right-hand neighbor of m', must have the bond k_{34} stretched just the correct amount to give it the motion it would have in a regular sinusoidal mode. Since the motion of atom 3 does conform to this sinusoid, atom 4 vibrates contentedly and obviously does not care about atom 2. Similarly, atom 2 is entirely free to vibrate as part of a regular band mode since it sees the neighbors to which it is bonded moving in a pattern characteristic of a regular band mode. Note that if this mode were a perfect sinusoid through atom 3, as indicated by the dashed line (Fig. 11), atom 4 would be giving a tremendous stretch to the k_{34} bond. This stretch is not needed in the defect chain because atom 3 is much lighter and thus needs much smaller forces to accelerate it. For this special model (linear chain with nearest-neighbor forces) the band modes look much like the unperturbed chain modes except for the jump in phase at the impurity atom. In particular, the impurity atom does not have any extra amplitude. This mode behavior is to be contrasted to the resonant modes discussed below.

The question often arises as to whether there is a valid q-space description for the vibrations of the defect chain. Figure 11 shows that for the band modes there is a regularity over the whole chain described by a single wave vector q, plus a jump in phase at the impurity. Thus in a special qualified sense there is a unique q state for each band mode. In two and three dimensions the band modes become much more complicated, with mixing of many unperturbed q states to form the new band modes of the defect crystal. In these latter cases there is no unique q but at best a range of q values which describes the band modes.

3. Local mode and band mode absorption

In Sec. II.B the dielectric function for the pure chain was discussed. Figure 12 shows the spectrum $\mathrm{Im}(\epsilon)$ for the defect chain of Fig. 7, where $m'=20$ amu. Since $\mathrm{Im}(\epsilon)$ is a series of delta functions, we plot a series of vertical bars whose height is the integrated strength S of each delta function. S is defined in Table II.2. The striking feature of Fig. 12 is that there are now 24 transverse modes (delta functions) in the $\mathrm{Im}(\epsilon)$ spectrum arising from vibrations with odd symmetry about the impurity. These are divided into a cluster of 11 acoustic band modes, 12 optic band modes, and the one local mode removed to higher frequency. The mode at 370 cm^{-1} is by far the strongest with $S=1.30$. This strength represents a decrease of about 20% from $S=1.667$ for

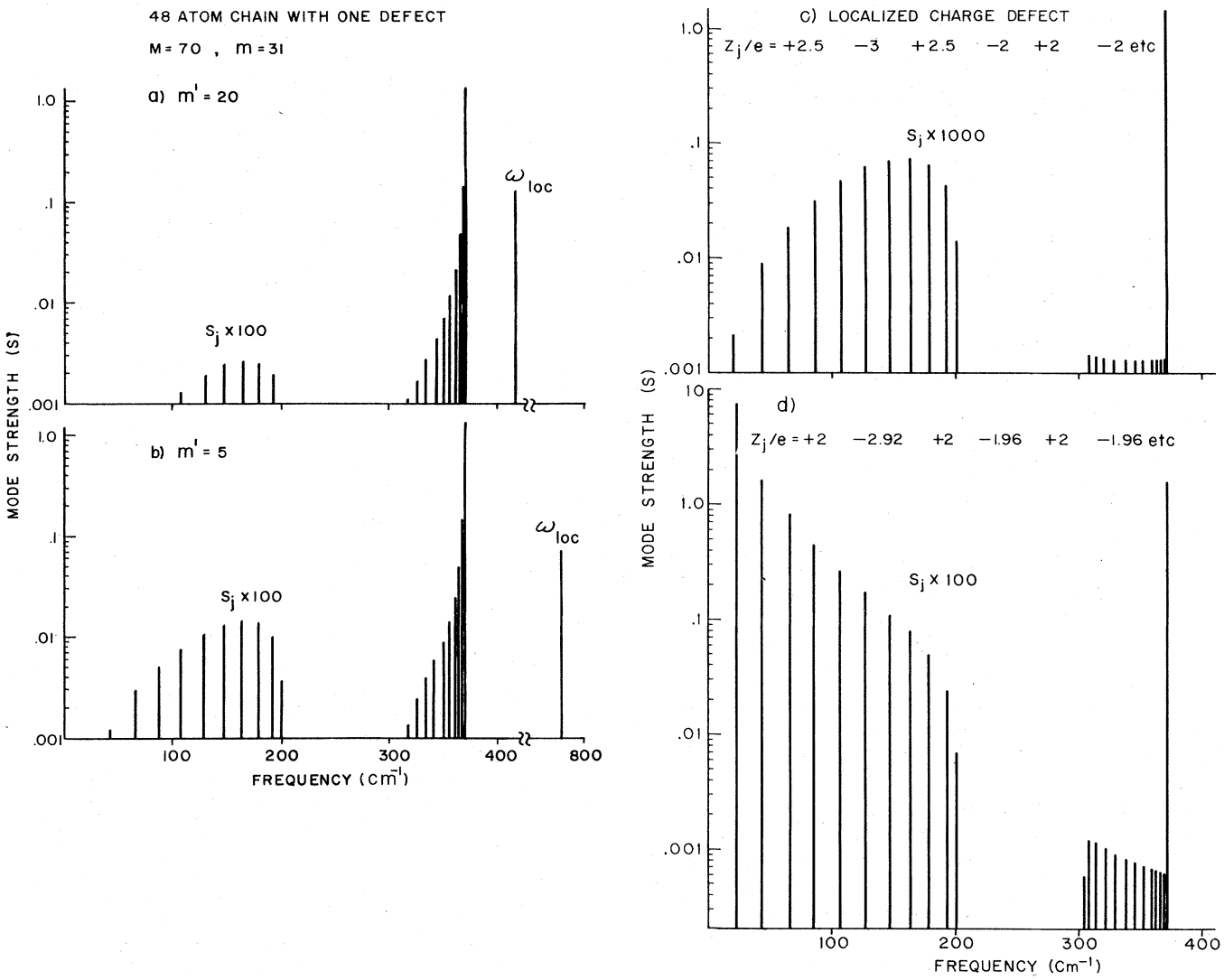

FIG. 12. Mode strengths for the 48-atom chain with one defect at atom site 2. Since Im(ϵ) is a series of delta functions, the integrated strength S of each mode is plotted (see Table II.2). In (a) and (b) the light atom is replaced by a lighter atom, causing a high-frequency local mode as well as absorption throughout the acoustic and optic bands. The charge of the impurity is taken equal to that of the atom it replaces (Table II.1). In (c) and (d) only a charge defect is introduced on atom 2. In (c) this charge is neutralized on the two nearest neighbors and in (d) it is neutralized over the entire chain.

the mode ω_{TO} of the pure chain. Note that our 48-atom chain has 24 unit cells, so that adding one impurity atom corresponds to 100/24 = 4.2 at.% defects. This is a very heavy doping compared to the 10^{-4}% typical of many local mode experiments. This large concentration causes all the new impurity modes to appear very strong and reduces the strength of the original lattice absorption, since its strength is "borrowed" by the impurity modes.

The impurity-mode strengths scale directly with concentration; thus the strengths shown in the figures may be scaled to predict the results for other concentrations. Figure 12 shows that the entire acoustic band and optic band have become active in infrared absorption. The acoustic band modes are weak for the mass defect m' = 20, but become stronger for m' = 5. In a realistic N-atom model, we expect the delta functions shown in Fig. 12 to merge as $N \to \infty$ giving continuous bands of absorption in the acoustic and optic band regions. The local mode will remain a delta function unless some specific mechanism is included in the model to couple it to the rest of the modes. Genzel (1969) has given an analytic treatment for the diatomic chain and derived the continuous absorption spectra for certain cases of both mass and force constant defects.

The broad bands of absorption discussed above will occur for many of the cases of defect chains studied below. We call this "band mode absorption." Its shape is always characteristic of the density of pure chain modes of appropriate symmetry. For infrared absorption the odd symmetry modes appear in the spectrum. Raman scattering selects even-symmetry modes. In addition the shape is modulated by a (generally) slowly varying function of frequency, which depends on the method of

coupling to the defect.

In the calculations for the mode strengths of the defect chain in Fig. 12(a) and (b) we have used $z'=2e$. That is, the impurity has the same charge as the ion it replaces. In real crystals the charges are seldom this simple. With the introduction of a defect there may be considerable rearrangement of charge on the defect and its neighbors. Leigh and Szigeti (1968) have considered this effect in detail. The importance of charge transfer and short-range polarization effects is illustrated by the experimental fact that Ge impurities in Si have five times the local mode absorption strength of B^- in Si even though the simplest point charge model suggests that the Ge should have zero charge. Such a simple model can be improved by putting z on the Ge atom and $-z$ on the nearest host Si atom. The local mode then has finite absorption proportional to z^2 (see Table II.2). In Fig. 12(c) and (d) two cases of charge defects are shown for a GaP chain with no mass or force constant defects. The mode frequencies and wavelengths remain as shown in Fig. 2 but there is now band mode absorption. Figure 12(c) shows the characteristic absorption shape in the acoustic band seen in the figures above. In Fig. 12(d) the charge defect is neutralized not at the nearest neighbors but by distributing the neutralizing charge uniformly over the entire chain. Here the low-frequency modes are strongly emphasized. This latter case is rather unphysical but does serve to emphasize the effects which can be associated with the charge distribution around the impurity.

4. The gap mode

We now consider the effect of replacing the light atom in the linear chain by a heavier "isotope." If we continue to use the mass defect parameter $\epsilon = 1 - m'/m$, then ϵ takes on negative values for such a substitution. Figure 10 shows the result of the calculation for the 48-atom linear chain. A new mode appears in the gap for any negative value of ϵ. This mode asymptotically approaches the top of the acoustic band as the substituted mass becomes very large. This particular behavior is changed if a different model is used. As discussed below, more realistic three-dimensional models show this mode dropping and entering the acoustic band when m' is made sufficiently large. A one-dimensional or three-dimensional model with no gap in the spectrum shows no new localized modes for negative ϵ except for possibly a quasilocalized resonant mode to be discussed below. Figure 13 shows the atom displacement patterns for three of the modes for $m' = 62$ amu. Mode 25 is the gap mode. In this mode, the impurity has most of the amplitude. Note that although the details of the motion are different, this mode, like the local mode of Fig. 7, consists principally of the impurity moving against its neighbors. There is a major difference in limiting behavior between the local mode and the gap mode, which should be noted. For $m' \to 0$, the local mode became completely localized at the same time that its frequency was pushed far above all band modes. The gap mode is constrained to lie in a finite frequency region and cannot be moved arbitrarily far (in frequency) from adjacent band modes. This feature prevents localization of all the mode amplitude on the defect. The bottom part of Fig. 13 shows the dielectric spectrum for the defect chain with $m' = 62$. As in Fig. 12, half of the band modes have become infrared-active and there is in addition a delta function absorption peak at the gap mode frequency.

5. Gap and local modes for heavy-ion replacement

All the modes discussed up to this point arise from replacing the light ion by an isotope. Figure 14 shows the effect of replacing the heavy ion ($M = 70$) by a lighter isotope. In this case two new localized modes appear simultaneously. We continue to call the lower-frequency localized mode the gap mode, since it occurs in the gap between the acoustic and optic bands, and the higher-frequency mode the local mode. For ϵ approaching 1, the local mode rises to very high frequency, as one expects intuitively. The gap mode, however, shows unexpected behavior. It approaches the center of the gap; thus its frequency cannot be related to the one-oscillator approximation $\omega = \sqrt{2k/M'}$. Figure 15 shows the atom motions for $M' = 5.6$ amu., i.e., $\epsilon = 0.92$. Mode 48 is the local mode. Its frequency of 760 cm^{-1} is well above all modes of the perfect chain. Its eigenvector is very similar to the local mode eigenvectors studied earlier in Fig. 9. Mode 24 is the gap mode. We note from the

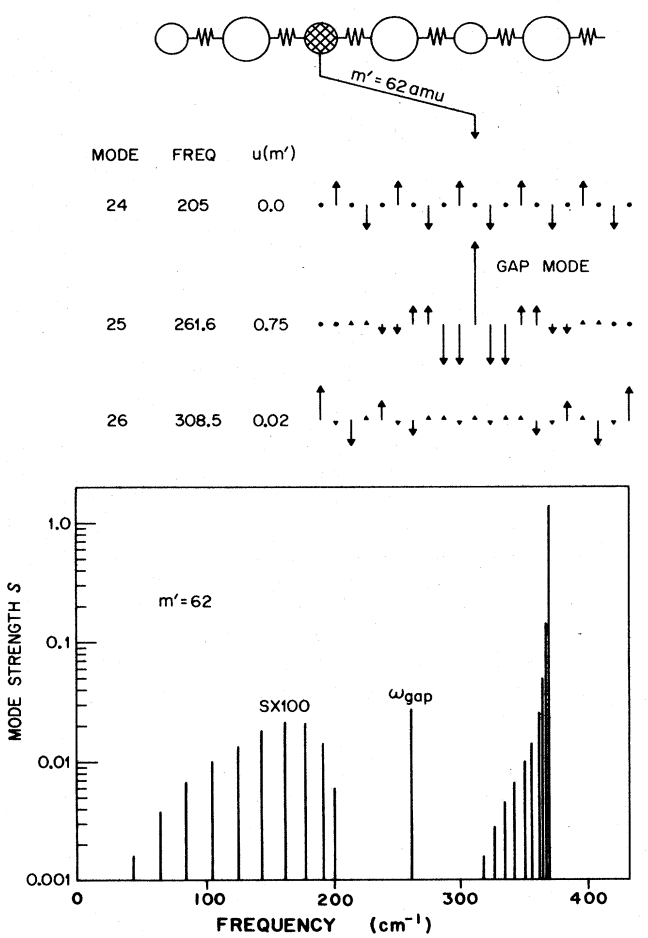

FIG. 13. Eigenvectors and absorption spectrum for a heavy substituent on the $m = 31$ site which causes a localized mode in the gap (mode number 25).

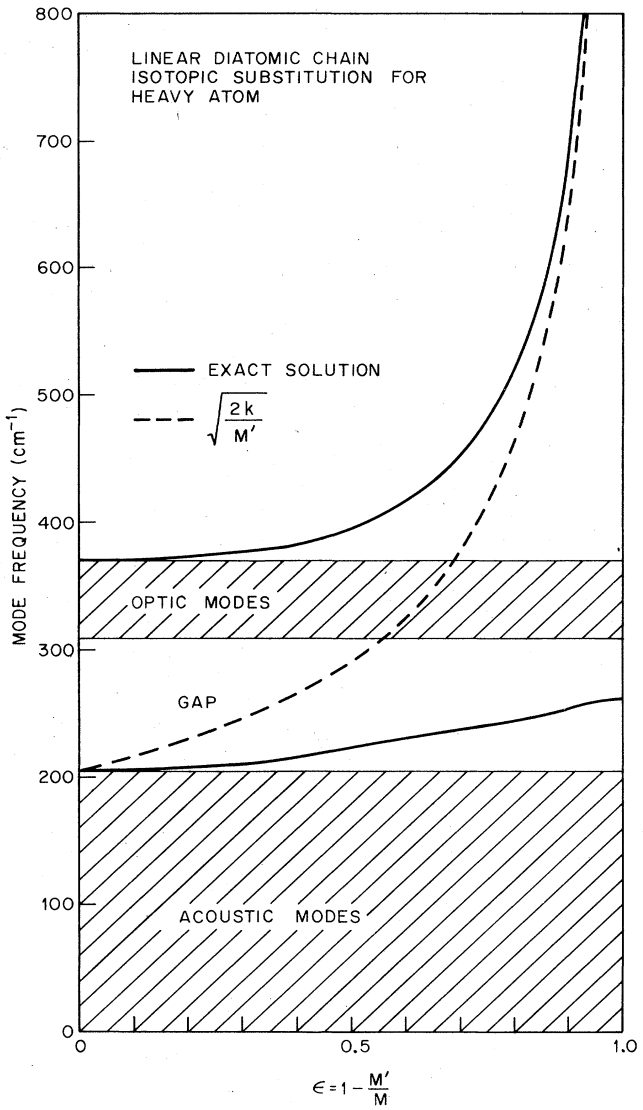

FIG. 14. Localized modes for substitutions on the $M=70$ site of the GaP linear chain (Table II.1). For this case two localized modes occur at once. The approximate solution is only useful for giving the higher-frequency mode near $\epsilon=1$.

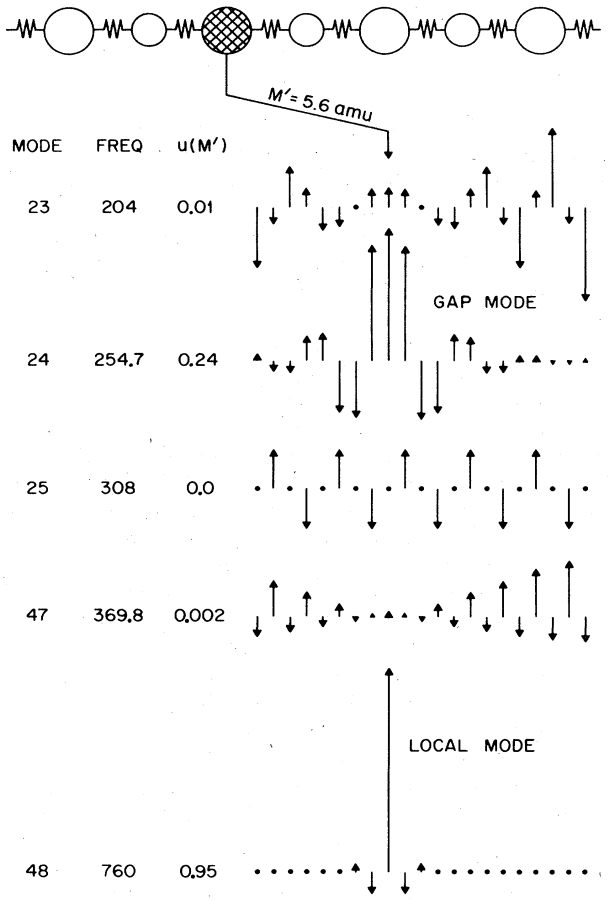

FIG. 15. Eigenvectors for the two kinds of localized modes for a light-atom substitution on the $M=70$ site. $M'=5.6$ corresponds to $\epsilon=0.92$ of the preceding figure. The localized mode which occurs in the gap is about four times less well localized than the high-frequency local mode. Reducing M' further does not increase the localization of the gap mode—its eigenvector and eigenfrequency change very little even in the limit $M' \to 0$.

eigenvector that the impurity mass plays almost no role in this type of motion. The impurity atom merely follows the ion on each side. It is easy to show that for the linear chain model in the limit of small M' the gap mode approaches the center of the gap in the ω^2 (rather than ω) spectrum. The gap mode of Fig. 15 should be contrasted with that of Fig. 13 arising from substitution on the lighter-ion site. Both are localized modes; however, the displacement pattern is quite different in detail for the two kinds of substitution.

6. Resonant modes

Substitution of a heavier isotope for the $M=70$ atom in the linear chain with nearest-neighbor forces results in no localized modes. The band modes become slightly infrared-active but no new absorption appears at high frequencies or in the gap. We now must emphasize the fact that the linear chain with nearest-neighbor forces and isotopic substitutions does not exhibit one very interesting class of defect modes—the resonant modes. This mathematical anomaly of the linear chain in fact delayed the recognition of these low-frequency modes which lie within the acoustic band.

Dawber and Elliott (1963) have shown that resonant modes arise in a three-dimensional model when an atom is replaced by a much heavier isotope. We can exhibit the same type of mode in the linear chain only by reducing the force constants on each side of one atom. Taking the linear chain of Fig. 2 we reduce the force constant on each side of atom 2 to k' and define the force constant defect parameter

$$\gamma = 1 - k'/k.$$

Figure 16 shows the new modes which result. As γ increases from 0 to 0.66, a localized mode drops from the lower edge of the optic band into the gap. Its eigenvector is very similar to the gap mode in Fig. 13 (mode 25) which resulted from replacing $m=31$ ion by a heavier isotope. As γ increases above 0.66, distinctly new

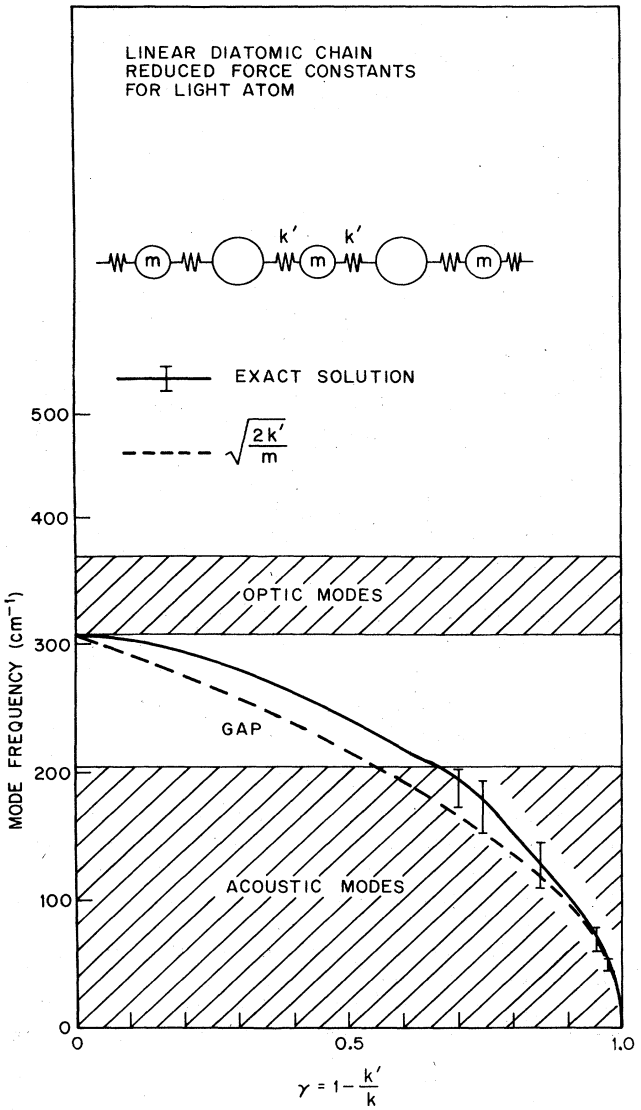

FIG. 16. The defect modes for a force constant reduction on the $m = 31$ atom. As γ increases, a gap mode is formed which decreases in frequency, then changes its character and enters the acoustic band. Once within the acoustic band, there is a group of eigenvectors or modes which have large amplitude near the impurity. The width in frequency of this group is given by the vertical bars. Such a group of modes is called a "resonant mode."

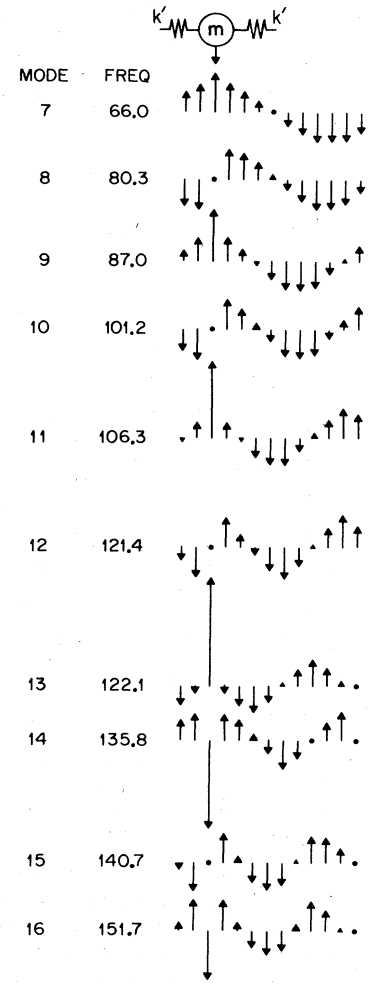

FIG. 17. Eigenvectors for several modes in the resonance region for $\gamma = 0.85$ (see preceding figure). Modes with even and with odd symmetry are perturbed from the pure chain eigenvectors. Note the relative amplitude reversal near the peak of the resonance as one passes from the eleventh to the thirteenth mode.

behavior occurs. A band of closely spaced modes within the acoustic continuum all have partially localized behavior. Vertical bars are used in Fig. 16 to show the width of the band. Figure 17 shows the atom motions for $\gamma = 0.85$. The vibrational amplitude does not die out far from the defect. The defect atom, however, has extra amplitude. These modes are localized in a special sense. All atoms vibrate in a sinusoidal pattern, but there is extra amplitude on the defect atom. For $\gamma = 0.85$ the extra amplitude is a maximum for modes near 125 cm^{-1}, which we call the frequency of the resonant mode.

Figure 17 clearly shows that there is not one but many localized modes. A probe which couples to some property of the defect will usually not be able to resolve individual modes, however, so that a measurement will show a broad response peaked near 125 cm^{-1}. This broad response is called "the resonant mode." It is not broad because of damping, but because it consists of an envelope of modes in each of which the defect vibrates with significant enhanced amplitude. Figure 18 shows the amplitude of vibration of the defect atom relative to the amplitude of the same atom type in a location removed from the defect, where the sinusoidal envelope is at a maximum. Again we note the "resonant" or "damped mode" appearance of the spectrum near 125 cm^{-1}. At higher frequencies in the optic band there is very little motion of the defect. The broad resonance shown in Fig. 18 is to be contrasted with the delta function peaks obtained earlier for the localized modes. Figure 19 shows the absorption strength spectrum for the resonant mode in a 48-atom chain. There is approximately a one thousand-fold increase in absorption strength in

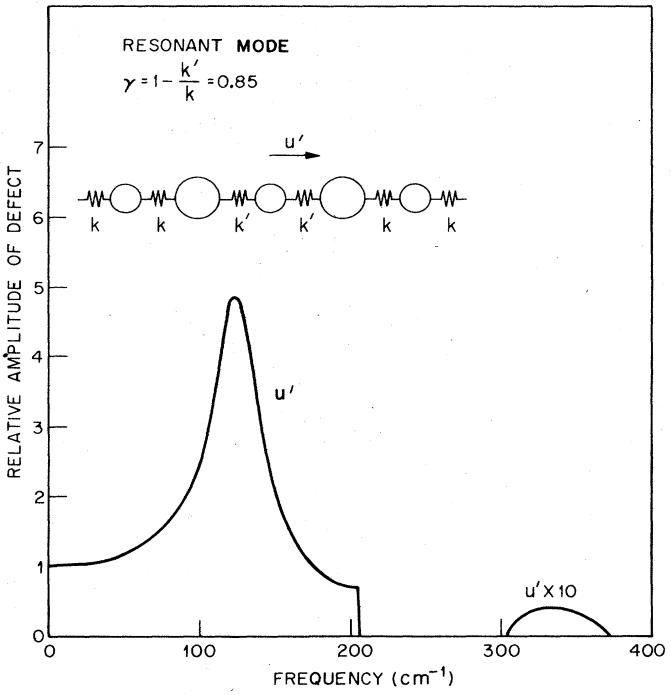

FIG. 18. Amplitude of defect atom relative to amplitude of atoms far removed for the case $\gamma = 0.85$. This function is only defined for even-symmetry modes. Note that finite amplitude exists in both the acoustic and optic band regions but there is a strong peak near 125 cm^{-1} connected with the resonant mode.

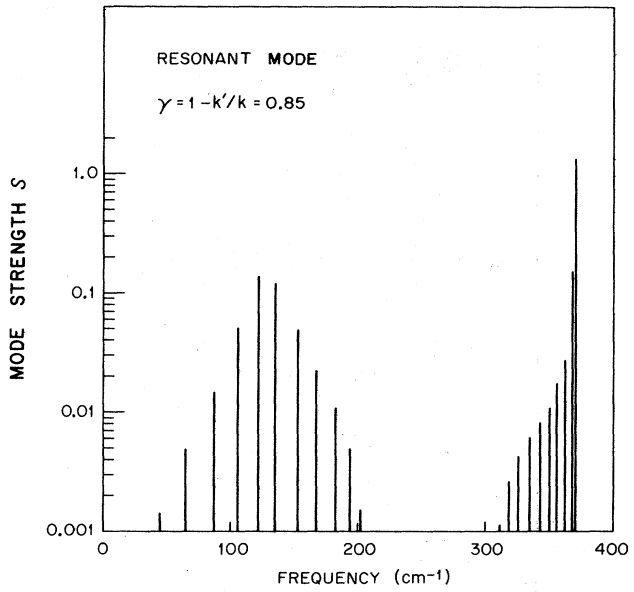

FIG. 19. Absorption spectrum for the resonant mode shown in preceding figures.

the acoustic band compared with all preceding calculations for mass defects. As might be expected from Fig. 18, the absorption shows a broad peak near 125 cm^{-1} plus some weak activity in the optic band.

The resonant mode exhibited by the linear chain model becomes much more narrow and moves to lower frequency as γ approaches 1 (Fig. 16). Li substituted for K in KBr is an example of a force constant defect (and mass defect simultaneously) which comes close to $\gamma = 1.0$. The weak binding of Li is found to cause a sharp absorption peak near 16 cm^{-1}, i.e., at very low frequencies near the lower edge of the acoustic band. Since very heavy substituents which might be expected to cause resonant mode behavior are usually tightly bound, most observations of resonant modes actually require significant softening of the force constant. Genzel, Renk, and Weber (1965) have presented linear chain calculations of resonant mode behavior for atoms which are both mass and force constant defects.

D. Vacancies and interstitials

Figure 20 shows two linear chain models which illustrate vacancy and interstitial defects. There is no simple physically realistic model for these defects which is comparable to the isotope model. The vacancy is denoted □. The simplest vacancy model consists of removing a host atom and its bonds to create a vacancy, then altering the nearest remaining bonds because of the static lattice relaxation which occurs about the defect. Mitani and Takeno (1965) have evaluated a similar model for a three-dimensional lattice. For the linear chain this model is attractive since it has only one parameter, the force constant defect $\gamma = 1 - k'/k$. We assume that the charge which has been removed is compensated for by small equal charge defects spread over the entire chain. There has been insufficient experimental work to confirm whether such a model is at all adequate. Figure 21 shows the localized and resonance modes which occur for a single vacancy on either a Ga-ion site or a P-ion site, i.e., for $\square_{Ga}$ or $\square_{P}$. For increased forces (negative γ) the P-vacancy mode lies somewhat higher than the Ga-vacancy mode. For $\square_{Ga}$ in GaP the large amplitude is localized on the two lighter ions (P ions) nearest the defect. For very long chains the modes occur as

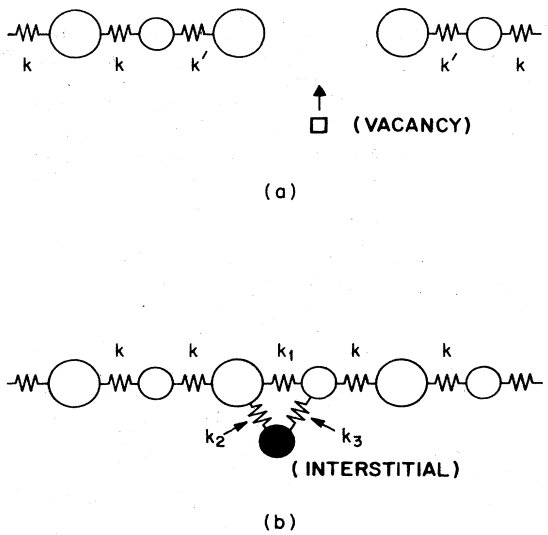

FIG. 20. Chain model of (a), a vacancy, and (b), an interstitial defect. The interstitial ion is drawn below the chain axis to avoid the bond k_1.

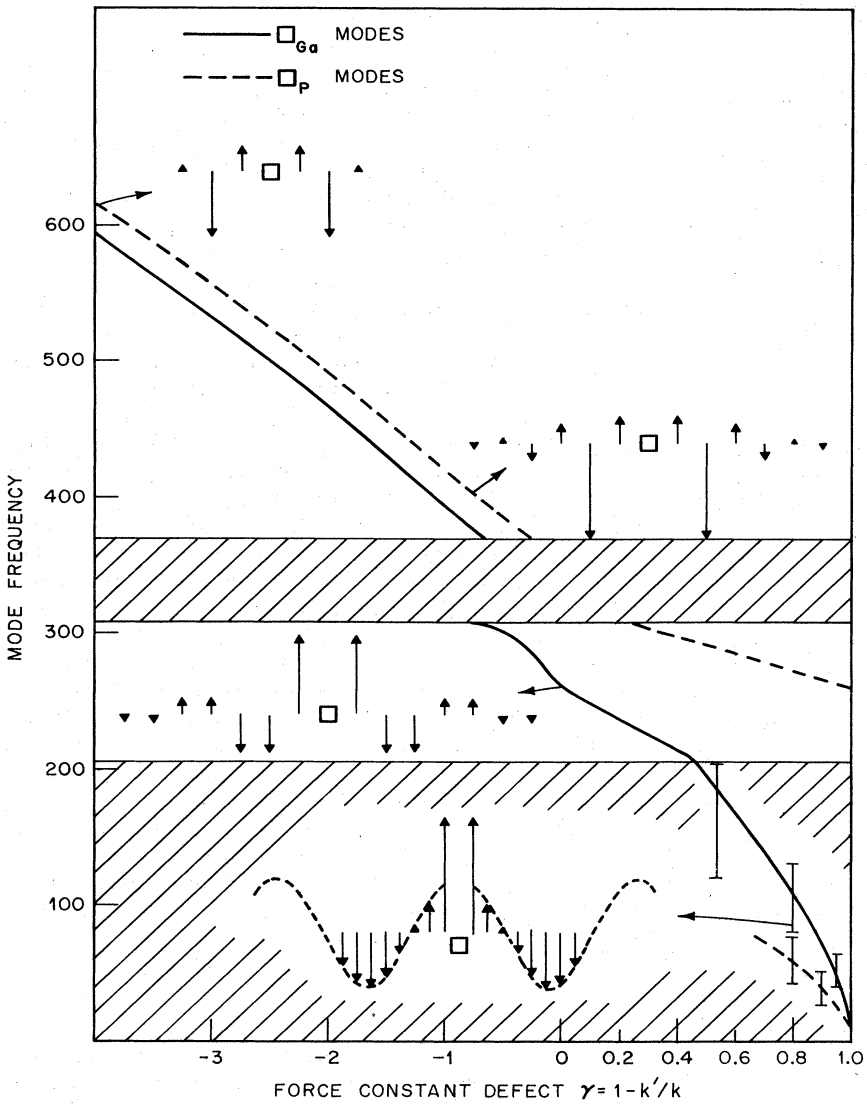

FIG. 21. Localized and resonance modes for the linear chain model with one vacancy. The GaP chain (Table II.1) is used and modes for vacancies on both the Ga and P site are calculated. Several typical eigenvectors for odd modes are shown.

degenerate pairs which can be taken to have symmetric and antisymmetric vibrational amplitudes about the vacancy. For the finite chains used here the degeneracy is lifted as soon as the amplitude becomes nonlocalized to the extent that there is finite amplitude at the chain ends which are connected by the periodic boundary conditions. For the 48-atom chain the splitting is negligibly small for all modes except the resonant modes. Note that a bond linking the nearest neighbors of the vacancy would split the degeneracy for a chain of any length. In Fig. 21 we have shown the antisymmetric (infrared-active) mode frequencies and eigenvectors. As in the case of the isotope defects discussed in earlier sections, the closer a defect mode comes to the band edge, the less localized it becomes.

For the vacancy on the Ga site when the force constant next to the defect is weakened, a gap mode appears which drops and penetrates the acoustic band, becoming a resonant mode. The vertical bars in Fig. 21 roughly delineate the breadth of the resonant mode. The eigenvector for one component of the resonance at $\gamma = 0.8$ is shown as an inset in the lower part of Fig. 21. The largest amplitude mode within the resonance occurs at 110 cm^{-1}. We plot the mode at 84 cm^{-1} and note the sinusoidal, i.e. bandlike behavior of all ions except the nearest neighbors of the vacancy. For $\square_P$ when $\gamma > 0$ a gap mode approaches the center of the gap and simultaneously a broad resonance appears at low frequencies. The resonant mode is resolvable only for $\gamma > 0.7$ for this case. Aside from details of the vibrational amplitude the vacancy model gives no generically new modes. Similar local modes, gap modes, and resonant modes have all been encountered in the earlier sections. This similarity makes the positive identification of vacancy modes from spectroscopic evidence alone quite difficult.

In Fig. 20 a model of a single interstitial is depicted. The interstitial ion is taken to lie between ions 3 and 4. It is evident that a reasonable parametrization requires the mass of the interstitial as well as several force constants (e.g., k_1, k_2, k_3). With so many parameters it be-

comes tedious to present general graphs of the modes. We have calculated several cases and find the same general conclusion as outlined above. For the interstitial there can be localized modes, gap modes, and resonant modes. In each case the large localized amplitude resides on the interstitial or in some cases on the lighter neighboring ion. While one or two cases of interstitial modes have been identified, very little model fitting has been carried out to date because of the complexity of this defect in the real three-dimensional case.

E. The case of many defects; the mixed crystal chain model

1. Introduction

In this section we continue our approach of using the linear chain to illustrate vibrational modes. For concreteness the masses appropriate to the mixed crystal $GaAs_xP_{1-x}$ are used, since this crystal has been much studied by infrared and Raman spectroscopy.

At the outset it must be stressed that there have been a disappointing lack of tractable theoretical models for describing mixed crystal vibrations. The situation here is very similar to that in the theory of the band structure of mixed crystals and of amorphous solids. In both problems there are exact techniques for describing the effect of one impurity atom. These techniques are then extended to mixed crystals by approximations which are questionable in many cases. For both band structure and lattice vibrations there is also the virtual-ion crystal model which replaces the individual host and impurity ions by a single "average" ion. For example, in $GaAs_{0.5}P_{0.5}$ the virtual ion would have a mass of 0.5 (70 + 31) amu. This model is conceptually simple, and once the properties of the virtual ion are fixed, one has a pure crystal problem in either band structure or lattice vibrations to solve. The coherent potential approximation (CPA) shows much promise in principle for providing models of mixed crystal vibrations. Elliott *et al.* (1974) have given an extensive review of this and other methods. Taylor (1973) has done a detailed approximate calculation using the CPA for two specific mixed crystals. Apart from these and other analytic techniques there has been a considerable effort in the mixed crystal lattice vibration problem using exact calculations on finite models. The linear chain model we use is one example. It suffers from being a one-dimensional model and from neglect of long-range forces and short-range polarization effects. The equations can be solved exactly, however. Dean has pioneered in this area, having considered chains containing as many as 200 000 atoms, and also having obtained solutions for some two- and three-dimensional structures. Hass *et al.* (1969) have presented some solutions for 40-atom chains which include the important feature of mode strength as well as frequency.

We will continue with our diatomic chain model, solving for mode frequencies, eigenvectors, and infrared strengths. We assure the reader that the model exhibits all the major effects that other more sophisticated models have shown and also that it is very useful in showing the way towards two other simple models which are most used in fitting experimental data.

2. The mixed GaAs–GaP linear chain

Figure 13 shows the effect of replacing one P ion in GaP by a much heavier ion. A gap mode of considerable strength appears, and some strength is also spread over adjacent formerly inactive modes. We will find that as more and more P ions are replaced by As ions and the gap mode increases in strength and finally becomes dominant. The modes near 370 cm^{-1} decrease in strength and finally become a P-ion local mode when only one P ion is left in our 48-atom chain. Since the impurity modes are all quite strong in the mixed crystal, they cause measurable effects in reflectivity, and we now compute the reflectivity spectra from the model to make closer contact with experiment. To conserve space many of the weaker modes, such as those below 200 cm^{-1} in Fig. 13, will not be shown in some of the plots. Figure 22 shows the modes for a 48-atom chain for several cases of moderate concentrations of impurities. For simplicity the force constant is fixed at 0.87×10^5 dynes/cm as used in most of the previous calculations (Table II.1). When this force constant is used with the masses appropriate to a GaAs linear chain, the TO mode occurs at 284 cm^{-1} (Fig. 22, top). This frequency is 14 cm^{-1} higher than ω_{TO} of real GaAs because of our choice of force constant. The figure shows the effect of adding one P ion, then three P ions, and finally the effects of three, then one As ion in GaP. From the figure we note that for 12.5% P in GaAs, there are three local modes. They are very closely spaced, however. The total strength of the three ($\Sigma S = 0.35$) is approximately three times the strength of the single local mode for the $GaAs_{0.958}P_{0.042}$ chain ($S = 0.12$), as might be expected. For the model we have been using there is an exact sum rule on the mode strengths S_j

$$\Sigma S_j = 1.667.$$

Thus as the local modes become stronger the main band must lose strength. In the lower part of Fig. 22 we note how the As gap mode increases in strength at the expense of the main GaP band in the $GaAs_{0.125}P_{0.875}$ mixed crystal. Figure 23 shows the calculated reflectance spectra for the same crystals. To obtain realistic spectra each mode has been given a width of $\Delta\omega_j = 0.025\omega_j$. While this is an arbitrary choice, such widths are often measured in mixed crystal spectra. The figure shows that pure GaP and pure GaAs each have one reststrahlen band. Here 4.2% impurity causes a second weak band to appear near the local or gap mode frequency. At 12.5% impurity the subsidiary reststrahlen bands acquire more strength, and in addition there is strong "fine structure" near these bands. Note that the reflectivity spectra are insensitive to very weak modes. In Fig. 24 the dielectric loss spectra are plotted for pure GaAs and for $GaAs_{0.875}P_{0.135}$. Since there is appreciable splitting of the transverse and longitudinal components of the principal mode and the main local modes, both the transverse [$\mathrm{Im}(\epsilon)$] and longitudinal [$\mathrm{Im}(-1/\epsilon)$] spectra are plotted. Here again finite linewidths have been inserted to give realistic spectra. Two main modes plus considerable fine structure are very evident in both the ϵ and $1/\epsilon$ spectra for the mixed crystal.

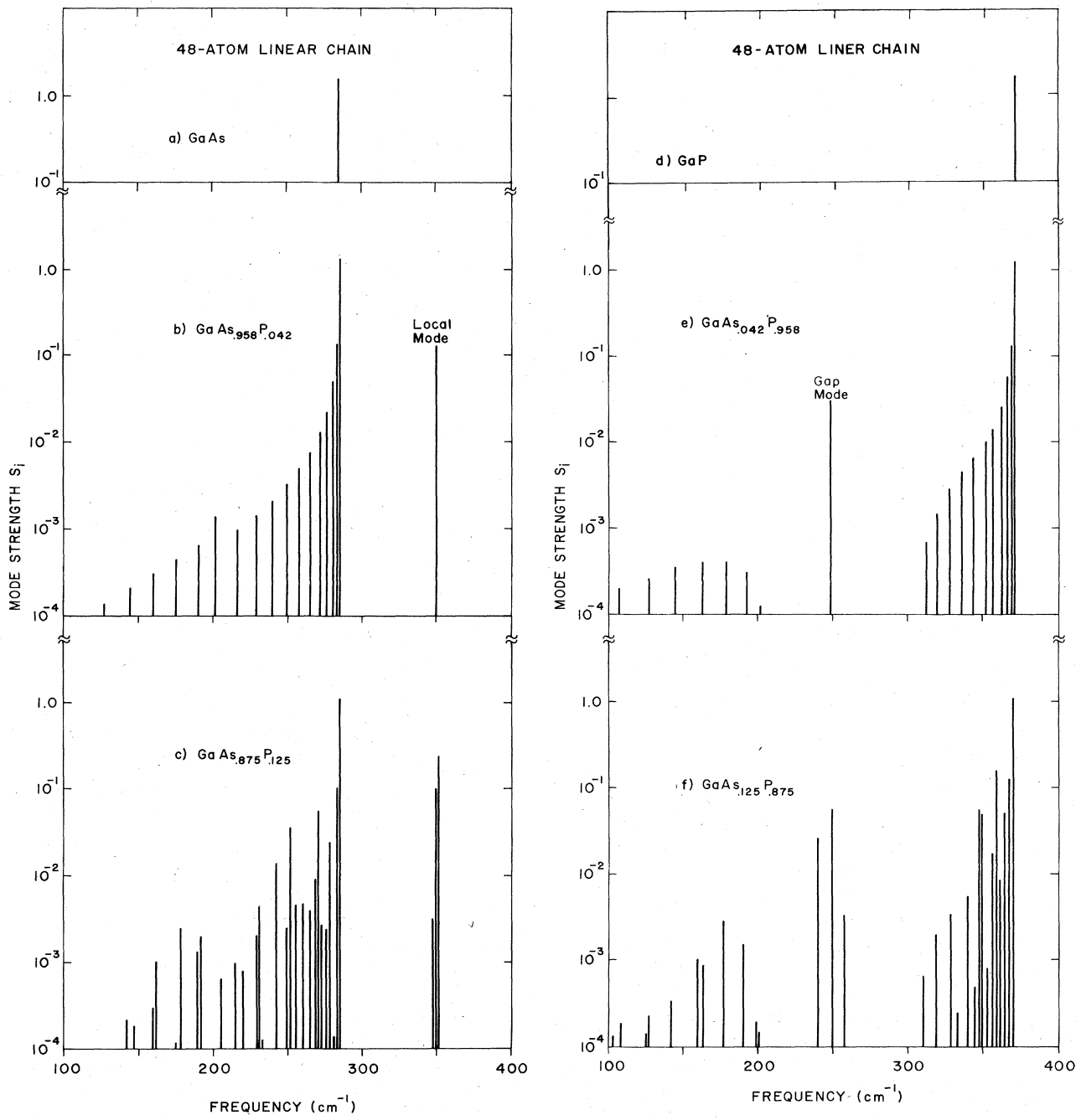

FIG. 22. Transverse mode frequencies and strengths for mixed crystals calculated from chain model. (a) Pure GaAs exhibits one mode. (b), (c) Increasing amounts of P cause local modes, gap modes, and band absorption. (d) Pure GaP with one TO mode. (e), (f) Increasing amounts of As cause gap modes and band absorption.

3. Two-mode behavior

If we ignore the weaker fine structure in the spectra shown in the preceding figures, a simple plot of mode frequency versus concentration may be constructed as shown in Fig. 25. The peaks of the strongest modes in the ϵ and $1/\epsilon$ spectra are plotted using the data in previous figures plus some data from additional calculations on 96-atom chains. The gross behavior shown in Fig. 25 has been termed "two-mode" behavior, since at any finite concentration there are two TO modes and two LO modes. Correspondingly, in the reflectance spectra there are two reststrahlen bands. The 48-atom chain shows, however, that even at 12% concentrations there is significant strength in other modes besides the main modes plotted in Fig. 25. To continue the diagram to $y = 0.5$ many more modes would have to be added to the figure, destroying its simplicity. We will return later to simpler models which show two-mode behavior for

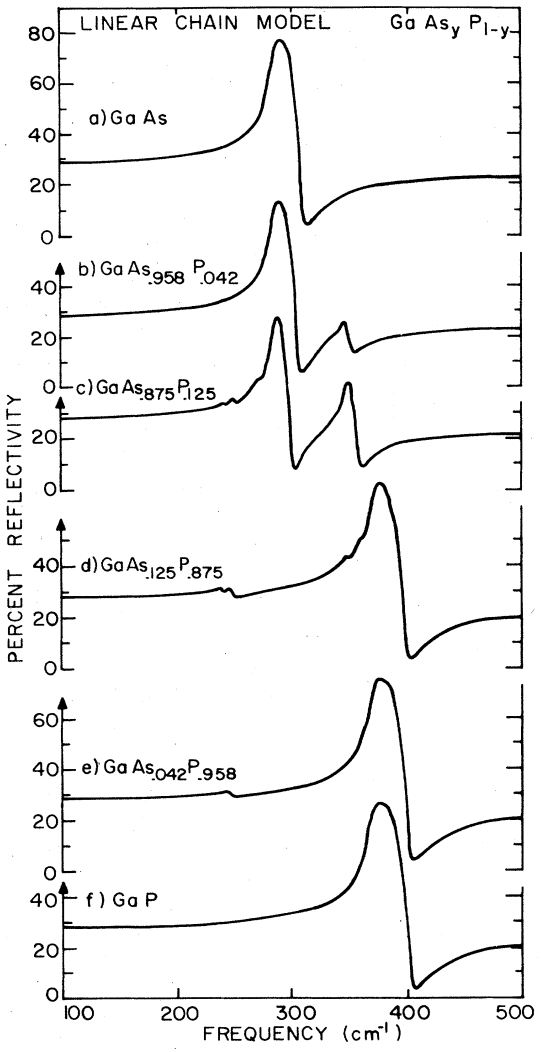

FIG. 23. Reflection spectra for modes shown in preceding figure. Each mode has had some damping included as described in the text. Note the considerable fine structure for the mixed crystals in (c) and (d).

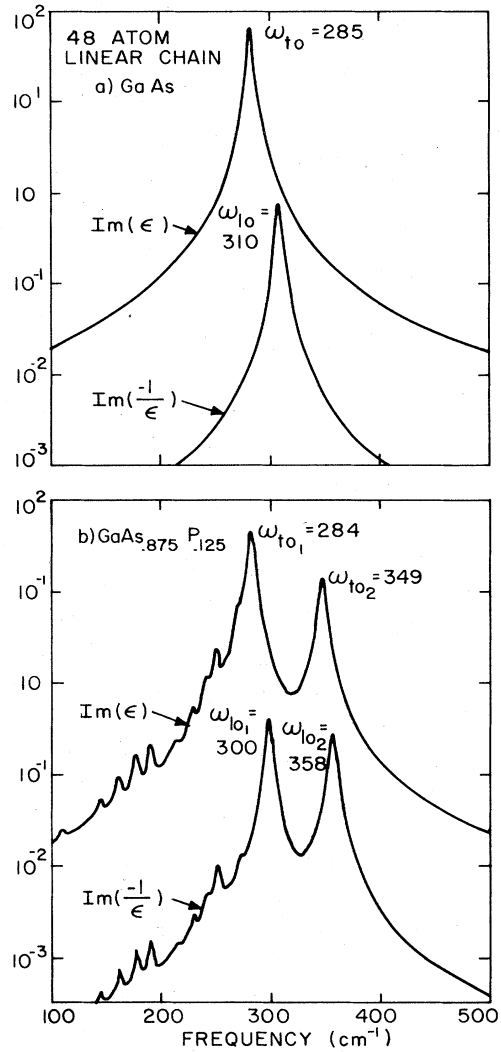

FIG. 24. (a) Dielectric spectra of pure GaAs calculated using $\epsilon_\infty = 9.0$ and the damping described in the text. (b) Dielectric spectra of a mixed chain showing two main modes plus many weaker peaks in both the transverse and longitudinal spectra.

all y, but note here that experiments clearly show fine structure like that described above, suggesting that two-mode behavior is an approximation and that any complete model must be able to exhibit more than two modes for a mixed crystal.

4. Dependence of modes on ion distribution

The figures discussed above with impurity concentrations up to 12.5% show several features which are specifically mixed crystal or high-concentration effects. The spectra deserve extra comment on two points related to the validity of the actual model used here. First, we stress that the calculation for Fig. 22(c) and Fig. 24 are based on a 48-atom GaAs chain with three As ions replaced by three P ions. Three localized modes appear. We could have achieved 12.5% P by using a 96-atom GaAs chain with six P ions, in which case there would be six local modes. The longer chain would reveal a very similar dielectric spectrum near the main mode and the local mode, however, once broadening was included. There would be more peaked structure below 220 cm^{-1}. The 48-atom chain has individual modes about 20 cm^{-1} apart in this acoustic band region. The broadening we have chosen does not cause such widely spaced modes to merge into a continuum of absorption which calculations on much longer chains show must exist. Genzel, Renk, and Weber (1965) have studied the linear chain with one defect analytically and find continuous absorption in the acoustic region in the limit of a very long chain. Their paper contains graphs of the absorption for various combination of mass defect, force constant defect, and charge defect in a NaCl linear chain model. In Fig. 26 their results for the dipole moment of the NaCl chain are reproduced for several cases of mass and force constant defect on the Na-ion site. Localized modes are ignored; only the band absorption is plotted. The continuous absorption within the acoustic and optic bands is clearly shown. A second

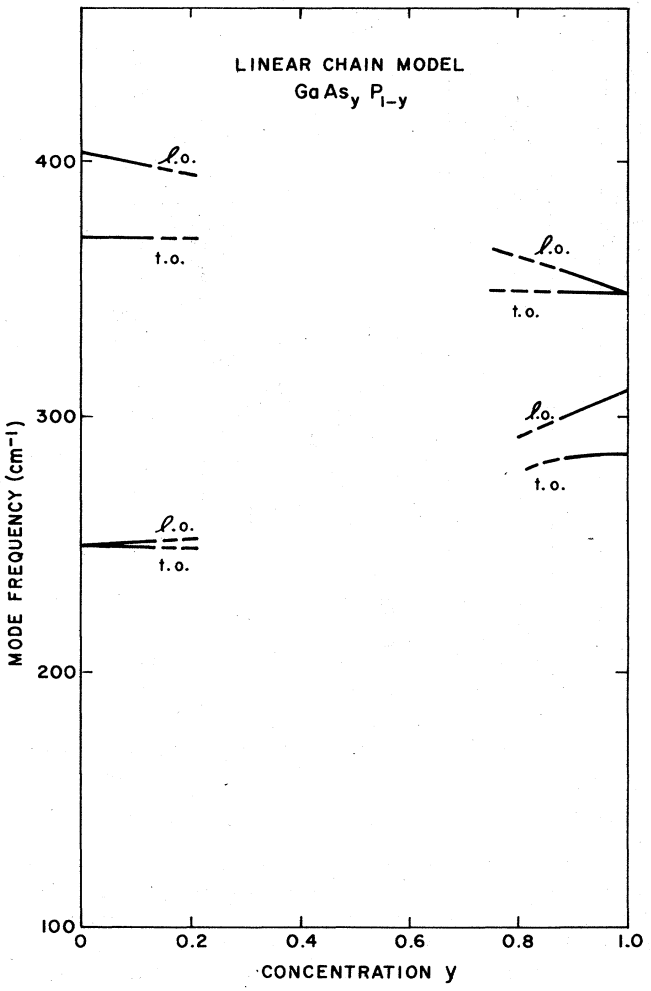

FIG. 25. Transverse and longitudinal mode frequencies near each end of the concentration range for the mixed chain of the preceding figures. Only the positions of the very strongest modes are plotted. This plot illustrates two-mode behavior.

point concerning the linear chain results has to do with the impurity-ion distribution. In one dimension as soon as two P ions are introduced, they partition the chain creating an "island" or cluster of GaAs between them. In three dimensions such islands are much less probable. "Island effects" are important and are predicted in three-dimensional mixed crystal models (Hori, 1968). Their probability of occurrence is far different in two- and three-dimensional systems. We merely stress at this point the importance of actual three-dimensional atomic arrangement in a detailed understanding of mixed crystal behavior.

A study of linear chain results for various compositions, various ion distributions, and various chain lengths suggests the following conclusions which are summarized in Fig. 27. For 12.5% P in GaAs the strongest mode is near 280 cm^{-1} and has an eigenvector which consists of Ga ions vibrating against As ions in all regions where As ions are two to three lattice spacings from P ions. The strong local mode at 349 cm^{-1} has an eigenvector which consists of the isolated P ions moving against their Ga neighbors in a localized mode, much as depicted in Fig. 7. The next strongest mode at 270 cm^{-1} is not highly localized but has largest amplitude for Ga vibrating against As in an island separated from the rest of the crystal by P ions. As Fig. 27 shows, the two most important islands are P–Ga–As–Ga–As–Ga–P and a P–Ga–As–Ga–P island with resonance near 250 cm^{-1}. Hori (1968) and his collaborators have discussed extensively the occurrence of islands and the spectral peaks which result from their vibrations. Our main point here is that these peaks are a characteristic mixed crystal effect, since it takes many impurity ions to isolate islands of host material. Some of the less localized modes have eigenvectors which resemble modes 24 or 25 in Fig. 3, i.e., the zone boundary modes of the perfect crystal. These kinds of modes may be described as perturbed zone boundary modes made active by the impurity-induced disorder. Finally, many of the weaker peaks below 200 cm^{-1} in Fig. 27 are characteristic of the short chain used here. These peaks can be expected to merge into a smooth absorption continuum in more realistic models, as has been mentioned above.

To conclude our discussion of the 12.5% mixed crystal we note that for the calculations presented thus far the ions were carefully distributed with always at least one As ion between adjacent P ions. If two P ions are allowed to fall on neighboring anion sites, there is a strong interaction between the ions, causing the local mode peak near 349 cm^{-1} (Fig. 27) to split. For two neighboring P-ions and a third more distant P-ion there are three peaks at 332, 349, and 360 cm^{-1}. The highest peak at 360 cm^{-1} contains two-thirds of the local mode strength and is a pair mode with the two P ions moving in phase. The isolated P ion still gives a mode at 349 cm^{-1}. The second member of the pair mode is infrared-inactive and is repelled to a frequency of 332 cm^{-1} well below the isolated local mode frequency. Dean (1967) has given an analytic treatment of pair modes for the monatomic chain. Figure 28 shows a plot of localized mode frequency for both the isolated atom defect and the two adjacent-atom defect. If two impurity atoms are inserted into the chain many lattice spacings apart, they can both vibrate independently in localized modes and both will have the same frequency given by the dashed curve in the figure. The strong repulsion of the two eigenfrequencies when the two isolated defects are placed together is evident from the figure.

The large effects associated with adjacent-pair defects and the island modes discussed above show that in forming a mixed crystal model we must carefully consider the distribution of ions, i.e., their order. Kittel (1968) has given a discussion of order under the heading "Elementary Theory of Order" in his Solid State Physics text. Space does not permit a discussion here of atom arrangements in three dimensions, but we will briefly consider possible structural configurations of a real GaAs$_y$P$_{1-y}$ mixture. We take the Ga sublattice to be perfect, and so we are really discussing the binary alloy As$_y$P$_{1-y}$ whose atoms must be distributed over an fcc lattice. Two extremes of behavior are at once apparent. There can be complete segregation where all of the As atoms cluster in one region and all the P in a second region. All second-neighbor anion-anion bonds in the alloy are then As–As or P–P except for the few across

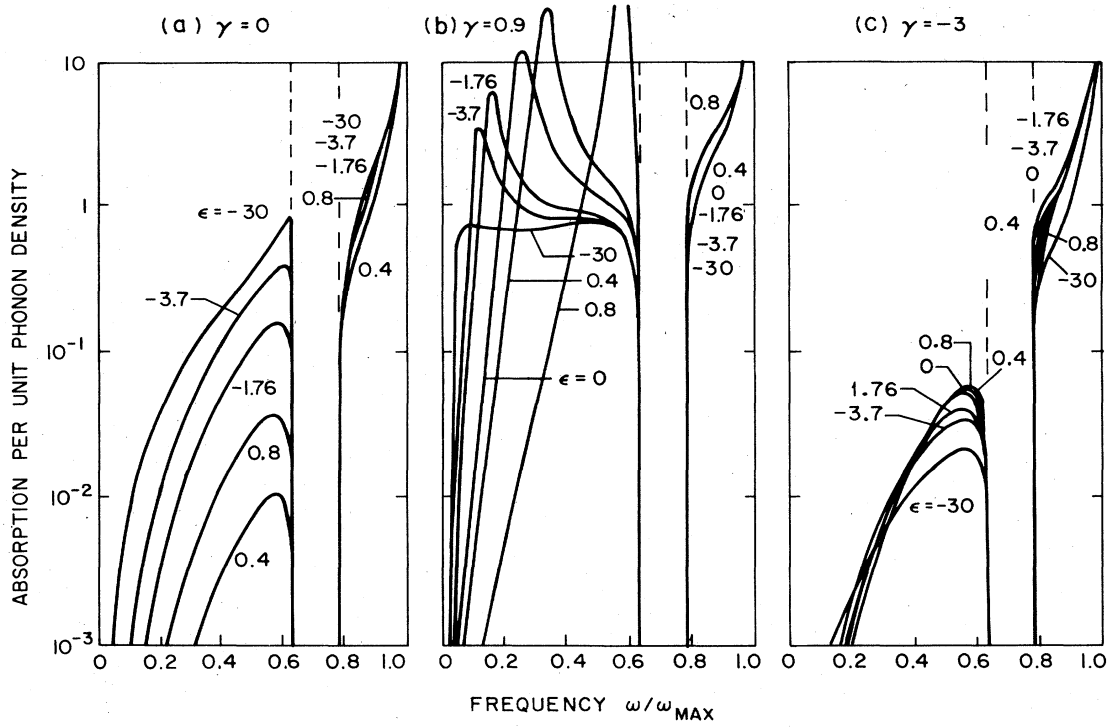

FIG. 26. Absorption spectra of band modes for a defect in an NaCl chain. γ and ϵ specify the force constant defect and mass defect, respectively, for the Na-ion site. Note the dramatic change in the spectral shape for a softened force constant in (b). Reproduced from Genzel *et al.* (1965).

the interface separating the regions. For this extreme of behavior the word "alloy" is inappropriate. The other extreme of behavior is the alloy with perfect long-range and short-range order for which $y = 0.25$ or $y = 0.75$ and cubic symmetry is preserved. The available sites divide into two unique groups: the face centers and the cube corners. Putting As ions on all face centers and P ions on all cube corners gives $GaAs_{0.75}P_{0.25}$. This structure can repeat indefinitely in space. In this structure, half of the anion–anion second-neighbor bonds are As–As and half are As–P. There are no P–P bonds. These are far different proportions than for the segregated mixture of the same composition described above. fcc alloys of $Cu_{0.75}Au_{0.25}$ have been studied and found to exhibit the type of order described here, but with a transition to a more disordered state as the temperature is raised.

The partially disordered state covers the considerable intermediate ground between the extremes mentioned above. The appropriate parameters used for its description are short-range order probabilities. For example, if we pick a P ion in the $As_{0.75}P_{0.25}$ ordered alloy, the probability of finding an As ion as nearest neighbor is 1.0, and as second-nearest neighbor is 0. In the segregated mixture these probabilities are both zero. We can picture an almost random alloy where this probability approaches 0.75 for far-distant neighbors. There is not enough energy gained from this configuration to force the whole crystal into this pattern. Probability considerations such as these play an important part in models for $GaAs_yP_{1-y}$ developed by Verleur and Barker (1966). The atomic arrangement of a real crystal may depend on conditions of growth as well as on the thermodynamic energies of certain configurations. For example, $GaAs_yP_{1-y}$ can be grown by vapor transport utilizing P_2 and P_4 molecules. It is easy to visualize localized clusters of P ions if a P_4 molecule arrives at the growth interface and the growth continues at a high rate with insufficient annealing to allow ion motion and exchange. Because of the dependence of the vibration frequencies on atomic arrangement, lattice spectra provide an important tool for studying atomic order.

F. Other mixed crystal models

1. The virtual-ion model

Figure 29 shows a linear chain virtual-ion model for $GaAs_yP_{1-y}$. There is no disorder since in this model all the anions are identical virtual ions with mass;

$$m = (y)75 + (1 - y)31 \text{ amu}. \tag{2.14}$$

At the bottom of the figure the mode frequencies are plotted as a function of concentration. At each concentration there is one doubly degenerate transverse mode and one longitudinal mode, i.e., one reststrahlen band. The mode frequencies decrease monotonically from pure GaP to pure GaAs with a downward curvature. The virtual-ion model is not applicable to $GaAs_yP_{1-y}$ since experimentally this mixed crystal shows two main reststrahlen bands. The model does qualitatively fit the spectra of mixed $Ba_ySr_{1-y}F_2$. For a detailed fitting in this latter case the virtual ion is described by an average mass (2.14), as well as averaged force constants and averaged effective charges, since these latter pa-

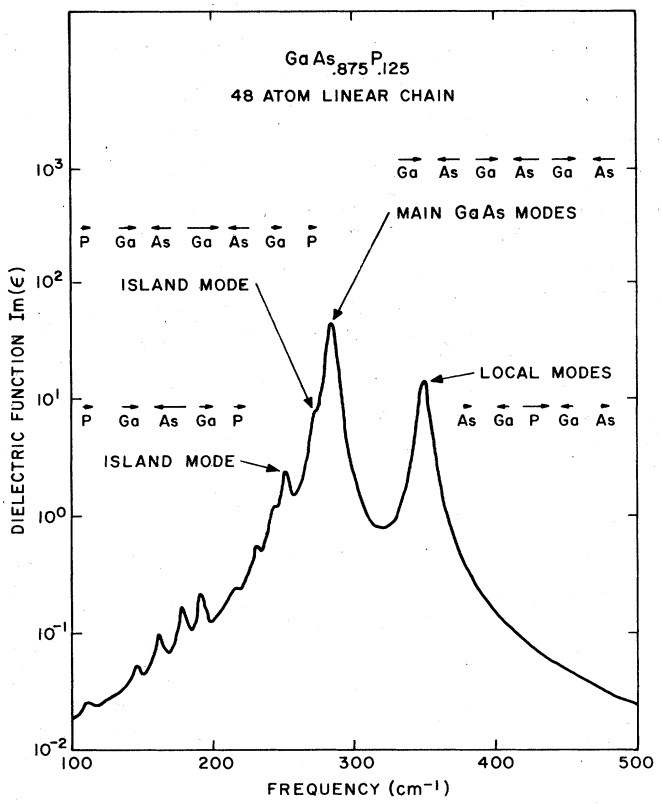

FIG. 27. Modes and eigenvectors in a mixed GaAs–GaP chain model. Besides the main GaAs-like mode and three almost degenerate and identical P-ion local modes (only one local mode eigenvector is shown), there are two strong island modes.

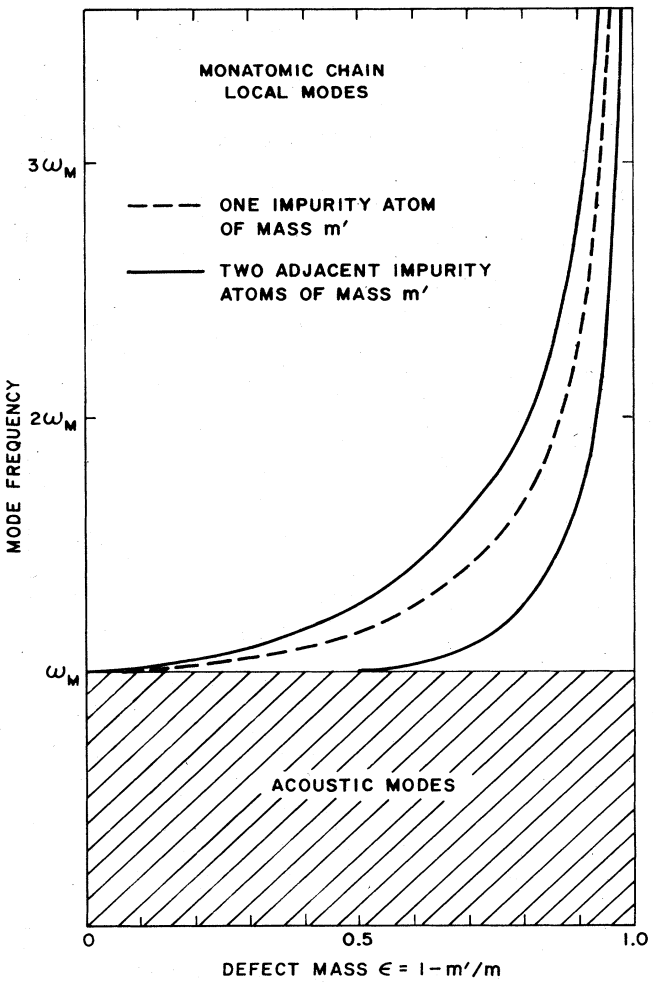

FIG. 28. Local mode frequencies for both a single and two adjacent light impurities in a monatomic chain calculated for the isotope model. The highest-frequency mode is symmetric and hence Raman-active but infrared-inactive, while the other local mode has reversed activity.

rameters are not the same in BaF_2 and SrF_2. A linear chain model of a mixed crystal where the two components have almost equal mass shows one main band of absorption at all concentrations plus weak subsidiary structure. The virtual-ion model is therefore a useful approximation for such cases if the weak structure can be ignored.

2. Isodisplacement models

A slightly more complicated model which gives two-mode behavior and can thus predict the gross behavior of $GaAs_xP_{1-x}$ has been proposed by Chen, Shockley, and Pearson (1966). To motivate this type of model, we note that in a diatomic crystal with perfect regularity equations for the long-wavelength ($q \approx 0$) modes can be written

$$m_g \ddot{x}_g = -k(x_g - x_p) + z_g E, \tag{2.15}$$

$$m_p \ddot{x}_p = -k(x_p - x_g) + z_p E. \tag{2.16}$$

We choose notation appropriate to gallium phosphide, write one-dimensional equations, and absorb local field effects into the coefficients so that E is the macroscopic electric field. x_g is the displacement of the Ga ion in every unit cell. The Ga ions all have the same displacement ("isodisplacement") since this is the definition of the $q = 0$ mode to which we have restricted ourselves. For the mixed crystal $GaAs_yP_{1-y}$ the equations of the isodisplacement model are

$$m_g \ddot{x}_g = -(y)k_a(x_g - x_a) - (1-y)k_p(x_g - x_p) + z_g E, \tag{2.17}$$

$$m_a \ddot{x}_a = -k_a(x_a - x_g) - (1-y)k_2(x_a - x_p) + z_a E, \tag{2.18}$$

$$m_p \ddot{x}_p = -k_p(x_p - x_g) - yk_2(x_p - x_a) + z_p E, \tag{2.19}$$

$$P_{\text{ion}} = \frac{x_g z_g + (y)x_a z_a + (1-y)x_p z_p}{V}. \tag{2.20}$$

Here P_{ion} is the lattice mode contribution to the polarization, and V is the unit cell volume. These equations are arrived at by assuming that Ga ions, P ions, and As ions are still isodisplacive in the mixed crystal. The force constants are weighted in the obvious manner by (y) or $(1-y)$ corresponding to the number of bonds each ion sees (Verleur and Barker, 1966; Chen *et al.*, 1966; Barker, 1968b). Equation (2.18) can be multiplied by (y), and (2.19) multiplied by $(1-y)$ to obtain a more natural set of equations with a symmetric force matrix. Note that k_2 is a second-neighbor (anion–anion) force constant which must be included to obtain a reasonable fit

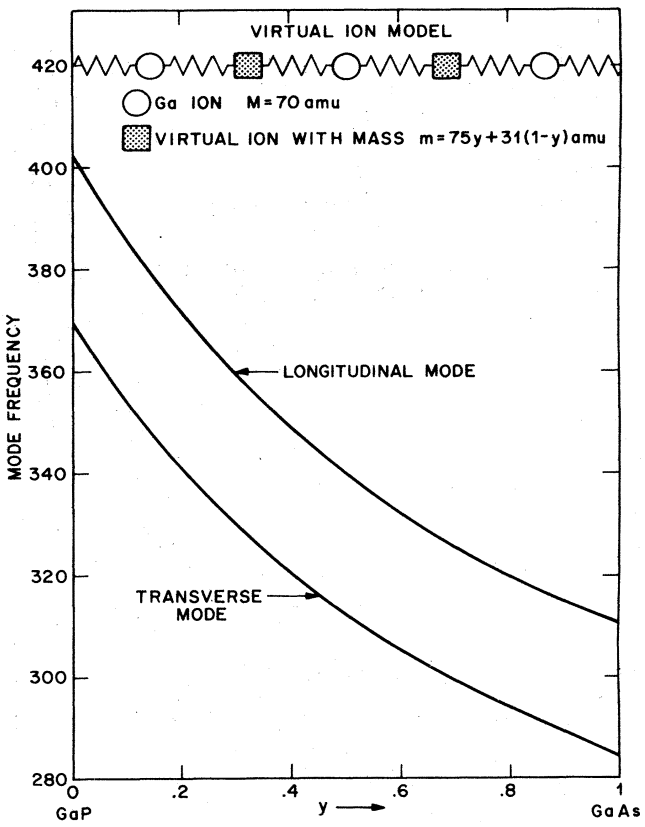

FIG. 29. Linear chain virtual-ion model of the mixed crystal $GaAs_yP_{1-y}$. The masses are given in the figure and force constants and charges in Table II.1.

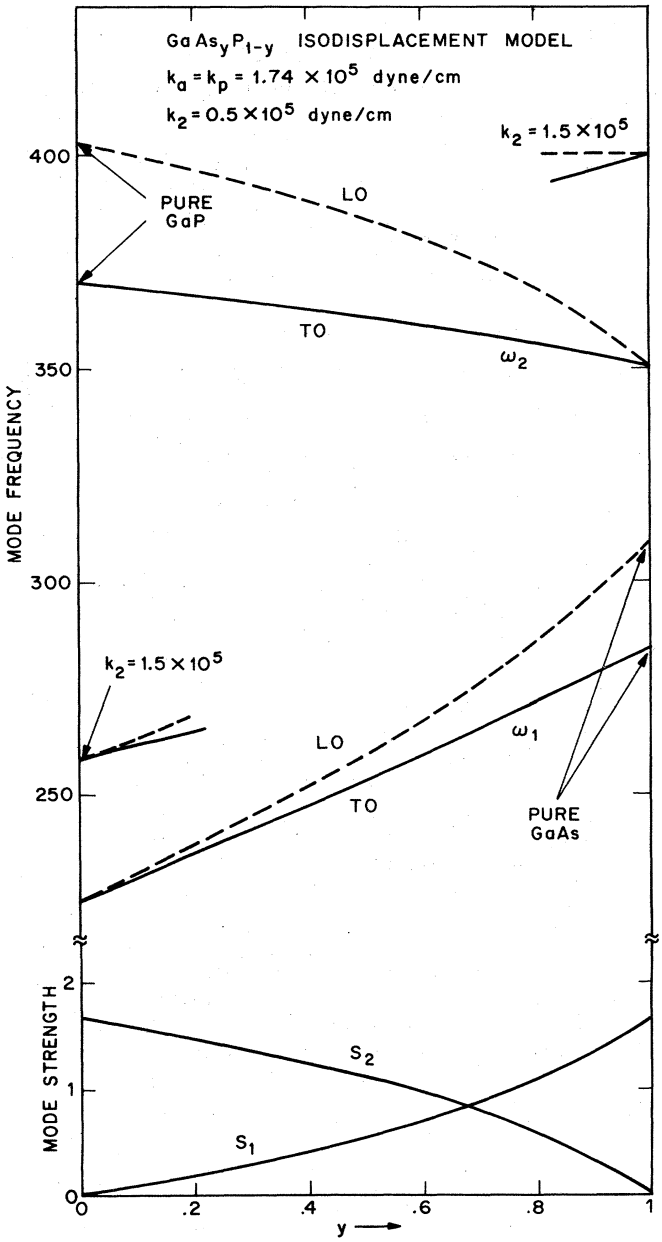

FIG. 30. Transverse and longitudinal mode frequencies of $GaAs_yP_{1-y}$ calculated with a three-coordinate isodisplacement model. In this simple example the force constants are fixed at the values shown in the figure, independent of concentration. Note that a larger value of k_2 raises the end points ("local modes") of the curves but not the main modes of pure GaAs or pure GaP. The lower part of the figure gives the transverse mode oscillator strengths of each band.

to the measured spectra of $GaAs_yP_{1-y}$. Figure 30 shows the modes obtained for $GaAs_yP_{1-y}$ using (2.17) to (2.20) with $\epsilon_\infty = 9$. The force constants are given in the figure. For simplicity we have chosen $k_a = k_p$ just as we did for the mixed crystal chain model. The parameters of Table II.1 are used and the optic mode frequencies evaluated from the poles and zeros of ϵ. The weak high-frequency mode observed as $y \to 1$ near 350 cm^{-1} (Fig. 30) has been called the phosphorus local mode (Verleur and Barker, 1966; Chen *et al.*, 1966). Strictly speaking, a localized mode cannot be defined within this model since there are no significant spatial coordinates. The eigenvector at $y = 0.99$ for the highest-frequency mode is $(x_g, x_a, x_p) = (0.008, -0.002, -1.384)$, which fits our intuitive picture of the localized mode—predominantly P vibrating against Ga. Similarly, the 225 cm^{-1} mode near $y = 0$ is suggestive of an As local mode, though the model is not complete enough to verify that this mode is localized, nor can we calculate whether this mode comes within a gap in the GaP density of states.

Chen *et al.* (1966) have given arguments for making the force constants in (2.17)–(2.19) depend on concentration because of the dilation of the average cell dimension as As is added to GaP. This procedure is necessary to obtain good fits in many cases. Verleur and Barker (1966) have noted that k_2 in (2.18) and (2.19) arises from including local field effects as well as from short-range forces. The actual short-range second-neighbor forces are found to be negative in shell models used to fit pure GaP and pure GaAs, while k_2 is usually positive in fits to actual mixed crystals. The above points merely emphasize that the force constants and charges in (2.17) to (2.20) are effective constants which may be difficult to relate to microscopic parameters. A major point worth emphasizing here is that this isodisplacement model exhibits two TO modes. It can exhibit no more since there are only three coordinates, and hence three de-

grees of freedom.[7] Verleur and Barker (1966) originally considered this model, then proposed a generalization of the model with more coordinates. They distinguish five different isodisplacive Ga-ion sublattices depending on whether a Ga ion is surrounded by four, three, two, one, or zero As ions. With many more coordinates they find many more modes and can thus fit the fine structure discussed previously. Their model simplifies to the model presented here if the five Ga coordinates are set equal by artificially joining all Ga ions with rigid rods so that there is only one unique Ga ion displacement, and similarly for the P ion and As ion coordinates. Because of the complexity of the model some later authors have called it a cluster model and mistakenly described it as being different from an isodisplacement model.

3. Five models of the mixed crystal

We conclude this introductory section on mixed crystals by computing the spectrum of a 50:50 mixed crystal by five different methods. The reflection spectra are shown in Fig. 31. In (a) a 48-atom chain has been used with the occupancy of anion sites determined by tossing a coin (heads—a P ion; tails—an As ion). We call this random occupancy. There are 46 active modes though some are negligibly weak. Modes which occur in forbidden regions between or above the band phonons of pure GaAs or GaP are somewhat localized. A few of the modes can be identified as vibrations of islands of GaAs or GaP. The spectrum clearly shows two main reststrahlen bands plus fine structure. Next a chain was generated using a conditional probability which favors different anions being next to each other. The actual anion sequence is given in the figure, with a and p used to represent As and P ions respectively. There are now four strong reststrahlen bands plus some additional weak structure as shown in (b). In Fig. 31(c) the spectrum of an ordered 48-atom chain has been calculated. Here the anion occupancy is As–P–As–P–As–P, etc. Such a chain may be viewed as a model of a crystal of perfect regularity with a four-atom primitive cell. There are three long-wavelength optic modes, two of which are infrared active, hence the two reststrahlen bands shown. The fourth model of the mixed crystal we consider is a virtual-ion model. The anion has a mass which is the average of the As- and P-ion masses. One mode obtains as was discussed for Fig. 29. Finally, in part (e) of Fig. 31 the isodisplacement model, discussed in the preceding section, is solved at $y = 0.5$. Two transverse and two longitudinal modes obtain causing two reststrahlen bands as shown in the figure. Models related to all five types in Fig. 31 have been used to fit vibrational spectra in mixed crystals.

G. Models for amorphous solids

Linear chain calculations may be used to model an amorphous or glasslike solid. Here the composition is regular but there is positional disorder. A study of (2.1) shows that in fact these equations, where x_j refers to displacement from equilibrium, do not depend on the disorder in equilibrium positions. The disorder must enter the equations through a distribution of force constants k. Two atoms which are close together would be expected to have a large force constant for the bond linking them, while two neighboring atoms which are

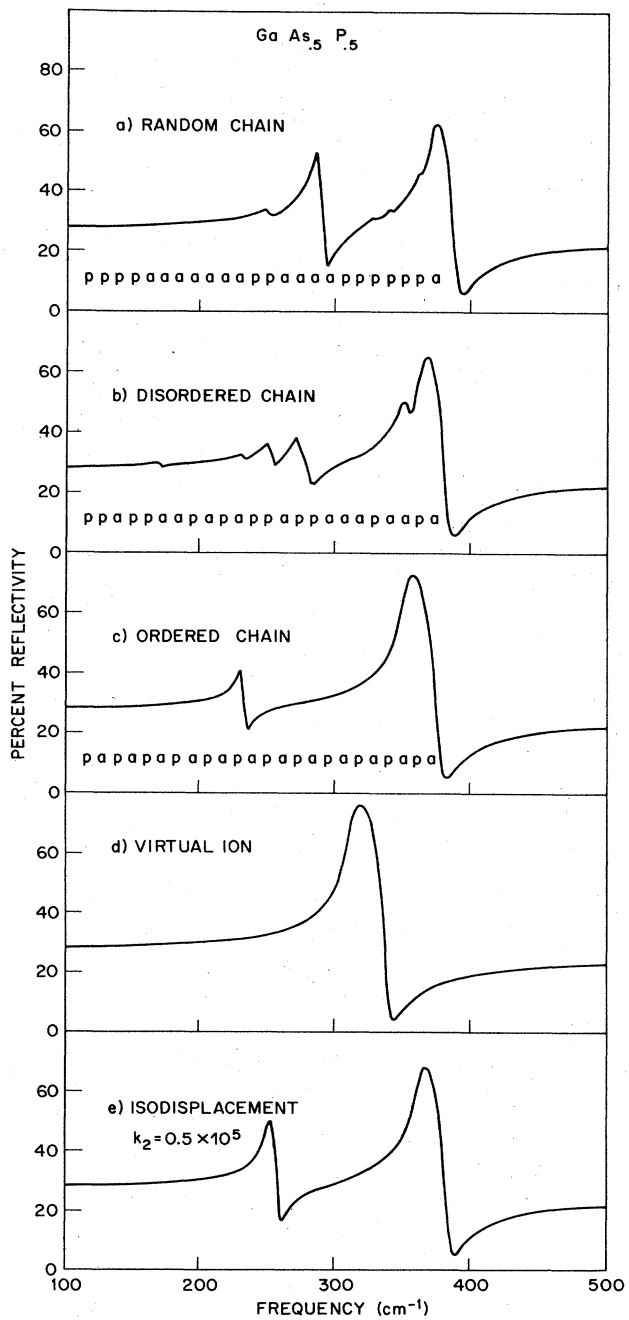

FIG. 31. Five different models for the reflection spectra of $GaAs_{.5}P_{.5}$. In (a), (b) and (c) a linear chain model is used with the ions distributed with different kinds of order as indicated in the figure. (d) shows the virtual-ion result and (e) the isodisplacement model result of the preceding figure. Some damping has been added to each mode in the figure to give realistic spectra.

[7] The model actually gives three modes, one of which corresponds to the $q = 0$ acoustic mode and has zero frequency.

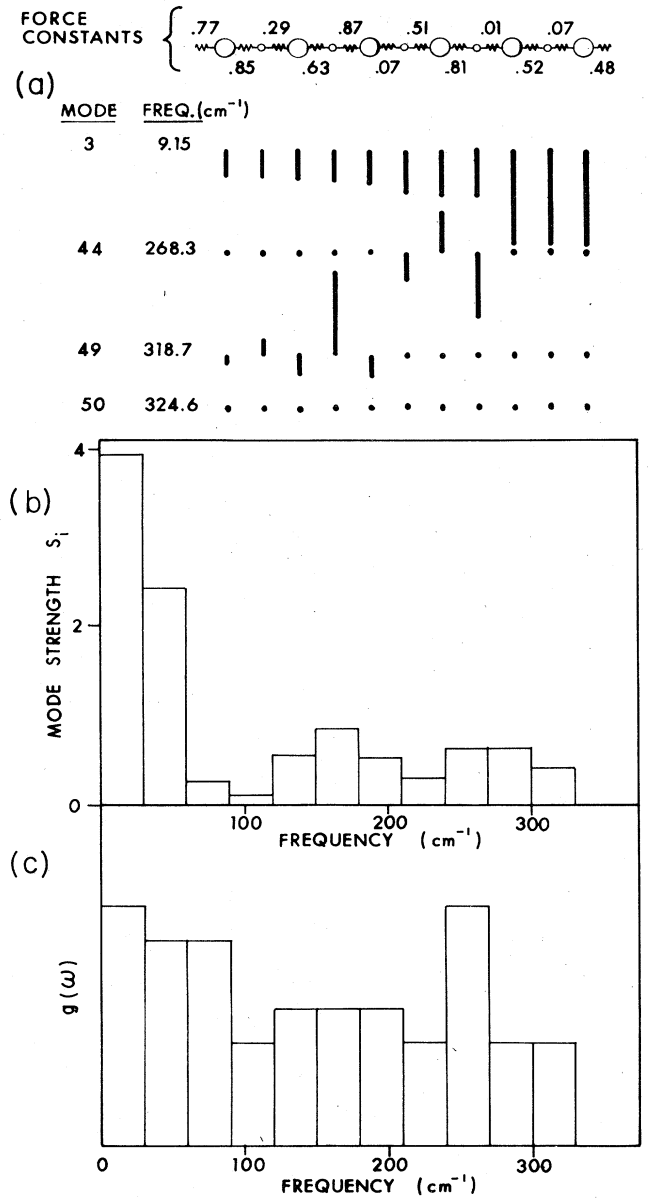

FIG. 32. Fifty-atom diatomic chain model with force constants chosen randomly from the range 0.01 to 0.87×10^5 dyne/cm and masses and charges of GaP. (a) shows a portion of the chain and four eigenvectors. The high-frequency modes are all localized. Mode 50 is localized 9 atoms to the left of the portion of chain shown here. (b) Gives the total mode strength in each 30 cm^{-1} interval. Total mode strength is not conserved here when the forces are varied. (c) The density of states shows many low frequency modes and no gap (c.f., Fig. 4).

much farther apart than the average spacing must be linked by a weak force constant. In Sec. X we discuss the situation where the bond presents a tunneling barrier rather than a harmonic barrier to motion of an atom. Such an anharmonic bond cannot be included within our technique, which assumes simple harmonic time dependence to allow the matrix inversion for the modes. Dyson (1953) has presented one of the earliest studies of the effects of random masses and random force constants on the dynamics of a linear chain. That work emphasizes exact calculation of frequency distributions, but does not examine eigenfunctions or mode strengths. Calculations for 50-atom chains with a range of force constants using Eq. (2.1) immediately show several facts. First, all modes become active in optical spectra. Figure 32 shows the infrared spectrum for a 50-atom diatomic chain. Second, the spectral pattern of mode activity (infrared or Raman) is exceedingly complex. It appears impossible to factor the optical spectra into a density-of-states factor times a slowly varying optical matrix element factor. Third, the lower-frequency portion of the spectrum consists of entirely delocalized modes, while the high-frequency region is entirely localized. The high-frequency modes typically consist of an island of three or four atoms vibrating against each other, with all other atoms remaining almost stationary.

We have used a table of random numbers to generate a set of force constants for the GaP chain. Forces between 0.01×10^5 and 0.87×10^5 dyne/cm are allowed. Spectra of real materials show that amorphous solids do possess a range of force constants. The solid does not, however, have any significant number of force constants above a certain upper limit—typically the equivalent force constant in the related crystalline modification. Figure 32 shows a calculated spectrum. Four eigenvectors are shown to depict the localization described above. Calculations with different choices of force constants only confirm the points made above. The linear chain allows unphysical features to appear, as has been noted earlier in Sec. II.E.4. There, islands were created by mass defects. Here a small force constant can partition the chain. We note the unusual effect of the weak force constant $k=0.01\times10^5$ on mode 3 (see figure). Such effects would be rare in three dimensions. The linear chain model appears useful only to introduce the subject of vibrations in amorphous solids. More realistic models must be much more complex. Unfortunately, the additional complexity usually makes rather tedious the examination of eigenfunctions in detail as we have done for the various chain models. Such models are discussed more fully in Sec. X.

III. GREEN'S FUNCTIONS FOR THE LATTICE VIBRATION PROBLEM

A. The simple two-atom lattice

1. The perfect lattice

In this section we give an elementary discussion of classical Green's functions for the lattice vibration problem. The use of Green's functions is essentially a method of solution for the equations of motion such as given in (2.1). The methods have been developed by Lifschitz, by Montroll and Potts, and by Maradudin and co-workers. A review article that is convenient for our purposes has been written by Elliott (1966). Of the several types of Green's function, we discuss only the classical Green's function or response function for the lattice. The full treatment of the Green's function method for lattices with defects lies properly within the scope of a theoretical review article. Such treatments may be found in the article by Elliott and in the recent review by Elliott, Krumhansl, and Leath (1974). There is a close correspondence between some of the aspects of the Green's function method and certain physical processes in a lattice vibration problem. We wish to illustrate these relationships and to derive the basic mass defect equation here using a very simple, but useful model.

We specialize the equations (2.1) to two particles with fixed boundary conditions. The model is shown at the top of Fig. 33

$$m\ddot{x}_1 = -kx_1 - k(x_1 - x_2) + F_1 , \tag{3.1}$$

$$m\ddot{x}_2 = -kx_2 - k(x_2 - x_1) + F_2 . \tag{3.2}$$

Assuming simple harmonic time dependence we search for solutions of the form $x_1\exp(-i\omega t)$, $x_2\exp(-i\omega t)$, with the forces

$$F_1 = f_1\exp(-i\omega t), \quad F_2 = f_2\exp(-i\omega t) .$$

Setting f_2 equal to zero we may solve for x_2 and substitute this in (3.1) to obtain

$$x_1 = f_1 \Big/ \left[2k - m\omega^2 - \frac{k^2}{2k - m\omega^2} \right] .$$

We define the classical Green's function as the mechanical response per unit force.[8] For the force applied to particle 1 we obtain

$$g(1,1,\omega) = x_1/f_1 = 1 \Big/ \left[2k - m\omega^2 - \frac{k^2}{2k - m\omega^2} \right] . \tag{3.3}$$

Note that the Green's function $g(1,1,\omega)$ is actually one element of a matrix. For the present simple model $g(2,2,\omega)$ has exactly the same form and represents the response of particle 2 to a force applied to particle 2 ($f_1 = 0$ and f_2 finite). The off-diagonal components of the Green's function response matrix simply represent the response of particle 2 to a force applied to particle 1 and vice versa. Figure 33 shows two of the Green's functions for the present system.

The Green's function g specifies the response of the system to a stimulus of arbitrary frequency. The natural modes of the system occur at the poles or resonances of g. From (3.3) there are two resonances which occur where

$$2k - m\omega^2 - k^2/(2k - m\omega^2) = 0. \tag{3.4}$$

It is easy to show that (3.4) is identical to the result obtained by setting the determinant of coefficients of x_j in (3.1) and (3.2) equal to zero. We do not pursue the determinant method since it avoids the introduction of g and lacks the extension to defect cases discussed below.

It is important to realize that the response function g has real and imaginary parts. For the simple model, specified by (3.1) and (3.2), the imaginary part of g consists of δ-functions centered on the resonant frequencies. To illustrate some of the points to be discussed below it is convenient to introduce a small amount of damping of the form $-\gamma m\dot{x}_j$ in (3.1) and (3.2). Such damping terms broaden each δ-function into a peak which is more easily plotted. Figure 33(b) shows the imaginary part of the Green's function for the case where γ is chosen to be approximately 1/10 of the resonant frequency. Finally, we note that the spectrum of the imaginary part of the Green's function in fact gives information on the density of states of the vibrating lattice. That is, it yields a peak at each normal mode of the lattice. From Fig. 33(b) it is apparent that the peaks are not properly normalized in the Green's function, the low-frequency peak appearing with greater weight than the upper peak. A weighting factor of ω corrects this feature and we find that the density of states is given by[9]

$$\nu(\omega) = (2m\omega/\pi)\,\mathrm{Im}[g(1,1,\omega)] . \tag{3.5}$$

Since the Green's function is a response function, its real and imaginary parts are connected by the Kramers–Kronig relations (Kittel, 1958). Thus from (3.5) a knowledge of the density of states of the lattice allows us to recreate the entire Green's function, both real and imaginary parts.

2. Defects in the two-atom lattice

For the simple two-particle model considered in the above section we may change any mass or any force constant and solve exactly for the new frequencies. To illustrate the Green's function method, however, we separate out the change in mass or force constant as a defect. Let us consider a change in mass of particle 1 by an amount δm

$$m \to m' ,$$

$$m' = m + \delta m . \tag{3.6}$$

Conceptually, we regard the δm term as an additional

[8] In contrast to the previous section, g and G are used here for Green's function in the perfect and in the perturbed lattices, respectively.

[9] Some authors include the mass in the definition of g so that m does not appear explicitly in the density of states expression. In three-dimensional problems, g has vector subscripts describing the direction of x_1 and f_1. In that case a trace over the vector subscripts is required in (3.5).

force which is driving the otherwise perfect lattice. Assuming simple harmonic time dependence, as before, the response of particle 1 is given by

$$x_1 = f_1 \Big/ \left[2k - m\omega^2 - \frac{k^2}{2k - m\omega^2} - \delta m\omega^2 \right] . \tag{3.7}$$

The value of separating m' into m plus the defect δm is now apparent; except for the δm term the denominator can be identified with the Green's function for the unperturbed lattice. Taking advantage of this identification we write (3.7) in the form

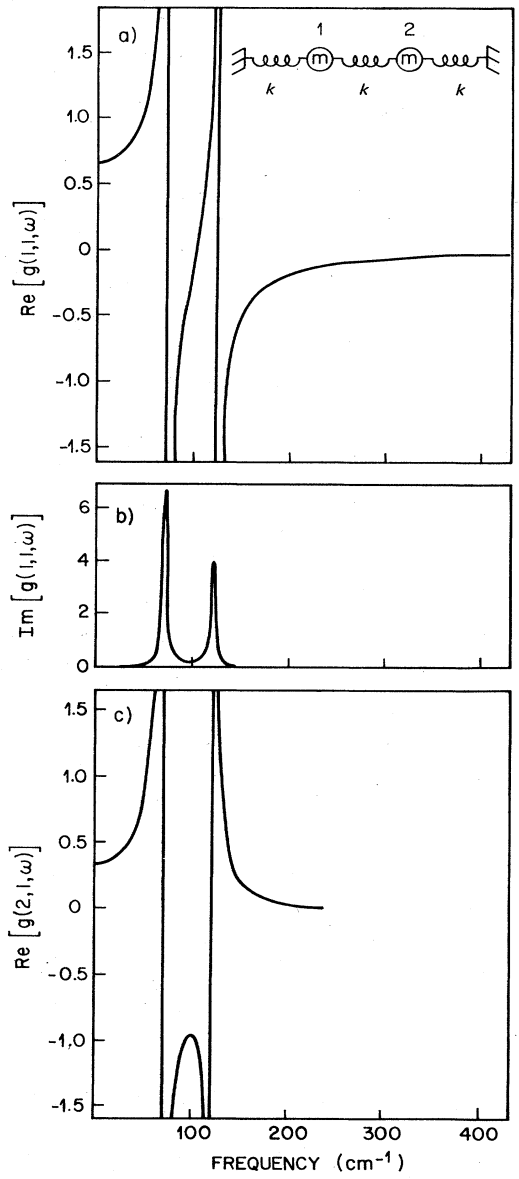

FIG. 33. Green's function for a one-dimensional two-atom system. The model is shown in the inset. (a), (b) show the Green's function $g(1, 1, \omega)$ which exhibits two resonances at $\omega_1 = 122$ cm^{-1} and $\omega_2 = 70.4$ cm^{-1}. (c) shows the response $g(2, 1, \omega)$ of atom 2 to a force applied to atom 1. This and the following figure use $k = 5000$ dyne/cm and $m = 17$ amu.

$$x_1 = f_1 / [\, 1/g(1, 1, \omega) - \delta m\omega^2] . \tag{3.8}$$

From (3.8) we can immediately write the condition for a resonance of particle 1 (i.e., the pole in the response) as

$$g(1, 1, \omega) = 1/\delta m\omega^2 . \tag{3.9}$$

Note that (3.9) is exact. It does not result from a perturbation expansion. It has the correct form for $\delta m \to 0$ which causes reversion to the unperturbed lattice problem. For finite values of δm (positive or negative) the new resonances occur where the unperturbed lattice Green's function $g(1, 1, \omega)$ crosses the "mass defect curve" $1/\delta m\omega^2$. Here (3.9) is the equation for modes in the defect crystal based on the mass defect or isotope assumption. In order to make contact with the literature we introduce the mass defect parameter ϵ which was used in Sec. II ($\epsilon = -\delta m/m$) and rewrite (3.9) to obtain the commonly quoted form

$$1 + m\epsilon\omega^2 g(1, 1, \omega) = 0 . \tag{3.10}$$

Given the Green's function of a lattice, solutions of (3.10) describe all the new modes which occur when a mass defect described by ϵ is introduced at one atom site. While the details of Green's function calculations may often be extremely complicated and tedious in their intermediate steps, there is clearly some direct physical content in (3.9) and (3.10). The unperturbed Green's function (3.3) tells us how soft the lattice is at a certain atom site. It gives the stiffness (mechanical impedance) of that site as a function of frequency. We can imagine measuring such a stiffness by reaching into the lattice with microscopic tweezers, shaking the atom, and observing the force required. The right side of (3.9) is the required stiffness of a defect mass δm if it is to vibrate at a given frequency. These two stiffnesses must match if the defect is to have a natural resonance.

Figure 34(a) shows a graphical solution of (3.9) for two cases of mass defects in the two-atom model. The dot–dash line in the figure is the mass defect curve for a heavy atom replacing the host atom on site x_1. We note that (3.9) is satisfied at two frequencies which are displaced below the original host lattice modes. That is, the graphical method has found two frequencies where the stiffness of the host lattice matches the stiffness of the heavy atom. Therefore, as expected, the addition of a heavier atom lowers the normal mode frequencies of the lattice. There can be only two resonances because our equations possess two degrees of freedom. Note that no matter how heavy the defect atom is made, the higher of the two new modes can never be displaced below the unperturbed lattice resonance near 70 cm^{-1}. The pinning of the new modes between the modes of the original unperturbed lattice was first discussed by Lord Rayleigh and is precisely stated in one of the many Rayleigh theorems on the vibrations of a collection of particles (Maradudin, Montroll, and Weiss, 1963). Note that for a heavy substitution one mode can be displaced all the way down to zero frequency for this model.

The dashed line in Fig. 34(a) results from considering a light substitution on the x_1 lattice site. The curve is drawn for $\delta m = -0.75$ m. Again there are two new modes and again all the modes but one are pinned (Rayleigh's

theorem). Note that the highest mode for increasingly large $|\delta m|$ can be made to resonate at an arbitrarily high frequency.

Figure 34(a) appears to show four solutions, i.e., there are four crossings of the curve $1/\delta m\omega^2$ with the real part of the Green's function. The Green's function $g(1,1,\omega)$ has real and imaginary parts as noted above, and this fact must be recognized in evaluating the resonance condition (3.9) or (3.10). Neglect of this point has sometimes led to erroneous results and the prediction of localized modes which cannot possibly exist. We recall from (3.7) that our procedure was to search for resonances in the system. Equation (3.9) was the resonance condition which leads to a pole in the response of particle x_1. This equation is complex, so that Fig. 34(a) which shows a plot of the real part does not tell the whole story. When searching for sharp resonances, the free variable ω at the solution point must be real or at most have a very small imaginary part. Consider the crossing of the two curves at the point n in Fig. 34(a). At this point we have a solution for the real part of (3.9). Note, however, that the Green's function g at the frequency n has an extremely large imaginary part shown in Fig. 33(b). The imaginary part of (3.9) has no solution near the point n. The potential solution suggested by the graphical method based on drawing the real part of g must therefore be discarded. This is a quite general rule for graphical solutions based on the real part of the response function; the crossing of a solution curve with nearly vertical portions of the Green's function does not result in a solution. This point can be further reinforced by going to the full Green's function for the perturbed lattice. From (3.7) we obtain directly for the Green's function G for the lattice with the defect included on atom site x_1

$$G(1,1,\omega,\delta m)=\frac{g(1,1,\omega)}{1-\delta m\omega^2 g(1,1,\omega)}\,. \tag{3.11}$$

The resonances of the defect may be examined by plotting G rather than examining only the resonance condition (3.9) which arises from setting the denominator equal to zero. Figure 34(b) shows a plot of the imaginary part of G. We plot the case $\delta m=-0.75$ m (i.e., a light impurity atom). Only two modes appear and we note that they occur where the mass-defect graph $1/\delta m\omega^2$ intersects the curved portions of the Green's function g. There is no mode structure at the other crossings discussed above.

Figure 34(b) illustrates the general result that for a light atom substitution the localized mode lies at a frequency above all the original modes of the host lattice and also becomes extremely narrow. The linewidth of the mode for the present model is naturally dependent on the way the damping was introduced. In our calculations we have included damping from particle x_2 only. Qualitatively, however, the behavior is correct. As a localized mode splits off from the band of lattice modes, it participates less and less in the band vibrations and less and less in the damping processes as its mass decreases. It is an easy matter to show that the eigenvector of the high-frequency mode in the case of the light substitution deviates from the eigenvector $(x_1,x_2)=(1,-1)$ of the host lattice and approaches $(1,0)$ in the limit of defect-atom mass approaching zero. In this limit there is perfect localization.

The equations for determining the defect vibrations which we have exhibited in (3.9) and (3.10) have an extremely simple form. This simple form is retained only for a single mass defect. Intuition suggests that disturbing the mass of particle 1 should only require the introduction of the Green's function for particle 1, as we have found in (3.9). Changing a force constant between particle x_1 and x_2 disturbs the dynamics of both particles, and we can expect that the equation for the new resonances in the lattice must include $g(1,1,\omega)$ and $g(2,1,\omega)$. This turns out to be the case. For the pres-

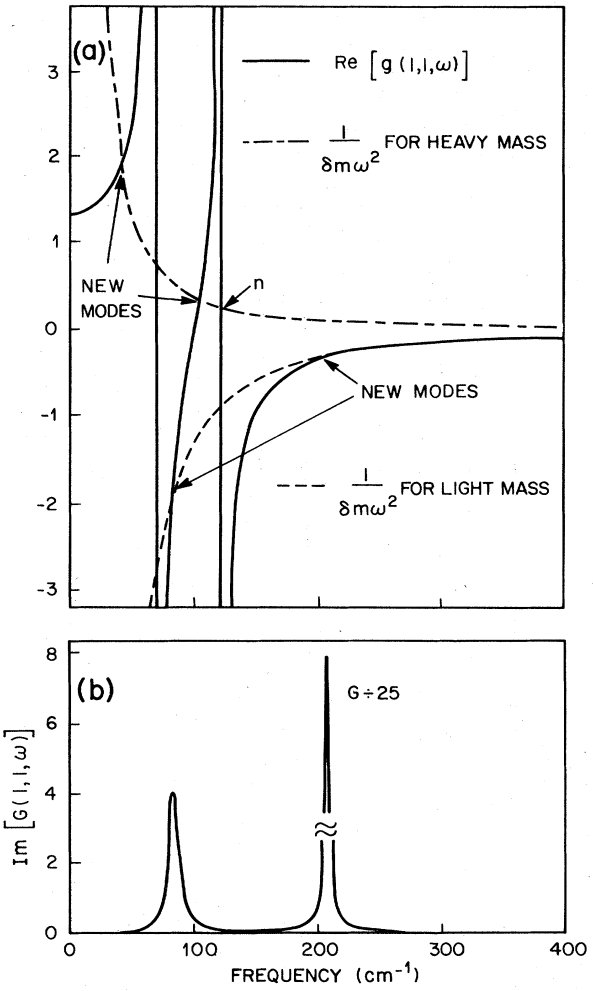

FIG. 34. Mass defect modes in the two-atom system. (a) A heavy mass with $\delta m=3m$ gives the dot-dash defect curve. The new modes occur at 41.7 cm^{-1} and 103.7 cm^{-1} where the defect curve intersects the pure crystal Green's function g. The dashed defect curve corresponds to $\delta m=-0.75m$ and gives modes at 83.5 cm^{-1} and 207.4 cm^{-1}. The intersection marked n (and the other similar intersection) yields no modes, as discussed in the text. (b) The Green's function for the defect crystal with atom 1 replaced by an atom with $\delta m=-0.75m$. The new resonances correspond to the dashed curve in (a). Note the large strength and narrow linewidth of the high-frequency mode, which is quite localized in the sense that atom 2 participates very little in the motion.

ent simple model the response of particle 1 for a force constant change can be written down explicitly, but the resonant denominator now contains complicated combinations of the two Green's functions mentioned. We do not illustrate any further solutions of defect problems here but merely note two points in constructing such solutions. First, the more localized the defect the simpler we can expect the structure of the equations to be. A defect which involves interactions between atom 1 and atoms up to five lattice sites away obviously involves a great many of the unperturbed lattice Green's functions, including $g(1,1,\omega)$ up to $g(1,5,\omega)$. Therefore, the more localized a defect the simpler the Green's function method becomes. Secondly, the method, while exact in principle, may require expansions or truncations in practice to obtain solutions. In spite of these practical restrictions on the method, it remains the most important theoretical tool in analyzing defect problems. It is worth noting that neutron scattering from crystals, Raman scattering, and infrared absorption may all be expressed in terms of Green's functions (Cowley, 1966). In cases where the unperturbed Green's function g may be impossible to calculate from first principles, it may be derived from one or more experiments. This g may then be used in equations such as (3.9) or (3.10) to calculate the properties of a lattice with defects.

B. Extension to the infinite chain and to real crystals

In Sec. III.A we have shown that a two-atom lattice has a Green's function matrix with two resonances. The diagonal element $g(1,1,\omega)$ was written down explicitly in (3.3). By setting the denominator of g equal to zero we find that the two resonances occur at

$$\omega^2 = k/m,$$

$$\omega^2 = 3k/m.$$

The Green's function (3.3) may be rewritten using these normal mode frequencies in the form

$$g(1,1,\omega) = \frac{1}{2m}\left[1/(\omega_1^2-\omega^2)+1/(\omega_2^2-\omega^2)\right]. \tag{3.12}$$

The factor 1/2 arises from the fact that there are two atoms. It is fairly easy to show that for a chain of N equivalent atoms the generalization of (3.12) is

$$g(1,1,\omega) = \frac{1}{Nm}\sum_{j=1}^{N}\frac{1}{\omega_j^2-\omega^2}, \tag{3.13}$$

i.e., the Green's function is simply a sum over the N resonances of the chain (Spitzer, 1971; Elliott, 1966). The weighting factor 1 for each resonance arises because all particles are equivalent. In three dimensions the form of (3.13) is essentially preserved and the mass defect problem again takes the simple form

$$1+m\epsilon\omega^2 g(1,1,\omega)=0. \tag{3.14}$$

For lattices more complicated than the monatomic case, the weighting factor for each term in the sum (3.13) depends on the eigenvector of each mode. Such a dependence is easily illustrated for a zone boundary mode in the diatomic chain. At this mode frequency one type of atom does not move (see Fig. 3, mode 24). If this is a type 1 atom, then the weighting must be zero for this mode in the sum for $g(1,1,\omega)$. Elliott (1966) and others have given the expression for g for a general lattice.

To illustrate the mass defect local mode in more detail we examine the case of $g(1,1,\omega)$ for $N=10$. We also remove the fixed boundary conditions of the model of Fig. 33 and use periodic boundary conditions. In this case the lowest mode frequency is zero. Figure 35(a) shows the Green's function g. If a mass defect is introduced at one of the lattice sites, the curve $1/\delta m\omega^2$ is superimposed on the figure, and intersections are read off to obtain the new modes as before. For δm positive or negative, ten new modes are obtained. As with the two-particle case, all but one of the new modes are pinned between the perfect lattice modes. In the case of a light atom substitution, one intercept lies above the highest mode of the perfect lattice (here 100 cm^{-1}) and may be pushed up without limit by increasing the magnitude of $|\delta m|$ towards m. This mode is the localized defect mode which we expect intuitively for a light sub-

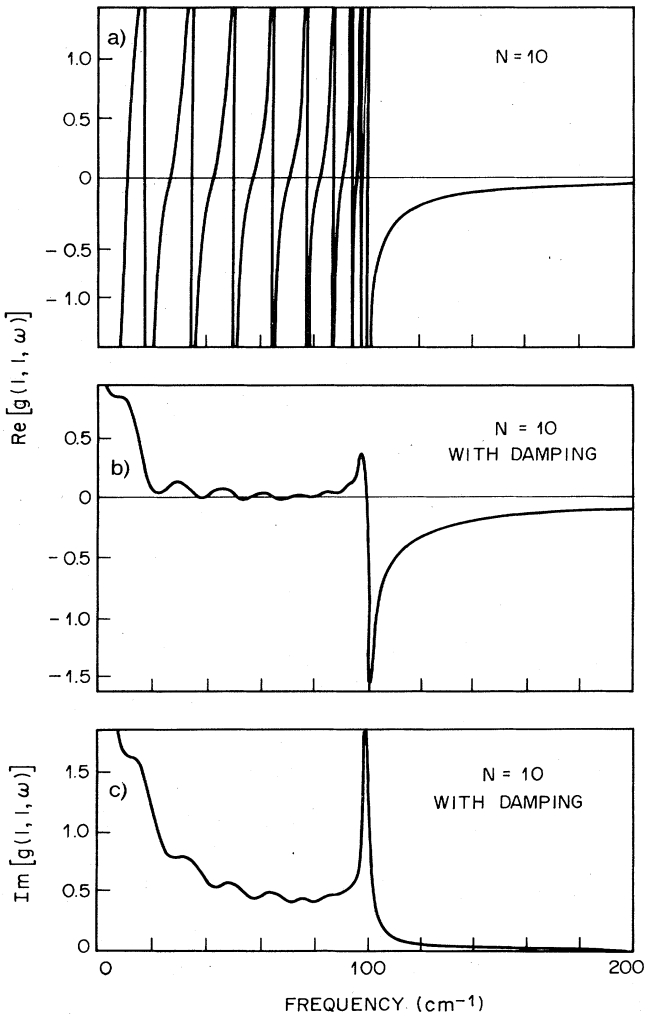

FIG. 35. Green's function for the perfect 10-atom lattice. In (b) and (c) sufficient damping has been included to merge the lattice modes and thus smooth the Green's function.

stituent atom.

We now wish to discuss the case of $N \to \infty$. Schematically the concepts of Fig. 35(a) still hold. For δm negative (a light mass) there are $N-1$ intersections of the mass defect curve with g below 100 cm^{-1} and there is in addition one high-frequency (local mode) intersection. The mathematics involved in dealing with the dense cluster of poles as $N \to \infty$ is extremely difficult. A more intuitive picture is obtained by making N fairly large but adding some damping to each mode to smear out the rapid oscillations in g. Figures 35(b) and (c) show the effect of such damping for $N=10$. Re$[g]$ and Im$[g]$ are now fairly smooth functions. A mass defect curve drawn on the Re$[g]$ graph yields two intersections for δm negative, only one of which is of interest. This intersection will occur above 100 cm^{-1} where Im$[g]$ is small so that we obtain a valid solution to (3.14) yielding a sharp local mode. We lose information on the dense cluster of band modes below 100 cm^{-1} using this method. In many cases the closely spaced band modes are not of interest, so that the method is practical and useful. Figure 35(b) and (c) can be imagined to arise from real damping or merely from a computational method (based on an undamped model) which samples the mode spectrum using a finite resolution. Such a technique results in histogram plots (see Fig. 4) which can be smoothed to obtain graphs like those shown in Fig. 35(b) and (c).

The monatomic linear chain represents one of the few models in which the limit $N \to \infty$ can be carried analytically for many of the calculations. The Green's function is

$$g(1,1,\omega) = \frac{1}{m\omega\sqrt{\omega^2 - \omega_m^2}} . \tag{3.15}$$

Figure 36 shows the real and imaginary parts of g for the chain with the same force constant k and mass m as the case chosen for $N=10$. The close relationship of Figs. 35 and 36 is obvious. From Fig. 36(a) we obtain two results for local modes in the linear chain. First, for a light mass defect, there is a solution of (3.14) as sketched in Fig. 36(a). Since all the curves in the figure have known analytic form we obtain for the intersection point

$$\omega^2 = \omega_m^2/(1-\epsilon^2), \quad (0<\epsilon<1). \tag{3.16}$$

This simple formula gives the local mode frequency in

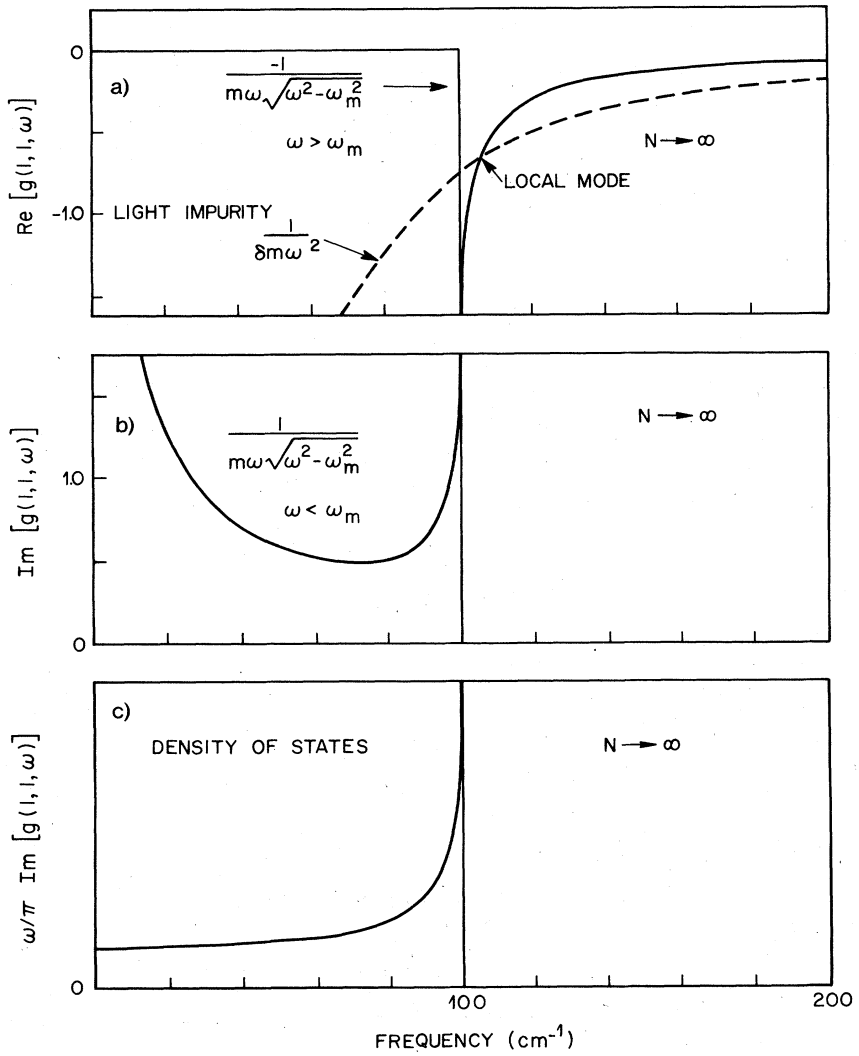

FIG. 36. Green's function for the infinite linear monatomic chain. The real part of g is plotted in (a) together with the mass defect curve for a substitution impurity lighter than the host atoms. One impurity localized mode is produced at the intersection frequency labelled in the figure. (b) shows the imaginary part of g and (c) the density of states derived from (b).

terms of the maximum frequency of the lattice ω_m, and the mass defect parameter ϵ. Secondly, for heavy substituents, there is no localized mode solution, as is obvious from the figure.

Dean (1967) has given the result (3.16) and also the Green's function equation for the case for two localized modes which occur when two identical light defects are placed on adjacent sites in the chain. Mazur, Montroll, and Potts (1956) have given expressions equivalent to (3.16) for localized modes and gap modes associated with mass defects in a linear diatomic chain. These formulas represent the only cases where (3.9) can be solved analytically. Green's functions are known for some models of three-dimensional crystals; however, Eq. (3.9) or (3.10) must be evaluated graphically or numerically.

We have noted above that there is no low-frequency in-band mode for a heavy atom substitution in the linear chain. This same result was found in Sec. II by direct calculation—a low-frequency mode could be obtained only by weakening the force constants. This is a special result associated with the linear chain and may be viewed as arising from the form of g in one dimension. Figure 36(c) shows the density of states for the linear chain. The one-dimensional system retains a finite density of states in the $\omega \to 0$ limit. In three dimensions we recall that at low frequencies (the Debye region) the density must vary as ω^2. In three dimensions, therefore, g has a far different form from that shown in the figure. Figure 37 shows the Green's function calculated for three-dimensional silicon. The figure is taken from the work of Elliott and Pfeuty (1967), who define Re$[g]$ to have the opposite sign from that adopted here. The mass defect curve for a light impurity is also shown in Fig. 37(b). Note for this three-dimensional case the mass defect curve for a heavy atom can intersect the Green's function at low frequencies (below 100 cm^{-1}) and moreover the imaginary part is small in this region [unlike Fig. 36(c)], allowing a sharp mode which is in contrast to the case of the linear chain. Elliott and Pfeuty have used the diagonal Green's function shown in Fig. 37, as well as certain other Green's functions for silicon, to calculate the localized vibrations of pairs of defects in silicon connected with mass changes and short-range force constant changes.

Figure 38 shows the modes to be expected for a light atom (carbon) substitution in silicon and for a heavy atom (germanium) substitution. The figure is taken from a review article by Maradudin (1966a). The Green's function is calculated by a Kramers–Kronig transform of a density of states supplied by Dolling which is based on experimentally observed phonon dispersion curves. Maradudin has effectively multiplied (3.9) through by ω so that the mass defect curves are hyperbolas $1/\delta m\omega$. The plotted curves appear different from Fig. 37 both for this reason and because the Green's functions used in the two figures are slightly different. From Fig. 38 we note that a carbon impurity yields one mode near $x = 1.2$ which is well above the maximum lattice frequency ω_m. The heavy germanium impurity yields one solution near $x = 0.86$. This should be a reasonably sharp mode since Im$[g]$ is small here. There are three other near crossings at lower frequencies. In these regions the approximate graphical method based on plotting Re$[g]$ is not very informative. Equation (3.9) obviously has damped solutions at these near intersections. The strengths and widths of these modes must be examined by plotting the Green's function of the defect (3.11). In

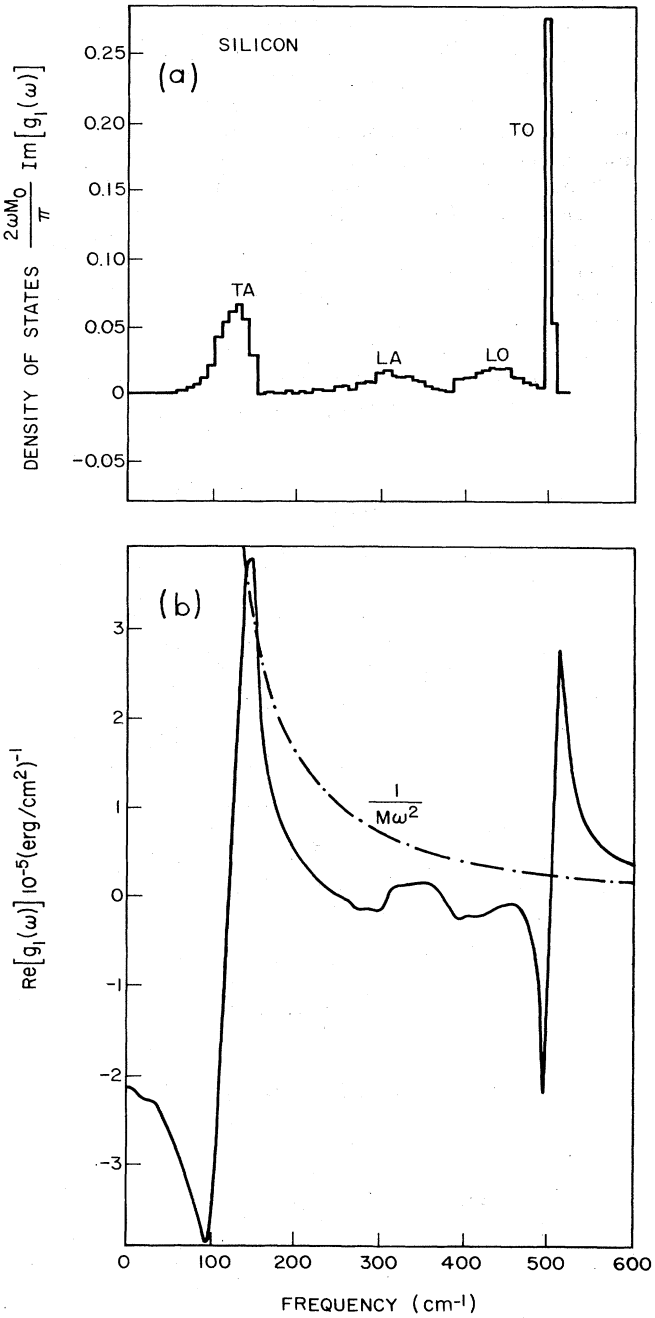

FIG. 37. (a) density of states of silicon and (b) the real part of the Green's function calculated by a Kramers–Kronig transform of the data in (a). The mass defect curve for a light impurity is sketched in the figure. Two localized modes are predicted; one just above TA near 150 cm^{-1} and the other at an extremely high frequency off the figure to the right. From Elliott and Pfeuty (1967).

this connection it is appropriate to recall that the information to determine the defect mode spectrum is contained in (3.11). Figures 37 and 38 represent a simplification based on examining the resonance condition using only the real part of the denominator of (3.11).

C. Summary

In the above sections we have examined the Green's function method in detail for the solution of the isolated mass defect problem. Elliott and Taylor (1967) have extended the method to crystals containing a finite concentration of defects. After making certain approximations and retaining only the terms of lowest order in concentration the results may be expressed in the form (3.9) but with a second term on the right which is proportional to concentration. In the case of light substituents the effect is to cause a band of impurity modes. Elliott *et al.* (1974) have given a general review of all methods used to attack the more general problem of disordered systems. The interested reader is referred to that article for the current status of the theoretical methods. In general the Green's function method depends on finding the function g of the perfect lattice. This function contains all the information on the dynamical response of each atom in the lattice. When a disturbance such as δm is introduced, the response of the perturbed system depends on g and on the parameters describing the disturbance. The new modes can be found from the resonances of the perturbed system. The method of solution involves finding the Green's function of the perturbed system [for example (3.11)] and perhaps approximation methods or graphical solutions to study the resonances or modes. Some of these methods will be treated in detail in the following chapters for specific impurity systems.

Finally, we must give a word of caution related to the application of these purely mathematical results to real crystals. The simple examples given above show that a light impurity gives a high-frequency localized resonance, while a heavy impurity is needed to produce a low-frequency defect mode. This simple picture arises from the mass defect approximation. In practice a light atom is a small atom. When it is placed in the lattice, we can imagine it to fit poorly (be "loose") and to cause relaxation of the positions of the nearly surrounding

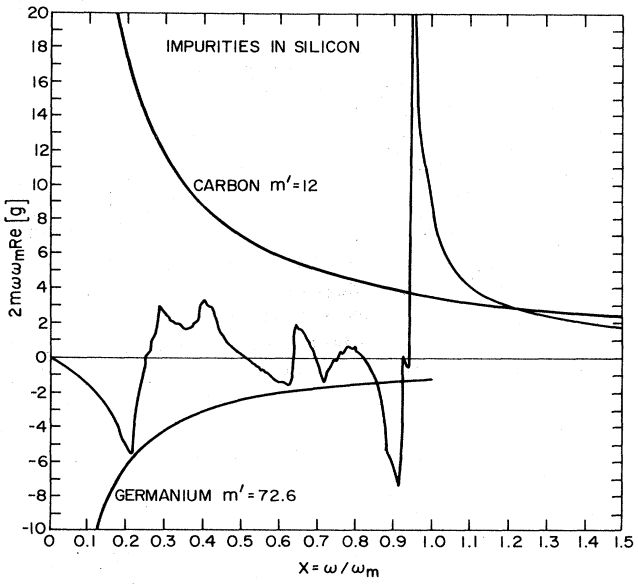

FIG. 38. Mass defect modes in silicon. ω times the Green's function is plotted using a different model from that used in the preceding figure. The mass defect curve for a substitution carbon atom predicts a mode near $x=1.2$. The heavy substitutional germanium atom gives four potential resonance solutions, all of which can be expected to be damped. From Maradudin (1966).

atoms. These two concepts of loose fit and lattice relaxation are hard to quantify and insert into a Green's function approach in a simple way. Their importance is clear, however, as will be seen in succeeding chapters where, for example, the light atom Li in KBr and Ne in solid argon produce low-frequency resonant modes. The Green's function method can predict such resonant modes by using weakened force constants. Unfortunately, such models usually need more parameters than can be fixed by experiment. To give a balanced view, the theoretical methods have been very useful for many cases of substitution where the substituent has close to the required ion size and valence. They have not been very helpful for many other defect systems, and it is perhaps here that experiment will show theory the direction which must be taken.

IV. DEFECT MODES IN SEMICONDUCTORS

A. The problem of crystal growth and charge compensation

This chapter must begin with a warning to scientists who attempt studies on impure or doped crystals. The physical chemist or crystal growth expert often cringes when an experimenter talks of making a crystal of silicon doped with lithium, or of CaF_2 doped with a trivalent rare earth ion, and then describes the spectra on the basis of the simple isotope substitution model. In CaF_2 doped with Er^{3+} at least eight distinct types of Er impurity centers have been observed. They are distinguished by the exact position of compensating charges which lower the symmetry and change the environment of the impurity. These are all thermodynamically related and their relative abundance depends on certain thermodynamic parameters and on the thermal history. This latter is particularly important since two crystals grown from the same "recipe" can be vastly different if one is cooled much more quickly than the other to room temperature. Thus the statement that a crystal A is doped with B is at best ambiguous and at worst may represent a situation which no one else will be able to duplicate. The most important factors to be considered when substitutions are made are ion size, charge, and electronegativity (Nassau, 1971). Fortunately, many of the semiconductors which have been studied do allow direct substitution on ion sites with little complication.

For most semiconductors and insulators, if the size of the impurity ion allows reasonable solubility, then the problem of charge compensation must be considered when substituting an impurity for a host ion in a crystal. If one considers U centers such as H^- for F^- in CaF_2, or C for Si in silicon, then local charge neutrality is maintained. Substituents like these are often called isoelectronic substituents. In the case of rare-earth ions on Ca^{2+} sites in CaF_2, the impurity ions may be present as either divalent or trivalent state. In the trivalent state, charge compensation may occur through the formation of F^- interstitials or, if heated in hydrogen, by H^- interstitials leading to several distinct types of center as described above.

In semiconductors the charge compensation process for nonisoelectronic substituents is usually different from the process in an insulator, being accomplished most often through the introduction of free carriers. If a Group III or V element is introduced as a substitutional impurity in a Group IV semiconductor host, the impurity is often an acceptor or donor with a very small ionization energy. Examples include B or Al in Si (acceptors) or P, As, or Sb in Si (donors). In each of these cases, the impurity state is sufficiently shallow (few hundredths of an eV) that the excess charge (electron or hole) accompanying the impurity is ionized at room temperature and the sample is electrically conductive. Thus charge compensation automatically occurs by the reaction $D \rightleftharpoons D^+ + e^-$ for donor impurities and $A \rightleftharpoons A^- + e^+$ for acceptor impurities. The presence of the free carriers (e^- or e^+) poses a serious problem in semiconductors when one attempts to measure vibrational mode absorption associated with the D^+ or A^- impurity.

The source of the difficulty in semiconductors is easily seen when one realizes that the absorption cross section for free carriers can be as much $\sim 10^3$ times larger than the local mode absorption cross section. The evaluation of free carrier absorption (Moss, 1959) can be a rather involved function of the energy band structure and the momentum conserving carrier scattering mechanism, and it is not our purpose to review it here. We instead consider a specific case for illustration. The free carrier absorption in p-type Si in the spectral range $500 \leq \nu \leq 700$ cm^{-1} is α (free carrier) $= 500$ to 1000 cm^{-1} for a hole concentration $[e^+] = 10^{18}$ cm^{-3}. It will be seen shortly that the peak α of the local modes of substitutional B in Si is ~ 2 cm^{-1} for a concentration $[B_{Si}] \sim 10^{18}$ cm^{-3}. The local mode frequencies for both ^{10}B and ^{11}B isotopes are within the spectral range specified above for the free carriers. It therefore is important that the carrier concentration and thus the carrier absorption be reduced without reduction of the $[B_{Si}]$. One suggestion might be to lower the temperature sufficiently that almost all of the carriers are frozen out, i.e., $A^- + e^+ \rightarrow A$; however, one has replaced free carrier absorption with photoionization in the spectral range of interest. The ionization threshold energy of B in Si is 0.045 eV or 360 cm^{-1}. The photoionization absorption is comparable to that of free carriers, so that the situation is not substantially improved.

The removal of free carriers may be accomplished by electrical compensation in three different ways. The first method involves double doping during growth of the crystal. If exact compensation is achieved, the reaction is $D^+ + e^- + A^- + e^+ \rightarrow D^+ + A^-$. If one's intent is to study the high-frequency modes of a light Group III impurity such as B_{Si}, then a heavy Group V impurity such as P, As, or Sb can be used (Newman and Smith, 1968; Angress *et al.*, 1965; Tsvetov *et al.*, 1967; 1968) for compensation, so that the compensating element does not introduce its own mode in the region of interest. Unfortunately, it is usually impossible by this method to obtain better than order of magnitude compensation for a substantial portion of the ingot. It is therefore generally necessary to use one of the two remaining methods to complete the compensation.

The second method involves the use of particle irradiation, usually bombardment by electrons or protons (Newman and Smith, 1968; Spitzer *et al.*, 1969a). Caution must be used in the interpretation of the resulting vibrational absorption, however, as the defects produced by the bombardment damage can themselves introduce new spectral features (Devine and Newman, 1970).

The third method involves compensating by diffusion under conditions where the solubility of the diffusant is controlled by the impurity to be compensated. The diffusant must be capable of diffusing distances of the order of a millimeter in experimentally reasonable times and at temperatures where the original dopant does not outdiffuse or precipitate. Si and GaAs, with band gaps greater than 1 eV, are likely candidates, while InSb and InAs, with much smaller gaps, would be very unlikely candidates for diffusion compensation (Spitzer, 1971).

One feature which has been omitted from the discussion thus far is ion pairing. That is, the D^+ ion and the A^- ion may take up nearest-neighbor positions. The D^+ ion is then no longer an isolated impurity in the host semiconductor, but a perturbed impurity at a site of low symmetry because of the nearby A^- impurity. In all three methods of compensation there exists the possibility that pairing will occur when the sample is held at temperatures where the defects or impurities are mobile. Indeed Fuller (1959) found ample evidence for ion pairing prior to the local mode observations of recent years. The prevalence of pairing, particularly when Li is used as the compensating diffusant, explains the large number of ion pair defect entries in Table IV.1.

Finally we note that most of the difficulties described above apply to direct absorption measurements by infrared methods. Raman scattering has been successfully carried out in silicon doped with hole concentrations $[e^+] \sim 10^{20}$ cm^{-3} and the boron local modes detected (Cerdeira *et al.*, 1974). In this measurement the carriers do, however, modify the measured spectrum, causing unusual mode shape and mode shifts, so that their presence must be taken into account for an accurate analysis.

B. Group IV crystals

1. Introduction

A great deal of the early defect mode studies were done in the Group IV semiconductors, and some of the

TABLE IV.1. Localized modes in semiconductors and metals.

Host and Impurity	Mode frequency (temperature) °K	Defect symmetry, Method of observation, [a] References, [b] Comments
Diamond		
N ?	1340(300)	T_d ?, A, 6
Silicon		
^{10}B	644(300), 646(80)	T_d, A, 1, 5, 7, 9, 14, 15, 16; R, 67
^{11}B	620(300), 622(80), ~230(300)	T_d, A, 1, 5, 7, 9, 14, 15, 16; R, 67; T, 79
^{10}B–^{7}Li	681, 584, 522(300); 683, 586, 523(80)	C_{3v}, A, 1, 5, 14, 17
^{10}B–^{6}Li	683, 584, 534(300)	C_{3v}, A, 1, 14, 17
^{11}B–^{7}Li	655, 564, 522(300); 656, 566, 523(80)	C_{3v}, A, 1, 5, 14, 17
^{11}B–^{6}Li	657, 564, 534(300); 659, 566, 536(80)	C_{3v}, A, 1, 5, 14, 17
^{11}B–^{11}B	615, 552.3(80)	D_{3d}, A, 2, 3
^{10}B–^{10}B	570(80)	D_{3d}, A, 2, 3
^{10}B–^{11}B	560(80)	C_{3v}, A, 2, 3
^{10}B–P	622, 653(80)	C_{3v}, A, 3, 5
^{11}B–P	600, 628(80)	C_{3v}, A, 3, 4, 5
^{10}B–As	625, 662(80)	C_{3v}, A, 3
^{11}B–As	604, 637(80)	C_{3v}, A, 3, 4
^{10}B–Sb	635, 668(80)	C_{3v}, A, 3
^{11}B–Sb	612, 643(80)	C_{3v}, A, 3, 4
As	366(80) Reson.	T_d, A, 6
P	441 Reson., 491(80) Reson.	T_d, A, 6
Ga–^{6}Li	521(300) Reson.?	C_{3v}, A, 8
Ga–^{7}Li	515(300) Reson.	C_{3v}, A, 8
Al–^{6}Li	525(300) Reson.?	C_{3v}, A, 8
Al–^{7}Li	520(300) Reson.	C_{3v}, A, 8
^{14}C	570(300), 573(80)	T_d, A, 3
^{13}C	586(300), 589(80)	T_d, A, 3
^{12}C	605(300), 680(80)	T_d, A, 3
O	Bands near 30, 500, 1100, 1200	10, 11 } Interstitial oxygen in bent Si–O–Si molecule.
^{12}C–^{16}O	1103.9(4.2), 586(300), 637(300), 684(300), 589(80), 640(80), 690(80)	A, 12, 13 } Some transition may be rotational as well as vibrational.
^{12}C + irrad.	922, 932(88)	Axial, A, 18, carbon probably interstitial

TABLE IV.1. Localized modes in semiconductors and metals. *(Continued)*

Host and Impurity	Mode frequency (temperature) °K	Defect symmetry, Method of observation,[a] References,[b] Comments
Germanium		
Si	389(300)	T_d, A, 19; R, 20; neutron, 87
Si–Si	476, 448(300)	D_{3d}, R, 20
^{16}O	855(300), 862(4)	C_{2v}, A, 21
^{18}O	818(?)	C_{2v}, A, 22
^{10}B	571(80)	T_d, A, 23
^{11}B	547(80)	T_d, A, 23
^{10}B–Li	518.5, 610(80)	C_{3v}, A, 23
^{11}B–Li	497, 582.5(80)	C_{3v}, A, 23
Ga–^{6}Li	379, 405(80)	C_{3v}, A, 24
Ga–^{7}Li	356, 380(80)	C_{3v}, A, 24
Ga–P	~343, 350(80)	C_{3v}, A, 24
^{31}P	343(80)	T_d, A, 24
SiC		
N	635(4)	C_{3v}, R, T, 25
H_{Si}	2977(1.3)	Axial, 73
D_{Si}	2210(1.3)	Axial, 73
Impurity–vacancy	536(45)	Resonant mode, 74
GaAs		
Al	362(80) ~371(4.2)	T_d, A, Refl., 27, 42 T_d, T, 85
P	355(80), 353(300) ~363(4.2)	T_d, A, R, Refl., 27, 40, 41, 58 T_d, T, 85
^{6}Li	350, 389, 401, 409.5, 426, 452(80)	?, A, 29, 30] The Li defect is now known to be complex involving two or more Li atoms and a native defect.
^{7}Li	364, 389, 394, 379, 383, 421(80)	?, A, 29, 30]
Te–^{6}Li	419, 510(80)	C_{3v}, A, 29, 31
Te–^{7}Li	391, 475(80)	C_{3v}, A, 29, 31
Mn–^{6}Li	391, 413, 419(80)	C_{2v}, A, 32
Mn–^{7}Li	365, 386, 391(80)	C_{2v}, A, 32
Cd–^{6}Li	377, 401, 423(80)	C_{2v}, A, 29, 32
Cd–^{7}Li	354, 375, 395(80)	C_{2v}, A, 29, 32
Zn–^{6}Li	361, 385, 404, 433(80)	?, A, 29, 32
Zn–^{7}Li	340, 361, 379, 405(80)	?, A, 29, 32
Si_{Ga}	384(80)	T_d, A, 33, 34, 35, 36
Si_{As}	399(80)	T_d, A, 33, 34, 35, 36
Si_{Ga}–Si_{As}	367, 393, 464(80)	C_{3v}, A, 33, 34, 35, 36
Si_{Ga}–$^{6}Li_{Ga}$	374, 379, 405, 470, 480, 487(80)	C_s, A, 33, 34, 35, 36
Si_{Ga}–$^{7}Li_{Ga}$	374, 379, 405, 438, 448, 455(80)	C_s, A, 33, 34, 35, 36
Si_{Ga}–Cu_{Ga}	374, 376, 399(80)	C_s, A, 33, 34, 35, 36
Si_{Ga}–Zn_{Ga}	378, ~382, 395(80)	C_s, A, 37
Mg–^{7}Li	318, 338, 348, 366, 377, 392(80)	?, A, 38, ^{6}Li also studied
Mg_{Ga}	326(80)	T_d, A, 38
$^{11}B_{Ga}$; $^{10}B_{Ga}$	517(77); 540(77)	T_d, A, 68
^{12}C; ^{13}C	582(77); 561(77)	T_d, A, 68

TABLE IV.1. Localized modes in semiconductors and metals. *(Continued)*

Host and Impurity	Mode frequency (temperature) °K	Defect symmetry, Method of observation,[a] References,[b] Comments
GaP		
Al	444.7(77)	T_d, A, R, 50, 51, 52
Si_{Ga}	465(80)	T_d, A, 39, 50
Si_{Ga}–Si_P	455.7(80)	T_d, A, 39, 50
^{11}B	569.7(77)	T_d, A, R, 50, 51, 52
^{10}B	593.8(77)	T_d, A, R, 50, 51, 52
^{14}N	493(4.2)	T_d, L, A, 53
O_i	1005(80)	T_d, A, 69
O_P	199, 229(1.6)	S, L, 84; Isotope shifts done
O_P?	464(77)	T_d, A, 50
C	606(20)	T_d, A, 57
As	272(300)	T_d, Refl., 58
S_P	ω_{LO} −6(20)	Bound phonon, L, R, Refl., 63, 64
Te_P	193(1.6) ω_{LO} −10(20)	S, L, 80, 82 Bound phonon, L, R, Refl., 63, 64
Si_{Ga}	ω_{LO} −10(20)	Bound phonon, L, R, Refl., 63, 64
Sn_{Ga}	72(5) ω_{LO} −19(20)	S, L, 83 Bound phonon, L, R, Refl., 63, 64
Se_P	ω_{LO} −7(20)	Bound phonon, Refl., 64
Cd	56(20.4)	S, L, 81, Complexed with a neighboring oxygen
Zn	48(1.6)	S, L, 81, Complexed with a neighboring oxygen
C_P	ω_{LO} −10(20)	Bound phonon, assignment uncertain, Refl., 67
Be_{Ga}	629(20)	A, 70
GaSb		
Al_{Ga}	316.7(77)	T_d, A, 47, 48
InSb		
Al	296(77)	T_d, A, 43, 44
P	293(77)	T_d, A, 45
AlAs		
Ga	252(300)	T_d, Refl., 46
InP		
^{10}B; ^{11}B	543.5(77); 522.8(77)	T_d, A, 77
As_P	223(300)	Refl., 75
InAs		
Ga_{In}	~240(300)	T_d, Refl., 50
P_{As}	303(300)	Refl., 75
CdS		
^6Li	474(100)	?, A, 59
^7Li	457(100)	?, A, 59
I_1 transition unknown impurity		
I_1	ω_{LO} −19, −26(1.2)	Anisotropic bound phonon, L, 65
Be_{Cd}	446(∥), 453(⊥)(100)	C_{3v}, A, R, 66
Se_S	182(∥), 186(⊥)(300)	C_{3v}, Refl., 60, 71

TABLE IV. 1. Localized modes in semiconductors and metals. *(Continued)*

Host and Impurity	Mode frequency (temperature) °K	Defect symmetry, Method of observation,[a] References,[b] Comments
CdSe		
Be_{Cd}	411(∥), 420(⊥)(100)	C_{3v}, A, 66
Te_{Se}	153(293)	S, Refl., 86, this mode may lie in a gap
S_{Se}	269(∥), 270(⊥)(15)	Refl., 60, 71
CdTe		
Zn_{Cd}	167(293)	S, Refl., 86
Be	391(4), 61(4) Reson.	T_d, A, 55, 56
Se_{Te}	170(300)	T_d, A, 54, Refl., 86
Li(?)	270(?)	?, A, 54
N. ZnS		
Be	490(100), 486(300)	R, A, 76
Se	220	Refl., R, 64
ZnSe		
^{7}Li	353(77), 336(77), 328(77), 318(77)	?, A, 60
Al	359(77)	T_d, A, 61
Al-$\square_{Zn}$?		?, A, 61
Be	450(100), 447(300)	S, R, A, 76, 88, 89
S	297(100)	S, A, Refl., R, 60, 62, 72
ZnTe		
Cd_{Zn}	153(293)	S, Refl., R, 86, this mode may be in the gap
S	270	S, Refl., 72
Be	415(100), 411(300)	S, A, 76
Metals		
In in Pb	77(0.83)	S, T, 78, Localized mode band (host crystal has $\omega_m = 73$ cm^{-1})
Au in Cu	80(300)	S, Neutron scattering, 90, well-defined resonant mode in acoustic band for 3% Au
W in Cr	Broad resonance	S, Neutron scattering, 91, resonant mode

[a] Key: A = absorption, R = Raman, Refl. = reflectivity, T = electron tunneling, L = luminescence, S = substitutional.

[b] The references for Table IV.1 are the following:

1. Spitzer, W. G., and M. J. Waldner, 1965, Appl. Phys. **36**, 2450.
2. Newman, R. C., and R. S. Smith, 1967, Phys. Lett. A **24**, 671.
3. Newman, R. C., and R. S. Smith, 1968, in *Localized Excitations in Solids*, edited by R. F. Wallis (Plenum, New York), 177.
4. Tsvetov, V., W. Allred, and W. G. Spitzer, 1968, in *Localized Excitations in Solids*, edited by R. F. Wallis (Plenum, New York), 185.
5. Tsvetov, V., W. Allred, and W. G. Spitzer, 1967, Appl. Phys. Lett. **10**, 326.
6. Angress, J. F., A. R. Goodwin, and S. D. Smith, 1968, Proc. R. Soc. Lond. A **308**, 111.
7. Angress, J. F., A. R. Goodwin, and S. D. Smith, 1965, Proc. R. Soc. Lond. A **287**, 64.
8. Devine, S. D., and R. S. Newman, 1969, J. Phys. Chem. Solids **31**, 685.
9. Newman, R. C., and R. S. Smith, 1967, Solid State Commun. **5**, 723.
10. Newman, R. C., 1969, Advances in Physics **18**, 545 for review.
11. Bosomworth, D. R., W. Hayes, A. R. L. Spray, and G. D. Watkins, 1970, Proc. R. Soc. A **317**, 133.
12. Newman, R. C., and J. B. Willis, 1965, J. Phys. Chem. Solids **26**, 373.
13. Newman, R. C., and R. S. Smith, 1969, J. Phys. Chem. Solids **30**, 1493.
14. Balkanski, M., and W. Nazarewicz, 1966, J. Phys. Chem. Solids **27**, 671.
15. Angress, J. S., T. Arai, A. R. Goodwin, and S. D. Smith, 1964, in *Physics of Semiconductors: Proceedings of the 7th International Conference*, edited by M. Hulin (Dunod, Paris), p. 1115.
16. Smith, S. D., and J. F. Angress, 1963, Phys. Lett. **6**, 131.
17. Balkanski, M., and W. Nazarewicz, 1964, J. Phys. Chem. Solids **25**, 437.
18. Bean, A. R., and R. C. Newman, 1970, Solid State Commun. **8**, 175.

TABLE IV.1. Localized modes in semiconductors and metals. *(Continued)*

19. Cosand, A. E., and W. J. Spitzer, 1971, J. Appl. Phys. **42**, 5241.
20. Feldman, D. W., M. Ashkin, and J. H. Parker, Jr., 1966, Phys. Rev. Lett. **17**, 1209.
21. Kaiser, W., 1962, J. Phys. Chem. Solids **23**, 255.
22. Whan, R., 1965, Phys. Rev. A **140**, 690.
23. Nazarewicz, W., and J. Jurkowski, 1969, Phys. Status Solidi **31**, 237.
24. Cosand, A. E., and W. G. Spitzer, 1967, Appl. Phys. Lett. **11**, 279.
25. Colwell, P. J., W. D. Compton, M. V. Klein, and L. B. Schein, 1970, in *Proceedings of the Tenth International Conference on the Physics of Semiconductors*, edited by S. P. Keller, J. C. Hensel, and F. Stern (USAEC, Oak Ridge), p. 484.
26. Smith, S. D., R. E. V. Chaddock, and A. R. Goodwin, 1966, in *Proceedings of the International Conference on the Physics of Semiconductors* (Suppl. to J. Phys. Soc. Japan, Vol. 21, Tokyo), p. 67.
27. Lorimer, O. G., W. G. Spitzer, and M. Waldner, 1966, J. Appl. Phys. **37**, 2509.
28. Spitzer, W. G., 1967, J. Phys. Chem. Solids **28**, 33.
29. Hayes, W., 1965, Phys. Rev. **138**, A1227.
30. Levy, M., O. Lorimer, and W. G. Spitzer, 1968, J. Appl. Phys. **39**, 1914.
31. Lorimer, O. G., and W. G. Spitzer, 1967, J. Appl. Phys. **38**, 2713.
32. Lorimer, O. G., and W. G. Spitzer, 1967, J. Appl. Phys. **38**, 3008.
33. Lorimer, O. G., and W. G. Spitzer, 1966, J. Appl. Phys. **37**, 3687.
34. Spitzer, W. G., and W. Allred, 1968, Appl. Phys. Lett. **12**, 5.
35. Spitzer, W. G., and W. Allred, 1968, J. Appl. Phys. **39**, 4999.
36. Spitzer, W. G., A. Kahan, and L. Bouthillette, 1969, J. Appl. Phys. **40**, 3398.
37. Allred, W. P., G. Cumming, J. Kung, and W. G. Spitzer, 1969, in *Galluim Arsenide, Proceedings of Second International Symposium*, Dallas, Texas, 1968 (Institute of Physics, London), p. 66.
38. Leung, P. C., L. H. Skolnik, W. P. Allred, and W. G. Spitzer, 1972, J. Appl. Phys. **43**, 4096.
39. Morrison, S. R., and R. C. Newman, 1974, J. Phys. C **7**, 627.
40. Kleinman, L., M. H. L. Pryce, and W. G. Spitzer, 1966, Phys. Rev. Lett. **17**, 304.
41. Chen, Y. S., W. Shockley, and G. L. Pearson, 1966, Phys. Rev. **151**, 648.
42. Ilegems, M., and G. L. Pearson, 1970, Phys. Rev. B **1**, 1576.
43. Goodwin, A. R., and S. D. Smith, 1965, Phys. Lett. **17**, 203.
44. Smith, S. D., R. E. V. Chaddock, and A. R. Goodwin, 1966, J. Phys. Soc. Japan, Suppl. II, **21**, 67.
45. Skolnik, private communication.
46. Ilegems, M., and G. L. Pearson, 1970, Phys. Rev. B **1**, 1576.
47. Hayes, W., 1964, Phys. Rev. Lett. **13**, 275.
48. Hayes, W., in *Localized Excitations in Solids*, edited by R. F. Wallis (Plenum, New York), p. 140.
49. Brodsky, M., and G. Lucovsky, 1968, Phys. Rev. Lett. **21**, 990.
50. Kachere, A. H., W. G. Spitzer, O. G. Lorimor, F. K. Euler, and R. N. Brown, 1974, J. Appl. Phys. **45**, 5475.
51. Hayes, W., H. F. MacDonald, and C. T. Sennett, 1969, J. Phys. C (Solid State Phys.) **2**, 2402.
52. Hon, D., W. Faust, W. G. Spitzer, and F. Williams, 1970, Phys. Rev. Lett. **25**, 1184.
53. Thomas, D. G., and J. J. Hopfield, 1966, Phys. Rev. **150**, 680.
54. Balkanski, M., R. Beserman, and L. K. Vodopianov, 1967, in *Localized Excitations in Solids*, edited by R. F. Wallis (Plenum, New York), p. 154.
55. Hayes, W., and A. R. L. Spray, 1969, J. Phys. C (Solid State Phys.) **2**, 1129.
56. Sennett, C. T., D. R. Bosomworth, W. Hayes, and A. R. L. Spray, 1969, J. Phys. C (Solid State Phys.) **2**, 1137.
57. Hayes, W., M. C. K. Wiltshire, and P. J. Dean, 1970, J. Phys. C **3**, 1762.
58. Verleur, H. W., and A. S. Barker, Jr., 1966, Phys. Rev. **149**, 715.
59. Mitsuishi, A., A. Manabe, H. Yoshinaga, S. Ibuki, and H. Komiya, 1966, J. Phys. Soc. Japan, Suppl. II, **21**, 72.
60. Balkanski, M., and R. Beserman, 1968, in *Proceedings of the 9th International Conference on the Physics of Semiconductors*, Moscow, 1968 (Nauka, Leningrad), p. 1042.
61. Ibuki, S., H. Komiya, A. Mitsuishi, A. Manabe, and H. Yoshinaga, 1967, in *II-VI Semiconducting Compounds Conference*, edited by D. G. Thomas (Benjamin, New York), p. 1140.
62. Brafman, O., I. F. Chang, G. Lengyel, S. S. Mitra, and E. Carnall, Jr., 1967, Phys. Rev. Lett. **19**, 1120.
63. Dean, P. J., D. D. Manchon, and J. J. Hopfield, 1970, Phys. Rev. Lett. **25**, 1027.
64. Barker, Jr., A. S., 1973, Phys. Rev. B **7**, 2507.
65. Reynolds, D. C., C. W. Litton, and T. C. Collins, 1971, Phys. Rev. B **4**, 1868.
66. Manabe, A., A. Mitsuishi, H. Komiya, and S. Ibuki, 1973, Solid State Commun. **12**, 337.
67. Nazarewicz, W., M. Balkanski, J. F. Morhange, and C. Sibenne, 1971, Solid State Commun. **9**, 1719.
68. Newman, R. C., F. Thompson, M. Hyliands, and R. F. Pert, 1972, Solid State Commun. **10**, 505.
69. Barker, Jr., A. S., R. Berman, and H. W. Verleur, 1972, J. Phys. Chem. Solids **34**, 123.
70. Barker, Jr., A. S., R. Berman, and M. Ilegems, (to be published).
71. Verleur, H. W., and A. S. Barker, Jr., 1967, Phys. Rev. **155**, 750.
72. Beserman, R., and M. Balkanski, 1970, J. Phys. Chem. Solids **31**, 355.
73. Choyke, W. J., and L. Patrick, 1972, Phys. Rev. Lett. **29**, 355.
74. Choyke, W. J., and L. Patrick, 1971, Phys. Rev. B **4**, 1843.
75. Kekelidze, N. P., G. P. Kekelidze, and Z. D. Makharadze, 1973, J. Phys. Chem. Solids **34**, 2117–2126.
76. Manabe, A., Y. Ikuta, A. Mitsuishi, H. Komiya, and S. Ibuki, Solid State Commun. **9**, 1499 (1971).
77. Newman, R. C., F. Thompson, J. B. Mullin, and B. W. Straughan, Physics Letters **33A**, 113 (1970).
78. Rowell, J. M., W. L. McMillan, and P. W. Anderson, Phys. Rev. Lett. **14**, 633 (1965).
79. Cullen, D. E., E. L. Wolf, and W. D. Compton, Phys. Rev. B **2**, 3157 (1970).
80. Dean, P. J., C. J. Frosch, and C. H. Henry, J. Appl. Phys. **39**, 5631 (1968).

TABLE IV.1. Localized modes in semiconductors and metals. *(Continued)*

81. Henry, C. H., P. J. Dean, and J. D. Cuthbert, Phys. Rev. **166**, 754 (1968).
82. Dean, P. J., Phys. Rev. **157**, 655 (1967).
83. Dean, P. J., R. A. Faulkner, and S. Kimura, Phys. Rev. B **2**, 4062 (1970).
84. Dean, P. J., and C. H. Henry, Phys. Rev. **176**, 928 (1968).
85. Andrews, A. M., H. W. Korb, N. Holonyak, Jr., C. B. Duke, and G. G. Kleiman, Phys. Rev. B **5**, 2273 (1972).
86. Vodopyanov, L. K., and E. A. Vinogradov, to be published.
87. Wakabayashi, N., R. M. Nicklow, and H. G. Smith, Phys. Rev. **4B**, 2558 (1971).
88. Tatsuno, K., A. Manabe, A. Mitsuishi, and S. Ibuki, Optics Commun. **10**, 346 (1974).
89. Yuasa, T., A. Mitsuishi, H. Komiya, and S. Ibuki, Jap. J. Appl. Phys. **9**, 1421 (1970).
90. Svensson, E. C., and B. N. Brockhouse, Phys. Rev. Lett. **18**, 858 (1967).
91. Moller, H. B., and A. R. Mackintosh, Phys. Rev. Lett. **15**, 623 (1965).

best comparisons with rigorous theories have been made here. From the list of defects and host crystals contained in Table IV.1 it is clear that some selectivity must be exercised in the discussion of this topic. There will be no attempt to discuss all the cases, but rather a few examples will be selected to illustrate the nature of the results and observed the effects. In some cases, the choice reflects the personal bias of the authors, while in other cases the examples omitted here have already been discussed extensively by Newman (1969) in his recent review. The latter category includes the important cases of O, (C–O) pairs, and B-substitutional donor pairs in Si.

It is of interest to note the difference in the experimental situation for the insulators and semiconductors. The insulators show many cases of gap modes and resonant modes, but only a few defects give high-frequency localized modes. In the semiconductors there are relatively few cases observed of in-band or resonance mode absorption, and the cases observed are frequently not well understood. However, as indicated in Table IV.1, defects giving rise to high-frequency localized modes are numerous.

The Group IV semiconductors, which include germanium and silicon, are of the diamond structure which consists of face centered cubic sublattices with a relative displacement of $\frac{1}{4}$ the body diagonal. There are two atoms in the primitive cell. The nearest-neighbor configuration for each atom is tetrahedral (T_d point group), and there is a center of inversion midway between any pair of nearest neighbors. The vibrational spectrum of the perfect lattice consists of six branches of which three are optical (two transverse and one longitudinal) and three are acoustical. Symmetry requirements impose a number of conditions on the frequencies at certain points and along symmetry lines of the Brillouin zone. An illustration is given in Fig. 39 where the dispersion curves for the normal modes of vibration of Si are shown. The degeneracy of the optical branches at $q = 0$ (Γ point), the degeneracy of the LO and LA branches at the X point, and the twofold degeneracy of both the TO and the TA branches along certain high-symmetry directions are examples of these restrictions. The degeneracy at the X point corresponds to the degeneracy of modes 24 and 25 in Fig. 3 when $M = m$ in the linear chain.

Infrared absorption and to a somewhat lesser degree Raman scattering of the pure crystals have been the subjects of several studies (Johnson, 1965). Since the crystals cannot have a first-order electric moment for the $\vec{q} \approx 0$ optical modes, single phonon absorption is forbidden and the crystals do not have a reststrahlen band. The modes are Raman allowed, however, and have been observed. The relatively weak absorption observed in the infrared in these crystals has been shown to be due to multiphonon processes and therefore need not concern us further here.

2. Localized vibrational modes of isolated impurities

Figure 40 shows the density of states of silicon calculated by Johnson (1965). Because of the degeneracy of the LO and LA branches at the X point, there cannot be a forbidden frequency region between the optical and acoustical branches, and hence no localized gap modes are possible in the Group IV materials. Dolling and Cowley (1966) have calculated and intercompared the lattice vibrations of diamond, germanium, silicon, and gallium arsenide. The latter three have very similar densities of states. In all these crystals localized modes must have frequencies above the top of the unperturbed frequency spectrum. There are several examples of high-frequency modes listed in Table IV.1. These include the cases of an isolated substitutional impurity (B, C, and Si in Ge); interstitials such as O in Si and Ge; paired impurities such as Li–B in Si, Li–B in Ge, B–As, B–Sb, B–P, and B–B in Si.

The simplest cases to discuss are those of the isolated substitutional impurities. These cases also contain some interesting contrasts. Carbon in silicon is a Group IV impurity in a Group IV host. Because of the matching valence of the impurity one expects that it should be assigned zero charge in a point charge model and hence should show little or no infrared absorption strength. Relatively strong infrared modes have been reported by Newman and Willis (1965) for ^{12}C, ^{13}C, and ^{14}C isotopes. Figure 41 shows an absorption spectrum for Si doped with ^{12}C and ^{13}C. The observations are consistent with the previous evidence that C is a substitutional impurity in Si (Newman, 1969). A single frequency is expected for a given C defect as the symmetry is T_d (tetrahedral), so that the vibrations along three orthogonal axes are degenerate. The local mode frequency calculated for ^{14}C using the Green's function method (Sec. III) applied to the mass defect model (Dawber and Elliott, 1963a, 1963b) is 610 cm^{-1}, compared to the experimental value of 573 cm^{-1}. Thus a decrease in force constant is required to obtain better agreement. An interesting feature, however, is the value of the absorption cross sec-

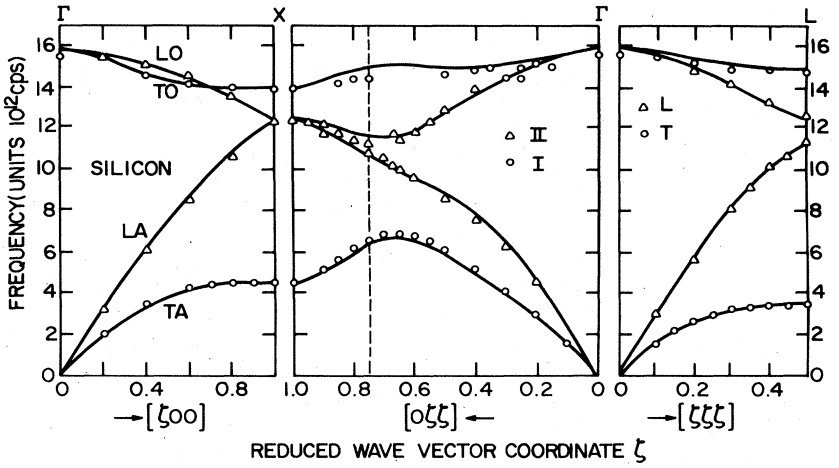

FIG. 39. The dispersion curves for the lattice vibrations in silicon at 296°K in three principal directions, determined by Dolling. The curves are fitted to the measurements using an 11 parameter shell model. From Brockhouse (1964).

tion[10] given by $\sigma_{loc} = \int_{band} \alpha_b(\nu)\, d\nu/N$, where $\alpha_b(\nu)$ is the absorption due to the band with the pure sample background subtracted and N is the defect concentration. The experimental value of σ_{loc} for carbon in silicon is 3×10^{-17} cm, where ν is in units of cm^{-1} (Newman and Willis, 1965). As will be seen, this is a larger value than that obtained from most other impurities in Ge or Si, including B_{Si}^{-} which is a charged acceptor. This result can be understood using the theory of Leigh and Szigeti (1967, 1968), which shows that the absorption is determined not only by the ionic charge on the impurity, but also by internal field effects. The point charge model used by most authors, in which the impurity carries a charge e in an uncharged lattice, is too simple for use in calculating the absorption strength. Recall that the one-oscillator model with a fully localized charge of $|e|$ and a mass of 16 amu gave $\sigma_{loc} = 3\times10^{-17}$ cm (Table II.1). A first principle prediction of the carbon local mode absorption strength cannot yet be given.

The case of the B local mode in silicon has received considerable experimental and theoretical work. B is the lightest of the simple donor or acceptor atoms which can be dissolved in the Group IV hosts, and thus should produce the most spatially localized impurity mode. When B is introduced as an impurity in the Si lattice, it is substitutional (a shallow acceptor) and must be electrically compensated for in absorption studies. Compensation techniques have already been discussed. In order to observe the isolated B_{Si}^{-} species of T_d symmetry, the compensation technique must employ species which do not readily ion pair with the boron. The method usually employed has been doping during growth with a donor and then completing compensation either by electron irradiation or by Li diffusion. Figure 42 shows some experimental results of Angress *et al.* (1964). The absorption cross section for the boron is approximately 0.2 that of the carbon. As in the case of carbon, the calculated frequency (mass defect model) of 664 cm^{-1} for Bi_{Si}^{11} is substantially higher than the observed value near 620 cm^{-1}.

The dependence of the B_{Si} local mode frequency upon

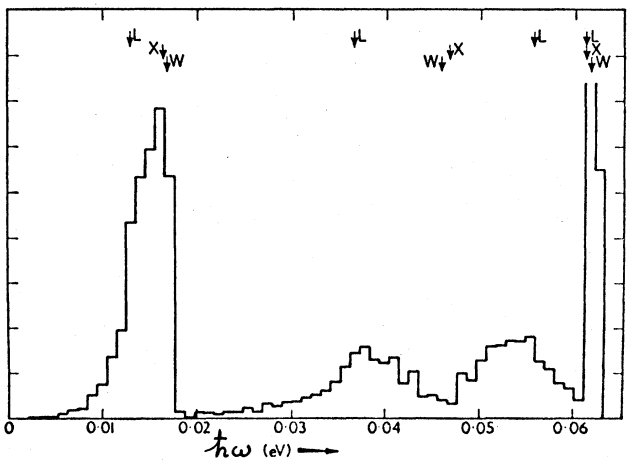

FIG. 40. Density of states for silicon. Some critical point energies are shown. From Johnson (1965).

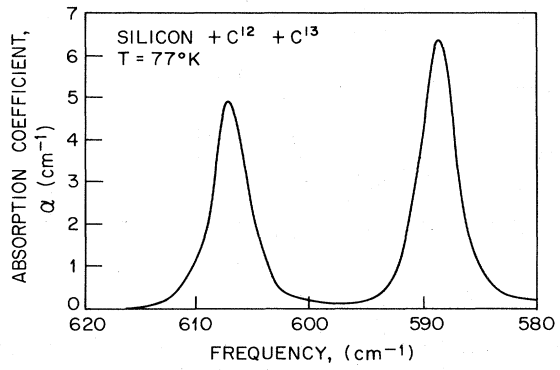

FIG. 41. Differential absorption spectrum of silicon doped with 43% ^{12}C and 57% ^{13}C compared with zone refined silicon. The total carbon concentration is approximately 10^{18}/cc. The two local modes occur at frequencies slightly below those predicted by the Dawber–Elliott calculations. From Newman and Willis (1965).

[10] The cross section defined here is not conventional, however, it is a practical quantity which can be related to model calculations. See Table II.2 for the value of σ_{loc} in the point charge one-oscillator model.

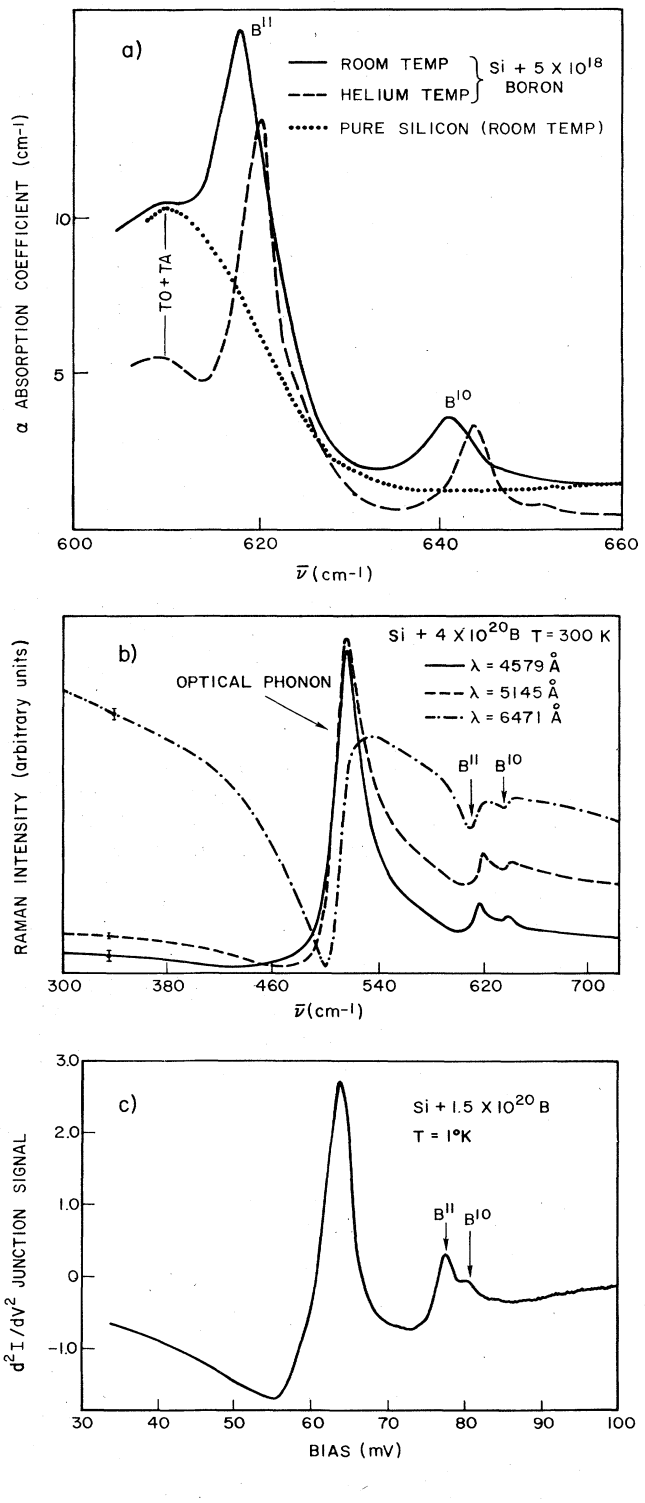

FIG. 42. Local mode due to boron in silicon at room and liquid helium temperatures. (a) Infrared absorption, compensation by phosphorus doping and 2 MeV electron bombardment. From Angress *et al.* (1964). (b) Raman scattering spectrum—no compensation. Error bars represent noise. Three laser wavelengths were used. From Cerdeira *et al.* (c) Electron tunnel junction spectrum showing optical phonon and local modes. From D. C. Tsui (private communication) (1974).

force constant changes has been investigated by Elliott and Pfeuty (1967), who include nearest-neighbor force constant variations in their Green's function calculations and show that it is possible to fit experiment by reducing the B–Si force constants.

Two methods which avoid the compensation problem are Raman scattering and electron tunneling. Cerdeira, Fjeldly, and Cardona (1974) have recently observed the boron local modes by Raman scattering. Their results are shown in Fig. 42. The presence of 4×10^{20} carriers (holes) causes a significant shift of the local modes to lower frequency and also Fano-type lineshape anomalies which depend on the wavelength of the exciting laser radiation. The tunneling method has detected the boron local mode but involves some complications in interpretation and the practical difficulties of making a suitable junction. A tunnel junction spectrum is shown in Fig. 42(c). While the local modes show clearly here, other similar systems do not show local mode structure in their tunneling spectrum. The factors which control the strength of these features in tunneling spectra are not understood at present.

Until recently there was no report of infrared absorption by isoelectronic impurities other than C in a Si or Ge host. However, Raman studies of Ge_xSi_{1-x} alloys by Feldman *et al.* (1966) showed a mode which was interpreted as the Si_{Ge} local vibration for x close to unity. Figure 43 shows some of the spectra. The frequency for $x=0.985$ is 389 cm^{-1}, which is very close to the calculated value of 394 cm^{-1}. In addition, for $x \lesssim 0.95$, Raman lines were observed at 448 and 476 cm^{-1}, both of which are greater than the maximum unperturbed Ge phonon

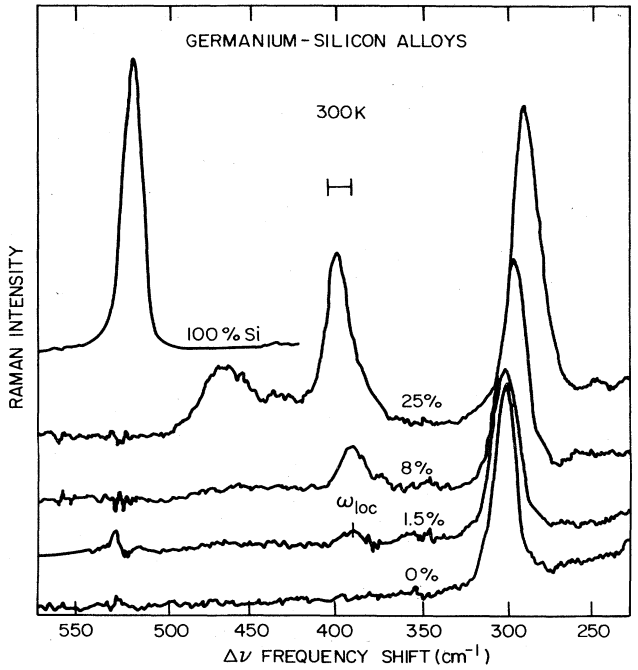

FIG. 43. Raman spectra of germanium-silicon alloys for several compositions. The instrumental resolution is indicated by the vertical lines. The isolated Si_{Ge} local mode occurs at 389 cm^{-1}. From Feldman *et al.* (1966).

frequency (305 cm^{-1}). These bands were attributed to the two Raman-active modes of the Si_{Ge}–Si_{Ge} nearest-neighbor pair defect (D_{3d} symmetry). Later Raman studies by Brya (1973) and by Renucci *et al.* (1971) suggest, however, that the 476 mode is not associated with isolated defect pairs. Wakabayashi *et al.* (1971) have observed the local mode near 380 cm^{-1} by neutron scattering. Their samples contain 9.2% Si, so that concentration broadening is significant. Some very recent absorption measurements by Cosand and Spitzer (1971) for $0.88 \leq x \leq 1.00$ show the local mode band near 390 cm^{-1}. Figure 44 shows their infrared results for several concentrations of Si. The absorption cross section $\sigma_{loc} \sim 1 \times 10^{-20}$ cm is essentially constant over the indicated range of x, as expected for noninteracting defects. The mass defect ϵ and the mode eigenvectors are similar for C_{Si} and Si_{Ge}. We note, however, that the σ_{loc} in the latter case is 10^3 smaller for C_{Si} in Si, in spite of the fact that each is an isoelectronic impurity in a homopolar crystal. There are a number of significant factors which could cause major differences for the two cases. The electronegativity values of Ge and Si are almost the same, while that for carbon is quite different; the tetrahedral covalent radii are similar for Si and Ge ($r_{Si}/r_{Ge} = 0.96$), while C is again different ($r_C/r_{Si} = 0.65$). It is well known that Si and Ge form a uniform solid solution over the entire range of mixtures, while C is only slightly soluble in Si and in large quantities forms the SiC compound. These differences point up the fact that the bonding and charge distributions are different in the two cases, requiring more detailed models than are presently available.

The case of Ge impurities in silicon tending to form resonant modes is discussed in Sec. 4 below. Several of the studies mentioned above include a wide range of concentrations of the Ge_xSi_{1-x} alloy and will be referred to again in Sec. IX.

3. Localized vibrational modes of defect pairs

B–Li pairs in Si were the first case in which localized modes of a defect pair were the subject of a detailed investigation, and remain today as the most thoroughly studied case in any semiconductor. The B is in a substitutional site and the Li is presumed to be in an interstitial site (Reiss and Fuller, 1956). Figure 45 shows a substitutional B impurity and one possible interstitial Li site. The Coulomb attraction and the mobility of Li favor the formation of $B_{Si}^- - Li_i^+$ pairs as shown in the figure. Experiments by Balkanski and Nazarewicz (1966), Spitzer and Waldner (1965a and b), Waldner *et al.* (1965), and Chrenko *et al.* (1965) show that when ^{7}Li compensated samples are measured, the 620 cm^{-1} band for isolated ^{11}B is replaced by bands at 655, 564, and 522 cm^{-1}. Analysis of the bands is carried out by using ^{10}B in place of ^{11}B and by compensating with ^{6}Li in place of ^{7}Li. A typical absorption spectrum is shown in Fig. 46, which illustrates the various isotope effects.

An early interpretation of the pair mode spectrum suggested that the effective force constant between the B and Li was small, causing the triply degenerate modes to split into two modes, one singly degenerate axial mode and a doubly degenerate mode at higher frequency orthogonal to the B–Li axis. This result now appears questionable, and Cosand (1971) has summarized various models for the mode separation and its relation to the $B_{Si}^- - Li_i^+$ ion spacing in the lattice.

The detailed calculations for B–Li pairs were done by Elliott and Pfeuty (1967) and by Pfeuty (1968), by use of a Green's function analysis. They find that reasonable results can be obtained with the substitutional B-interstitial Li defect pair model if one makes a number of assumptions concerning force constants. Terms are included representing a harmonic but anisotropic interaction between the B and Li. It is also necessary to lower the force constant for the B–Si bond opposite the Li and the second-neighbor force constants between the B and those Si atoms which are also nearest neighbors of the Li. The model has a predominantly Li vibration near 522 cm^{-1} for ^{7}Li, and near 534 cm^{-1} for ^{6}Li. With these assumptions and force constant changes, quite good agreement is obtained between calculated and experimental values, as shown in Table IV.2.

The Li participation in the pair modes is not yet well

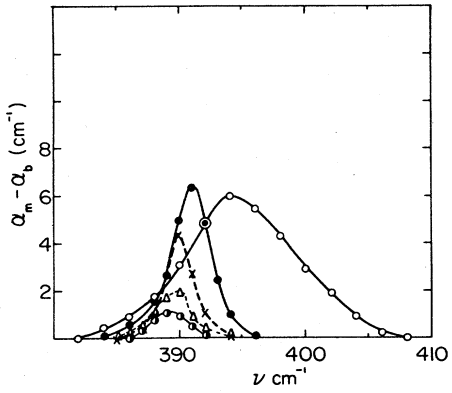

FIG. 44. Absorption coefficient at 80 K for the Si local mode in Ge-rich Ge–Si alloys. The background absorption has been subtracted off. In order of increasing strength the alloy compositions are 0.6%, 1.5%, 2.5%, 4.5%, and 12.0% silicon. From Cosand and Spitzer (1971).

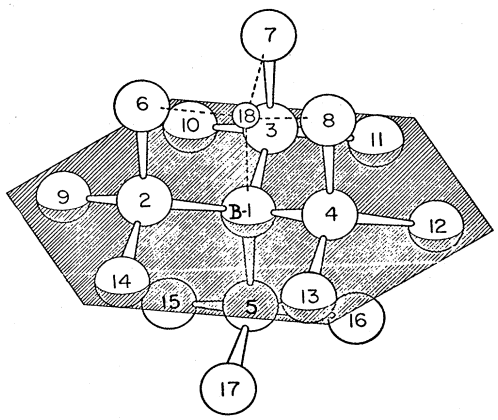

FIG. 45. An impurity site (B1) in a diamond lattice with its four first neighbors (2–5), twelve second neighbors (6–17), and a tetrahedral interstitial site (18). From Cosand (1971).

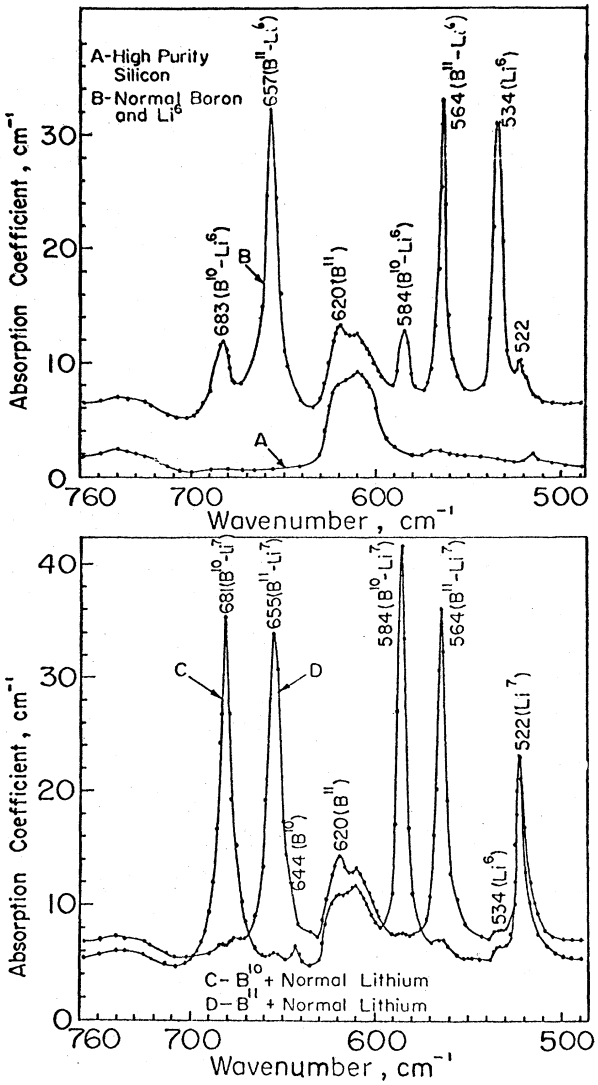

FIG. 46. Absorption spectra for boron- and lithium-doped silicon: (A) high-purity silicon; (B) boron and ^{6}Li doping; (C) ^{10}B and Li; (D) ^{11}B and Li. From Spitzer and Waldner (1965b).

understood. One might expect two Li modes, an axial and a doubly degenerate transverse mode, similar to those of the B. The small isotope shift between the observed ^{7}Li and ^{6}Li bands is qualitatively understood by noting that the maximum phonon frequency for pure Si is between 520 and 525 cm^{-1}. Therefore the Li modes are not highly localized and considerable motion of the neighboring Si must be involved. Indeed, the 522 cm^{-1} band for ^{7}Li may be a resonant mode lying within the silicon optic band. One is forced to conclude that either the Li modes are not significantly split by the interaction or that the other, presumably axial Li mode, is at a lower frequency and has not been observed, perhaps because of a high density of band modes at its frequency.

The B–Li defect model has recently been extended by Cosand (1971) to Si-rich Ge–Si alloys. The presence of the Ge causes an asymmetric broadening of the B modes. The broadening effects could be explained as the result of second neighbors to the B being randomly distributed between Ge and Si atoms, which changes the B–Si force constants. Some weak split-off bands were also observed which were attributed to B with a Ge first neighbor. This small observed strength may be an indication that B and Ge tend to avoid nearest-neighbor sites (Cosand, 1971).

4. In-band and resonant modes

Several defects have been shown to produce band mode absorption (i.e., absorption in the range of the host lattice phonons) in Group IV materials. For the present purposes we will discuss the Si host, as it is the one most extensively studied. The simplest (though by no means completely understood) case is probably that of Ge–Si alloys at the Si-rich end of the composition range (Cosand and Spitzer, 1971). The introduction of Ge produces pronounced bands near 125, 405, and 485 cm^{-1} as shown in Fig. 47. There is some question as to whether these peaks represent resonant mode frequencies or simply density of states peaks in the silicon phonon spectrum shown in Fig. 40. All three bands lie close to peaks in the density of states function; however, two of the bands (125 and 485 cm^{-1}) also lie close to resonance or near-resonance positions as calculated by Maradudin

TABLE IV.2. Comparison of B–Li pair mode frequencies in silicon.[a]

Defect	Mode	Observed frequency (cm^{-1})	Calculated frequency (cm^{-1})
^{10}B–^{6}Li, ^{11}B–^{6}Li	Primarily Li	534	533
^{10}B–^{7}Li, ^{10}B–^{7}Li	Primarily Li	522	522
^{10}B–^{6}Li(^{10}B–^{7}Li)	Primarily B transverse mode	683(681)	678(678)
^{10}B–^{6}Li(^{10}B–^{7}Li)	Primarily B axial mode	584(584)	584(584)
^{11}B–^{6}Li(^{11}B–^{7}Li)	Primarily B transverse mode	657(655)	655(651)
^{11}B–^{6}Li(^{11}B–^{7}Li)	Primarily B axial mode	564	565.5

[a] From Pfeuty (1968).

(1966a) for Ge in Si (see Fig. 38). Dawber and Elliott (1963b) have calculated the mode spectrum for As in Si. Since As has a mass close to that of Ge, this calculation is also relevant to Ge_{Si} and is shown in Fig. 47. Both theoretical calculations show some similarities to the measured spectra. At the present time this lack of close agreement appears typical of most resonant mode experiments.

Angress *et al.* (1964, 1965, 1968) have observed band mode absorption in Si containing B plus a heavy substitutional donor, either P, As, or Sb, and with final compensation produced by electron irradiation. They also studied P-doped Si compensated by neutron irradiation. Some of their results are shown in Fig. 48. The most prominent band was near 441 cm^{-1}, which was attributed to a phosphorous resonance. A number of weaker bands were observed and some attributed to impurity resonances, while others were related to impurity activation of lattice modes. In general it was found that the "in-band" absorption due to B was in reasonable agreement with the predictions of Dawber and Elliott [Fig. 48(c)], while P and As absorption were not in agreement. In view of the later work of Leigh and Szigeti, the lack of success of the impurity point charge model used by Dawber and Elliott for P_{Si} is not unexpected.

A particularly interesting case is the recent prediction of a near-resonance absorption at 225 cm^{-1} for B-doped Si. In this calculation, Bellomonte and Pryce (1968) used a density of states for Si obtained from an analysis by Johnson and Loudon (1966) of the neutron results of Dolling (1963). This density of states is significantly different from others in the literature and leads to a boron resonance absorption, as opposed to boron's merely activating the regular band modes of the silicon. Angress *et al.* (1965, 1968) independently observed a small peak near 227 cm^{-1} (see Fig. 48). This result illustrates the necessity of having accurate information concerning the density of states for reliable resonant-mode calculations.

Finally we wish to note one possible class of localized modes which is conspicuous by its absence. In Fig. 21 vacancy modes for the linear chain were illustrated. Corresponding modes must exist for $\square_{Si}$ (vacancy on a Si site) in silicon, though probably only the low-frequency solutions (resonant modes) would occur in a real crystal. The silicon vacancy is observed in electron spin resonance experiments, is mobile above approximately 100°K, and can exist in several charge states (Watkins, 1972). Since the vacancy is perhaps the most basic intrinsic defect, there is considerable theoretical interest in band strengths and lattice relaxation about this defect. Note that the fundamental breathing mode of the neutral vacancy would be Raman active, but other motions, as well as modes of the charged vacancy, would be infrared active. It would be extremely valuable to detect these localized vibrations by optical methods.

C. III-V compound semiconductors

1. Introduction

The compound semiconductors have proved to be a rich field for localized mode studies, but there are very few experimental results of either resonant modes or band absorption. The III–V compound crystals usually crystallize in the zinc blende structure $A_{III}B_V$, which is produced by placing the Group III element on one sublattice of the diamond structure, called A, while the Group V element is placed on the other, or B, sublattice. Thus each atom is tetrahedrally coordinated with four atoms of the other type. Since there is no longer a center of inversion as in Si, a first-order electric moment is allowed and the TO modes near $\vec{q}=0$ are active in infrared absorption as well as in Raman scattering. The TO and LO mode frequencies near $\vec{q}=0$ are now split, and the LO–LA degeneracy at the zone edge in the ⟨100⟩ direction (*X* point) is lifted, allowing the possibility of a gap in the phonon spectrum. Figure 49 shows the phonon dispersion curves of GaAs. Comparison with Fig. 39 shows the splittings referred to at high-symmetry points. The dispersion curves of GaP are very sim-

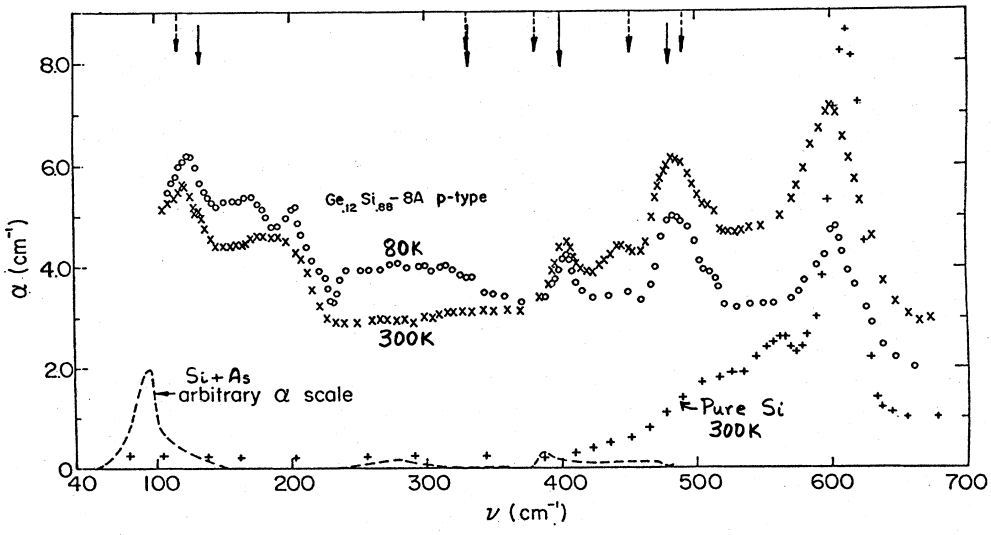

FIG. 47. Absorption coefficient for $Ge_{0.12}Si_{0.88}$ compared with Si. Dashed curve is absorption predicted by Dawber and Elliott for a heavy impurity (As) in Si. Dashed arrows are positions of resonance and near-resonance modes as calculated by Maradudin (see Fig. 38). Solid arrows indicate peak positions in the histogram for the vibrational spectrum of Si. From Cosand and Spitzer (1971).

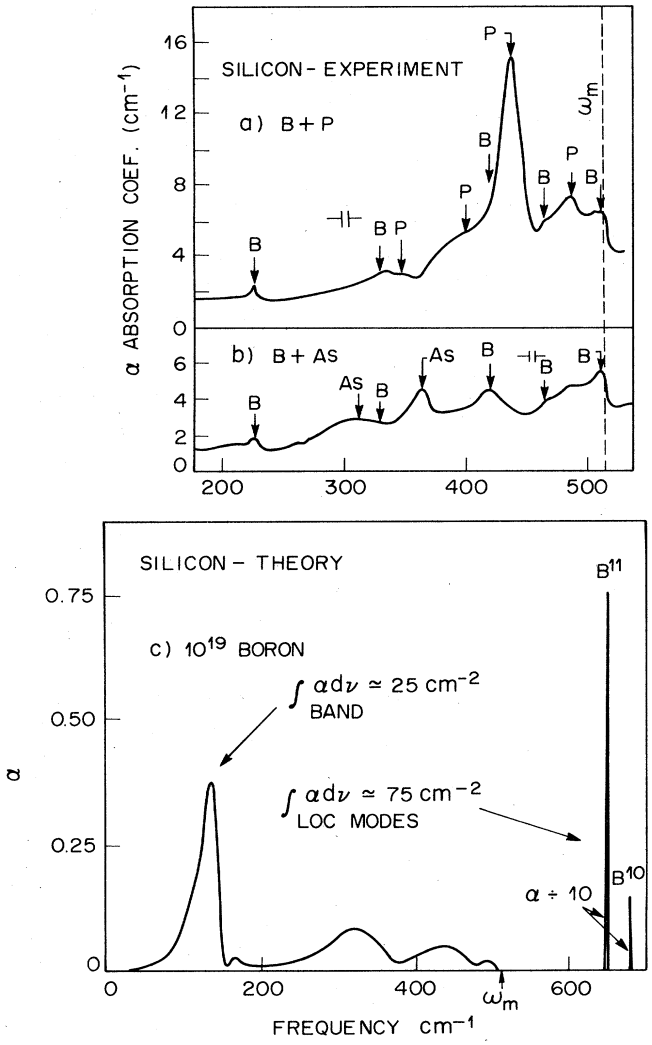

FIG. 48. The absorption spectra of silicon doped with boron and phosphorus (a) and boron and arsenic (b). From Angress *et al.* (1968). (c) Absorption spectra calculated from the theory of Dawber and Elliott, showing impurity-activated band modes and local modes. From Elliott (1966).

ilar in shape to GaAs, but there is a wide gap between the acoustic branches and the optic branches. Figure 50 compares GaAs and GaP. From the figure it is evident that gap modes will be possible in some of the III–V compounds.

In the case of the isoelectronic substitution of a Group III or Group V impurity in a III–V material, the defect will not contribute free carriers, and hence electrical compensation is not a problem. This is why the reader will note a number of such cases given in Table IV.1, for example, Al or P in GaAs, GaSb, and InSb; Al and B and N in GaP. When one introduces impurities from the II, IV, and VI columns, then the impurities are generally electrically active, i.e., they are donors or acceptors, and reduction of the carrier concentration is required for infrared absorption measurements. In many cases impurity compensation is not easy to achieve. In some cases, particle irradiation does not tend to produce well compensated material. A happy exception is GaAs, and this explains the rather long list of defects observed in that material. The energy gap of GaAs is 1.4 eV, which is larger than that for Si, allowing Li diffusions to be done at temperatures up to ~1000°C (Spitzer, 1971). Samples a millimeter thick can be uniformly Li diffused in a few hours at 600°C. In addition, both electron and neutron irradiation tend to produce defects which compensate for any impurity originally present.

The materials GaAs and GaP are excellent hosts for the study of high-frequency local modes for a number of additional reasons. Both Ga and As are fairly heavy, and hence there are a large number of relatively light impurities which are candidates for introducing local modes. In many cases the impurities have large enough solid solubilities that detection by infrared absorption is relatively easy, and in some cases correlation with transport properties also becomes possible. The masses of Ga and As are sufficiently close that for theoretical purposes one can approximate this diatomic system by a monatomic system. In addition, the phonon spectra of pure GaAs and GaP have been measured and the density of states fairly well established (see Fig. 50).

For the above reasons we will restrict our discussion to GaAs and GaP. We will not discuss all the defects, but will concentrate on the details of several cases of particular interest. As will be seen, the studies are not complete and in some cases interpretations in the literature of the last few years are obviously in error.

2. Models for localized modes in diatomic crystals

It is appropriate here to review models for the frequencies of localized modes since there are very few detailed model calculations for the III–V semiconductors. In contrast with the case of the Group IV semiconductors, the diatomic structure causes far more parameters to be needed for realistic models of the host crystal even before the defect is introduced into the problem. Beginning with the simplest possible model we have the one-oscillator approximation discussed in Sec. II (2.13):

$$\omega_{\rm loc} = \omega_{\rm TO}\sqrt{m/m'}. \tag{4.1}$$

In the equation m' is the mass of the impurity, and the one "parameter" which is a force constant has been written as two parameters, here $\omega_{\rm TO}$ and m. In the spirit of the mass defect model we hope that this parameter may be evaluated from some knowledge of the pure host crystal. In fact an examination of actual local mode frequencies observed in several III–V semiconductors shows that there is no unique choice for the parameter. An easy choice which is correct in the limit of very small m' is to choose the transverse optic mode frequency for $\omega_{\rm TO}$ and the reduced mass of the two constituent host atoms for m. Consideration of a range of experimental results shows that the model gives results which are 10 to 20% low in typical cases. As might be expected, there are several immediate objections to such a simplified model. One is simply that the form presented here does not distinguish whether the substitution is taking place on the A or B sublattice. In spite of this objection an extension of the one-oscillator model

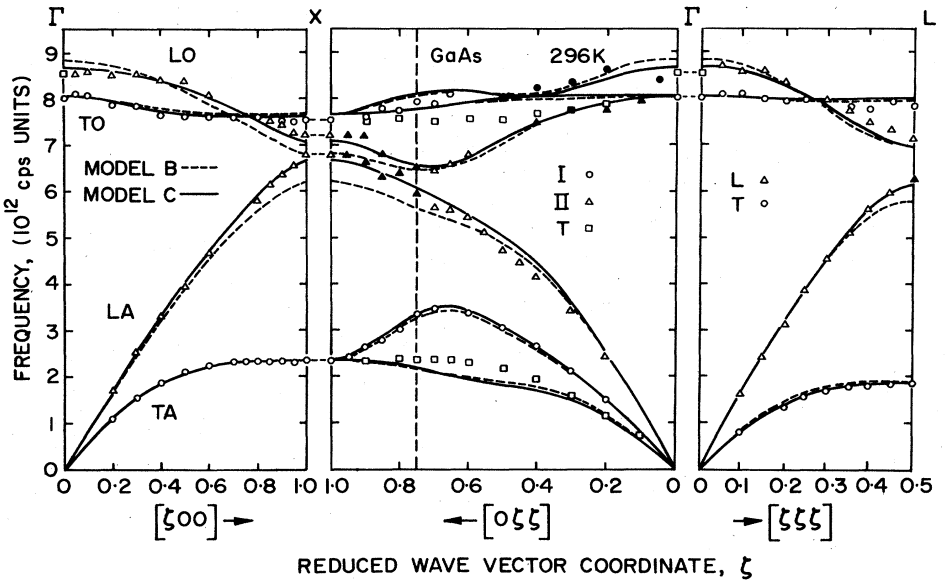

FIG. 49. Theoretical dispersion curves for gallium arsenide at 296 °K, calculated on the basis of two different modifications of the dipole approximation model, Model B(ii)—dotted lines; Model C(i)—solid lines. From Dolling and Waugh (1965).

forms the basis for most of the detailed analyses of local modes in many defect systems. The defect potential implicit in (4.1) is $V(x)=Ax^2$. The most common extension of the model is to make it three-dimensional and to add anharmonic terms. For a defect atom at a site of tetrahedral symmetry the potential is (Elliott *et al.*, 1965)

$$V=A(x^2+y^2+z^2)+Bxyz+C_1(x^4+y^4+z^4)+C_2(y^2z^2+z^2x^2+x^2y^2)+\cdots \quad (4.2)$$

For only A nonzero, a single local mode frequency is calculated as given by (4.1). The anharmonic terms allow the second and third harmonics to have a finite infrared strength. In particular, if the second harmonic is observed, it establishes the presence of the term $Bxyz$ in V, confirming that the defect site has tetrahedral symmetry. Elliott *et al.* (1965) have given detailed results for the potential (4.2), including the calculation of the temperature dependence of intensities, of line shifts and widths, and the appearance of sidebands. This three-dimensional anharmonic form of the one-oscillator model is thus capable of correlating and predicting a great many results on local modes. The parameters A, B, C_1, C_2, etc. are not derived from first principles or from properties of the host. They are fit to some of the data. The use of (4.2) goes well beyond the mass defect model—it actually establishes the form of the short-range defect potential once it has been fit to sufficient data on the fundamental, second, and third harmonic absorption. Note that since even the parameter A is fit to experimental results, (4.2) is not usually used to predict the occurrence of localized modes.

Returning to harmonic mass defect models, Allen (1970) has suggested a two-parameter (two-oscillator) model to evaluate local mode frequencies in the III–V semiconductors. He derives the model from considerations of an impurity mass vibrating against some other mass which represents the nearest neighbors in the actual lattice. The parameters are evaluated by actually fitting to some observed local mode frequencies. Quite reasonable predictions are then made for other local mode frequencies using the model. The equation for the local mode is given by

$$\omega_{\rm loc}^2=A(1/m'+1/\beta m_{nn}), \quad (4.3)$$

where m_{nn} is the mass of an atom neighboring the impurity, and A and β are the parameters of the model. This model does distinguish between A and B sites through m_{nn}. Note that (4.1) and (4.3) give the same behavior for very light mass impurities, but different limiting behavior for large mass impurities.

As the impurity mass increases from very small values, the mode must be much more extended in real space as the frequency of the local mode approaches the frequencies of band modes of the host. Models like those discussed above can be expected to become poor approximations in this limit (large m'), since they do not contain the band modes. In order to obtain more realistic models one is naturally led to the linear chain calculations such as those presented in Sec. II. In fact the simple models described by (4.1) and (4.3) can be shown to correspond to special one-atom and two-atom linear chains. Linear chains which contain more atoms can naturally have more parameters; for example, second-neighbor and third-neighbor forces. Multiatom chains allow the spatial extent of the localized mode to be evaluated as well as the local mode frequency.

Lucovsky *et al.* (1970) have proposed using a diatomic linear chain with one type of force constant between nearest-neighbor ions. If the masses in such a chain model are chosen to be the masses of the real crystal then this is a one-parameter model. The authors write down the analytic form for the localized mode frequencies which have been derived earlier by Mazur, Montroll, and Potts (1956). The analytic form can be expressed as simple combinations of two parameters. Lucovsky *et al.* now abandon the original linear chain and treat these two parameters as basic, relating them to the

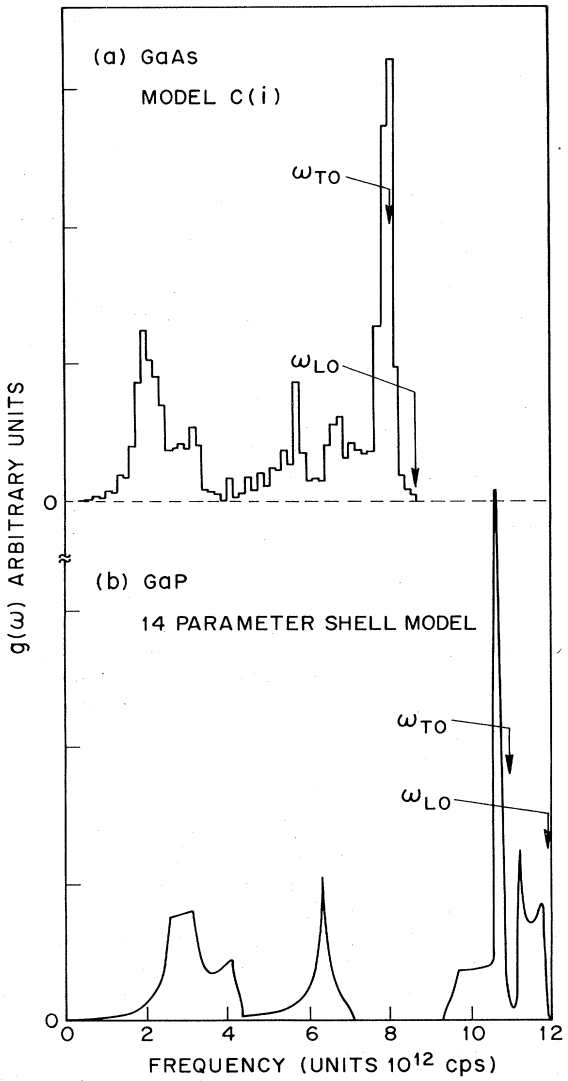

FIG. 50. (a) Calculated frequency distribution for gallium arsenide at 296 °K, based on Model C(i) of Fig. 49. (b) Frequency distribution for gallium phosphide from the work of Yarnell *et al.* (1968).

measured ω_{TO} and ω_{LO} frequencies of the real host crystal. In this way they have a procedure which can predict local mode frequencies using only data on the host. The new ingredient which is used in applying the model is the assumption that localized modes will not actually be observed if the mode predicted in this manner lies inside the optic or acoustic band of the real crystal. In this way they surmount one shortcoming of the linear chain model: it predicts a local mode for any light substitution on a host ion site contrary to the results for three-dimensional crystals. Other difficulties of the linear chain model remain, however. For example, resonant modes cannot appear in the model. Using the model the authors are able to establish a large list of predictions for local mode frequencies which in many cases are quite close to observed modes and in other cases can serve as predictions where no local mode has yet been observed.

Barker and Berman (1974) have also used a diatomic linear chain model to predict local mode frequencies. They use the masses of the crystal being modeled as fixed parameters and choose three force constants as three adjustable parameters. The forces chosen are those between nearest neighbors, those linking anions, and those linking cations. The three force constants are chosen to actually fit some observed localized modes in the crystal. Figure 51 shows the results of this linear chain model for local modes in GaP. The suggestion of Lucovsky *et al.* has been included by drawing in the experimentally observed band edges in the figure. The occurrence of a sharp spectral feature is to be expected only where the local mode solution curve emerges from the band. Note that there is a gap mode for heavy-ion substitution on the Ga site. This is in contrast to the simple nearest-neighbor force constant linear chain where no such mode can exist. This mode occurs in the gap of the chain but falls inside the optic band of real GaP. It is not clear at this stage whether modes of this type will be observable. Substitutional local modes which have been observed in GaP are included in Fig. 51 as solid points.

The absorption strength of the localized mode can be evaluated from the chain model once a charge is assigned to the impurity, and the localization can be evaluated from the eigenvectors. Figure 52 shows the mode strength for the localized and gap modes assuming isoelectronic defect ions in the Barker–Berman chain model. The band modes will also acquire infrared activity which can be calculated and was shown for several cases in Sec. II using a model with nearest-neighbor forces.

We now briefly describe a more detailed model for prediction of localized mode frequencies in several III–V and II–VI compounds. Gaur *et al.* (1971) have used a rigid ion model to describe the host crystal. The parameters of this model are fixed by knowledge of the three elastic constants and the ω_{TO} and the ω_{LO} optic mode frequencies. The model is therefore more detailed than a linear chain model but certainly much simpler to handle than a shell model which must have neutron dispersion curves to determine the parameters. The impurity ion is assumed to be a mass defect only. Figures 53(a)–(c) show the results of some of these calculations for several semiconductors with the zinc blende structure. The calculations give localized modes above the optic band when the mass of the impurity is less than some critical mass. This fact explains the termination of the solution curves at the low ϵ end in the figures. It is interesting to note the close correspondence of the two localized mode solutions for cases where the host crystal is nearly "monatomic." For example, in gallium arsenide the atomic masses are within 7% of each other. The approximation is often made for purposes of calculating ω_{loc} that the lattice vibrations of GaAs are very similar to those of silicon except for a frequency scaling factor (Lorimor, Spitzer, and Waldner, 1966; Verleur and Barker, 1966). Using such an approximation, substitutions on the gallium sites and the arsenic sites are equivalent. The validity and the degree of approximation resulting from this assumption can immediately be tested using the figures.

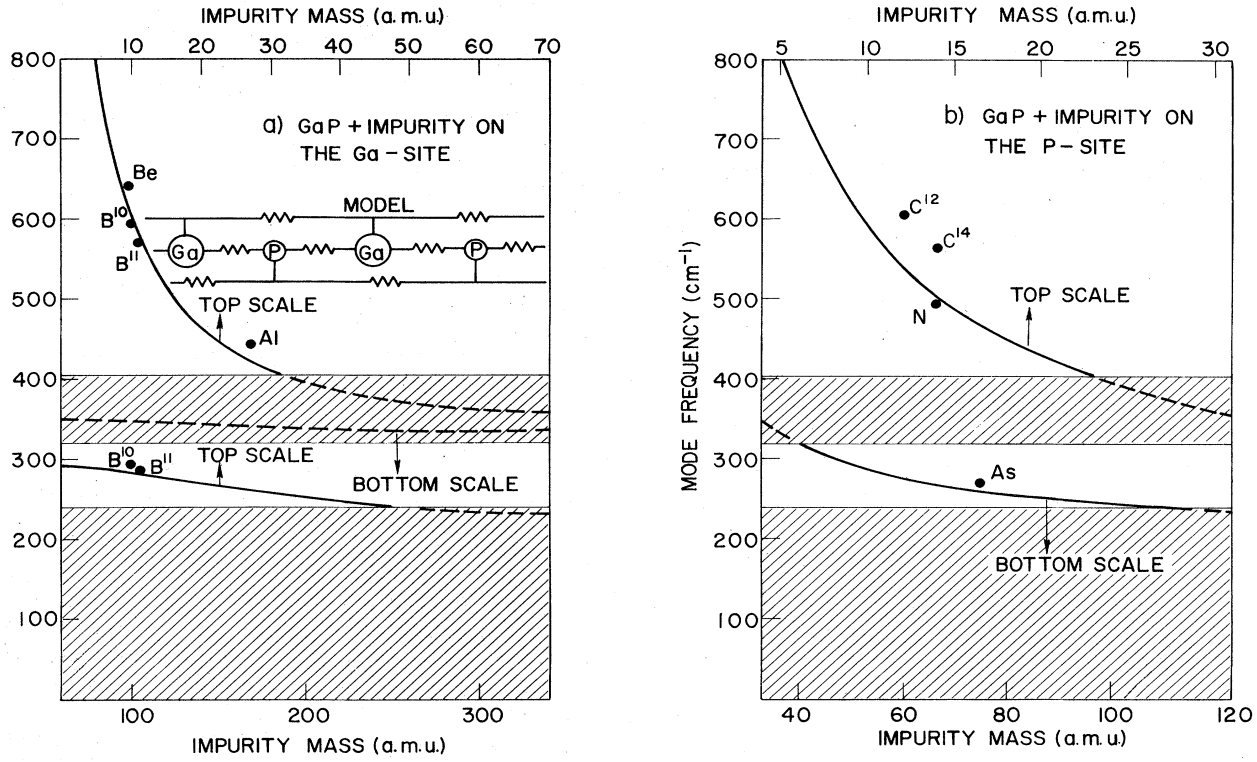

FIG. 51. (a) Local mode frequencies from a three-force-constant linear chain model. Isotopic substitutions are made on a Ga-ion site. The form of the model is shown in the inset. The force constants are chosen to make $\omega_{TO} = 358$ cm^{-1}, the optic branch very flat, and to approximately fit the N_P local mode. The forces are 0.813×10^5 (Ga–P), 0.16×10^5 (P–P) and 0.15×10^5 dyne/cm (Ga–Ga). The shaded regions mark the acoustic and optic band positions in real GaP. (b) Local and gap mode frequencies for isotopic substitutions on the P-ion site. The solution curve is shown dashed where it enters the shaded regions. We assume that well-localized modes cannot exist here.

Little work has been done on more fundamental impurity mode models in any of the compound semiconductors. While new knowledge is being gained at an increasing rate because of the technical importance of these materials, at the present time a fundamental model of the host requires too many unknown parameters. In addition, a fundamental model of the host crystal is not sufficient for many of the situations of practical interest. This is because the localized modes correspond not to simple substitutional mass defects but to force constant plus mass defects or more complicated interstitial defects or combinations of several defects. An example of the latter situation is the Li–Li–O defect cluster in GaP. The localized modes associated with this center have been studied by photoluminescence (Dean, 1971). At least three force constants, which are unique to this defect, must be introduced to explain some of the modes observed. In a similar fashion we find that, for many other compound semiconductors, experimental studies of localized modes have led to rather specialized models which introduce *ad hoc* force constants and which involve only the defect and the nearest-neighbor atoms rather than the entire crystal. Talwar and Agrawal (1975) have made a study of the force constant changes needed to make a particular model agree with known local mode frequencies. The force constant changes needed are as large as ±60% in some cases and appear unrelated to any obvious impurity atom parameter.

3. Gallium phosphide

Gallium phosphide is one of the most important compound semiconductors from the point of view of light-emitting electronic devices. In the "as-grown" form, it usually has a rich luminescence spectrum which exhibits many localized modes as sidebands on electronic transitions. These modes often result from the unintentional inclusion of impurity atoms during growth. At present the most important impurities from the point of view of the manufacture of light-emitting diodes are Zn, O, and N. Using the mass defect model, it is apparent that O and N can cause localized modes (see for example Figs. 51 and 53). It is worth noting at this point that in spite of great interest in the O local mode and in spite of tremendous efforts to find this mode, it has not positively been identified to date for the substitutional position O_P in the GaP lattice. O at an interstitial site has been identified and is of technical interest, since this form of O is inactive in the light-emitting process and hence robs the crystal of active O while it is being doped.

It is now well established that GaP has a wide gap between its acoustic and optic bands. This is clearly il-

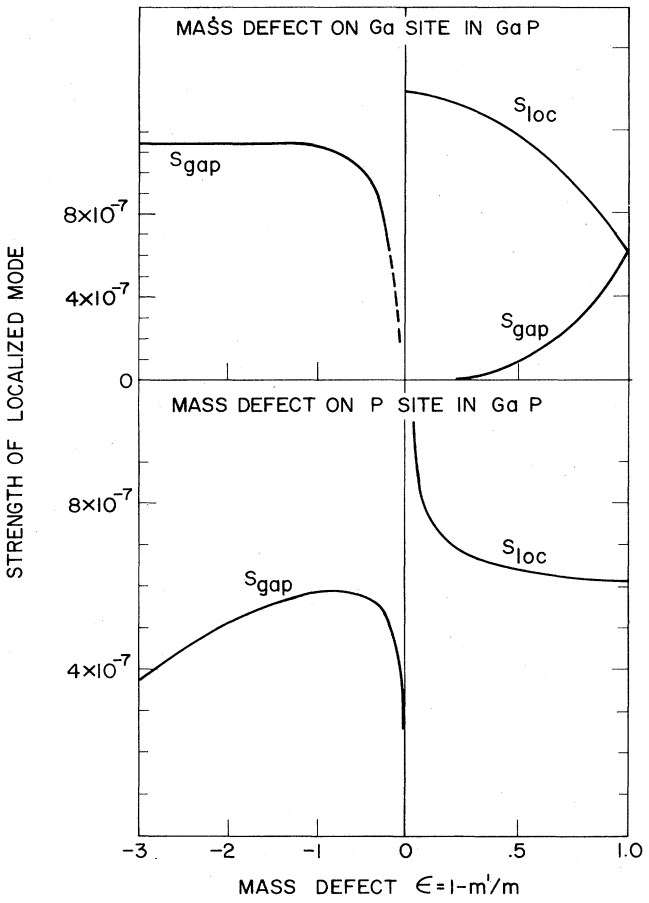

FIG. 52. Local and gap mode strengths for the model of Fig. 51. The impurity is assumed to have the same dynamic charge ($\pm 2e$) as the ion it replaces. Local field effects are neglected and a standard concentration of 10^{16} impurities/cc is assumed. Note the enhancement of S_{loc} as ϵ drops below 1.0 from the cooperative motion of the neighboring host ions.

lustrated for the shell model of Fig. 50 and the one-dimensional model of Fig. 2. GaP is therefore a good host for the study of gap modes.

Spitzer *et al.* (1969b) made one of the earliest studies of vibrational modes of defects in GaP. While several impurity species were considered, positive identification was made of ^{11}B and ^{10}B. The method of identification illustrates the importance of isotopes in local mode studies. The two local modes resulting from the two isotopes of B are well separated and maintain a strength ratio of about 4 to 1. This is exactly the ratio of the natural abundances of these two isotopes, giving a strong indication that the correct assignment is B. Some of the other assignments made by Spitzer *et al.* have proved to be correct, while other peaks observed by them have not been assigned to any known impurity even to this date. A listing of the known localized modes which have been connected with specific impurities is listed in Table IV.1. Figure 54 shows both localized modes and gap modes for the two isotopes of B in gallium phosphide. Hayes, MacDonald, and Sennett (1969) have also seen combination bands consisting of the simultaneous excitation of a gap mode and a local mode. These are shown in the bottom part of the figure. Lightowlers (1972) has carefully measured the B local mode absorption and the concentration of boron in several gallium phosphide crystals. For the ^{11}B local mode, he finds $\int \alpha d\lambda = 0.6 \times 10^{-6}$ for 10^{16} impurities per cc or $\sigma_{loc} = 0.19 \times 10^{-16}$ cm. This measurement of the absorption coefficient is the most accurate to date in a compound semiconductor. The value is about three times larger than for B in silicon and in fact is close to the model value given in Table II.1 which neglects local field effects.

Hayes, MacDonald, and Sennett (1969) have made calculations of the local and gap mode frequencies of B_{Ga} using the Green's function method and the mass defect model of Sec. III. Certain approximations are made in the characteristic equation (3.10), including using Debye functions for the acoustic mode density of states and a single delta function to represent the entire optical band density of states. The authors predict frequencies that are about 12% high for the local mode, and 15% low for the gap modes. It is typical of the situation in the compound semiconductors that this model, based on a sophisticated Green's function method, yields less accurate predictions than the simple linear chain model illustrated in Fig. 51.

The spectra of both Spitzer *et al.* and Hayes *et al.* show a sharp mode at 606 cm^{-1} [see Fig. 54(a)]. This mode has been shown by Hayes, Wiltshire, and Dean (1970) to be the local mode of ^{12}C. The mode shifts to 564 cm^{-1} for the ^{14}C isotope. These local modes are believed to arise from carbon on the P lattice site.

Barker *et al.* (1973) have made a search for oxygen local modes in gallium phosphide. Typical undoped crystals grown from the melt show as many as 20 to 50 impurity vibration bands. The problem in this system is not in finding local modes but in assigning them. A major sharp peak near 1000 cm^{-1} has been assigned to O_i. Figure 55 shows a pair of nearest-neighbor Si atoms in pure silicon connected by a [111] bond. It is fairly well established that oxygen can break this bond and form the Si–O–Si system pictured to the right of the figure. Newman (1969) has discussed the O_i localized vibrational mode in both Si and Ge. By analogy with the Si–O–Si system and also with the stable $GaPO_4$ crystal form, we expect that the Ga–O–P impurity configuration can occur in the GaP lattice (Barker *et al.*, 1973). Figure 55(b) shows the absorption of two crystals which are known to contain oxygen. In addition to the 1000 cm^{-1} mode assigned to the interstitial oxygen, many other high-frequency modes appear in the region of a prominent three-phonon band centered near 1100 cm^{-1}. Some of these modes have been tentatively assigned to pair vibrations involving oxygen together with other light impurities by Barker *et al.* Models of the isolated O_i local mode and of the pair local modes developed by the authors all involve *ad hoc* assumptions about force constants. While the force constants are reasonable in comparison with other semiconductors, a definitive test of the model requires measurement involving the ^{18}O isotope. Attempts to introduce ^{18}O into the GaP crystals have proved unsuccessful thus far.

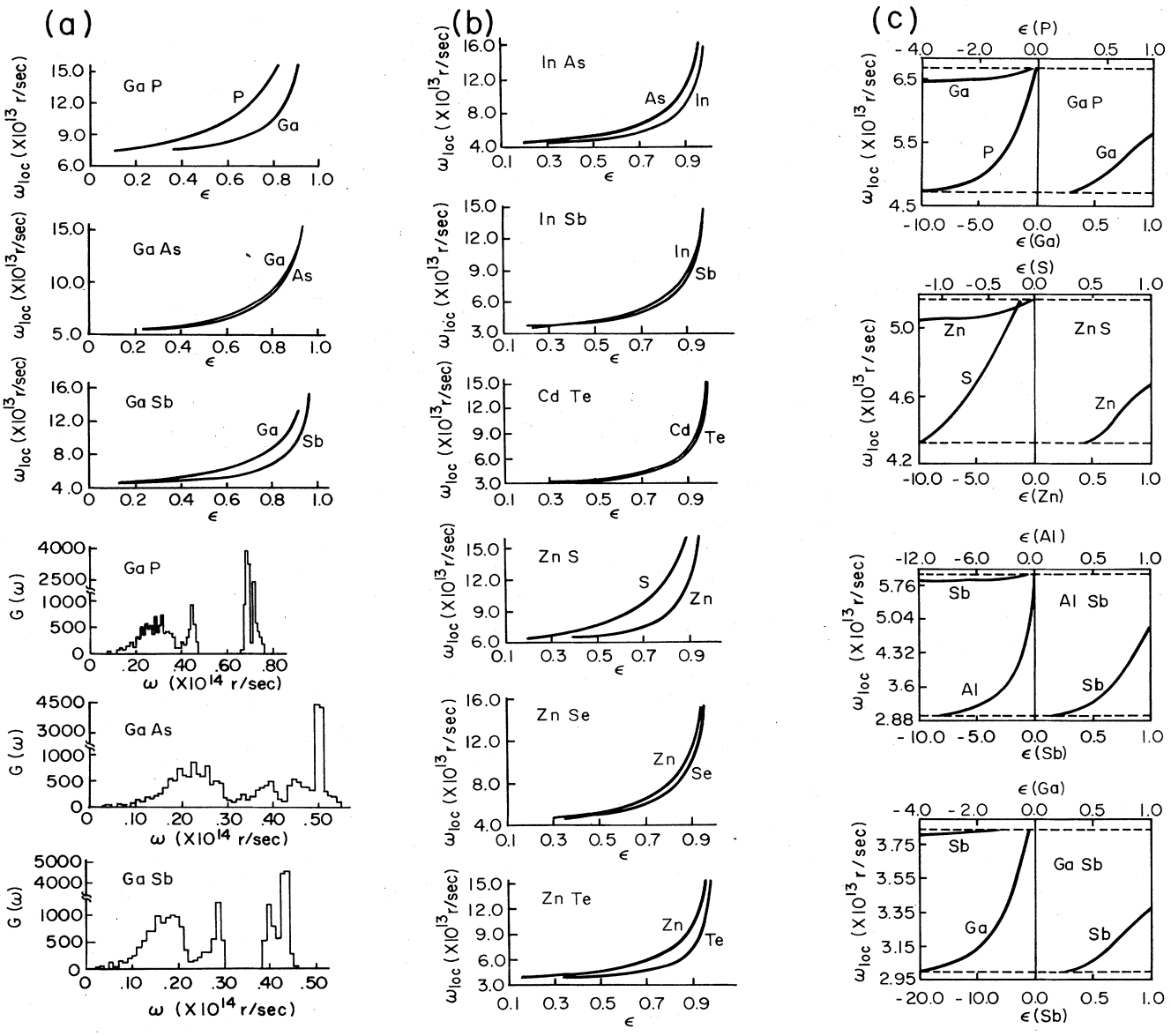

FIG. 53. (a) Localized mode frequency as a function of mass defect parameter for substitutions in GaP, GaAs, and GaSb. The calculations are based on a modified rigid-ion model and the mass defect approximation is used. The three histograms show the calculated frequency distributions of the host crystals. From Gaur *et al.* (1971). (b) Localized mode calculations for InAs, InSb, CdTe, ZnS, ZnSe, and ZnTe from the model described in Fig. 53(a). (c) Gap mode calculations for GaP, ZnS, AlSb, and GaSb from the model described in Fig. 53(a). The curves are marked by the ion being replaced.

4. Gallium arsenide

The measurement and assignment of local modes in gallium arsenide has proceeded faster than in other compound semiconductors. This is probably because compensation can be achieved for both donor and acceptors by lithium diffusion or by electron bombardment. Since there are two readily available isotopes of lithium, this flexibility has allowed the detailed study of any particular local mode complex by several different methods. One of the benefits of the local mode studies has been to give insight into the nature of various lithium defects. We discuss below the case of manganese–lithium modes, silicon local modes, and the modes due to lithium complexes in gallium arsenide. Considerable additional local mode work in gallium arsenide may be found by referring to various specific cases listed in Table IV.1.

Neutron diffraction studies of the phonon dispersion in GaAs are shown in Fig. 49. The figure shows that the highest frequency of the lattice occurs at the zone center. At room temperature this frequency is $\omega_m = 291$ cm^{-1}. The figure shows also that, unlike gallium phosphide, gallium arsenide has no gap in the phonon density of states. Figure 50 shows a density of states histogram based on a model fitted to the dispersion curves of the

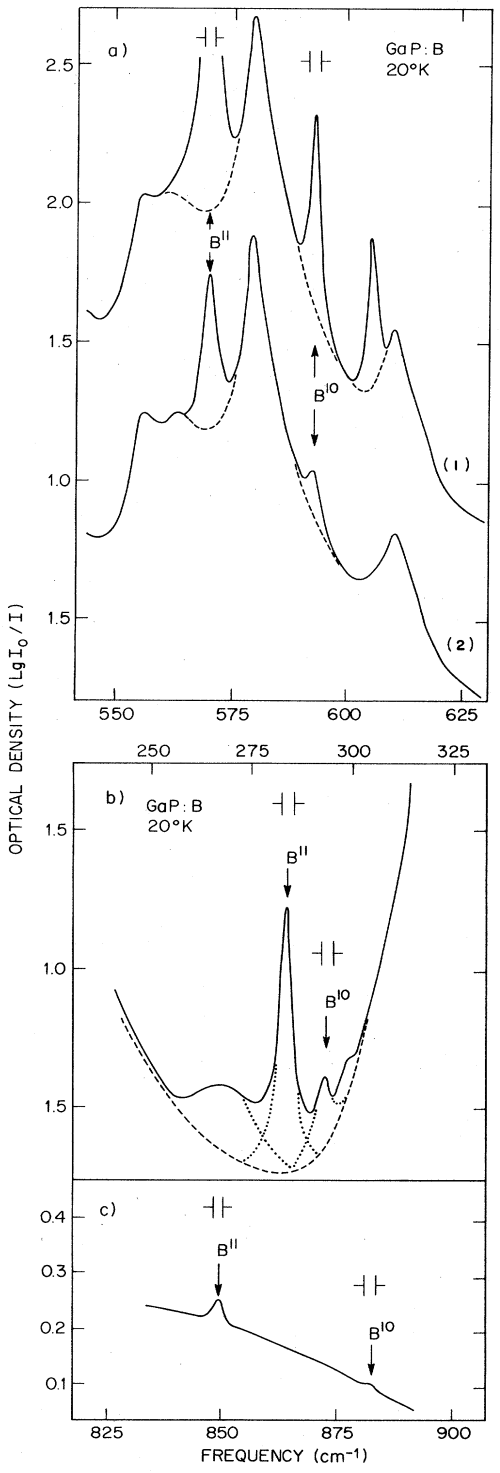

FIG. 54. Local modes, gap modes, and overtone modes of B in GaP. (a) Optical density at 20 °K of 1 mm thick (1) Malvern and (2) BT crystals of GaP containing boron. The spectra are not corrected for variation in background due to instrumental effects. (b), (c) Optical density of a 1 mm thick Malvern crystal of GaP at 20 °K containing boron. The top energy scale refers to (b) and the bottom energy scale to (c). The broken line on (b) represents an estimated optical density for pure GaP in the gap mode region. From Hayes *et al.* (1969).

previous figure. The histogram appears to show a narrow gap in GaAs; however, an examination of Fig. 49 shows that the density of states cannot go to zero anywhere in the range O to ω_m. Sharply localized gap modes are not to be expected therefore in GaAs.

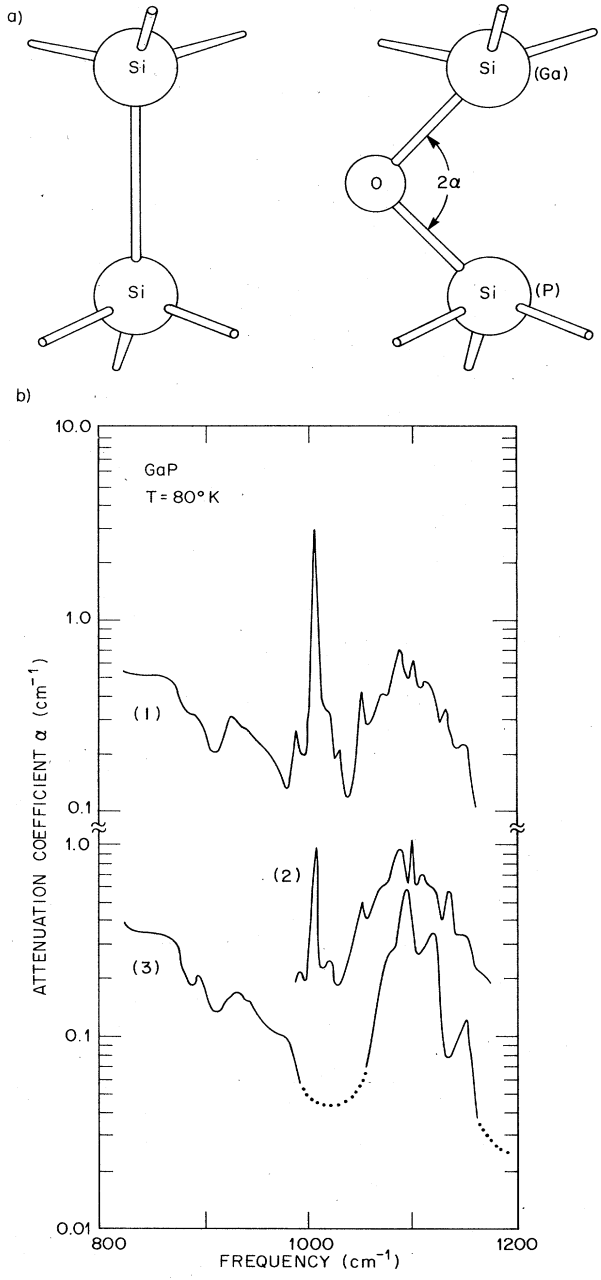

FIG. 55. (a) Si–Si pair joined by a [111] bond in pure silicon (left), and a sketch of an interstitial oxygen (right) between the two silicon atoms or between a Ga–P pair in GaP. (b) (1) Absorption spectrum of an oxygen-doped LEC sample of GaP. (2) Spectrum of an undoped LEC GaP sample. The prominent peak near 1000 cm^{-1} is assigned to interstitial oxygen. (3) Composite spectrum of several samples chosen to exhibit low absorption. This curve probably represents the intrinsic absorption of pure GaP. From Barker *et al.* (1973).

a. (Mn–Li) pairs

Manganese is known to be a relatively deep acceptor in GaAs with an ionization energy of ~0.1 eV, and it is generally assumed to be substitutional on the Ga sublattice (Chapman and Hutchinson, 1967). When diffused with Li, the resulting material is well compensated. Infrared measurements by Lorimor and Spitzer (1967b) show three principal bands of nearly equal strength, as shown in Fig. 56. All of these bands show an isotope in changing from ^{7}Li to ^{6}Li which is close to $\Delta\nu/\nu = -\Delta M/2M$ where ΔM and M relate to the Li masses. This is simply the one-oscillator result (2.13) which implies complete localization at the Li. The predicted and experimental shifts for the 391 cm^{-1} band are both 28 cm^{-1}.

Since the Li is a donor, most studies have assumed the species to be interstitial, $Li_i^+ + e^-$. The Li_i^+, being a highly mobile species at temperatures only slightly above room temperature, is expected to be ion paired with the Mn_{Ga}^-. There are two different types of tetrahedral interstitial positions for the Li_i^+, one with four Ga nearest neighbors and the other with four As neighbors. Thus the possible simple pairs are Mn_{Ga}^--Li_i^+(Ga) and Mn_{Ga}^--Li_i^+(As). Lorimer and Spitzer (1967b) proposed models involving the second choice and distortion of the As cage in an attempt to fit the observed spectra. They had only fair success.

Recent EPR measurements (Title, 1969) of the Mn center in Li-compensated GaAs:Mn and GaP:Mn support a Mn–Li pair model, although the principal symmetry axis observed at the Mn_{Ga} site in these measurements is in the ⟨110⟩ direction. This direction corresponds to neither of the above pairs. Title has shown that the observations are consistent with a Mn–Li pair axis corresponding to the second pair if one assumes that the symmetry at the Mn site is determined primarily by a special type of distortion of the As neighbor configuration.

Title has also pointed out that the published infrared and EPR data are explicable in terms of a center $(Mn_{Ga}-2\,Li_i)^+$ where the two Li each occupy an interstitial site coordinated by the Mn_{Ga} and three Ga atoms. In this case the EPR spectrum can be explained without invoking significant lattice distortion. If the Li were weakly coupled, then the lack of axial symmetry would lead to three identical absorption lines for each Li. Subsequent attempts to observe new modes in ^{6}Li + ^{7}Li diffused samples were unsuccessful, in agreement with a model where the Li motions are essentially independent of one another.

There are several objections to the two-lithium model of the defect center. One concerns the donor nature of such a center. Another is connected with the unexplained results for Zn_{Ga}^-–Li_i^+ (Lorimor and Spitzer, 1967b). In this case four Li bands are observed. Recent results for GaAs with Mg–Li pairs suggest that one Li per defect is the most likely situation (Leung *et al.*, 1972). While the exact form of these particular pair defects has not yet been confirmed, the work serves as a good example of the considerations necessary for an experimentalist to make a firm assignment to the spectra. It should be obvious that one set of absorption spectra on one crystal can seldom establish the nature of a defect center.

b. Si impurities

A large number of high-frequency localized modes have been observed in infrared absorption for Si in GaAs. Spitzer (1971) has recently reviewed the absorption spectra. The unusual electrical behavior as a function of silicon concentration has led to the speculation by Queisser (1966) and Kressel (1968) that Si can exist in different defect states, i.e., Si_{Ga}, Si_{As}, and Si_{Ga}–Si_{As} nearest-neighbor pairs. The first should be a shallow donor, the second a shallow acceptor, and the third possibly a deep acceptor or electrically inactive. When Li compensation is used there is the possibility of

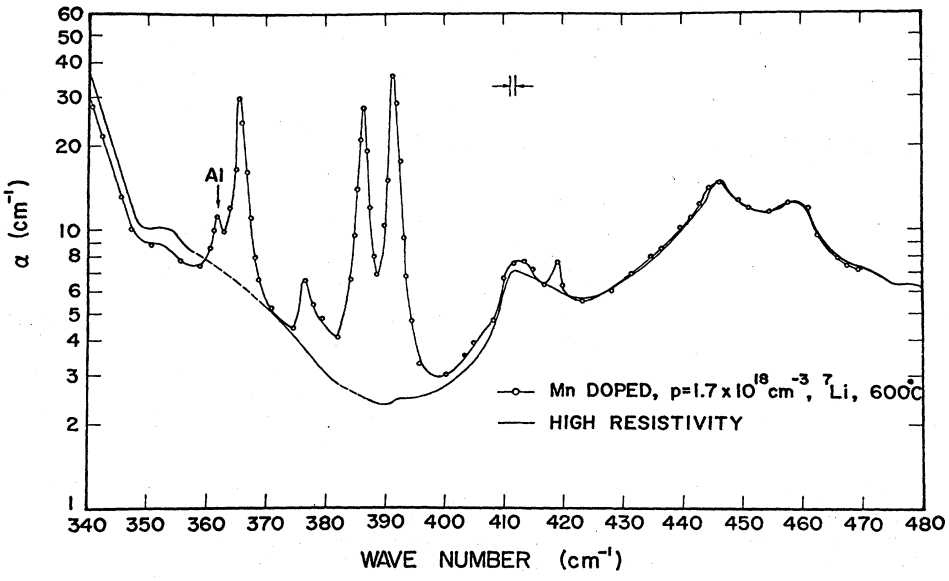

FIG. 56. Absorption at 77 K of Mn-doped GaAs compensated by ^{7}Li diffusion. From Lorimor and Spitzer (1967b).

Si_{Ga}–Li_{Ga} pairs. It is clear that a complicated system of local modes is possible for the compensated Si-doped samples.

A prominent band at 384 cm^{-1} has been attributed to isolated Si^{+}_{Ga}. It is the only band appearing at low Si concentration, and its frequency is independent of whether Li or Cu is used for compensation. The estimated frequency for the local mode Si^{+}_{Ga} with T_d symmetry is 378 cm^{-1}, obtained by scaling the Green's function results for the Si lattice. As the Si concentration is increased, a new band appears at 399 cm^{-1} which is interpreted as Si^{-}_{As} acceptors. The increase from 384 to 399 cm^{-1} is only partially accounted for by the change in mass defect, and therefore the force constant of the Si_{Ga} defect must be slightly lower than that for Si_{As}.

When samples with Si concentration greater than 10^{18} cm^{-3} are measured, several new bands appear. One suggested defect center is the Si_{Ga}–Si_{As} nearest-neighbor pair. This center has C_{3v} symmetry and hence does not have a center of symmetry. The modes are illustrated in Fig. 57. Application of the Elliott and Pfeuty (1967) theory leads to four infrared-active frequencies with $\omega_1 > \omega_2 > \omega_3 > \omega_4$. Using the mass defect theory, the predicted frequencies for Si_{Ga}–Si_{As} are 419, 390, 369, and 327 cm^{-1}. The 390 and 369 cm^{-1} are in reasonable agreement (1%) with observed modes. The 419 cm^{-1} is quite low compared to a mode at 464, but this mode is very sensitive to the Si–Si force constant which has not been adjusted in the calculation. The low-frequency mode calculated to be 327 cm^{-1} falls close to the ω_m = 295 cm^{-1} and may not have been observed yet (Spitzer, 1971).

Additional modes observed in GaAs:Si are all sensitive to the choice of the compensating species and are attributed to the Si_{Ga}–X_{Ga} defect shown in Fig. 58, where X is ^{6}Li, ^{7}Li, or Cu. This defect has lower symmetry than that of Fig. 57 and hence six bands are expected as all degeneracies are lifted. Table IV.3 shows the assignments of Spitzer and Allred (1968). Spitzer (1971) has listed several additional experiments and arguments for the mode assignment. It is clear that many of the mode assignments have been made on the basis of plausibility. Defects like Figs. 57 and 58 are entirely reasonable, however, and can be expected in other compound semiconductors.

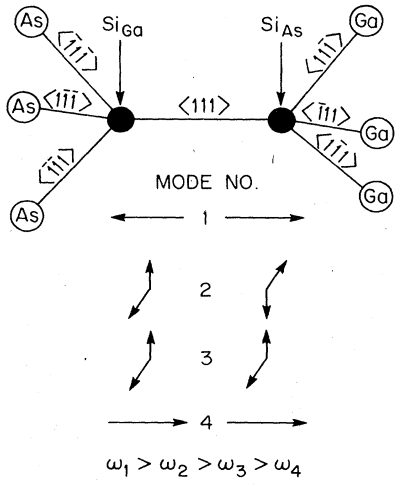

FIG. 57. Model for (Si_{Ga}–Si_{As}) pair defect in GaAs. Approximate displacement vectors for the localized modes are shown. Modes 2 and 3 are doubly degenerate. From Spitzer and Allred (1968).

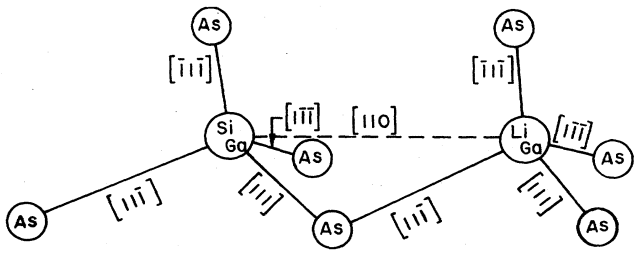

FIG. 58. A model for an undistorted (Si_{Ga}–Li_{Ga}) pair in GaAs showing nearest neighbors to the substitutional impurities. From Spitzer and Allred (1968).

c. Li impurities

Hayes (1965) was the first to study the high-frequency vibrational modes of Li in GaAs. He found that when Li was diffused into undoped GaAs at temperatures between 750 and 850°C, a series of bands were observed above ω_m. All of the prominent bands showed approximately a full Li isotope shift. They were tentatively attributed to various Li defects such as Li_i, Li_{Ga}, and complexes

TABLE IV.3. Impurity modes in GaAs doped with Si and compensated with lithium or copper. [a]

Band no.	Defect	Impurity	Mode frequency (cm^{-1}) ^{6}Li		Cu
1	Al_{Ga}	Al	···	362	···
2	Li–lattice defects		352		
3		Li	389		
4			406		
5	Si_{Ga}–Li_{Ga}	Li_{Ga}	470		
6			480		
7			487		
9		Si_{Ga}	374		
11			379		
15			405		
9	Si_{Ga}–Cu_{Ga}	Si_{Ga}			374
10					376
14					399
12	Si_{Ga}	Si_{Ga}	···	384	···
14	Si_{As}	Si_{As}	···	399	···
8	Si_{Ga}–Si_{As}	Si_{Ga}–Si_{As}	···	367	···
13			···	393	···
16			···	464	···

[a] From Spitzer and Allred (1968).

involving vacancies and oxygen. This work was extended by Levy *et al.* (1968), who showed that there were seven bands and that for diffusions in the range 700–1000°C the largest bands followed a dependence of

$$\int \alpha d\nu \propto \alpha \exp(-E/k_B T_D),$$

where $E \sim 1.0$ eV, and T_D is the Li diffusion temperature. These authors concluded that there were at least four types of Li defects. One was identified as that due to Li_i with T_d symmetry.

It is now known that the defect assignments mentioned in the above paragraph are wrong. Levy and Spitzer (1973) have conducted an extensive series of experiments using simultaneous diffusion of ^{6}Li and ^{7}Li. The importance of doing such experiments is easy to illustrate. Consider a double lithium defect which consists of two lithium sites near to each other but inequivalent. If this lithium complex had been responsible for one of the modes observed in the studies mentioned above, then changing the doping from ^{6}Li to ^{7}Li would merely shift the observed mode to a new frequency, which would correspond approximately to the simple mass defect formula. Doping simultaneously with ^{6}Li and ^{7}Li causes four modes to appear, the ^{6}Li–^{6}Li mode, the ^{7}Li–^{7}Li mode, the ^{6}Li–^{7}Li mode, and the ^{7}Li–^{6}Li mode. If the two lithium sites had been equivalent, the two latter modes would coalesce into one, yielding a three-mode spectrum. A complex consisting of three lithium sites obviously gives an even more complicated series of lines when simultaneous diffusion is used. In addition to observing the number of modes, the strengths can be correlated with the structure of the complex. For example, in the case of the two Li sites given above, it is obvious that if the two sites are equivalent, the two equivalent ways of obtaining the ^{6}Li–^{7}Li local mode vibration cause this absorption mode to be approximately twice as strong as either the ^{6}Li–^{6}Li or ^{7}Li–^{7}Li mode complex. In addition to carrying out the double diffusions, Levy and Spitzer have made careful studies of the effects of the temperature at which diffusion is done and of the effects of long annealing and rapid quenching, both with and without lithium sources present. One important result of this latter study is to show that lithium itself is responsible for the defect center. A high-temperature anneal without lithium, plus a subsequent lithium diffusion, does not produce the defect center responsible for the local modes. Five types of complex have been noted in the GaAs:Li system. The local mode bands have been arbitrarily assigned the numbers 1 to 5 and a prime is used to designate the mode that results when the ^{7}Li is replaced by ^{6}Li. New mixed modes which appear when double diffusion is used are denoted by adding the letters a or b. Figure 59 shows the spectrum of a GaAs sample diffused with equal amounts of ^{6}Li and ^{7}Li. If we pick complex type 4 for example, we see from the figure that it exhibits three modes. The mode 4a is the new feature which has been revealed by the studies of Levy and Spitzer; it suggests that the complex responsible for mode 4 consists of two Li atoms in equivalent positions. Figure 60 shows a two-dimensional model for the acceptor complex thought to be responsible for mode type 4. The two Li atoms are bound by springs to the

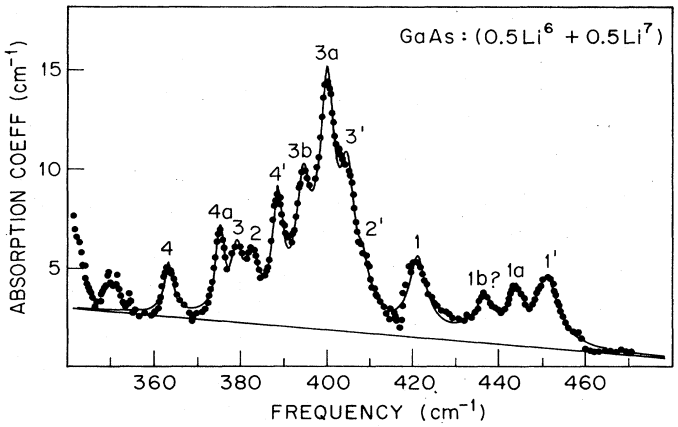

FIG. 59. Absorption of GaAs at liquid nitrogen temperature after simultaneous diffusion with ^{6}Li and ^{7}Li. The solid curve results from a fitted set of Lorentzian resonances which is used to evaluate the mode strengths, frequencies, and linewidths. From Levy and Spitzer (1973).

host lattice and also to the native defect. The native defect is known to be present at each complex but has not been identified. The major conclusions of this study, based on using simultaneous diffusion of the two Li isotopes and on various temperature and quenching cycles, are the following. Five major absorption bands occur in Li-diffused GaAs which is originally undoped. Each of these bands arises from a localized vibrational mode of a different Li complex. Each complex involves two or three Li atoms. Finally, the quantitative measurements of the amount of Li present imply that there are always other Li defects present which do not contribute to the absorption measured in this spectral range.

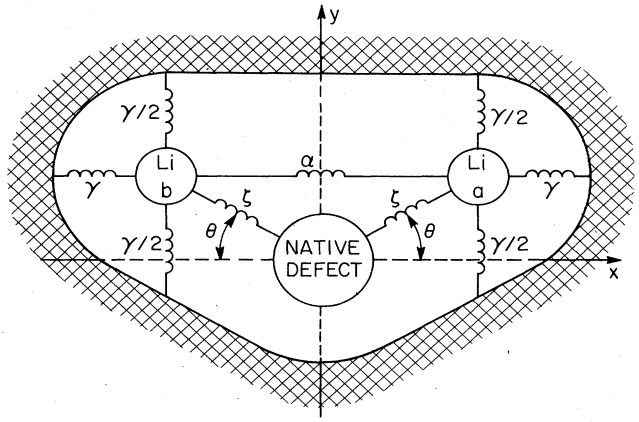

FIG. 60. Two-dimensional spring and point-mass model of the acceptor complex with two equivalent Li sites (band 4 of Fig. 59). The symbols α, γ, and ζ denote spring constants. Both the host lattice (shown as a cross-hatched wall around the complex) and the native defect are assumed immobile. From Levy and Spitzer (1973).

D. II-VI Compound semiconductors

1. Introduction

When we consider the semiconductor systems starting with the Group IV crystals, then the III–V compound, and finally the II–VI compounds, we find increasing difficulty in preparing the pure materials, increasing difficulty in introducing known impurities, and increasing difficulty in achieving charge compensation. In the II–VI compound semiconductors we also find a more complex crystal system, since most of the compounds crystallize in the wurtzite structure. This crystal structure belongs to the hexagonal system, so that infrared absorption or reflection studies must be done on oriented crystals. We can expect the local mode frequency for an isolated substitutional impurity to have one value for vibrations along the c axis and another value for vibrations in the ab plane. Because of the difficulties connected with crystal growth, most of the studies to date have involved isoelectronic substitutions in the II–VI system. In particular, a great many of the studies have been concerned with substitutions among the Group VI–A elements S, Se, Te. The ease of substitution within this group of elements is illustrated by the fact that one of the early studies of CdSe:S was performed on a crystal which was thought to be CdSe (Verleur and Barker, 1967a). The sulfur was an unintentional contaminant apparently contained in the source of Se. In the sections below we discuss substitutions in CdSe and CdS, which are wurtzite crystals, as well as in CdTe which is one of the few II–VI compounds which has the zinc blende (cubic) structure. At the present time the chemistry of these cadmium compounds must still be regarded as being in a primitive state. Many absorption lines and luminescent lines which occur reproducibly are still labeled as being due to unknown impurities. While we do not discuss in detail any other II–VI compounds, some other known modes are listed in Table IV.1. The known modes occur principally in the zinc compound semiconductors, which are probably the next most thoroughly investigated class after the cadmium compounds.

2. CdSe and CdS

The mixed crystal $CdSe_xS_{1-x}$ has been investigated by several groups and is discussed thoroughly in Sec. IX. In a low-temperature reflectivity study, Verleur and Barker (1967a) found the local mode of S_{Se} due to a 1.5% contamination of S in a nominally pure CdSe crystal. Figure 61 shows the reflectivity spectrum at 15°K for vibrations parallel to the c axis. A weak mode is easily detected near 270 cm^{-1}. The authors find that scaling the Dawber and Elliott result for silicon predicts a S_{Se} local mode at 285 cm^{-1}. Since the silicon model gives an isotropic result, no prediction could be made of the expected anisotropy in the local mode frequency. Experimentally, Verleur and Barker find the local mode vibration perpendicular to the c axis to be about 1.0 cm^{-1} higher than the vibration parallel to the c axis. In addition to this anisotropic splitting of the local mode, the concentration of S is sufficient to cause the transverse wave to split off from the longitudinal wave local mode. A careful Kramers–Kronig analysis of the reflectivity shown in Fig. 61 shows that the TO and LO components are split by about 1.5 cm^{-1} for the case shown in the figure. This TO–LO splitting can be expected to go to zero as the concentration of S goes to zero. Verleur and Barker have also measured a CdS crystal with 23% Se present. While this is hardly a low enough concentration to be considered a suitable crystal for local mode studies, the fitting of the whole range of crystals and the data from this concentration extrapolate to give an impurity mode near 185 cm^{-1} for Se_S. Balkanski and Beserman (1968) have made a more detailed study of the impurity mode for Se_S vibrations in CdS. They find a sharp mode at 182 cm^{-1} for vibrations parallel to the c axis and 186 cm^{-1} for vibrations perpendicular to the c axis. The authors suggest that CdS has a very small or vanishing density of states in this region so that the impurity modes may be gap modes.

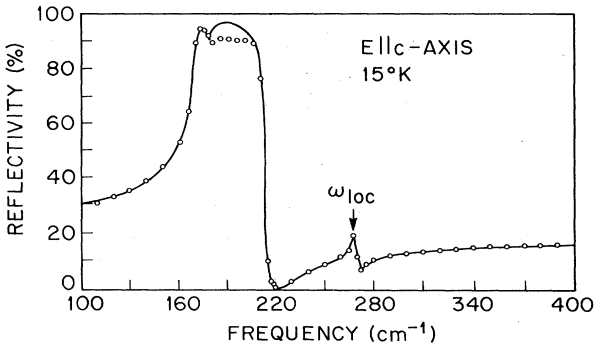

FIG. 61. Theoretical fit, based on model (solid line) of far-infrared reflectivity spectrum of $CdSe_{0.985}S_{0.015}$ at 15 °K with $E \parallel$(c-axis). Open circles are experimental points. From Verleur and Barker (1967a).

Manabe *et al.* (1973) have measured local mode absorption lines due to Be in CdS and CdSe. Unlike the studies mentioned above, these local mode measurements were made in absorption and by Raman scattering. The authors see the fundamental and second harmonic absorption frequencies as shown in Fig. 62 for

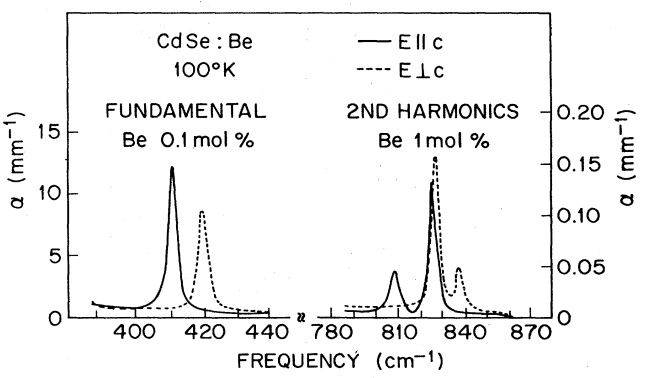

FIG. 62. Infrared absorption spectrum of Be-doped CdS at 100 °K for two different polarizations of light. The anisotropy of the localized mode and its harmonic is easily detected. From Manabe *et al.* (1973).

CdSe. From the observed anisotropy splitting and the appearance of the second harmonic, a local oscillator model is constructed including potential terms up to third order in the Be ion displacement. While a unique fit is not possible from the measured data, a set of potential coefficients is obtained which predicts the lines generally to within 1 cm^{-1}. The anharmonic coefficients are found to be substantially smaller in CdSe than in CdS. Further progress in understanding localized vibrations in this crystal and in most of the other II–VI compounds must await other developments, particularly more knowledge of the host crystal dispersion curves.

3. CdTe—Anharmonic effects and sidebands

Table IV.1 shows that two or three localized modes and one resonant mode have been identified in CdTe. While many of the fundamental properties of CdTe are not accurately known, a considerable effort has gone into understanding the mode connected with Be impurities. This has included detailed fitting of temperature effects on local mode linewidth and line shift and also on the strength and shape of sidebands. Studies of this type had previously been carried out only in ionic crystals. Such studies will be discussed in Sec. V in considerable detail. Since anharmonic theories have generally not been applied to semiconductors, we indicate here areas of agreement and disagreement between the experiments and such a detailed theory in the case of CdTe. Hayes and Spray (1969) have measured the infrared absorption of CdTe doped with Be. They find the fundamental local mode at 391 cm^{-1} at 4°K. They observe the second and two third harmonics of the local mode as well as sideband structure on the high-frequency side of the local mode. Figure 63 shows the local mode and sideband structure at 4°K. In a related study Sennett *et al.* (1969) find in addition a resonant mode at 61 cm^{-1} connected with Be impurities. These authors construct a shell model for the lattice vibrations in CdTe, based on the $\vec{q}=0$ lattice vibration frequencies which are known and on the measured elastic constants. In addition the high- and low-frequency dielectric constant are used to determine the effective charges in the model. Using the shell model and the isotope approximation for the Be impurity, the Green's function method is used to predict the local mode frequency. Figure 64 shows the appropriate Green's function (A) and the mass defect curve (B). Localized modes will occur where the two curves cross or nearly cross as described in Sec. III. To the far right of the figure (not shown) a crossing occurs at 417 cm^{-1}. This must be considered good agreement with the experimental value of 391 cm^{-1} for the localized mode, since the model has been based on host crystal properties unconnected with the local mode and the isotope approximation has been used. Figure 64 also shows a near crossing near 60 cm^{-1}. This is the resonant mode and is in good agreement with the measured frequency. Another solution near 160 cm^{-1} gives a very weak resonance when the imaginary part of the function is included in the calculation.

Hayes and Spray use their measured frequencies of fundamental, second, and third harmonic modes to fit

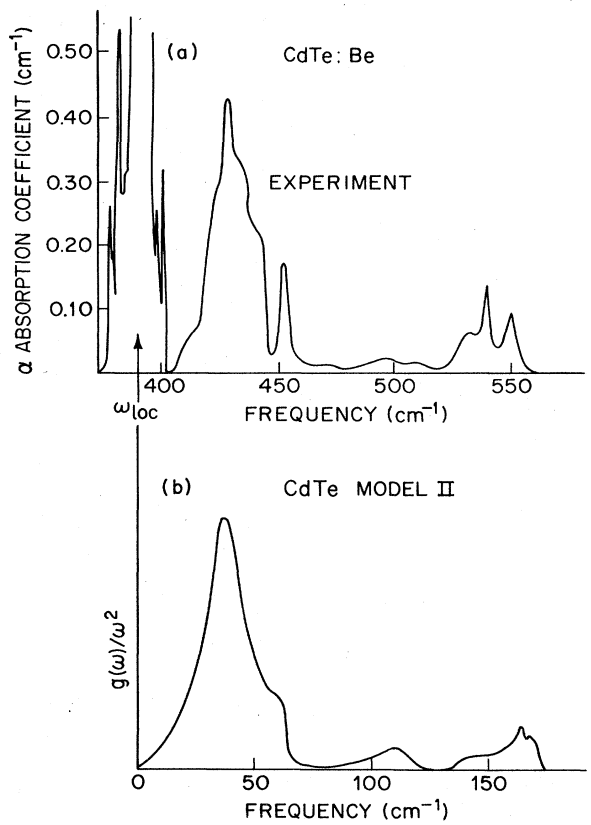

FIG. 63. (a) The fundamental of the local vibrational mode of Be in CdTe at 4 K with high-energy lattice sidebands. The sharp lines near the fundamental are due to Be-ions in sites perturbed by other lattice defects. From Hayes and Spray (1969). (b) Shape function $g(\omega)/\omega^2$ calculated from the density of states of a shell model. This function gives a reasonable fit to the sidebands shown in (a). From Sennett *et al.* (1969).

the four potential parameters of a localized anharmonic oscillator. Once this has been done, the intensity ratio of the second harmonic to the fundamental can be calculated. It involves in the numerator the cubic anharmonic potential coefficient squared and is calculated to be 1/130. The measured value is much larger, being 1/27. This discrepancy is thought to be due to the neglect of coupling between the impurity and the lattice modes in the model. Using the method of Elliott *et al.* (1965) the authors then include coupling between the local oscillator and the lattice oscillators. The latter are assumed to have a Debye spectrum. This coupling still gives too small an intensity ratio. An approximate argument which involves the second-order dipole moment mechanism is shown to be able to account for the measured intensity ratio.

The cubic anharmonicity which allows the observation of the higher harmonics discussed above also causes the sideband absorption shown in Fig. 63. Using the theory of Elliott *et al.* the integrated intensity of the sideband structure has been calculated and reasonable agreement with experiment has been obtained. A separate calculation of the shape of the sideband absorption has been carried out by Sennett *et al.* (1969). Using the

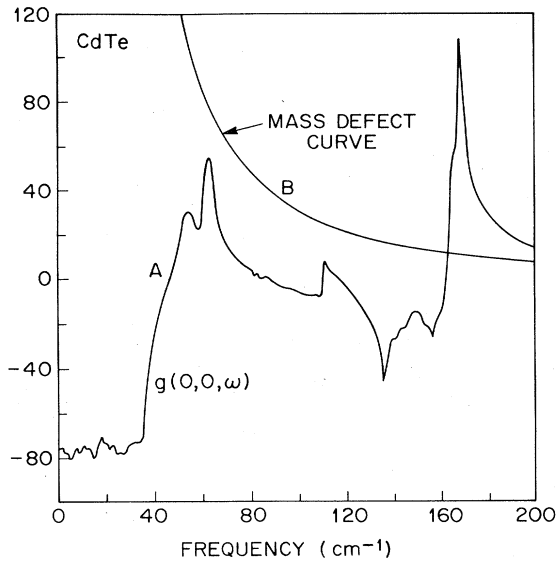

FIG. 64. A: Principal part of the Green's function for the Cd site in CdTe. B: Mass defect parameter $(\epsilon M\omega^2)^{-1}$ for a Be impurity as a function of ω. The ordinate is arbitrary. Crossings or near crossings of A and B give defect mode resonances. From Sennett *et al.* (1969).

Debye approximation for the host crystal phonons, the sidebands should have a shape given by $g(\omega)/\omega$, where $g(\omega)$ is the vibrational density of states. Timusk and Klein (1966), using a more detailed model appropriate to KBr:H, find that the band mode contribution should have a shape determined by certain projections of the perturbed density of states divided by ω^3. The CdTe experiments suggest that the shape is approximately $g(\omega)/\omega^2$. Figure 63 shows this shape function for CdTe. Reasonable agreement is seen to exist when Fig. 63(a) and (b) are intercompared. The success of such a simple functional form is surprising in view of the extremely complicated form of the theoretical expressions. Section V presents a case where only even symmetry lattice modes couple to the impurity to produce sidebands. Finally, the cubic anharmonicity also causes a temperature dependence of the strength of the local mode fundamental. The theory for this effect has been discussed by Takeno and Sievers (1965) and involves the Debye–Waller factor. The measured temperature dependence of the local mode fundamental of Be is found to agree quite well with this theory and to predict a Debye temperature of 290°K as compared with the value 200°K obtained from specific heat measurements.

The theory of Elliott *et al.* predicts that the frequency of the fundamental and harmonics of the local mode should be temperature dependent and depend on the fourth-order anharmonic coefficient. Hayes and Spray have given a rough evaluation of this effect for CdTe:Be using the theory and find that the fourth-order coefficient is considerably larger than the coefficient needed to explain the value of the energy levels in the anharmonic potential. The authors point out that the decrease in local mode frequency as the temperature is raised may be connected more directly with the thermal expansion of the crystal, which has not been included in the anharmonic theory. Other sources of both positive and negative mode shifts which depend on anharmonicity are possible. An assessment of the relative importance of each is difficult at the present time. Finally, the anharmonicity of the binding of the impurity atom can also cause a temperature dependence in the linewidth of the local mode. In the case of Be in CdTe this process must occur through a fourth-order anharmonic process. For such a process the limiting behavior at high temperatures is predicted to give a linewidth going as T^2. The experiments do show this dependence for temperatures above 100°K. Hayes and Spray note that band phonons scattering off the defect can also give a T^2 dependence to the linewidth; however, they suggest that the fourth-order process is dominant. In conclusion it should be noted that the rather detailed application of models to CdTe, though not one hundred percent successful, has allowed the development of a shell model with associated Green's functions as well as anharmonic local potentials which will be useful in the interpretation of future work on impurity vibrations in CdTe and other related compounds.

E. The bound optical phonon localized mode

A new type of localized mode has been observed by Dean, Manchon, and Hopfield (1970) in GaP by Raman scattering. Figure 65 shows this mode for S, Te, and

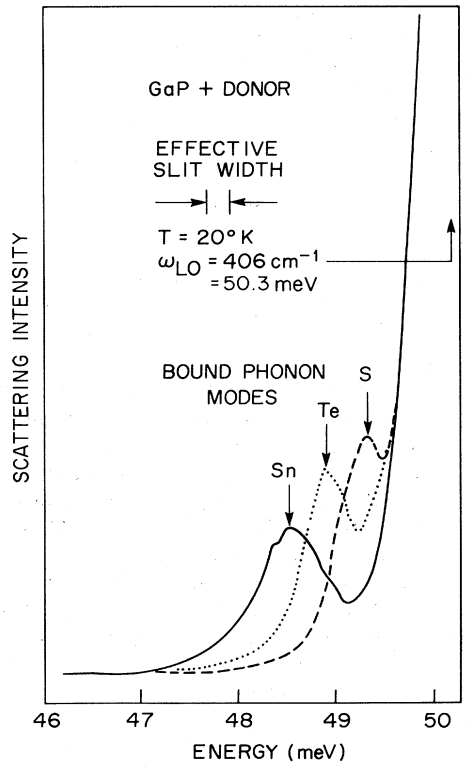

FIG. 65. Raman scattering of 5145 Å laser light from GaP containing ~10^{18} neutral Sn, Te, or S donors. The bulk $\vec{q}=0$ LO phonon is off scale at this gain setting. The small peaks are the new localized modes. From Dean *et al.* (1970).

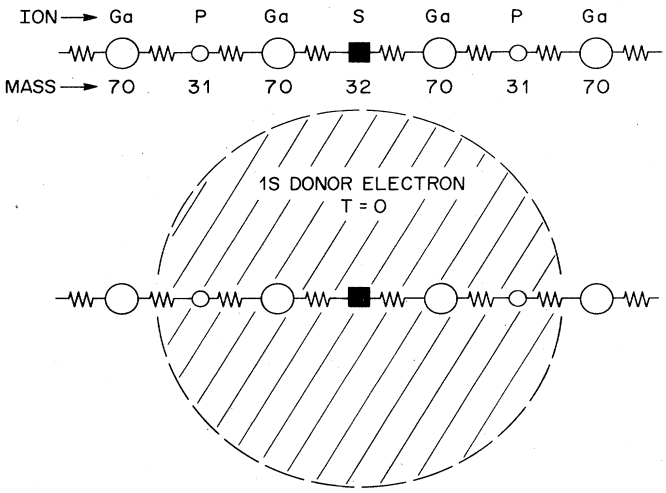

FIG. 66. Sketch of neutral donor giving rise to a bound optical phonon. At the top a S atom replaces a P atom in GaP with little mass change. Below, the donor wave function is sketched—it emcompasses several nearby ions of the host. The spring constants within the wave function are effectively reduced, leading to a new optic mode inside, which has a lower frequency than the bulk optic mode.

Sn impurities substituted for P. The mode occurs within the optic band of the host at energies slightly below ω_{LO}, the zone center longitudinal optic (LO) mode. The authors describe this mode as an optical phonon bound to the impurity center. They give a quantum theory for this binding based on the hydrogenic levels of the donor impurity. The important point to note is that the local mode frequency is not directly dependent on the mass of the impurity. Figure 66 presents this concept heuristically. The impurity ion S is a donor and has an extended electronic wave function associated with the loosely bound electron which influences the surrounding host lattice. In the real three-dimensional crystal the electronic cloud of the impurity extends over approximately 100 GaP unit cells and modifies the binding forces of all these host atoms. Such large impurity wave functions can be expected to occur in narrow gap semiconductors. In the linear chain pictured in Fig. 66 we could modify all the force constants within the electronic cloud to simulate this effect. The linear chain then has new optic modes. The local mode consists of ion motions principally within the electronic cloud. For most cases observed to date the modified force constants would need to be 4 to 6% lower than the unperturbed force constants. Barker (1973) has developed a simple macroscopic dielectric theory for the sphere of modified GaP within the donor electron cloud. The theory gives the bound phonon local mode frequency and linewidth. Good agreement is obtained with infrared and Raman studies of such modes in GaP.

Figure 67 shows the bound phonon local mode for Si in GaP in an infrared spectrum. The mode is seen as a prominent dip on top of the reststrahlen band in the reflectivity spectrum. Kramers–Kronig analysis allows the derivation of the absorption spectrum. For a wide range of impurities the local mode frequency is independent of the mass of the impurity, as required by the theory. If one compensates the crystal, removing the electron from the region of the impurity but leaving the impurity ion present, the mode disappears as expected on the basis of the above theories. Bound phonon local modes have also been observed for certain impurities in CdS by Reynolds *et al.* (1971).

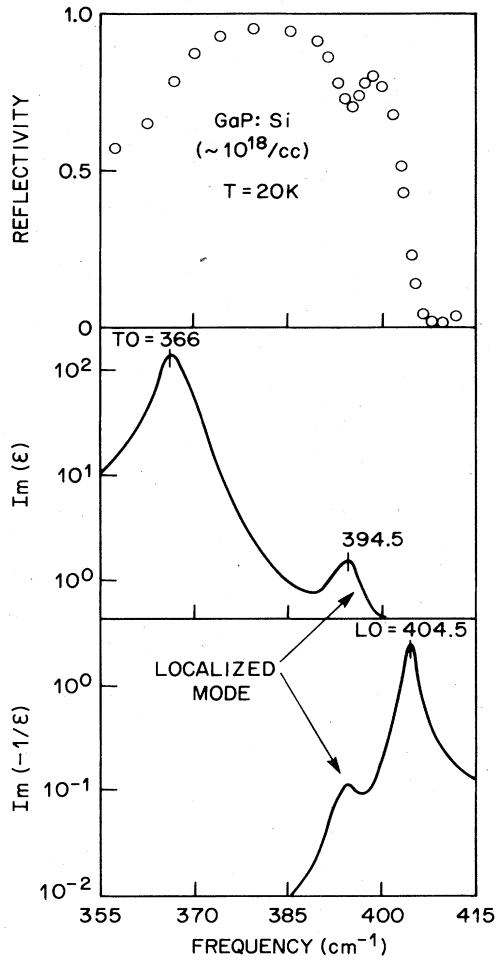

FIG. 67. Infrared spectrum of GaP doped with Si. The reflectivity data of the top shows the bound phonon localized mode as a dip. A Kramers–Kronig analysis shows TO and LO components as small peaks near 394 cm^{-1}. From Barker (1973).

F. Conclusions

The work discussed here on the semiconductor systems is not complete but is a representative sample. Almost all of the discussion centers on absorption, as little Raman work has been done. It is expected that in the future there will be an increased effort to correlate the results of different experimental techniques with infrared measurements. An example is the EPR work on the GaAs:Mn–Li system. The authors believe that the local mode measurements are a diagnostic tool of significant value. In a number of cases such as B–Li, B–B, O, and C in Si, detailed information concerning the defect composition and symmetry are obtained which help in

establishing reasonable defect models. It should be stressed here that a resourceful experimenter is a key ingredient in defect mode assignment. In most cases the mode is identified with a defect configuration by making tests—changing the impurity isotope, changing the lattice, making stress measurements, using results from EPR, etc. In almost no case is comparison with a first-principles calculation a convincing proof of an assignment.

In this section we have seen the first effects of leaving the isolated defect and proceeding towards the fully disordered solid. Cosand (1971), for example, found new modes due to different nearest-neighbor environments and also broadening effects due to random variation in more distant neighbors in the Ge–Si alloys. There are several areas in which the diagnostic possibilities have not yet been fully exploited. The use of high-frequency local modes for measuring impurity segregation coefficients (Skolnik, Allred, ans Spitzer, 1971), irradiation-induced damage centers (Devine and Newman, 1970), and ion-implanted impurities (Skolnik *et al.*, 1972) has already been demonstrated. A new and critical role for defects has been found in the utilization of defect vibrations to promote a defect reaction such as diffusion (Weeks, Tully, and Kimerling, 1975). Defect spectroscopy could lead to important results here which have a direct connection with the lifetime of semiconductor devices which fail because of defect diffusion.

V. IONIC CRYSTALS—LOCAL AND GAP MODES

A. Introduction

Experiments on the defect states in ionic crystals began with work on the electronic properties (Hilsch and Pohl, 1933, 1936, 1938). About 20 years after the electronic transition of the substitutional hydride ion was discovered, Schaefer (1960) observed defect-induced lattice absorption from the same center (Fig. 1). Since that time many investigators have been drawn to the study of the lattice defect problem in alkali halide crystals, mainly because these crystals have been easy to grow and purify. Consequently the alkali halide crystal has become the "fruit fly" for the study of lattice impurity modes. A vast literature of experiment and theory has grown up around these crystals and a number of reviews have already been written.

Maradudin *et al.* (1963) first presented a theoretical review of the defect problem. Then Maradudin (1963, 1965) presented more specific theoretical reviews of the effects of point defects on the dynamical properties of crystals. Finally Maradudin (1966a, 1966b) reviewed in some detail both the theoretical and experimental aspects of the effects of defects on the vibrations of crystals. About the same time Ludwig (1967) reviewed lattice dynamics theory with about 100 pages devoted to the defect problem. Fritz (1968a) reviewed the experiments on the *U* center, and Klein (1968) has described the experimental and theoretical progress on impurity modes up to 1967. Sievers (1971) surveyed the experimental situation in 1968. Most recently Maradudin *et al.* (1971) have reviewed the theoretical aspects of the lattice dynamics of solids, with about 150 pages devoted to a general theoretical description of the effects of defects, and Bäuerle (1973) has reviewed *U*-center modes in alkali halides. Sherman and Wilkinson (1973) have reviewed experimental data with emphasis on polyatomic defects in alkali halides.

In this section we shall concentrate mainly on the spectroscopic results that have been obtained on spatially localized vibrational modes in ionic crystals. Some successful studies have been reported on impurities in silver halides (Hattori *et al.*, 1973), the rare earth trifluorides (Jones and Satten, 1966), and the II–VII compounds (Elliott *et al.*, 1965; Shamu *et al.*, 1968; Harrington *et al.*, 1970; Jones *et al.*, 1968; Chambers and Newman, 1969); but most measurements have dealt with the hydride ion in alkali halide crystals. Some investigators have studied the substitutional H^- and D^- ion (Schäfer, 1960; Price *et al.*, 1960; Mitsuishi and Yoshinaga, 1962; Mirlin and Reshina, 1964; Dötsch *et al.*, 1965; Fritz *et al.*, 1965; Timusk and Klein, 1966; Sievers and Pompi, 1967; Bäuerle and Fritz, 1967; Dötsch, 1969; Dötsch and Mitra, 1969; and Montgomery *et al.*, 1972). Other investigators have looked at interstitial H^- impurities (Fritz, 1962; Bäuerle and Fritz, 1968; Dürr and Bäuerle, 1970) or pair spectra (Mirlin and Reshina, 1966; Barth and Fritz, 1967; de Souza *et al.*, 1970 and 1973). The frequencies associated with all these lattice defect combinations are recorded in Table V.1.

With the discovery of a local mode, the experimental approach is to vary as many experimental parameters as possible, one at a time, to characterize the particular lattice-defect combination. By varying isotopic mass, crystal strain, temperature, or polarization some information on the dynamics of the impurity and the local impurity potential can be determined. We shall begin with experiments which indicate that the local mode acts as a simple oscillator and then consider experiments which demonstrate the anharmonic effects associated with the local mode.

B. The impurity potential

1. Local mode isotope effects

The simplest potential which one can use to describe the local mode in the static lattice is a quadratic form consistent with the defect symmetry. For O_h or T_d symmetry the potential has spherical symmetry

$$V(r) = Ar^2 = \tfrac{1}{2}M^*\omega^2 r^2, \tag{5.1}$$

where M^* is the defect mass. This is just the one-oscillator expression (4.2) restricted to harmonic terms only. An isotope-induced frequency shift of the localized mode which varies inversely as the square root of the isotopic mass would be a clear indication that the vibrational motion is indeed associated only with the impurity, i.e., that (5.1) is appropriate.

By examining Table V.1 we can determine how accurately Eq. (5.1) describes the experimental situation. The smallest isotope shift has been observed in $AgCl:Li^+$, namely 1.043 compared with the value $\sqrt{7/6} = 1.080$ predicted by Eq. (5.1). The rather low value implies considerable motion of the atoms neighboring the defect, as was illustrated for several cases in Figs. 2–8. The absorption coefficient for the $AgBr:Li^+$ data is shown in Fig. 68. The absorption spectrum of AgBr containing natural Li is shown in curve (a). The clearly visible localized modes lie 60 cm^{-1} above $\omega_m = 135$ cm^{-1}. The spectrum consists of two distinct peaks with Lorentzian shape, corresponding to the two isotopes of Li. The ratio of the integrated absorption intensity of the low-frequency band to the high-frequency band is 92/8, which is very close to the natural abundance of the two lithium isotopes. Here the isotope shift is 1.074, indicating a much more localized mode. When natural Li is replaced by enriched Li (Fig. 68), the high-frequency band becomes stronger and the low-frequency band becomes weaker, confirming the assignment to Li impurities.

The local mode associated with the H^- ion is two or three times the maximum phonon frequency of the lattice, in contrast to the Li case. Therefore, better agreement between the measured isotope shift and the one-oscillator model of (5.1) is to be expected. Inspection of Table V.1 indicates that the predicted frequency ratio $(\sqrt{2/1})$ is within 5% of the measured values for all of the ionic crystals. Note that the isotope frequency ratio is different for the different crystals. Even if we restrict our attention to alkali halide crystals the measured frequency ratio is not a constant. Although the measurement of a frequency shift due to an isotopic

TABLE V.1. Localized modes in ionic crystals.

Crystal	Mode frequency (cm^{-1}) (Irreducible representation, Temp. °K)	Defect symmetry, Method of observation,[a] References,[b] Comments	
H^- (substitutional)			
^6LiF	$1028.9(T_{1u}, 20)$	O_h, A, 1	
^7LiF	$1025(T_{1u}, 20)$	O_h, A, 2, 3	
NaF	$858.9(T_{1u}, 20)$	O_h, A, 2, 3, 4	
NaCl	$562.5(T_{1u}, 57)$	O_h, A, 4, 5, 6	
NaBr	$496(T_{1u}, 57)$	O_h, A, 4, 5, 6	
NaI	$426.8(T_{1u}, 10)$	O_h, A, 4, 7	
KF	$725.5(T_{1u}, 100)$	O_h, A, 4	
KCl	$503.8(T_{1u}, 100)$	O_h, A, 4, 5, 6, 8, 9	
KBr	$446.7(T_{1u}, 100)$	O_h, A, 4, 5, 8, 9, 10	
KBr	$886.3(T_{2g}, 10), 904.5(E_g, 10), 894.8(A_{1g}, 10)$	O_h, R, 11	Second harmonic
KI	$383.9(T_{1u}, 100)$	O_h, A, 4, 5, 6	
KI	$753.1(T_{2g}, 10), 767.9(E_g, 10), 759.9(A_{1g}, 10)$	O_h, R, 11	Second harmonic
RbF	$703.1(T_{1u}, 100)$	O_h, A, 4	
RbCl	$476(T_{1u}, 90)$	O_h, A, 4, 5, 6	
RbBr	$425(T_{1u}, 90)$	O_h, A, 4, 5, 6	
RbI	$360(T_{1u}, 57)$	O_h, A, 4, 5	
CsCl	$423.1(T_{1u}, 100)$	O_h, A, 4, 12	
CsBr	$365(T_{1u}, 100)$	O_h, A, 4, 12	
CsI	$290(T_{1u}, 100)$	O_h, A, 12	
CaF_2	$957.8(T_2, 290), 965.6(T_2, 20)$	T_d, A, 13; R, 14	5×10^{20} imp/cm^3
CaF_2	$1903(T_2, 290), 1919.8(T_2, 20), 1895(A_1, 16)$	T_d, A, 13; R, 14	Second harmonic
CaF_2	$2912(T_2, 20), 2825(T_2, 20)$	T_d, A, 13	Third harmonic
SrF_2	$885.3(T_2, 290), 893.2(T_2, 20)$	T_d, A, 13; R, 14	6×10^{20} imp/cm^3
SrF_2	$1759(T_2, 290), 1775.9(T_2, 20), 1747(A_1, 16)$	T_d, A, 13; R, 14	Second harmonic
BaF_2	$798.2(T_2, 290), 806.6(T_2, 20)$	T_d, A, 13; R, 14	9×10^{19} imp/cm^3
BaF_2	$1580(T_2, 290), 1596(T_2, 20), 1566(A_1, 16)$	T_d, A, 13; R, 14	Second harmonic
LaF_3	1168, 816(4.2)	D_3, A, S, 15	4×10^{18} imp/cm^3
PrF_3	1183, 866(4.2)	D_3, A, S, 15	4×10^{18} imp/cm^3
NdF_3	1194, 882(4.2)	D_3, A, S, 15	4×10^{18} imp/cm^3

TABLE V.1. Localized modes in ionic crystals. *(Continued)*.

Crystal	Mode frequency (cm^{-1}) (Irreducible representation, Temp. °K)	Defect symmetry, Method of observation,[a] References,[b] Comments		
D^- (substitutional)			Isotope effect	
LiF	$746(T_{1u}, 20)$	O_h, A, 3	I = ratio of local mode frequency, with H^- and D^-	$I = 1.373$
NaF	$614.7(T_{1u}, 20)$	O_h, A, 2, 3		$I = 1.398$
NaCl	$408(T_{1u}, 90)$	O_h, A, 6		$I = 1.384$
NaBr	$361(T_{1u}, 90)$	O_h, A, 6		$I = 1.380$
NaI	$317.8(T_{1u}, 10)$	O_h, A, 7		$I = 1.34$
KCl	$360.4(T_{1u}, 100)$	O_h, A, 4, 6, 8, 9		$I = 1.398$
KBr	$320.4(T_{1u}, 100)$	O_h, A, 4, 8, 13		$I = 1.394$
KBr	$635.0(T_{2g}, 10), 644.4(E_g, 10)$	O_h, R, 11		$I = 1.396, 1.403$
KI	$278.6(T_{1u}, 100)$	O_h, A, 4, 5		$I = 1.378$
KI	$543.4(T_{2g}, 10), 550.2(E_g, 10)$	O_h, R, 11		$I = 1.386, 1.396$
RbCl	$339(T_{1u}, 90)$	O_h, A, 6		$I = 1.404$
CsCl	$302(T_{1u}, 100)$	O_h, A, 12		$I = 1.404$
CsBr	$259(T_{1u}, 100)$	O_h, A, 12		$I = 1.409$
CsI	$207(T_{1u}, 100)$	O_h, A, 12		$I = 1.401$
CaF_2	$689(T_2, 290), 694.3(T_2, 20)$	T_d, A, 13; R, 14		$I = 1.391$
CaF_2	$1374(T_2, 290), 1384(T_2, 20)$	T_d, A, 13	Second harmonic	
CaF_2	$2093(T_2, 20), 2047(T_2, 20)$	T_d, A, 13	Third harmonic	
SrF_2	$635.8(T_2, 290), 640.4(T_2, 20)$	T_d, A, 13; R, 14		$I = 1.395$
SrF_2	$1267(T_2, 290), 1277(T_2, 20)$	T_d, A, 13; R, 14	Second harmonic	
BaF_2	$572(T_2, 298), 576(T_2, 16)$	T_d, R, 14		$I = 1.40$
BaF_2	$1133(A_1, 16), 1150(T_2, 16)$	T_d, R, 14	Second harmonic	
LaF_3	833(4.2), 584(4.2)	D_3, A, S, 15		$I = 1.40, 1.40$
PrF_3	866(4.2), 622(4.2)	D_3, A, S, 15		$I = 1.40, 1.39$
NdF_3	882(4.2), 632(4.2)	D_3, A, S, 15		$I = 1.40, 1.40$
$^6Li^+$ (substitutional)				
AgCl	$228.3(T_{1u}, 2)$	O_h, A, 16		
AgBr	$205.9(T_{1u}, 2)$	O_h, A, 16		
$^7Li^+$ (substitutional)				
AgCl	$218.9(T_{1u}, 2)$	O_h, A, 16	I = ratio of local mode frequency with ^6Li and ^7Li.	$I = 1.043$
AgBr	$191.8(T_{1u}, 2)$	O_h, A, 16		$I = 1.074$
Na^+ (substitutional)				
AgBr	$166.7(T_{1u}, 2)$	O_h, A, 16		

TABLE V.1. Localized modes in ionic crystals. *(Continued)*.

Crystal	Mode frequency (cm^{-1}) (Irreducible representation, Temp. °K)	Defect symmetry, Method of observation, [a] References, [b] Comments	
H_i^- (interstitial)			
KCl	851(20)	T_d, A, 17	
KBr	795(20)	T_d, A, 17, 18	
KI	721(20), 718(10)	T_d, A, 17, 19	
RbCl	800(20)	T_d, A, 17	
$SrTiO_3$	3513(120)	Probably interstitial bonded to O. A, 26, splits below 102 °K phase transition.	
CaF_2	1298(290), 1312(20)	O_h, A, 20	
D_i^- (interstitial)			
KI	518(10)	T_d, A, 19	$I = 1.386$
CaF_2	938(290)	O_h, A, 20	$I = 1.39$
H_i^0 (interstitial)			
CaF_2	640(100)	O_h, A, 21	3×10^{19} imp/cm^3
$H^-:H^-$ (pair)			
KCl	463.5, 512.5, 535(77)	C_{2v}, A, 22	
$D^-:D^-$ (pair)			
KCl	331.5, 375.5, 368(77)	C_{2v}, A, 22	$I = 1.40, 1.39, 1.4$
$Na^+:H^-$ (pair)			
KCl	503, 534, 432(65)	C_{4v}, A, 23, 24	
$K^+:H^-$ (pair)			
NaCl	559, 514, 686(78)	C_{4v}, A, 23	
RbCl	476, 493, 432(20)	C_{4v}, A, 24	
RbBr	426, 443, 388(20)	C_{4v}, A, 24	
$Rb^+:H^-$ (pair)			
KCl	500, 483, 550(65)	C_{4v}, A, 24	$I = 1.39$
KBr	444, 426, 494(20)	C_{4v}, A, 24	
$Cs^+:H^-$ (pair)			
KCl	500, 455.5, 617.5(78)	C_{4v}, A, 23	

TABLE V.1. Localized modes in ionic crystals. *(Continued)*.

Crystal	Mode frequency (cm^{-1}) (Irreducible representation, Temp. °K)	Defect symmetry, Method of observation,[a] References,[b] Comments
Rare earth : H_i^- (pair)		
$CaF_2 : La^{3+}$	976.9, 1121.7(20)	C_{4v}, A, S, 20
$CaF_2 : Ce^{3+}$	988.9, 1130.1(20)	C_{4v}, A, S, 20
$CaF_2 : Pr^{3+}$	994.7, 1115.0(20)	C_{4v}, A, S, 20
$CaF_2 : Nd^{3+}$	1001.5, 1119.4(20)	C_{4v}, A, S, 20
$CaF_2 : Eu^{3+}$	1009.9, 1092, 9(20)	C_{4v}, A, S, 25
$CaF_2 : Sm^{3+}$	1011.6, 1117.3(20)	C_{4v}, A, S, 20
$CaF_2 : Gd^{3+}$	1017.0, 1104.2(20)	C_{4v}, A, S, 20
$CaF_2 : Tb^{3+}$	1029.3, 1112.8(20)	C_{4v}, A, S, 20
$CaF_2 : Dy^{3+}$	1033.1, 1103.3(20)	C_{4v}, A, S, 20
$CaF_2 : H_0^{3+}$	1035.9, 1094.6(20)	C_{4v}, A, S, 20
$CaF_2 : Er^{3+}$	{1036.3, 1086.6(20)} {1037.6, 1081.2(20)}	C_{4v}, A, S, 20
$CaF_2 : T_m^{3+}$	1043.5, 1087.3(20)	C_{4v}, A, S, 20
$CaF_2 : Yb^{3+}$	1043.4, 1074.6 1049.8, 1100.7(20)	C_{4v}, A, S, 25
$CaF_2 : Lu^{3+}$	1042.5, 1072.0(20)	C_{4v}, A, S, 20
$CaF_2 : Y^{3+}$	1028.9, 1074.8(20)	C_{4v}, A, S, 20
Rare earth : H^-, D^-, T^- (substitutional)		
$CaF_2 : Ce^{3+} : H^-$	1235(12)	S, 27
$: D^-$	893(12)	S, 27
$: T^-$	739(12)	S, 27
$SrF_2 : Ce^{3+} : H^-$	1103(12)	S, 27
$: D^-$	802(12)	S, 27
$: T^-$	669(12)	S, 27

[a] A = absorption, R = Raman, S = electronic sideband.

[b] The references for Table V.1 are the following:

1. Sievers, A. J., and R. L. Pompi, 1967, Solid State Commun. **5**, 963.
2. Dötsch, H., W. Gebhardt, and C. Martius, 1965, Solid State Commun. **3**, 297.
3. Dötsch, H., 1969, Phys. Status Solidi **31**, 649.
4. Price, W. C., and G. R. Wilkinson, 1960, Final Tech. Report No. 2 (December 1960) on U. S. Army Contract DA-91-591 EUC-130801-4201-60 (R& D260), U. S. Army, through the European Research Office.
5. Schäfer, G., 1960, Phys. Chem. Solids **12**, 233.
6. Fritz, B., U. Gross, and D. Bäuerle, 1965, Phys. Status Solidi **11**, 231.
7. Bäuerle, D., and B. Fritz, 1967, Phys. Status Solidi **24**, 207.
8. Mirlin, D. N., and I. I. Reshina, 1964, Fiz. Tverd. Tela **6**, 3078 [Sov. Phys.–Solid State **6**, 2454(1964)].
9. Mitsuishi, A., and H. Yoshinaga, 1962, Prog. Theor. Phys. (Kyoto) Suppl. **23**, 241.
10. Timusk, T., and M. V. Klein, 1966, Phys. Rev. **141**, 664.
11. Montgomery, G. P., W. R. Fenner, M. V. Klein, and T. Timusk, 1972, Phys. Rev. **5**, 3343.
12. Dötsch, H., and S. S. Mitra, 1969, Phys. Rev. **178**, 1492.

TABLE V.1. Localized modes in ionic crystals. *(Continued)*.

13. Elliott, R. J., W. Hayes, G. D. Jones, H. F. Mac donald, and C. T. Sennett, 1965, Proc. R. Soc. Lond. **289**, 1.
14. Harrington, J. A., R. T. Harley, and C. T. Walker, 1970, Solid State Commun. **8**, 407.
15. Jones, G. D., and R. A. Satten, 1966, Phys. Rev. **147**, 566.
16. Hattori, T., K. Ehara, A. Mitsuishi, S. Sakuragi, and H. Kanzaki, 1973, Solid State Commun. **12**, 545.
17. Fritz, B., 1962, J. Phys. Chem. Solids **23**, 375.
18. Dürr, U., and D. Bäuerle, 1970, Z. Phys. **233**, 94.
19. Bäuerle, D., and B. Fritz, 1968, Phys. Status Solidi **29**, 639.
20. Jones, G. D., S. Yalsiv, S. Peled, and Z. Rosenwacks, 1968, in *Localized Excitations in Solids*, edited by R. F. Wallis (Plenum, New York), p. 512.
21. Shamu, R. E., W. M. Hartmann, and E. L. Yasaitis, 1968, Phys. Rev. **170**, 822.
22. deSouza, M., A. G. Góngora, M. Aegerter, and F. Lüty, 1970, Phys. Rev. Lett. **25**, 1426.
23. Mirlin, D. N., and I. I. Reshina, 1966, Sov. Phys.–Solid State **8**, 116.
24. Barth, W., and B. Fritz, 1967, Phys. Status Solidi **19**, 515.
25. Chambers, D. N., and R. C. Newman, 1969, Phys. Status Solidi **35**, 685.
26. Klukhuhn, A. F. W., J. Bruining, B. Klootwijk, and J. van der Elsken, 1970, Phys. Rev. Lett. **25**, 380.
27. Jacobs, I. T., G. D. Jones, K. Žďánský, and R. A. Satten, 1971, Phys. Rev. B **3**, 2888.

mass change is usually a straightforward experiment, the interpretation of the small differences between alkali halide crystals is still not completely understood. Below we examine whether these differences can be accounted for within the framework of the harmonic approximation.

When the H^- or D^- ion replaces the heavy ion in an alkali halide crystal (see Table V.1) the ratio of the hydride to deuteride frequency is without exception smaller than when H^- or D^- replaces the light ion in the lattice. In the former case the local mode originated essentially from the top of the acoustic branch, while in the latter case it started at the bottom of the optic branch. In the second case the H^- and D^- modes end up further from the normal lattice modes, are better approximated by an isolated Einstein oscillator, and produce a frequency ratio closer to $\sqrt{2/1} = 1.414$. The formalism associated with this statement can be found in Maradudin *et al.* (1963). Such a behavior is a characteristic property of a harmonic local mode in a diatomic lattice.

Proper calculations of local mode frequencies require a knowledge of the eigenfrequencies and eigenvectors of the host crystal vibrational modes as well as the mass and force constant changes introduced by the impurity ion. The isotope shifts can be easily calculated within the harmonic approximation by using a simple three-dimensional model exploited by Mitani and Takeno (1965). This model is extremely useful when extensive three-dimensional shell model calculations are not available.

Mitani and Takeno calculated the frequencies of local modes for a substitutional defect in a diatomic simple cubic lattice of the NaCl type with host ion masses M_1 and M_2. A relatively simple equation for the eigenfrequency of the infrared-active local mode can be obtained if central and noncentral force constants are set equal to each other. When the local mode frequency is much larger than ω_m an analytic solution can be obtained (as contrasted with the graphical method described in Sec. III). Only one parameter, K', the nearest-neighbor force constant for the impurity ion, appears in the solution. This parameter can be eliminated by fitting the hydride local mode frequency. The deuteride frequency is then predicted and compared with experiment.

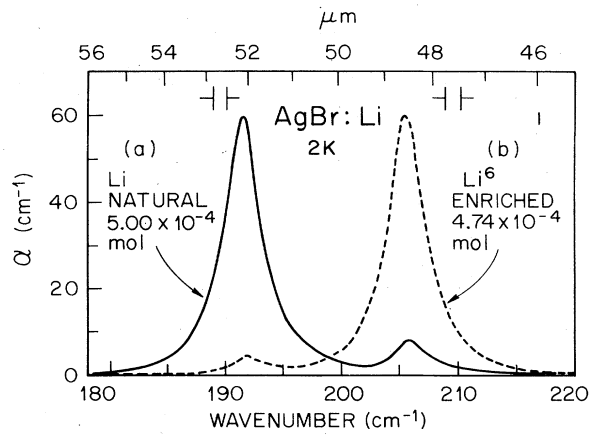

FIG. 68. The isotope shift for the AgBr:Li^+ local mode. After Hattori *et al.* (1973).

The Mitani-Takeno model has been solved by Nolt *et al.* to give the eigenfrequency of the infrared-active mode in the following form:

$$M_1\omega_1^2 g_0\left(\left(\frac{\omega}{\omega_1}\right)^2\right)=\frac{(1-\gamma)-\gamma(1-\epsilon)(\omega/\omega_1)^2}{\epsilon(1-\gamma)-\gamma(1-\epsilon)(\omega/\omega_1)^2}, \tag{5.2}$$

with ω_1 equal to the frequency of the top of the acoustic branch and M_1 the heavier mass in the diatomic lattice, so $M_1' \ll M_1$. $g_0((\omega/\omega_1)^2)$ is the real part of the Green's function defined by Mitani and Takeno, and ϵ and γ are mass and force constant defect parameters (Sec. II). Equation (5.2) is comparable to the mass defect equation (3.9) except now both mass and force constant parameters enter the defect term on the right side. For the high-frequency region of interest here where $\omega/\omega_1 \gg 1$, Sievers and Pompi (1967) have shown that the asymptotic expansion of the left-hand side of (5.2) is

$$M_1\omega_1^2 g_0\left(\left(\frac{\omega}{\omega_1}\right)^2\right)\cong\frac{(\omega/\omega_1)^2}{(\omega/\omega_1)^2-1}\left\{1+\left[6\left(\alpha^2\left(\frac{\omega}{\omega_1}\right)^2-1\right)\times\left(\left(\frac{\omega}{\omega_1}\right)^2-1\right)\right]^{-1}\right\}, \tag{5.3}$$

where $\alpha=\omega_1/\omega_2$, with ω_1 equal to the top of the acoustic branch, and ω_2 equal to the bottom of the optic branch. The right-hand member of (5.2) contains the defect parameters, so that a mass change of the impurity ion changes the right side of (5.2) but not the left, while a mass change of the host lattice has the opposite effect.

We now calculate the hydride–deuteride frequency ratio for NaCl using the model described above. By fitting the experimentally determined local mode frequency for NaCl:H^- from Table V.1, we determine the effective force constant ratio to be $K'/K=0.32$, indicating a large softening of the lattice around the impurity. This is perhaps to be expected because the H^- ion has a smaller ionic radius than the Cl^- ion that it replaces. The impurity mass is then changed by a factor of 2, and the D^- frequency ratio is calculated. The result is

$$\omega(H^-)/\omega(D^-)=1.409.$$

The ratio is less than the ratio given by the one-oscillator model, but still not as small as the experimental value of 1.384.

The lattice-defect system can be investigated from another point of view by studying the H^- frequency shift due to an isotopic mass change in the host crystal lattice. So far it has only been possible to obtain isotopically pure ^{6}LiF and ^{7}LiF. By fitting the experimentally determined local mode frequency for ^{7}LiF:H^-, the effective force constant ratio is found to be $K'/K=0.25$ from (5.3). As no gap occurs between the optic and acoustic branches, the zone boundary frequencies are set equal to each other ($\omega_1=\omega_2$). The calculated frequency ratio for the change in host crystal is 1.0011, which is much too small to account for the experimentally measured ratio of 1.0038. Apparently anharmonic contributions, though not large, must play a significant role in determining the local mode frequency. This conclusion is substantiated by more complete local calculations (MacDonald, 1966).

When long-range electrostatic forces are taken into account, it has been shown by Jaswal and Montgomery (1964), using the rigid-ion and deformation-dipole models, by Fieschi *et al.* (1965, 1964), using the shell model, by Page and Strauch (1967), using the breathing shell model, and by Striefler and Jaswal (1969a), including relaxation, that the central force constant between the impurity and its nearest neighbors has to be decreased by about 50% to obtain agreement with experiment. Most of the model calculations lead to a H^-/D^- isotope frequency ratio of 1.40 (Fritz, 1968).

Before turning to anharmonic properties of local modes it should be noted that a number of calculations have been carried out on the dynamics of isotopic substitution in LiH and LiD mixed crystals (Benedek, 1967; Hardy, 1962; Montgomery and Hardy, 1965; Elliott and Taylor, 1967; Jaswal and Hardy, 1968; and Striefler and Jaswal, 1969b), but as yet only one experimental result has been published on these systems (G. Wolfram *et al.*, 1972).

2. The static anharmonic potential

A number of the spectroscopic properties of the U-center local mode both in alkaline earth fluorides and in alkali halides have been accounted for by using the extended one-oscillator model described in (4.2). That is, the H^- ion is assumed to reside in a static anharmonic potential having the symmetry of the host lattice at the impurity site. For the alkaline earth fluorides Elliott *et al.* (1965) used a Hamiltonian

$$\mathcal{H}=Ar^2+Bxyz+C_1(x^4+y^4+z^4)+C_2(x^2y^2+y^2z^2+z^2x^2) \tag{5.4}$$

which is a Taylor's expansion of the energy to fourth order in the displacement of the impurity ion. This adiabatic approximation is physically reasonable since the local mode frequency is about three times the largest lattice mode frequency, suggesting that the impurity samples the average lattice. For the low-lying energy levels, the effects of B and C will be small. The spherical oscillator where only $A\neq 0$ has equally spaced levels at $E=\hbar\omega(n+3/2)$, with degeneracies 1, 3, 6, 10, ... etc. In the tetrahedral potential these degenerate levels are split. For the sites of cubic symmetry, O_h, $B=0$ but again the cubic potential terms split the degenerate levels of the spherical oscillator.

The energy relative to the unperturbed ground state has been found by Elliott *et al.* (1965) to be

$$E(\Gamma)=n\hbar\omega+[\mu_1(\Gamma)C_1+\mu_2(\Gamma)C_2]\left(\frac{\hbar}{2M^*\omega}\right)^2-\frac{\lambda(\Gamma)B^2\hbar^2}{24M^{*3}\omega^4}. \tag{5.5}$$

The positions and forms of the first few vibrational levels for T_d and O_h symmetry are shown in Table V.2.

The energy level diagrams for the lowest states are shown in Fig. 69. For T_d symmetry electric dipole transitions are allowed from the singlet A_1 ground state only to the T_2 triply degenerate excited states. As shown in Table V.1 transitions to all four T_2 states have been observed in CaF_2, enabling the constants ω, B, C_1, and C_2 in (5.5) to be determined (Elliott *et al.*, 1965). Al-

TABLE V.2. Positions and forms of the lower vibrational energy levels for T_d and O_h symmetry (after Elliott *et al.*, 1965). The wave functions are designated by the quantum numbers of the harmonic oscillators in the x, y, and z directions. The last two lines of this table form a complete set.

n	T_d Symmetry	O_h	Wave functions	μ_1	μ_2	λ
0	A_1	A_{1g}	$\|000\rangle$	9	3	1
1	T_2	T_{1u}	$\|100\rangle$	21	7	5
2	A_1	A_{1g}	$1/\sqrt{3}[\|200\rangle + \|020\rangle + \|002\rangle]$	45	15	21
2	E	E_g	$1/\sqrt{2}[\|200\rangle - \|020\rangle]$	45	9	3
2	T_2	T_{1g}	$\|011\rangle$	33	15	13
3	A_1	A_{1u}	$\|111\rangle$	45	27	25
3	T_1	T_{2u}	$1/\sqrt{2}[\|102\rangle - \|120\rangle]$	57	21	15
3	T_2	T_{1u}	$1/\sqrt{2}[\|102\rangle + \|120\rangle]$	$\begin{pmatrix} 57 & 0 \\ 0 & 81 \end{pmatrix}$	$\begin{pmatrix} 25 & 2\sqrt{6} \\ 2\sqrt{6} & 15 \end{pmatrix}$	$\begin{pmatrix} 27 & 6\sqrt{6} \\ 6\sqrt{6} & 13 \end{pmatrix}$
3	T_2	T_{1u}	$\|300\rangle$			

though the A_1, T_2, and E transitions should be active in Raman scattering, only the A_1 and T_2 have been observed (Harrington *et al.*, 1970). These measurements confirm the infrared results. The Raman scattering spectrum for H^- in BaF_2 is shown in Fig. 70.

For O_h symmetry electric dipole transitions are allowed from the singlet A_{1g} ground state to the T_{1u} triply degenerate excited states. Only the lowest transition to the first T_{1u} state has been observed. Complementary Raman scattering measurements (Montgomery *et al.*, 1972) on the lowest $A_{1g} \rightarrow A_{1g}$, $A_{1g} \rightarrow T_{1g}$, and $A_{1g} \rightarrow E_g$ transitions provide the necessary information to evaluate the coefficients in (5.5). The coefficients for CaF_2 and for KI are given in Table V.3.

The anharmonic potential can also be probed by the addition of an applied dc electric field to the sample. The perturbation Hamiltonian is then

$$\mathcal{H}_E = -e(\vec{E} \cdot \vec{r}). \tag{5.6}$$

The local mode infrared absorption in CaF_2 has been measured in the presence of an external electric field by Hayes and MacDonald (1967). They found the electric field Hamiltonian to be

$$\mathcal{H}_E = \frac{\hbar E_{\text{loc}} e^* B}{2M\omega^2} (\zeta_1\eta_2\eta_3 + \zeta_2\eta_3\eta_1 + \zeta_3\eta_1\eta_2), \tag{5.7}$$

where e^* is the effective charge of H^-, and E_{loc} is equal to the Lorentz local field correction times the applied electric field. The applied dc field is considered along an arbitrary direction $(\zeta_1, \zeta_2, \zeta_3)$ relative to the crystal axes. Here (η_1, η_2, η_3) refers to the motion of the charged impurity and hence to the polarization of the incident infrared field. Although individual H^- ions occur in sites which lack inversion symmetry, the crystal as a whole has a center of symmetry. There are as a consequence, two H^- ions in the electric unit cell. They give identical energy level patterns, symmetric about the unperturbed line, when E is in the [001] and [110] directions. However, when E is in the [111] direction they give rise to separate energy levels which still maintain the symmetry of the perturbation pattern about the unperturbed line. The calculated splitting of the T_2 states by an electric field in the [111], [110] and [100] directions is shown in Fig. 71.

With the electric field along the [111] direction Hayes and MacDonald (1967) were not able to resolve the mode splitting. With a spectral slit width of 1.5 cm^{-1} and a natural linewidth estimated to be about 0.5 cm^{-1} they found that the line broadened by less than 20% in a 90 kV/cm electric field. From these measurements the

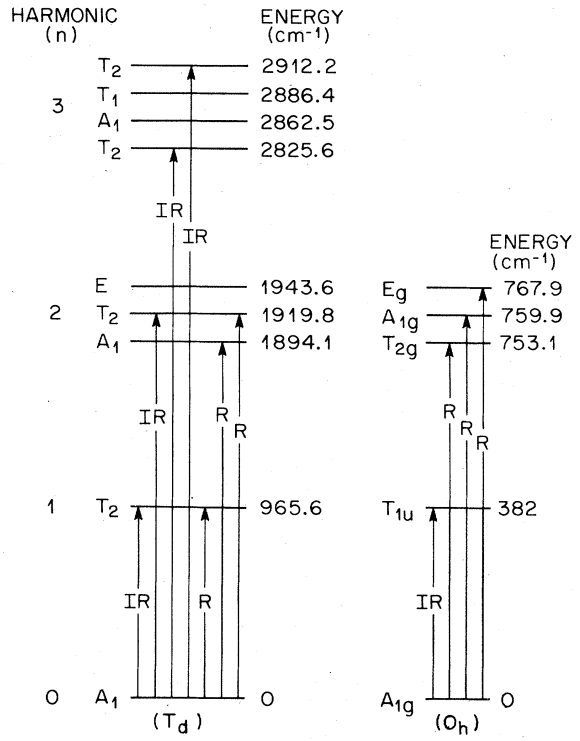

FIG. 69. Energy level diagram for the H^- ion in $CaF_2(T_d)$ and also in $KI(O_h)$. The observed infrared- and Raman-active modes are indicated by the full vertical lines.

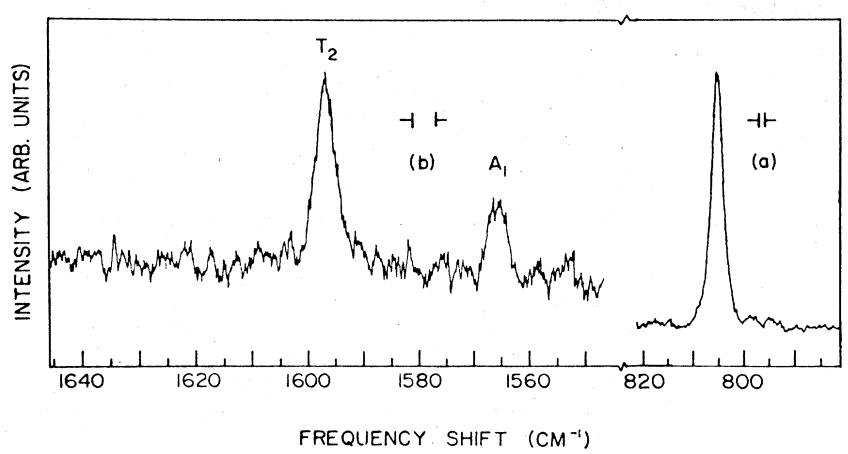

FIG. 70. Raman spectra of BaF_2:H^- at 16 °K. (a) Fundamental T_2 transition, (b) Second harmonics of A_1 and T_2 symmetry. (The second harmonic of E symmetry which is not observed is predicted to occur at 1617 cm^{-1}. Instrumental resolution is indicated for each trace.) After Harrington *et al.* (1970).

coefficient of the cubic term is estimated in Table V.3. This value was obtained assuming e^* to be one electron charge.

Although no electric field measurements have as yet been made on the U center in alkali halide crystals, the energy changes have been calculated (Clayman *et al.*, 1971). For O_h symmetry the defect site has inversion symmetry, so a linear electric field effect will not be possible. It has been noted that the second-order electric field effect operator has the same symmetry and even parity as does the uniaxial stress operator (Gebhardt, 1967). This leads to the same selection rules for both perturbations. The Hamiltonian for this second-order electric field effect, which is a symmetric expression in the direction cosines ζ_i and η_i, is

$$\mathcal{H}_E = \frac{\hbar e^{*2} E_{\rm loc}^2}{2M^3\omega^5}\left\{\left(4C_1+\frac{4C_2}{3}\right)+\left(2C_1-\frac{C_2}{3}\right)\right.$$
$$\times[(2\zeta_3^2-\zeta_1^2-\zeta_2^2)(2\eta_3^2-\eta_1^2-\eta_2^2)$$
$$+3(\zeta_1^2-\zeta_2^2)(\eta_1^2-\eta_2^2)]+2(-3C_1+2C_2)$$
$$\left.\times(\zeta_1\zeta_2\eta_1\eta_2+\zeta_2\zeta_3\eta_2\eta_3+\zeta_3\zeta_1\eta_3\eta_1)\right\}. \quad (5.8)$$

In (5.8), ζ_i refers to the external field, and η_i refers to the polarization of the incident radiation with respect to the crystal axes. The calculated splittings of the T_{1u} state by an electric field in the [111], [110] and [100] directions are shown in Fig. 71. For the dc field along [100] the T_{1u} state splits into an A_1 and an E state. For the applied field parallel to [110] the degeneracy is completely removed as the levels split into A_1, B_1, and B_2 states. Hence from the slopes of the infrared absorption as a function of $(E)^2$ the anharmonic potential coefficients can be obtained.

In this section we have seen that the anharmonic one-oscillator model can describe the measured impurity mode spectra quite well. With this model we can re-examine the frequency ratio for the isotopic mass substitution. The previous section showed that the harmonic models gave frequency ratios greater than the experimental frequency ratios. From (5.5) and Table V.2 the anharmonic A_{1g} to T_{1u} mode transition energy is

$$\hbar\Omega = \hbar\omega + (3C_1 + C_2)(\hbar/M\omega)^2. \quad (5.9)$$

From Table V.3 $(3C_1 + C_2) > 0$. An examination of (5.9) shows that the anharmonic isotope effect will be *larger* than the harmonic isotope effect calculated earlier. This

TABLE V.3. The coefficients of Eq. (5.5) determined from spectroscopic measurements on U-centers. Both alkaline earth fluorides and alkali halide values are given.

Host crystal	ω (cm^{-1})	$\lvert B\rvert$ 10^{+12} erg/cm^3	C_1 10^{19} erg/cm^4	C_2 10^{19} erg/cm^4	Reference [a]
KBr : H^-	444.6	0	0.986	−2.30	1
KBr : D^-	318.2	0	0.986	−2.30	1
KI : H^-	377.8	0	0.576	−1.356	1
KI : D^-	272.3	0	0.576	−1.356	1
CaF_2 : H^-	981.1	7.87	−2.32	−1.01	2
SrF_2 : H^-	907.4	6.20	−1.80	−2.19	2
BaF_2 : H^-	827.2	3.98	−1.70	−8.5	2

[a] The references for Table V.3 are the following:

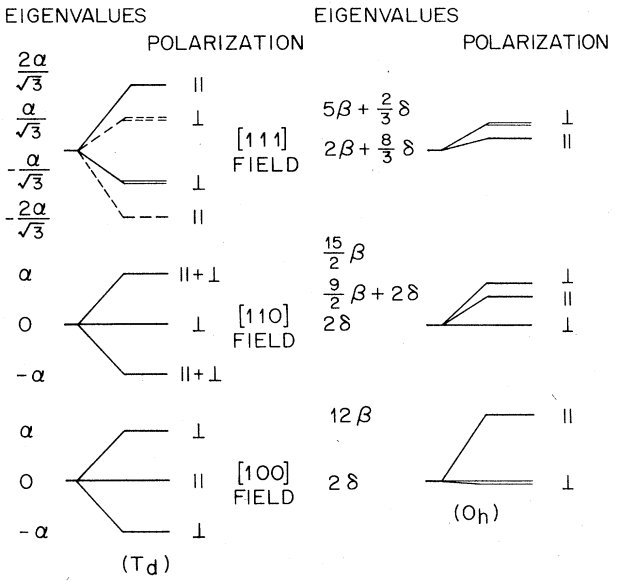

FIG. 71. Calculated splittings of the lowest-frequency infrared local mode transition with an electric field. For T_d symmetry the splitting parameter α is $e^*E_{\rm loc}B/m\omega^2$ as given in (5.7). For O_h symmetry the splitting parameters are $\beta = C_1\hbar(e^*E_{\rm loc})^2/2m^3\omega^5$ and $\gamma = C_2\hbar(e^*E_{\rm loc})^2/2m^3\omega^5$ as described in (5.8).

important discrepancy between theory and experiment has not yet been resolved.

C. Anharmonic coupling to the lattice

1. Sidebands of the H^- local mode

In addition to the main U-center absorption band, Schäfer (1960) also observed sidebands in his original work. Fritz (1964) first proposed that these were caused by anharmonic coupling between the local mode and perturbed band modes. The temperature-dependent absorption spectrum in the frequency region of the local mode is shown for KBr:H^- in Fig. 72. At room temperature there is one broad and relatively structureless band. This sharpens up considerably as the crystal is cooled. At 90K a prominent peak exists in the center of the spectrum, plus a broad region of sidebands one to three orders of magnitude lower than the peak intensity in the main band. At lower temperature a great deal of sideband structure can be resolved. Experimental investigations on sidebands have been carried out by Fritz (1965), Elliott *et al.* (1965), Mitra and Brada (1965), Dötsch *et al.* (1965), Fritz *et al.* (1965), Timusk and Klein (1966), Fritz *et al.* (1968), Dötsch (1969), and MacPherson and Timusk (1970).

The experiments establish two main facts: (1) The difference between sideband and main band frequencies is not affected by D^- substitution, and (2) the sidebands are almost symmetrically displaced from the main band to higher and lower frequencies. The low-frequency component freezes out completely at low temperatures, as shown in Fig. 72.

Physically the processes can be described in terms of two-phonon absorption. A local mode quantum is virtually excited by one absorbed photon. This state decays into a final state in which one local mode quantum is created and one lattice mode quantum is either created (summation or Stokes band) or destroyed (difference or anti-Stokes band). In this framework any peak in the density of phonons at ω_i, provided that there is strong enough coupling of the local mode to these phonons, would lead to sideband peaks at roughly

$$\omega_+ = \omega_{\rm loc} + \omega_i \text{ Stokes sideband,}$$

and

$$\omega_- = \omega_{\rm loc} - \omega_i \text{ anti-Stokes sideband.}$$

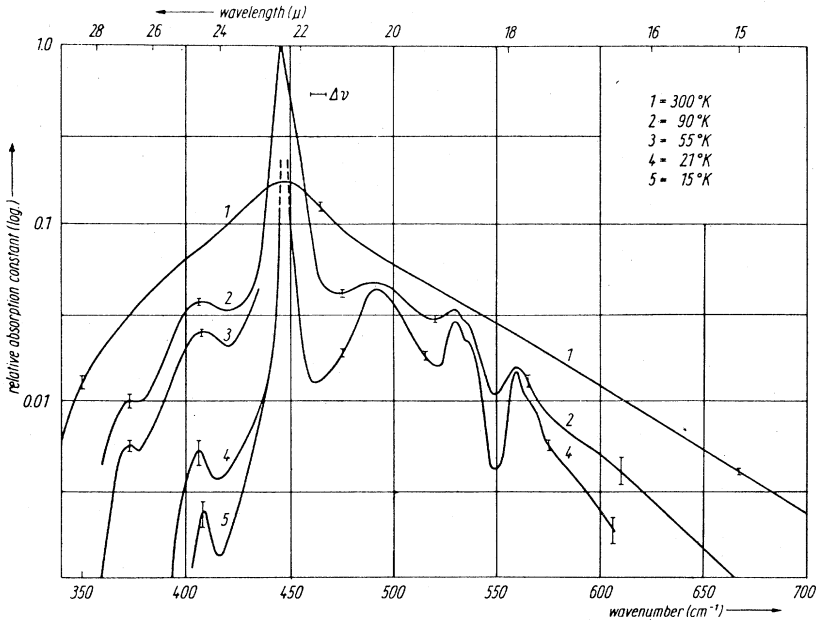

FIG. 72. Impurity-induced absorption in KBr:H^- as a function of temperature. The absorption constant is given on a logarithmic scale. After Fritz *et al.* (1965).

Figure 63 showed the Stokes sideband of a local mode in CdTe. Figure 73(a) shows the high-frequency sideband structure of KI:H^- (MacPherson and Timusk, 1970). Figure 73(b) shows the phonon density of the pure material as obtained from neutron scattering data (Dolling *et al.*, 1966). The general decrease of absorption in the sideband with increasing frequency is quite striking. We recall that in CdTe:Be the phonon density of states had to be weighted by approximately $\omega^{-3/2}$ to fit the observed sidebands. KI:H^- also shows a sharp localized mode in the region of the phonon gap near 94 cm^{-1}.

Theoretical studies of the sideband spectra have been made by Elliott *et al.* (1965), Timusk and Klein (1966), Nguyen Xuan Xinh (1966, 1967), Bilz *et al.* (1966), Page and Dick (1967), Gethins *et al.* (1967), and MacPherson and Timusk (1970). A concise review of the progress on this problem up through 1967 has been given by Klein (1968). It was found that the theory developed by Timusk and Klein (1966), which attempts to explain the shape of the sideband spectrum in terms of the anharmonic coupling of the H^- ion to its nearest neighbors, was qualitatively correct. The sideband spectrum could be calculated by taking an anharmonic coupling term of the form Q^2q_i where the local mode coordinate is denoted by Q and the rest of the lattice normal modes by $\{q_i\}$. The agreement with experiment was achieved without the use of any parameter fitted to sideband shape. The single adjustable parameter of the model—the nearest-neighbor force constant—is fitted to the local mode frequency itself.

The Timusk–Klein model has been extended by Gethins *et al.* (1967) to allow for lattice relaxation around the impurity. Because the H^- ion has a smaller ionic radius than the halide ion it replaces, the neighbors of the H^- ion move until counteracted by an exchange repulsion. Because the forces between ions are not perfectly harmonic, this change of position results in a change of force constants. The change will be largest (apart from the change between the H^- ion and its nearest neighbors) for the interionic distances which are most changed; namely, between the nearest neighbors of the H^- ion, and their nearest neighbors in the direction away from the H^- ion. These are the fourth neighbors to the H^- ion and are shown in Fig. 74. The change in force constants coupling the H^- ion to its second and third neighbors can be expected to be small, because these force constants are themselves small.

Using the above model, MacPherson and Timusk (1970) have calculated the sideband spectra for the H^- in KCl, KI, NaF, NaCl, and NaBr, and fitted these calculations to their experimental results by varying the force constant Δg (Fig. 74). Figure 73 shows the calculated fit they obtained to their experimental measurements. Although some small discrepancy still remains between the widths and relative strengths of the predicted peaks, they conclude that the salient features of the sideband spectrum of the H^- local mode in the sodium and potassium halides can be explained in terms of a simple shell model for the defect. This fact indicates that the effects of breathing shell modes (Schroder, 1966), charge changes at the defect site, other force constant changes, and anharmonic corrections should be relatively minor. It is important to note from Fig. 73 that while the sidebands do reflect some features of the density of states

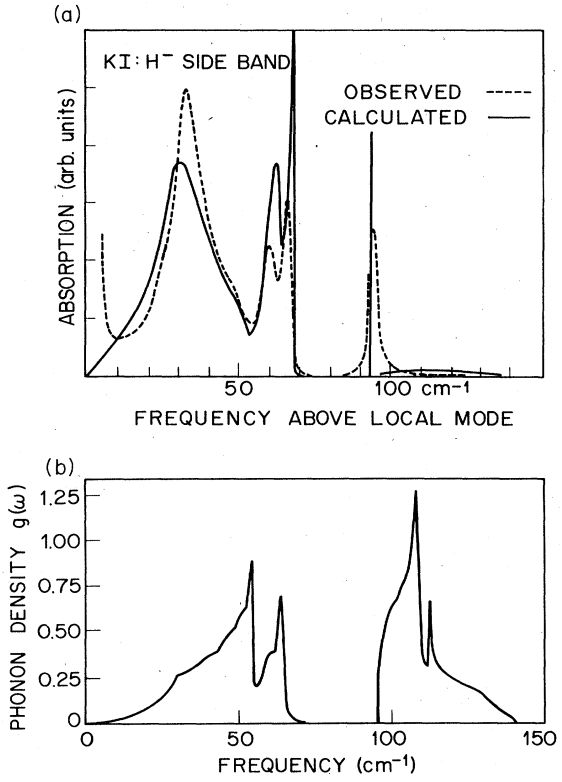

FIG. 73. (a) Observed and calculated sideband absorption of the H^- ion localized mode in KI. (MacPherson and Timusk, 1970). (b) One-phonon density of states for KI. (Dolling *et al.*, 1966).

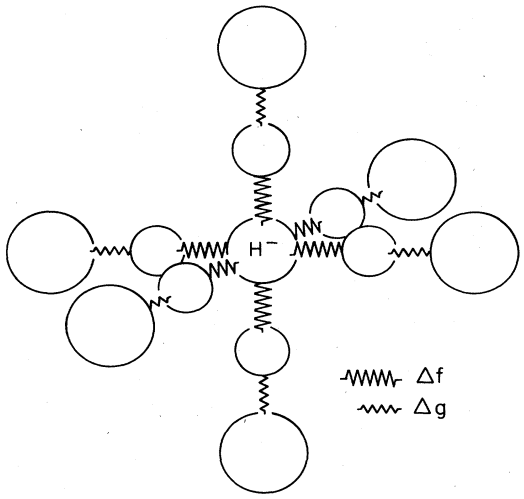

FIG. 74. The "molecule" of force constant changes introduced by insertion of the H^- ion, an alkali halide crystal. The ion at the center is the H^-. Its first-neighbor (alkali) atoms are shown, as well as its fourth-neighbor (halide) atoms. The spring constant Δf is determined by the local mode frequency; the spring constant Δg is an adjustable parameter. After Gethins *et al.* (1967).

$g(\omega)$, simply scaling $g(\omega)$ by a factor like ω^{-2} or ω^{-3} does not give a detailed fit to the sidebands. The reason for this effect in the infrared sideband spectrum of an alkali halide is simply that even lattice modes are effective at modulating the local mode, while odd lattice modes are not. Thus certain components of $g(\omega)$ (the odd modes) do not appear in the sideband envelope.

2. Intensity of the local mode peak

In discussing the intensity of the integrated absorption due to a local mode it is important to be quite clear as to how much of the absorption spectrum is being discussed. If the potential energy is purely harmonic the spectrum consists of a single line at $\omega_{\rm loc}$. The integrated absorption coefficient is temperature independent (Wilson *et al.*, 1955). When anharmonic terms are included this line may shift, broaden, and change in strength, but in general the anharmonicity would also induce other lines to appear elsewhere in the spectrum. These lines may be described in the language of molecular spectroscopy as combination bands, overtones, etc. or in solid-state terms as sidebands, two-phonon transitions, etc. The original line near $\omega_{\rm loc}$ would then be referred to as the fundamental or as the "zero-lattice-phonon" (ZLP) line. We are concerned with the intensity of this line only, and not with the complete absorption spectrum associated with the local mode. For the complete absorption spectrum there exists a sum rule

$$\int \alpha(\omega)\,d\omega = \text{const.}$$

This result has been derived by Strauch (1969) for an anharmonic system with a linear dipole moment using the anharmonic one-phonon Green's function. Since this is a very useful result, we give an alternative simple proof (Alexander *et al.*, 1970).

The Hamiltonian for the harmonic local mode Q is $\mathcal{H}(Q)$ and for the harmonic lattice mode q, $\mathcal{H}(q)$ so that the total Hamiltonian may be written

$$\mathcal{H} = \mathcal{H}(Q) + \mathcal{H}(q) + \mathcal{H}'(Q,q),$$

where $\mathcal{H}'(Q,q)$ describes the anharmonic part of the potential. The dipole moment is $M = e^*Q$, where e^* is the effective charge. Allowing for negative contributions from stimulated emission, the absorption coefficient may be written as

$$\alpha(\omega) = Av_i \sum_f{}' |\langle f|M|i\rangle|^2 \omega_{fi}\,\delta(|\omega_{fi}| - \omega)\,, \tag{5.10}$$

where $\hbar\omega_{fi}$ is the transition energy $E_f - E_i$. Here $|i\rangle$ and $|f\rangle$ are eigenstates of $\mathcal{H}$ with eigenvalues E_i and E_f, and Av_i indicates a thermal average over the states $|i\rangle$.

By expanding the commutator $[Q,[H,Q]]$ one finds that

$$\sum_f (E_f - E_i)|\langle f|Q|i\rangle|^2 = \frac{\hbar}{2M_Q}\,, \tag{5.11}$$

for all i, where M_Q is the mass associated with the local mode. This may be recognized as a disguised version of the Thomas–Reich–Kuhn f sum rule of atomic spectra. Combining (5.10) and (5.11) it follows that

$$\int_0^\infty \alpha(\omega)\,d\omega = \frac{\hbar e^{*2}}{2M_Q} = \text{constant}. \tag{5.12}$$

In contrast with the above sum rule, which is exact for an anharmonic system with a linear dipole moment, we are interested in the temperature dependence $I(T)$ of the more restricted spectrum given by

$$I(T) = \int_{ZPL} \alpha(\omega)\,d\omega. \tag{5.13}$$

Measurements by Fritz (1968) on the U center in KCl indicate that $I(T)$ drops by about 20% between 4K and 300K. A similar decrease in intensity is observed for the U center in CaF_2 by Elliott *et al.* (1965). A number of investigators have identified the intensity change with a "Debye–Waller factor" (Takeno and Sievers, 1965; Mitra and Singh, 1966) analogous to the well-known cases in x-ray, neutron scattering, the Mössbauer effect, and electronic optical absorption by defects (Maradudin, 1966a; Silsbee and Fitchen, 1964). The reason behind the application of the Debye–Waller factor has been that the anharmonic coupling term which produces the sidebands involves linear coupling to the lattice modes and by analogy will result in a Debye–Waller factor for the zero-lattice-phonon mode. The temperature dependence has the form (Alexander *et al.*, 1970)

$$I(T) = \exp\left\{-S_0\bar{A}^2\left[1 + 4\left(\frac{T}{\theta_c}\right)^2 \int_0^{\theta_c/T} \frac{x\,dx}{e^x - 1}\right]\right\}, \tag{5.14}$$

where $S_0 = 9\omega_c^2/4Mv^2\hbar\omega_D^3$ contains a cutoff frequency ω_c which is less than the Debye frequency ω_D. Here $\theta_c = \hbar\omega_c/k_B$, v is the Debye velocity, and M the average ion mass appropriate to the Debye modes. For O_h symmetry, the strain coupling parameter $\bar{A}$ is made up of the coupling coefficients A, B, C for the three symmetry types as follows

$$\bar{A}^2 = \frac{A^2(A_{1g})}{48} + \frac{B^2(E_g)}{12} + \frac{3C^2(T_{2g})}{16}\,. \tag{5.15}$$

The validity of the above approach has been examined by Hughes (1968). He concludes that the Debye–Waller factor is applicable in the vibrational case when the local mode frequency is much greater than the frequency of the anharmonically coupled lattice modes and when the temperature dependence arises from coupling terms of the form Q^2q_i in the Hamiltonian. Hughes' calculations are compared with the experimental data in Fig. 75. In Fig. 75(a) the calculated temperature dependence from the Debye–Waller factor is given by curve A for the anharmonic coupling constant determined by Bilz *et al.* (1966) for KCl:H^- and is given by curve B when the coupling constant is reduced by a factor of 2. The points are the experimental data. The calculated curve is compared with experiments on CaF_2:H^- in Fig. 75(b). The solid curve is the calculated temperature dependence from the Debye–Waller factor using the anharmonic coupling constant determined by Elliott *et al.* (1965). Again the experimental points are the circles. With appropriate coupling constants the calculations are successful.

3. The effects of lattice strain

The Grüneisen constant γ for a mode with frequency ω is a dimensionless number given by

$$\gamma \equiv -\frac{d\ln\omega}{d\ln V}, \tag{5.16}$$

$$= \frac{1}{\omega\chi}\left(\frac{\partial\omega}{\partial P}\right)_T, \tag{5.17}$$

where measurements are performed at constant temperature, V is the crystal volume, and χ is the bulk crystal compressibility. From theoretical models of the dependence of the frequency on interionic spacing, the Grüneisen constant can be calculated from (5.16), and from experimental measurements of the frequency shift as a function of pressure the Grüneisen can be calculated from (5.17). One assumes that the U-center local mode obeys a relation similar to (5.16) so that a local mode Grüneisen constant may be defined

$$\gamma_{\rm loc} \equiv -d\ln\omega_{\rm loc}/d\ln V_{\rm loc}\ . \tag{5.18}$$

Some calculations have been made on the relation between the local volume change around the defect and the volume change in the lattice (Benedek and Nardelli, 1968). But most investigators have assumed that the two quantities are identical. In this case (5.18) simplifies to

$$-\Delta\omega_{\rm loc} = \omega_{\rm loc}\gamma(\Delta V/V),$$
$$= A(\Delta V/V). \tag{5.19}$$

For small frequency shifts a linear relation exists between the shift and the lattice strain. In the previous two sections a linear coupling to lattice phonons has played a central role in understanding the experimental results. If one assumes that the linear coupling to dynamic strains (phonons) is the same as to the static strain of the same symmetry, then an independent measure of the anharmonic coupling coefficient is available by using (5.19).

Local mode frequency shifts have been measured by Shotts (1973) for the H^- ion in NaCl, KCl, and KBr with crystal strains of up to 1%. These strains are large enough to observe that (5.19) breaks down as shown in Fig. 76. The hydrostatic coupling coefficients $A(A_{1g})$ are recorded in Table V.4.

The presence of foreign alkali or halogen ions in the crystal has been observed to perturb the local mode frequency. In mixed crystals new lines appear which are shifted to both higher and lower frequencies with respect to the main U-center absorption line. Groups of these new lines have been identified with perturbed U centers which have foreign ions in one of the nearest three shells of neighboring ions (Merlin and Reshina, 1966; Barth and Fritz, 1967). In addition to these secondary absorption lines which are identified in Table V.1, the entire absorption spectrum undergoes a concentration-dependent frequency shift and broadening which is related to the change in the average lattice constant of the mixed crystal.

The lattice constant dependence of the main local mode absorption has been obtained by Barth and Fritz (1967). They studied the concentration-dependent shift and broadening of all lines in KCl:H^- and KCl:D^- doped with Rb. The position of the local mode absorption versus doping concentration is shown in Fig. 77. The frequency $\omega_{\rm loc}$ measured at 20°K is a linear function of the Rb concentration. On the top of Fig. 77 a lattice parameter scale is also given, which is based on the findings of Gnädinger (1953), who showed that the lattice constant in this system at room temperature follows closely the

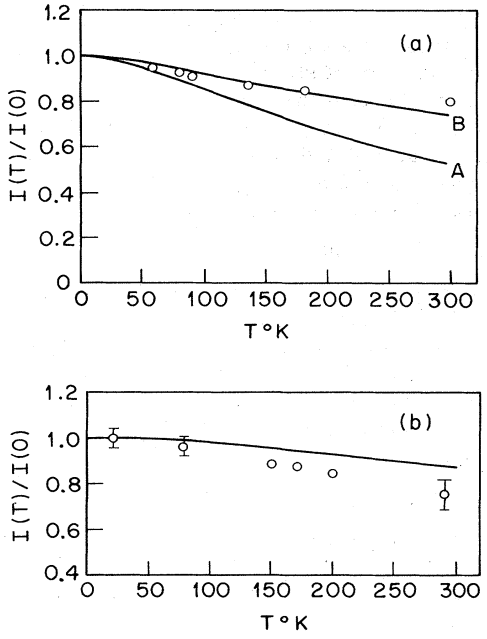

FIG. 75. (a) Calculated curves of $I(T)/I(O)$ versus temperature for KCl:H^-: (A) The Debye-Waller factor; (B) The Debye-Waller factor with an anharmonic coupling constant one-half the size of that in (A). The points are experimental data. (b) Calculated curve of $I(T)/I(O)$ versus temperature for CaF_2:H^-. The circles are experimental data. After Hughes (1968).

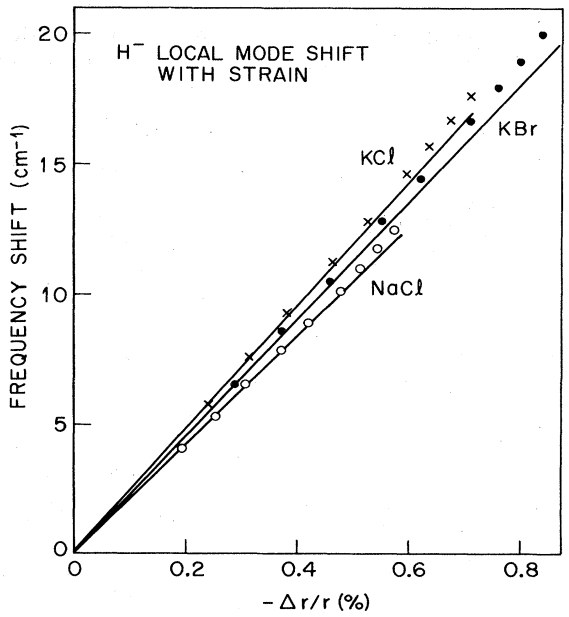

FIG. 76. Frequency shift of the U-center mode versus hydrostatic strain. The sample temperature was 41 °K. After Shotts (1973).

TABLE V.4. Anharmonic coupling coefficients for U centers with $O_h(T_d)$ symmetry in ionic crystals.

Host lattice	A (cm^{-1}/unit strain)	B (cm^{-1}/ unit strain)	C (cm^{-1}/unit strain)	Reference [a]
NaF	940 ± 60	510 ± 30	150 ± 5	1
NaCl	680 ± 2			2
KCl	772 ± 2			2
	840 ± 80	270 ± 30	120 ± 10	3
KBr	730 ± 2			2
	750 ± 75	240 ± 20	220 ± 20	4
KI	310 ± 50	130 ± 25	220 ± 50	3
CaF_2	940 ± 35	105 ± 35	1120 ± 35	4

[a] The references for Table V.4 are the following:

1. Dötsch, H., 1969, Phys. Status Solidi **31**, 649. Compliance factors from Vallin, J. K. Marklund, J. O. Sirkström, and O. Beckman, 1966, Ark. Fys. (Sweden) 32, 515.
2. Shotts, W. J., Ph.D. Thesis, Cornell University, 1973. Compressibility from Sharko, A. V., and A. A. Botaki, 1971, Sov. Phys.-Solid State **12**, 1796.
3. Fritz, B., J. Gerlach, and U. Gross, 1968, in *Localized Excitations in Solids*, edited by R. F. Wallis (Plenum, New York), p. 504. Source of compliance factors not given.
4. Dürr, U., and D. Bäuerle, 1970, Z. Phys. **233**, 94.
5. Hayes, W., and H. F. MacDonald, 1967, Proc. R. Soc. Lond. A **297**, 503. Compliance factors given.

Vegard relation (Vegard, 1921)

$$\bar{a} = a_1 + (a_2 - a_1)x. \tag{5.20}$$

In this equation, a_1 and a_2 are the lattice constants of the two components KCl and RbCl, and x is the molar concentration of component 2. From their measurements Barth and Fritz (1967) deduced a relation between frequency shift $\Delta\omega_{loc}$ and the average lattice constant change $\Delta\bar{a}$. Using the relation $\Delta V/V = 3\Delta a/a$ we can express their result as

$$-\Delta\omega_{loc} = 555(\Delta V/V)\ \text{cm}^{-1}.$$

This independent measure of the hydrostatic coupling coefficient is in reasonable agreement with the hydrostatic coupling coefficient recorded in Table V.4. Harrington and Walker (1971) have given a different interpretation of H^- and D^- local mode perturbations in BaF_2. They explain the concentration dependence $c^{1/2}$ observed in the linewidth as a mass perturbation of the host lattice rather than a lattice constant perturbation.

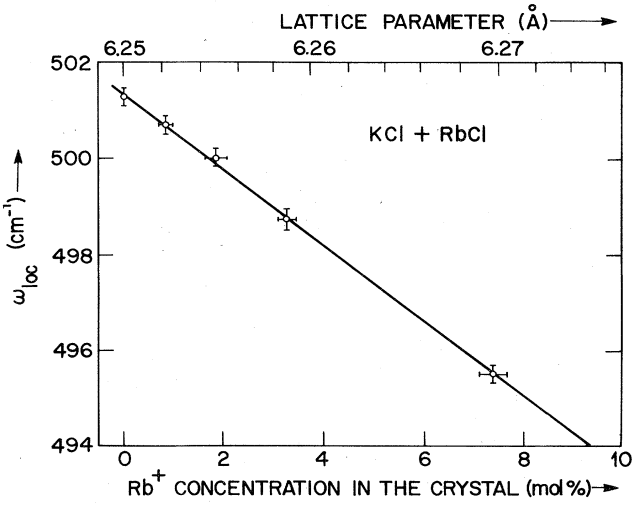

FIG. 77. Position of the H^- local mode peak in KCl doped with RbCl at 21 °K. The lattice parameter is interpolated using a Vegard relation. After Barth and Fritz (1967).

The hydrostatic pressure dependence of the U-center sideband in KBr has been measured by Shotts and Sievers (1973) to deduce the pressure dependence of structure in the density of states. They observed a linear dependence with pressure of a sideband feature which arises from a localized region of the Brillouin zone, a saddle point at [0.6, 0.6, 0] on the longitudinal acoustic branch (Ward and Timusk, 1972). The experimentally determined Grüneisen constant is

$$\gamma(0.6, 0.6, 0) = 1.93 \pm 0.1\,(\text{expt}).$$

Although in a simple calculation this constant is the same for all phonons, a detailed calculation in three dimensions results in different Grüneisen constants for different regions of k space. Using a shell model potential adjusted to fit neutron diffraction data, Cowley and Cowley (1965) have calculated the Grüneisen constant for the saddle point to be

$$\gamma(0.6, 0.6, 0) = 1.91\,(\text{theory}),$$

giving excellent agreement between theory and experiment.

The A_{1g} type strain (hydrostatic pressure) is only one kind of distortion which can perturb the T_{1u} local mode excited state. To identify all other lattice distortions which will influence the local mode we need to examine the appropriate matrix element for the excited state, which is

$$\Delta\omega = \langle\psi(T_{1u})|\mathcal{H}'|\psi(T_{1u})\rangle\,. \tag{5.21}$$

For these matrix elements to be invariant under all sym-

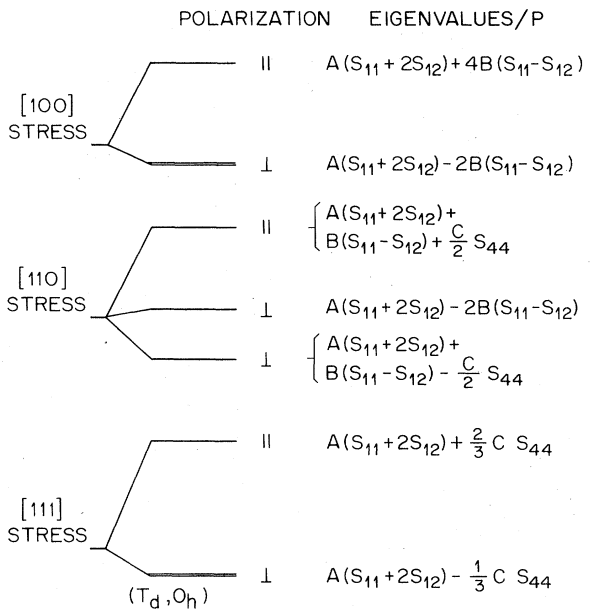

FIG. 78. Calculation of the splitting of the T_{1u} (T_2) states with applied stress in the [100], [110], and [111] directions. The polarization of the electric dipole absorption from the ground state is given. After Nolt and Sievers (1967).

metry operations of the octahedral group O_h, they must transform like the A_{1g} representation (Tinkham, 1964). Thus the stress perturbation must transform according to the representations contained in the direct product of

$$T_{1u} \times T_{1u} = A_{1g} + E_g + T_{2g},$$

showing that the only modes which interact with the excited state of the resonant mode are the long-wavelength distortions of A_{1g} (spherical), E_g (tetragonal and orthorhombic), and T_{2g} (trigonal) symmetry. Three coupling coefficients, $A(A_{1g})$, $B(E_g)$, and $C(T_{2g})$, determine the dependence of the local mode frequency upon the strain components. For the case of T_d symmetry only modes of symmetry A_1, E, and T_2 couple to the excited state of the local mode.

The form of the general stress Hamiltonian coupling to degenerate electronic states has been discussed by Schawlow *et al.* (1961) and Gebhardt and Maier (1965). Similar considerations apply to the vibrational problem treated here.

The stress Hamiltonian may be written as (Hayes and MacDonald, 1967)

$$\begin{aligned}\mathcal{H}_p = P\{&A(S_{11}+2S_{12}) + B(S_{11}-S_{12}) \\ &\times[(2\xi_1^2-\xi_2^2-\xi_3^2)(2\eta_3^2-\eta_1^2-\eta_2^2)+3(\xi_1^2-\xi_2^2)(\eta_1^2-\eta_2^2)] \\ &+CS_{44}(\xi_1\xi_2\eta_1\eta_2+\xi_2\xi_3\eta_2\eta_3+\xi_3\xi_1\eta_3\eta_1)\},\end{aligned} \tag{5.22}$$

where the light ion has displacement with direction cosines (η_1, η_2, η_3), and the stress P has direction cosines $(\xi_1 \xi_2 \xi_3)$ relative to the crystal axes. The parameters S_{ij} are compliance factors appropriate to the impurity environment. The term A shifts the center of gravity of the T_{1u} states (or in T_d symmetry the T_2 states); this term will also affect the position of the ground state. The degeneracy of the $T_{1u}(T_2)$ states is raised by the terms in B which have tetragonal and orthorhombic symmetry, and by the terms in C which represent a shear. The calculated splittings of the local mode for stress applied along different crystal axes is summarized in Fig. 78.

The measured stress-induced shifts in KCl:H$^-$ for the different stress and polarization directions are shown in Fig. 79(a). From the slopes of these lines, the coupling coefficients in Fig. 78 can be determined. These coupling coefficients are given in Table V.4 for NaF, KCl, KI, and CaF_2.

The measured shifts in KI:H$^-$ are shown in Fig. 79(b). The main band shifts measured in the [100] direction are qualitatively similar in KCl and KI. The dotted curve shows the stress effect on the sideband gap mode shown in Fig. 73(a). From these measurements the symmetry of this mode has been identified as A_{1g}. For the H$^-$ centers of T_d symmetry in CaF_2 the splitting of both the fundamental and second harmonic T_2 modes have been measured. In addition, with the application of a shear strain, Hayes and MacDonald (1967) have observed new transitions which correspond to an admixture of the T_2 states with the infrared inactive A_1 and E levels belong-

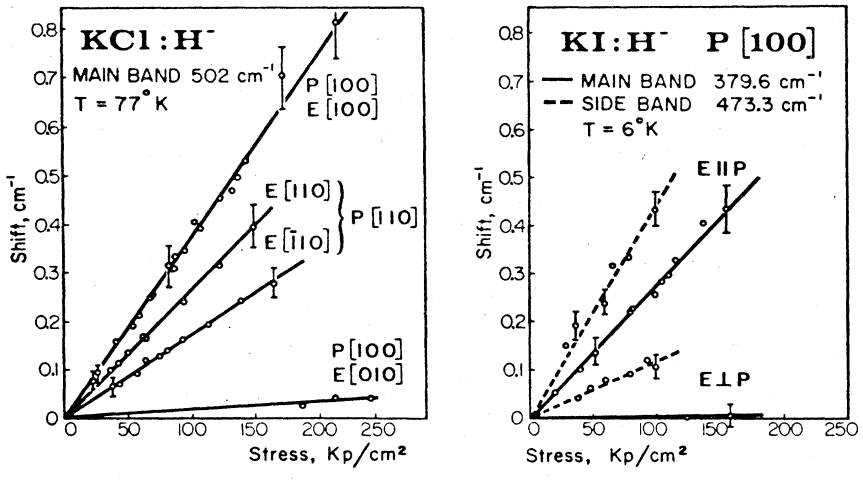

FIG. 79. Splitting of the U-center local mode bands under uniaxial stress. The side band corresponds to the excitation of a gap mode at 93.7 cm^{-1}. After Fritz *et al.* (1968).

ing to $n=2$.

One comparison of the effective anharmonic coupling coefficient, as obtained from thermal measurements, with that determined from applied lattice strain results has been reported. The effective anharmonic coupling coefficient $\bar{A}$ can be obtained directly from the Debye–Waller factor which describes the temperature dependence of the zero lattice phonon peak $I(T)/I(0)$ (5.14). From the measurement of Fritz *et al.* (1968), Alexander *et al.* (1970) find that

$$\bar{A}(\text{thermal}) = 350(\text{cm}^{-1}/\text{unit strain}).$$

From uniaxial stress measurements using bulk elastic compliances they find using (5.15)

$$\bar{A}(\text{stress}) = 150(\text{cm}^{-1}/\text{unit strain}).$$

They conclude that this is reasonable agreement justifying the concepts involved in correlating the two types of measurements.

4. Temperature dependence of the local mode frequency and linewidth

The contribution of anharmonic terms in the potential energy to the broadening and shift of the absorption lines due to localized modes has been discussed widely in the literature (Maradudin, 1966b; Elliott *et al.*, 1965; Klein, 1968; Ivanov, 1966; Bilz, 1966; Kühner and Wagner, 1968; Ipatova, 1968; and Gethins, 1970). To interpret the available data we follow the discussion by Klein.

The various processes contributing to the width and shift can be divided into two types: decomposition processes and scattering processes. Both can be regarded as broadening the absorption line by limiting the lifetime of the excited local mode state, and although this approach to the problem does not give detailed line shapes, etc., it does provide a simple framework for discussing features such as temperature dependence.

In a decomposition process the local mode excited state decays into one or more phonons. One-phonon decay can result from anharmonic terms such as Q^3q, and schematically we can represent these by a transition

$$|1\rangle|n_q\rangle \rightarrow |0\rangle|n_q+1\rangle\,.$$

Conservation of energy requires $\omega_{\text{loc}} = \omega_q$ which cannot occur for a localized mode above the band mode spectrum. Two-phonon decay of the local mode originates from coupling terms such as Qqq'. For these the relaxation rate can be written as (Klein, 1968)

$$\frac{1}{\tau_2} = \sum_{\omega_{\text{loc}}=\omega_q+\omega_{q'}} A(q,q')(1+\bar{n}_q+\bar{n}_{q'}), \tag{5.23}$$

where A is the appropriate coupling coefficient, and $\bar{n}$ denotes the equilibrium value of the phonon occupation number at temperature T. The limiting temperature dependences for two-phonon decay rates are

$$\begin{aligned} &1/\tau_2 \sim \text{const. (low } T\text{)},\\ &1/\tau_2 \sim T \text{ (high } T\text{)}. \end{aligned} \tag{5.24}$$

Similarly, three phonon decays have the limiting temperature dependence

$$\begin{aligned} &1/\tau_3 = \text{const. (low } T\text{)},\\ &1/\tau_3 = T^2 \text{ (high } T\text{)}. \end{aligned} \tag{5.25}$$

Scattering processes were first proposed by Elliott *et al.* (1965). They broaden the absorption line by limiting the lifetime of the over-all excited state of the form $|1\rangle|\ldots n_q \ldots\rangle$. Schematically, the transition involved is of the type

$$|1\rangle|\ldots n_q, n_{q'}, \ldots\rangle \rightarrow |1\rangle|\ldots n_q \pm 1, n_{q'} \mp 1, \ldots\rangle,$$

and can be brought about by anharmonic terms like Q^2q (taken to second order in perturbation theory) or Q^2qq' (taken to first order). In either case these transitions give a relaxation rate (Klein, 1968)

$$\frac{1}{\tau_{\text{sc}}} = \sum_{\omega_q=\omega_{q'}} C(qq')n_q(n_{q'}+1). \tag{5.26}$$

Using a Debye approximation for the phonons, McCumber and Sturge (1963) and McCumber (1964) treated processes like those above to obtain the linewidth

$$\Delta\Gamma_{\text{sc}} = \Gamma(T) - \Gamma(0) = \beta\left(\frac{T}{\theta_c}\right)^7 \int_0^{\theta_c/T} \frac{x^6 e^x}{(e^x-1)^2}\,dx\,, \tag{5.27}$$

where $k\theta_c/\hbar$ is an effective cutoff frequency. This formula exhibits the limiting behavior

$$\begin{aligned} &\Delta\Gamma_{\text{sc}} \sim T^7, \quad T \ll \theta_c \quad \text{(low } T\text{)}\,,\\ &\Delta\Gamma_{\text{sc}} \sim T^2, \quad T \gg \theta_c \quad \text{(high } T\text{)}\,. \end{aligned} \tag{5.28}$$

The scattering process also gives rise to a frequency shift

$$\Delta\omega_{\text{loc}} = \omega_{\text{loc}}(0) - \omega_{\text{loc}}(T) = \delta\left(\frac{T}{\theta_c}\right)^4 \int_0^{\theta_c/T} \frac{x^3\,dx}{(e^x-1)} \tag{5.29}$$

which has the limiting behavior

$$\begin{aligned} &\Delta\omega_{\text{loc}} \sim T^4 \quad \text{(low } T\text{)}\,,\\ &\Delta\omega_{\text{loc}} \sim T \quad \text{(high } T\text{)}\,. \end{aligned} \tag{5.30}$$

In the above expressions, β is positive but δ may be positive or negative.

In addition to the two-phonon process given by (5.29), there will be a frequency shift from the anharmonic terms which give rise to thermal expansion. This contribution can be estimated through the hydrostatic strain coupling coefficient A by

$$\Delta\omega_{\text{ex}} = A[\Delta a/a(0)], \tag{5.31}$$

where $a(0)$ is the low-temperature lattice parameter, and $\Delta a = a(T) - a(0)$.

The temperature dependence of the center frequency and linewidth of many local modes have been measured (Elliott *et al.*, 1965; Fritz *et al.*, 1965). The measurements by Dötsch (1969) on LiF and NaF illustrate the two possible limiting examples. The temperature dependence of the half-width of the local mode of H^- and D^- in these two alkali halides is shown in Fig. 80. The low-temperature half widths are very different for these two materials. Because of the small mass of lithium, the local mode frequency in LiF:H^- is close enough to the maximum frequency of LiF that a two-phonon decay process is possible. That is $\omega_{\text{loc}} < 2\omega_m$. The damping is found to be very large and the half width can be resolved

easily at low temperatures. In fact two-phonon decay is possible for three out of the four defect-lattice combinations shown in Fig. 80, namely, LiF:H^-, LiF:D^-, and NaF:D^-. From (5.23) one obtains the approximate relation

$$\Gamma_2 \sim ctnh(\hbar\omega_{H^-,D^-}/4kT). \tag{5.32}$$

In Fig. 80(a) the experimental data are given by curve 1 and curve 2. The temperature dependence described by (5.32) is given by curves 3 and 4. Curve 5 is obtained by subtraction and refers to the scattering process (5.27).

For NaF:H^- shown in Fig. 80(b) Dötsch found a three-phonon decay scheme necessary because $\omega_{loc} > 2\omega_m$. The absence of a two-phonon decay contribution explains the smaller half-width of the H^- band. Although the three-phonon decay scheme has the correct limiting temperature dependence (T^2) at high temperature (5.25), the scattering process described by (5.26) is believed to play the dominant role here (Fritz, 1968). In Fig. 80(b), Γ_{sc} (5.27) is fitted to the experimental data points of NaF:H^- with a $\theta_c = 350°K$ (curve 1). From specific heat $\theta_D = 400°K$. It has been observed for most alkali halide crystals that $\theta_c < \theta_D$, presumably because of a preferred coupling of the local mode to long-wavelength acoustic phonons (Bilz *et al.*, 1965). The fit of curve 1 using this reasonable value for θ_c is excellent. Curve 2 shows the two-phonon decay of NaF:D^- according to (5.32).

One-shell model calculation has been made by Gethins (1970) on the temperature-dependent linewidth of U-center local modes in KBr. Gethins calculated the linewidth from parameters adjusted to fit the U-center sidebands in an anharmonic Green's function calculation. The expressions are related to the results of McCumber and Sturge; however, in this calculation the exact phonon density of states is used and there are no adjustable parameters. The linewidth resulting from the calculation is a factor 6 too small in the high-temperature (T^2) region (Shotts, 1973).

The temperature-dependent shift of local mode bands has been observed by several investigators (Elliott *et al.*, 1965; Fritz *et al.*, 1965; Dötsch, 1969). It is usually observed to be linear at temperatures near room temperature, as would be suggested by (5.31) rather than (5.29). Figure 81 indicates that the situation is not simple. Both increases as well as decreases in the mode frequency are observed when the temperature is lowered. Even a reversal of sign can take place, as shown in Fig. 81. Presumably scattering contributions such as (5.29) as well as thermal lattice expansion play a role here.

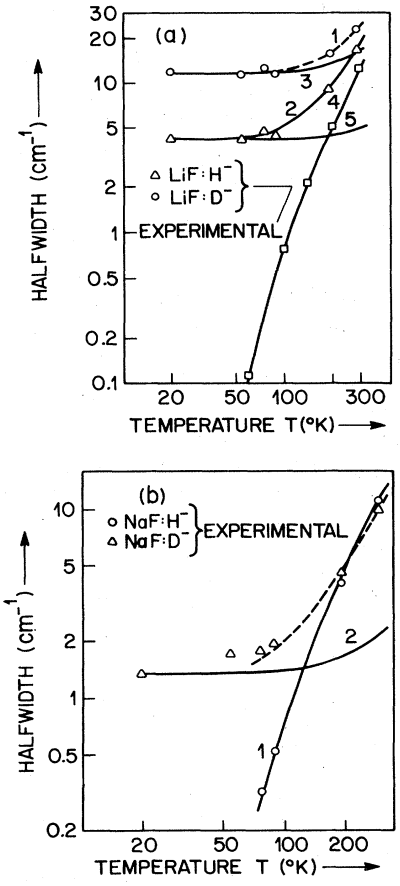

FIG. 80. (a) The temperature dependence of the half widths of LiF:H^- and LiF:D^-. Curves 3, 4, 5 are theoretical fits. (b) The temperature dependence of the half widths of NaF:H^- and NaF:D^-. Curves 1, 2 are theoretical fits. After Dötsch (1969).

D. Pair modes

In a number of alkali halides, high concentrations (~1 mole %) of impurities have been found to result in

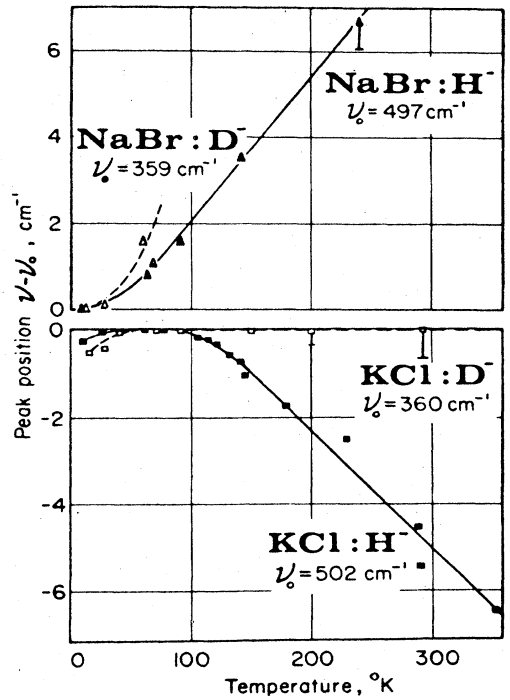

FIG. 81. Temperature-dependent shift of local mode peaks. After Fritz (1968).

vibrational modes involving pairs of impurity ions. The first such mode discovered (de Souza *et al.*, 1970; de Souza and Lüty, 1973) was due to pairs of U centers (H^- and D^- ions) in KCl and resulted in three infrared-active modes near the single U-center line at ~500 cm^{-1}. The pairs are oriented along the [110] crystal direction. The frequencies and strengths of these and all the other pair modes discovered to date are presented in Table V.1.

For a model of the U-center pairs, de Souza and Luty proposed two harmonic oscillators, coupled to the rigid lattice by the same "springs" that act on the single U-center. The two ions are coupled to each other by a spring whose three parameters are fitted from the three pair mode frequencies. The frequencies of the D^-D^- and some of the H^-D^- pair modes predicted by the model are in good agreement with observed values.

E. Gap modes from monatomic impurities

1. Gap mode measurements

Our review of local modes in ionic crystals has demonstrated that (with a few exceptions, which are listed in Table V.1) the defect must consist of an H^- or D^- ion in order to produce an infrared-active localized mode at frequencies that are larger than the maximum frequency ω_m of the host lattice. In contrast with this situation, lower-frequency localized modes have been observed for a variety of impurities at frequencies corresponding to the gap region between optic and acoustic phonon branches (gap modes). Only five alkali halide crystals have such a gap, LiCl, NaBr, NaI, KBr, and KI. Gap modes have been observed in all but LiCl. Some of the early work has been described in the reviews listed at the beginning of Sec. V. In addition measurements on gap modes up through 1966 have been reviewed by Hadni (1967), Sievers (1968, 1969), and Genzel (1969). The experimental results on gap modes are brought up to date in Table V.5.

One of the first observations of a gap mode was made by measuring the electronic emission spectrum associated with rare earth ions in alkali halide host lattices (Wagner and Bron, 1965). The emission spectra of Eu^{2+} and Yb^{2+} consist of broad bands which arise from transitions of the type $4f^n \rightleftarrows 4f^{n-1}5d$. Many of these broad bands show a long series of sharp vibronic lines when measured near liquid helium temperatures. One such spectrum is shown in Fig. 82. The important vibrational frequencies are obtained from the interval between successive lines of the vibronic series. For this particular example the frequency is 79 cm^{-1}. The gap in KI extends from 69.7 to 96.5 cm^{-1} so the important lattice vibration is a gap mode. Wagner and Bron have concluded the following: (1) The rare earth vacancy impurity has C_{2v} symmetry, (2) the electronic transitions can be coupled only to normal modes of A_1 symmetry, (3) the local lattice is strongly distorted, and (4) a strong electron–lattice coupling is present. These measurements first illustrated that it is possible to measure gap modes even when they do not have an electric dipole moment or when their frequency does not occur in a transparent region of the host crystal.

Gap modes have also been observed by measuring vibrational sideband spectra. For monatomic impurities, gap modes have been discovered in this way in $KI:H^-$ (Fritz *et al.*, 1965; Timusk and Klein, 1968; and MacPherson and Timusk, 1970), in $KBr:H_i^-$ (Dürr and Bäuerle, 1970) and in $KI:H_i^-$ (Bäuerle and Fritz, 1968). The sideband spectrum for $KI:H^-$ is shown in Fig. 73(a) with the gap mode at 93 cm^{-1}. Note that the sideband spectra obey the Raman selection rules. This means that a symmetric or even symmetry gap mode couples strongly to the impurity to create a sideband. Uniaxial stress measurements on this gap mode by Fritz *et al.* (1968), shown in Fig. 79, indicate that this mode belongs to the A_{1g} irreducible representation of the O_h symmetry group. This result has been confirmed by Raman scattering measurements by Montgomery *et al.* (1972). Their experimental results are shown in Fig. 83. In order to determine the presence or absence of the A_{1g} gap mode, one needs to subtract the two-phonon scattering from the host lattice. The difference spectrum shows a distinct peak near 95 cm^{-1}.

Most gap modes have been discovered by absorption spectroscopic techniques with the sample at low temperatures, as indicated in Table V.5. The reason for this is that although the host ionic crystal is opaque for frequencies less than the transverse optic mode at room temperature, the crystal becomes remarkably transparent as the temperature is decreased. This is just the well-known "freezing out" of the two-phonon absorption which usually dominates the spectral region near the gap.

2. Gap mode isotope effects

The most complete experimental investigation of infrared-active gap modes has been on the systems $KI:Cl^-$ (Sievers, 1965; Sievers *et al.*, 1965; Nolt *et al.*, 1967, Shotts and Sievers, 1974) and $KI:e^-$ (Bäuerle and Fritz, 1968; Bäuerle and Hübner, 1970). The Cl^- gap mode in nominally pure KI was observed at about 77 cm^{-1}, as shown in Table V.5. As the sample temperature is increased to 15°K the sharp doublet does not change appreciably except to appear on a broad background absorption. This background absorption becomes strong enough by 15°K to dominate the absorption in this frequency region. It results from two-phonon difference band absorption described in the previous section.

Sievers *et al.* (1965) treated the substitutional Cl^- impurity as a mass defect and calculated the gap mode for potassium iodide. The calculation of the eigenfrequencies and eigenvectors of the perfect lattice was based on Karo and Hardy's deformation dipole model (1963) of ionic crystals, which gave an incorrect gap for KI according to later inelastic neutron scattering data (Dolling *et al.*, 1966). Later a high-resolution study by Nolt *et al.* (1967) showed that the local mode was really a doublet due to the two stable chlorine isotopes, ^{35}Cl and ^{37}Cl. A high-resolution study by Shotts and Sievers (1974) of this frequency region is shown in Fig. 84. The points are the experimental data and the solid curve represents the superposition of three Lorentzian line shapes. The isotope shift is 0.33 cm^{-1}. These three lines have been explained by a model first described by Benedek (1970), which includes the splittings resulting

TABLE V.5. Gap modes in alkali halide crystals.

Crystal	Mode frequency (cm^{-1}) (Irreducible representation, Temp. °K)	Defect symmetry, Method of observation,[a] References,[b] Comments
e^- (substitutional)		
KBr	99.60(T_{1u}, 1.2)	O_h, A, 1, 2
KBr	99.07(–, 1.2)	C_{4v}, A, 1, 2
KBr	98.50(–, 1.2)	D_{4h}, A, 1, 2
KI	82.62(T_{1u}, 1.2)	O_h, A, 1, 2
KI	81.98(–, 1.2)	C_{4v}, A, 1, 2
KI	81.19(–, 1.2)	D_{4h}, A, 1, 2
H^- (substitutional)		
KI	93.7(A_{1g}, 90)	O_h, V, 3, 4, 5; R, 6
Na^+ (pair)		
KI	76.02, 84.14(–, 4.2)	A, 7
Cl^- (substitutional)		
NaI	82.9(T_{1u}, 1.2)	O_h, A, 8, 9
KBr	95(T_{1u}, 4.2)	O_h, A, 10, 20
KI:^{35}Cl	77.10(T_{1u}, 1.2)	O_h, A, 11, 12, 13
KI:^{37}Cl	76.79(T_{1u}, 1.2)	O_h, A, 11, 12, 13
Cl^- (pair)		
KI	27.02, 80.26, 82.84	A, 7
Br^- (substitutional)		
KI:^{79}Br	88.94(T_{1u}, 4.2)	O_h, A, 7
KI:^{81}Br	88.47(T_{1u}, 4.2)	O_h, A, 7
Br^- (pair)		
KI	73.8(–, 4.2)	A, 7
Cs^+ (substitutional)		
KI	83.5(T_{1u}, 1.2)	O_h, A, 11
$A_g{}^+$ (substitutional)		
KI	86.2(T_{1u}, 1.2)	O_h, A, 13
$A_g{}^+$ (?)		
KI	78(–, 1.2)	A, 14
H_i^- (interstitial)		
KBr	98.7(T_2, –)	T_d, A, V, 15
KI	86.7(T_2, –)	T_d, A, V, 16
e^-: Na^+		
KI	80(–, 1.2)	A, 2
Rare earth vacancy		
KI:Eu^{2+}	79(A, 10)	C_{2v}, 5, 17
KI:Yb^{2+}	79(A, 10)	C_{2v}, 5, 17
OH^- (substitutional)		
NaBr	129(–, 7)	C_{4v}, V, 5
KI	86.2, 86.9, 89(–, 6)	C_{4v}, A, 18, 19 — The assignment of these lines has been questioned by Ref. 20.
OD^- (substitutional)		
KI	82.5, 86.2, 88.8, 8, 94.3(–, 6)	C_{4v}, A, 19 — The assignment of these lines has been questioned by Ref. 20.

TABLE V.5. Gap modes in alkali halide crystals. *(Continued)*.

Crystal	Mode frequency (cm^{-1}) (Irreducible representation, Temp. °K)	Defect symmetry, Method of observation,[a] References,[b] Comments
CN^- (substitutional)		
NaBr	110, 123(–, 7)	V, 30, 31
NaI	72, 74, 94(–, 1.2)	A, 21
	93(–, 7)	V, 30, 32
KI	81(–, 4.2)	A, 21, 22, 29
	83(–, 7)	V, 30, 27
NCO^- (substitutional)		
NaBr	117, 123, 127(–, 100)	C_{3v}, V, 30
NaI	91, 105(–, 100)	C_{3v}, V, 23, 30
KBr	97.4, 99.7(–, 100)	C_{3v}, V, 23, 30
KI	77.8, 82.2(–, 100)	C_{3v}, V, 23
	78.8(–, 4.2)	C_{3v}, A, 29
	78,82(–, 100)	C_{3v}, V, 30
BO_2^- (substitutional)		
KI	88(–, 100)	V, 31
N_3^- (substitutional)		
NaBr	124(–, 100)	V, 31
NaI	105(–, 100)	V, 31
KBr	97(–, 100)	V, 31
KI	80(–, 100)	V, 31
NO_2^- (substitutional)		
NaBr	109(E_g, 6)	O_h, R, 28
NaI	84,93(–, 2)	A, 21
KI	71.0(–, 2), 79.7(–, 2)	S, 24; A, 25, 26; V, 27
	76(E_g, 6)	O_h, R, 28
NCS^- (substitutional)		
NaI	89, 101(–, 40)	V, 30
KI	79, 83(–, 40)	V, 30
NO_3^- (substitutional)		
NaBr	105, 113, 128(–, 77)	V, 32
NaI	86(–, 77)	V, 32
KBr	95(–, 77)	V, 32
KI	73.3, 78.4, 88.2(–, 2)	A, 22, 25
	74 89(1, 100)	V, 31
	73 88(–, 77)	V, 32, 27
CO_3^- (substitutional)		
KI	94.1(–, 6)	A, 20

[a] Key: A = absorption, R = Raman, S = electronic sideband, V = vibrational sideband.

[b] The references for Table V.5 are the following:

1. Bäuerle, D., and B. Fritz, 1968, Solid State Commun. **6**, 453; 1968, Phys. Status Solidi **29**, 639.
2. Bäuerle, D., and R. Hübner, 1970, Phys. Rev. B **2**, 4252.
3. Fritz, B., U. Gross, and D. Bäuerle, 1965, Phys. Status Solidi **11**, 231.
4. Timusk, T., and M. V. Klein, 1968, in *Physics of Color Centers*, edited by W. B. Fowler (Academic, New York), p. 521.
5. MacPherson, R. W., and T. Timusk, 1970, Can. J. Phys. **48**, 2176.
6. Montgomery, G. P., W. R. Fenner, and M. V. Klein, 1972, Phys. Rev. B **5**, 3343.
7. Ward, R. W., and B. P. Clayman, 1974, Phys. Rev. B **9**, 4455.
8. Hadni, A., G. Morlot, and R. Casarotto, 1967, Compt. Rend. **265**, B767.
9. Timusk, T., and R. W. Ward, 1969, Phys. Rev. Lett. **22**, 396.
10. Nolt, I. G., R. A. Westwig, R. W. Alexander, and A. J. Sievers, 1967, Phys. Rev. **157**, 730.
11. Sievers, A. J., 1965, in *Low Temperature Physics*, edited by J. G. Daunt, D. O. Edwards, F. J. Milford, and M. Yagub (Plenum, New York) LT9, Pt. B, p. 1170.
12. Sievers, A. J., A. A. Maradudin, and S. S. Jaswal, 1965, Phys. Rev. **138**, A272.

TABLE V.5. Gap modes in alkali halide crystals. *(Continued)*.

13. Kirby, R. D., 1971, Phys. Rev. Lett. **26**, 512.
14. Kirby, R. D., I. G. Nolt, R. W. Alexander, and A. J. Sievers, 1968, Phys. Rev. **168**, 1057.
15. Dürr, U., and D. Bäuerle, 1970, Z. Phys. **233**, 94.
16. Bäuerle, D., and B. Fritz, 1968, Phys. Status Solidi **29**, 639.
17. Wagner, M., and W. Bron, 1965, Phys. Rev. A **139**, 223.
18. Renk, K. F., 1967, Z. Phys. **201**, 445.
19. Grisar, R. G. J., K. P. Reiners, K. F. Renk, and L. Genzel, 1967, Phys. Status Solidi **23**, 613.
20. Becker, C. R., 1970, Solid State Commun. **8**, 337.
21. Lytle, C. D., 1965, M. S. Thesis, Cornell University, Materials Science Center Rt MSC No. 390.
22. Sievers, A. J., 1969, in *Elementary Excitations in Solids*, edited by G. Nardelli and A. A. Maradudin (Plenum, New York), p. 220.
23. Decius, J. C., J. L. Jacobson, W. F. Sherman, and G. R. Wilkinson, 1965, J. Chem. Phys. **43**, 2180.
24. Timusk, T., and W. Staude, 1964, Phys. Rev. Lett. **13**, 373.
25. Sievers, A. J., and C. D. Lytle, 1965, Phys. Lett. **14**, 271.
26. Renk, K. F., 1965, Phys. Lett. **14**, 281.
27. Narayanamurti, V., W. D. Seward, and R. O. Pohl, 1966, Phys. Rev. **148**, 481.
28. Evans, A. R., and D. B. Fitchen, 1970, Phys. Rev. B **2**, 1074.
29. Shotts, W. J., 1973, Ph.D. Thesis, Cornell University.
30. Cundill, M. A., and W. F. Sherman, 1968, Phys. Rev. **168**, 1014.
31. Cundill, M. A., and W. F. Sherman, 1966, Phys. Rev. Lett. **13**, 570.
32. Metselaar, R., and J. Van Der Elsken, 1968, Phys. Rev. **165**, 359.

from both the Cl^- isotopes and the K^+ nearest-neighbor isotopes.

Nolt *et al.* (1967) tried to compare the experimental results for the isotope shift with the predictions of the simple lattice model described by Mitani and Takeno (1965) [see (5.2) and (5.3)]. They calculated the frequencies of the gap modes for a lattice system consisting of a point defect with mass and nearest-neighbor force constants taken to be different from those of the host lattice. Long-range interaction forces which introduce coupling between the components of motion, as well as polarizability effects and lattice distortions, are not considered in this model. With the lattice coupling confined to nearest neighbors only and with central and noncentral force constants set equal to each other, a solution for the eigenfrequency of the infrared-active gap mode is found using (5.3). Only a knowledge of the frequencies at the top and bottom of the gap are required to determine the form of $g_0((\omega/\omega_1)^2)$ in this region. The impurity mode frequency of 77 cm^{-1} is reproduced with (5.3) if the impurity nearest-neighbor force constant is 38% of the host lattice force constant. The internal consistency of this fit can be tested from the isotope shift data. The shift in frequency associated with the chlorine mass change and the force constant given above is 1.74 cm^{-1} compared to the measured value of 0.33 cm^{-1}. This lack of agreement is disappointing. One must conclude that the isotope shift data is a sensitive probe of the lattice defect system, hence the lattice defect model. The simple chain model (Fig. 13) showed that gap modes are not well localized, reinforcing the implication that more than nearest neighbors must be included in a good model of the defect.

The more rigorous calculations of Benedek and Maradudin (1968) support the above conclusion. They used a refined model of the impurity ion which takes into account the mass difference, the change in nearest-neighbor central forces, and also the change in nearest-neighbor noncentral forces. They also use more reliable models for the dynamical properties of the host crystal,

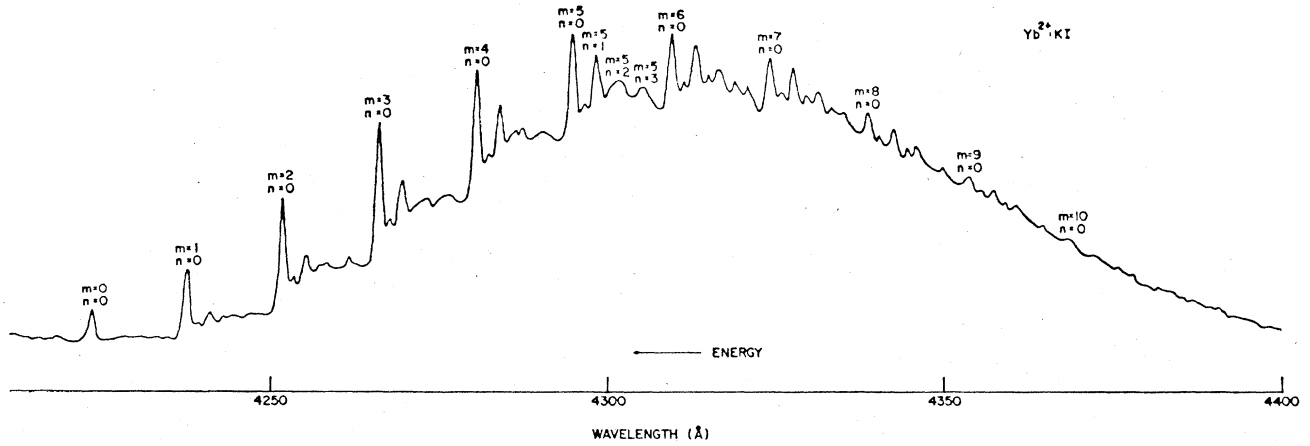

FIG. 82. Major and minor vibronic intervals observed on the lowest energy emission band of $KI:Yb^{2+}$ at 10 °K. The gap mode frequency of 79 cm^{-1} is obtained from the interval between successive lines of the vibronic series. After Wagner and Bron (1965).

such as Cowley's shell model III (Cowley *et al.*, 1963) and the deformation dipole model of Karo and Hardy (1963), but with the position and width of the gap adjusted to fit the inelastic neutron data. They found that neither the deformation dipole nor the shell model calculations can correctly predict the experimental isotope shift with only nearest-neighbor force constant changes. From the calculations Benedek and Maradudin conclude that the position of the gap mode must be very sensitive to the range of the perturbation in the host crystal. Because of elastic relaxation around the defect, force constant changes should be included for other than nearest neighbors. In addition anharmonicity of the interionic forces is expected to contribute a small shift to the frequencies of gap modes calculated in the harmonic approximation, and to make a small contribution to the isotope shift. Benedek and Maradudin do not estimate the magnitude of this latter effect.

More recently Bäuerle and Hübner (1970) have shown that the gap mode frequency and isotope shift for Cl^- can be fit with a model similar to that used by Gethins *et al.* (1967), where changes in both nearest-neighbor and fourth-nearest-neighbor force constants are allowed. (This model has been described in connection with the U-center local mode and is shown in Fig. 74.) Unfortunately, the calculation represents a two-parameter fit to only two separate pieces of experimental data. This comparison does not yet test the accuracy of the model.

Gap modes associated with F centers (an anion vacancy occupied by an electron) in KBr and KI give complementary information to that obtained for the KI:Cl^- gap modes, in that isotope shifts associated with a mass change in the host lattice can be resolved. The physical characteristics of the eigenvector associated with this mode have been described by Bäuerle and Fritz (1968) in their original paper. As the impurity mass is decreased with respect to the heavy host mass in the crystal, the gap mode frequency increases but approaches a finite value (Fig. 14) for the limiting case of vanishing impurity mass (i.e., e^- center). The displacements are such that the nearest neighbors of the e^- center move with the same amplitude while the fourth-nearest neighbors to the defect move with somewhat reduced amplitude and with the opposite phase (compare mode 24, Fig. 15). The displacements are not localized at the defect center itself, as in the case of the localized mode. It is worth noting that the corresponding gap mode for the H^- ion has been searched for but apparently does not exist (Sievers, 1968).

Benedek and Mulazzi (1969) have calculated this F center gap mode absorption using Hardy's deformation dipole models for the lattice phonons. When they allowed an inward elastic relaxation of the neighbors they were able to fit the measured frequency given in Table V.5.

Recent measurements by Bäuerle and Hübner (1970) on the isotope shifts associated with host lattice mass changes provide more experimental data with which lattice models can be tested. Their experimental measurements on the F-center gap mode in KI is shown in Fig. 85. Lines A, B, and C are associated with the F center. The lower-frequency line at 80 cm^{-1} is probably due to a perturbation of the F center by Na^+ ions (F_A centers). The ratio of the integrated absorptions of the three lines is

$$I_A : I_B : I_C \rightarrow 193:28:1 \text{ (expt)}.$$

Similar results have been obtained for F centers in KBr. The frequencies and relative intensities of the individual peaks of the F-center gap mode can be explained by the presence of two isotopes in the host crystal, ^{39}K and ^{41}K, which have a natural abundance ratio $^{39}K:^{41}K = 93:7$.

The usual gap mode is associated with O_h symmetry for all nearest neighbors consisting of ^{39}K. Replacements of ^{39}K by ^{41}K on one or two of the six nearest-neighbor sites will reduce the gap mode symmetry to C_{4v}, D_{4v}, or C_{2v}. Within the model used, two ^{41}K atoms along the direction of vibration give the strongest perturbation to the mode and reduce its frequency below the

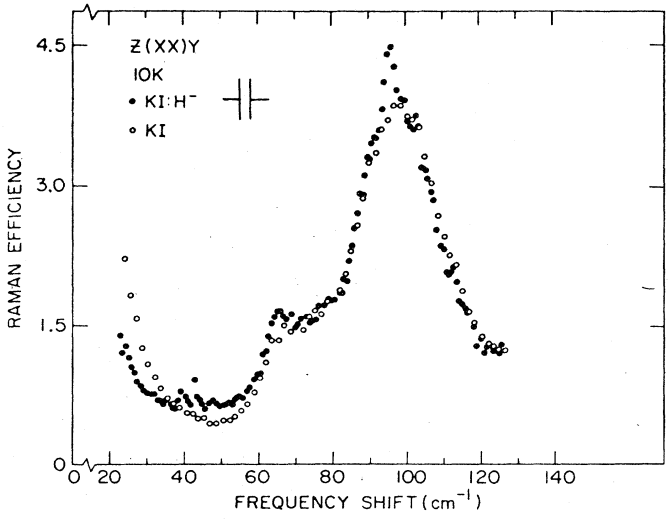

FIG. 83. Raman spectra of KI:H^- and pure KI at low frequency. The large band between 80 and 120 cm^{-1} is due to the two-phonon scattering from the host crystal. Note the localized A_{1g} gap mode at 95 cm^{-1} in the doped sample. After Montgomery *et al.* (1972).

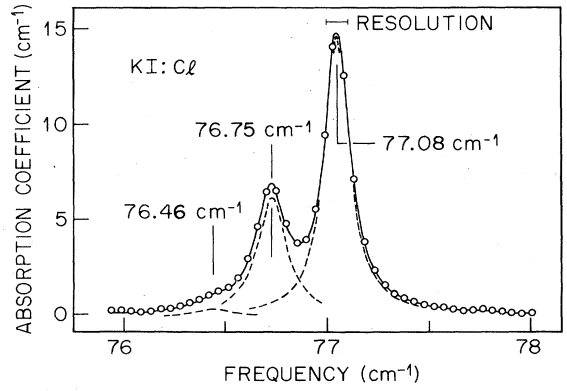

FIG. 84. High-resolution trace of the gap mode absorption in KI:Cl^- between 76 and 78 cm^{-1}. The dots are the experimental data and the solid curve represents the superposition of three Lorentzian line shapes. The sample is at 4.2 °K. After Shotts and Sievers (1974).

A mode position. One ^{41}K atom along the direction of vibration reduces the frequency somewhat less.

The relative intensities are obtained by noting that the probability of n F centers having i ^{41}K nearest-neighbor ions can be written as

$$b(i)=\sum_n P_i(n). \tag{5.33}$$

For the natural abundance ratio of ^{39}K:^{41}K Bäuerle and Hübner evaluate the probabilities P_i in (5.33) and obtain $b(0)=65.5\%$; $b(1)=27.7\%$; and $b(2)=5.9\%$.

In order to compare the relative frequencies of these three configurations with the relative intensities of the measured lines, the polarization and the degree of degeneracy in the modes must be taken into account. The relative intensities for the three modes which correspond to the various O_h symmetry-breaking perturbations are

$$\begin{aligned} A &= 2b(0)+\tfrac{4}{3}b(1)+\tfrac{12}{15}b(2),\\ B &= \tfrac{2}{3}b(1)+\tfrac{16}{15}b(2),\\ C &= \tfrac{2}{15}b(2). \end{aligned} \tag{5.34}$$

Inserting the values for $b(i)$ yields

$$I_A:I_B:I_C=210:30:1 \text{ (theory)}$$

in good agreement with the measured ratios.

Bäuerle and Hübner have also fitted the gap mode frequency by using the breathing shell model (Schroder, 1966) to describe the host lattice eigenvectors and eigenvalues. They find that the positions of the gap mode depend strongly on the change in the force constant between first-nearest neighbors and fourth-nearest neighbors. For any fixed value of the nearest-neighbor force constant, the gap mode frequencies can be shifted over the total gap region by a variation of the fourth-nearest-neighbor force constant within reasonable limits. This once again indicates that a realistic model for the description of defects can not be restricted in real space. A large region around the center will be perturbed by the relaxation of the surrounding lattice. This is apparently true not only for the soft F center and H^- center but also for Cl^- ions in potassium iodide. The gap mode with its somewhat extended eigenvector is a more sensitive probe of these perturbations than a high-frequency localized mode.

3. Anharmonic coupling of gap modes to the lattice

No significant measurements on the temperature dependence of the infrared-active gap modes have yet been made. The reason is not a lack of interest but rather

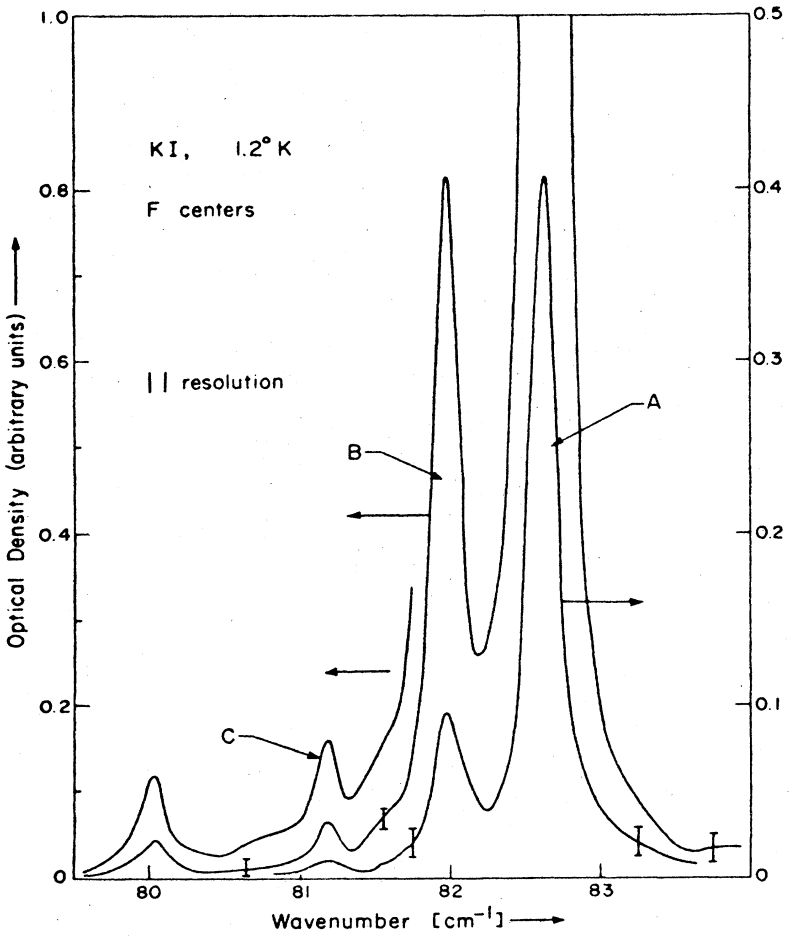

FIG. 85. The F-center gap mode absorption spectrum in KI. The positions of the lines are given in Table V.5. The resolution is 0.1 cm^{-1}. After Bäuerle and Hübner (1970).

TABLE V.6. Anharmonic coupling coefficients for gap modes with O_h symmetry in potassium iodide.

Impurity	A (cm^{-1}/unit strain)	B (cm^{-1}/unit strain)	C (cm^{-1}/unit strain)	Reference [a]
e^-	125±40	35±15	···	1
Cl^-	110±25	···	···	2
Ag^+	220±50	···	···	2

[a] The references for Table V.6 are the following:
1. Bäuerle, D., and R. Hübner, 1970, Phys. Rev. B 2, 4252. (Used local compliances.)
2. Patterson, M., 1973, M. S. Thesis, Cornell University; Materials Science Center R. MSC Number 2016. (Used compliances of the bulk crystal.)

that the temperature-dependent absorption coefficient associated with the background "difference" processes of the host lattice rapidly masks the impurity-induced absorption in the gap region above about 15°K, as mentioned earlier.

A few measurements of the hydrostatic coupling coefficient of the gap mode to the lattice (5.19) have been reported (Patterson, 1973) and one uniaxial strain measurement has been made on the F-center gap mode (Bäuerle and Hübner, 1970). The measured parameters are recorded in Table V.6. A comparison of the coupling coefficients for gap modes (Table V.6) and for local modes (Table V.4) indicates that the local modes are coupled much more strongly (~5×) to the lattice than are the gap modes. In fact, the gap modes have roughly the same size coupling coefficient as does the transverse optic mode for the pure crystal. For potassium halides, Postmus *et al.* (1968) find that the hydrostatic coupling coefficient for the $q=0$ transverse optic modes is

$$A(TO) \sim 110 \text{ (cm}^{-1}\text{/unit strain)}$$

in reasonable accord with the gap mode values listed in Table V.6.

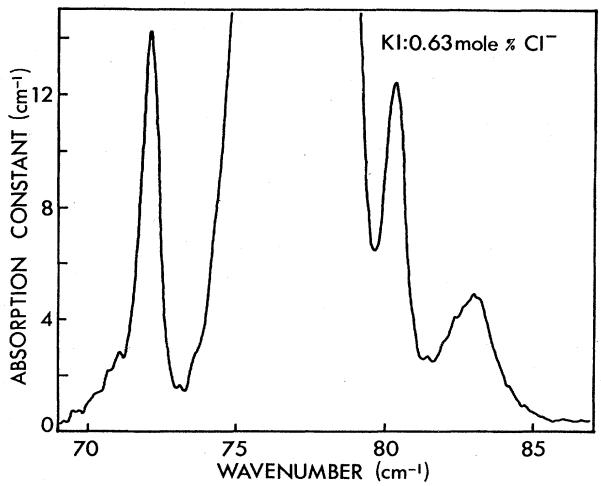

FIG. 86. Cl^--induced gap modes in KI at 4.2 °K. The mode at 77 cm^{-1}, which peaks off-scale, is a doublet due to isolated ^{37}Cl and ^{35}Cl impurities. The three modes shown are pair modes. The instrumented resolution is 0.21 cm^{-1}. After Ward and Clayman (1974a).

4. Pair modes in the gap

Recently, several infrared-active pair modes have been discovered (Ward and Clayman, 1974a) in the gap region of KI (70–96 cm^{-1}). Three lines are due to Cl^-, two due to Na^+, and one due to Br^-; all have strengths proportional to the impurity concentrations squared. The frequencies are given in Table V.5. The absorption constant versus frequency for KI heavily doped with Cl^- (0.63 mole %) is shown in Fig. 86. Three pair modes are observed. To analyze the KCl:Na^+ pair Jaswal (1972) has taken a molecular model consisting of the two Na^+ ions and their 15 nearest neighbors, vibrating in an otherwise rigid lattice. The reduction in force constant required to fit the mode frequency was in fair agreement with the results of a first-principles calculation by Templeton (1973) of the lattice relaxation around the Na^+ ions. The molecular model was extended by Ward and Clayman (1974b) to describe successfully the pair modes in KI:Cl^- and KI:Na^+. In both cases, the most likely configuration for the defect has the impurities lying along the [110] direction.

F. Gap modes from molecular impurities

1. Early work

The first studies of polyatomic ions isolated in alkali halide crystals (Maslakowez, 1928; Keteloar *et al.*, 1956; Decius and Maki, 1958; and Price *et al.*, 1960) illustrated that the internal molecular modes were only slightly modified by the matrix. More recent measurements on samples at low temperatures have invariably produced complex spectra. Almost all spectroscopic techniques have been used to advantage on these defect systems.

Timusk and Staude (1964) observed phonon structure in the NO_2^- electronic absorption at 400 mμ wavelength in the alkali halides at 4.2°K. For KI:KNO_2 and NaBr:$NaNO_2$, sharp structure was observed on the high-frequency side of the electronic (or electronic plus molecular vibration) transition with a frequency shift corresponding to the gap region of the host crystals. At about the same time, Narayanamurti (1964) observed temperature-dependent sidebands associated with the near-infrared stretching vibration of CN^- in KCl. The sideband structure indicated that the CN^- molecular motion changed from hindered rotation, to libration, to tunneling as the sample temperature was decreased from

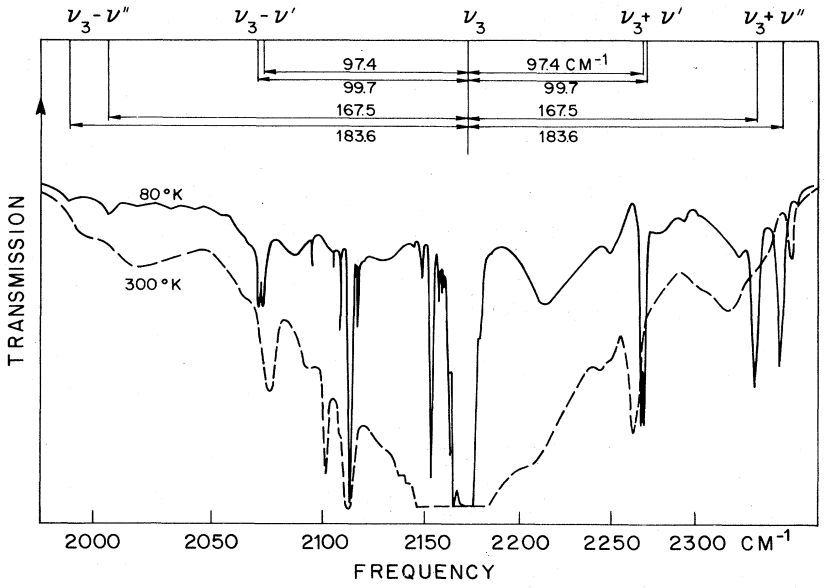

FIG. 87. The infrared spectrum of NCO^- in KBr, showing the gap and localized modes in combination with the internal stretching vibration ν_3. The sharp features on the low-energy side of the main line are due to small traces of the various isotopic species of NCO^- as they occur in natural abundances. After Decius *et al.* (1965).

room temperature. In 1965 Decius *et al.* identified gap modes by observing the sidebands associated with the near-infrared stretching mode of NCO^- in KBr and KI. The absorption curve for NCO^- isolated in KBr is shown in Fig. 87. The sharp features about 20 cm^{-1} to the low-energy side of the main ν_3 absorption line are due to small traces of the various isotopic species of NCO^- as they occur in natural abundance. The lines near ±98 cm^{-1} are due to gap modes, while the lines near ±170 cm^{-1} are due to local modes. Sharp absorption lines in KI:NO_2^- were observed directly in the far-infrared by Sievers and Lytle (1965) and by Renk (1965). These absorption lines were tentatively identified as gap modes.

One unanswered question associated with all of this early work was to what extent could one distinguish between librational motion of the molecule and the localized mode motion of the molecule and its neighbors. If such a distinction could be made, then to what extent would a specific assignment for one molecular lattice combination apply to the same molecule in a different lattice? Recent studies have had to face this problem; we review here mainly this later work.

2. CN^- gap modes

The CN^- molecule has been studied in a number of alkali halide host lattices by Seward and Narayanamurti (1966). They used near-infrared spectroscopy, thermal conductivity, and specific heat measurements to obtain a detailed picture of the motion associated with this molecular ion. Figure 88 shows some infrared results. They found that most of features observed with CN^- in alkali halides can be explained with the cosine potential for angular motion first used by Pauling (1930).

$$V = (V_0/2)(1 - \cos 2\theta). \tag{5.35}$$

The Schrödinger equation for this potential is known as Mathieu's equation and can be solved exactly. When $kT \ll V_0$ the molecules occupy energy states below the top of the barrier. (Here $V_0 \sim 25$ cm^{-1}.) In the harmonic approximation these librational energy levels correspond to those of a harmonic oscillator.

The selection rules for the degenerate librator have been worked out by Hexter and Dows (1956). They showed that in the near-infrared vibrational spectrum the strongest transitions involve no changes in the librational quantum number, i.e., they arise from the

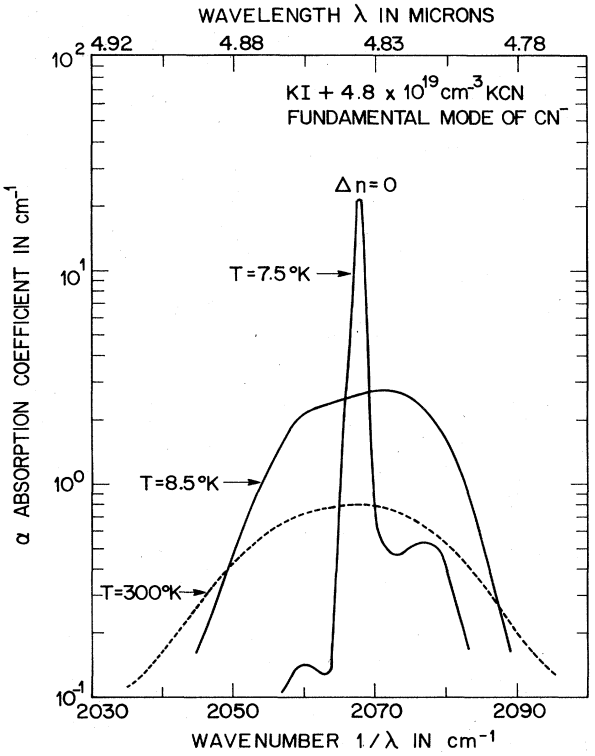

FIG. 88. Absorption spectra of KI:CN^- near the fundamental stretching vibration. CN^- concentration is 4.8×10^{19} cm^{-3}. After Seward and Narayanamurti (1966).

transition $\Delta n = 0$ which is called the Q branch. Because of anharmonicity, weaker transitions $\Delta n = \pm 1, \pm 2, \ldots$, etc. are allowed. The $\Delta n = \pm 1$ transitions are clearly seen in Fig. 88 as weak sidebands on the $\Delta n = 0$ peak in the low-temperature vibrational spectrum.

The eigenstates of (5.35) with energies large compared to V_0 correspond closely to those known for free molecules. The free rotor energy levels are given by

$$\hbar\omega_j = BJ(J+1),$$

where J is the rotational quantum number. Each level is $(2J+1)$-fold degenerate. The selection rules for the vibrating rotor are $\Delta J = \pm 1$. The transitions with $\Delta J = +1$ and $\Delta J = -1$ give rise to the R and P branches, respectively, while the transitions with $\Delta J = 0$ (the Q branch) are now forbidden (see also Sec. VII, Fig. 131).

The results of the above simple theory may be briefly summarized as follows: at low temperatures ($kT \ll V_0$), the near-infrared spectrum should consist of a strong Q branch with weak satellites separated from the fundamental by multiples of the librational frequency. At high temperatures ($kT \gg V_0$), the spectrum should approximate that known for free molecules, i.e., it should consist of P and R branches with a missing central Q branch.

Figure 88 shows this evolution as a function of temperature. Below about 20°K the motion of the molecule can best be described as librational. Between 20 and 85°K the molecule performs hindered rotational motion, i.e., in this temperature range a significant number of molecules occupy energy states both above and below the barrier. Seward and Narayanamurti point out that clear P and R maxima are to be expected in KI at high temperature because the cavity at the missing I^- ion is large and hence the barrier to rotation should be low. At high temperatures the rotational P, Q, and R branches for the C–N stretching band in KI:CN^- merge to form a single broad band in Fig. 88. This is analogous to what is observed in liquids and is caused by rotational diffusion. The rotating vibrator makes a collision before it turns more than a radian or so. This prevents the rotational branches from developing. The role of intermolecular rotational collisions in a liquid is presumably played in KI:CN^- by phonon emission or absorption processes that change the rotational state of the CN^-. Klein and co-workers have drawn this analogy in their Raman work on NaCl:OH^- (Peascoe and Klein, 1973) and on KCl:OH^- and KBr:OH^- (Peascoe *et al.*, 1974). Among theoretical discussions of the liquid case are papers by Kivelson and Keyes (1972) and Bratoz *et al.* (1970).

At low temperatures Seward and Narayanamurti note a sharp sideband absorption at 83 cm^{-1} from the $\Delta n = 0$ transition. They conclude that this line is caused by either of the following two mechanisms: (1) Since the CN^- ion possesses symmetry $C_{\infty v}$ two translational gap modes of symmetry A_1 and E_1 should be allowed. The absence of a second gap mode from the observed spectrum might be explained through rapid reorientational motion of the CN^- ion about its two axes of inertia, which causes it to behave like an ion of spherical symmetry. (2) The center of mass of the ion may not coincide with the center of the large highly polarizable I^- cavity. Translational or librational motion around this off-center position may be responsible for the absorption in the gap region.

In far-infrared absorption measurements on KI:CN^- Lytle and Sievers (1965) observed a strong absorption at 81 cm^{-1}. A high-resolution trace of this impurity-induced absorption taken by Shotts (1973) is shown in Fig. 89. The broad absorption at 81 cm^{-1} is due to CN^-, the sharp absorption line at 78.8 is due to substitutional NCO^- (see Table V.5). The linewidth for CN^- is about 10 times that of Cl^- (Fig. 5-17) or NCO^-. Evidently the gap mode widths for CN^- and NCO^- are governed by different couplings. We conclude that low-lying motional states of the molecule can show up in the far infrared as a simple broadening of the gap mode.

3. NCO^- gap modes

The near-infrared spectra from NCO^- molecules in many alkali halide crystals have been investigated in some detail by Cundill and Sherman (1968). The measured frequencies of gap modes are given in Table V.5. They have unravelled the eigenvectors of the gap modes discovered by Decius *et al.* (1965) by measuring the frequency shifts associated with isotopic substitution in the molecule. Figure 90 shows schematically the local and gap mode frequency shifts. The ^{12}C to ^{13}C shift in the four bands is found to be very small. Oxygen substitution affects only the lower component of each doublet while nitrogen substitution affects primarily the upper components. Note that cases 1, 2, and 4 in Fig. 90 have identical total mass, which governs the center of mass motion.

The contribution of the defect neighbors to the gap mode and local mode motion has been estimated by first calculating the isotope shift associated with torsional motion of a rigid molecule and then scaling down this value to fit the experimentally measured number. One scaling factor is associated with each of the four bands. These scaling factors are then taken as a measure of the delocalization of the motion. For example, for the 97.4 cm^{-1} band the measured shift is 1/7 of the predicted shift for a strictly localized torsional oscillator, thus 6/7 of the energy of the mode is associated with the mo-

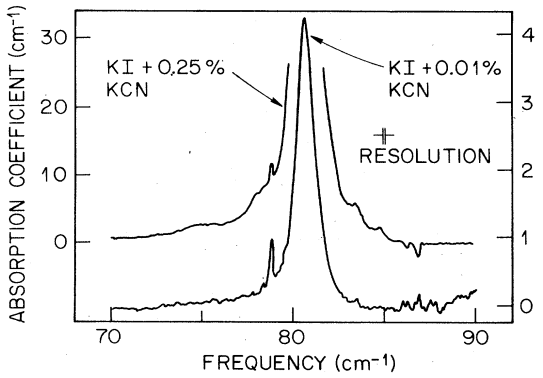

FIG. 89. Far-infrared gap mode for KI:CN^-. The absorption line at 81 cm^{-1} is due to CN^-, and the sharp line at 78.8 is due to NCO^-. Sample at 4.2°K. After Shotts (1973).

tion of the neighbors. For the 183.6 cm^{-1} band only 1/4 of the energy is associated with the neighbors, and so on.

Cundill and Sherman assume that the NCO^- molecule is oriented in a ⟨111⟩ direction as shown in Fig. 91. Their calculations of the force constants operating between the NCO^- and its neighbors when the NCO^- is rotated indicate that the two rings of nearest neighbors play a dominant role. The 97.4 cm^{-1} line is assigned to torsional motion of the NCO^- about an axis perpendicularly dividing the C–N band, accompanied by an in-phase movement of the nearest neighbors (the potassium rings) as shown in Fig. 91. The 99.7 band corresponds to a large nitrogen amplitude, again with nearest neighbors moving in phase. The 167.5 cm^{-1} band is due to a large oxygen amplitude torsional mode, with the nearest neighbors moving out of phase, and the 183.6 cm^{-1} band is due to a large nitrogen amplitude motion. Figure 91 shows schematically the four vibrations which are described above. The dotted lines in the figure represent the planes of nearest- and next-nearest neighbors. Cundill and Sherman have shown that their calculated modes are self-consistent in that they can reproduce the observed delocalization factors while satisfying the requirements of zero net translation and zero net angular momentum.

Cundill and Sherman have not carried out isotope shifts on other alkali halide crystals doped with NCO^-; however, all the crystals with phonon gaps show similar sideband spectra. They conclude that this motion is a general feature of the polyatomic impurity ion such as NCO^-, N_3^-, and BO_2^- in alkali halide crystals. The gap modes consist of a librational motion of the polyatomic impurity, with the nearest neighbors participating in the motion. The center of mass of the polyatomic ion does not move.

It is possible to estimate the anharmonic coupling coefficient of the librational gap mode to the lattice from the hydrostatic pressure measurements of Cundill and Sherman (1968). The effects of pressures up to 50 kbars on the sideband structure were measured using a modified Drickamer-type of optical cell at temperatures in the range 90 to 500°K (Drickamer *et al.*, 1957; Sherman, 1966). From their measurements on KBr:NCO^- at 90°K with pressures up to 20 kbars we calculate the hydrostatic coupling coefficient from (5.19) to be $A = 130$ cm^{-1}/unit strain. This coefficient is about the same size as has been determined for gap modes associated with monatomic impurities (Table V.6) and for the transverse optic mode at $q = 0$. It is interesting that the spherical anharmonic lattice coupling coefficient is approximately equal for librational and center of mass type gap modes.

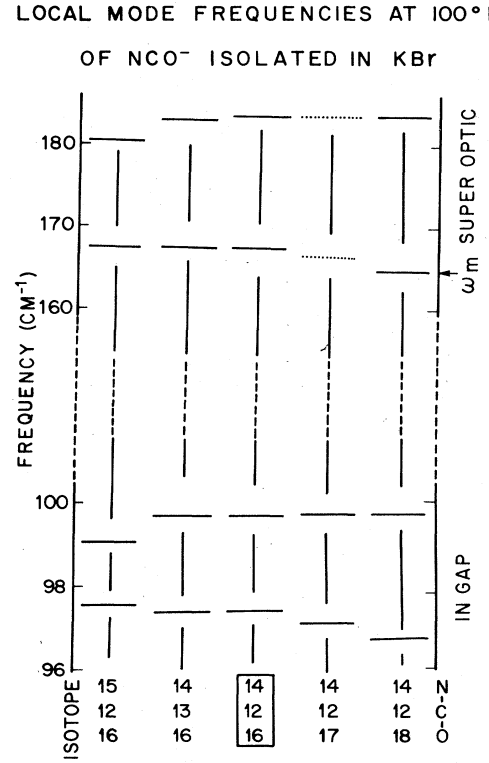

FIG. 90. Local and gap mode frequencies found in combination with ν_3 (NCO^-) isolated in KBr for the various isotopic species. After Cundill and Sherman (1968).

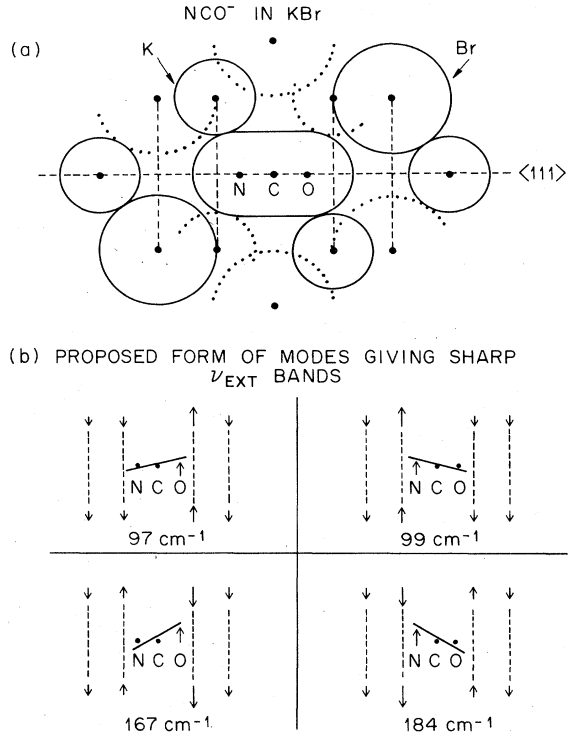

FIG. 91. (a) The KBr environment surrounding an NCO^- impurity. Its axis is oriented in a ⟨111⟩ direction and the schematic representation is drawn to scale using Goldschmidt radii. The small circles represent K^+ ions, the large circles Br^- ions. Ions in the plane of the paper are presented as solid circles; ions out of this plane are shown dotted. Note particularly how the NCO^- is held between two rings of K^+ ions, each composed of one ion in the plane of the paper and two out of this plane. (b) The proposed eigenvectors for the gap and local modes in KBr:NCO^-. The dotted lines represent the planes of nearest and next-nearest neighbors. After Cundill and Sherman (1968).

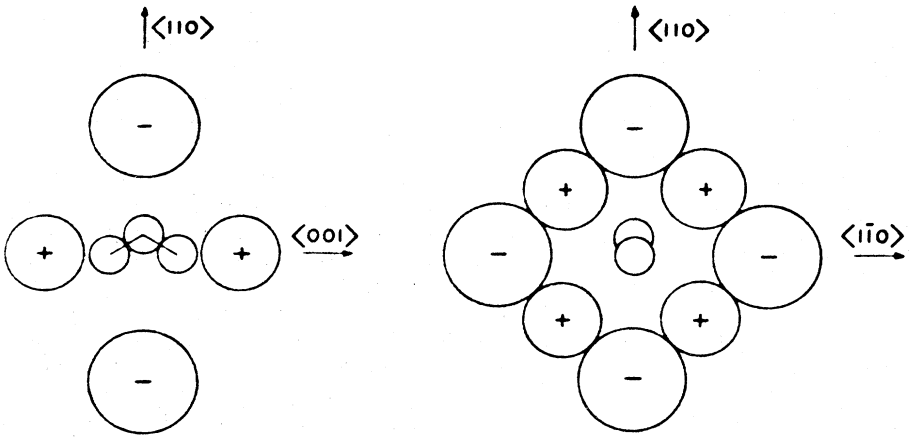

FIG. 92. Probable equilibrium orientation of the nitrite ion at low temperatures in alkali halides. In KI the ion may be in an off-center position displaced towards the halide ion nearest the nitrogen atom. After Evans and Fitchen (1970).

4. NO_2^- gap modes

The nitrate molecule has a bent O–N–O form of C_{2v} symmetry and represents a more complex defect than the linear molecules which we have considered above. In the alkali halide crystal the symmetry axis of the NO_2^- molecule lies in a [110] direction and the molecular plane is a (100) plane as shown in Fig. 92.

Spectral features in the gap of the lattice vibration frequencies of KI have been observed by far-infrared absorption (Lytle and Sievers, 1965; Renk, 1965); as sidebands in the uv (Timusk and Staude, 1964; Avarmaa, 1968; Avarmaa and Rebane, 1969; Evans and Fitchen, 1970); as infrared sidebands (Narayanamurti *et al.*, 1966; Metselaar and Van der Elsken, 1968; Cundill and Sherman, 1968), and in the Raman spectra (Evans and Fitchen, 1970). These features have been attributed variously to translational modes of the NO_2^- ion in its cavity, high-frequency librational modes, or perturbed lattice modes of the host crystal. As Table V.5 indicates, all spectral techniques have identified gap modes of some sort.

Most measurements have been carried out on KI:NO_2^-. The uv absorption shows a gap mode at 70 cm^{-1}; the Raman scattering another mode at 76 cm^{-1}; the near-infrared sideband work shows three modes at 71, 79, and 80.5 cm^{-1}; and the far-infrared two modes at 71 and 79.9. The highest-resolution measurements on KI:NO_2^- have been made in the far infrared by Hughes (1970). His results are shown in Fig. 93. Peak (a) is a gap mode due to NO_2^-; peak (b) NO_3^-; peak (c) unknown; peak (d) Cl^-; peak (e) NO_3^-; peak (f) unknown, possibly an isotope effect or NCO^-; peak (g) NO_2^-; peak (h) unknown, possibly due to F centers; peaks (i) and (j) unknown, possibly

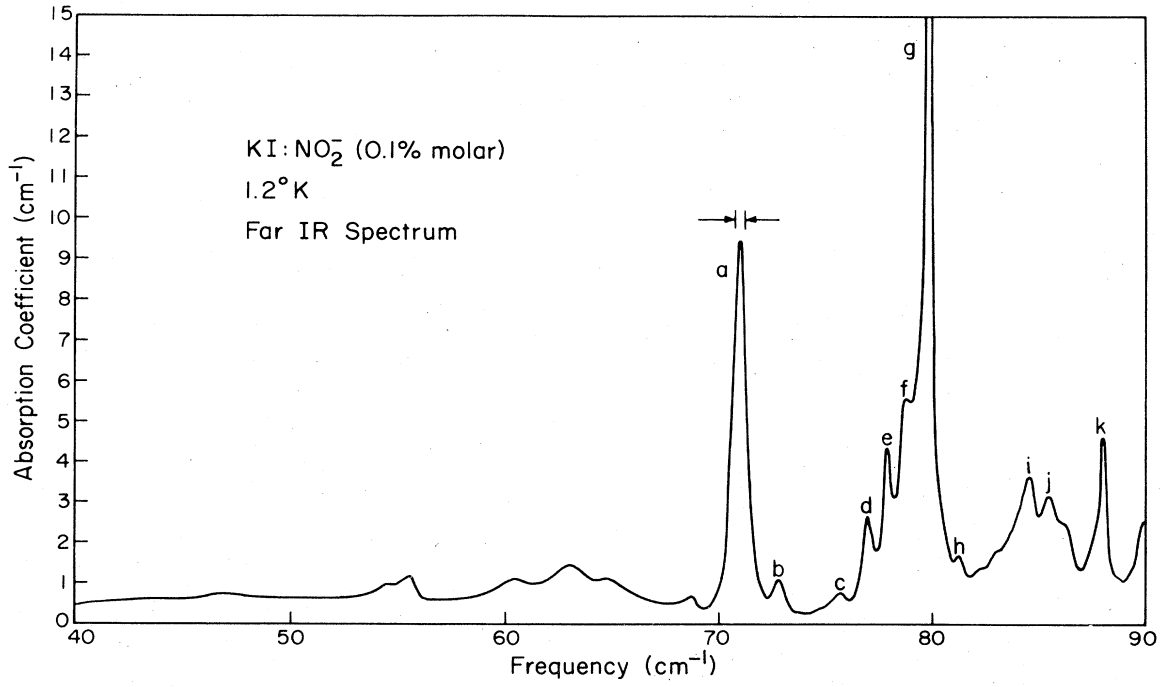

FIG. 93. Far-infrared spectrum of KI:NO_2^- at 1.2 °K. After Hughes (1970).

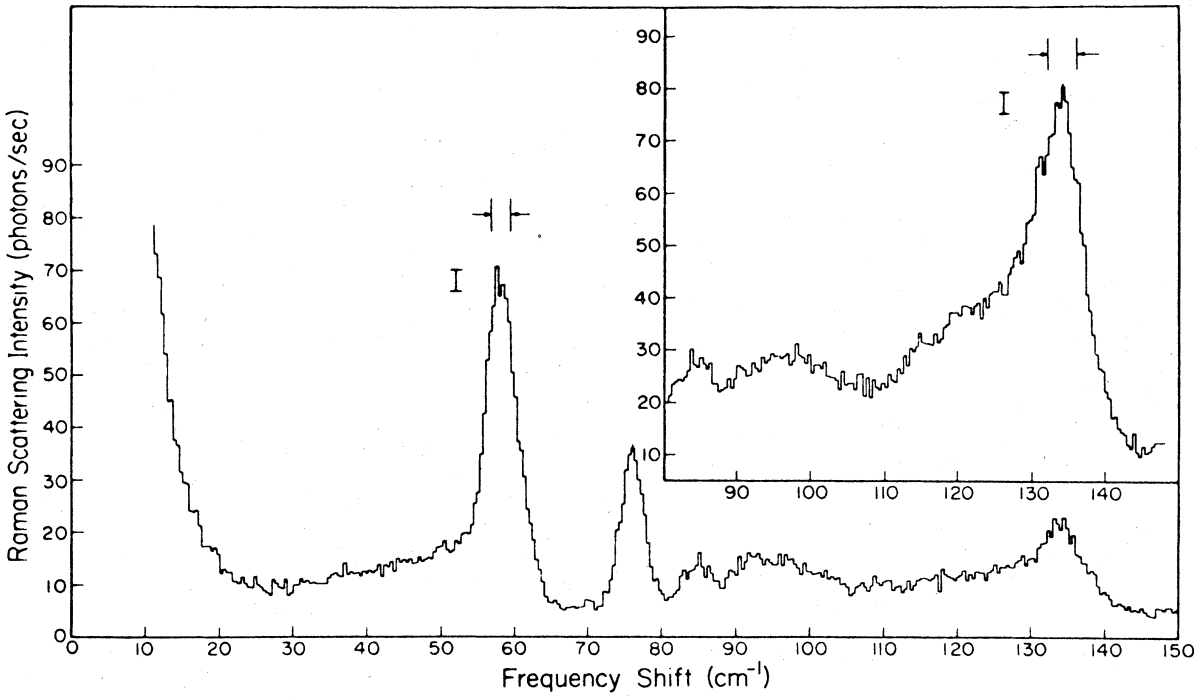

FIG. 94. Unpolarized Raman spectrum of KI:NO_2^- at 6 °K. Insert shows part of the spectrum at higher sensitivity. After Evans and Fitchen (1970).

due to OH^-; peak (k) NO_3^-.

The low symmetry of the NO_2^- ion suggests that only modes which transform according to the A_1 representation (both infrared- and Raman-active) couple with the nondegenerate electronic transitions. One interpretation of the experimental results is to identify the mode at 71 cm^{-1} (Fig. 93) with the A_1 representation. To do this we must assume the C_{2v} symmetry of the impurity center lifts the threefold degeneracy of the infrared-active T_{1u} mode and produces three infrared-active nondegenerate modes transforming as the A_1, B_1, and B_2 representations of the C_{2v} point group. This model is appealing, but the experimental results do not completely support it. Three modes are expected in the far infrared but only two have been observed; moreover, from group theoretical arguments only two sideband modes are to be expected in the near infrared, and three have been observed. Narayanamurti *et al.* (1966) propose that some of the gap modes must be of the librational type, e.g., torsional motion about the center of mass, as occurs for NCO^-.

The Raman scattering measurements have provided complementary information which enabled Evans and Fitchen to propose yet another model. The gap mode in KI:NO_2^- as determined by Raman scattering measurements is shown in Fig. 94. This unpolarized spectrum shows that only one Raman-active mode occurs in the gap region and the frequency of this mode (76 cm^{-1}) does not correspond with that obtained by any previous spectroscopic measurements. It is known that for substitutional monatomic defects in alkali halide crystals the Raman-active modes and infrared-active modes are mutually exclusive because of the inversion symmetry of the site. Evans and Fitchen conclude from their measurements that parity must still be a good quantum number even with a C_{2v} defect in the crystal. Because of the small size of the NO_2^- ion with respect to the I^- ion that it replaces, the molecule may not distort the cubic symmetry of the cavity. Combining all the experimental information they propose that the Raman peak corresponds to an E_g gap mode and the other gap modes must be associated with a translational motion of the NO_2^- ion. Isotope shift measurements would obviously provide the next step in understanding the dynamics of the bent molecule and resolving the question of whether the NO_2 infrared-active gap modes are torsional or translational in character.

VI. IONIC CRYSTALS: ACTIVATED BAND MODES, RESONANT MODES, AND TUNNELING STATES

A. Activated band modes

In an alkali halide lattice a substitutional monatomic impurity is at a site of inversion symmetry. Odd-parity band modes become infrared active, while even-parity modes become Raman active. One might anticipate that the defect-induced far-infrared absorption spectrum would follow the density of T_{1u} modes of the lattice, while the defect-induced Raman spectrum would silhouette the density of A_{1g}, E_g, and T_{2g} modes of the lattice. To some extent this does occur (for example, in the case of an isotopic defect), but when the impurity-lattice mismatch is large, low-lying resonances sufficiently alter the absorption spectrum so that the unperturbed density of phonon states can no longer be directly observed. For this latter case investigations have centered on delineating the anharmonic properties of the low-lying resonances themselves. The dramatic spectroscopic properties of resonant modes and tunneling states provide useful probes of the local lattice potential at the defect site. We begin this section by describing those experiments where measured activated band modes have been compared with a harmonic lattice theory.

1. Activated band modes detected by far-infrared absorption

The first experiments on activated band modes in alkali halide crystals have been reviewed by Maradudin (1966a, b), Klein (1968), Genzel (1969), and Sievers (1969). In most of these early experiments a detailed comparison of theory with experiment was not yet practical. In the last few years quantitative models have played a more important role, and the agreement between theory and experiment is now quite encouraging. We shall first look at the work on the defect-activated Van Hove singularities.

Ikezawa and Nasu (1973) have measured the isotope-induced far-infrared absorption in NaCl and KCl at higher resolution (0.5 cm^{-1}) than previously done by Klein and MacDonald (1968), and have clearly observed absorption peaks associated with a number of Van Hove singularities.

Ward and Timusk (1972) have made an extensive investigation of the far-infrared absorption of single crystals of KBr containing small amounts of Li^+, Na^+, Tl^+, Sm^{++}, Cl^-, F^-, OH^-, and O_2^- and also of crystals of KCl containing Li^+, Na^+, Sm^{++}, Eu^{++}, F^-, Br^-, I^-, and O_2^-. They find that the structure of the single-phonon-induced absorption is essentially independent of the impurity used, depending mainly on the lattice dynamics of the host crystal. Van Hove singularities characteristic of the density of states have been observed for nearly all the impurities used and have been found to agree very well with those predicted by the potassium halide shell model calculations.

The impurity-induced spectra for KBr are shown in Figure 95. The calculated curves shown dotted are based on the shell model of Cowley *et al.* (1963) for KBr, and the defect model of Woll *et al.* (1968). Two force constant changes are employed, the impurity to nearest-neighbor force constant change and the nearest-neighbor to fourth-nearest-neighbor force constant change shown as Δg in Fig. 74.

Shifts of Van Hove singularities with varying impurity concentration have been observed. Extrapolations to zero-defect concentration have provided the highest-resolution measurements to date of phonon frequencies in KBr and KCl at liquid helium temperatures. The far-infrared spectrum between 60 and 95 cm^{-1} of KBr containing two different impurity concentrations of Na^+ is shown in Fig. 96. The discontinuities in the spectrum are marked A, B, C, and D, and one can see from the vertical dashed line at B that the positions of these discontinuities move to higher frequencies as the concentration is increased. Detailed comparison of the experimental spectra with impurity calculations based on the shell model of the alkali halides has shown that, in the absence of impurity resonances, the main features of the induced absorption can be understood in terms of the relatively simple model mentioned above. The model is unable to predict the correct absorption intensity when low-frequency impurity resonances are present, however. Recently Ward *et al.* (1975) have completed a similar study of singular points in KI.

The impurity-induced absorption spectrum of NaCl containing Ag^+, Li^+, K^+, F^-, Br^-, and I^- ions have been measured by MacDonald *et al.* (1969) over a similar frequency range but at a much lower resolution than Timusk and Ward (1972). Although the Van Hove singularities cannot be identified in these experiments, a number of features of the absorption spectra can be fit quite well with shell model calculations. MacDonald *et al.* used a shell model similar to those used to fit neutron-determined dispersion curves (Woods *et al.*, 1960, 1963; Cowley *et al.*, 1963; Dolling *et al.*, 1968, 1966). A final adjustment of the shell model parameters was made by a comparison with the band mode absorption due to the natural isotopes of chlorine in sodium chloride (Klein and MacDonald, 1968). These shell model results were used to evaluate the unperturbed Green's functions of the perfect lattice and a point ion model was used to describe the defect. Five point ion models were introduced to fit the data of six chemical impurities. Although the data does not fit the models in all cases, these calculations represent the first systematic probing of the properties of the defect space and it is useful to summarize some of their results.

For Br^- and I^- MacDonald *et al.* found that a model which included the central force constant changes between the defect and its six nearest neighbors and also its 12 next-nearest neighbors gave good agreement with experiment. The comparison between experiment and theory for NaCl:Br^- is shown in Fig. 97. This model is consistent with the expectations from a simple rigid-ion substitution. The rigid-ion representations are shown schematically in Fig. 98. In this picture both I^- and Br^- are larger than Cl^-. Figures 98(a) and 98(b) show the defect electron distributions almost overlapping with those of the second-nearest neighbors. Both first- and second-nearest neighbors should be affected in agree-

ment with the defect model.

For the F^- impurity in NaCl the best fit to the experimental data was obtained using a lattice relaxation model. This model takes account of changes in the nearest-neighbor central force constants and in the central force constant between the nearest neighbors and the fourth-nearest neighbors of the defect. This more complex model is consistent with our expectations from the rigid-ion picture. The fluorine impurity, which is shown in Fig. 98(c), is much smaller than the Cl^- it replaces, and hence a reduction in the nearest-neighbor central force constant is expected. This should be offset to some extent by an inward relaxation of the nearest-neighbor sodium ions, which would in turn lead to a reduction of the force constant linking the nearest neighbor with the fourth-nearest neighbor. The relaxation model was first proposed by Gethins *et al.* (1967). The comparison of theory and experiment for NaCl:F^-, as shown in Fig. 99, is quite good.

Although the other three impurity calculations by MacDonald *et al.* (1969) do not fit as well with experiment as the three we have outlined here, the rigid-ion model stands out as a reasonable description of the defect space. Also it is clear from this work that the most widely used defect model in the past, which simply involves changes in the central force constant coupling the defect to its six nearest neighbors, is not realistic for many lattice-defect combinations (Benedek and Nar-

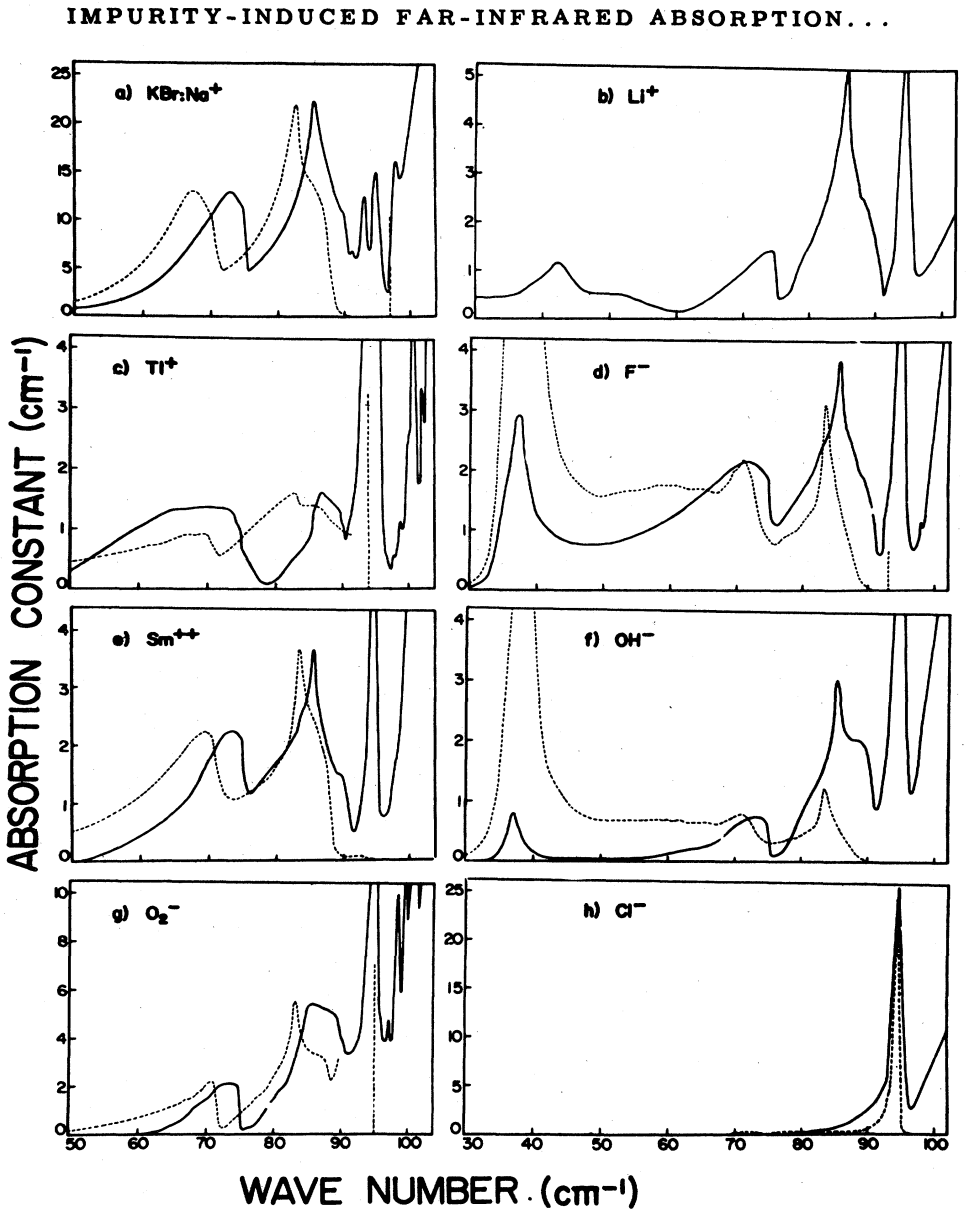

FIG. 95. Induced far-infrared absorption due to different impurity ions in KBr: (a) Na^+, (b) Li^+, (c) Tl^+, (d) F^-, (e) Sm^{2+}, (f) OH^-, (g) O_2^-, and (h) Cl^-. The calculated curves shown dotted are based on a shell model. After Ward and Timusk (1972).

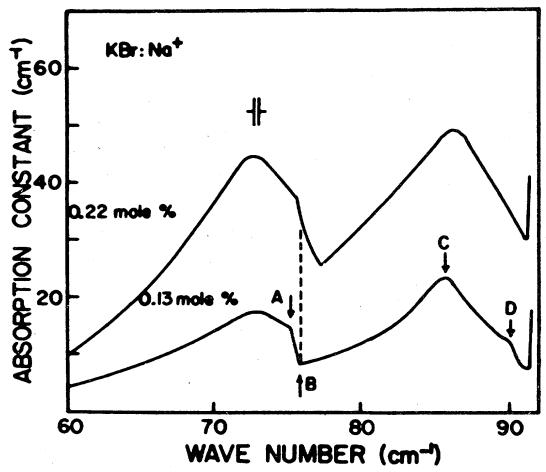

FIG. 96. Far-infrared absorption between 60 and 95 cm^{-1} of KBr containing two different impurity concentrations of Na^+. The Van Hove singularities in the spectrum are marked A, B, C, and D. The spectral resolution is given by the frequency interval between the arrows. After Ward and Timusk (1972).

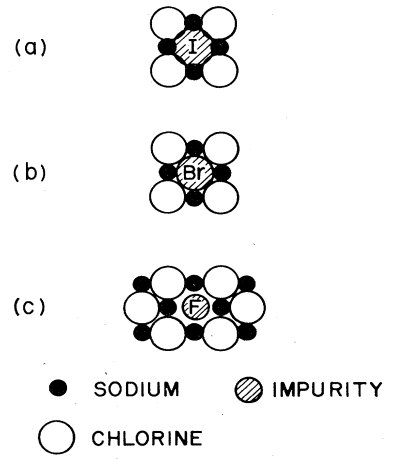

FIG. 98. Rigid-ion representations of the substitutional chemical impurities in NaCl. After Macdonald *et al.* (1969).

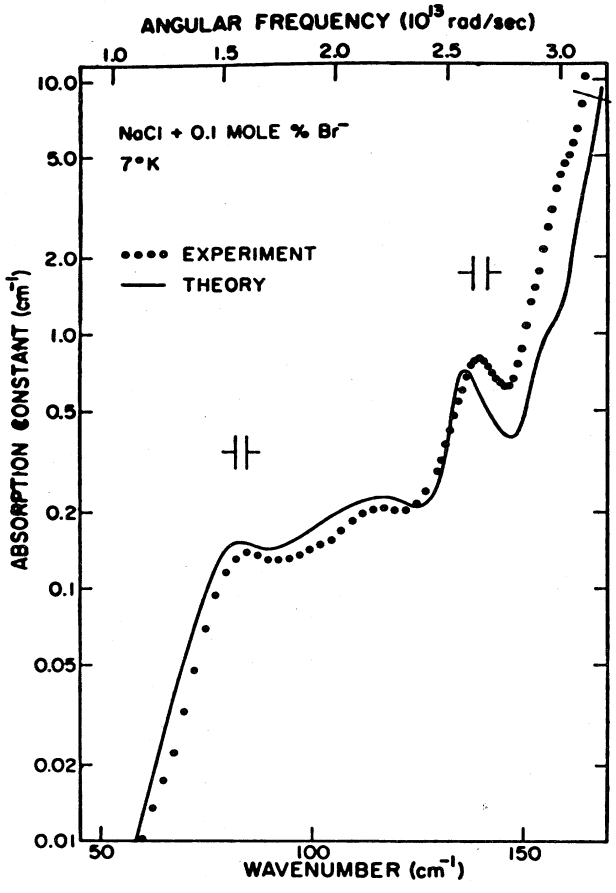

FIG. 97. Induced far-infrared absorption due to Br^- in NaCl. A comparison of theory and experiment with the change in the nearest-neighbor force constant set equal to the change in the next-nearest neighbor force constant. After Macdonald *et al.* (1969).

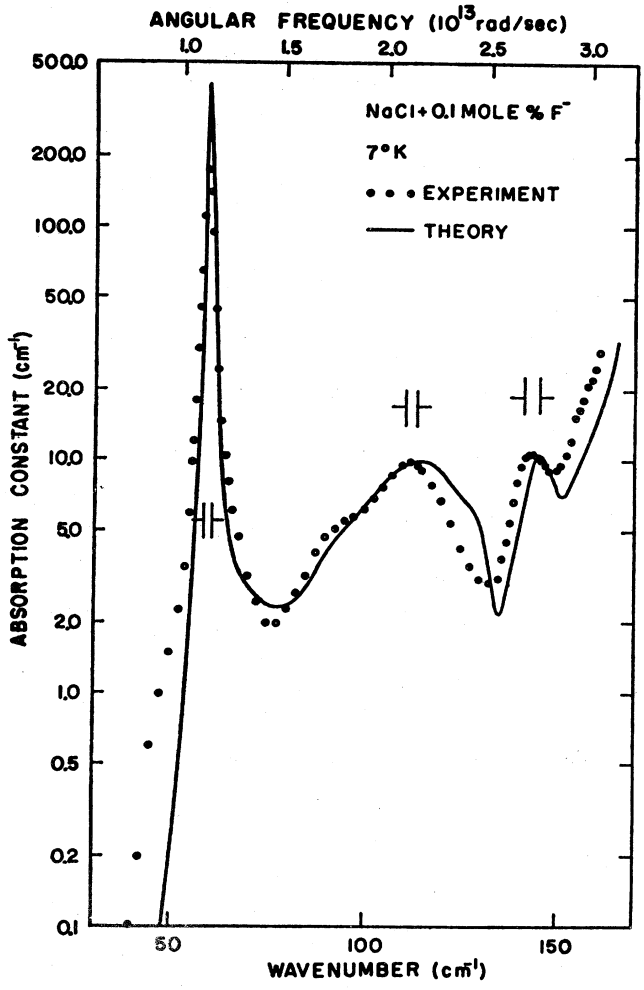

FIG. 99. Impurity-induced far-infrared absorption due to F^- in NaCl. Experiment is compared with theory using a model which allows for inward relaxation of the nearest neighbors. After Macdonald *et al.* (1969).

delli, 1968a).

Hayes *et al.* (1973) have measured the far-infrared absorption of CaF_2 at 1.8°K doped with Co^{2+}, Y^{3+}, La^{3+}, Sm^{2+}, and Tm^{3+}. Figure 100 shows these results. A simple model incorporating a lattice Green's function, a mass change at the impurity site, and a change of nearest-neighbor central force constant has been used to calculate the infrared absorption. Reasonable agreement with experiment was found (see Fig. 100), with ion size the dominant factor in determining the change of central force constant required to obtain agreement with experiment. The crystal field levels of the ground $^3H_6$ state of Tm^{3+} have not been established in CaF_2. There may well be electronic levels of Tm^{3+} in the low-frequency region in addition to the phonon absorption. Such levels may require high-resolution spectroscopy to be observable.

2. Activated band modes detected by Raman scattering

Raman scattering is caused by vibration-induced changes in the electronic polarizability of the system. Although the technique is less sensitive than far-infrared absorption spectroscopy, it has two advantages in the alkali halide host crystals. In the pure crystal, infrared radiation is strongly absorbed in a first-order process by the transverse optic phonon mode (ω_{T0}). This absorption masks all impurity absorption effects above a certain frequency. Secondly, Raman scattering is forbidden in first order for the rocksalt structure because all of the atoms are at centers of inversion and the first-order polarizability derivatives are identically zero. Impurity-induced scattering therefore has no strong background to compete with.

When an impurity is introduced into the lattice, much of the frequency region in the neighborhood of the transverse optic mode is completely opaque to far-infrared radiation. However, because the inversion symmetry is now destroyed at the neighboring sites to the impurity, certain atomic displacements of the neighbor atoms have nonzero first-order polarizability derivatives. The impurity also represents a departure from translational symmetry. This implies that atomic displacements responsible for Raman scattering need not correspond to optic phonons from the center of the zone. The first-order Raman spectrum in a perturbed crystal is a continuum reflecting the density of states for those atomic displacements rendered Raman-active by the presence of the impurity. The Raman technique has proved to be complementary to far-infrared absorption spectroscopy.

A number of the early studies were made on crystals containing F centers (an anion replaced by an electron). Raman scattering from F centers in KCl and NaCl was observed by Worlock and Porto (1965), and discussed theoretically by Kleinman (1964), Benedek and Nardelli (1967), and Henry and Slichter (1968). A combined experimental and theoretical investigation of F centers in KF, NaBr, and RbF was made by Buchenauer *et al.* (1969). While one can see effects of the lattice phonons in these studies, they are complicated by the large force constant perturbations produced by the F center. Further, the experiments were done with a resonance enhancement arising from the coincidence between the exciting laser frequency and the absorption band for the F center. This results in some subtle complications in the spectra shapes. The same remarks pertain to the Raman spectra of F_A(Li) centers in KCl observed by Fritz (1968b).

First-order Raman scattering has been observed from mixed KBr:KCl crystals by Hurrell *et al.* (1968). The induced scattering approximately silhouetted the projected density of states of A_{1g} symmetry modes of KBr. Kaiser and Möller (1969, 1970a, 1970b, 1972) have observed first-order impurity-induced scattering in NaCl:Ag^+ both from isolated silver impurities and also from impurity pairs, while the first-order Raman scattering in gold-doped alkali halides has been investigated by Jain and Sehgal (1970). Measurements of first-order impurity-induced scattering in cesium halides have been made by Buchanan *et al.* (1974). Raman scattering from the mixed crystal $KCl_{1-x}Br_x$ (Nair and Walker, 1971) and also from $KBr_{1-x}I_x$, $KCl_{1-x}I_x$, and $K_{1-x}Rb_xCl$ (Nair and Walker, 1973) has been observed and analyzed in detail.

One of the most complete experimental and theoretical studies for a lattice-defect system with small force constant changes is that by Harley *et al.* (1971) on the Raman scattering in Tl^+-doped alkali halides. Experimental Raman spectra have been obtained for KCl, KBr, KI, and RbCl doped with Tl^+ ions. The experimental E_g and T_{2g} Stokes spectra for KI:Tl^+ at 15°K is shown in Fig. 101. All crystals show strong features of E_g symmetry and rather weaker T_{2g} spectra. First-order A_{1g} structure has not been observed. Figure 101 also shows the results of theoretical calculations in which the host lattice phonon frequencies and polarization vectors were obtained from the breathing shell model of Schröder (1966). No nearest-neighbor force constant changes were required to fit the experimental data. The absence of A_{1g} features would be explained by an accidental cancellation of two polarizability components.

Since the force constants are only weakly perturbed for the above system, the defect-induced spectra can be simply explained in a qualitative way. Harley *et al.* (1971) assume that the Raman process takes place via a virtual excited electronic state of the Tl^+ ion, and that

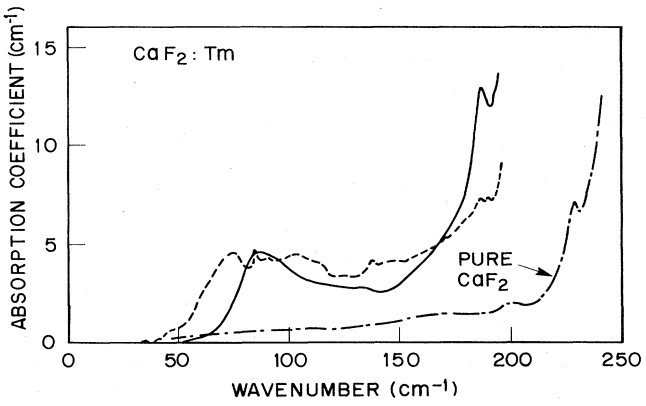

FIG. 100. Measured (broken line) and calculated (full line) absorption of CaF_2 doped with 0.1 at.% Tm^{3+}. The chain line gives the absorption of undoped CaF_2. After Hayes *et al.* (1973).

only the motion of the nearest neighbors appreciably modulates the Tl^+ electronic wave functions. Therefore the defect-induced Raman spectra should be most intense in regions of the phonon spectrum where the nearest neighbors of the Tl^+ vibrate with large amplitudes. This will be at frequencies in the acoustic phonon region in KI, but in the optic phonon region in RbCl. The experimental spectra show these effects. In addition there are gaps in which no Raman scattering occurs that correspond well with the gaps between the acoustic and optic phonon regions of the host lattice.

Harley *et al.* (1969) have also calculated the impurity-induced far-infrared absorption spectra for the odd-parity T_{1u} resonances, using the $Tl^+ - K^+$ mass difference and unchanged force constants. For polarizable defects the use of the unperturbed force constants for the odd-parity T_{1u} modes involves an additional assumption beyond those used for the even-parity modes. For the T_{1u} calculations, they assumed that (in the language of the shell model) the defect's core–shell force constant and core and shell charges were unperturbed. Recent measurements by Kahan (1973) have shown that the measured T_{1u} resonance in KCl:Tl^+ is in good agreement with these calculations. The data are shown in Fig. 102. For a Tl^+ concentration of $8.6\times10^{19}/cm^3$ with the crystal at 1.2°K, a resonance is observed at 39 cm^{-1} with a half width of 9 cm^{-1}. From the theory the resonance is predicted at 43 cm^{-1} with a width of 10 cm^{-1}. Apparently Tl^+ acts like an isotopic defect, since only a mass change is required to fit the observed spectrum. Previously Pohl (1968) had argued that Tl^+ was but one among many possible isotopiclike defects in potassium halides.

In contrast with the Tl^+ impurity in potassium halides, the Ag^+ impurity in NaCl is more difficult to understand and so better illustrates the complete lattice-defect problem. Montgomery *et al.* (1972) have made a detailed experimental and theoretical study of the defect-induced far-infrared and Raman spectra of the NaCl:Ag^+ system. The E_g Raman spectra at three temperatures are shown in Fig. 103. The room temperature spectrum is in good agreement with previously published results by Möller *et al.* (1970). As the sample is cooled, the E_g resonance peak shifts to higher frequencies and narrows, and additional structure is revealed. Low-temperature Raman data reveal many singularities pertaining to pure and perturbed phonons. Only a few of the singularities can be assigned to particular phonon critical points. The theoretical calculations are based on the lattice relaxation model described earlier (see Fig. 74). The calculated unperturbed T_{2g} Raman spectrum fits the data well. A large peak in the E_g spectrum is explained as an incipient resonance caused by relatively large *decreases* in the central force constants. The infrared spectrum is fit well by assuming somewhat smaller central force constant *decreases*. The A_{1g} Raman spectrum requires an *increase* of the nearest-neighbor central force constant. The results then imply that symmetry-dependent Coulomb contributions to force constant changes must result from the lattice relaxation. Unfortunately the discovery of symmetry-dependent force constant changes also introduces new parameters in sufficient number into the defect–lattice problem so that a fit is always possible.

Impurity-induced Raman scattering in SrF_2 and BaF_2 has been reported by Chase *et al.* (1973). Measurements were made of the impurity-induced Raman scattering spectra due to Eu^{2+} impurities substituting for the cations. Typical spectra are shown in Fig. 104. Chase *et al.* found that the data could not be fitted to a nearest-neighbor coupling model like that used previously to fit

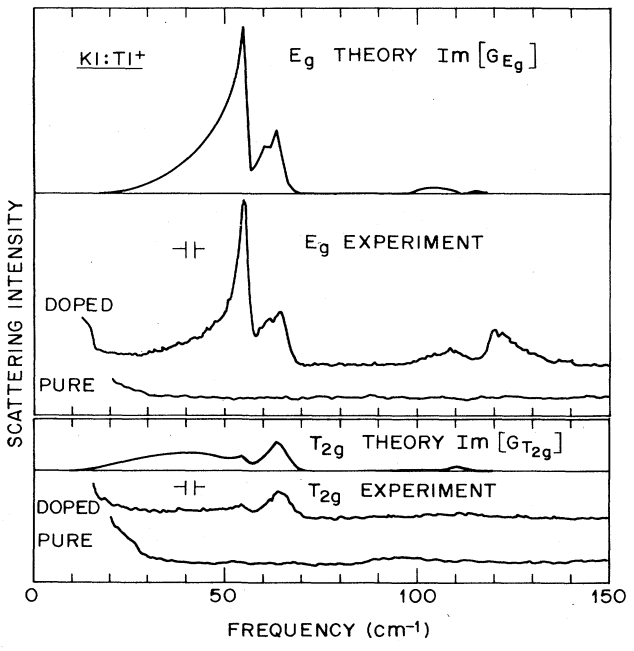

FIG. 101. Experimental and theoretical Raman spectra for KI:Tl^+: above E_g component, below T_{2g} component. The temperature of the experiments was 15 °K and the instrumental gain was the same for both the doped and pure crystals and for the E_g and T_{2g} spectra. The theoretical curves are for zero force constant change and were computed using 0 °K breathing shell model phonons. They have been normalized to reflect the experimental intensities. After Harley *et al.* (1971).

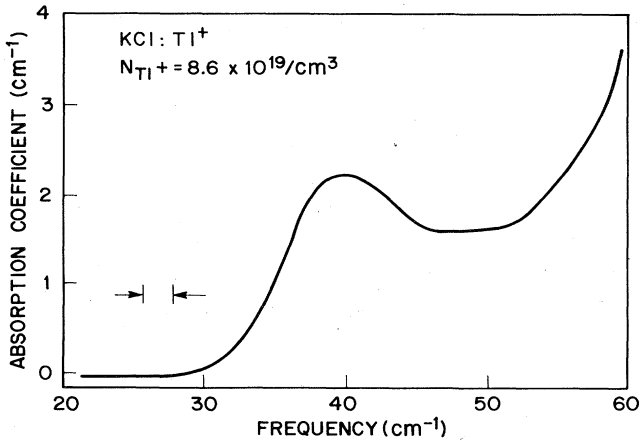

FIG. 102. Impurity-induced absorption spectrum in KCl:Tl^+. The sample temperature was 1.2 °K. The spectral resolution is represented by the separation of the two arrows. After Kahan (1973).

successfully the Tl^+ impurity in several alkali halides (Harley *et al.*, 1971). They concluded that the nearest-neighbor coupling model will give an adequate fit to the impurity-induced spectra only in hosts in which all ions in the unit cell vibrate with approximately equal amplitudes in the optic-phonon region. The fluorite lattice does not share the major advantage mentioned at the beginning of this section for alkali halide crystals. The large signal from the T_{2g} mode in the E_g and E_g-plus-A_{1g} traces dominates the spectrum in the region around 250 cm^{-1}. In addition some two-phonon scattering occurs at higher frequencies in all three traces. Both of these intrinsic scattering processes interfere with observations of the impurity-induced scattering.

3. Activated band modes seen in sideband spectra

A number of mechanisms can give rise to phonon sidebands of a high-frequency transition. In Sec. V we have already shown that anharmonic coupling of the *U*-center local mode to the lattice produces sidebands. Similarly coupling between an internal molecular vibration and a lattice mode can in the anharmonic approximation lead to a combination band in the infrared spectral region. Broad bands are observed with an intensity distribution related to the frequency distribution of lattice modes (see for example Metselaar and Van der Elsken, 1968, and Sherman and Wilkinson, 1973); however, no quantitative comparison of the experimental results with a realistic lattice model has yet been made.

The most detailed comparison between theory and experiment has been carried out for sidebands to electronic transitions. Sidebands to forbidden transitions have been observed by Bron and Heller (1964), Bron (1965), Timusk and Buchanan (1967), Bron (1969), Buchanan and Woll (1969), Kühner and Wagner (1970), and Kühner *et al.* (1972). Forbidden transitions can be made allowed by absorption or emission of a phonon; the sideband produced in this way will in general reflect some odd-parity projection of the phonon density of states. The parent zero-phonon line is either absent or very faint due to weak magnetic-dipole or defect-induced electric dipole processes, and multi-phonon sidebands are absent. The one-phonon sideband strength is calculated by second-order perturbation theory.

A good example of such a sideband is seen in the fluorescence spectrum of Sm^{2+} in KBr. On the low-energy side of the $^5D_0 \rightarrow {}^7F_0$ line at 6890 Å is the distinct sideband shown in Fig. 105. The 6890 Å line is strictly forbidden in cubic symmetry for electric dipole radiation, as it corresponds to a transition between two states of even parity. The presence of electric fields, however, would lower the symmetry and make the following transitions possible: the zero-phonon line, arising from the static field from the positive ion vacancy, which is necessary for electrical neutrality, and the sideband arising from the time-varying electric field of phonons in the crystal. Timusk and Buchanan (1967) assume that the electric field from the phonons is responsible for the

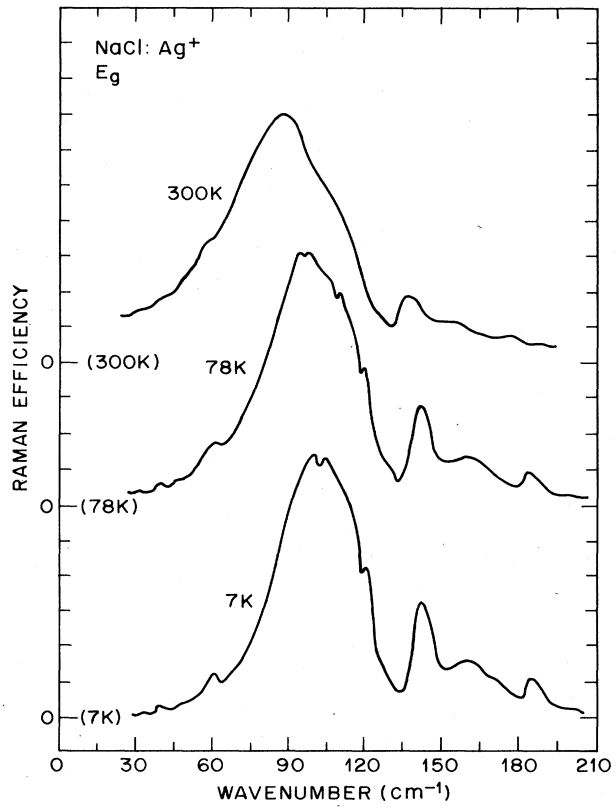

FIG. 103. The E_g Raman spectrum of NaCl:Ag^+ at three temperatures. Each vertical division represents 400 counts/sec at 300 °K, 200 counts/sec at 78 °K, and 100 counts/sec at 7 °K. The curves have been shifted vertically for easier viewing, and the zero levels for each temperature are indicated. After Montgomery *et al.* (1972).

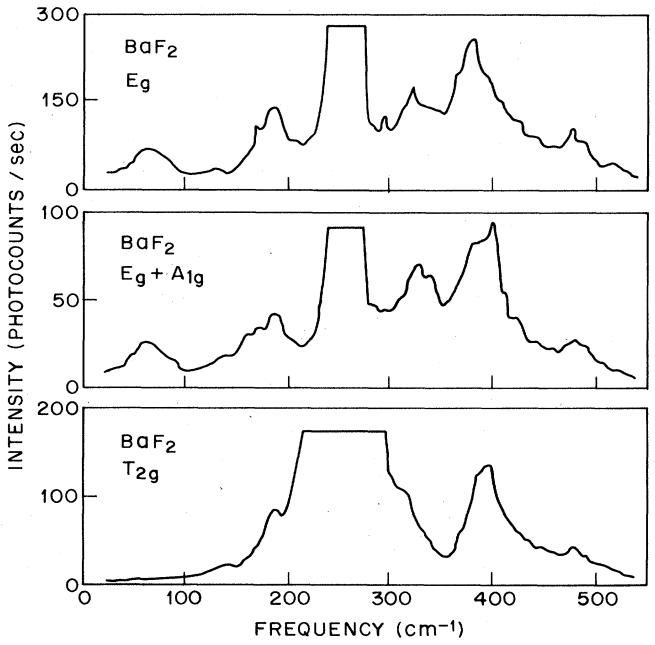

FIG. 104. Raman spectra of BaF_2:Eu^{2+}. The impurity-induced scattering is partially obscured by the strongly allowed T_{2g} vibration of the host near 250 cm^{-1}. After Chase *et al.* (1973).

sideband, and a detailed shape is calculated by the use of the phonons of pure KBr as determined from neutron measurements. The electric field due to the phonons is calculated by the Ewald method. The theoretical sideband is also shown in Fig. 105. With the exception of a few peaks that can be attributed to local modes, all the important features of the observed sideband agree with the curve given by the model.

Sidebands to allowed transitions have been observed by Timusk and Staude (1964), Avarmaa and Rebane (1969), Rebane and Saari (1971), and Rolfe *et al.* (1973). These allowed transitions often exhibit strong multiphonon sidebands corresponding to even-parity phonons. The sidebands arise from transitions between harmonic oscillator states of the phonons with displaced equilibrium positions. A characteristic of this Frank–Condon or overlap mechanism is that the relative intensities of all the multiphonon lines of a given mode are given by the simple Poisson distribution.

The emission spectra of O_2^- ions dissolved in alkali halide crystals consist of a series of zero-phonon lines separated by approximately 1000 cm^{-1}. This frequency corresponds to the separation of the vibrational levels of the O_2^- in the ground state. Each zero-phonon line is accompanied by multiphonon sidebands. Rolfe *et al.* (1973) have made high-resolution measurements of such emission spectra at 2°K in the alkali halides NaCl, KCl, KBr, KI, RbCl, RbBr, and RbI. The sidebands are produced by the interaction of even-parity lattice modes with the allowed $T_g \leftarrow T_u$ transition corresponding to O_2^- emission.

A spectrum of KBr:O_2^- measured by Rolfe *et al.* (1973) is shown in Fig. 106. They found that most of the sideband structure can be explained by coupling with A_{1g} lattice modes perturbed by relatively small changes in nearest-neighbor force constants. The calculated spectrum is also shown for comparison. In two other cases (KCl and RbCl) they found it necessary to add T_{2g} mode coupling, or to consider changes in other force constants, to obtain better agreement between calculated and observed sidebands. A residual spectrum at very low frequencies cannot be explained by the above hypothesis and it is assigned to a second-order coupling to librations of the O_2 ion.

In summary we have found that the harmonic lattice models can readily describe the far-infrared absorption, Raman scattering, and sideband spectra associated with the lattice-defect system for a variety of cases. Now let us turn to examine those lattice-defect combinations in which the impurity does not fit well into the lattice in some sense and the harmonic approximation is no longer adequate.

B. Resonant modes

Some lattice-defect combinations have been discovered which contain resonances near zero frequency. Examples are KBr:Li^+, Sievers and Takeno (1965); NaI:Cl^-, Clayman *et al.* (1969); NaCl:Cu^+, Weber and Nette (1966); NaCl:Ag^+, Weber (1964); KI:Ag^+, Sievers (1964); and CsI:Tl^+, Genzel *et al.* (1969). A complete listing of resonant modes is given in Table VI.1. In all cases where sharp low-frequency resonances have been observed, the impurity ion has a smaller ionic radius than the host ion it replaces. Matthew (1965) first showed with an intuitively appealing model how such low frequencies could occur for small ions in crystals.

Assume an impurity ion is surrounded by six nearest neighbors (NaCl structure) at a distance a, and the other ions in the crystal are at unperturbed lattice sites at distance r_0 from one another, where r_0 is the interatomic distance for the perfect crystal. All ions are rigidly fixed except for the impurity ion which moves a distance x from its normal lattice site along a cubic [100] axis.

The potential energy of the crystal $V(x)$ has the power expansion

$$V(x) = V_0 + Kx^2/2 + Bx^4 + Cx^6 + \cdots . \tag{6.1}$$

For normal cation substitutions, the term $K/2$ is large and positive, providing a strong restoring force on the particle to bring it back to its equilibrium configuration at $x = 0$. To estimate the magnitude of $K/2$ for small

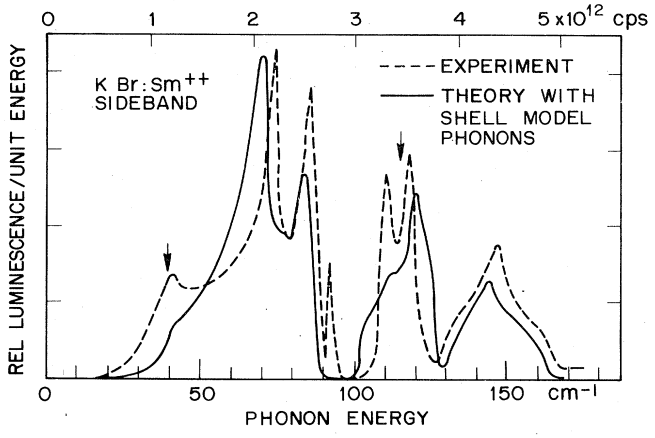

FIG. 105. The theoretical sideband for simple ions compared with the experimental sideband of K Br: Sm^{2+}. The sample was at 7°K. After Timusk and Buchanan (1967).

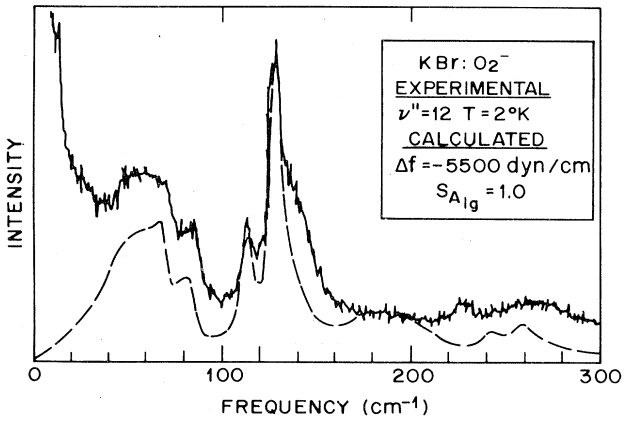

FIG. 106. The experimental and calculated (dashed) sidebands in the emission spectrum of O_2^- in KBr. The sample is at 2°K. Coupling to A_{1g} lattice modes and a slightly weakened nearest-neighbor free constant is assumed. The coupling to librations is very weak in K Br. After Rolfe *et al.* (1973).

TABLE VI.1. Resonant modes and tunneling states in ionic crystals.

Crystal	Mode frequency (cm^{-1}) (Irreducible representation, Temp. °K)	Defect symmetry, Method of observation, [a] References, [b] Comments
$^{6}Li^{+}$ (substitutional)		
NaCl	45.3(T_{1u}, 1.4)	O_h, A, 1
KCl	39.5(–, 4.2)	O_h, A, 1; H, 2; D, 3; P, 4 (Transitions involving tunneling states)
	1.15(T_{1u}, 4.2)	
KBr	17.71(T_{1u}, 4.2)	O_h, A, 5, 6
	43.7, 53.5(–, 4.2)	
$^{7}Li^{+}$ (substitutional)		
NaCl	43.7(T_{1u}, 1.4)	O_h, A, 1
KCl	42.1(–, 4.2)	O_h, A, 1; H, 2; D, 3; P, 4 (Transitions involving tunneling states)
	0.82(T_{1u}, 4.2)	
KBr	16.07(T_{1u}, 4.2)	O_h, A, 5, 6
$^{7}Li^{+}$ (pairs)		
NaBr	35.6(–, 4.2)	A, 7
$^{6}Li^{+}$ (pairs)		
NaBr	36.3(–, 4.2)	A, 7
F^{-} (substitutional)		
NaCl	59.2(T_{1u}, 2)	O_h, A, 8
NaBr	6×10^{-3}(–, 1)	O_h, H, 9
F^{-} (pairs)		
NaCl	32.2, 37.6, 39.8, 44.2, 48.1(–, 4.2)	A, 10 (Symmetry not yet determined)
$F^{-}K^{+}$ (pairs)		
	16.5(–, 4.2)	A, 38
Na^{+} (pairs)		
KCl	44(–, 4.2)	D_{4h}, A, 11
$^{35.5}Cl^{-}$ (substitutional)		
MnF_2	35.79(–, 2)	A, 12
NaI	5.438, 55(T_{1u}, 4.2)	O_h; A, 13
$^{37}Cl^{-}$ (substitutional)		
NaI	5.286, 54.9(T_{1u}, 4.2)	O_h, A, 13
Cl^{-} (pairs)		
KI	36.2(–, 4.2)	A, 37
K^{+} (substitutional)		
CsBr	86(T_{1u}, 6)	O_h, A, 14
$^{63}Cu^{+}$ (substitutional)		
NaCl	23.57(T_{1u}, 4.2)	O_h, A, 6
$^{65}Cu^{+}$ (substitutional)		
NaCl	23.20(T_{1u}, 4.2)	O_h, A, 6
Cu^{+} (substitutional)		
NaCl	40(E_g, 10), 48($A_{1g}+T_{2g}$, 10)	O_h, R, 15
Br^{-} (substitutional)		
$KMnCl_3$	14.9(–, 2)	O_h, A, 16
I^{-} (substitutional)		
KCl	52(–, 4.2)	O_h, A, 24

TABLE VI.1. Resonant modes and tunneling states in ionic crystals. *(Continued)*.

Crystal	Mode frequency (cm^{-1}) (Irreducible representation, Temp. °K)	Defect symmetry, Method of observation, [a] References, [b] Comments
Ag^+ (substitutional)		
NaCl	52.5(T_{1u}, 4.2)	O_h, A, 17, 18
	59.4(E_g, 7)96(E_g, 7)	O_h, R, 19, 20
NaBr	48.0(T_{1u}, 4.2)	O_h, A, 8
NaI	36.7(T_{1u}, 4.2)	O_h, A, 8
KCl	38.8(T_{1u}, 4.2)	O_h, A, 8
	45(E_g, 110)	O_h, R, 42
KBr	33.5(T_{1u}, 4.2)	O_h, A, 8
KI	16.35(E_g, 1.2)	O_h, A, 21
	25(A_{1g}, 1.2)	
$^{107}Ag^+$ (substitutional)		
KI	17.37(T_{1u}, 4.2)	O_h, A, 6
$^{109}Ag^+$ (substitutional)		
KI	17.23(T_{1u}, 4.2)	O_h, A, 6
Ag^+ (substitutional)		
RbCl	21.3, 26.5, 36.7(T_{1u}, 1.2)	O_h, A, 1 (Transitions involving tunneling states)
Ag^+ (pairs)		
NaCl	47.2	R, 22
In^+ (substitutional)		
CsBr	11.0(T_{1u}, 6)	O_h, A, 23
CsI	12.2(T_{1u}, 6)	O_h, A, 23
I^- (substitutional)		
KCl	52(T_{1u}, 1.2)	O_h, A, 24
Tl^+ (substitutional)		
KCl	39(T_{1u}, 1.2)	O_h, A, 24
RbBr	52(T_{1u}, 4.2)	O_h, A, 25
RbI	47(T_{1u}, 4.2)	O_h, A, 25
CsBr	16.95(T_{1u}, 6)	O_h, A, 23
CsI	14.1(T_{1u}, 6)	O_h, A, 23
Y^{3+} (substitutional)		
CaF_2	9.4(–, 4.2)	A, 44
Eu^{2+} (substitutional)		
MnF_2	16.05, 42(–, 2)	D_{4h}, A, 26
Eu^{2+} + vacancy		
NaCl	48, 210(–, 10)	C_{2v}, S, 27
KCl	45, 196(–, 10)	C_{2v}, S, 25
RbCl	38, 183(–, 10)	C_{2v}, S, 25
KBr	37, 110(–, 10)	C_{2v}, S, 25
KI	19(–, 10)	C_{2v}, S, 25
Yb^{2+} + vacancy		
NaCl	45, 208(–, 10)	C_{2v}, S, 25
KCl	44, 203(–, 10)	C_{2v}, S, 25
RbCl	42, 183(–, 10)	C_{2v}, S, 25
KBr	37, 108(–, 10)	C_{2v}, S, 25
KI	19(–, 10)	C_{2v}, S, 25

TABLE VI.1. Resonant modes and tunneling states in ionic crystals. *(Continued)*.

Crystal	Mode frequency (cm^{-1}) (Irreducible representation, Temp. °K)	Defect symmetry, Method of observation, [a] References, [b] Comments
	OH^- (substitutional)	
LiF	1.8	K, 28
NaF	$0.4(T_{1u}), 0.2(T_{1u} - E_g)$	H, 29
NaCl	$2, 9.3, 10.2, 12.2, 15.6, 22(T_{1u}, 4.2)$	O_h, A, 1, K, 30
	$3.2, 21(E_g, 4.2)$	O_h, R
	$11.5, 13.7–14.2(T_{2g}, 4.2)$	O_h, R
KCl	$0.4(T_{1u}, 4.2), 0.2(T_{1u} - E_g, 4.2)$	O_h, P, 32, 33
	32(–, 1.7)	A, 41
	25(–, 4.6)	O_h, V, 34
	$32(T_{2g}, 8)$	O_h, R, 40
	37.5(–, 1.7)	A, 41
KBr	30(–, 5)	O_h, V, 34
	$36(T_{2g}, 8)$	O_h, R, 40
RbCl	27(–, 4.5)	V, 34
	30(–, 1.7)	A, 41
KI	3.7, 8.2(–, 4.5)	V, 34
	OD^- (substitutional)	
KBr	35(–, 1.7)	A, 41
	CN^- (substitutional)	
NaCl	58(–, 27)	R, 39
KCl	$1.2(T_{1u}, 4.5)$	O_h, V, 35
	$16(T_{1u}, 1.2)$	A, 24
	12(–, 4.2)	V, 28
	15.9(–, 20)	R, 40
	16.4, 18.6(–, 5)	42 Deduced from neutron scattering by coupled defect-phonon modes
KBr	12(–, 2)	V, 36
	13.2(–, 12)	R, 39
KI	11, 38(–, 1.36)	V, 36
	$0.49(T_{1u}, 2), 0.25(T_{1u} - E_g, 2)$	H, 28
RbCl	19	V, 28

[a] Key: A = absorption, R = Raman, S = electronic sideband, V = vibrational sideband, P = paraelectric resonance, H = heat capacity, D = dielectric constant, K = thermal conductivity.

[b] The references for Table VI.1 are the following:

1. Kirby, R. D., A. E. Hughes, and A. J. Sievers, 1970, Phys. Rev. B **2**, 481.
2. Harrison, J. P., P. P. Peressini, and R. O. Pohl, 1968, Phys. Rev. **171**, 1037.
3. Lakatos, A., and H. S. Sack, 1966, Solid State Commun. **4**, 315.
4. Herendeen, R. A., and R. H. Silsbee, 1969, Phys. Rev. **188**, 645.
5. Sievers, A. J., and S. Takeno, 1965, Phys. Rev. **140**, A1030.
6. Kirby, R. D., I. G. Nolt, R. W. Alexander, and A. J. Sievers, 1968, Phys. Rev. **168**, 1057.
7. Templeton, T. L., 1973, Ph.D. Thesis, unpublished, Simon Fraser University.
8. Sievers, A. J., 1969, in *Elementary Excitations in Solids*, edited by A. A. Maradudin and G. F. Nardelli (Plenum, New York), p. 193.
9. Rollefson, R. J., 1972, Phys. Rev. B **5**, 3235.
10. Becker, C. R., and T. P. Martin, 1972, Phys. Rev. B **5**, 1604.
11. Templeton, T. L., and B. P. Clayman, 1971, Solid State Commun. **9**, 697.
12. Bäuerle, D., 1971, Phys. Rev. B **4**, 2347.
13. Clayman, B. P., I. G. Nolt, and A. J. Sievers, 1969, Solid State Commun. **7**, 7.
14. Becker, C. R., 1971, Solid State Commun. **9**, 13.
15. Ganguly, B. N., R. D. Kirby, M. V. Klein, and G. P. Montgomery, 1972, Phys. Rev. Lett. **28**, 307.
16. Sievers, A. J., 1966, unpublished.
17. Weber, R., 1964, Phys. Lett. **12**, 311.
18. MacDonald, H. F., M. V. Klein, and T. P. Martin, 1969, Phys. Rev. **177**, 1292.
19. Kaiser, R., and W. Möller, 1969, Phys. Lett. **28A**, 619.
20. Montgomery, G. P., M. V. Klein, B. N. Ganguly, and R. F. Wood, 1972, Phys. Rev. B **6**, 4047.
21. Kirby, R. D., 1971, Phys. Rev. B **4**, 3557.
22. Möller, W., R. Kaiser, and H. Bilz, 1970, Phys. Lett. **32A**, 171.

TABLE VI.1. Resonant modes and tunneling states in ionic crystals. *(Continued)*.

23. Prettl, W., and E. Siep, 1971, Phys. Status Solidi 44, 759.
24. Kahan, A. M., 1973, Ph.D. Thesis, Cornell University, Materials Science Center Rept. MSC No. 1906 (unpublished).
25. Shotts, W. J., 1973, Ph.D. Thesis, Cornell University, Materials Science Center Rept. MSC No. 2063.
26. Alexander, Jr., R. W., and A. J. Sievers, 1967, in *Optical Properties of Ions in Crystals*, edited by H. M. Crosswhite and H. W. Moos (Interscience, New York), p. 391.
27. Wagner, M., and W. E. Bron, 1965, Phys. Rev. **139**, A223.
28. Narayanamurti, V., and R. O. Pohl, 1970, Rev. Mod. Phys. 42, 201.
29. Harrison, J. P., G. Lombardo, and P. P. Peressini, 1968, J. Phys. Chem. Solids **29**, 557.
30. Rosenbaum, R. L., C. K. Chau, and M. V. Klein, 1969, Phys. Rev. **186**, 852.
31. Peascoe, J. G., and M. V. Klein, 1973, J. Chem. Phys. **59**, 2394.
32. Dreyfus, R. W., 1969, Solid State Commun. **7**, 827.
33. Peressini, P. P., J. P. Harrison, and R. O. Pohl, 1969, Phys. Rev. **180**, 926.
34. Wedding, B., and M. V. Klein, 1969, Phys. Rev. **177**, 1274.
35. Lüty, F., 1974, Phys. Rev. B **10**, 3667,3677.
36. Seward, W. D., and V. Narayanamurti, 1966, Phys. Rev. **148**, 463.
37. Ward, R. W., B. P. Clayman, and S. S. Jaswal, 1974, Solid State Commun. **14**, 1335.
38. Ishigama, M., C. R. Becker, T. P. Martin, and W. Prettl, 1972, Phys. Status Solidi **54**, K81.
39. Callender, R., and P. S. Pershan, 1970, Phys. Rev. A **2**, 672.
40. Peascoe, J. G., W. R. Fenner, and M. V. Klein, 1974, J. Chem. Phys. **60**, 4208.
41. D. R. Bosomworth, 1967, Solid State Commun. **5**, 681.
42. Möller, W., and R. Kaiser, 1972, Phys. Status Solidi **50**b, 155.
43. Walton, D., H. A. Mook, and R. M. Nicklow, 1974, Phys. Rev. Lett. **33**, 412.
44. Campbell, J. A., E. A. Schiff, and A. J. Sievers, 1975, Phys. Lett. **51**A, 470.

ions in ionic crystals, Matthew (1965) assumes that four interatomic forces need to be considered.

The first contribution to $K/2$ is from the point ion electrostatic potential. Applying Laplace's theorem to a cubic array of point ions, the restoring force for a displacement x of the impurity ion is zero, i.e., $K_c/2 = 0$.

The second contribution is from the nearest-neighbor repulsive interactions with a Born–Mayer potential

$$V_{\text{rep}} = \lambda_{+-} \exp[-r_{ij}/\rho] \quad (i, j \text{ nearest neighbors}).$$

The contribution to $K/2$ from this potential is

$$\frac{K_{\text{rep}}}{2} = \lambda_{+-} \exp\left(-\frac{a}{\rho}\right)\left[\frac{1}{\rho^2} - \frac{2}{a\rho}\right]. \tag{6.2}$$

The third contribution is from the electronic polarizability. The nearest-neighbor ions to the impurity are given a polarizability α, while the impurity ion is assumed unpolarizable. The rest of the lattice with regards to its electronic polarizability is treated as a spherical cavity of radius $\sqrt{2}\, r_0$ and dielectric constant ϵ. If dipoles are induced in the lattice purely by the ionic dipole ex at the impurity site, the dipoles induced on the nearest neighbors are $2\alpha ex/a^3$ along $\pm[100]$, and $\alpha ex/a^3$ along $[0 \pm 10]$ and $[00 \pm 1]$. These produce an electric field which tends to pull the ion away from the central site. The contribution to $K/2$ from work done against the reaction field is

$$\frac{K_{\text{n.n. pol.}}}{2} = \frac{-6\alpha e^2}{a^6}, \tag{6.3}$$

due to the nearest neighbors and

$$\frac{K_{\text{lattice pol.}}}{2} = -\frac{(\epsilon - 1)}{1 + 2\epsilon} \frac{e^2}{2\sqrt{2}\, r_0^3}, \tag{6.4}$$

due to the rest of the lattice outside the spherical cavity.

The fourth and final contribution is from the deformation polarization. When the impurity ion moves a distance x it induces on the neighboring anions deformation dipoles $\gamma(ex)$ opposite in direction to the electronic dipoles. If we neglect the deformation dipoles induced on the smaller cation the contribution to K is

$$\frac{K_{\text{def}}}{2} = 2\gamma e^2/a^3. \tag{6.5}$$

The various contributions to $K/2$ for KBr:Li^+ are computed in Table VI.2. The contributions to $K/2$ for K^+ in KBr are also computed for comparison in Model 1. Models 2 and 3 illustrate that for Li^+ with zero and with a small amount of nearest-neighbor relaxation, the repulsive contribution is small enough so that the Li^+ ion is unstable at the normal lattice site. Model 4 gives an indication of just how far the nearest neighbors must relax inward before the Li^+ ion is stable at the normal lattice site.

From these admittedly rough calculations it is evident that the balance between the repulsive forces (which push the ion toward the center) and the polarization and electrostatic forces (which pull the ion off-center) is extremely delicate. The resulting net restoring force is small, leading to low-frequency modes. More elaborate calculations by Dienes *et al.* (1966), Wilson *et al.* (1967), and Quigley and Das (1967, 1969) have confirmed these ideas. On the basis of the above arguments, low-frequency resonances or lattice instabilities are to be expected for a large number of small-ion substitutions. In the linear chain model (Fig. 16), force constant reductions of 10 times or more were required to push the resonant mode to low frequencies.

Table VI.1 indicates that a large number of sharp resonances have now been observed experimentally. Just why these resonant modes are so narrow can be understood using a simple model developed by Sievers and Takeno (1965). This model leads to an analytic solution for the resonant frequency and the linewidth of a low-frequency resonance. Although the model is not applicable to ionic crystals where long-range Coulomb forces are present, it does provide an intuitive feel for the properties of resonances in general.

TABLE VI.2. Calculated nearest-neighbor force constant for Li in KBr. After Matthews, 1965.

Model	System	a [A]	$(K/2)$ Rep	(K/2) NN pol.	(K/2) Lattice pol.	$(K/2)$ Def	$(K/2)$ Total
1	KBr : K^+ [b]	3.29	1.53	−0.45	−0.05	0.19	1.22
2	KBr : Li^+ [b]	3.29	0.42	−0.45	−0.05	···	−0.08
3	KBr : Li^+ [b]	3.16	0.60	−0.57	−0.05	···	−0.02
4	KBr : Li^+ [b]	3.06	0.79	−0.70	−0.05	···	+0.04

[a] Units of $K \equiv [\text{cgs} \times 10^4]$.

[b] The following parameters from Born and Huang (1954) are used in these calculations:

$r_0 = 3.29\,R$, $\alpha_{Br} = 4.13 \times 10^{-24}$ cm^3, $\epsilon = 2.33$,

K^+–Br^- bond: $\lambda_{+-} = 3.93 \times 10^{-9}$ ergs, $\rho = 0.334$ Å,

Li^+–Br^- bond: $\lambda_{+-} = 0.82 \times 10^{-9}$ ergs, $\rho = 0.348$ Å.

Here γ was estimated to be 0.15 from Hardy (1962).

To derive the resonant frequency and the linewidth we consider a diatomic lattice of the NaCl type containing a substitutional impurity. The masses in the host lattice are M_1 and M_2. They are connected to their nearest neighbors by harmonic springs having central force constant and noncentral force constant both equal to K. The impurity of mass M_1' substitutes for a mass M_1. The springs connecting the impurity to its nearest neighbors have central and noncentral force constant equal to K'. Using the Green's function methods described in Sec. III we write the equation for the eigenfrequency of the infrared-active resonance (Takeno, 1967)

$$D(\omega^2) = 0, \tag{6.6}$$

where

$$D(\omega^2) = \frac{K'}{K} + \left(\frac{K'}{K} - 1\right)\frac{M_1'}{M_1}\left(\frac{\omega}{\omega_1}\right)^2 + \left\{\left(\frac{M_1'}{M_1} - 1\right)\frac{K'}{K} - \left(\frac{K'}{K} - 1\right)\frac{M_1'}{M_1}\left(\frac{\omega}{\omega_1}\right)^2\right\} M_1\omega^2 g_0(\omega) \tag{6.7}$$

with $g_0(\omega) = g_0'(\omega) + i\,(sgn\,\omega)\,g_0''(\omega)$ and

$$g_0'(\omega) = \frac{-3}{2M_1\omega_1^2},$$

$$g_0''(\omega) = \frac{3\pi(1 + M_2/M_1)^{1/2}\,\omega/\omega_1^3}{8M_1},$$

for $(\omega/\omega_1)^2 \ll 1$, where ω_1 is the frequency at the top of the acoustic branch.

If in Eq. (6.7) we assume that the resonance is sharp, i.e., that $\mathrm{Re}[D(\omega^2)]$ is varying rapidly compared with the magnitude of $\mathrm{Im}[D(\omega^2)]$, then the resonant frequency is obtained by setting

$$\mathrm{Re}[D(\omega^2)] = 0.$$

To second order in K'/K ($\ll 1$) (Page, 1974) this gives

$$\left(\frac{\omega_0}{\omega_1}\right)^2 = \frac{1}{2}\frac{M_1}{M_1'}\frac{K'}{K}\left[1 - \frac{1}{2}\frac{K'}{K}\right]. \tag{6.8}$$

At very low frequencies $\omega_0^2 = 6K'/M_1'$ which is just the one-oscillator result.

Again assuming a sharp resonance so only $\mathrm{Re}[D(\omega^2)]$ is varying rapidly near ω_0, we obtain the width Γ by

$$\Gamma\left|\frac{d}{d\omega}\,\mathrm{Re}[D(\omega^2)]\right|_{\omega=\omega_0} = 2\,\mathrm{Im}[D(\omega_0^2)]. \tag{6.9}$$

The width depends strongly on the relative magnitude of

$$\left|\left(\frac{M_1'}{M_1} - 1\right)\frac{K'}{K}\right| \quad \text{compared with} \quad \left|\left(\frac{K'}{K} - 1\right)\frac{M_1'}{M_1}\left(\frac{\omega_0}{\omega_1}\right)^2\right|.$$

If the first expression is larger, then

$$\Gamma = \frac{3\pi}{8}\left|\frac{M_1'}{M_1} - 1\right|\left(1 + \frac{M_2}{M_1}\right)^{1/2}\frac{\omega_0^4}{\omega_1^3}. \tag{6.10}$$

On the other hand, if the second expression is larger, then

$$\Gamma = \frac{3\pi}{8}\left|\left(\frac{K'}{K} - 1\right)\frac{M_1'}{M_1}\right|\left(1 + \frac{M_2}{M_1}\right)^{1/2}\frac{\omega_0^6}{\omega_1^5}. \tag{6.11}$$

It is interesting to compare Eq. (6.10) and (6.11) with the results for a simple mass defect, i.e., $K' = K$ in Eq. (6.7). In this case

$$\Gamma_{md} = \frac{\pi}{8}\left(1 + \frac{M_2}{M_1}\right)^{1/2}\left|\frac{M_1'}{M_1} - 1\right|\frac{\omega_0^2}{\omega_1}.$$

If there is both a force constant change and a mass change then $\Gamma \sim \Gamma_{md}K'/K$ if Eq. (6.10) holds, while if Eq. (6.11) holds the impurity is decoupled by another factor of K'/K. For more realistic calculations of frequency and linewidth which include Coulomb interactions, the reader should consult articles by Klein (1968), Benedek and Nardelli (1967), Benedek and Maradudin (1968), Timmesfeld (1968), Prettl and Siep (1971), Martin (1971), and Ram and Agarwal (1972).

The idea of a resonance consisting of a number of perturbed phonon modes in which the impurity ion has a large amplitude has not been particularly helpful in understanding the experimental results because these modes have a strong anharmonic character, as we shall soon show.

The current approach has been to interpret the experimental measurements on sharp spectral features at low frequencies in terms of an effective oscillator Hamiltonian which consists of a harmonic component and anharmonic coupling terms like those used in Eq. (5.4) to describe the U-center local mode. However there is a fundamental difference between these two limits. In

each case one starts by expanding the potential of the crystal in coordinates Q_i which transform according to some row of an irreducible representation of the symmetry group of the Hamiltonian centered on the impurity ion. One of the Q_i's, for example, is the infrared-active T_{1u} mode. For the U center it is a normal mode of the perturbed crystal, while for the low-frequency resonant mode, the $Q_{T_{1u}}$ is not a normal mode of the system; instead the $Q_{T_{1u}}$ is a linear superposition taken from the continuous spectrum up to the highest frequency of the crystal. Figure 17 shows such a resonant mode situation. With a suitably large decrease in the force constants, the $Q_{T_{1u}}$ resonant mode does approach an eigenmode of the crystal with a well-defined frequency.

The effective oscillator Hamiltonian of the resonant mode problem has some close analogies with the effective spin Hamiltonian long used in the paramagnetic resonance field. To relate the resonant mode $Q_{T_{1u}}$ with the true normal modes $q_{T_{1u}l}$ of the perturbed crystal we note that in general

$$Q_{T_{1u}} = \sum_l \langle Q_{T_{1u}} | l \rangle q_{T_{1u}l} , \tag{6.12}$$

where the $q_{T_{1u}l}$ obey a harmonic oscillator Hamiltonian.

A picture of the eigenvector associated with resonant mode vibrations can be obtained by examining Fig. 107. In this figure the relative amplitudes for T_{1u} resonances in the asymptotic limit of zero frequency are shown. To obtain these amplitude patterns, Page (1974) assumed weakened nearest-neighbor longitudinal force constants at the impurity and realistic host crystal phonons. The relative amplitudes for impurity-induced T_{1u} resonances at zero frequency in various alkali halides, also calculated by Page (1974), are shown in Table VI.3. In all cases the mode consists essentially of the impurity ion vibrating against the rest of the crystal lattice. Therefore, at least in this limit, the resonant mode is intuitively simple though the extent of the host lattice involvement varies substantially from host to host.

Probably the biggest advantage to treating resonant modes as normal modes of the system is that analogies can be made with the extensive work which has been done on the normal modes of molecules in gases. For example, the observation of resonant mode isotopic effects can lead one to look for an analogue of the Teller–Redlich product rule, or the influence of anharmonicity can lead one to look for Fermi resonances, overtones, or combination vibrations (Herzberg, 1964). Just how far this analogy can be taken is still under investigation, but the next few sections will provide some guidelines.

1. Isotope effects on odd-parity resonant modes

When a small impurity ion in an alkali halide is replaced by an isotopic ion of the same element it is reasonable to expect that the potential energy function and configuration of the atom are changed by only negligible amounts. The vibration frequency may be appreciably altered because of the change in mass involved. In particular, a mode of vibration in which the ion in question is oscillating with a larger relative amplitude will give a greater isotopic change in frequency than a mode in which the ion is moving with a small relative amplitude. Consequently, the isotopic frequency ratios provide information on the extent to which the surroundings participate in the motion.

Isotope shifts have been measured for four different lattice defect combinations by Kirby *et al.* (1968) and Clayman *et al.* (1969). The experimental results for NaCl:Cu^+, KI:Ag^+, KBr:Li^+, and NaI:Cl^- are summarized in Table VI.4. The resonance frequency for the light impurity isotope in each of the four systems is listed in the second column, and these frequencies are each less than 15% of the maximum frequency of the host lattice. The experimentally observed ratios are given in column 3. Ratios appropriate to the one-oscillator behavior are tabulated in the fourth column. Except for KBr:Li^+, the experimental ratios are very nearly equal to the corresponding one-oscillator ratios, which suggests that the defect is moving alone in these systems. Sievers and Takeno (1965) obtained an Einstein oscillator or one-oscillator isotope effect by using a lattice model which involved equal nearest-neighbor longitudinal and transverse force constants. Since the force constants in this model are all positive and couple to nearest neighbors, a low-frequency resonance may be achieved only by reducing the nearest-neighbor force constant so that the defect and host are decoupled. In this situation an Einstein oscillator behavior necessarily results.

Benedek and Nardelli (1967) and Klein (1968) have used more realistic models to calculate the isotope shifts for resonant modes in NaCl:Cu^+, KI:Ag^+, and KBr:Li^+. These authors employed the nearest-neighbor

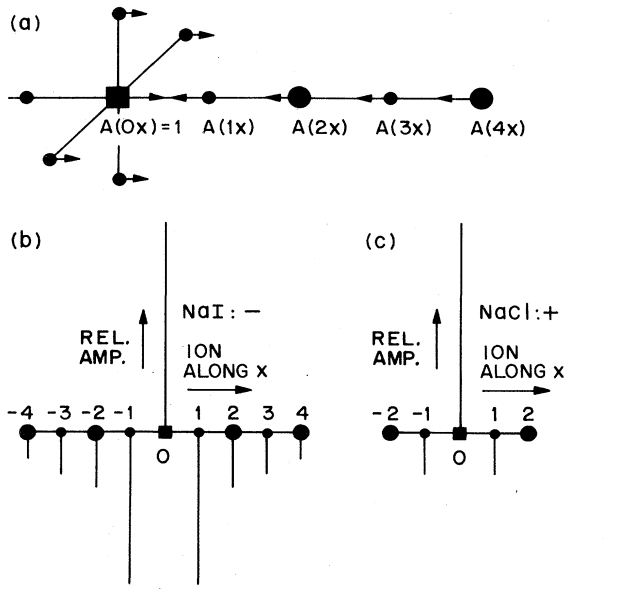

FIG. 107. Schematic representation of the relative amplitudes in the vicinity of the impurity of T_{1u} resonances of zero frequency. (a) Shows the mode and defines the four neighbors listed in Table VI.3. Computed values of these amplitudes for five different alkali halide systems are given in Table VI.3. In (b) and (c) the calculated relative amplitudes for ions along the x axis are plotted to scale for negative and positive defects in NaI and NaCl, respectively. After Page (1974).

TABLE VI.3. Force constant weakenings and relative amplitudes for impurity-induced T_{1u} resonances of zero frequency in alkali halides. These quantities are independent of the systems' mass and were computed with longitudinal nearest-neighbor force constants changed using host lattice phonons of the breathing shell model.[a] The fractional force constant changes δ_c/k_l listed here were obtained by dividing δ_c by the value of the unperturbed nearest-neighbor overlap (shell–shell) force constant of the breathing shell model. The defect displacement is unity. The neighbors are identified in Fig. 107. After Page (1974).

System	δ_c $10^4 \frac{\text{dyn}}{\text{cm}}$	δ_c/k_l	A $(1x)$	A $(1'x)$	A $(2x)$	A $(3x)$	A $(4x)$
NaCl:+	−1.51	−0.560	−0.204	0.0443	−0.009 54	−0.0144	−0.001 56
NaI:−	−1.13	−0.612	−0.732	0.115	−0.266	−0.199	−0.0716
KCl:+	−1.46	−0.597	−0.369	0.0691	−0.126	−0.0939	−0.0377
KBr:+	−1.33	−0.611	−0.310	0.0543	−0.108	−0.0778	−0.0336
KI:+	−1.19	−0.630	−0.262	0.0464	−0.103	−0.0740	−0.0356

[a] Schröder, U., 1966, Solid State Commun. 4, 347.

force constant perturbation while the host phonons were obtained from the deformation dipole model (Hardy, 1962) and the shell model of Cowley *et al.* (1963), respectively. The calculated shifts are much smaller than the measured or the Einstein oscillator shifts. This discrepancy comes about because a realistic lattice model in an ionic crystal insures that the long-range Coulomb interaction is present, so that the defect neighbors can never be uncoupled from the defect itself.

Krumhansl (1968) and Krumhansl and Matthew (1968) have argued that Einstein oscillator behavior may be a rather general property of impurity resonances in the low-frequency limit, but cautioned that this assumption might not apply to ionic crystals.

Page (1974) has reviewed the entire problem and calculated the above isotope shifts, as well as that for NaI:Cl^-, again employing the nearest-neighbor force constant perturbation and the breathing shell model for the host phonons, but using increased accuracy. His calculated values are given in Table VI.4, column 5. In his model the effective mass associated with the resonance can be written as

$$M^* = M_I + F, \tag{6.13}$$

where M_I is the impurity mass, and F is the mass enhancement term. Working in the zero-frequency limit, he derived a model-independent expression for F in terms of the host lattice masses and amplitudes. The expression shows that F is always positive and hence that Einstein oscillator or one-oscillator behavior is an upper bound on the isotope shift in any harmonic model. For the nearest-neighbor force constant change model, F is a function of just the unperturbed host crystal phonons, and Page's computed values are given in the sixth column of Table VI.4. His isotope shift expression is

$$\frac{\omega_l}{\omega_h} = \left(\frac{M_h + F}{M_l + F}\right)^{1/2}, \tag{6.14}$$

where l and h denote light and heavy substituents, respectively. For ionic crystals in this model, the above isotope shift is always substantially less than the one-oscillator shift (2.13). The frequency ratios for NaCl:Cu^+ and KI:Ag^+ are seen to be in agreement within the experimental and theoretical uncertainties. On the other hand, the agreement between theory and experiment is very bad for KBr:Li^+ and NaI:Cl^-. The bad agreement for KBr:Li^+ is expected since the measured shift for this system is greater than the Einstein oscillator limiting value of the harmonic approximation. As we shall see in the next section KBr:Li^+ is indeed a very

TABLE VI.4. Ratios of resonant mode frequencies for impurity isotope substitutions. Subscripts l and h denote light and heavy isotopes, respectively. Measured values of the frequencies for the lighter isotopes are listed in the second column, while the experimentally observed frequency ratios are given in column three. Ratios appropriate to Einstein oscillator behavior are tabulated in the fourth column. The calculated ratios listed in the fifth column are based upon the defect-nearest neighbor force constant change model described by Page (1974). In his model quantity F must be added to the impurity mass to obtain the effective mass of the resonant mode. F is a function of the unperturbed host crystal phonons and is given in the sixth column. After Page (1974).

System	ω_l (cm^{-1}) (exp)	$(\omega_l/\omega_h)_I$ (exp)	$(m_h/m_l)^{1/2}$	$(\omega_l/\omega_h)_I$ (calc)	F (amu)
NaCl: $(Cu\ 63–65)^+$	23.6	1.016 ± 0.002	1.0157	1.0142 ± 0.0006	6.97
KI: $(Ag\ 107–109)^+$	17.4	1.008 ± 0.002	1.0093	1.0072 ± 0.0003	30.5
KBr: $(Li\ 6–7)^+$	17.7	1.105 ± 0.004	1.0801	1.015 ± 0.004	26.8
NaI: $(Cl\ 35–37)^-$	5.4	1.029 ± 0.008	1.0282	1.008 ± 0.003	97.6

anharmonic system. The situation for NaI:Cl^- is clear-cut, as the calculated ratio falls far below the range of experimental values. The assigned experimental ratio of 1.029 is very close to the Einstein oscillator value of 1.0282, and the large discrepancy between the computed and observed shifts is reflected in the large deviation of the calculated amplitude pattern from that for uncoupled or Einstein oscillator behavior.

Page (1974) has also calculated the host isotope shift for the same model. An example of such a system would be the substitution of (Cl^{35}) by (Cl^{37}) in the NaCl:Cu^+ system. The host isotope shift can be written as

$$\frac{\omega_L}{\omega_H} = \left(\frac{M_h + [1 + (\Delta m/m)]F}{M_h + F} \right)^{1/2} . \tag{6.15}$$

In this derivation Δm, the change in the host ion mass, m, is assumed to be the same in both sublattices. This approximation is strictly correct only for a monatomic lattice. For a one-oscillator model where the impurity is uncoupled (so that $F = 0$), no host isotope shift is expected to occur.

Kahan (1973) has measured the host isotope shift of $NaCl^{35.5}$:(Cu^{63}) to $NaCl^{37}$:(Cu^{63}) to be

$$[(\omega_L/\omega_H) - 1] = (0.8 \pm 0.8) \times 10^{-3} \quad \text{(experimental)}.$$

For Page's model the expected shift is

$$[(\omega_L/\omega_H) - 1] = 2 \times 10^{-3} \quad \text{(theory)}.$$

Unfortunately the experimental errors are too large to determine whether or not the amplitude pattern in Table VI.3 does describe the NaCl:Cu^+ lattice defect system correctly. More precise measurements of all isotope shifts must be obtained experimentally before much more progress can be expected in this area.

2. Resonant mode anharmonic potential

A phenomenological resonant mode oscillator which describes successfully all the experiments to date on the NaI:Cl^- resonant mode has the following Hamiltonian (Clayman *et al.*, 1971):

$$\mathcal{H} = \frac{P^2}{2M^*} + \frac{M^*}{2}\omega^2(x^2 + y^2 + z^2) + C_1(x^4 + y^4 + z^4) + C_2(x^2y^2 + y^2z^2 + z^2x^2). \tag{6.16}$$

This Hamiltonian represents an anharmonic oscillator in a site of cubic symmetry and has the same form as Eq. (5.4), which was used to describe the U-center local mode. Here M^* is the effective mass of the oscillator, and ω is the harmonic resonant mode frequency. C_1 and C_2 are the fourth-order anharmonic coefficients. Higher-order terms have not been necessary. Unlike the localized mode case, the atoms of the host crystal do not provide a static potential at low frequencies in which the impurity ion vibrates. They are all vibrating themselves. Consequently in Eq. (6.16) x, y, and z are interpreted as normal coordinates rather than as particle displacements. The lower the frequency ω, the better defined the mode becomes and the more exact is (6.16).

Small electric-field-induced frequency shifts of the resonant mode have been used to probe the quartic anharmonic terms in (6.16). The Hamiltonian describing the motion of the resonant mode in the presence of the external electric field is identified with (5.6). The observed resonant mode peak in the infrared absorption spectrum is due to the electric dipole transition from the ground state of A_{1g} symmetry to the triply degenerate (in the absence of the electric field) first excited state of T_{1u} symmetry. As the defect site has inversion symmetry, a linear electric field effect is not possible. The second-order Stark effect for the resonant mode is shown in Fig. 108. Two polarization directions are shown with the applied D. C. field along the [110] crystal direction. Notice that the frequency shift varies with the square of the electric field, as expected (Clayman *et al.*, 1971).

The Hamiltonian for the second-order electric field effect is given by (5.8). From measurements of the electric-field-induced second-order shifts in the frequency of the resonant mode for different experimental geometries, the values of the quartic anharmonic coefficients C_1 and C_2 can be obtained.

In terms of the model parameters of Eq. (5.5) the transition energy is

$$\hbar\Omega = \hbar\omega + (3C_1 + C_2)(\hbar/M^*\omega)^2 . \tag{6.17}$$

We use Ω for the mode frequency, which includes anharmonic effects, and ω for the harmonic approximation. From the electric field experiment Clayman *et al.* (1971) find that the anharmonic contribution to the transition energy is 7%. It is small, confirming the validity of the perturbation approach. With this degree of an-

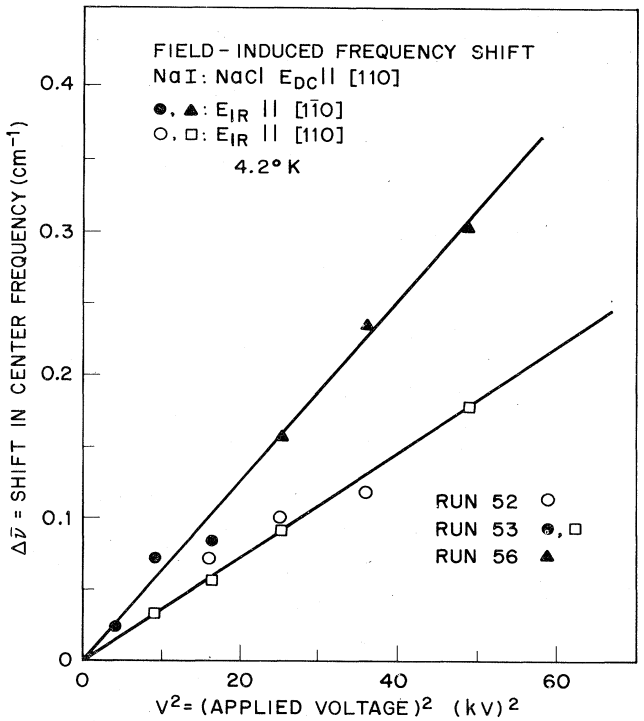

FIG. 108. Second-order Stark effect for a resonant mode. E_{dc} || [110] and two polarization directions of the infrared radiation are shown. The center frequency is at 5.43 cm^{-1} for no applied electric field. After Clayman *et al.* (1971).

harmonicity determined for the one-oscillator model, one can also predict the frequency shifts that result from isotopic mass substitution. For NaI:Cl^- the value obtained is

$$\Omega(35)/\Omega(37) = 1.030.$$

This is consistent with the value of 1.028 ± 0.008 reported by Clayman *et al.* (1969).

A further test of the model has been obtained from temperature dependence measurements by Clayman (1971). He observed that the centroid of the absorption line shifted to larger frequencies as the sample temperature was increased from 4.2°K.

From Eq. (6.17), if $(3C_1 + C_2) > 1$, the transitions between excited states for different n values all occur at higher frequencies than the $0 \rightarrow 1$ transition. This behavior can be readily understood by noting that the sign of the anharmonic terms causes the resultant potential to approach that of a square well at high excitation energies. Although at low temperatures the $0 \rightarrow 1$ transition dominates the observed spectrum, as the temperature is increased, the populations of the excited states increase quickly and transitions between excited states begin to dominate. The upward shift of the absorption frequency and the temperature dependence of the relative strengths of the transitions is explicable on the basis of thermal population effects for an anharmonic oscillator.

The success of the anharmonic oscillator model in explaining the NaI:Cl^- experimental results suggests that one try the same approach for KBr:Li^+. Fourth-order anharmonicity can cause the anomalously larger $^6Li \rightarrow {}^7Li$ isotope shift in BKr but the crucial test is whether or not the anharmonic oscillator model can self-consistently explain *both* the isotope shift and the electric field shifts. Clayman *et al.* (1971) have found that the quartic perturbation in Eq. (6.16) must be very large (33%) to explain the isotope shift. On the other hand, to explain the small electric field shifts in KBr:Li^+ the quartic term must be 50 times smaller. Furthermore, the value of $(3C_1 + C_2)$ is negative, which makes the isotope shift smaller than that of an harmonic oscillator. Equation (6.16) does not correctly describe the properties of the KBr:Li^+ mode.

Quigley and Das (1969) and Wilson *et al.* (1967) have performed calculations to determine the minimum energy configuration of Li^+ in KBr. Their results indicate that the potential-energy minima for the impurity ion are displaced in the [111] direction from the center of the host ion (K^+) cavity. The barriers on the [110] directions between adjacent equilibrium sites are small; Quigley and Das find that they are smaller than the Li^+ vibrational zero-point energy. Gomez (1968) has pointed out that such a well can explain the large $^6Li \rightarrow {}^7Li$ isotope shift in KBr. Clayman *et al.* (1971) have shown that this type of potential also gives a small Stark effect as well. They introduced the central barrier as a perturbation to a harmonic well, fit the isotope effect, and found the parameters changed the $0 \rightarrow 1$ transition energy by 22%. This potential is shown in Fig. 109. Finally they calculated the electric-field-induced shift in the $0 \rightarrow 1$ transition energy to be 0.03 cm^{-1} for an external field of 70 kV/cm. This value is compared with the experimentally observed shift of 0.08 ± 0.03 cm^{-1} (Kirby and Sievers, 1968). Consequently a potential well which has displaced energy minima, but barriers which are small compared to the impurity zero point energy, causes a large isotope shift but only a small electric field shift. Although the potential in Fig. 109 may appear anomalous on first inspection, similar but different potential functions have long been used to understand the ring puckering vibrations of closed molecular chains (Chan *et al.*, 1966).

NaCl:Cu^+ has both a large impurity mass and a high resonant frequency, so the expected electric-field-induced shifts due to fourth-order anharmonicity which varies as $M^{*-3}\omega^{-5}$ [see Eq. (5.8)] would be only $\sim 10^{-4}$ as large as the NaI:Cl^- shifts. A shift this small would be unobservable. The experimental results on NaCl:Cu^+ show that no shift or broadening in excess of 0.005 cm^{-1} occurs at 120 kV/cm. A potential similar to that which explains the KBr:Li^+ results possibly could be used here as well.

3. Even-parity modes, overtones, and combination bands

The far-infrared absorption spectrum of KI:Ag^+ is shown in Fig. 110 (Kirby 1971). The spectrum is complicated with at least five Ag-induced absorption lines in addition to the well known T_{1u} resonant mode at 17.3 cm^{-1}, and a strong gap mode at 86.2 cm^{-1}. The observed absorption spectrum varies linearly in absorption strength with the Ag^+ concentrations; consequently,

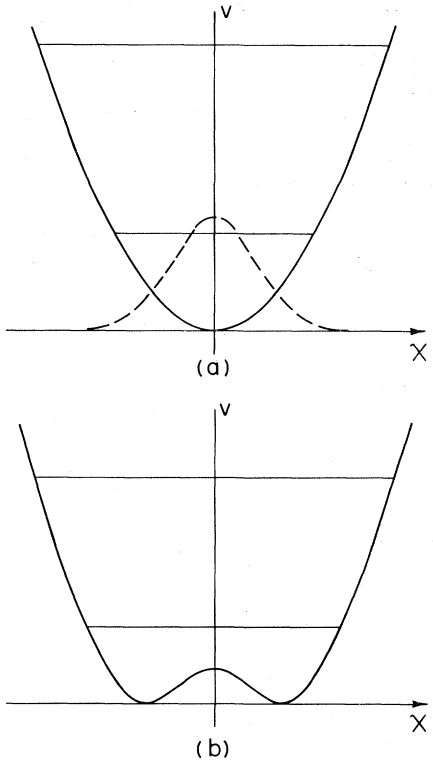

FIG. 109. One-dimensional harmonic oscillator with a central barrier. (a) Harmonic well with two lowest states. Dashed curve shows the perturbing potential used. (b) Anharmonic well with two lowest states. Parameters are appropriate for KBr:Li^+. After Clayman *et al.* (1971).

pair modes, which we shall consider later, are not observed here. By means of electric field shifts in the far-infrared absorption spectrum, and also by means of Raman scattering, Kirby has identified two even-parity resonant modes. The E_g symmetry Raman scattering spectrum is shown in Fig. 111. The center frequency is at 16.1 cm^{-1}. A self-consistent identification of the absorption spectrum is obtained with the absorption at 29.8 cm^{-1} in Fig. 110 identified as the $T_{1u}+E_g$ combination band, and the absorption at 44.4 cm^{-1} as the $T_{1u}+A_{1g}$ combination band.

The near degeneracy of the T_{1u} and E_g resonances in KI:Ag^+ produces a remarkable electric field effect on the absorption spectrum. The odd-parity electric field mixes the two modes of opposite parity, and both of the mixed modes are seen in the infrared absorption spectrum. The frequency shifts versus external field are shown in Fig. 112. The upper set of data correspond to the T_{1u}-like mode, while the lower set correspond to the E_g-like mode. The solid curves were obtained using an anharmonic oscillator model described below.

To estimate the properties and interactions of the one odd and two even resonant modes, Kirby assumed that each mode could be represented by a harmonic oscillator, so that the Hamiltonian for the entire system is

$$\mathcal{H}_0 = \mathcal{H}_{T_{1u}} + \mathcal{H}_{E_g} + \mathcal{H}_{A_{1g}} ,$$

where the effective mass of the T_{1u} mode is taken as the silver ion mass, and the mass for the two even modes is taken as the iodine mass. To include the effects of anharmonicity he expanded the potential energy in powers of the harmonic coordinates. Because of the inversion symmetry about the defect site, the T_{1u}-mode coordinates enter only in even powers. The cubic interaction between the T_{1u} mode and the even-parity modes is written as

$$\mathcal{H}' = V_A r^2 Q_{A_{1g}} + V_E[(3z^2 - r^2)Q_{E_{g1}} + \sqrt{3}\,(x^2 - y^2)Q_{E_{g2}}] . \tag{6.18}$$

The second-order perturbed energies for the anharmon-

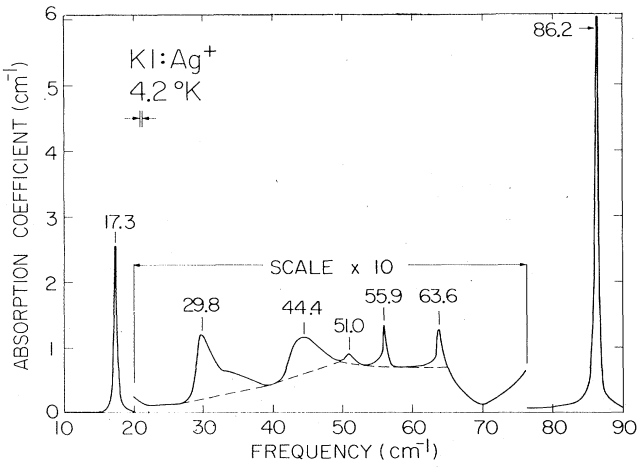

Fig. 110. Far-infrared absorption spectrum of KI:Ag^+ at 4.2 °K. The instrumental resolution is 0.25 cm^{-1}. Combination resonances appear at 29.8 and 44.4 cm^{-1}. After Kirby (1971).

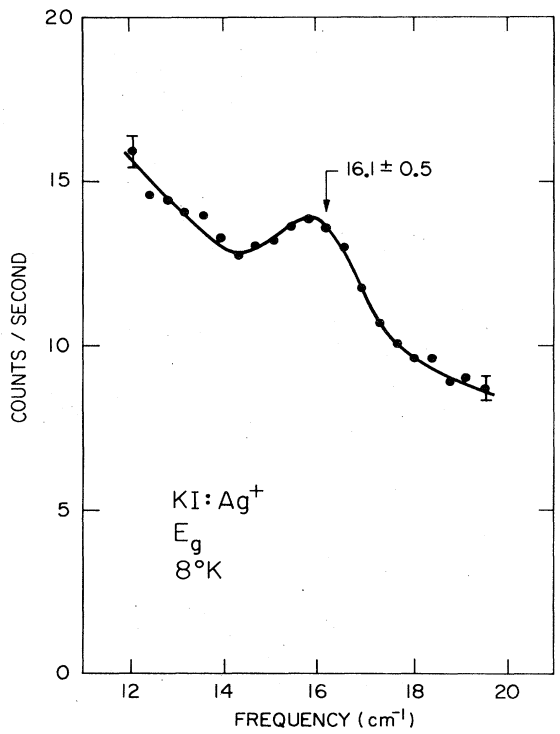

FIG. 111. E_g symmetry Raman scattering spectrum of KI:Ag^+ at 8 °K. The scattering geometry is $z(yx)y$, with $x \parallel [110]$, $y \parallel [110]$, $y \parallel [\bar{1}10]$, and $z \parallel [001]$. The instrumental resolution is 2 cm^{-1}. After Kirby (1971).

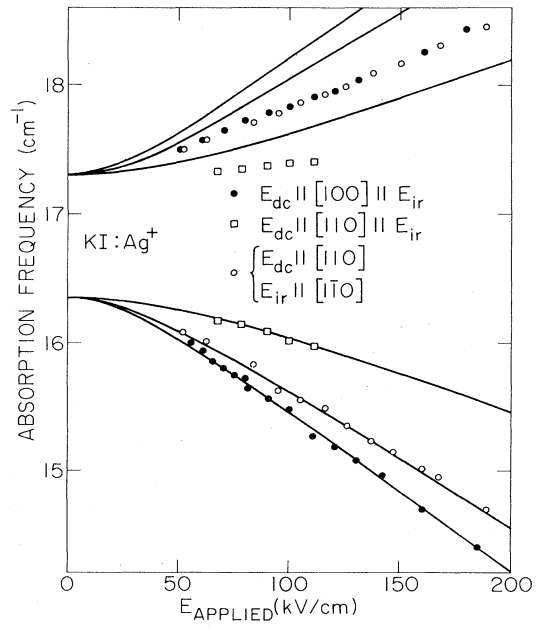

FIG. 112. Frequency vs external electric field results for the T_{1u} and E_g symmetry resonances in KI:Ag^+. The solid curves were fitted using the harmonic oscillator model described in the text. After Kirby (1971).

ic oscillator model are recorded in Table VI.5.

Kirby (1971) determined V_A and V_E by fitting the strengths of the combination bands, since these quantities are independent of cubic and quartic terms not included in (6.18). Unfortunately the fitted coupling coefficients are so large that the anharmonic contributions to the oscillator energies are of the same size as the harmonic contributions, so that these perturbation calculations can provide only qualitative results.

The form of the coupling terms used in the perturbation has been verified to some extent by the electric field results. Since the E_g and T_{1u} modes are nearly degenerate, the application of an electric field (5.6) leads to a mixing of the two modes and results in the field-induced shifts

$$\delta(E) = \pm(\Delta^2 + R^2E^2)^{1/2} , \tag{6.19}$$

where the + and − signs are to be associated with the T_{1u} and E_g modes, respectively, 2Δ is the zero field separation, and

$$R = 2e\hbar V_E/(2\omega_T - \omega_E)\omega_E M_T(M_T M_E \omega_T \omega_E)^{1/2} .$$

The value of V_E obtained from Fig. 112 is in good agreement with the sideband fit described above.

Raman-active resonant modes and overtones have also been observed in NaCl:Cu^+ by Ganguly *et al.* (1972). The combined Raman spectrum is shown in Fig. 113. This spectrum contains an E_g resonant mode and also reveals the three components of the first overtone of the 23.5 cm^{-1} infrared-active resonant mode. The frequencies of the E_g resonance and the E_g component of the overtone are shifted as a result of a strong anharmonic coupling between them. Their line shapes and strengths are considerably altered by an interference between the Raman amplitudes. Additional evidence for strong anharmonic coupling between modes is provided by the existence of combination bands in the far infrared at 64 and 69 cm^{-1} (Montgomery and Kirby, 1971).

Möller and Kaiser (1972) have observed a strong Raman-active E_g resonance at (45 ± 2) cm^{-1} in KCl:Ag at 110°K. The absorption coefficient of the T_{1u} activated spectrum in KCl:Ag at 5°K was observed earlier by Sievers (1968). A strong resonant mode absorption at 38.6 cm^{-1} was measured, as well as a weak absorption at 78 cm^{-1}. Kirby has noted that this $T_{1u}+E_g$ cm^{-1} combination resonance again indicates strong anharmonic coupling between odd- and even-parity modes.

TABLE VI.5. Perturbed transition energies from the anharmonic oscillator model, where

$$U_E = V_E \frac{\hbar}{M_T\omega_T}\left(\frac{\hbar}{2M_E\omega_E}\right)^{1/2}$$

and

$$U_A = \frac{V_A\hbar}{2M_T\omega_T}\left(\frac{\hbar}{M_A\omega_A}\right)^{1/2}.$$

After Kirby (1971).

Final state	Perturbed transition energy
$\|100;00;0\rangle$	$\hbar\omega_T - \frac{4U_E^2}{\omega_E} - \frac{4U_E^2}{2\omega_T+\omega_A} - \frac{8U_A^2}{\omega_A} - \frac{2U_A^2}{2\omega_T+\omega_A}$
$\|000;10;0\rangle$	$\hbar\omega_E - \frac{3U_E^2}{2\omega_T-\omega_E} - \frac{3U_E^2}{2\omega_T+\omega_E}$
$\|000;00;1\rangle$	$\hbar\omega_A - \frac{3U_A^2}{2\omega_T-\omega_A} - \frac{3U_A^2}{2\omega_T+\omega_A}$
$\|100;10;0\rangle$	$\hbar\omega_T+\hbar\omega_A - \frac{4U_E^2}{\omega_E} - \frac{4U_E^2}{2\omega_T+\omega_E} - \frac{8U_A^2}{\omega_A} - \frac{5U_A^2}{2\omega_T-\omega_A} - \frac{7U_A^2}{2\omega_T+\omega_A}$
$\|100;00;1\rangle$	$\hbar\omega_T+\hbar\omega_E - \frac{4U_E^2}{\omega_E} - \frac{11U_E^2}{2\omega_T+\omega_E} - \frac{7U_E^2}{2\omega_T-\omega_E} - \frac{8U_A^2}{\omega_A} - \frac{2U_A^2}{2\omega_T+\omega_A}$

4. Anharmonic coupling to the lattice

1. Lattice strain

An alloy of two alkali halides has an average lattice constant intermediate to the lattice constants of the two constituents (Havighurst *et al.*, 1925). This method of varying the lattice constant has been successfully exploited to study the U-center system, as has been described in Sec. V.

Clayman *et al.* (1967) have alloyed KCl or KI with KBr:Li^+ to study the effect of the lattice constant change on the resonant mode frequency. The dependence of mode frequency and linewidth on lattice constant has been found to be linear. The center frequency of the absorption versus fractional change of the lattice constant is shown in Fig. 114. With the addition of KCl to the lattice, the center frequency shifts to higher frequencies and the line broadens; the center frequency shifts to lower frequency and again the line broadens upon the addition of KI. The frequency of the maximum optical density is shown where it differs appreciably from the centroid frequency. The average lattice constant $\bar{a}$ is

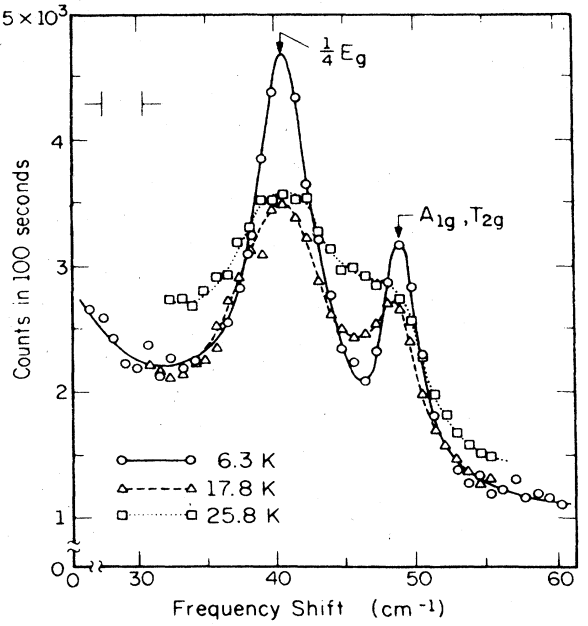

FIG. 113. Combined Raman spectrum of NaCl:Cu^+ at moderate resolution showing strong temperature dependence. The copper concentration was $3\times10^{18}/cm^3$. After Ganguly *et al.* (1972).

calculated from the measured alloy concentration by Vegard's relation [see (5.20)].

The linear dependence of mode frequency upon lattice constant has been explained by Hughes (1968). He applied the strain broadening theory of Stoneham (1966), and included the uniform dilation of the lattice necessary to make the surface stresses vanish. The result was a Lorentzian line whose frequency shift and width vary linearly with lattice constant change. Using the strain coupling parameters determined from uniaxial stress measurements (Nolt and Sievers, 1968), he calculated that

$$\Delta\omega = -440(\Delta V/V) \quad \text{(calculated)}$$

in good agreement with the experimentally determined value

$$\Delta\omega = -470(\Delta V/V) \quad \text{(experimental)}.$$

Hughes' result for the strain broadening of the line is too large by a factor of 2, but this can be explained by the nonrandom distribution of impurities.

Another method of altering the lattice constant is to use hydrostatic pressure. Using He gas as the pressure medium, Kahan and Sievers (1971) and Kahan *et al.* (1975) have made low-temperature hydrostatic pressure measurements on a number of resonant mode systems. Lattice constant changes of the same magnitude as for the alloy experiments have been obtained with a higher degree of accuracy because of the absence of disorder-induced broadening. The measured stress coupling coefficients are recorded in Table VI.6. Column 3 of this table gives the hydrostatic coupling coefficients. Because the frequency shifts for a 1% linear strain are on the order of the oscillator frequency itself, Eq. (5.19), which assumes that the frequency shift varies linearly with strain, is not particularly useful here.

The above results can be described by the anharmonic oscillator model of (6.18). That is, third-order anharmonic coupling is assumed to be important for all resonant modes. The lowest-order coupling that will produce a hydrostatic pressure shift is of the form

$$\mathcal{H}' = -\tfrac{1}{2}V_A r^2 \epsilon_{A_{1g}} , \tag{6.20}$$

where V_A is the coupling constant, and $\epsilon_{A_{1g}} = \Delta V/V$, the hydrostatic strain.

The Hamiltonian for the system becomes

$$\mathcal{H} = (P^2/2M^*) + \tfrac{1}{2}(k_0 - V_A\epsilon_{A_{1g}})r^2 , \tag{6.21}$$

where k_0 is the force constant of the unperturbed oscillator. The effective force constant in the presence of hydrostatic strain is

$$k_{\text{eff}} = k_0 - V_A\epsilon_{A_{1g}}$$

so

$$\frac{\Delta k}{k_0} = -V_A\epsilon_{A_{1g}} = \frac{\omega^2 - \omega_0^2}{\omega_0^2} . \tag{6.22}$$

At zero strain the anharmonic coupling coefficient, V_A, is related to the hydrostatic coupling coefficient, A, and the resonant mode Grüneisen constant, γ, (5.18) by

$$\frac{V_A}{2} = \frac{A}{\omega_0} = \gamma_r . \tag{6.23}$$

For a variety of resonant modes the force constant does vary linearly with strain as illustrated in Fig. 115. Here KI:Ag^+ is anomalous in this respect, for in addition to the linear contribution the resonant mode contains a large quadratic dependence on strain. From the experimental data it is projected that the frequency shift for KI:Ag^+ will reach a maximum value at 6% lattice strain and then decrease for large lattice strains (Kahan *et al.*, 1975). If one assumes that coupling to dynamic strains is the same as to static strains, then for most resonant mode systems linear coupling is sufficient, while for KI:Ag^+ one should include quadratic coupling as well.

With the application of uniaxial stress along crystallographic directions, the coupling of the resonant mode excited state to lattice distortions of different symmetry can be distinguished (Nolt and Sievers, 1968; Subashiev,

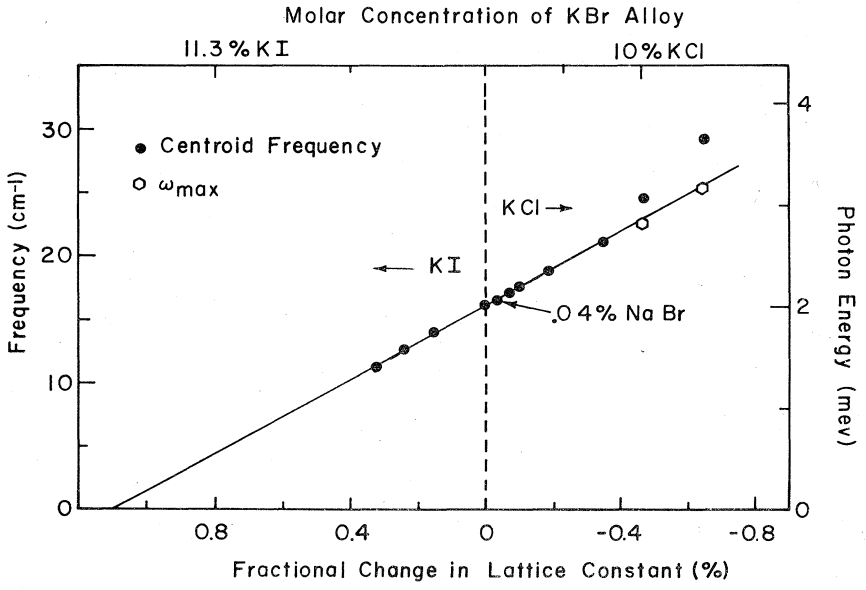

FIG. 114. Li^+ resonant mode absorption frequency in KBr alloys. The average lattice constant is calculated by using the Vegard relation [see Eq. (5.20)]. After Clayman *et al.* (1967).

TABLE VI.6. Stress coupling coefficients for infrared-active resonant modes. The center frequencies of these modes are given in Table VI.1.

Defect system	A ($S_{11}+2S_{12}$) (cm^{-1}/kbar)	A (cm^{-1}/unit strain)	B ($S_{11}-S_{12}$) (cm^{-1}/kbar)	B (cm^{-1}/unit strain)	CS_{44} (cm^{-1}/kbar)	C (cm^{-1}/unit strain)	References [a]
NaCl : Li^+	0.67	530, 440 [b]	1.3	620, 440 [b]			1
NaCl : F^-	0.83	670, 560 [b]	1.0	470, 350 [b]			1
NaCl : Cu^+	0.43 ± 0.17	230 [b], 350	0.90 ± 0.07	170 [b]	0.62 ± 0.39	−80 [b]	2
	0.59 ± 0.1	470					3
	0.50	400, 330 [b]	0.90	420, 295 [b]			1
NaI : Cl^-	0.18 ± 0.03	97	0.42 ± 0.07	124			4
KBr : Li^+	1.6 ± 0.2	480 [b], 830	1.0 ± 0.1	312 [b], 360	3.1 ± 0.4	144 [b], 170	5
	1.7 ± 0.2	880					3
KI : Ag^+	1.0 ± 0.3	225 [b], 390	1.6 ± 0.2	246 [b], 510	−0.4 ± 0.2	266 [b], −15	5
	0.94 ± 0.1	360					
CsBr : Tl^+	1.7 ± 0.3	800 [c]					6
CsI : Tl^+	0.69 ± 0.1	264 [c]					3
	1.0 ± 0.4						6
CaF_2 : Y^{3+}	0.220	630					7

[a] The references for Table VI.6 are the following:

1. Busse, G., 1972, Ph.D. Thesis, Universität Freidburg i. Br. (unpublished).
2. Busse, G., W. Prettl, and L. Genzel, 1968, Phys. Lett. **27A**, 438.
3. Kahan, A. M., M. Patterson, and A. J. Sievers, 1975, "Far Infrared Properties of Lattice Resonance Modes: 6 Hydrostatic Pressure Measurements," unpublished.
4. Clayman, B. P., 1969, Ph.D. Thesis, Cornell University, Materials Science Center Rep. MSC Number 1026 (unpublished).
5. Nolt, I. G., and A. J. Sievers, 1968, Phys. Rev. **174**, 1004.
6. Prettl, W., and E. Siep, 1971, Phys. Status Solidi, **44**, 759.
7. Campbell, J. A., E. A. Schiff, and A. J. Sievers, 1975, Phys. Lett. **51A**, 470.

[b] Local stress coupling coefficients calculated by Benedek, G., and G. F. Nardelli, 1968, Phys. Rev. **167**, 837.

[c] Room temperature compliance constants were used. [Tosi, M. P., 1964, in *Solid State Physics*, edited by F. Seitz and D. Turnbull (Academic, New York), Vol. 16, p. 44.]

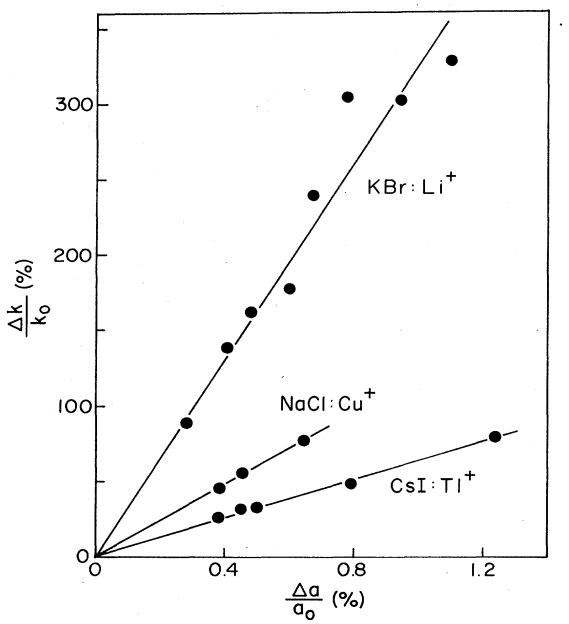

FIG. 115. Linear dependence of the resonant mode force constant on lattice strain. After Kahan *et al.* (1975).

1970). These coupling coefficients can be estimated from the slopes of the absorption frequency versus applied stress data if the stiffness constants of the crystal are known. The stress coupling coefficients for distortions of spherical, A, tetragonal and orthorhombic, B, and trigonal, C, symmetry are given in Table VI.6. The stiffness constants of the pure host crystal at 4.2°K have been used to obtain most of these values. The stiffness constants for most of the alkali halides are contained in Table VI.7. A problem which has received little attention to date is associated with modifying the stiffness constants to account for a softening of the lattice in the neighborhood of the impurity (Benedek and Nardelli, 1968b).

The influence of local stress fields on resonant modes has also been observed for plastically deformed crystals. Busse and Haider (1970) have attempted to use the resonant mode frequency shifts in NaCl:Cu$^+$ to probe the local lattice distortion near dislocations. Shifts on the order of 1 cm^{-1} have been resolved and related to the deformation.

b. Temperature dependences of resonant modes

One simple explanation of the temperature dependence of the resonant mode intensity lies in the anharmonicity

TABLE VI.7. Compliance constants of some ionic crystals at 4.2°K.

Crystal	$S_{11}+2S_{12}$ 10^{-3}(kbar)$^{-1}$	$S_{11}-S_{12}$ 10^{-3}(kbar)$^{-1}$	S_{44} 10^{-3}(kbar)$^{-1}$	References[a]
LiF	0.4775	1.216	1.54	2
LiCl	0.9421	2.629	3.715	1
NaF	0.6481	1.168	3.449	1
NaCl	1.253	2.169	7.513	1
NaBr	1.477	2.622	9.346	1
NaI	1.867	3.375	12.80	3
KF	0.974	1.608	7.485	1
KCl	1.691	2.330	15.08	4
KBr	1.907	2.75	19.7	5
KI	2.618	3.16	27.2	4
RbCl	1.787	2.74	20.3	1
RbBr	2.078	2.951	24.48	1
RbI	2.544	3.509	34.2	1
CsBr	1.816	4.163	10.0	6
CsI	2.313	5.144	12.1	6
CaF_2	0.350	0.85	2.783	7
SrF_2	0.447	1.23	3.023	8
BaF_2	0.533	1.876	3.931	9

[a] The references for Table VI.7 are the following:

1. Lewis, J. T., A. Lehoczky, and C. V. Briscoe, 1967, Phys. Rev. **161**, 877.
2. Briscoe, C. V., and C. F. Squire, 1957, Phys. Rev. **106**, 1175.
3. Claytor, R. N., and B. J. Marshall, 1960, Phys. Rev. **120**, 332.
4. Norwood, M. H., and C. V. Briscoe, 1958, Phys. Rev. **112**, 45.
5. Galt, J. K., 1948, Phys. Rev. **73**, 1460.
6. Vallin, J., O. Becman, and K. Salema, 1964, J. Appl. Phys. **35**, 1223.
7. Huffman, D. R. and M. H. Norwood, 1960, Phys. Rev. **117**, 709.
8. Gerlich, D., 1964, Phys. Rev. **136A**, 1366.
9. Gerlich, D., 1964, Phys. Rev. **135A**, 1331.

of the resonant mode itself, i.e., terms such as x^4 in the potential. These have been shown to be important for the interpretation of some electric field experiments (Clayman *et al.*, 1971). Terms such as these will break down the regular spacing of the harmonic oscillator levels so that the $0 \rightarrow 1$ transition does not coincide with the $1 \rightarrow 2$ and higher transitions. If the shift in levels is larger than the linewidth of the individual transitions, then only the $0 \rightarrow 1$ transition contributes effectively to the line strength and its intensity will decrease as the ground state is thermally depopulated. Assuming that the anharmonicity is not too large, so that we can still use the harmonic oscillator partition function, we find for a one dimensional oscillator that

$$I(T)/I(0) = [1 - \exp(-\hbar\omega/kT)]^2 . \tag{6.24}$$

The temperature dependence of the nondegenerate resonant mode in $MnF_2:Eu^{2+}$ follows Eq. (6.24) very closely (Alexander *et al.*, 1970). In addition the $1 \rightarrow 2$ transition has been identified as a line appearing about 1.5 cm^{-1} higher in energy than the $0 \rightarrow 1$ line. The total integrated intensity of the main line plus the sideband remains essentially temperature-independent as predicted by Eq. (5.12). Thus for MnF_2 the anharmonicity of the resonant mode itself gives a simple, satisfactory explanation of the temperature dependence of the absorption strength.

For a three-dimensional oscillator which would be appropriate for the alkali halide case, the first excited state is threefold degenerate but only one state is important for each polarization, thus

$$I(T)/I(0) = [1 - \exp(-\hbar\omega/kT)]^4 . \tag{6.25}$$

Line strengths have been measured for a number of resonant modes, namely: $KBr:Li^+$ and $KI:Ag^+$ (Takeno and Sievers, 1965); $NaCl:Cu^+$ (Weber and Nette, 1966; Weber and Siebert, 1968; Alexander *et al.*, 1970); $NaI:Cl^-$ (Clayman, 1971); and $CsBr:Tl^+$ and $CsI:Tl^+$ (Genzel *et al.*, 1969; Prettl and Siep, 1971).

The temperature dependences of the resonant mode absorption of $CsI:Tl^+$ and $CsBr:Tl^+$ are shown in Figure 116. For both systems the absorption strength is nearly independent of temperature. Figure 117 shows a plot of the absorption strength versus temperature for three other resonant mode systems, $KBr:Li^+$, $NaCl:Cu^+$, and $KI:Ag^+$. The solid line for a simple three-dimensional harmonic oscillator $0 \rightarrow 1$ transition, as given by Eq. (6.25). The temperature scale has been normalized by setting $\hbar\omega = kT_0$. The temperature dependence of the $NaCl:Cu^+$ resonance is very similar to that observed for $CsI:Tl^+$.

For these systems it appears that the explanation in terms of the resonant mode anharmonicity does not work except perhaps for $KBr:Li^+$ and $NaI:Cl^-$. (Previously we have noted that such a model was successful in explaining the temperature dependence of $NaI:Cl^-$.) Since stress-induced shifts of these systems, which give another measure of the anharmonicity, suggest that the resonances in Fig. 117 are rather similar, it is somewhat unsatisfactory to accept an explanation for $KBr:Li^+$ which fails for the other two. Also there is no evidence for a resolved $1 \rightarrow 2$ transition in any of these systems. It appears that anharmonicity of the resonant mode itself is not the answer for these three alkali halide modes.

The problem of anharmonic coupling of the resonant mode to the lattice modes has been investigated by Alexander *et al.* (1970). They assumed a linear coupling of the resonant modes to a Debye spectrum of modes. The assumption implicit here is that the linear coupling to dynamic strains (phonons) is the same as to the static strain of the same symmetry. Using Eq. (5.14) they found that the measured strain coupling coefficients were a factor of 10 too small to explain the temperature dependence data. Thus it appears that this model cannot explain the temperature dependence either.

Alexander *et al.* (1970) were the first to realize that linear coupling *between* resonant modes of different symmetries was the appropriate anharmonic coupling mechanism for understanding the anomalous temperature-dependent properties of infrared-active resonant modes. It was previously inferred from thermal con-

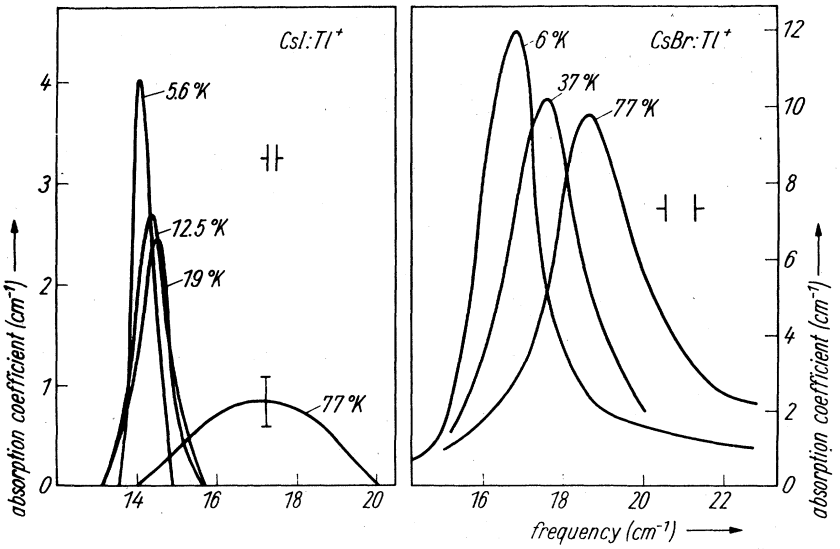

FIG. 116. Temperature dependences for Tl^+ resonant modes in CsI and CsBr. The impurity concentrations were 1.5×10^{-2} mole% Tl^+ in CsI, and 6.4×10^{-2} mole% Tl^+ in CsBr. After Prettl and Siep (1971).

ductivity measurements that an impurity, can induce an infrared-active resonant mode, as well as inactive modes of similar frequency. Such modes were observed in KI:Ag^+ (Bauman and Pohl, 1965), KBr:Li^+ (Bauman *et al.*, 1967), and NaCl:Cu^+ (Caldwell and Klein, 1967).

Assuming one even mode with resonant frequency ω_E as the appropriate coupling agent, Alexander *et al.* (1970) have found that the strength of the infrared-active resonant mode is given by

$$I(T) = \exp(-P_E) Z_0(C_E), \tag{6.26}$$

where

$$P_E = S_E(2\bar{n}_E + 1),$$

and

$$C_E = S_E \operatorname{csch}(\hbar\omega_E/2kT).$$

In Eq. (6.26), $\bar{n}_E$ denotes the equilibrium value of the even resonant mode occupation number at temperature T, and S_E is a dimensionless linear coupling parameter. Alexander *et al.* have calculated the S_E from the strain coupling coefficients by assuming that the even mode involves motion only of the defect nearest neighbors, so that one is dealing with one of the A_{1g}, E_g, T_{2g} modes of an octahedron. Making an identification between the strain at the defect site and the displacement of the nearest neighbors, they calculate the way the energy of the resonant mode transition depends on the even-mode normal coordinates. This in turn gives the following values for S_E, corresponding to an even mode of particular symmetry, namely,

$$S(A_{1g}) = \frac{3A^2}{4m\hbar\omega_A^3 a^2}, \tag{6.27}$$

$$S(E_g) = \frac{6B^2}{m\hbar\omega_E^3 a^2}, \tag{6.28}$$

and

$$S(T_{2g}) = \frac{2C^2}{3m\hbar\omega_T^3 a^2}, \tag{6.29}$$

where m is the mass appropriate to the even mode, and a is the nearest-neighbor distance. For each of the three systems considered there is some measure of agreement with the value of S_E from the temperature-dependent data.

This linear coupling model also produces sidebands at $\omega \pm \omega_E$ with strength $\sim S_E$ compared to the resonant mode strength. Such sidebands have been observed by Kirby (1971) and Montgomery and Kirby (1971). Kirby (1971) has attempted to fit the temperature dependence of the line strength of the T_{1u} mode in KI:Ag^+. Using the values of the anharmonic coupling coefficients determined from the strengths of the combination bands, his perturbation calculation predicts that the integrated absorption strength of the T_{1u} mode at 15°K should be 66% of the low-temperature strength, while the experimentally determined number is 20%.

The even resonant modes can contribute to the scattering mechanism for line broadening and frequency shift since they are really many modes rolled into one, and excitations could be scattered from one normal mode to the others. In this limit the temperature dependence of the linewidth (which is the analogue of (5.27) is

$$\Delta\Gamma_{sc} = \beta \sinh^{-2}(T_E/2T), \tag{6.30}$$

while the temperature dependence of the center frequency (which is the analogue of (5.29) is

$$\Delta\omega_{sc} = \delta[\coth(T_E/2T) - 1]. \tag{6.31}$$

Alexander *et al.* (1970) have obtained good agreement over the entire temperature range studied for the linewidths and center frequencies of KBr:Li^+, NaCl:Cu^+, and KI:Ag^+. Thus there appears to be a great deal of internal consistency in the idea that the infrared-active resonant mode is coupled most strongly to other resonant modes of even symmetry. Although the temperature dependences have been described here under "Anharmonic Coupling to the Lattice," the current evidence for most infrared-active resonant modes is that such coupling is weak and the coupling to even-parity resonant modes determines the resonant modes anharmonic behavior.

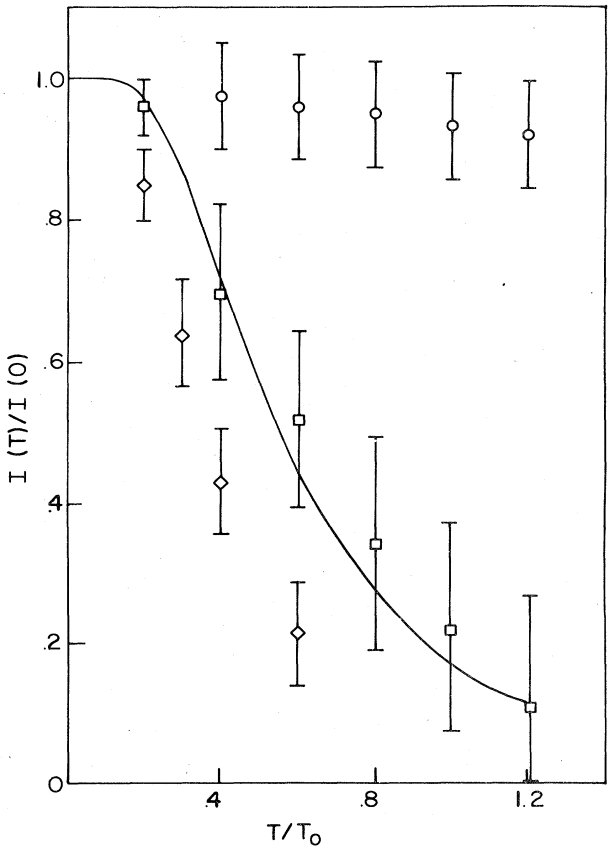

FIG. 117. Normalized absorption strength $I(T)/I(O)$ versus normalized temperature (T/T_0) for three resonant mode systems, where $kT_0 = \hbar\omega$. O—NaCl:Cu^+; □—KBr:Li^+; and ◇—KI:Ag^+. The curve is for the $0 \rightarrow 1$ transition of the three-dimensional oscillator model described by Eq. (6.25). After Alexander *et al.* (1970).

5. Resonant pair modes

A number of defect systems exhibit resonant pair modes when the impurity concentration is on the order of 1 mole %. Raman scattering from silver pairs in NaCl were first observed by Möller *et al.* (1970). A

sodium pair mode has been observed in the far-infrared absorption spectrum of KCl by Templeton and Clayman (1971), and a fluorine pair mode in NaCl by Becker and Martin (1972). The frequencies associated with these and other pair modes are given in Table V1.1.

A large number of pair-induced resonant modes have been associated with fluorine pairs in NaCl. A high-resolution spectrum of this system is shown in Fig. 118. Kirby (1969) showed that these absorption lines did not change with electric field and hence were not tunneling transitions. Becker and Martin (1972) have found that the five lowest-frequency lines in Fig. 118 vary quadratically with the impurity concentration. They have concluded that two pair configurations are required to explain all of the absorption lines. One configuration has the impurities aligned along the [110] axes (D_{2h} symmetry) and the other has the impurities aligned along the [100] axes (D_{4h} symmetry). If only impurities themselves are assumed to vibrate appreciably, then the D_{2h} symmetry center will contribute three lines, and the D_{4h} symmetry center will contribute two lines.

Using the Green's function method with a nearest-neighbor force constant change, Haridason *et al.* (1973) have calculated the infrared-active and Raman-active pair modes for both of the configurations described above. With a weakened nearest-neighbor force constant, a qualitative identification of the infrared absorption lines has been possible. Five different Raman-active resonant pair modes are predicted for fluorine pairs but none have been observed to date.

The only positive identification of a pair mode symmetry has been made by Templeton and Clayman (1972). They applied uniaxial stress to KCl:Na single crystals along high symmetry directions and observed that the Na^+–Na^+ pair mode frequency shifted for polarizations parallel and perpendicular to the stress direction. From the observed shifts and the known quadratic dependence on the line strength on Na^+-ion density, the site symmetry of the pair mode was deduced. The stress shift for the [100] oriented crystal is shown in Fig. 119 for two different polarizations. There are seven different possible symmetry systems associated with a defect pair in a cubic crystal. For each of the symmetry systems, Kaplyanskii (1964) has tabulated the splitting patterns and intensity ratios of the various components for stress applied to the crystal along the [100], [110], and [111] directions. A comparison with the measured splitting patterns enabled Templeton and Clayman (1972) to make the tetragonal assignment. Another interesting feature of Fig. 119 is the kink in the frequency shift versus stress graph. A similar kink for the [110] oriented crystal was found, but not for the [111] oriented crystal. The smaller slope at large strain suggests that the lattice has undergone some change which stiffens the lattice around the pair.

Jaswal (1972) has approximated the KCl:Na^+ pair system by a molecular model consisting of two Na^+ ions and their 15 nearest neighbors vibrating in an otherwise rigid lattice. The reduction in the force constant required to fit the mode frequency of Templeton and Clayman was in fair agreement with the results of a first-principles calculation by Templeton (1973) of the lattice relaxation around the Na^+ ions.

Resonant pair modes have also been studied in NaBr:Li^+ (Templeton, 1973), where an isotope has been identified in NaCl:K^+ F^- (Ishizama *et al.*, 1972), where a mode at 16.5 cm^{-1} was measured, and in KI:Cl^- (Ward and Clayman, 1974).

6. Resonant modes in other ionic crystals

Resonant modes have been observed in $KMnCl_3$: Br^- (Sievers, 1966), in MnF_2 doped with europium (Alexander,

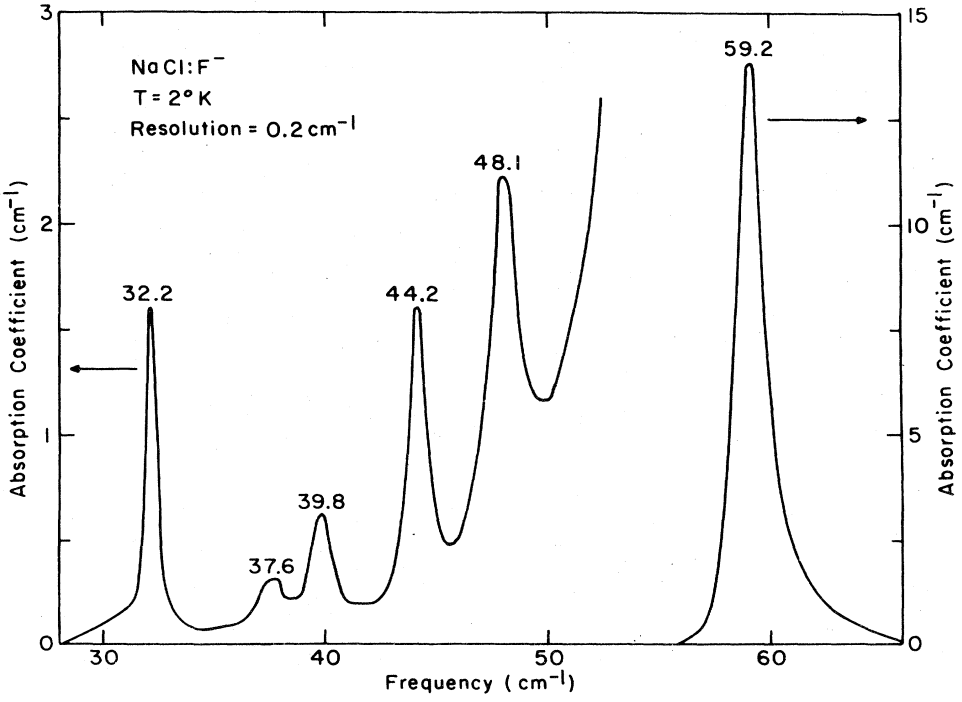

FIG. 118. Far-infrared absorption spectrum of NaCl with 0.08 mole% fluorine. The absorption by isolated fluorine ions occurs at 59.2 cm^{-1}. All other absorption lines are associated with fluorine pairs. The sample temperature was 4.2 °K. After Kirby (1969).

1967), and in $CaF_2:Y^{3+}$ (Campbell *et al.*, 1975). Impurity-induced absorption is observed for MnF_2 doped with any rare earth ion. Crystals doped with La, Nd, Sm, Eu, Gd, Tb, Ho, Er, Tm, and Yb have been studied between 5 and 50 cm^{-1}. Figure 120 (a) summarizes the experimental results (Alexander, 1968). The width of the bars is proportional to the linewidth observed. The absorption associated with the antiferromagnetic resonance of the host is not shown. Also not shown in Fig. 120(a) is the continuous absorption, which roughly follows the density of unperturbed phonon states.

Here Nd, Gd, Tb, Dy, Ho, and Er are expected to be present as +3 ions in MnF_2. Sm, Eu, Tm, and Yb may be present as either +2 or +3 ions. In these latter systems, no information exists as to the valence state of the rare earth impurity.

The spectra associated with Tm and Eu in MnF_2 are shown in Fig. 120(b). $MnF_2:Eu^{2+}$ has been the easiest spectrum to interpret. Two modes have been observed (also see Table V1.1). Both modes are nonmagnetic and have been identified with lattice resonant modes. The ratio of the absorption strengths for the two lines is found to vary from crystal to crystal. Also no polarization effect has been observed for those two lines. These experimental results suggest that more than one type of center is being observed.

The Eu^{2+} free ion is in a $^8S_{7/2}$ state, so the ion ground state will not be greatly influenced by the local crystal field and there will be no low-lying electronic states. The Eu^{3+} free ion is in a $^7F_0$ state, so the ground state is nondegenerate and cannot be split by the local crystal field. The next electronic state is several hundred wave numbers above the ground state, so again there are no electronic transitions below 100 cm^{-1}. The absorption lines which stem from lattice modes must be associated with more than one kind of center. Presumably, both Eu^{2+} and Eu^{3+} are present. The Eu^{3+} ion must have a compensating vacancy close to the Eu^{3+} site producing a dramatic effect upon the Eu^{3+} resonant mode frequency.

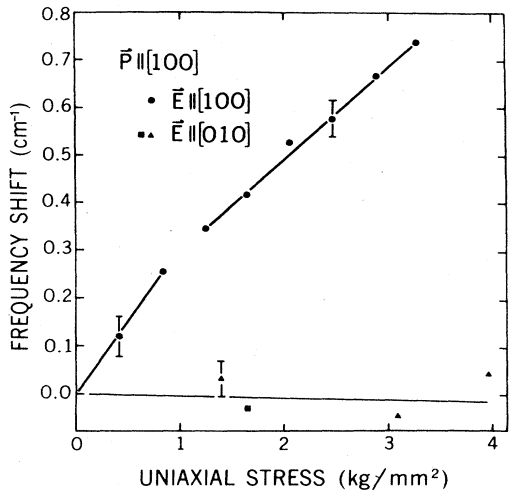

FIG. 119. Frequency shift versus stress for pair modes in KCl:NaCl. The stress is along the [100] crystal direction for light along [100] and [010]. The unstressed line frequency is 43.92 cm^{-1}. After Templeton and Clayman (1972).

Because of the similarity in chemical properties and mass of all the rare earth ions, defect-induced modes are expected to be related throughout the series but with the added complication that low-lying electronic states will also occur in this frequency range. We can expect that interactions between electronic states and resonant modes will be explored in systems such as these by tuning the electronic states with an external magnetic field.

C. Tunneling states in alkali halides

A number of defect-host combinations produce isolated dipoles in alkali halide crystals. The impurities divide naturally into two groups: (1) those which have intrinsic dipoles such as OH^-, CN^-, or NO_2^-, and (2) those in which the defect–host combination itself pro-

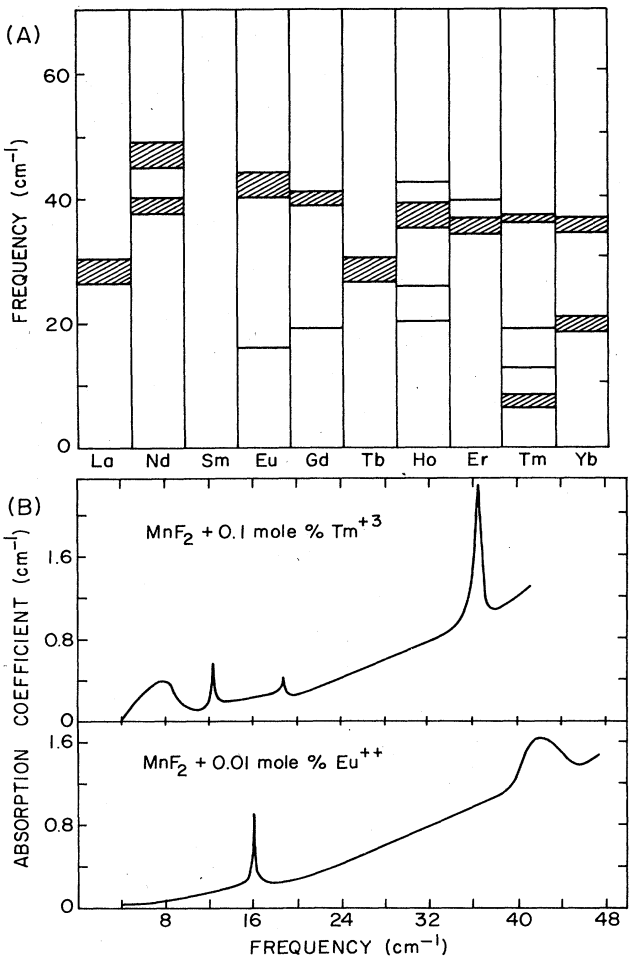

FIG. 120. (a) Schematic representation of impurity-induced absorption lines in MnF_2 doped with various rare-earth ions. The 5 to 50 cm^{-1} region was investigated. After Alexander (1968). (b) *Upper:* The impurity-induced absorption spectrum of $MnF_2:Tm^{3+}$ at 4.2 °K. Three sharp absorption lines are found at 12.42± 0.1 cm^{-1}, 18.60± 0.1 cm^{-1}, and 36.5± 0.1 cm^{-1}. By 34 °K these lines are no longer observable. *Lower:* The impurity-induced absorption spectrum of $MnF_2:Eu^{2+}$ at 4.2 °K. The sharp line is observed at 16.05± 0.1 cm^{-1}. The antiferromagnetic resonance of the host MnF_2 is not shown. After Alexander and Sievers (1967).

duces an effective dipole such as for Li^+ in KCl, F^- in NaBr, or Ag^+ in RbCl. A number of reviews on this subject have already appeared in the literature. Smoluchowski (1969) considered the experimental and theoretical progress on the properties of off-center substitutional ions up through (1968), and Krumhansl (1969) outlined the problems associated with interacting tunneling systems. A discussion of the vibrational sideband data which supports the models of librating molecules in alkali halide crystals has been given in a review by Sherman and Wilkinson (1973). However, the most complete review on tunneling states associated with molecular impurities and off-center substitutional impurities in alkali halides has been published by Narayanamurti and Pohl (1970). Since this latter review was completed a number of studies on off-center ions have appeared in the literature. In addition a great deal of work on substitutional molecular dipoles is in progress (Beyeler, 1974a, b; Lüty, 1974a, b, c). As our review is constructed to complement the review by Narayanamurti and Pohl (1970) it will reflect the bias of the more recent published work toward off-center ions. For completeness, however, the frequencies of both low-lying states of ions and of molecules are recorded in Table VI.1.

1. The statics of off-center ions

Lombardo and Pohl (1965) were the first to observe an electrocaloric effect for an ionic crystal doped with a monatomic impurity, namely, $KCl:Li^+$. As a similar effect previously had been observed in $KCl:OH^-$ (Kuhn and Luty, 1965), Lombardo and Pohl (1965) and also Sack and Moriarty (1965) suggested that the small Li^+ ion might not be stable at the normal lattice site. It would sit off-center in the cage of the nearest neighbors, thus providing a dipole moment. This hypothesis has proved to be correct (Narayanamurti and Pohl, 1970).

The electrocaloric effect, which is the electric analogue of adiabatic demagnetization, is still the most sensitive probe for determining whether or not mobile off-center ions exist in crystals. The technique is to apply a large electric field to the crystal while it is in thermal contact with a heat reservoir, then remove first the reservoir and second the electric field, in that order, and measure the associated temperature drop in the sample due to paraelectric cooling.

A search for off-center ions for a large number of defect–lattice combinations has now been made using paraelectric cooling as a test. The results are summarized in Table VI.8. Most of the systems give negative results. So far only three systems, $KCl:Li^+$, $NaBr:F^-$, and $RbCl:Ag^+$, appear to contain mobile off-center defects.

Matthew (1965) showed qualitatively that when a small impurity ion replaces a large host ion in an alkali halide the large decrease in the repulsive potential can lead to an instability at the normal lattice site (see Sec. VI.B). More detailed calculations by Wilson *et al.* (1967) and Quigley and Das (1969) indicate that there may be exceptions to this rule, since the actual position of the ion depends primarily upon a delicate balance of repulsive and polarization energies. A large repulsive interaction tends to keep the ion in place, while a high polarizability will tend to move it off the normal lattice site.

The procedure for theoretically determining the off-center susceptibility of a particular defect–lattice combination is straightforward. It involves a calculation of the variation of the interaction energy for small displacements. The total energy of the crystal depends upon both the displacements of the impurity and the displacements of the host ion from their lattice sites. The sign of the determinant, made up from second derivatives of the energies with respect to the impurity displacement and host ion displacement, indicates whether a particular configuration is stable or not. If all ions except the impurity are permitted to relax then the total energy of the crystal can be minimized and the host ion displacements determined. The sign of the determinant calculated for these host ion displacements and a small impurity displacement along a major crystallographic direction indicates whether the impurity is stable on the ideal lattice site in a relaxed configuration.

The most elaborate calculation has been carried out by Wilson *et al.* (1967). Up to 24 displacement parameters were employed to account for relaxation of the surroundings of the impurity. This enabled the experimentors to allow the impurity and 26 additional ions (the first-, second- and third-nearest neighbors) to relax. The polarization energy of an additional 66 ions was calculated, as well as the polarization energy of the relaxed ions. Their predictions for off-center behavior are compared with the paraelectric cooling results in Table VI.8. The correlation is about 50%. One explanation for this poor agreement between theory and experiment is that the impurity ion could be "frozen" in an off-center position. At least in one case, $KBr:Li^+$, this has been shown by stress measurements on the resonant mode not to be the case (Nolt and Sievers, 1968).

Quigley and Das (1967, 1969) have also calculated the off-center behavior of $KCl:Li^+$ and $KBr:Li^+$. They allowed the impurity and the nearest-neighbor positions to vary and assumed the other ions to be held rigid and unpolarizable. They performed minimum energy configuration calculations for a range of lattice parameters and found that the configurations were rather sensitive to the particular lattice parameter chosen. We show their calculated values for the energies of the impurity and its nearest-neighbor cluster as a function of [111] displacement, ζ, of the impurity ion in Fig. 121. For $KBr:Li^+$ at 2°K, the central barrier between diametrically opposite [111] wells is 2 meV, and the barrier between adjacent wells is 0.7 meV. Thus in KBr the Li^+ ion is not even quasilocalized in an off-center well, since the ion has enough zero point energy (~2 meV) to overcome all barriers. Plots of the $KCl:Li^+$ configuration energy as a function of the impurity displacement ζ are shown in Fig. 121(b) for four KCl lattice values. The figure illustrates that the off-center well depth at 2°K is only one-third of the room temperature depth. Although the 2°K $KCl:Li^+$ configuration is not as strongly off-center as the room temperature configuration, the well depth is still large enough to give an off-center configuration, in qualitative agreement with experiment.

Quigley and Das (1969) also predicted that 7 kbar hydrostatic pressure would be sufficient to establish a

strong on-center KCl:Li^+ configuration. The experimental measurements on the pressure dependence of the isotope effect by Kahan *et al.* (1975) agree with this prediction. From all the evidence it now appears that the introduction of low-temperature lattice constants into the calculations by Wilson *et al.* (1967) would have produced better agreement with the paraelectric cooling results in Table VI.8.

2. Dynamics of off-center ions

The important features of the low-lying vibrational states associated with off-center ions are easily enumerated with a simple one-dimensional model in which we have tunneling between two wells. The impurity is assumed to move in a double-well truncated harmonic oscillator potential, Fig. 122(a), where

TABLE VI.8. Off-center (?) ions in alkali halide crystals.

System	Theory (References) [a]	Paraelectric cooling (References) [a]
KCl : e^-	···	No (1)
KBr : H^-	···	No (1)
NaCl : Li^+	Yes (2)	No (3)
KCl : Li^+	Yes (2, 4)	Yes (1)
NaBr : Li^+	Yes (2)	No (5)
KBr : Li^+	Yes (2), No (5)	No (6, 3)
RbCl : Li^+	···	No (3, 7)
NaCl : F^-	···	No (5)
KCl : F^-	No (2)	No (6)
NaBr : F^-	Yes (2)	Yes (5, 6)
KBr : F^-	No (2)	···
RbCl : F^-	···	No (5)
KCl : Na^+	No (2)	···
RbCl : Na^+	···	No (7)
KCl : Rb^+	···	No (1)
RbCl : K^+	···	No (5)
NaCl : Cu^+	Yes (8)	No (3)
KCl : Cu^+	Yes (8)	No (5, 3)
KBr : Cu^+	···	No (5)
RbCl : Cu^+	Yes (8)	No (5)
RbBr : Cu^+	Yes (8)	···
NaCl : Ag^+	No (8)	···
KCl : Ag^+	No (8)	No (1)
RbCl : Ag^+	Yes (8)	Yes (9, 10)
RbBr : Ag^+	No (8)	No (9, 10)
RbI : Ag^+	···	No (5)
CsBr : Na^+	···	No (3)

[a] The references for Table VI.8 are the following:

1. Lombardo, G., and R. O. Pohl, 1965, Phys. Rev. Lett. **15**, 291.
2. Wilson, W. D., R. D. Hatcher, G. J. Dienes, and R. Smoluchowski, 1967, Phys. Rev. **161**, 888.
3. Kapphan, S., 1970, Ph.D. Thesis, University of Utah (unpublished).
4. Quigley, R. J., and T. P. Das, 1969, Phys. Rev. **177**, 1340.
5. Rollefson, R. J., 1972, Phys. Rev. B **5**, 3235.
6. Lombardo, G., and R. O. Pohl, 1966, Bull. Am. Phys. Soc. **11**, 212.
7. Lombardo, G., 1971, Ph.D. Thesis, Cornell University (unpublished).
8. Wilson, W. D., R. D. Hatcher, R. Smoluchowski, and G. J. Dienes, 1969, Phys. Rev. **184**, 844.
9. Kapphan, S., and F. Luty, 1968, Solid State Commun. **6**, 907.
10. Kapphan, S., and F. Luty, 1972, Phys. Rev. B **6**, 1537.

$$V=\begin{cases}\frac{1}{2}m\omega^2(x+x_0)^2, & x<0,\\ \frac{1}{2}m\omega^2(x-x_0)^2, & x>0,\end{cases} \tag{6.32}$$

where ω is the frequency of the particle in a single well and the rest of the lattice is assumed to be rigid. We express the lowest states as linear combinations of the ground states $|a\rangle$ and $|b\rangle$ of the unperturbed harmonic oscillators. The energies are given by the secular equation

$$\begin{vmatrix} E_0-E & H_1-SE \\ H_1-SE & E_0-E \end{vmatrix}=0,$$

where $E_0=\langle a|H|a\rangle=\langle b|H|b\rangle$, $H_1=\langle a|H|b\rangle$ and $S=\langle a|b\rangle$. We get one symmetric and one antisymmetric solution, with energies

$$E_\pm=(E_0\pm H_1)/(1\pm S). \tag{6.33}$$

If the barrier between wells is large compared to the zero-point energy, then $S\ll 1$. In this case the solution can be simplified to

$$E_{g\pm}\approx\hbar\omega\pm\delta, \tag{6.34}$$

where

$$\delta=\hbar\omega x_0(m\omega/\pi\hbar)^{1/2}\exp[-(m\omega/\hbar)x_0^2], \tag{6.35}$$

and 2δ is the energy splitting due to tunneling.

With a perturbation, Δ, applied so that the two wells become inequivalent, the potential has the form shown in Fig. 122(b). The secular equation can be written as

$$\begin{vmatrix} E_{g+}-E & -\Delta \\ -\Delta & E_{g-}-E \end{vmatrix}=0,$$

and the energy splitting ϵ between the two lowest levels is

$$\epsilon=2(\delta^2+\Delta^2)^{1/2}. \tag{6.36}$$

The effect of a large perturbation, $\Delta\gg\delta$, is to nearly localize the particle in one well, with only a small fraction $\delta/2\Delta$ of the wave function in the other well and the energy difference between the two states determined entirely by the perturbation.

Gomez *et al.* (1969) have generalized this model to the three-dimensional problem. Three types of off-center minima are considered: (1) six wells along the six [100] axes (XY_6), (2) eight wells along the eight [111] axes (XY_8), and (3) twelve wells along the twelve [110] axes (XY_{12}). Each well is assumed to have a three-dimensional oscillator form. Thus a given well can be described by its three curvatures or force constants and its distance r_0 from the central lattice site. Each well by itself corresponds to a three-dimensional harmonic oscillator. If the wells were infinitely deep then these

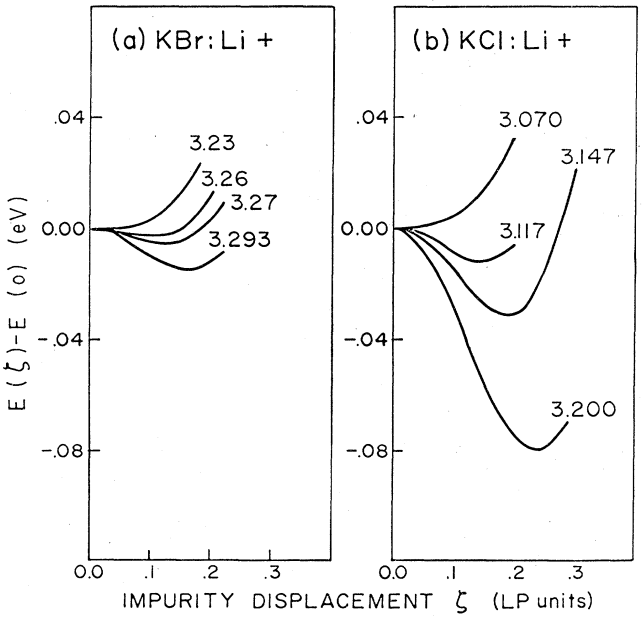

FIG. 121. Energies of the impurity and its nearest-neighbor cluster as a function of the [111] displacement ζ of the impurity ion. The energies are measured relative to those of the corresponding centrosymmetric configurations ($\zeta=0$). (a) KBr:Li^+ energies for the four lattice-parameter values indicated (in units of Å). 3.293 is the room temperature lattice parameter, 3.26 is the 2 °K lattice parameter. (b) KCl:Li^+ energies for the four lattice parameters indicated. 3.147 corresponds to 300 °K, while 3.117 corresponds to 2 °K. After Quigley and Das (1969).

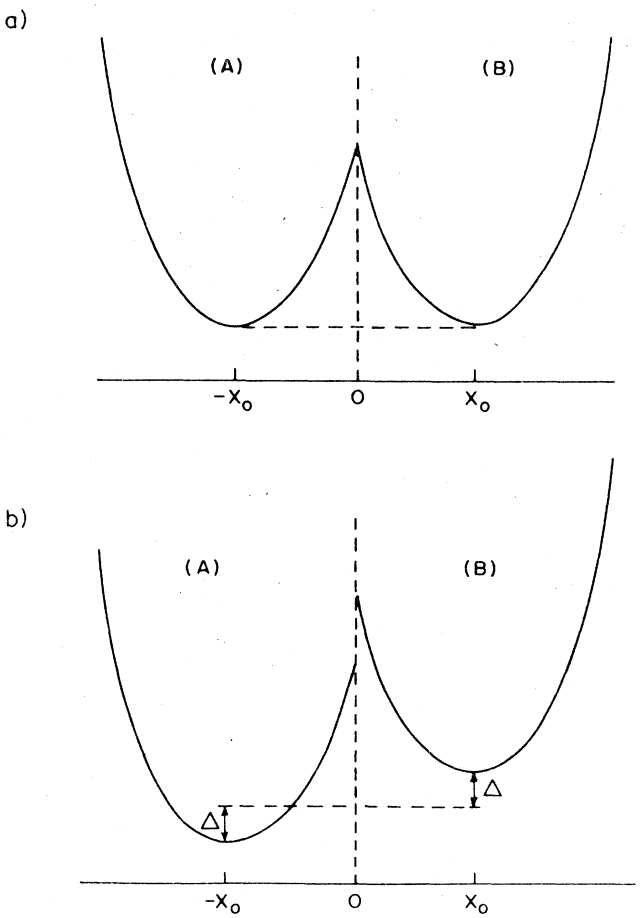

FIG. 122. Double-well harmonic oscillator for tunneling calculation. (a) Wells equivalent (b) wells inequivalent. After Rollefson (1972).

individual well eigenstates would represent the eigenstates of the off-center ion and there would be n-fold degeneracy (because of the $n=6$, 8, or 12 identical wells of the XY_6, XY_8, and XY_{12} models). These individual well states are called pocket states. If the wells are not infinitely deep, the actual states of the system will be linear combinations of the product states. These linear combinations must transform according to the irreducible representation of the O_h group. The important feature of the three-dimensional case is that more energy levels occur than for the one-dimensional case. This model is usually referred to as the "GBK model."

The kinds of experiments which can be used to probe the potential can be most easily visualized with the one-dimensional model. From (6.35), the transition energy varies exponentially with the impurity mass and also with the lattice constant, so isotopic mass substitution and hydrostatic pressure are important variables in exploring the potential. From (6.36), we see that uniaxial stress and dc electric field can be used to tune the transition energy. With these parameters the symmetry of the defect and its effective elastic and electric dipole moment can be determined.

a. NaBr:F⁻

Rollefson (1972) has made a systematic study of the NaBr:F⁻ system using specific heat, paraelectric cooling, thermal conductivity, and dielectric relaxation measurements. As yet no optical experiments have been reported. He found from measurements of the dielectric constant under applied stress that the fluorine ion tunnels between potential minima displaced from the lattice site in the ⟨110⟩ direction. The low-temperature specific heat contribution is found to be much broader in temperature than that given by the GBK model of Gomez *et al.* (1967). In addition the relaxation rate of the impurity ion is at least three orders of magnitude slower in NaBr:F⁻ (10^5 sec^{-1}) than what had been previously observed in KCl:Li⁺ (Narayanamurti and Pohl, 1970). By taking into account the effect of dc lattice strains on the tunneling motion, Rollefson has obtained good agreement with the NaBr:F⁻ specific heat data. Thus NaBr:F⁻ represents a tunneling system in the limit of small tunneling probability, S, while KCl:Li⁺ is characteristic of a system with a large tunneling probability.

b. RbCl:Ag⁺

Controversial results have existed for some time on the properties of this lattice defect combination. Originally Dreybodt and Fussgaenger (1966) suggested that displaced Ag⁺ impurities could explain some features of the temperature dependence of the Ag⁺ uv absorption band in RbCl. Nolt (1967) measured the infrared absorption spectrum of RbCl:Ag⁺, finding three absorption lines at 21.3, 26.5, and 36.7 cm^{-1}. He also observed stress-induced dichroisms consistent with an off-center defect. The stress effect for the pressure along a [100] axis is shown in Fig. 123. The increase in the integrated absorption in the vicinity of 36 cm^{-1} is approximately twice as large as the decrease that occurs for the two lower-frequency lines.

Paraelectric cooling was first observed in RbCl:Ag⁺ by Kapphan and Lüty (1968). They concluded that the defect had a [111] orientation. Bridges (1972) observed the paraelectric resonance spectrum and obtained an upper limit of $\delta \sim 0.1$ cm^{-1} for the tunneling splitting.

The far-infrared dichroisms associated with stress and electric field were studied and analyzed by Kirby *et al.* (1970) and found to be compatible with a [110] defect rather than with a [111] defect. They found that the system can be understood in terms of the classical limit of the GBK model (Gomez *et al.*, 1967). Because the tunneling splitting is so small, it can be ignored in considering the far-infrared absorption spectrum. One treats the twelve equivalent pocket sites expected for a [110] defect. In each of these sites the vibrational motion of the impurity occurs in a local potential well of C_{2v} symmetry, so that the first excited state consists of

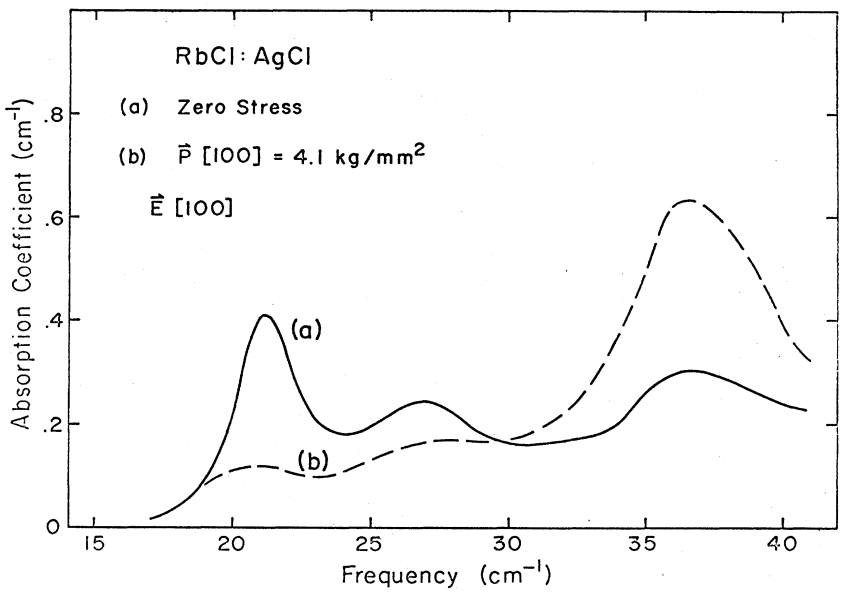

FIG. 123. Stress-induced dichroism in RbCl:Ag⁺. The increase in the integrated absorption in the vicinity of 36 cm^{-1} is approximately twice as large as the decrease that occurs for the two lower-frequency lines. The sample temperature is 2 °K. After Nolt (1967).

three levels corresponding to A_1, B_1, and B_2 irreducible representations of the C_{2v} symmetry group. The optically active transitions between the ground state and these three excited state levels give rise to the three absorption lines. The direction of field- and stress-induced absorption changes in the three components of the far-infrared spectrum agree qualitatively with the expectation of reorientation dichroism of [110] oriented electric and elastic dipoles.

The details of the dynamics of the above paraelectric defect have been explored by Kapphan and Lüty (1972) using the electrodichroism of the Ag^+ uv absorption both in RbCl and in RbBr. The static electro-optic measurements reveal for both systems paraelectric behavior from [110]-oriented dipoles, with dipole moment values of 0.78 and 0.95 eÅ for RbCl:Ag^+ and RbBr:Ag^+, respectively. Measurements of the time-dependent electrodichroism after rapid changes of the electric field show the existence of two relaxation processes whose rates differ by several orders of magnitude. Figure 124 summarizes the results of a large set of experiments in which the electrodichroism time dependence of an optic band (A-band) was studied. An electric field along [100], [111], or [110] was switched on, then off, and decay curves measured for both RbCl:Ag^+ and RbBr:Ag^+ function of temperature. Each point was obtained from a time-dependent absorption curve by taking the time value at which the absorption had changed by $1/e$. The complex relaxation behavior can be quantitatively accounted for by a [110] dipole which is based on predominance of 90° reorientation over 60° reorientation. This behavior, which cannot be explained for a dipole in an octahedral crystal field, is attributed to dressing of the dipoles by a strong E_g lattice distortion, which allows easy rotation within a {100} plane, but inhibits the change of this plane by 60° dipole reorientation. The observed temperature and field dependence of the relaxation rates indicate reorientation by tunneling processes at $T > 5°K$, and classical thermally activated reorientation at higher temperature.

c. KCl:Li^+

The physical properties of the four-level tunneling multiplet in KCl :Li^+ have been reviewed by Narayanamurti and Pohl (1970). Some additional work has been completed since that time and will be discuss-

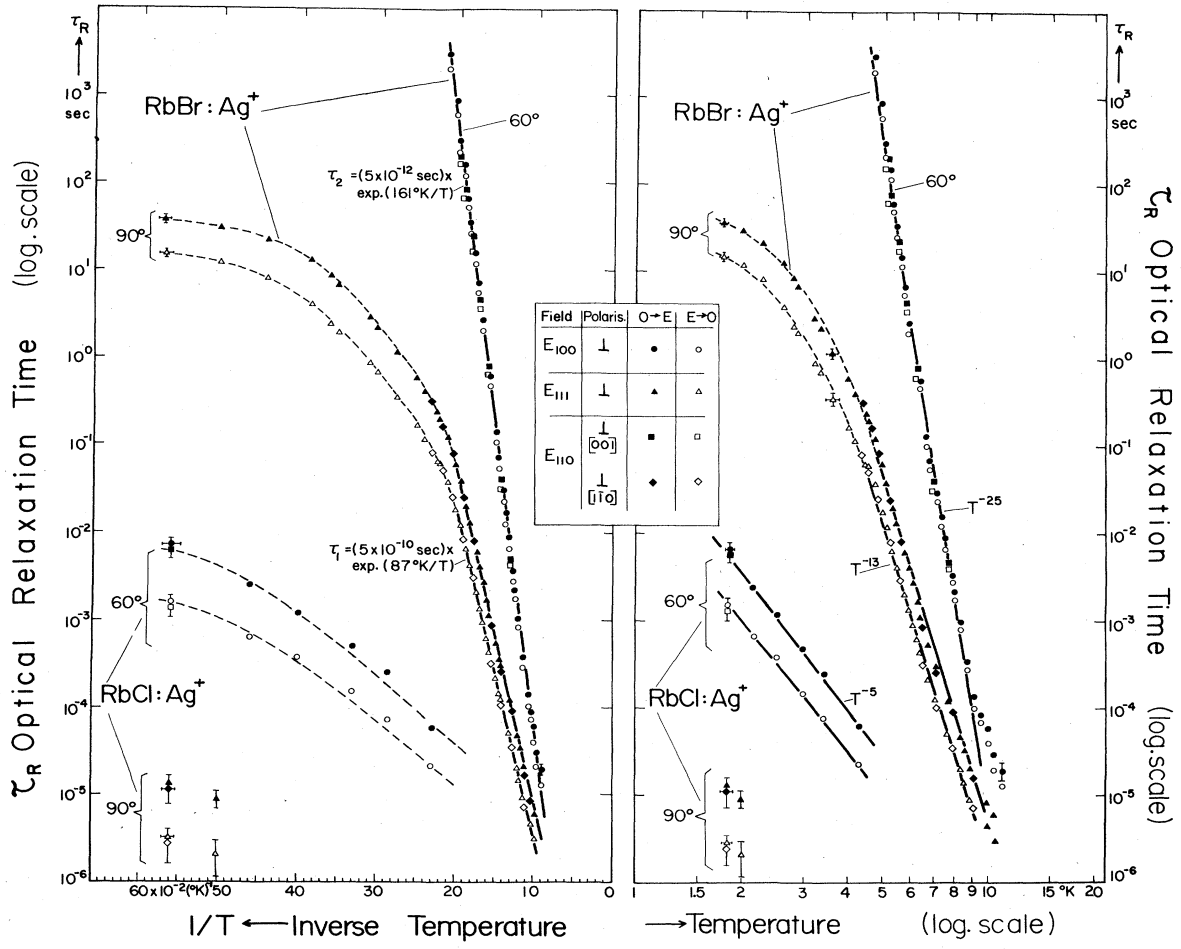

FIG. 124. Optical relaxation time of Ag^+ in RbBr and RbCl measured for different field directions and switching operations, as indicated, as a function of temperature, plotted logarithmically against $1/T$ (left-hand side) and against $\ln T$ (right-hand side). During temperature variation, the electric field strength was adjusted to keep approximately a constant Boltzmann factor over the whole range ($pE/kT = 2.0 \pm 0.05$ for RbBr, and $pE/kT = 3.0 \pm 0.7$ for RbCl). After Kapphan and Lüty (1972).

ed here. Extending the work of Alderman and Cotts (1970) on the stress-induced quadrupole splitting of ^{7}LiNMR in KCl, Irwin and Cotts (1971) measured the electric-field-induced quadrupole splittings of the ^{7}LiNMR. The results are in agreement with the [111] tunneling model of Gomez *et al.* (1967), with eight equivalent off-center potential minima.

Larson and Silsbee (1972) investigated stress effects in the paraelectric resonance spectrum and found that the tunneling model with equal tunnel splittings adequately describes the experimental data. Kirby *et al.* (1970) measured the ^{6}Li and ^{7}Li infrared absorption spectrum for applied electric fields up to 130 KV/cm, producing tunneling transitions on the order of 10 cm^{-1}. In all cases they found that the tunneling levels are well described by the model of Gomez *et al.* (1967), assuming a Li^+ dipole moment of 1.14 eÅ for both ^{6}Li and ^{7}Li.

Hetzler and Walton (1970, 1973a, 1973b) have measured the energy spacing of the four-level tunneling multiplet with an ingenious phonon spectrometer. They find that the four energy levels associated with the multiwell potential consisting of eight wells in the [111] directions are not equally spaced, as had been previously assumed. If tunneling along the cube edge predominates, then equally spaced levels are to be expected; however, if tunneling along a face or body diagonal is important, the level spacing will not be equal. These experimental results were the first indication that tunneling through the body diagonal was important for KCl:Li^+.

Excited state transitions of the KCl:Li^+ system around 40 cm^{-1} were first observed by Sievers (1969). Kirby *et al.* (1970) have studied the temperature dependence and isotope effect of these excited states. The most surprising feature of the higher levels in KCl:Li^+ is that they show a *negative* isotope shift. The experimental data is shown in Fig. 125.

Kirby *et al.* have attempted to explain the double feature in the absorption spectra of Fig. 125(a) by assuming the symmetry of the local oscillator is C_{3v}. Under these conditions the oscillator cannot be characterized as spherical, so the resonant mode excited state is no longer triply degenerate. The excited state consists of two levels, a singlet A, and a doublet E. The next step in the analysis is to take into account tunneling of the impurity ion between the equilibrium sites. If the small tunneling rate (high barrier) approximation is also assumed to be valid for the resonant mode excited state levels, then the tunnel transitions are as shown in Fig. 125(b). This model explains some of the temperature dependence features of the absorption spectrum, but does not explain the negative isotope shift.

Harrison *et al.* (1968) have used the Devonshire model to describe the 40 cm^{-1} band. This model is equivalent to the resonant mode model if we consider only the energy levels in the ν_E excited state multiplet, in Fig. 125(b), presumably by assuming $\nu_A \gg \nu_E$. The use of the Devonshire model has an advantage, namely that it can take into account the changes in transition probability which occur because the excited state is not in the extreme tunneling limit. This model tends to make the isotope shift smaller, but it does not make it negative.

Pandey *et al.* (1973, 1974) have attempted to explain these results by introducing a model in which the far-infrared lines correspond to translational motion of the impurity in the matrix cage. Any departure from the single harmonic oscillator isotope effect they identify with coupling of the impurity motion to the lattice motion through the rotation–translation coupling effect (which is described in Sec. VII) and through the anisotropic part of the crystalline field. They are able to fit the observed transitions, but in addition predict another absorption line at 26.7 cm^{-1}. They claim this transition has been observed, but in fact no absorption line associated with isolated KCl:Li impurities has ever been reported in this frequency region (Kirby *et al.*, 1970; Kahan *et al.*, 1975).

The transition region where the Li^+ ion is at the normal lattice site in KCl has been studied by Kahan *et al.* (1975). The frequency shifts produced by hydrostatic pressure have been measured for both tunneling and excited state modes. The tunneling mode (1.15 cm^{-1} for ^{6}Li at zero strain) increases to 30 cm^{-1} at 1.1% strain. These results are shown in Fig. 126. A second line close in frequency to the tunneling line is identified with another transition within the tunneling multiplet, indicating that the four tunneling levels in the ground state manifold are not equally spaced, confirming the results of Hetzler and Walton (1970). The 40 cm^{-1} absorption band splits into three lines with increasing hydrostatic strain.

The isotope shift associated with the tunneling transition was also measured as a function of lattice strain and is shown in Fig. 127. For large strains the isotope shift in KCl:Li^+ is about the same magnitude, 8%, as has previously been found for KBr:Li^+ at zero strain. For KBr:Li^+ at high strain the isotope shift is less than 3% (Kahan and Sievers 1971).

In analyzing their results Kahan *et al.* (1975) note that the GBK model is inappropriate for handling states near or above the potential barrier, as it relies on a perturbation calculation employing the tunneling matrix element between adjacent wells. Instead they use the same double harmonic oscillator potential but calculate the energy levels directly. This potential fails to describe adequately the pressure dependence of the five absorption lines in Fig. 125, even at relatively low strains. The potential becomes too close to a harmonic oscillator too quickly to explain the higher-frequency lines as the potential is adjusted to the frequency of the tunneling mode. They find that it is possible to fit the data at zero strain with almost any double well potential by varying its parameters in an appropriate manner. The presence of a large barrier is much more significant than the details of the potential. They conclude that the more anharmonic square well with a square barrier is a better model, in that it fits the data over a larger strain interval.

The square well model breaks down when the strain is increased to 0.6%. The Li^+ ion in KCl is on-center by this point, having achieved the new configuration at roughly 0.5% strain. A detailed comparison of the experimental results for KCl:Li^+ and KBr:Li^+ demonstrates that KCl:Li^+ at 0.65% strain is almost identical to KBr:Li^+ at zero strain. The higher-frequency transitions in this limit correspond to overtone transi-

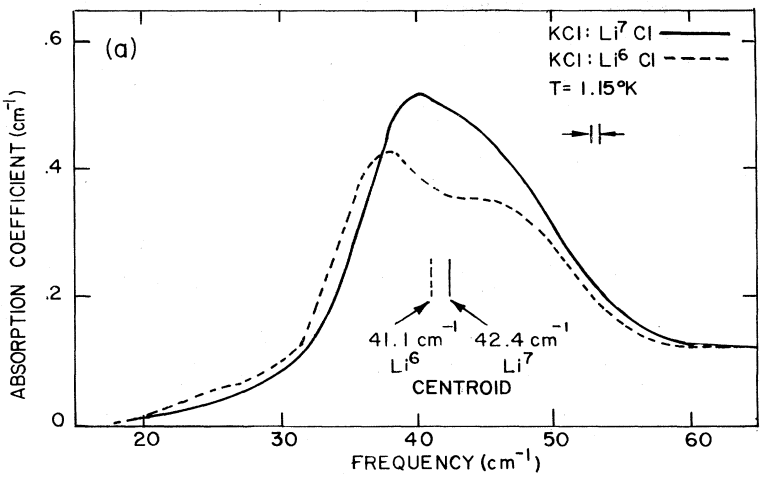

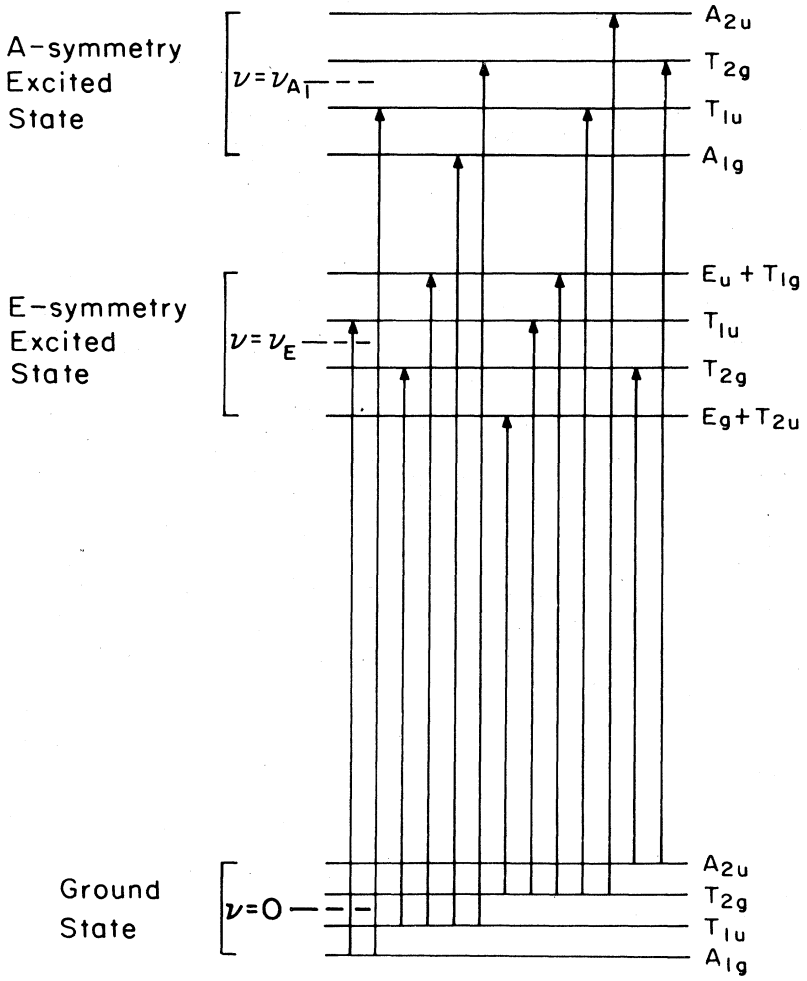

FIG. 125. (a) Isotope effect for the resonant mode excited state in KCl:^{6}Li; ^{7}Li. (b) Energy-level scheme resulting from the extension of the [111] tunneling model to the resonant mode excited states. The arrows indicate the optically active transitions. After Kirby (1969).

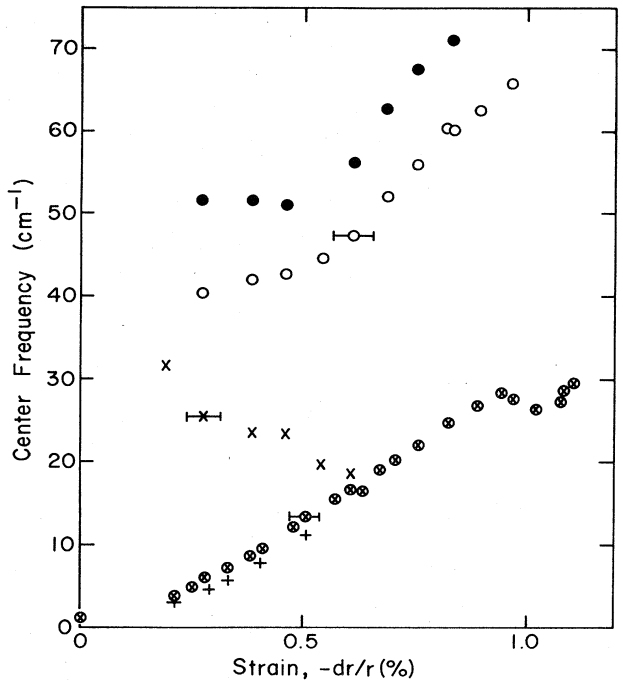

FIG. 126. Strain dependence of the KCl:^{6}Li absorption frequencies. The three high-frequency lines are not resolved at zero strain. The sample temperature is 4.2 °K. The error bars show the estimated error in the pressure measurement. After Kahan *et al*. (1975).

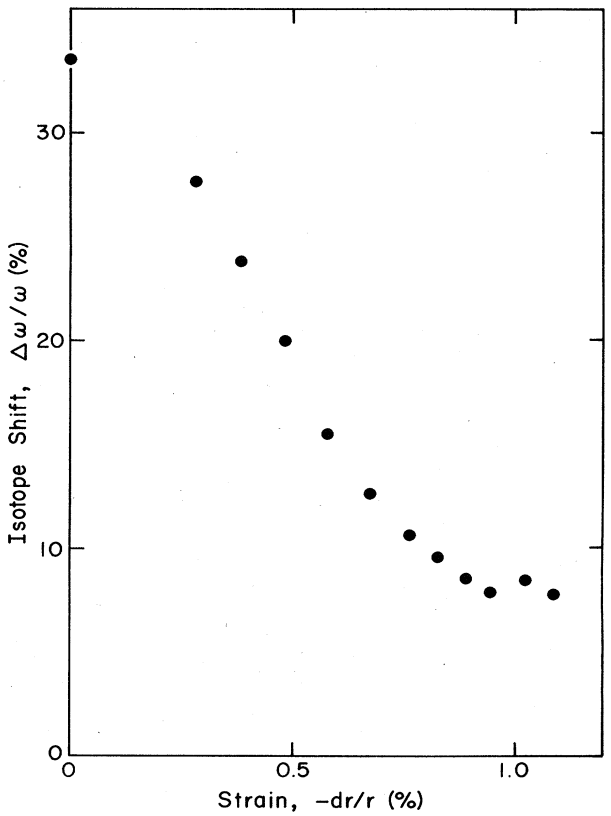

FIG. 127. Strain dependence of the KCl:Li^+ isotope effect for the lowest $A_{1g} \rightarrow T_{1u}$ transition. Here $\Delta\omega$ equals $\omega(^6\text{Li}) - \omega(^7\text{Li})$ and is divided by the average of the two frequencies on the ordinate. After Kahan *et al*. (1975).

tions of an anharmonic oscillator.

No model has been found which fits the isotope shift and the five transition frequencies over the entire strain interval. Apparently this combination of experimental probes is particularly sensitive to the specific form of the potential. Experiments such as these could provide a means of deriving a better semiempirical repulsive potential.

The influence of electric dipole interactions for high concentrations of Li in KCl has been studied by Fiory (1971). He observed a maximum in the dc dielectric constant due to the dipoles at a temperature which is proportional to the average interaction energy. A remnant polarization is observed at low temperatures which is caused by parallel-aligned pairs of dipoles experiencing a reorientation barrier. There is the possibility of polarization waves analogous to spin waves, although none have been observed; presumably they are heavily damped.

VII. IMPURITIES IN VAN DER WAALS CRYSTALS

A. Introduction

In 1954 Norman and Porter and also Whittle *et al.* proposed that argon and nitrogen be used as matrix supports for the isolating of molecules and photoproduction of free radicals. In the ensuing interval a great deal of effort has been directed along these lines. Although matrix isolation has emerged as a general method, its use in the spectroscopic determination of the structure of free radicals is still the most important chemical application. A complete discussion of the early studies can be found in Bass and Broida (1960). Substantial progress has been made in recent years in experimental techniques (reviewed by Hallam and Scrimshaw, 1973), infrared measurements on monomers, dimers, and trimers, etc. (reviewed by Hermann, 1969, and by Hallam, 1973), and in the theoretical understanding of static matrix effects on molecular normal modes (reviewed by Hermann, 1969, and by Barnes, 1973). In the large body of spectroscopic measurements described above, most deal with a disordered specimen, that is, the material under investigation was formed by condensing the molecular and the matrix gas on a cold substrate at liquid helium or liquid hydrogen temperature. The spectroscopic properties of the molecule stand out, but the dynamics of the matrix defect system is not observed. Our review will not treat this work, but instead concentrate on a small subset of papers where some evidence for local, band, resonant modes, or tunneling states, have been found.

The noble gases form face-centered-cubic crystals at low temperatures. This crystal binding is caused by the weak short-range attraction between these atoms with spherical charge distributions due to fluctuating multipole or van der Waals forces. The 6–12 potential given by

$$U_{ab} = 4\epsilon\left[\left(\frac{\sigma}{r_{ab}}\right)^{12} - \left(\frac{\sigma}{r_{ab}}\right)^{6}\right], \tag{7.1}$$

where ϵ and σ are the Lennard-Jones parameters, has been widely used as a representation of the attractive (van der Waals) and repulsive interactions, respectively, between two atoms separated by r_{ab}. Such a representation has been used by Horton and Leech (1963), Nijboer and DeWetle (1965), and Grindlay and Howard (1965) to calculate the dispersion curves and frequency spectrum of rare gas solids at 0 °K. Neutron scattering techniques have been used to measure the phonon dispersion relations for a number of noble gas solids. Measurements have been made on the dispersion curves of krypton by Daniels (1967); of argon by Egger *et al.* (1968) and Batchelder *et al.* (1970); of neon by Leake *et al.* (1969); and of helium by Minkiewiez *et al.* (1968).

The density of states for argon calculated from the results of the inelastic neutron scattering of Batchelder *et al.* (1970) is shown in Fig. 128(a). Their dispersion curve measurements were consistent with a Lennard-Jones potential where the parameters were determined entirely from other macroscopic measurements on argon.

B. Monatomic impurities

Jones and Woodfine (1965) first investigated the far-infrared absorption in solid argon containing the heavier atoms krypton or xenon as an impurity. They used samples up to 25 cm in path length, condensed from the vapor in low-temperature absorption cells. Between 20 cm^{-1} and 140 cm^{-1} they found some frequency-independent absorption in pure argon, which they attributed to scattering at bubbles or grain boundaries, but there was

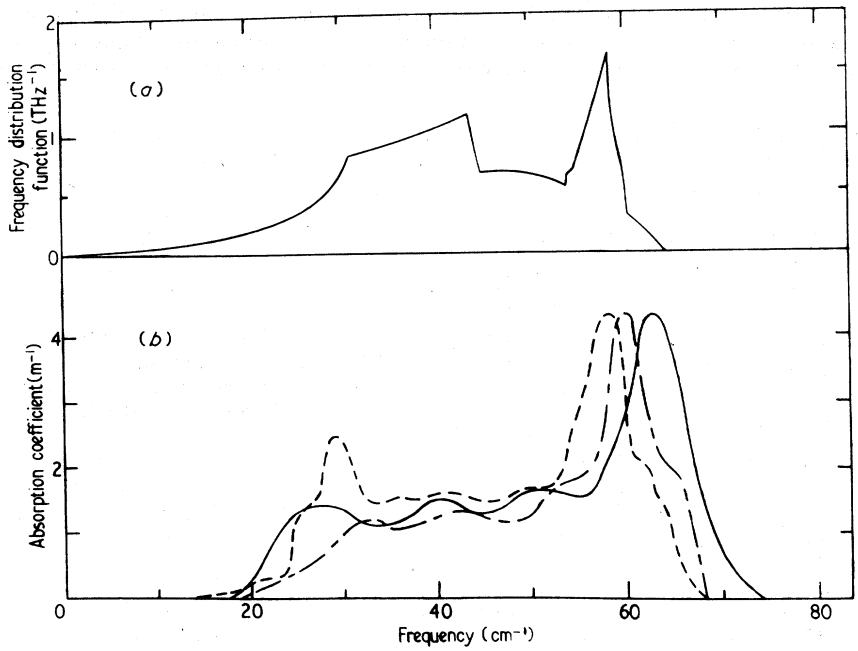

FIG. 128. (a) Density of states calculated from the results of inelastic neutron scattering data. After Batchelder *et al.* (1970) and Keeler and Batchelder (1972). (b) Absorption coefficient of argon doped with 1% krypton at 2 °K. Solid curve experimental data, Keeler and Batchelder (1972); dashed curve, Hartmann and Elliott (1967); dot-dash curve, Martin (1967).

no selective absorption attributable to two-phonon or multiphonon processes or to defect-induced absorption caused by vacancies. However, in argon containing fractions of $\frac{1}{2}$ to 2% krypton or $\frac{1}{2}$% xenon there was absorption distributed over a broad frequency region around 60 cm^{-1}. The absorption strength was roughly proportional to the amount of impurity present, and larger for the heavier impurity. These workers encountered considerable difficulty in growing and cooling the large transparent specimens required for far-infrared transmission studies. More recently, measurements have been made on specimens grown at high pressure by Obriot *et al.* (1970). Quantitative comparison of their results with the theoretical models is made difficult by the elevated temperature of their measurements (77°K). Finally, Keeler and Batchelder (1972) have measured the far-infrared absorption in solid argon with krypton and neon impurities. The impurity-induced absorption coefficient for 1% krypton in argon is shown in Fig. 128(b). A comparison with the density of states in Fig. 128(a) illustrates that the impurity produces a weak infrared activation of the host phonon spectrum due to the difference in polarizability of the defect and host atom.

Detailed calculations of the impurity-induced absorption in rare gas matrices were first made by Hartmann and Elliott (1967), who treated both the lattice and the defect in the shell model approximation. They did not change the nearest-neighbor force constant of the defect, but only its core shell force constant and its mass. Their calculated absorption curve is given by the dashed curve in Fig. 128(b). Martin (1967) has calculated the absorption coefficient for Ar:Kr by using a shell model in describing the lattice dynamics of the host atoms. The substitutional defect differs explicitly in its mass and nearest-neighbor force constant. Martin's calculated absorption coefficient, shown in Fig. 128(b) by the dash-dot curve, also is in fairly good agreement with the experimental results.

Keeler and Batchelder (1972) have also measured the absorption coefficient of 0.15% neon in argon at 2°K. The absorption for this lightly doped specimen was much smaller than for the krypton samples and no broad absorption bands were observed between 10 and 100 cm^{-1}. They did observe a strong absorption peak at 28 cm^{-1} which is shown in Fig. 129. (A local mode had been predicted by Hartmann and Elliott). In retrospect it is possible to understand the position of this low-frequency resonant mode if one assumes that the much larger argon atoms do not relax in towards the smaller neon atom. Cohen and Klein (1974) can get essentially exact agreement with the experimental data by adjusting the nearest-neighbor force constant of the impurity atom. The resulting configuration is reminiscent of that described in Sec. VI for KBr:Li, that is, a delicate balance occurs between the repulsive forces, which stabilize the neon atom at the normal lattice site, and the polarization forces, which tend to destabilize it. For neon almost complete cancellation occurs. Along these lines it is interesting to note that no absorption was observed for Ar:He between 10 and 100 cm^{-1}. This negative result can be easily understood if the He atom resides in an off-center configuration, since tunneling transitions appropriate to this configuration would occur at frequencies much smaller than 10 cm^{-1}. The reader is referred to Sec. VI for a discussion of such tunneling states in ionic crystals. Although the work on monatomic defects in rare gas matrices is not so extensive as for alkali halides, the same pattern is emerging, i.e., the dominant factor which determines the frequency of local modes, resonant modes, or tunneling states is the extent of the lattice relaxation around the impurity, not the difference in mass between the impurity and the host atom.

C. Molecular impurities

1. Homonuclear

The fundamental near-infrared absorption band of H_2 and D_2 has been studied in dilute solutions of Ar:H_2 by Kriegler and Welsh (1968) and of Ar:D_2 and Kr:H_2 by DeRemigis and Welsh (1970). Transparent H_2-doped argon and krypton crystals, suitable for observing the near-infrared spectrum, were produced by slow cooling

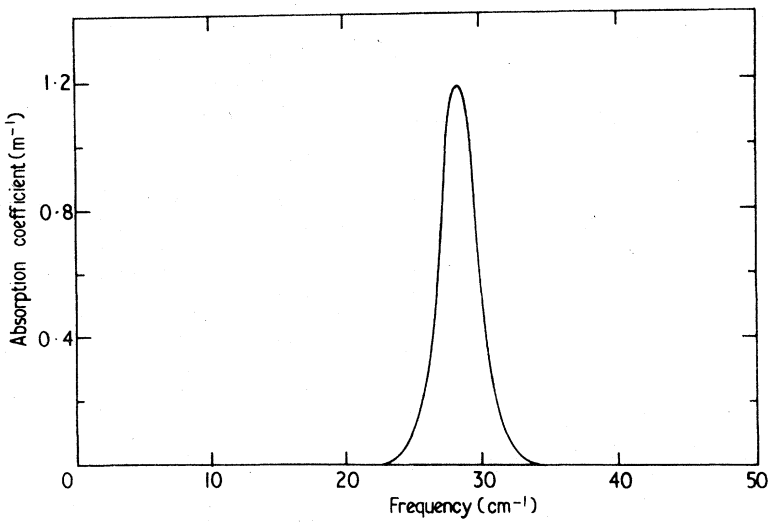

FIG. 129. Absorption coefficient of argon doped with 0.15% neon at 2°K. Resolution not given. After Keeler and Batchelder (1972).

of an absorption cell containing liquid argon or krypton in which hydrogen had been dissolved under moderate pressure. Samples 10 to 20 cm in length were prepared in this manner.

The experimental results for krypton doped with 1.21 mole% H_2 is shown in Fig. 130. The instrumental resolution is 3 cm^{-1}. The maxima in this spectrum are grouped into three sets of lines, each falling in the region of one of the H_2 transitions, Q, $S(0)$, and $S(1)$, corresponding to the vibration–rotational transitions with $J=0\rightarrow J=0$, $J=0\rightarrow J=2$, and $J=1\rightarrow J=3$, respectively. The positions of the $Q(0)$, $S(0)$, and $S(1)$ transitions for the free molecule are marked on the frequency axis. The structure found from Ar:H_2 and Ar:D_2 is essentially the same. Each of the three H_2 transitions gives rise to the same symmetrical pattern of five lines, consisting of a central component q, flanked by a higher-frequency pair of components, r' and r, and a lower-frequency pair, p' and p. The q components are associated with purely H_2 transitions (zero phonon lines) and the other components consist of combinations of the H_2 transitions with transitions of the lattice vibrational spectrum. Both local modes and resonant modes have been observed, and the frequencies are recorded in Table VII.1.

The local mode isotope shift is

$$\frac{\omega_{H_2}}{\omega_{D_2}} = 1.4 \approx \left(\frac{M_{D_2}}{M_{H_2}}\right)^{1/2} = 1.41 ,$$

in good agreement with the isotope shift expected for the one-oscillator model. The resonant mode has a mass shift of

$$\frac{\omega_{Ar}}{\omega_{Kr}} = 1.33 \approx \left(\frac{M_{Kr}}{M_{Ar}}\right)^{1/2} = 1.44 .$$

Again good agreement is found with a one-oscillator model. There is another interesting feature associated with the mass effect. The local mode shift given above is that expected for a mode of odd symmetry, while the resonant mode shift is that expected for a mode of even symmetry. The observation of both symmetry types in the same sideband spectrum implies that the impurity site cannot have inversion symmetry, hence cannot be at an argon site in a fcc. lattice. Kriegler and Walsh (1968) have already noted that the inversion symmetry at the impurity site cannot explain the presence of the zero phonon lines, and they suggested that the structure of solid argon may be hcp. in the neighborhood of the H_2

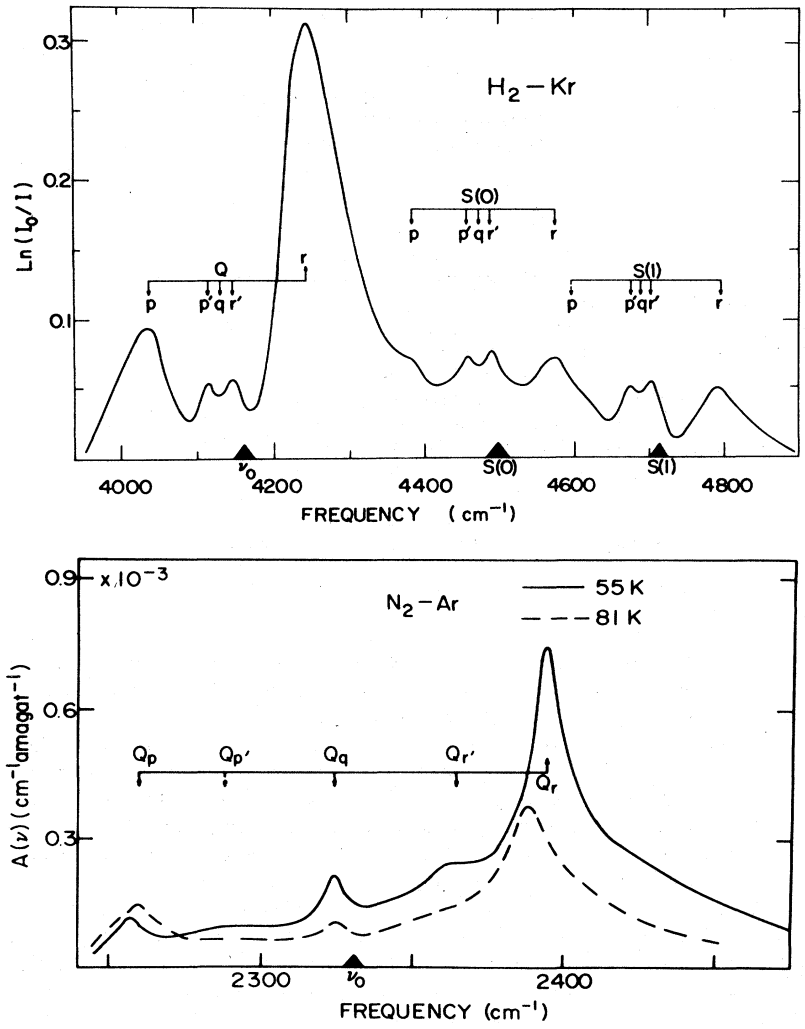

FIG. 130. *(upper)* Absorption band associated with the fundamental vibration of hydrogen in solid krypton. The Kr contained 1.21 mol% H_2 and a 40 cm path. Q, $S(0)$, and $S(1)$ correspond to the vibration-rotational transitions for a free H_2 molecule with $J=0\rightarrow J=0$, $J=0\rightarrow J=2$ and $J=1\rightarrow J=3$, respectively. After DeRemigis and Welsh (1970). *(lower)* Absorption band associated with the fundamental vibration of nitrogen in solid argon at 55 and 81 °K. The Ar was doped with 2.1 mole% nitrogen and a 40 cm absorption path. The triangle on the abscissa axis indicates the frequency of the band origin for the free N_2 molecule. After DeRemigis *et al.* (1971).

TABLE VII.1. Impurity activated lattice absorption in noble gas matrices.

Matrix	Mode frequency (cm^{-1})	(Temp. °K)	Method of observation, [a] References, [b] Comments
Ne (substitutional)			
Ar	28 (2)		A,1; Resonant mode
H_2 (substitutional)			
Ar	22,112 (82)		V,2; Resonant mode, local mode
Kr	16,106 (82)		V,3; Resonant mode, local mode
D_2 (substitutional)			
Ar	22,79 (82)		V,3; Resonant mode, local mode
N_2 (substitutional)			
Ar	39,70 (55)		V,8; Band mode, local mode
HCl (substitutional)			
Ne	93 (--)		A,4; Deposition at liquid He temp.
Ar	75 (12)		V,5,6; Average frequency
	73 (--)		A,4; Deposition at liquid He temp.
K	63 (12)		V,5,6,7; Average frequency
	62 (--)		A,4; Deposition at liquid He temp.
Xe	45 (7)		V,6,7; Average frequency
	49 (--)		A,4; Deposition at liquid He temp.
DCl			
Ar	72 (--)		A,4; Deposition at liquid He temp.
Kr	58 (--)		A,4; Deposition at liquid He temp.
Xe	49 (--)		A,4; Deposition at liquid He temp.
HBr			
Ar	78 (12)		V,5
	72 (--)		A,4; Deposition at liquid He temp.

[a] Key: A = absorption, V = vibrational side band.

[b] The references for Table VII.1 are the following:

1. Keeler, G. J., and D. N. Batchelder, 1972, J. Phys. C **5**, 3264.
2. Kriegler, R. J., and H. L. Welsh, 1968, Can. Journ. Phys. **46**, 1181.
3. De Remigis, J., and H. L. Welsh, 1970, Can. Journ. Phys. **48**, 1622 (1970).
4. Katz, B., A. Ron, and O. Schnepp, 1967, J. Chem. Phys. **46**, 1926.
5. Bowers, M. T., and W. H. Flygare, 1966, J. Chem. Phys. **44**, 1389.
6. Verstegen, J., M. P. H. Goldring, S. Kimel, and B. Katz, 1966, J. Chem. Phys. **44**, 3216.
7. Keyser, L. F., and G. W. Robinson, 1966, J. Chem. Phys. **44**, 3225.
8. De Remigis, J., H. L. Welsh, R. Bruno, and D. W. Taylor, 1971, Can. Journ. Phys. **49**, 3201.

impurity. Supporting evidence is based upon the observations of Barrett *et al.* (1965, 1966), who found that under certain circumstances, especially in the presence of some impurities, a finite fraction of the argon crystallized in the hcp. structure.

The near-infrared band associated with N_2 dissolved in solid argon has been studied by DeRemigis *et al.* (1971). The fundamental absorption band was measured for a few different N_2 concentrations in the range 0.95 to 2.2 mole%. Typical profiles are shown in Fig. 130 for the two extreme temperatures used, 55° and 81°K. The spectrum at 55°K consists of four maxima (Q_r, $Q_{r'}$, Q_p, and $Q_{p'}$) situated more or less symmetrically about the calculated frequency of the band frequency ν_0 for the gas phase. A weak central component Q_q occurs close to ν_0. The nomenclature corresponds to that used above to describe H_2 and D_2.

In order to determine whether or not rotational motion of the N_2 molecule contributes to the sideband structure, DeRemigis *et al.* have also examined the backscattered Raman spectra from 20-cm long samples. They found no evidence of a rotational spectrum in N_2-doped argon even though a very strong rotational spectrum was observed when an equivalent amount of N_2 gas was put in the cell. They conclude that the spectrum consists of combination bands of lattice modes and the N_2 vibrational transition. The two prominent features are identified with a local mode at 70 cm^{-1} and a band mode at 39 cm^{-1}.

Again, to explain the appearance of the zero-phonon N_2 vibrational line, it is necessary to assume that the local symmetry around the defect is not fcc. but instead hcp.

2. Heteronuclear

a. Near-infrared

The remaining investigations described in this section have not used ordered rare gas matrices but instead a dilute concentration of a molecular gas-rare gas mixture deposited as a film on a low-temperature substrate. The near-infrared transmission spectra of these films have shown that many molecules still rotate to some extent at low temperatures. Such molecules are methane (Cabana *et al.*, 1963; Cabana *et al.*, 1965; Frayer and Ewing, 1967; Hopkins *et al.*, 1968), water (Catalano and Milligan, 1959; Redington and Milligan, 1962, 1963; Glasel, 1960; Robinson, 1963), HCl and DCl (Schoen *et al.*, 1962), NH_2 (Robinson and McCarthy, 1959), and HF (Robinson and Von Holle, 1966; Bowers *et al.*, 1966). The rotational transitions observed for hydrogen halide molecules trapped in noble gas matrices are given in Table VII.2. An even larger number of trapped species do not rotate in rare gas matrices (Hallam, 1973).

To decide qualitatively whether or not a molecule rotates in the matrix, one makes an analogy with the gas phase spectra. The energies for the vibrational-rotational transitions in HCl gas are shown in Fig. 131(a). At room temperature two bands, the P and the R band, are observed as shown in Fig. 131(b). In the solid if the molecule exhibits only small deviations from the P and R branch of the gas phase then the crystal barrier opposing rotation can be assumed small. Molecules with rotational energies much less than the barrier height will exhibit a strong Q (no rotation) branch and weak P and R branches. In the limit of a large barrier the rotational energy levels must reduce to librational energy levels, as was first indicated by Pauling (1930) and extended by Devonshire (1936) to diatomic molecules in an octahedral cage.

One of the best illustrations of a trapped molecule which still rotates at low temperatures was obtained by Schoen *et al.* (1962). They measured the near-infrared absorption spectrum of HCl in solid argon matrices at 4°and 20°K and concluded that the observed spectral features were consistent with the existence of quantized molecular rotation in the matrix. Lines in the matrix spectra which correlate with the $R(0)$ and $P(1)$ transitions of gaseous HCl were identified, and their reduced separation, when compared with the free molecular transition, seemed to imply a hindrance to free rotation as a consequence of a barrier created by the local environment. These preliminary results served as a starting point for many experimental and theoretical studies of hydrogen halides in rare gas matrices.

A number of papers have appeared in which the stretching vibration frequency region of hydrogen halides has been measured with some precision. In the first of these, Bowers and Flygare (1966) studied the near-infrared spectrum of HCl, DCl, HBr, and DBr; Verstegen *et al.* (1966) measured the spectrum of HCl in Ar, Kr, and Xe; Keyser and Robinson (1966) measured the infrared spectrum of HCl and DCl in Kr and Xe, and Mann *et al.* (1966) obtained high-resolution spectra on HCl, DCl, HBr, and DBr in Ar and Kr.

The spectrum of HCl (with chlorine isotopes in natural abundance) trapped in Ar at 20 °K and 4.2 °K is shown in Fig. 132. The $R(0)$ and $P(1)$ transitions can be identified from the temperature dependence of the spectrum. From these and other more recent studies we have compiled in Table VII.2 the measured $\frac{1}{2}[R(0)-P(1)]$ frequencies for hydrogen halides. {For a free rotor the lowest-frequency rotational transition, $J=0\rightarrow J=1$, is approximately equal to $\frac{1}{2}[R(0)-P(1)]$.} The predicted lowest energy rotational transition from the near-infrared results is compared in column 5 of Table VII.2 with the experimentally measured far-infrared frequency (column 6) for the molecule in a rare gas matrix.

b. Far-infrared

Far-infrared absorption studies have been made on three of the hydrogen halides in rare gas matrices, namely, HF, DF, and HCl. In the measurements on HF and DF by Robinson and Van Holle (1966) and Mason *et al.* (1971) it was found that the far-infrared absorption frequency corresponded almost exactly to that expected for a pure rotation spectra in Ne. As the experimenters proceeded to heavier matrices the rotational transition for HF increased in frequency, while for DF no such systematic change was observed. Also in most of these heavier matrices the rotational transition was observed to be split. (They also observed doublets of comparable intensity in the mid-infrared vibrational spectrum as well). One such far-infrared doublet is shown in Fig. 133 for Ar:HF. The frequencies of the rotational transitions are recorded in Table VII.2.

The far-infrared data on HCl is somewhat uneven. Barnes *et al.* (1969), in an interferrometric study of small molecules in Ar matrices, determined the spectrum of Ar:HCl from 8 to 120 cm^{-1}. They observed an absorption line at 18.6 cm^{-1} which they assign to the $J=0\rightarrow J=1$ transition of HCl. This value is in good agreement with the near-infrared results recorded in Table VII.2. Von Holle and Robinson (1970) have measured the spectrum of HCl in solid Ne, Ar, Kr, and Xe. In Ar at 18 cm^{-1} they find a doublet with a splitting of 0.8 cm^{-1}, while in Kr they find a broad line at 19 cm^{-1}. These experimental results are shown in Fig. 133. The Xe:HCl spectrum showed one wing of a line that lies just below the 16 cm^{-1} limit of their grating spectrometer. No absorption was observed for Ne:HCl. Inspection of Table VII.2 shows that qualitatively all of these results are consistent with the near-infrared assignment of a nearly free rotor.

A number of other absorption bands in Ar:HCl have been observed in the far-infrared. The interpretation of some of these additional bands is still not clear. We have brought together the different assignments which have been proposed in Table VII.3. Much of the confusion in the interpretation of spectra appears to arise from H_2O contamination. Mason *et al.* (1971) have noted that H_2O lines always appear in premixed gas samples. They eliminated this impurity by a simultaneous spray-on technique in which rare gas passes directly from a molecular sieve trap to the cooled window.

TABLE VII.2. Rotational transitions of diatomic molecules trapped in noble gas matrices.

Matrix	Near ir frequency (cm^{-1})		References [a]		Far ir frequency (cm^{-1})	References [a]
	$R(0)$	$P(1)$		$\frac{R(0)-P(1)}{2}$	($J=0\rightarrow J=1$)	
HF						
Gas	4000.94	3920.39	1	40.34	41.9	2
Ne	3992.0	...	1	...	39.8	1
Ar	3962.0	3875.0	1,3	43.5	43.4 (Doublet)	1
Kr	3956.0	3867.0	1,3	44.5	45.4 (Doublet)	1
Xe	3953.0	3852.0	1,3	50.5	50.5 (Doublet)	2
DF						
Gas	2928.01	2885.08	1	21.46	22.0	1
Ne	2924.9	...	1	...	21.6	1
Ar	2896.4	2859.4	1	18.5	19.8	1
Kr	2886.0	2855.9	1	15.05	24.6 (Doublet)	1
Xe	2870.0	...	1	...	...	1
HCl						
Gas	2905.7	2864.6	4	20.55	...	...
Ne	2900.0	2872.0	5	14.0	No abs < 16	6
Ar	2887.5	2853.6	5, 7, 8	17.0	17.6, 18.6 (Doublet)	6, 9
Kr	2872.5	2837.5	5, 7, 8 10, 11	17.5	19	6
Xe	2858.0	2822.4	7, 8, 11	17.8	abs below 17	6
DCl						
Gas	2100.9	2079.5	4	10.7	...	...
Ar	2088.9	2069.2	5, 10, 11	9.8	...	...
Kr	2079.0	2058.3	5, 8, 10 11	10.3	...	...
Xe	2069.0	2048.5	5, 8	10.2	...	...
HBr						
Gas	2575.0	2542.1	4	16.4	...	...
Ar	2569.1	2550.1	5, 12	9.5	...	...
Kr	2551.6	2532.0	5, 10	9.8	...	...
DBr						
Gas	1848.2	1831.3	4	16.4	...	...
Ar	1843.1	1834.3	5, 8	4.4	...	...
Kr	1833.0	1821.5	5, 10	5.7	...	...
HI						
Gas	2242.4	2217.6	4	12.6	...	...
Ar	2255.0 2246.0	...	12	...	...	...
Kr	2232.0	2214.0	12	9.0	...	...

[a] The references for Table VII.2 are the following:

1. Mason, M. G., W. G. Von Holle, D. W. Robinson, 1971, J. Chem. Phys. **54**, 3491.
2. Robinson, D. W., and W. G. Von Holle, 1966, J. Chem. Phys. **44**, 410.
3. Bowers, M. T., G. I. Kerley, and W. H. Flygare, 1966, J. Chem. Phys. **45**, 3399.
4. *Tables of Wavenumbers for the Calibration of Infrared Spectrometers* (Butterworths, London 1961).
5. Bowers, M. T., and W. H. Flygare, 1966, J. Chem. Phys. **44**, 1389.
6. Von Holle, W. G., and D. W. Robinson, 1970, J. Chem. Phys. **53**, 3768.
7. Verstegen, J., M. P. H. Goldring, S. Kimel, and B. Katz, 1966, J. Chem. Phys. **44**, 3216.
8. Keyser, L. F., and G. W. Robinson, 1966, J. Chem. Phys. **44**, 3225.
9. Barnes, A. J., J. B. Davis, H. E. Hallam, and G. F. Scrimshaw, 1969, Chem. Commun., 1089.
10. Mann, D. E., N. Acquista, and D. White, 1966, J. Chem. Phys. **44**, 3225.
11. Brunel, L. C., and M. Peyron, 1966, Compt. rend. **262**, 1297.
12. Barnes, A. J., H. E. Hallam, and G. F. Scrimshaw, 1969, Trans. Faraday Soc. **65**, 3159 (1969).

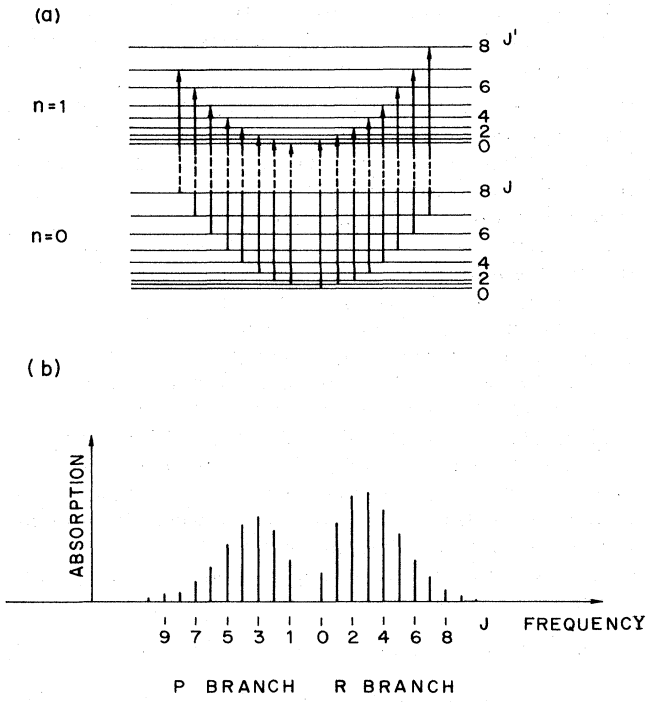

FIG. 131. (a) Energy level diagram and transitions for the vibration-rotation band of a diatomic molecule. The spacing between the rotation levels has been exaggerated compared with that between the vibrational levels. Transitions with $\Delta J=+1$, counting from the J value of the lowest vibrational state, correspond to the R branch and those with $\Delta J=-1$ belong to the P branch. For large molecule-lattice interactions $\Delta J=0$ is a permitted transition; such transitions belong to the Q branch. (b) Schematic absorption spectrum of HCl gas at 300 °K corresponding to the transitions in (a).

The absorption at 73 cm^{-1} in Table VII.3 arises from impurity-activated lattice phonons. From the density of states shown in Fig. 128 it is apparent that this absorption is due to a local mode. This identification of a lattice contribution confirms the original supposition of Verstegen *et al.* (1966). They had proposed that the high-frequency sideband of the near-infrared HCl stretching vibration was a combination transition, in which both the HCl vibration and the translational local mode quantum numbers changed by 1. The local mode frequencies for HCl, DCl, and HBr are given in Table VI.1. The far-infrared studies illustrate that impurity-activated phonon absorption can be readily correlated with the near-infrared measurements. Where both measurements have been made the agreement is quite good. Unfortunately, many of the near-infrared workers did not publish spectra over a large enough frequency region to include the frequency interval of interest here. Because the near-infrared measurements probe lattice modes in the excited molecular vibrational state, while the far-infrared measurements probe those associated with the ground vibrational state, we can conclude from the experimental results in Table VII.1 that the effect from internal molecular vibration on the lattice spectrum must be small.

D. Molecular impurity models

The near- and far-infrared spectroscopic data on diatomic molecules have provided some mysteries and some answers concerning the motion of diatomic molecules in a rare gas matrix. We have seen that:

(1) Doublet spectral lines appear in the near-infrared vibrational band of HF, but not for DF or HCl.

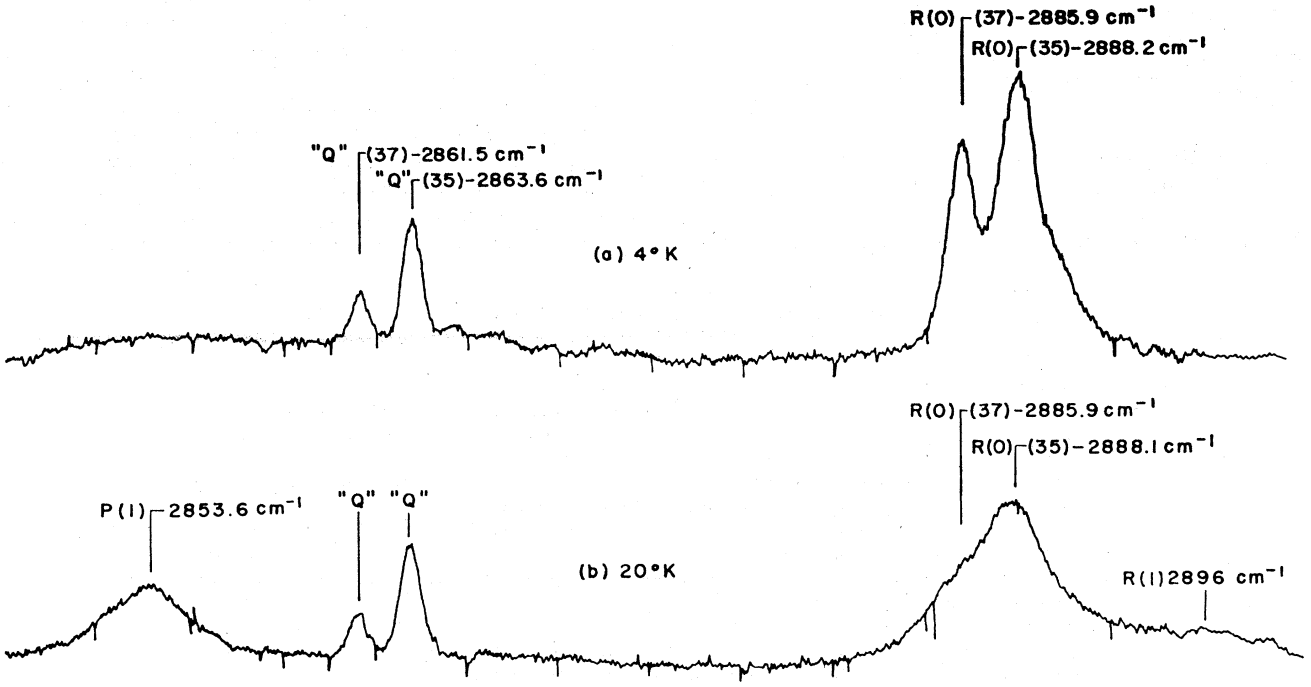

FIG. 132. The infrared spectrum of HCl (chlorine isotopes in natural abundance), trapped in an argon matrix at 20 °K and cooled to 4.2 °K. Ratio of HCl:argon, 1:1000. After Mann *et al.* (1966).

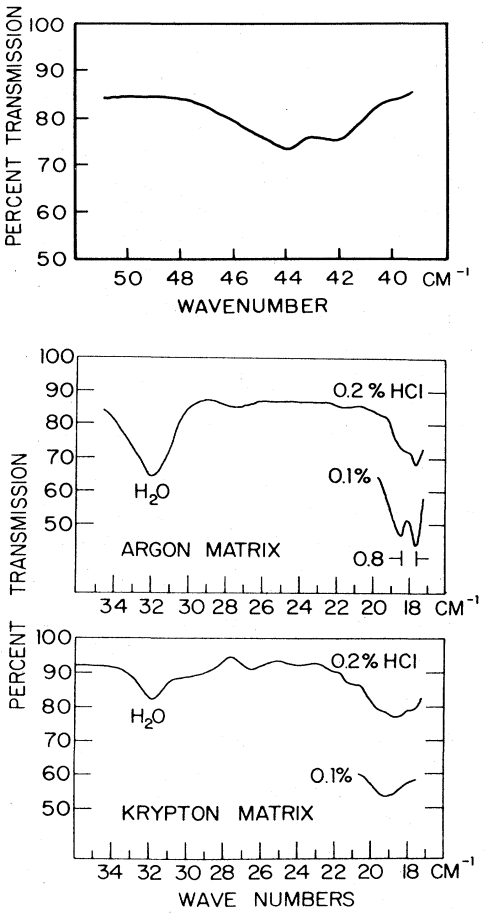

FIG. 133. *(upper)* Double absorption line attributed to the $J=0 \rightarrow J=1$ transition of HF isolated in an argon matrix. After Mason *et al.* (1971). *(lower)* Spectra of HCl isolated in argon and krypton matrices. Water impurity lines are also shown. The 0.1% HCl curves are displaced downward so that the ordinate scale applies only to the 0.2% HCl spectra. After Von Holle and Robinson (1970).

(2) Doublet spectral lines appear in the far-infrared rotational spectra of HF, DF, and HCl in different matrices.

(3) The rotational frequency of HF increases with increasing matrix mass, while the frequency of DF does not; and the frequency of HCl decreases with increasing matrix mass.

It may be that items (1) and (2) appear because the matrix symmetry is hexagonal at the impurity site (Von Holle and Robinson, 1970), but at present this explanation does not consistently explain all the available data. Item (3) is a direct consequence of the local dynamics of the molecule, and we shall outline the partial solution of this problem here.

The theory for the rotation of trapped molecules in noble gas lattices has been considered by Devonshire (1936), Cundy (1938), Babloyantz (1959), Friedmann (1962), Flygare (1963), Friedmann and Kimel (1963, 1965, 1967), Keyser and Robinson (1966), Bowers *et al.* (1966), Mann *et al.* (1966), and Pandey (1968). Rotational shifts of the free rotor have been induced by means of two perturbations: the electrostatic barrier perturbation, hindering rotation, and a coupling between the translation of the molecule and its rotation.

The Hamiltonian which includes both of these effects can be written as

$$\mathcal{H} = \mathcal{H}(\text{trans}) + \mathcal{H}(\text{rot}) + \mathcal{H}(\text{xtal}) + \mathcal{H}(\text{rot–trans}) \qquad (7.2)$$

where $\mathcal{H}$(trans) is identified with the harmonic oscillator Hamiltonian appropriate to a local or resonant mode, $\mathcal{H}$(rot) is the Hamiltonian of a free rotor, $\mathcal{H}$(xtal) describes the influence of the local crystal field at the free rotor, and $\mathcal{H}$(rot–trans) the mixing of the rotational translational motions. In the barrier model where the molecule is treated as a hindered rigid rotor only the second and third terms of Eq. (7.1) are retained. Devonshire first calculated the rotational energy levels for a diatomic molecule in a field of octahedral symmetry, the symmetry possessed by the substitutional sites of rare gas lattices, in 1936. This theory has been used by Bowers and Flygare (1966) for hydrogen halides, but did not give a consistent fit with all the near-infrared measurements. In particular the isotope effect on $\frac{1}{2}[R(0)-P(1)]$ in Table VII.2 was not explained.

For the crystal field model, rotations occur about the center of interaction rather than the center of mass; this interaction point between the two atoms is identical for all isotopic species. For a given crystal field

TABLE VII.3. Assignment of absorption mechanism in far ir spectrum of Ar : HCl.

Ar : HCl Absorption frequency (cm^{-1}) [a]	Katz *et al.* [b] (1967)	Barnes *et al.* [c] (1969)	Von Holle and Robinson (1970) [d]
18	Freq. not measured	HCl rotation	HCl rotation
35	Observed—no assignment	Imp. act. phonons	H_2O rot. at 33 cm^{-1}
48	Not observed	Imp. act. phonons	H_2O rot. at 47 cm^{-1}
73	Imp. act. phonons	Imp. act. phonons	Freq. not measured

[a] Barnes *et al.* have also observed two additional lines at 97 and 115 cm^{-1} which they have identified as imp. act. phonons.

[b] Katz, B., A. Ron, and O. Schnepp, 1967, J. Chem. Phys. **46**, 1926.

[c] Barnes, A. J., J. B. Davis, H. E. Hallam, and G. F. Scrimshaw, 1969, Chem. Commun., 1089.

[d] Von Holle, W. G., and D. W. Robinson, 1970, J. Chem. Phys. **53**, 3768.

strength the perturbation on the rotational spectrum should be greater for the isotope with the smaller rotational transitions. Inspection of the data on HCl and DCl in Table VII.2 shows that the HCl rotational transition is perturbed more strongly than the DCl rotational transition, although the HCl rotational transitions are larger, a result which is not possible from crystal field effects alone.

The introduction of rotational–translational coupling explains qualitatively the data in Table VII.2. The Hamiltonian of the system is now represented by terms 1, 2, and 4 in Eq (7.2). The coupling between rotation and translation comes about because of the difference between the center of electrical interaction and the center of mass for heteronuclear molecules. The strength of this coupling term depends on the distance between these two points. Using second-order perturbation theory, Friedmann and Kimel (1963, 1965) first calculated the perturbation upon the rotational energy levels.

A more general solution to the problem of rotation translation coupling has been obtained by Keyser and Robinson (1966). They constructed a matrix Hamiltonian which treats the translational modes of HCl and DCl and the strength of the translation-rotation as parameters. The perturbed energy levels are found by direct diagonalization of the truncated matrix. They show that for a heteronuclear diatomic rotor in a cubic lattice, the translational–rotational states form a basis for the irreducible representations of a group isomorphous with D_{2h}. This property allows considerable factorization of the Hamiltonian matrix. These approaches have been reviewed recently by Turrell (1972) and Barnes (1973).

Bowers *et al.* (1966) have interpreted the vibration-rotation spectra of the substitutional HF in terms of a translation-rotational coupling model different from that given earlier. They claim that a term in the potential energy which accounts for the shift of the molecular center of mass with respect to the center of the lattice site is equivalent to the center of interaction model described by Friedmann and Kimel. For HF they found that the barrier hindering rotation in the lattice appears to be much smaller than this rotational-translational coupling. The interpretation based upon their model shows two definite features: (1), the frequencies for the molecular translational motions are very small in all cases (about one half the rotational energy of HF) and (2), the center of mass at equilibrium appears to be further from the center of the lattice site as one proceeds to the larger rare gases. This latter point leads to the interesting possibility of a potential maximum at the center of the lattice site. Potentials of this form observed for ionic crystals are described in Sec. VI.

The most convincing feature of the translation rotation coupling model is that the red shifted rotational transitions in DF-doped solids and the blue shifted rotational transitions in HF-doped solids can be readily interpreted. By coupling a translational mode to a rotational mode, the energy difference between the new mixed modes increases with respect to the difference between the energy levels of the unperturbed system (mixing and repulsion). If in the unperturbed system the vibrational energy is larger than the rotational energy, then in the coupled system the rotational transition energy will be decreased with respect to the unperturbed energy, while if the vibrational transition energy is smaller than the rotational transition energy the converse is true. The dependence of the energy levels upon the translational frequency has been worked out for HF by Bowers *et al.* (1966) and we show their calculated mixed mode scheme in Fig. 134.

Although no low-frequency translational modes have been observed for HF, the far-infrared experiments on Ar:Ne by Keeler and Batchelder (1972) give some evidence to justify this approach. Ne and HF have the same mass and roughly similar sizes, both much less than the argon atom they replace. For Ne a resonant mode is observed at 28 cm^{-1} which is larger than the rotational spacing of DF but smaller than HF. In terms of Fig. 134 the normalized translational frequency for DF would be greater than 1 and the rotational transition ($N=0, J=1$) would correspond to a smaller frequency in units of the rotational constant B than for HF, where the normalized translational frequency would be less than 1.

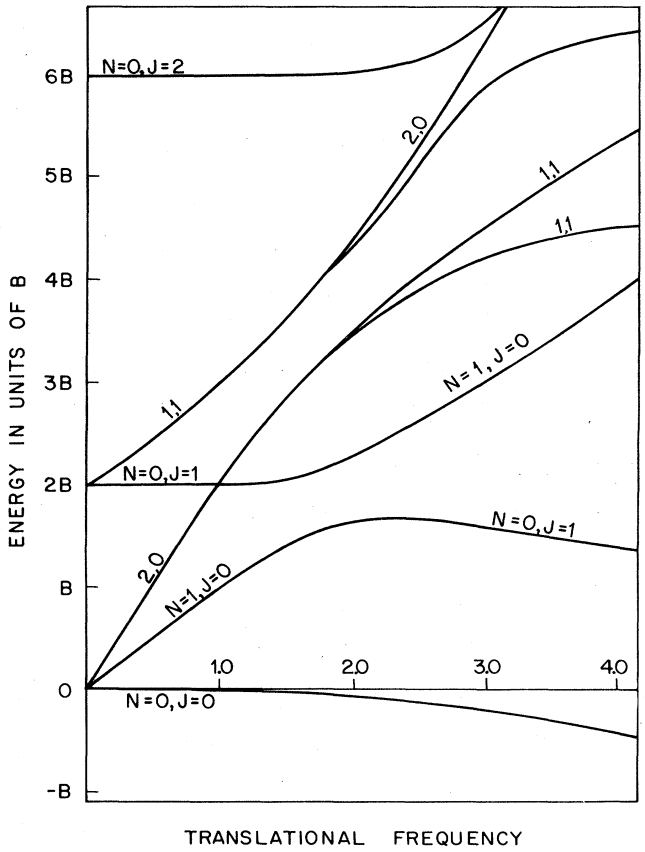

FIG. 134. Dependence of the energy levels upon the translational frequency of the molecule. Both energy and frequency are given in units of the rotational constant B. These curves were calculated for HF ($R_0 = 0.08$ Å). The energy levels are labeled by a translational quantum number N (sum of the quantum numbers for the three directions of motion) and by J, the rotational quantum number. Not all of the levels are shown. From Bowers *et al.* (1966).

Mannheim and Friedmann (1970) have extended the rotational–translational coupling model to include coupling of the diatomic molecule with the lattice vibrations of the crystal. They recognized that polar molecules can be used as a lattice probe since an indirect coupling of the light with the lattice is produced by the rotational translational coupling. Their mechanism is as follows: the light couples to the rotation of the polar molecule, the rotation couples to the translation, and the translation of the defect couples to the lattice vibrations. The only lattice modes which are optically active are those in which the defect is in motion.

In conclusion the rotational–translational coupling can explain qualitatively the spectral features which are observed experimentally for heteronuclear molecules, and at this stage one cannot expect more. The fundamental unsolved problem is that *a priori* the frequency of the translational mode cannot be theoretically calculated. Even for the simple problem of a monatomic defect (Ne) in a rare gas lattice (Ar), theoretically a high-frequency local mode was predicted while experimentally a low-frequency resonance was observed (Sec. VII.B). The degree of local lattice relaxation around the defect is still an unknown quantity. Without being able to theoretically estimate the relaxation, one cannot predict whether local modes, resonant modes, or tunneling states should be assigned to the translational motion of the impurity. To break out of this impasse we still need to do a great deal of experimental work. Raman and far-infrared spectra of good quality rare gas crystals and also ionic crystals containing heteronuclear molecules can provide the needed information on impurity dynamics and lattice relaxation.

VIII. IMPURITIES TRAPPED IN ORGANIC CLATHRATE STRUCTURES

A. Introduction

An example of impurities very weakly coupled to a lattice occurs for gas atoms trapped in the organic crystal β-quinol clathrate. When quinol $C_6H_4(OH)_2$ is crystallized from a solution containing a large concentration of trappable molecules, the β phase is formed. This β-quinol clathrate has an open structure which contains regularly spaced cavities of approximately 8 Å diameter in which small foreign molecules can be trapped during formation (Palin and Powell, 1947). The actual preparation of these clathrates occurs by slow crystallization from hot solutions of recrystallized quinol in *n*-propanol in the presence of the appropriate impurity gas under pressure (Parsonage and Staveley, 1959). Fractional cage occupancies can be varied from about 7% to 80% depending on the applied gas pressure.

In these clathrates, which have a local trigonal symmetry at the cage site (Meyer and Scott, 1959), one molecule at most can be trapped in each hole. The crystal structure in the neighborhood of one of these holes is shown in Fig. 135. The internuclear distance across a diameter of the cavity is about 8 Å, but the physical size of the electron wave functions associated with the quinol molecules reduces the cage diameter to about 3 or 4 Å. The spacing between the cages is such that there are two nearest neighbors along the *c* axis at 5.5 Å, whereas the next-nearest and third-nearest neighbors lie at distances greater than 9 Å. There are three cages per unit cell (Allen, 1966).

Although the clathrate lattice is indeed complex, the analysis of the experimental data on the trapped species has proven to be remarkably straightforward. This fact may account for the sustained interest in the compound over the years. A review of the infrared spectra of clathrates was recently published by McKean (1973). The reader is referred to this work for a discussion of the near-infrared properties and mention of some preliminary Raman work.

Clathrate crystals containing trapped atoms and molecules first attracted widespread attention after the successful analysis of some of the in room temperature thermodynamic properties (van der Waals, 1956a; van der Waals and Platteeuw, 1959). Using classical statistical mechanics and a cell model for the local potential (Lennard-Jones and Devonshire, 1937, 1938), van der Waals and Platteeuw were able to calculate the room temperature vapor pressure of the trapped molecules and the heat of formation. Their predictions agreed with experiments conducted near room temperature (Evans and Richards, 1954; van der Waals, 1956b). Although a variety of experimental measurements have been reported since that time on clathrate compounds, the far-infrared absorption measurements and the complementary heat capacity experimental results provide a fairly clear picture of the impurity lattice dynamics. With these two techniques, low-lying energy states associated with impurity translation or translation plus rotation were observed for the trapped molecules.

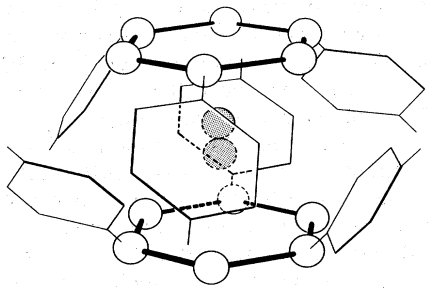

FIG. 135. Structure of a β-quinol clathrate cage containing a trapped diatomic molecule (shaded). The heavy black lines represent indirect bonds formed by hydrogen atoms between neighboring oxygens (unshaded spheres), not direct bonds. The hexagons represent benzene rings. From Burgiel *et al.* (1965).

B. Resonant modes

The simplest case, that of rare gases trapped in clathrates, was studied by Burgiel *et al.* (1965). They measured the absorption spectra of the clathrates containing Ar, Kr, and Xe from 15 to 85 cm^{-1}. The absorption frequencies are recorded in Table VIII.1. The temperature dependence of the absorption spectrum of argon in β-quinol is shown in Fig. 136. The absorption line at about 36 cm^{-1} stems from the trapped argon atoms, and the line strength arises through dipole moments induced by interaction between the gas molecule and the clathrate cage. The strong absorption line at 67 cm^{-1} is due to the host lattice. The continuous absorption which occurs over the entire frequency range probably arises from the impurity-induced activity which the host lattice modes acquire because of the breakdown of translational symmetry.

When the temperature of the clathrate is increased, the absorption line associated with an argon or krypton impurity tends to broaden and shift to higher frequencies. In contrast, the xenon clathrate spectrum is nearly independent of temperature. Another interesting feature is the shift of the strong lattice mode from 67 cm^{-1} to 72 cm^{-1} in the xenon clathrate. It is interpreted as a stretching of the cage walls by the large Xe atom. A summary of the temperature dependence data is given in Fig. 136(b).

To test whether or not the low-frequency absorption line can account for all the impurity-induced motion, the optical results can be compared with heat capacity measurements. An analysis of the motions of argon and krypton in β-quinol from heat capacity measurements has been made by Staveley and co-workers (Parsonage and Staveley, 1960; Grey and Staveley, 1963), using the cell model theory of van der Waals (1956a). This model assumes a rigid cage or cell of 24 atoms, each of which interacts with the trapped molecule via a Lennard-Jones six-twelve potential. In the region above 120°K, good agreement between the experiments and the theory was obtained using the parameters evaluated by van der Waals from other experiments. Grey and Staveley estimated the specific heat at lower temperatures by evaluating the energy levels for the Lennard-Jones

TABLE VIII.1. Characteristic spectral features of trapped species. Atoms and molecules ordered by mass.

Trapped species	Absorption peaks (cm^{-1}) (Temp. °K)	Remarks	References [a]
Ar	35.5(1.2)	Trans. mode	1
K	36.0(1.2)	Trans. mode	1
Xe	43.5(1.2)	Trans. mode	1
H_2	–(1.2)	No absorption between 15 and 85 cm^{-1}	1
CH_4	31, 82(1.2)	Large impurity distorts cages	1
HCN	20–40(90)	Weak, hindered rotation	2
N_2	53.5(1.2); 52.5(90)	Trans. mode	1, 2
CO	55.2; 81.5(1.2)	Trans. mode; hindered rot. mode	1
NO	46.5; 33.0(1.2)	Trans. mode; hindered rot. mode	1
O_2	40(1.2)	Trans. mode	1
CH_3OH	73(80)	Trans. mode	3
HCl	52; 18(1.2)	Trans. mode; rotational mode	4
H_2S	75, 57; 22(10)	Trans. modes; rotational mode	3, 5
D_2S	79, 74, 57; 20(10)	Transtational modes; rotational mode	5
CO_2	74(90)	Trans. mode	2
SO_2	32(1.2)	Very broad absorption	1
NF_3	–(1.2)	No absorption between 15 and 85 cm^{-1}	1
HBr	$\lesssim$16(1.2)		4
H_2Se	74, 57, 44; 10(10)	Trans. modes; rotational mode	5
D_2Se	80, 75, 54, 44(10)	Transtational modes	5
Pure α-quinol	42, 60, 67	Lattice modes, 67 cm^{-1} strong	1

[a] The references for Table VIII.1 are the following:

1. Burgiel, J. C., H. Meyer, and P. L. Richards, 1965, J. Chem. Phys. **43**, 4291.
2. Davies, P. R., 1969, Disc. Faraday Soc. **48**, 181.
3. Barthel, C., X. Gerbaux, and A. Hadni, 1970, Spectrochim. Acta. **26A**, 1183.
4. Allen, S. J., 1966, J. Chem. Phys. **44**, 394.
5. Gerbaux, X., C. Barthel, A. Hadni, and M. M. Pradhan, 1973, Spectrochim. Acta. **29A**, 1695.

potential numerically. In Figure 137 this calculation, the dashed curve, is compared with the experimental results for Kr trapped in β-quinol.

Burgiel *et al.* (1965) have also used the cell model. They assign the single low-frequency absorption line to the translational motion of the atom within its cell. They use this absorption line and its temperature dependence to evaluate the parameters of a one-dimensional Poschl–Teller potential well. This model, while more simplified then the Lennard-Jones model, has the advantage of giving the energy eigenvalues in analytical form and thus allowing a simple physical interpretation of its parameters. The solid curve in Figure 137 shows the calculated heat capacity using the infrared data and the Poschl–Teller potential.

A comparison of the two calculations shown in Fig. 137 illustrates that they are equally good or bad depending on the temperature range in question. At high temperatures both calculations fit the experimental heat capacity date reasonably well. They give a value which is less than the classical value for an Einstein oscillator, $C/R \sim 3$, but larger than the classical value for a free particle in a box, $C/R \sim \frac{3}{2}$. At low temperatures, however, neither calculation fits the experimental heat capacity data. This result is particularly striking with the calculation by Burgiel *et al.* because the far-infrared data provide the low-lying energy levels directly. To improve the agreement between experiment and calculation, apparently the cell model must be modified.

Burgiel *et al.* have proposed that correlation between motions of neighboring molecules may be important. For a set of harmonic oscillators the heat capacity rises approximately exponentially, while that of an assembly of coupled oscillators with a Debye spectrum rises more slowly. The high temperature limit is the same in both cases. A correction for collective modes of motion may improve the agreement between theory and experiment, though such a correction cannot be calculated from the infrared data.

A different approach which would improve the agreement between the theoretical and experimental heat capacity would be to use a resonant mode model instead of

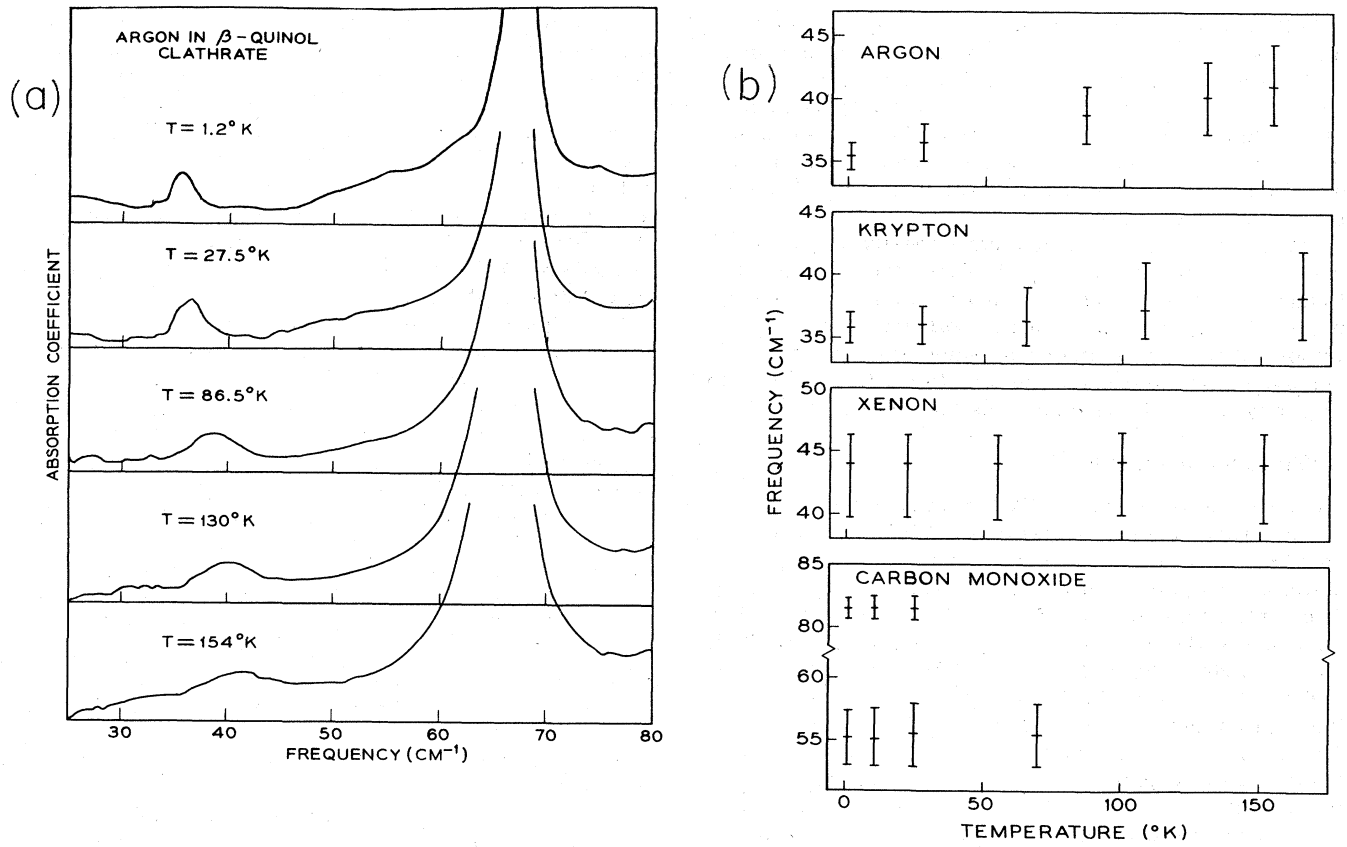

FIG. 136. (a) Temperature dependence of the absorption spectrum of argon in β-quinol clathrate. (b) The frequency of absorption for several trapped atoms and CO as a function of temperature. The bars indicate the widths of the absorption lines, not the uncertainties in their frequencies. From Burgiel *et al.* (1965).

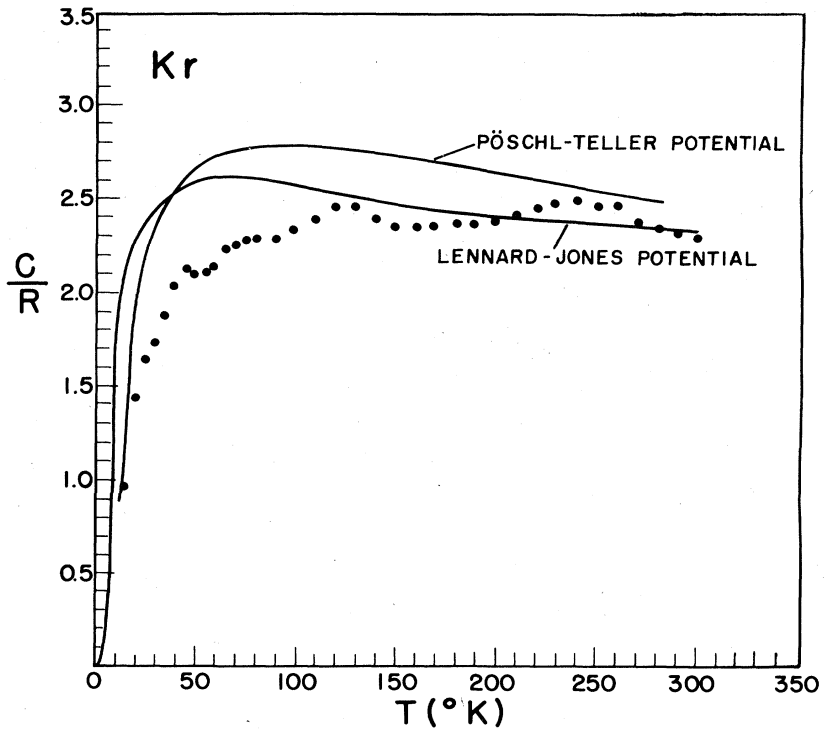

FIG. 137. Specific heat of Kr trapped in β-quinol—data of Parsonage and Staveley. The solid curve was calculated by Burgiel *et al.* from infrared data using the Poschl–Teller potential. The dashed curve was calculated by Grey and Staveley using quantum statistics and Lennard–Jones potential. From Burgiel *et al.* (1965).

a cell model. This model would include the impurity motion which occurs in many lattice modes in addition to the low-lying rattling model. Only some fraction of the impurity atom degrees of freedom would then appear as an Einstein or Poschl–Teller oscillator contribution to the heat capacity; the remainder would appear as a small additional contribution to the Debye-like spectrum of the host lattice.

The one approach assumes that impurity-impurity coupling is important, while the other treats isolated impurities but removes the condition of a rigid lattice. Which of these two different possibilities is the more important for the β-quinol clathrates has not yet been resolved; for the present the simple rattling mode of the impurity in a rigid cage remains the state of the art.

C. Molecular impurities

In addition to measuring the far-infrared spectra of trapped rare gases, Burgiel *et al.* (1965) also investigated the far-infrared spectra of a variety of trapped diatomic and polyatomic gases in β-quinol. Their work is complemented by that of Allen (1966), who studied in some detail the far-infrared properties of trapped HCl, and by Davies (1969), Barthel (1970), and Gerbaux *et al.* (1973). A listing of the trapped molecular species and the characteristic spectral features of each is given in Table VIII.1. These investigators required two kinds of transitions to explain the measured spectra of polar molecules.

For polar molecules, which possess a permanent dipole moment, infrared absorption occurs for both the translational and rotational motion. On the other hand, for molecules with no permanent dipole moment the inversion symmetry of the cavity insures that no dipole moment will be induced for purely rotational motion, and the spectrum resembles that induced by monatomic gases.

As shown in Table VIII.1, there are absorption lines for most of the diatomic molecules, and the frequency decreases systematically as the molecular weight increases. Burgiel *et al.* have attributed these lines to translational motion because they are observed in molecules without permanent dipole moments. The lines with maxima at 81.5 cm^{-1} for CO, at 33.0 cm^{-1} for NO, and at 18 cm^{-1} for HCl are attributed to hindered rotation. For HCl Allen found that the 52 cm^{-1} line was not changed by DCl substitution, but that the 18 cm^{-1} line was shifted appreciably.

For CO and NO, two gases with permanent moments, Burgiel *et al.* were able to estimate the barrier height of the potential which inhibits free rotation. These estimated barrier heights, 1240°K and 230°K, indicate that tunneling processes may be important here. Particularly in the large barrier limit such processes will influence both the low-temperature heat capacity and the far-infrared spectrum. Measurements below 15 cm^{-1} on these systems would be particularly valuable.

Unlike CO and NO, which are strongly hindered rotors exhibiting librational oscillations, HCl has been found by Allen (1966) to be very nearly a free rotor with a rotational spacing of 18 cm^{-1}, which is in fact less than the free value of 21 cm^{-1}. This red shift of 3 cm^{-1} can be explained by the translation-rotation coupling model of Friedman and Kimel (1964). This model assumes that the coupling arises in the solid because the molecule does not rotate about the center of mass. For HCl in the β-quinol clathrate Allen (1966) found that a difference between center of mass and center of rotation of 0.095 ± 0.015 Å successfully explains both the red shifted rotational frequency and the enhanced absorption of the translational mode. Allen also showed that the concentration and temperature dependence of the HCl rotational frequency was due to dipole–dipole interactions between the trapped molecules.

IX. MIXED CRYSTALS

A. Introduction

This section is less self-contained than many of the preceding sections. The reader who wants to understand the models and significance of many of the fine features of the experimental work is expected to have read Sec. II, where the mathematical models are discussed in detail. Some of the earliest calculations done by Matossi (1950) are discussed, however, in the next section. Original details on the isodisplacement model (discussed in Sec. II) may be found in the two papers where it was developed: Verleur and Barker (1966) and Chen, Shockley, and Pearson (1966). Short reviews of mixed crystal work have been given by Barker (1968b) and Lucovsky *et al.* (1968) in the Proceedings of the Conference on Localized Excitations in Solids. Several other papers on experimental work on mixed crystals also appear in the Conference Proceedings. Finally, a more extensive review, including references and experiments up through 1970, has been published by Chang and Mitra (1971).

There has been a sustained interest in and a progression of experimental papers on mixed crystals since the mid-1960's. Aside from their intrinsic physical interest, certain mixed semiconductors have recently become important in the solid state laser field. In constructing a junction laser it has been found important to profile the index of refraction in a specific way. This may be done by controlling the mixed crystal composition as a function of distance. While we do not review the electronic properties of mixed crystals, it is clear that an understanding of the vibrational properties is increasingly important in this area. Finally we note that mixed crystals can serve the function of providing a bridge between the concepts and phenomena of isolated impurities and the properties of amorphous or fully disordered solids. Since the atomic composition x can be varied in many cases from 0% to 100%, we can hope to see local modes evolve and broaden into major lattice bands in a continuous way. In several systems this has been done for the optic $q \approx 0$ modes by optical studies, and in one or two systems some neutron scattering data has begun to illuminate the behavior for nonzero q. For this subject concerning random defects of significant (not low) concentrations, the experiments are ahead of detailed first-principles calculations and hence can provide very important guidelines.

B. Early work

Kruger and co-workers have reported one of the earliest infrared studies of mixed crystals (Kruger *et al.*, 1928). This work was carried out before the modern methods of reflectivity analysis were available. The motivation was the study of the microscopic structure of mixed alkali halides via the lattice vibrations. Figure 138 shows their result for NaCl+KCl. They plot the infrared wavelength where maximum signal was observed (probably close to the peak of the reststrahlen band) versus the composition of the mixed crystal. In the three systems studied (Table IX.3) these workers observed a smooth shift of this maximum with concentration. For the system shown in Fig. 138 they also observed a decay after 11 months of the maximum into two maxima showing ion migration and reversion of the mixed crystal into separate components. In the TlCl+KCl system their spectra show subsidiary structure which we now know to be important as a sign of possible two-mode behavior. Matossi in 1950 used a periodic chain model to analyze the results of Kruger *et al.* He used the chain AC BC AC BC... with only nearest-neighbor force constants to analyze the 50% mixed crystal $A_yB_{1-y}C$. Note that this model has perfect periodicity with a four-atom unit cell, so that it cannot describe the random distribution of atoms in any way. His model can be regarded as a four-coordinate isodisplacement model (see discussion in Sec. II). Because of the two coordinates for the C sublattice and the inversion center at B, Matossi obtains a Raman-active mode involving relative motion of the two C ions in each cell. In addition there is a strongly infrared-active mode corresponding to the obvious A and B versus C motion, and a weaker mode involving predominantly A versus B. Matossi was unaware of the fine structure and two-mode behavior which have subsequently been measured in some alkali halides. He therefore compares his strong infrared mode with the experiments and somewhat neglects the other modes. Since he does not indicate the extension to concentrations other than $y = 0.5$, we do not use Matossi's calculations as a mixed crystal model. Nevertheless, his paper serves as an excellent introduction to certain mixed crystal models and a complete understanding of his solutions (both frequencies and

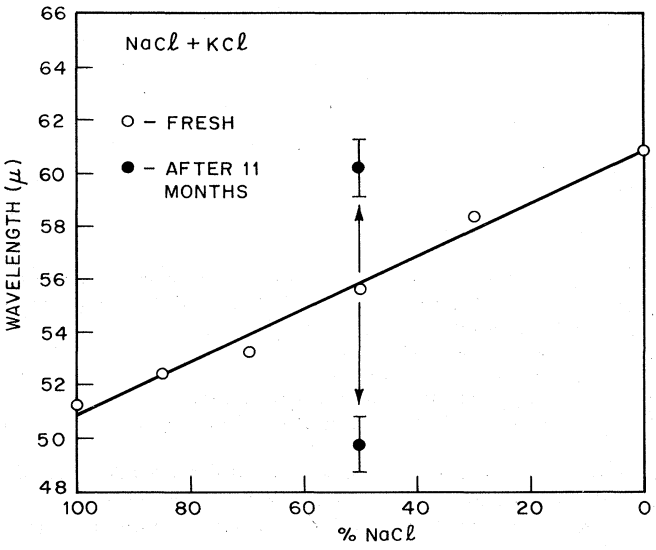

FIG. 138. Wavelength of reflection maximum in the system NaCl+KCl plotted against concentration. Note that this system is unstable, as indicated by the spectrum taken after eleven months. The appearance of a single peak which varies smoothly with concentration typifies one-mode behavior for the freshly prepared samples. From Kruger *et al.* (1928).

TABLE IX.1. Mixed III–V crystals with zinc-blende structure.[a]

	GaP	GaAs	GaSb	InP	InAs	InSb	AlAs
GaP	366[b], 403 Barker (1968a)	Verleur *et al.* (1966) Chen *et al.* (1966) Strahm *et al.* (1969)R Andrews *et al.* (1972)T 2 Mode	d	Lucovsky *et al.* (1971) Andrews *et al.* (1972)T 1 mode + structure	e	d e	$Ga_{1-x}Al_xAs_{1-y}P_y$ Lucovsky *et al.* (1974) 3 modes plus structure
GaAs		268, 291 Haas (1967) Cochran *et al.* (1961)	Lucovsky and Chen (1970) 1–2 Mode	e	Brodsky *et al.* (1968) Lucovsky and Chen (1970) 1–2 Mode	e	Ilegems and Pearson (1970) Andrews *et al.* (1972)T 2 Mode
GaSb			225, 233 Picus *et al.* (1959)	d e	e	Brodsky *et al.* (1970) 1–2 Mode	e
InP				304, 338 Picus *et al.* (1959) Haas (1967)	Oswald (1959) Kekelidze *et al.* (1973) 2 Mode	d	c e
InAs					209, 233 Haas (1967) Picus *et al.* (1959)	Lucovsky and Chen (1970) 1–2 Mode	c
InSb						174, 183 Haas (1967) Picus *et al.* (1959)	c e
AlAs							360, 390 Ilegems and Pearson (1970)

[a] Nitrides and borides do not crystallize in zinc blende structure.
[b] ω_{TO} and ω_{LO} at 300 °K for pure crystals.
[c] Al–In generally not miscible.
[d] Sb–P generally not miscible.
[e] A quaternary compound. No work reported.
[f] All studies are by infrared except for those noted as R = Raman, T = electron tunneling.

eigenvectors) serves as a basis for the understanding of the models discussed in this review. We merely note here that when second-neighbor forces are included, the weak infrared mode identified by Matossi can be made to fall at frequencies higher or lower than the main mode and in fact can borrow enough strength to become the main mode. His model when extended can therefore show the one- or two-mode behavior discussed in Sec. II.

C. Optic modes observed in infrared and Raman spectra

1. Two-mode systems

Tables IX.1–IX.5 show all (both one- and two-mode) systems which have been studied, subdivided in a fairly natural way by valence and crystal structure. Most, but not all, are of the $A_yB_{1-y}C$ type. In Fig. 139 the infrared-active modes in the mixed III–V semiconductor $Ga_yAl_{1-y}As$ are plotted. Ilegems and Pearson (1970)

TABLE IX.2. II–VI mixed crystals (ternary and quaternary).

	Pure crystal ω_{TO} (cm^{-1})	ω_{LO} (cm^{-1})	Mixed crystal: structure, references, and mode behavior
CdSe	$\perp c$-177	210	Wurtzite: ir, Balkanski *et al.* (1966);
	$\parallel c$-169	210	ir + model, Verleur and Barker (1967a);
+			ir, R, Parrish *et al.* (1967); electron
CdS	$\perp c$-242	307	tunneling, Lubberts (1971); 2-mode
	$\parallel c$-235	305	behavior.
ZnSe	206	252	Zinc blende: ir, R, Brafman *et al.* (1968);
+			2-mode behavior.
ZnS	270	350	
CdS	See above		Wurtzite: ir, Lucovsky *et al.* (1967); 1-
+			mode plus fine structure.
ZnS	$\perp c$-270	348	
	$\parallel c$-265	347	
HgTe	116	139	Zinc blende: ir, Carter *et al.* (1971); R,
+			Mooradian *et al.* (1971); ir, Baars and
CdTe	140	171	Sorger (1972); data scanty for large Cd
			conc.; 2-mode.
ZnSe	206	252	Zinc blende quaternary: ir, Barker and
+			Yim.
GaP	366	403	
CdTe	See above		Zinc blende: ir, R, 2-mode studied 0% to
+			60% Mg, Nakashima *et al.* (1973).
MgTe	~235	~320	
CdS	See above		Wurtzite: ir, 1-mode plus secondary
+			structure, Lucovsky *et al.* (1967); R,
ZnS	See above		Vavilov (1971).
CdTe	141	166	Zinc blende: ir, 2-mode, Harada and
+			Narita (1971), also measure local modes
ZnTe	172	204	in the mixed crystals; Vodopyanov *et al.*
			(1972), note 1-mode behavior at low Zn conc.
CdTe	See above		Zinc blende: ir, 2-mode, Vinogradov *et al.*
+			(1973); Gorska and Nazarewicz (1974).
CdSe	167	210	
ZnTe	See above		Zinc blende: R, 1-mode plus weak structure
+			on TO, Nakashima *et al.* (1971).
ZnSe	See above		
CdSe	See above		Wurtzite near 50%, polytypes at other
+			concentrations, R, probably 1-mode,
ZnSe	See above		Brafman (1972).

have measured the reflectivity spectra and analyzed the results using the three-coordinate isodisplacement model discussed in Sec. II. This type of model is often denoted REI for "random element isodisplacement" model (Chen *et al.*, 1966). The fit of the model to the measured points is good, considering the scatter in the experiments. To obtain the fit the authors have included a concentration-dependent term in the short-range force constants. (A concentration dependence of the long-range forces arising from the local field correction is explicitly included in the fundamental equations.) Chen *et al.* (1966) have outlined a relationship between the short-range forces and the lattice parameter involving the Gruneisen constant. For reasons indicated in Sec. II (see also Chang and Mitra, 1968), it appears unlikely that there should be any such relationship which is fundamental. The argument Chen *et al.* use is based on the Gruneisen relation

$$\Delta\omega/\omega = \gamma(\Delta V/V)\,, \tag{9.1}$$

where V is crystal volume, and γ the Gruneisen constant. If we identify ω with the optic mode near $q=0$ and introduce a force constant k by the proportionality $\omega^2 \sim k$, we obtain

$$\Delta k/k = 6\gamma(\Delta a/a)\,, \tag{9.2}$$

where $a \sim V^{1/3}$ is a linear cell dimension. For $GaAs_yP_{1-y}$ Chen *et al.* take $\gamma = 0.97$. Equation (9.2) then suggests

TABLE IX.3. Alkali and alkaline-earth mixed crystals.

	Pure crystal ω_{TO} (cm^{-1})	Pure crystal ω_{LO} (cm^{-1})	Mixed crystal: structure, references, and mode behavior
KCl + NaCl	141 164	201 260	Unstable structure; ir, Kruger *et al.* (1928), data scanty, probably 1-mode.
KBr + KCl	113 141	157 201	Cubic; r-Nair and Walker (1971); ir, Fertel and Perry (1969); 1-mode; zone boundary Raman active modes; CPA theory, Taylor (1973).
RbI + KI	75 103	100 135	Cubic: ir, Fertel and Perry (1969); 1–2 mode; CPA theory, Taylor (1973).
RbBr + KBr	~88 113	? 157	Cubic: neutron, Buyers and Cowley (1968); 1-mode type behavior except in LA branch near zone boundary.
KI + KBr	103 113	135 157	Cubic: R and x-ray, Nair and Walker (1973). Single crystals not obtained at many intermediate compositions. Zone boundary vibrational features identified.
RbCl + KCl	~118 114	? 201	Cubic: R, Nair and Walker (1973); ir, Mitsuishi (1965); ir, Kruger *et al.* (1928); probably 1-mode for infrared modes. Raman spectra show strong E_g feature identified as TO (L point).
TlCl + KCl	~66 141	~170 201	ir-Kruger *et al.* (1928), data scanty, probably 2-mode. Note the pure compounds crystallize in different structures.
LiD + LiH	450 580	835 ~1220	Cubic: ir, Montgomery and Hardy (1965); anomalous mode behavior; theory, Jaswal and Hardy (1968).
KI + KCl	103 141	135 201	Cubic: R, Nair and Walker (1973). One composition studied. Spectrum similar to KCl + KBr; main feature an activated mode.
BaF_2 + SrF_2	184(240 [a]) 217(285 [a])	326 374	Cubic: R, Chang *et al.* (1966); ir, Verleur and Barker (1967b); ir, Barker and Verleur (1967); R, Lacina and Pershan (1970); 1-mode.
SrF_2 + CaF_2	217(285 [a]) 257(322 [a])	374 463	Cubic: R, Chang *et al.* (1966); ir, Verleur and Barker (1967b); R, Lacina and Pershan (1970); 1-mode.
AgBr + AgCl	90 120	135 200	Cubic: ir and second order R, Bootz *et al.* (1974); 1-mode.

a force change of approximately six times the lattice dilation in passing from $y = 0$ to $y = 1$. Table IX.6 shows some collected results for crystals which have been fitted by isodisplacement models. A factor near 6 is seen to relate the force constant and lattice parameter changes on passing from the $y = 0$ to $y = 1$ crystal for many of the mixed systems, thus Eq. (9.2) does appear to be empirically useful. $Ga_yAl_{1-y}As$ and $Co_yNi_{1-y}O$ are seen to deviate considerably, though the reason for the latter case may lie in the special requirements of mode degeneracy, imposed by Chang and Mitra in analyzing this one-mode system. The more complex isodisplacement model of Verleur and Barker (1966) does not require the concentration-dependent force constants given by (9.2). This is because the model introduces four different force constants between Ga and As, depending on whether there are 0, 1, 2, or 3 nearest-neighbor Al ions. Since the number of nearby Al ions depends on the concentration, the same

TABLE IX.4. Polar mixed crystals—oxides and fluorides.

	Pure crystal ω_{TO} (cm^{-1})	Pure crystal ω_{LO} (cm^{-1})	Mixed crystal: structure, references, and mode behavior
CoO	400	580	Cubic: ir, Gielisse *et al.* (1965); 1-mode.
+			
NiO	348	575	
$KNiF_3$	151	165	Cubic perovskite: ir, Barker *et al.* (1968); 1-mode behavior for highest- and lowest-frequency modes; 1–2 mode behavior for intermediate modes.
	242	306	
	439	527	
+			
$KMgF_3$	164	192	
	296	360	
	446	550	
$KTaO_2$	~90	184	Cubic perovskite but phase change for Na > 0.7: ir, R, Perry and Tornberg (1969); 1-mode behavior for most but not all bands.
	200	421	
	546	838	
+			
$NaTaO_3$	Noncubic		
$KTaO_3$	See above		Cubic perovskite over part of composition range: one composition studied; ir, Barker (1967).
+			
$KnbO_3$	Cubic only above 410 °C		

end result is obtained—mode frequencies shift with composition. This model, however, allows identification of specific local environment of Ga, say, as opposed to the one average environment described by the three-coordinate model.

Chang and Mitra (1970) have also fitted the $Ga_yAl_{1-y}As$ data in Fig. 139 and obtain the same results with a similar model which omits local field corrections by using effective force constants.[11] From Fig. 139 the upper mode branches are seen to extrapolate to 357 cm^{-1} for the local mode of Al_{Ga} in GaAs. This is in reasonable agreement with the local mode frequency of 362 cm^{-1} measured at 80 °K (Table IV.1). Figure 139 is typical of the spectra of two-mode crystals where the $y = 0$ and $y = 1$ host crystals have well-separated modes (cf. Fig. 30). The tables show other two-mode systems.

2. One-mode systems and the question of the missing modes

Figure 140 shows the reflection spectra of a mixed crystal where the two pure crystals have almost degenerate mode frequencies. The spectra illustrate one-mode behavior. There is evidence of weak (perhaps second-order) bands in the 400–450 cm^{-1} region in CoO. The somewhat sharper weak bands in the $y = 0.50$ mixed crystal suggest that the bands here might be a mixed crystal effect. Figure 141 shows the analysis by Gielisse *et al.* (1965) of the data in terms of the transverse optic mode frequency ω_{TO} and the effective charge q^*. The decrease in ω_{TO} and increase in q^* with y combine to give a longitudinal optic mode frequency near 575 cm^{-1} (not shown) which is almost independent of y. A virtual-ion model of the type described in Sec. II can fit the data of Fig. 141 when both the effective charge and force constant are taken to be concentration dependent. The success of such a simple model might have been expected from the close similarity of Co and Ni with respect to mass and outer electron configuration.

Barker and Verleur (1967) and Barker (1968a) have discussed the application of a three-coordinate isodisplacement model to spectra like those shown in Fig. 140. The application to a one-mode crystal is a test of the model, since one hopes that a model which describes the presence of two types of cation (Co and Ni) will fit one-mode crystals by merely varying some parameters. For an appropriate choice of parameters in the three-coordinate model, two transverse optic modes occur but one is very weak for all concentrations, yielding at most some fine structure above or below the main transverse optic frequency. The frequency of the weak mode is controlled principally by the Co–Ni force constant used in the model, and this frequency can be chosen to coincide with the structure near 450 cm^{-1} in the mixed crystal. The eigenvector of the stronger mode in the model has Co and Ni moving together in phase, confirming that the virtual-ion model is indeed appropriate for the strong mode. The weaker mode of the model consists of Co vibrating against Ni with the O ion remaining almost stationary. Such a mode has a very small infrared strength since the two ions are positive and the net dipole moment arises only from the small difference in their effective charge and amplitude. This is essentially the same weak mode discussed by Matossi (1950). Chang and Mitra (1968) have taken a completely different approach in using the three-coordinate isodisplacement model to fit

[11] Chang and Mitra treat their polarization equation quite differently than Barker (1968) or Ilegems and Pearson (1970). Essentially they average z^2 while the latter authors treat the charge z at the same level as the mass and force constants. This latter method can be thought of as averaging z. In $Ga_yAl_{1-y}As$ the difference between the methods is quite small.

TABLE IX.5. Other mixed crystals.

Pure crystals	Modes (cm^{-1})	Comments and references
Bi + Sb	73, 99 (Raman) 115, 155 (Raman)	R, Zitter and Watson (1974); Lannin ( ) complicated 2-mode behavior; modes are ir inactive.
Ge + Si	301 (Raman) 520 (Raman)	R, Feldman *et al.* (1966); ir, Cosand and Spitzer (1971); electron tunneling, Logan *et al.* (1964); theory, Barker (1968b).
Te + Se	Strongest 92 $\perp c$ TO modes 86 $\parallel c$ Strongest 138 $\perp c$ TO modes 104 $\parallel c$	ir and theory, Geick and Hassler (1969); 1-mode behavior plus strong extra mode for $0.2 < y < 0.8$.
Pb + In	Metal Metal	Electron tunneling, Rowell *et al.* (1965); high-frequency indium modes seen at low In concentrations.
HgI_2 + $HgBr_2$	13, 41, 141 (Raman) –, 59, 188 (Raman)	R, Nakashima *et al.* (1974); layer structure orthorhombic crystals; complex mode structure with some 1- and some 2-mode behavior.
CuBr + CuCl	132 TO, 166 LO 170 TO, 210 LO	R, ir, Murahashi *et al.* (1973); 2-mode behavior plus anomalously strong gap mode at CuCl end of concentration range.
$HgCr_2Se_4$ + $ZnCr_2Se_4$	59, 171, 275, 289 86, 226, 276, 302	ir on powders–Wakamura *et al.* (1973); spinel structure; 5 principle modes in 40–340 cm^{-1} range; lowest modes show 2-mode behavior; rest show 1-mode behavior.
Pt + Ni	Transverse acoustic branch studied along (001) direction	Neutron scattering for 5% and 30% Pt. Kunitomi *et al.* (1973). Resonance mode near 120 cm^{-1} causes gap in acoustic branch.
$Pd_{0.45}$ + $Ni_{0.55}$	All acoustic branches studied along principal symmetry directions	Neutron scattering, Kamitakahara and Brockhouse (1972); one mode behavior of all modes. Virtual-ion model fitted to dispersion curves.

cases of one-mode crystals. They assume that such systems do not have local modes or weak subsidiary modes (see by contrast Te_ySe_{1-y} below) and they therefore force the second optic mode given by the three-coordinate model either to fall at zero frequency or to be degenerate with the first optic mode. This method gives mathematically satisfying solutions which, however, are somewhat unphysical. The first method they propose yields equations which cannot be approached in a continuous fashion and it therefore appears unsuitable for studying the transition from two-mode to one-mode behavior. This solution requires the second-neighbor force constant to be large and negative. Their second method deserves more comment. The forcing of a degeneracy on the system and thus in a sense eliminating the second optic mode appears attractive for explaining one-mode behavior. The degeneracy arises in the limiting case of $k_{12} = 0$ in the discussion given by Barker and Verleur (1967). In this limit the two modes have eigenvectors which are not determined by the equations, as is usual in a case of degeneracy. The driven response has one peak or mode which selects the linear combination of eigenvectors corresponding to the "virtual-ion-like" motion, i.e., Co and Ni together vibrating against oxygen. If one has no independent evidence of weak extra modes, the choice of whether to choose a model with the second mode degenerate or just very weak but nondegenerate cannot be resolved. From Table IX.6 it may be noted that the degeneracy condition in $Co_yNi_{1-y}O$ requires quite large force constant changes compared with the lattice dilation. This might be taken as a warning that the degeneracy method is not appropriate. A thorough investigation of the best method of fitting the one-mode $Co_yNi_{1-y}O$ system (or any similar system) must involve checking any weak structure near the main mode to see whether it is first

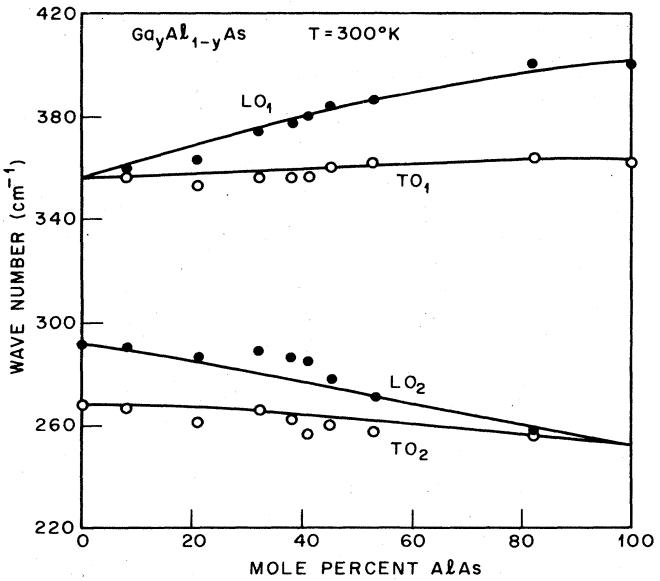

FIG. 139. TO and LO mode frequencies as obtained from a Kramers–Kronig analysis of the mixed crystal spectra, plotted versus alloy composition. The solid lines are calculated from the REI model. From Ilegems and Pearson (1970).

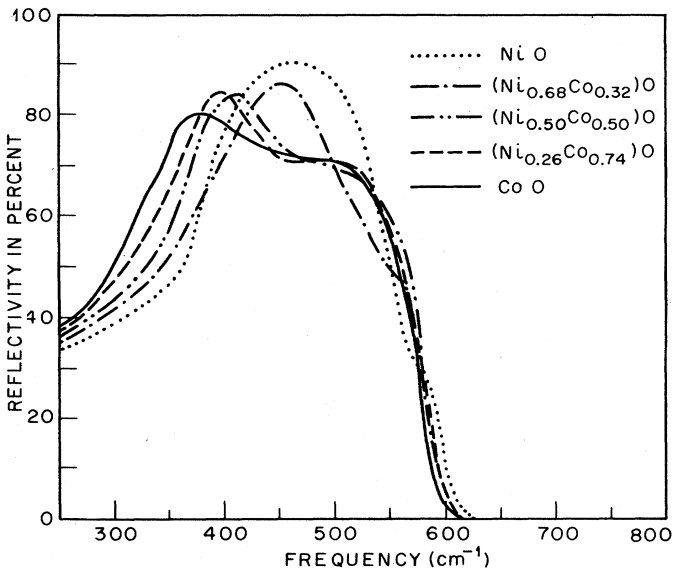

FIG. 140. Reflectivity spectra of the mixed crystal series NiO+CoO. From Gielisse *et al.* (1965).

order (e.g., by temperature dependence). In addition high-pressure experiments can be used to actually measure the coefficient in Eq. (9.2) which is applicable to the system. Knowledge of this coefficient puts an additional constraint on the force constants and can be used to check any proposed model of the system. Additional comments on the applications of the isodisplacement model to one-mode systems are made below for other crystals.

Figure 142 shows a linear chain model of $Co_{0.5}Ni_{0.5}O$ with a random distribution of the cations. In part (a) the eigenvector for part of the chain corresponding to the strong infrared mode is shown. As in the isodisplacement mode, Co and Ni both vibrate against O ions, giving a large dipole moment. In part (b) one of the weaker modes is shown. It corresponds roughly to the weaker mode in an isodisplacement model of the usual type, where the second optic mode has not been caused to be degenerate or to fall at zero frequency. Note that we cannot achieve an exact correspondence between the isodisplacement model and the linear chain model since one has three coordinates and three modes and the other has N (=48 here). The point we now wish to make is that the weaker mode [Fig. 142(b)] can be thought of as a zone boundary mode activated by the disorder. In part (c) of the figure the zone boundary acoustic mode of pure CoO (or NiO) is shown. It is obvious that the weak infrared mode is a small perturbation of this zone boundary mode. In fact, however, the eigenvector of the weak infrared mode is a linear combination of many modes of the unperturbed pure chain, so that the identification with the pure chain zone

TABLE IX.6. Dependence of force constants on composition in isodisplacement models.

Mixed crystal	Lattice parameter change	Force constant change	Reference
$GaAs_yP_{1-y}$	3.7%	21.6%	Chen *et al.* (1966)
$In_yGa_{1-y}P$	8%	40%, 50% [a]	Barker (unpublished)
$Ga_yAl_{1-y}As$	0.1% [b]	0.6%, 34% [a]	Ilegems and Pearson (1970)
		15%	Chang and Mitra (1970)
$ZnSe_yS_{1-y}$	4.3%	18%	Chang and Mitra (1968)
$CdSe_yS_{1-y}$	4.3% [c]	13%	Chang and Mitra (1968)
Bi_ySb_{1-y}	5%	30%	Zitter and Watson (1974)
$Co_yNi_{1-y}O$	1.8%	25%	Chang and Mitra (1968)

[a] The two values refer to two different force constants in the model.
[b] Somewhat uncertain because of the limited accuracy of the x-ray measurements.
[c] Average of c axis and a axis changes.

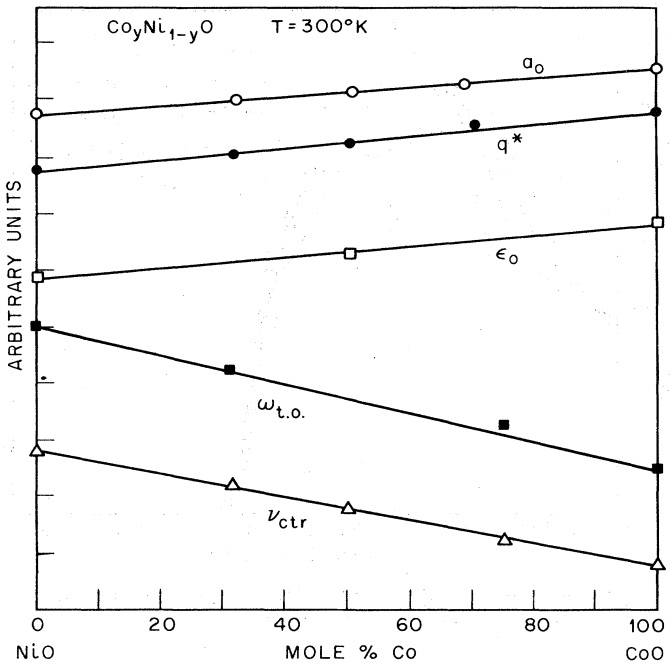

FIG. 141. Lattice constant (a_0), effective ionic charge (q^*), dielectric constant (ϵ_0), transverse optical mode frequency (ω_{TO}), and center frequency (ν_{ctr}) versus composition in the series NiO+CoO. From Gielisse *et al.* (1965).

boundary mode is qualitative. In Fig. 27 some eigenvectors for the mixed crystal $GaAs_{0.875}P_{0.125}$ were shown. In that case the eigenvectors were much more mixed so that identification of weak optic modes with zone boundary modes of the pure crystals was more difficult. Several authors have suggested that weak structure in a mixed crystal spectrum might be a normally inactive mode made active by the disorder. Usually there is a lack of supporting arguments since the pure crystal spectra throughout the Brillouin zone are unknown. This is the case for CoO and NiO. An exception is a recent study of KCl_yBr_{1-y} by Raman scattering (Nair and Walker, 1971). Here the pure crystal phonon-dispersion curves are known in detail. A weak peak in the mixed crystal spectra near 120 cm^{-1} is identified as a TO(X) zone boundary phonon. Further progress in identifying and classifying weak structure in mixed crystals must await detailed models which are more realistic than the linear chain model. Some principals emerge clearly, however, from the simple models studied to date. First, labeling of mixed crystal spectral features by pure crystal modes of sharp wave vector can only be done in a qualitative manner. In some systems where the mass or force constant perturbations are large, such labels are probably useless and impossible to verify. Secondly, the appearance of only one peak in the infrared or Raman spectra should not tempt one to completely eliminate or forget other possible modes. The atoms and hence the degrees of free-

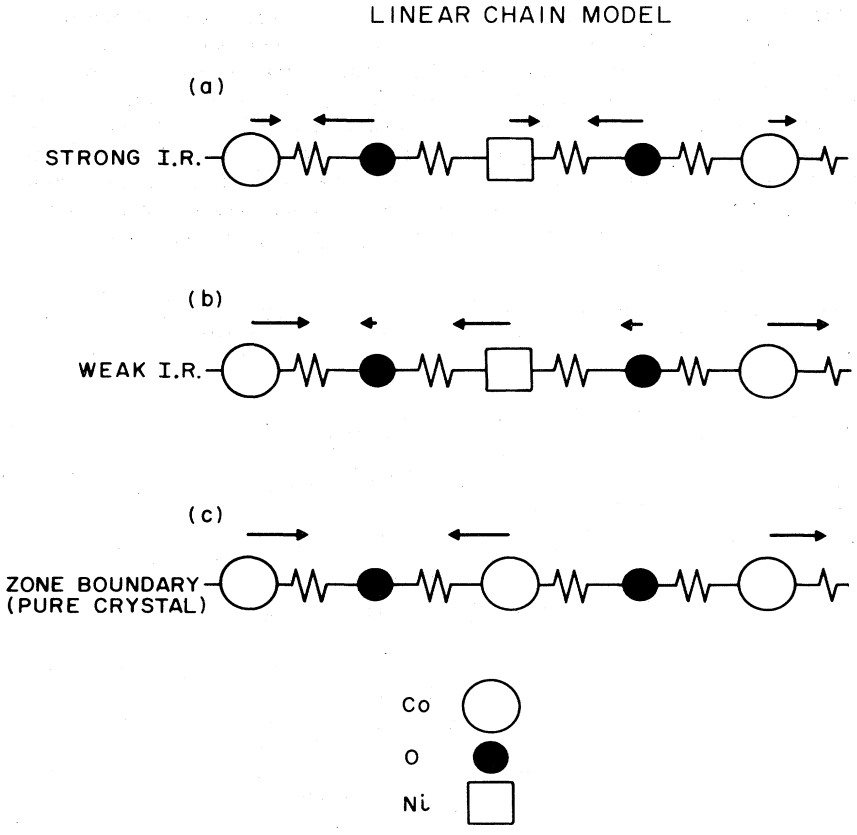

FIG. 142. Linear chain model for $Co_{0.5}Ni_{0.5}O$. Only nearest-neighbor bonds are indicated for simplicity. In (a) the strongest infrared mode is shown. In (b) the most prominent of the many weak infrared modes is shown. (c) is the zone boundary eigenvector of the highest-frequency acoustic mode of pure CoO.

dom are really there in the crystal. We have seen how accidental near cancellation of dipole strength makes such modes weak—some other spectroscopic technique should then be used if possible to search for the modes.

3. One-mode systems with structure

Figure 143 shows the Raman-active mode for two related mixed crystals, $Ba_ySr_{1-y}F_2$ and $Sr_yCa_{1-y}F_2$, from the work of Chang, Lacina, and Pershan (1966). In the pure crystals the infrared-active and Raman-active modes belong to different irreducible representations and hence are completely independent modes, unlike the situation in the zinc blende structure semiconductors. The Raman-active mode consists of the two F ions in the primitive cell moving against each other as shown in Fig. 144. This motion can occur independently along each of the three cube axes giving a threefold degenerate mode. In the mixed crystal there is a surprisingly linear variation of this mode frequency with composition y. Figure 145 shows the mode linewidth as a function of y; the mode approximately doubles its linewidth near

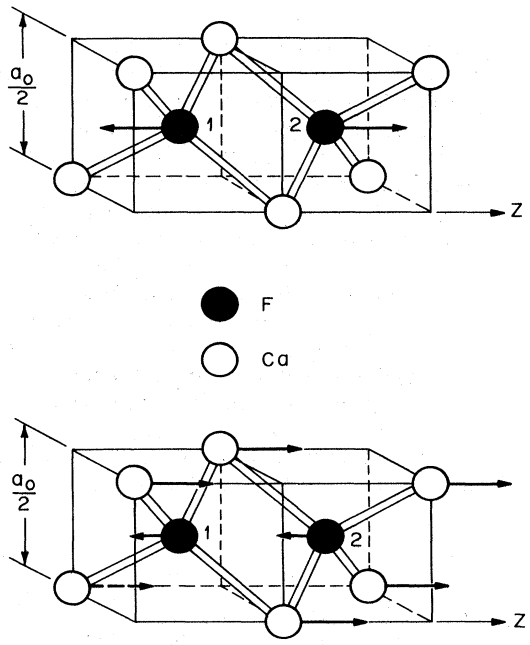

FIG. 144. Primitive cell of the CaF_2 (fluorite) structure containing two F ions at the centers of metal-ion tetrahedra. The structure is cubic, the standard x-ray cell of side a_0 containing four formula units. Arrows show the Raman mode eigenvector in (a) and the infrared mode eigenvector in (b).

$y = 0.5$. A search of the infrared spectrum (Verleur and Barker, 1967b) at the Raman mode frequency (with negative results) shows that the mixed crystal Raman mode maintains to a considerable extent its orthogonality to the infrared modes in spite of the disorder. Pershan and Lacina (1970) have described a Green's function theory which proceeds beyond the one-defect method to include terms dependent on concentration. While many approximations must be made, they predict trends which are consistent with the mode frequency and

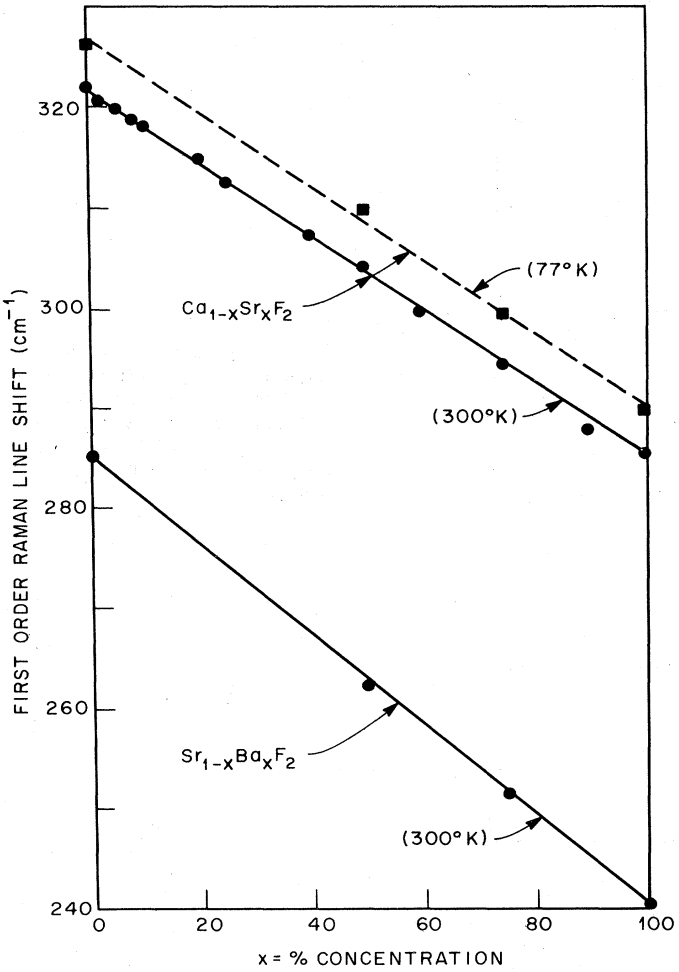

FIG. 143. The first-order Raman frequency of mixed crystals $Ca_{1-x}Sr_xF_2$ and $Sr_{1-x}Ba_xF_3$ as a function of the concentration x. In the pure crystals, there is only one first-order Raman vibration. From Chang, Lacina, and Pershan (1966).

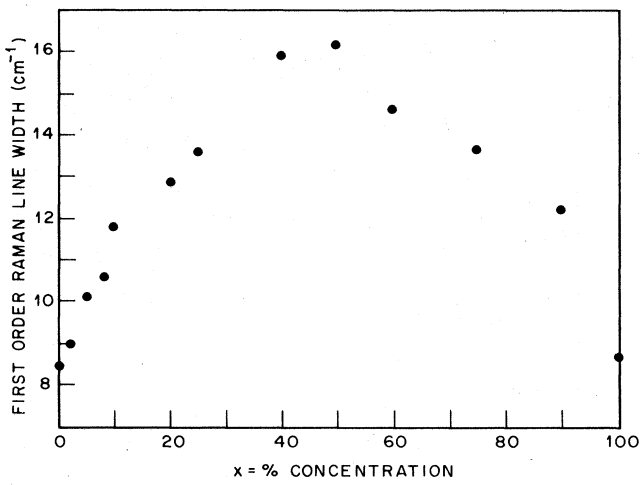

FIG. 145. The total linewidth measured at half-intensity of the first-order Raman-scattered light from the mixed crystals $Ca_xSr_{1-x}F_2$ at room temperature. The instrumental linewidth is 4.7 cm^{-1}. From Chang, Lacina, and Pershan (1966).

linewidth.

Verleur and Barker (1967b) have studied the infrared spectra of $Ba_ySr_{1-y}F_2$ and $Sr_yCa_{1-y}F_2$. Figure 146 shows the spectra of one system. The spectra were taken at 90 °K to remove some temperature-dependent second-order structure which hampers the search for weak modes connected with true mixed crystal effects. The data in Fig. 146 may be analyzed by a Kramers–Kronig method and show one strong and one weak peak in the $\mathrm{Im}(\epsilon)$ and in the $\mathrm{Im}(-1/\epsilon)$ spectra. These peak frequencies are plotted in Fig. 147. The modes are numbered ω_{TO1} for the weak mode, and ω_{TO5} for the main mode, for consistency with the model discussed below. The strengths S_1 and S_5 of the TO modes shown in Fig. 147 should be contrasted with the strengths S_1 and S_2 shown in Fig. 30 for a two-mode crystal.

Verleur and Barker (1967b) have fitted 18-coordinate isodisplacement models to the barium–strontium fluoride and strontium–calcium fluoride mixed crystal spectra. The smallest conceivable set of isodisplacements would be four [u(Ba), u(Sr), $u(F_1)$, and $u(F_2)$] in $Ba_ySr_{1-y}F_2$, the two distinguishable F coordinates being required to describe the Raman mode. Because of the introduction of many more coordinates, the authors are able to introduce more probabilities than the y and $1-y$ terms which occur in a three-coordinate model. This freedom allows the evaluation of an order parameter β as discussed in Sec. II (Verleur and Barker, 1966, 1967b). Figure 148 shows the infrared modes given by the model and Fig. 149 the transverse mode strengths. Note that a cluster of four closely spaced modes ($i=1$ to 4) actually gives the structure called ω_{TO1} in Fig. 147. Figure 150 shows the actual fit to reflectivity achieved for the $y=0.5$ crystal. The authors also fit the Raman data of Chang *et al.* discussed above. The parameter β must be set near zero for all fits, indicat-

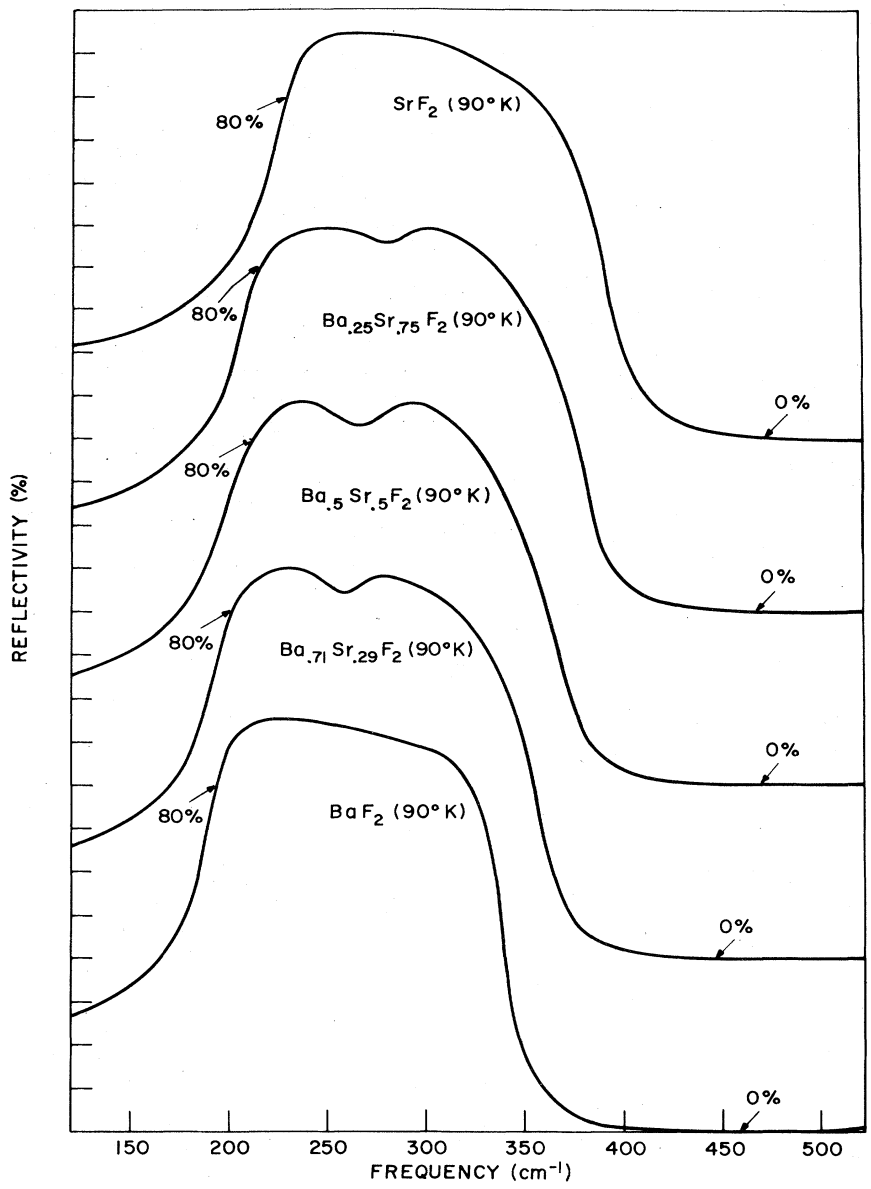

FIG. 146. Comparison of experimental reflectivity spectra at 90 °K of the pure crystals BaF_2 and SrF_2 with three mixed crystals of $Ba_ySr_{1-y}F_2$. From Verleur and Barker (1967b).

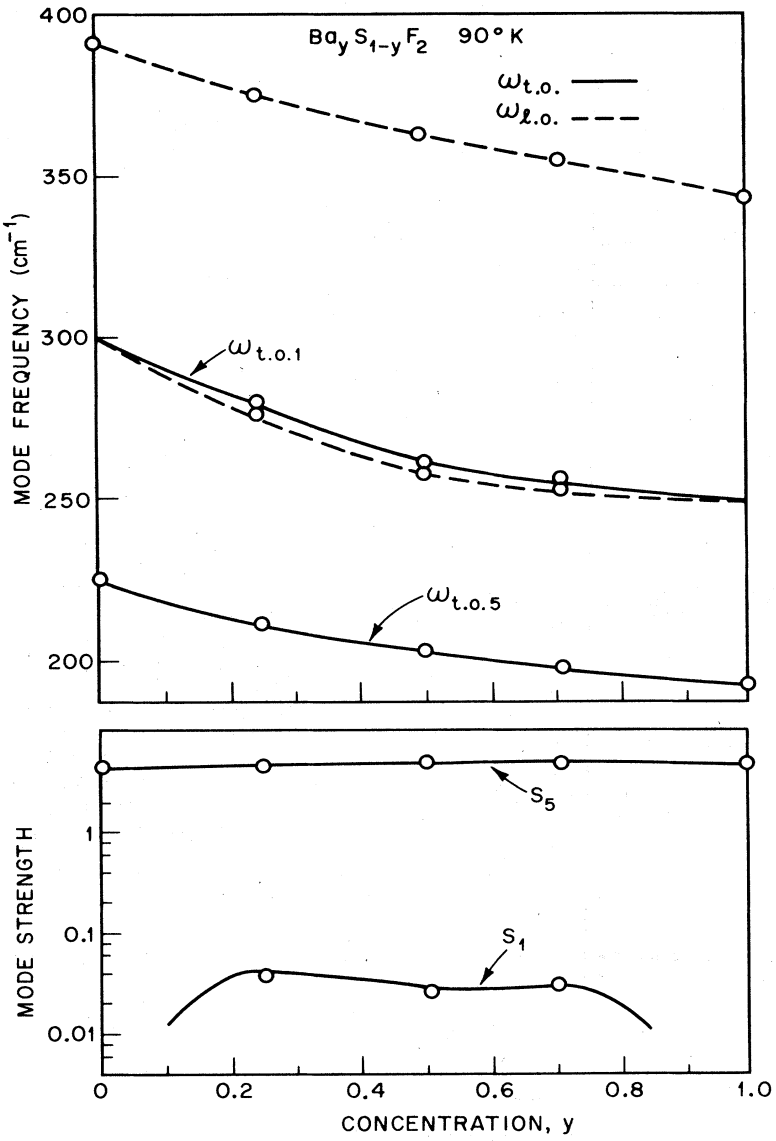

FIG. 147. Measured mode frequencies for five crystals from the system $Ba_ySr_{1-y}F_2$. The curves are merely smooth extrapolations. The strong mode is labeled ω_{TO5} and its strength is given in the lower part of the figure. The strength of ω_{TO1}, the weak mode, can only be determined for the three mixed crystals, but must approach zero at $y=0$ and $y=1$. Data taken from Verleur and Barker (1967b).

ing a near random arrangement of cations. An interesting feature of this isodisplacement model is the prediction of groups of modes below the frequency of the main reststrahlen band. The predicted strength of these modes is insufficient to cause measurable structure in the reflectivity. A search has been made in transmission using very thin samples and low temperatures to reduce the usual two-phonon absorption in the same region. On comparing a mixed crystal with a pure crystal it is found that there is considerable extra absorption in the 50 to 150 cm^{-1} frequency range, but it consists of a broad band unresolvable into components. It therefore remains an open question as to whether the model has correctly predicted this absorption. The model may be showing the correct trend, but just as with the finite linear chain model it can show only a few isolated modes where a more complete model would show a continuum of band absorption.

4. Two-mode systems with structure

Figure 151 shows the infrared reflectivity of $GaAs_yP_{1-y}$. There are two main bands for each composition, one near 270 cm^{-1} and the other near 360 cm^{-1}. Because these frequencies are near the TO frequencies of pure GaAs and GaP these bands have been called the GaAs band and GaP band. The gross appearance of the spectra is like that of Fig. 139, i.e., a two-mode system. However, there is considerable fine structure in each band which is first order (Verleur and Barker, 1966). Figure 152 shows a Raman spectrum for a $y=0.15$ crystal measured by Strahm and McWhorter (1969), which confirms the presence of fine structure. Chen *et al*. (1966) have fitted the transverse optic mode frequencies with a three-coordinate isodisplacement model. Barker (1968b) and Chang and Mitra (1968) have extended this three-coordinate model to include ion

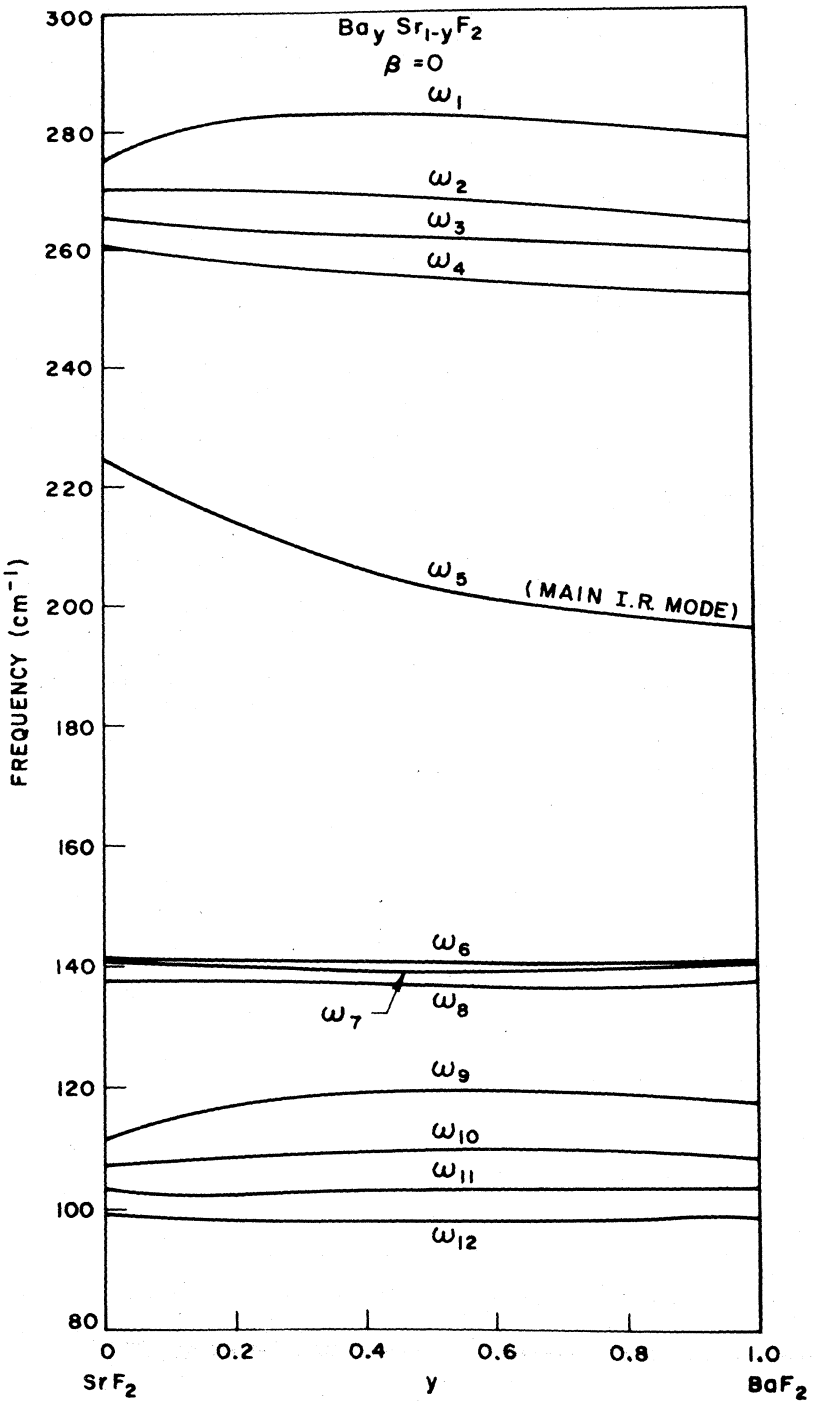

FIG. 148. Infrared-active mode frequencies for $Ba_ySr_{1-y}F_2$ versus composition (y) computed from the model for $\beta = 0$. In this and succeeding figures the model is evaluated for $T = 90\,°K$. From Verleur and Barker (1967b). Here ω_5 is to be compared with ω_{TO5} of the preceding figure and the group $\omega_1 - \omega_4$ with ω_{TO1}.

charges, so mode strengths can be evaluated. This allows the calculation of both transverse and longitudinal optic mode frequencies. The results of Chang and Mitra are shown in Fig. 153. Verleur *et al.* (1966) developed a thirteen-coordinate model in order to explain the main TO and LO modes and the fine structure. Since a thirteen-coordinate isodisplacement model yields twelve optic modes, it might be argued that a five- or six-coordinate model would be more appropriate to the spectra. Thirteen coordinates are suggested by the different possible nearest-neighbor ion configurations in three dimensions. To date no one has been able to suggest how to pick the five or six most significant coordinates (parenthetically we note that even the Green's function method faces the same essential problem). Figure 154 shows the frequencies of the five strongest TO and LO modes. Figure 151 shows the fits achieved with the thirteen-coordinate model. The fit

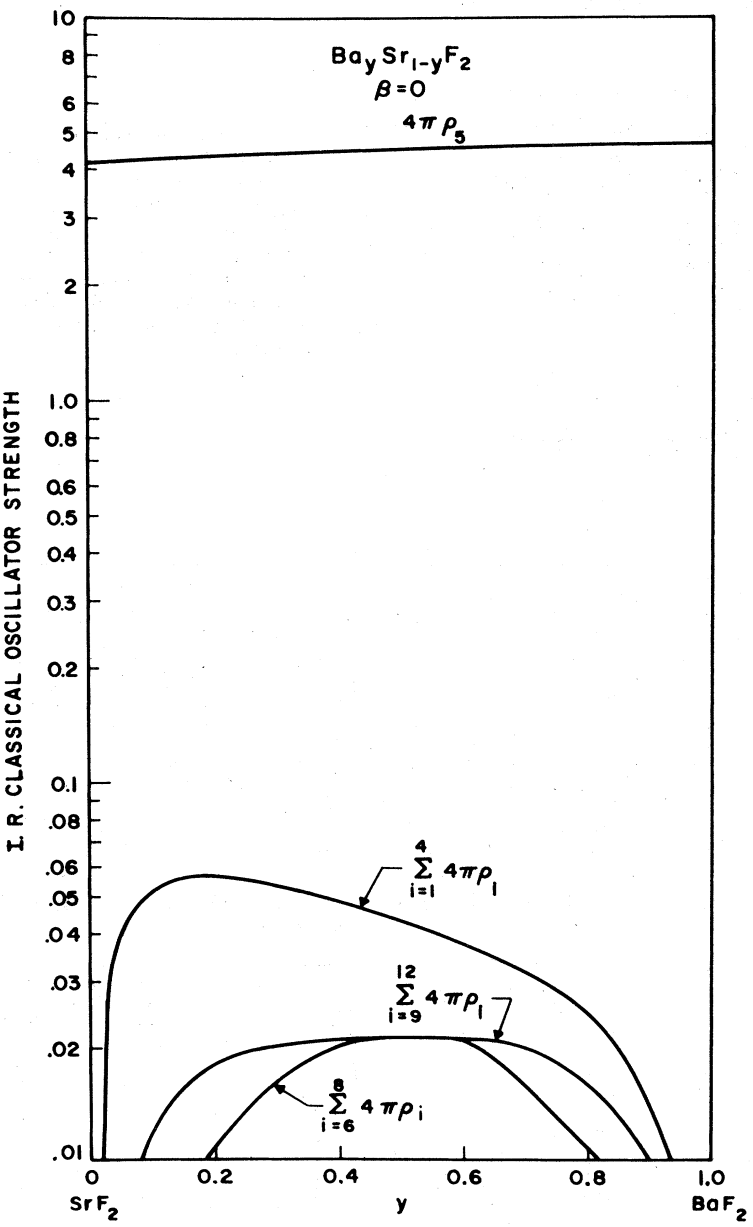

FIG. 149. Infrared-active mode strengths for four groups of modes in $Ba_ySr_{1-y}F_2$ versus composition (y) computed from the model used in the preceding figure. $4\pi\rho_5$ is to be compared with S_5 of Fig. 148 and the curve immediately below with S_1.

is quite good for the reflectivity. In contrast to the mixed fluorite crystals, the order parameter β requires large positive values for the fits, indicating a tendency for neighboring anions to be of the same type. Strahm and McWhorter (1969) have fit the same model to their Raman data but criticized some of the details of certain modes.

As in the case of the mixed fluorite crystals discussed above, there are some low-frequency (100–140 cm^{-1}) weak modes predicted by the $GaAs_yP_{1-y}$ model (Verleur and Barker, 1966). It is of interest that Strahm and McWhorter find weak Raman-active bands at 100 cm^{-1} and 210 cm^{-1} in additon to those shown in Fig. 152. In the thirteen-coordinate model of $GaAs_yP_{1-y}$, the eigenvectors of the modes near 100 cm^{-1} (Verleur and Barker, 1966) consist of entire units of primitive cells vibrating against each other. This suggests that short-wavelength (perturbed zone boundary) vibrations may cause absorption in the 100–140 cm^{-1} range. Pure GaAs and pure GaP have broad peaks in the one-phonon density of states near 100 cm^{-1}. The low-frequency modes may therefore be thought of as induced acoustic mode activity, though it is premature to classify such modes without a better model of the mixed crystal. Nearly all the isodisplacement models developed to date define coordinates which depend on nearest-neighbor configurations and are associated with long-wavelength vibrations (see, however, Barker, 1968b). Such coordinates are unsuitable for describing the shorter-wavelength lattice vibrations, so that further progress in understanding the fine structure must be coupled to the development of better models, as mentioned previously.

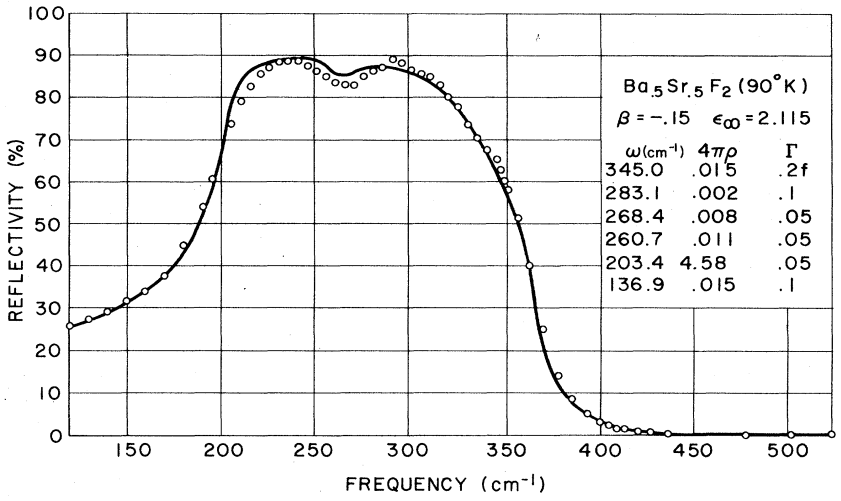

FIG. 150. Theoretical fit (solid line) to experimental reflectivity data for $Ba_{0.5}Sr_{0.5}F_2$. The oscillator parameters and β value are listed in the figure. f denotes a second-order mode not obtained directly from the model. From Verleur and Barker (1967b).

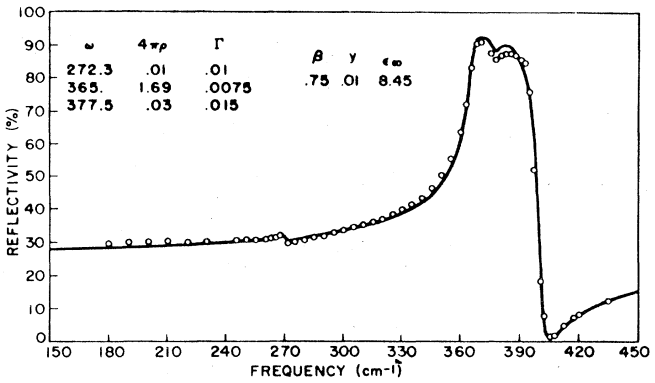

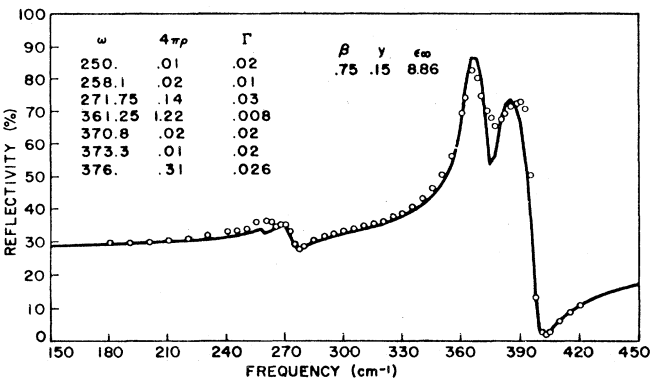

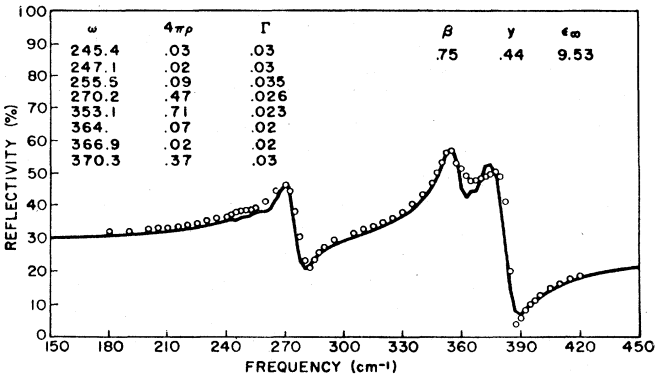

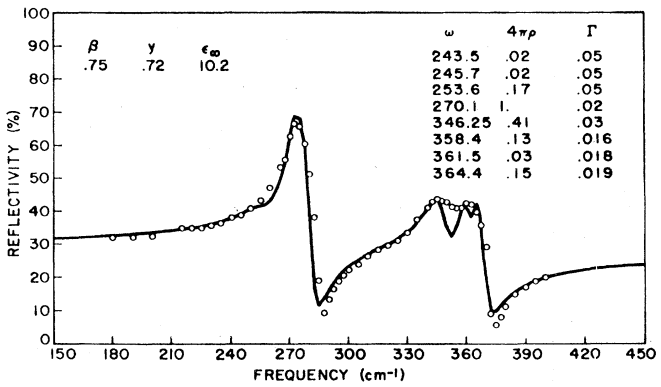

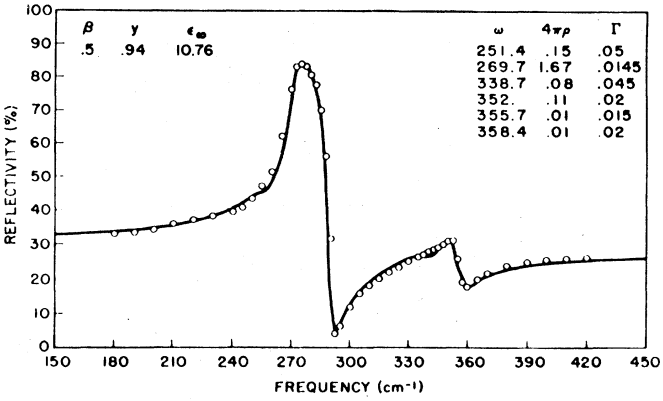

FIG. 151. Infrared spectra of $GaAs_yP_{1-y}$. The points are the measured reflectivity at 300 °K. The solid curves are calculated from the listed modes which are predicted by a thirteen-coordinate isodisplacement model. From Verleur and Barker (1966).

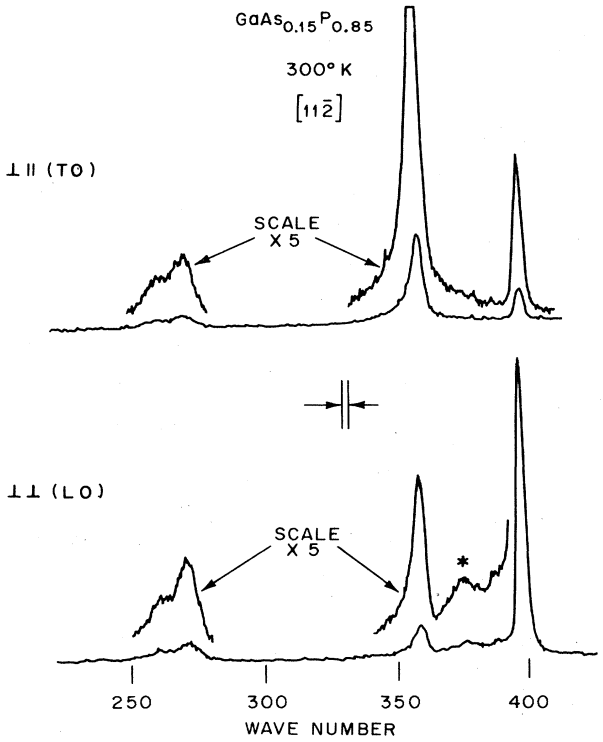

FIG. 152. Polarized Raman spectra of room temperature $GaAs_{0.15}P_{0.85}$. The spectrum of LO phonons is expected in the ($\perp\perp$) configuration and of TO phonons in the ($\perp\parallel$) configuration. Internal reflections of the laser beam and scattered light prohibit complete separation. The strongest fine structure is marked *. From Strahm and McWhorter (1969).

D. One-mode versus two-mode behavior

Lucovsky, Brodsky, and Burstein (1970) have attempted to establish criteria for predicting one- or two-mode behavior in mixed crystals. Their procedure essentially examines the behavior of each mixed system in the $y \to 0$ and $y \to 1$ limit where local mode theories are applicable. Using actual data for the local mode frequencies or estimates based on a simple linear chain mass defect model, they correlate their predictions and observations for a wide variety of mixed crystals. Figure 155(a) shows the simplest application of these ideas for a case like $GaAs_yP_{1-y}$. In the figure the limiting frequencies of the main reststrahlen band near $y=0$ and $y=1$ are plotted by the open and solid points. Near $y=0$ there is a localized mode in the gap (whose existence could be determined by measurement or by a model calculation). Near $y=1$ there is a localized mode at frequencies above the reststrahlen band of the $y=1$ compound. The solid lines show the most obvious interpolation scheme using four lines with no line crossings. This leads to two-mode behavior, i.e., two main TO and LO modes over most of the composition range. Note, however, that there are many other possibilities and extensions. Figure 155(b) is similar to Fig. 155(a) except that near $y=1$ there is a strong local mode plus a weaker pair mode, say, at slightly lower frequencies. The pair mode is not predicted of course by three-coordinate isodisplacement models. Simple probability arguments suggest that this mode would have a strength which varies as y^2 while the local or gap mode strength varies as y for small y. A six-line interpolation scheme is shown in Fig. 155(b). The spectra near $y=0.5$ may now look like two modes plus fine structure or three modes, depending on the actual frequencies of the modes. To date most mixed crystals which might fall into this category can be classified fairly naturally as two-mode plus weak structure. The criterion of Lucovsky *et al.* depends on a comparison of the host crystal atom masses with the mass being substituted at each end of the composition range. Essentially, if a gap and a local mode are formed near the end points as illustrated in Fig. 155(a), then the mixed crystal is predicted to exhibit two-mode behavior. Matsuda (1967) has suggested a different criterion also based on the masses involved. Chang and Mitra (1971) have reviewed the above criteria and have proposed a more complicated criterion which includes the force constant for the minor component as well as the masses of all the atoms involved. Harada and Narita (1971) have included more detail by considering the size of the second-neighbor force constant. For the crystal $A_yB_{1-y}C$ their criterion includes the force F_{AB}. Essentially the criterion hinges on noting that if F_{AB} is large, then the A and B ions must move together, which prevents two-mode behavior. Barker *et al.* (1968) have noted the importance of certain forces which can only be measured in the mixed crystal and which can essentially control the formation of one or two modes.

Elliott *et al.* (1974) have also considered the criteria discussed above and note the rather crude nature of the models (one-dimensional models, isodisplacement models, etc.) used to derive the criteria. They propose a criterion based on the coherent potential approximation applied to crystals of the type $A_yB_{1-y}C$. Assuming that the width of the optic band is given by $\omega_{LO}-\omega_{TO}$ and that the band has a parabolic density of states (and also that the acoustic band can be neglected), they derive the condition

$$\left|1-\frac{\mu}{\mu'}\right| > \frac{\epsilon(0)-\epsilon(\infty)}{\epsilon(0)+\epsilon(\infty)} \tag{9.3}$$

for two-mode behavior over the entire composition range. (Here μ is the reduced mass of the host crystal, and μ' the reduced mass corresponding to the minor constituent.) They apply (9.3) to a list of 21 crystals and predict the observed behavior with only one serious discrepancy. Because of the assumptions and inclusion of the dielectric constants as determining parameters, (9.3) cannot be applied to nonpolar modes. All of the above criteria depend on the masses and most of them depend on the force constants in some way. Equation (9.3) attempts to introduce the width of the optic branch which depends on its dispersion. This may be the most important feature of the force constants which should be considered. Note that flat optic branches allow localized eigenvectors with little extra energy cost. The ability to localize allows B ions, for example, to vibrate with large amplitude even in the presence of many A ion second neighbors which are remaining stationary. Flat branches, therefore, favor two-mode

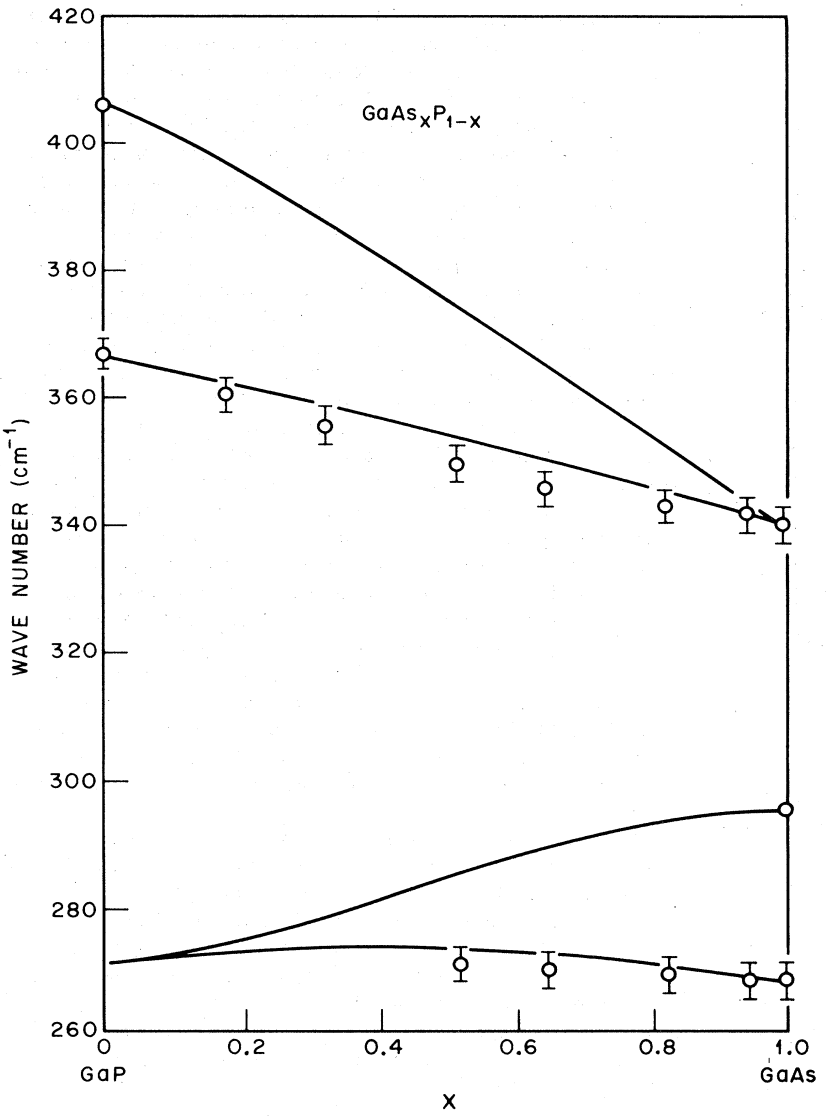

FIG. 153. Three-coordinate isodisplacement model of $GaAs_xP_{1-x}$. From Chang and Mitra (1968).

behavior. In the limit of very narrow dispersionless branches, the right side of Eq. (9.3) approaches zero, so that for reasonable mass differences two-mode behavior will result.

Figure 155(c) shows a mixed crystal system with a high-frequency local mode at both $y = 0$ and $y = 1$. The four-line interpolation scheme shown would be called one-mode behavior, though it is possible for this mode configuration to have a two-mode appearance near $y = 0.05$ if the upper mode has large strength. The Te_ySe_{1-y} system serves as an example (Table IX.5). Figure 156 shows the strongest of the $E\|$ c-axis modes in this system. Geick and Hassler (1969) have measured the spectra and applied an eighteen-coordinate isodisplacement model. The large number of coordinates arises partly from the necessity of considering displacements in three dimensions for this anisotropic crystal system. The authors have presented the TO mode frequencies and the mode strength. We have used this data to calculate the LO mode frequencies, shown as dashed lines, for better comparison with the previous figure. Geick and Hassler conclude that the higher-frequency mode is probably a local mode near $y = 0$ and $y = 1$ but has a very mixed character involving motion of all ions near $y = 0.5$.

It should now be apparent that the designation "two-mode" is somewhat arbitrary and can only be confirmed by a study of the spectra at several concentrations. Most authors have adopted the definition given by Barker and Verleur (1967) which *defines* Fig. 155a as two-mode behavior. There are two points worth noting in discussing figures like 155. First, TO and LO modes must alternate (for polar modes), with the lowest-frequency mode being a transverse mode. These modes will obey the Lyddane–Sachs–Teller relation. Secondly, any pair of lines which come close together represents a weak mode. The TO mode is a pole in the dielectric function and the LO mode a zero. As the strength of a TO mode goes to zero, the pole and zero coalesce. It is easy to show from the isodisplacement model (Sec. II) that for

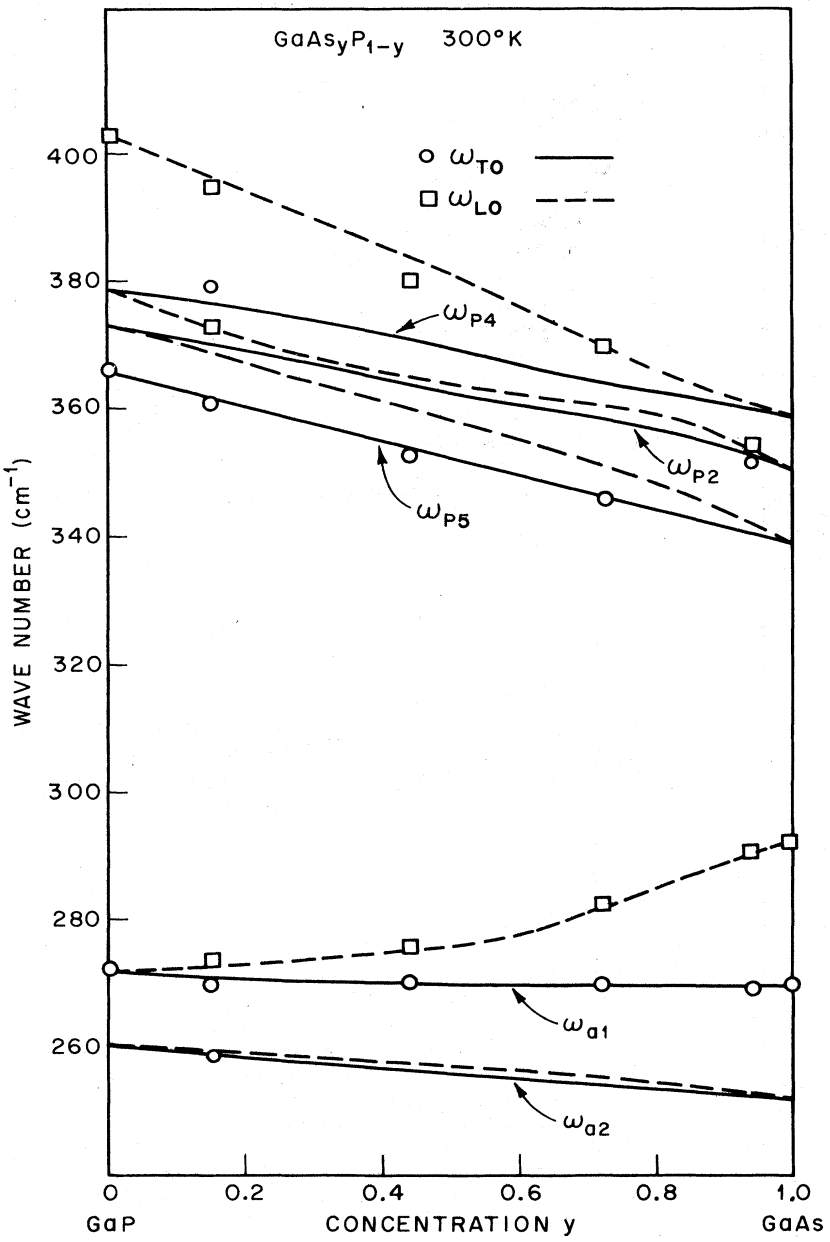

FIG. 154. Frequencies of the five strongest modes calculated from the thirteen-coordinate model of Verleur and Barker. Transverse modes are solid, and longitudinal modes dashed lines. The points merely mark the most prominent structure obtained by a Kramers–Kronig analysis of the measured reflectivity. Data shown in Fig. 151.

the usual local or gap mode near $y=0$, its strength will go as y and the frequency separation of the corresponding TO and LO components will go as y also. Near $y=1$, the same condition holds, but the dependence is on $(1-y)$. Maradudin and Oitmaa (1969) have given a more microscopic derivation leading to the same result.

Finally we discuss one of the asymmetric possibilities depicted in Fig. 155(d). Near $y=1$ there is a high-frequency local mode, but near $y=0$ one TO–LO pair coalesces to a weak mode marked f within the reststrahlen band of the $y=0$ host crystal. There seems no reason that the mode at f cannot be a localized mode even though it must vibrate at a frequency where the dielectric function of the host crystal is negative. Such a localized mode is known for the donor impurity case shown in Fig. 67. In practice the two-phonon damping can be large for f because its frequency is not very high. This mode might be expected to have a width similar to the width of ω_{TO} or ω_{LO} due to such processes. In the tables we have denoted the behavior being discussed here [Fig. 155(d)] as "one-two mode." Near $y=1$ there are two reststrahlen bands in Fig. 155(d), but near $y=0$ there is one band with a small dip on top due to the mode f. Since the dielectric function near f is dominated by the strong ω_{TO} and ω_{LO} modes, infrared methods are unsuitable for detection of this mode. More promising possibilities are Raman scattering or luminescence. Barker *et al.* (1968), Brodsky *et al.* (1968), and Lucovsky and Chen (1970) have discussed several one-two mode mixed crystals (see Tables). Figure 157 shows one-two mode behavior for the mixed alkali halide $Rb_yK_{1-y}I$.

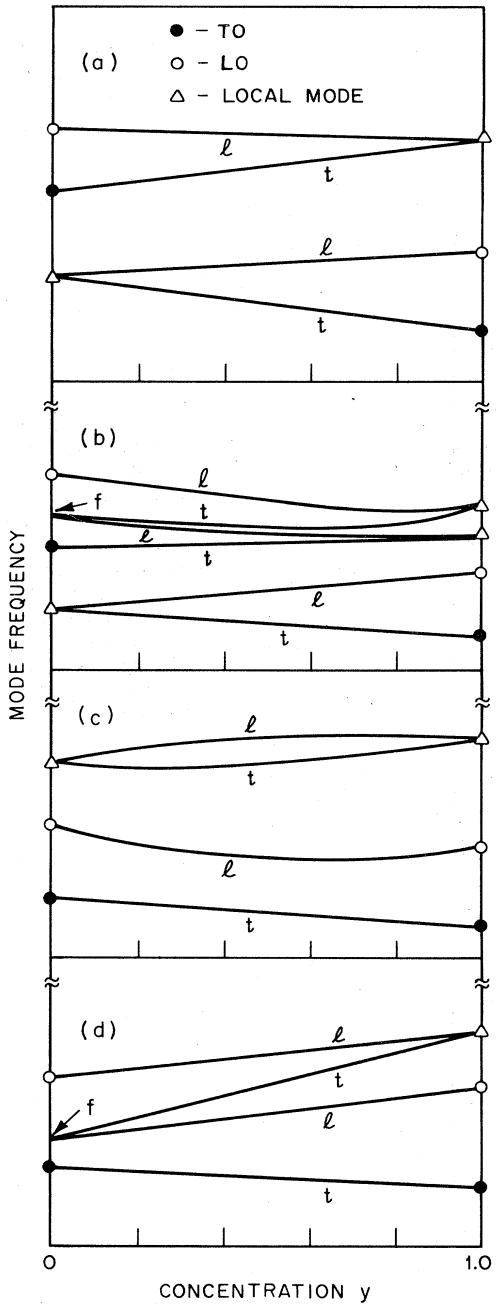

FIG. 155. Schematic representation of some simple polar mode patterns in mixed crystals. Part (a) shows two-mode behavior. Part (b) shows a more complicated two-mode behavior. In part (c) there is one main TO–LO pair at all concentrations plus a weaker mode at high frequency. (d) shows one-two mode behavior.

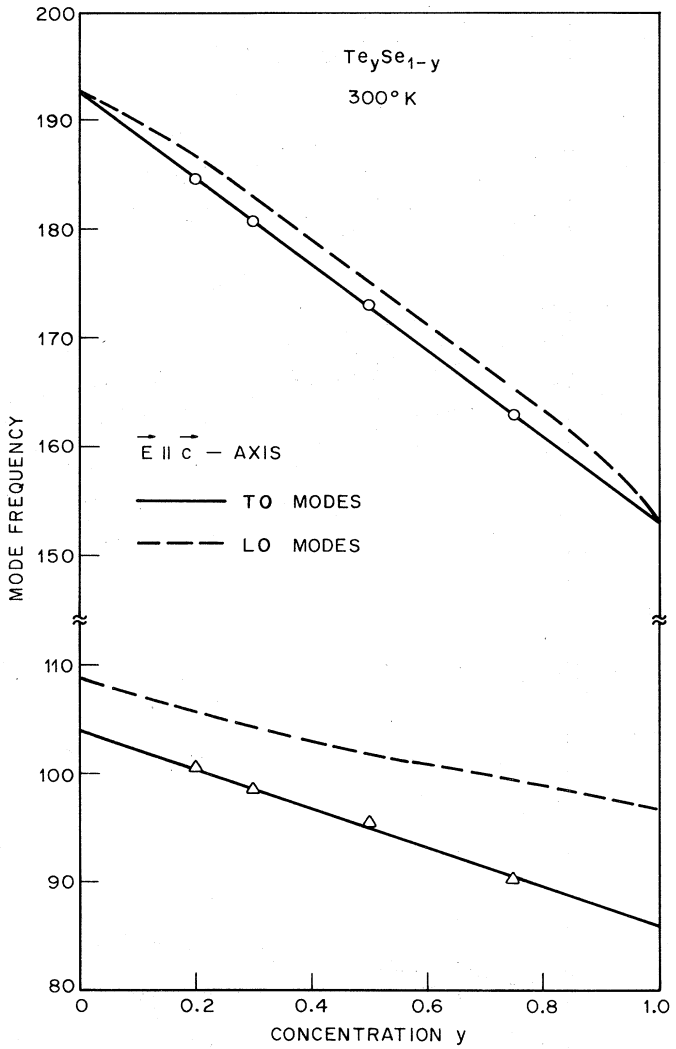

FIG. 156. A_2 symmetry optic modes in Te_ySe_{1-y}. For the pure crystal, group theory predicts one infrared mode. The points are taken from Geick and Hassler. The LO mode frequencies have been calculated from their data and extrapolated to other y values using the strengths given by their model. Note that the high-frequency mode, though weaker, does cause a prominent reststrahlen band in the reflection spectra, giving two modes at $y = 0.5$.

Note that there is a trivial inversion of this data compared with the example of Fig. 155(d). In $Rb_yK_{1-y}I$ the pole and zero which coalesce outside of the main LO–TO pair do so at lower rather than higher frequency and near $y = 0$ rather than $y = 1$. The solid lines are the result of a three-coordinate isodisplacement model fit by Fertel and Perry (1969). The fit is good, though the frequencies of the weaker modes have not been established experimentally near $y = 0$ and $y = 1$. The data do establish this crystal as a one-two mode system. The center mode in $KNi_yMg_{1-y}F_3$ shows exactly the same structure as that shown in Fig. 157, while the higher and lower-frequency bands show simple one-mode behavior. A six-coordinate REI model fit by Barker *et al.* (1968) has established that it is the large mass ratio Ni/Mg which causes the one-two mode behavior here.

A more complicated case of mixed mode system is shown in Fig. 158 for Bi_ySb_{1-y}. There are no infrared-active modes. There are two Raman modes which can be labeled TO and LO to designate atom vibration directions transverse and longitudinal with respect to the crystalline c axis. It is clear from the data (Zitter and Watson, 1974; Lannin, 1975) that two pure crystal modes decrease in strength in the mixed crystal regime, while

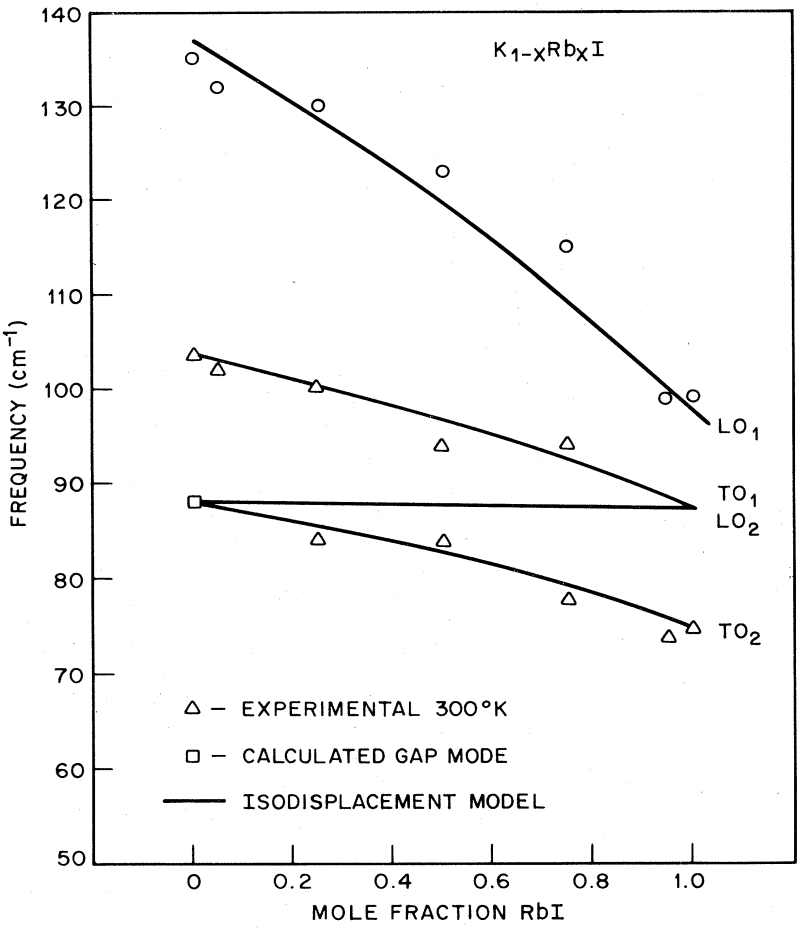

FIG. 157. Transverse and longitudinal optic modes in the KI+RbI mixed crystal. This system shows one-mode behavior near $x=1$, but two-mode behavior near $x=0$. From Fertel and Perry (1969).

one strong mixed crystal mode appears between 10 and 95% Bi. The solid curves in Fig. 158 show a fit given by an eight-coordinate isodisplacement model which must include coupling between TO and LO modes in the mixed crystal. The fit requires reasonable assumptions about the Sb–Bi force constants. X-ray diffractometer studies indicate some macroscopic inhomogeneities; however, a simple analysis suggests a ±17% composition spread at most.

These last examples illustrate the point that there is a wide variety of possibilities for optic mode behavior beyond the simple one- or two-mode models used for the cubic–diatomic mixed crystals. The work of Zitter and Watson (1974) and of Geick and Hassler (1969) on Te_ySe_{1-y} shows that the isodisplacement model can be useful in understanding the gross behavior of such systems. The one-dimensional chain model is also useful in examining the various situations which can arise, since mode frequencies and strengths can be evaluated easily and some assessment can be made of the significance of weak modes. This latter point must be emphasized since the three-coordinate isodisplacement model is so idealized that it allows little evaluation of the crystal structure or ion distributions form the model parameters. Significant theoretical progress must await the application of Green's function techniques to three-dimensional models or the solution of classical models with many more degrees of freedom.

E. More complex mixed crystal systems

Up to this point we have considered substitutions on only one sublattice of the pure host crystal. Many more general substitution schemes can be imagined; however, we will restrict our attention here to one subset of crystals which has actually been grown. We can consider mixing the diatomic crystal AB with another diatomic

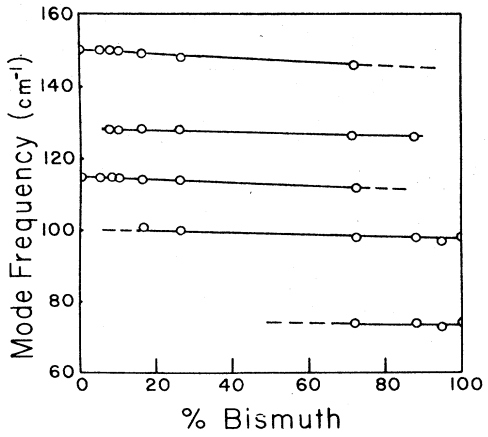

FIG. 158. Raman optical mode frequencies of Bi_ySb_{1-y}. The data are shown by points. The curves are calculated from an isodisplacement model. From Zitter and Watson (1974).

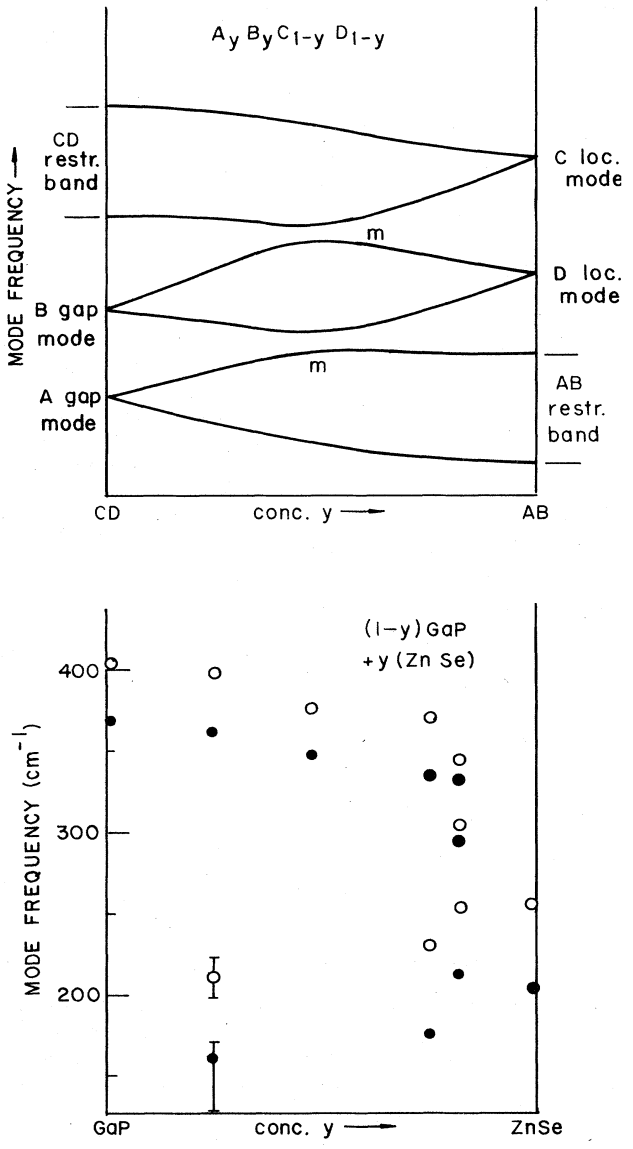

FIG. 159. (a) A possible mode (three TO and three LO) graph as a function of concentration for a quaternary mixed crystal. Near $y = 0$ and $y = 1$ there is one principal reststrahlen band and two weak localized modes. Anti-crossings occur near the points m. (b) Mode structure found in $Zn_ySe_yGa_{1-y}P_{1-y}$. Some frequency regions could not be studied carefully because of interference peaks in the thin samples used. From Barker and Yim (unpublished).

crystal CD. If A and C are cations, then we expect the chemical formula $A_xB_xC_{1-x}D_{1-x}$. If the compounds AB and CD are very similar, we might expect the more general mixed crystal $A_xB_yC_{1-x}D_{1-y}$. Using the simplest isodisplacement model point of view we merely have to add one more equation to the set of equations (2.17)–(2.19), as well as one extra term to the polarization equation (2.20). The four equations for these four degrees of freedom will yield one zero-frequency mode as before and three optic modes. From the types of mode graph already illustrated in Fig. 155, it is evident that many types of behavior are possible. Figure 159 illustrates a simple case in which the compound CD is composed of extremely light elements. On the right side of the mode graph the elements CD must each result in a local mode if the structure is well behaved, in the sense of the isotope model having applicability. At the left side, if we assume that the elements AB are both heavy, then we might have two low-frequency localized modes, perhaps occurring in a gap of the compound CD. Within the isodisplacement model these end point modes can be linked up as shown in the figure. Mixed modes with an anticrossing must occur near the point m (see figure) since the eigenvector for the D-ion local mode must merge with the CD reststrahlen band. Similarly, the B gap mode must finally be connected with the AB reststrahlen band. If these anticrossings near m produce a rather close approach of the poles and zeros of the dielectric function, then, near 50% concentration, the material will have an over-all one-mode reststrahlen spectrum, while at other concentrations it will appear to have a three-mode spectrum.

Several mixed III–V+II-VI semiconductor compounds have been successfully prepared. For example, ZnSe+GaP is a completely miscible quaternary alloy system (Yim *et al.*, 1970). A reflectivity study has been made of some compositions of alloys from this system and the preliminary results are shown in the lower part of Fig. 159. It is evident that some of the features to be expected from a general mode graph such as shown at the top of the figure are in fact observed in this mixed crystal system. Certain modes appear to be missing, however, in these preliminary results. Experimentally, this lack of mode structure could be due to anomalously large linewidth for certain modes or to the merging of weak mode structure with interference peaks, which complicated the spectra for several of the very thin samples used here. Work in this area will probably proceed only as fast as the technical importance of these crystals leads to new crystal growth efforts.

X. STRUCTURAL DISORDER—AMORPHOUS SYSTEMS

A. Introduction

In the preceding sections we have discussed infrared and Raman spectra for crystals in which the disorder arises from impurity atoms substituted for a host atom. Usually the crystal can be treated as if the atom positions still maintain a regular periodic array and the principal perturbation is only one of a mass change. Experimentally, such crystals show fairly sharp x-ray diffraction lines. In the present section we consider the effect of disorder in the periodic arrangement itself. Figure 160 shows examples of the two kinds of disorder. In (a) the disorder discussed in preceding chapters is shown. In (b) is shown the widely quoted representation of glass[12] proposed by Zachariasen (1932). The figure schematically depicts a two-dimensional A_2B_3 solid. There are no impurity atoms. Differing bond lengths and bond angles cause a loss of both short-range and long-range order in this amorphous system which would have been present in crystalline A_2B_3. Locally, however, each A atom always sees three B atoms as nearest neighbors, and each B atom always sees two A atoms. In many amorphous or glassy systems it has been found that valence is locally satisfied. For example in amorphous germanium, each Ge atom has four nearest neighbors. These neighbors are found at approximately the same distance and bond angle as in crystalline Ge. The key point is that local valence (i.e., four nearest neighbors) can be satisfied even in a very disordered structure, as shown in the figure. Thus in comparing related crystalline and amorphous materials, the great differences show up in atom spacings and angles from a particular atom to second or more distant neighbors. The present chapter deals with amorphous materials such as those discussed by Zachariasen. The working definition of an amorphous system is that its x-ray diffraction pattern lacks sharp rings or spots, consisting of a few broad halos (Bagley, 1974).

Unfortunately, the above definition does not lead to precise concepts when discussing the atomic structure of amorphous solids (Bagley, 1974; Grigorovici, 1974). The Zachariasen picture has been criticized since its inception (Hägg, 1935; Zachariasen, 1935), but no single model has taken its place. Figure 160(c) shows schematically one main opposing school of thought. This figure might be titled the microcrystalline model of the amorphous state. Here we imagine identifiable crystallites which are randomly oriented, and probably badly strained, joined by irregular bonds and atom bridges to each other. If the crystallites are small enough (~ 15 Å) and/or strained enough, this solid will also lack sharp x-ray diffraction lines. Only in the past year have any vibrational models of both the random network type [Fig. 160(b)] and the microcrystalline type [Fig. 160(c)] been constructed and intercompared. These models are mentioned below. While a review of the amorphous state is beyond our scope here it is important to give the reader two warnings. First, there may be no unique amorphous state for most materials. By its very nature the state is thermodynamically unstable or metastable and can transform with time or with thermal cycling. Different preparation techniques may yield different forms of the same solid. Secondly, presently available measurement techniques may not be able to distinguish between different models (Bagley, 1974). It appears that the major spectral peaks are insensitive to the details of sample preparation in many cases. It is in this area of model checking that optical spectra may play an important role in the future. If

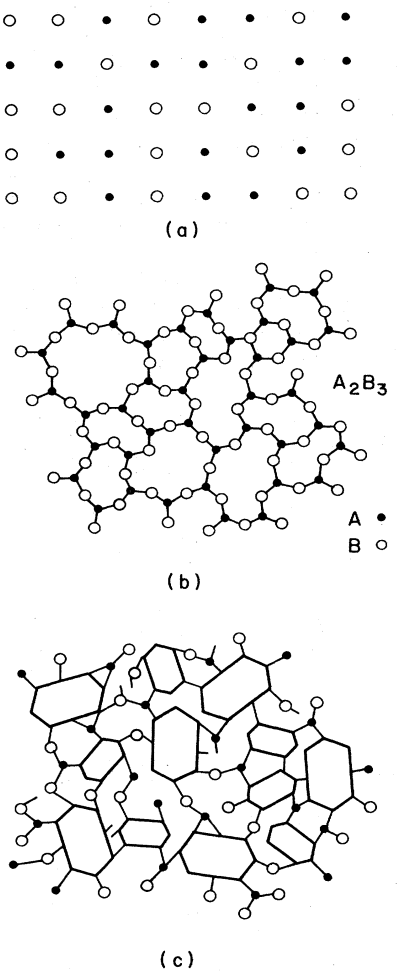

FIG. 160. Schematic representations of (a) substitutional disorder, (b) random network, and (c) microcrystallite disorder in two dimensions. Note the retention of local valence in (b). The crystallites shown by the regular polygons in (c) can be imagined to have regular structure internally with some superimposed strain caused by the irregular bonds at the surface atoms. (a), (b), from Dean (1967).

[12]Some authors define a glass as an amorphous solid which can be prepared from a melt. Others use amorphous and glassy synonymously. The adjectives vitreous and glassy are equivalent.

models can be developed for optical spectra which depend on second-neighbor parameters, then comparison of theory with experiment could lead to progress in understanding the amorphous state.

The absence of periodicity in amorphous solids and glasses allows many modes of the system to be both infrared-and Raman active. The perfect periodicity of a crystal causes cancellation of dipole moments (infrared activity) and polarizabilities (Raman activity) for all modes except those at $\vec{q}=0$. In the amorphous systems this perfect cancellation can no longer occur. The amorphous solids therefore have spectra which show intense broad features, and the problem becomes one of relating these features to the structure and state of order present in the solid. Figure 161 shows an example of spectra for fused quartz (SiO_2) and compares it with the similar spectra for crystalline quartz (α–SiO_2). From the figure we note there is a merging in the fused quartz of many sharp features of crystalline quartz in the 100–500 cm^{-1} region. The fused quartz shows only broad features. The contrast with Fig. 1 (H local mode) is striking. There is little use in amorphous systems for the one-oscillator model exploited in earlier chapters. In spite of the structural complexity, many of the vibrational modes in amorphous systems are localized. This seems intuitively obvious since perfect periodicity is needed to prove the Bloch theorem on plane wave states. At a somewhat deeper theoretical level, proofs that randomness causes localization are extremely difficult and only exist for very specialized and narrowly defined systems (Halperin, 1968).

From Fig. 161 we note that both types of quartz exhibit modes all the way up to about 1250 cm^{-1}, which is typically the highest frequency which occurs in oxide

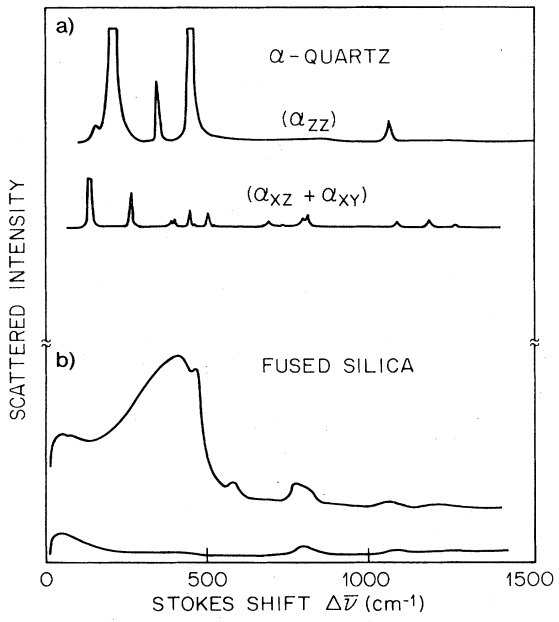

FIG. 161. (a) Raman scattering from α-quartz at 300 °K. From Scott and Porto (1967). (b) Raman scattering from fused silica at 300 °K (Tobin and Baak, 1968). Upper curve E perpendicular to direction of exciting beam; lower curve E parallel to direction of exciting beam.

materials, whether of glassy form or crystalline form. There are new features in the glass system at frequencies below 100 wave numbers. We will treat this very-low-frequency region in a later section. Several systems which occur in both the glassy and crystalline form have now been shown to have features similar to Fig. 161. Markov and Reshetnyak (1972) have studied $CdGeP_2$ by infrared reflectivity. They find in the glassy spectra, similar to fused quartz, a considerable broadening and loss of detail. Finkman and Tauc (1973) have measured the reflectivity of In_2Te_3 which has zinc blende structure with one-third of the cation sites vacant. In passing from an ordered to a disordered arrangement of vacancies, many sharp phonon modes merge into a few very broad bands. Spectra for some other materials have been reviewed by Lucovsky (1974).

There have been very few theoretical calculations which explain either the Raman or infrared spectra of an amorphous system. Most theories attempt to ascribe the absorption directly to the density of vibrational states. The calculation of the density of vibrational modes in itself is a formidable task, even without the additional complication of calculating the optical matrix elements. In Sec. IX. B we describe some calculations on very simple models and in the following sections list some experimental results, together with the models chosen by the various authors to help explain their results.

Leadbetter (1968) has given a review of the properties of glasses—particularly noting the indications of anomalous low-frequency vibrational modes which affect the thermal properties. Tauc (1974) has recently reviewed both the vibrational and electronic optical properties of amorphous systems. An excellent source of recent work on all aspects of amorphous systems may be found in the Amorphous and Liquid Semiconductor Conference Proceedings edited by Stuke and Brenig (1974).

B. Model calculations

We first note that the equation of motion for the linear chain (Sec. II) does not contain the position coordinate of each atom explicitly. Therefore the calculations carried out there for mixed crystals do provide a rough model for amorphous systems. The assumption which must be made is that the structural disorder can be simulated by the mass disorder of the mixed crystal model. The principal results to be noted are the broadening of structure, which was sharp in the regular chain, and the induced infrared activity for practically all modes in both the acoustic and optic bands. These results of Sec. II qualitatively explain the broad spectra of Fig. 161. Payton and Visscher (1968) have calculated the density of vibrational modes for a three-dimensional diatomic lattice with disorder in the value of the force constants. Figure 162 shows the results as the disorder increases from top to bottom. The model solid consists of $6\times6\times40$ atoms connected by central and noncentral nearest-neighbor force constants. The force constants γ are chosen randomly from within the range indicated in part (b) and part (c) of the figure. In part (a) there is no disorder and the density of states shows an acoustic band and an optic band separated by a gap, together with

some sharp structure within each band. The two main features to note as the disorder is increased are the loss of the sharp features and the broadening of both the acoustic and the optic band until finally the gap is removed. If optical absorption is connected with one of the sharp features in the spectrum of Fig. 162(a), then one would expect it to become broadened also, giving a qualitative explanation of the behavior shown in Fig. 161.

Dean and co-workers have calculated the vibrational density of states for glassy structures using explicit models for the random positions of the ions involved. Bell and Dean (1966) constructed atomic models of silica (SiO_2) based on the SiO_4 tetrahedron, with the silicon cation at the center. The models are physically constructed on the basis of random network theory, with metal rods representing bonds and polystyrene spheres representing the ions. The Si–O–Si angle can take any value within a range from about 120° to 160°. The mean value of this angle is 140°. The O–Si–O angle remains near the ideal tetrahedral angle for a regular structure (109.5°). The Si–O bond lengths also vary throughout the model but to a smaller extent than the variation in bond angle. Once a model of several hundred ions is constructed, the actual position coordinates of each ion are measured and radial distribution functions are calculated. These distribution functions agree quite well with measured x-ray radial distribution functions. The vibrational spectra are calculated from the physical model by adopting a central force constant of 4.0×10^5 dyne/cm and a noncentral force constant of 3/17 times this value. This model, therefore, unlike the one described in Fig. 162, has identical force constants throughout, but randomness in the angles of the bonds and the positions of the atoms. Figure 163 shows the calculated spectrum assuming fixed-end boundary conditions. Slightly different results are obtained when the boundaries are left free. Some of the individual modes have been identified and are labelled in the figure. Modes labeled B contain predominantly Si–O–Si bond-bending vibrations. In modes labelled R the oxygen atoms perform an Si–O–Si rocking motion roughly perpendicular to the bond plane. Modes labelled C have extremely intricate atomic motion, with the largest part of the vibrational energy residing in the Si ion. Finally, the modes labelled S are predominantly Si–O–Si bond-stretching vibrations in which the O moves in opposition to its two Si neighbors and roughly parallel to a line joining the two nearest Si ions. Bell, Dean, and Hibbens-Butler (1970) have considered the localization of the modes which are shown in the top part of Fig. 163. They define a quantity called the participation ratio, denoted by p_c, which gives roughly the number of atoms which participate in a given mode. p_c is shown in the lower part of Fig. 163 for the SiO_2 model with fixed-end boundary conditions. As can be seen from the figure, the localization is most severe in the midfrequency range for those modes of the B type.

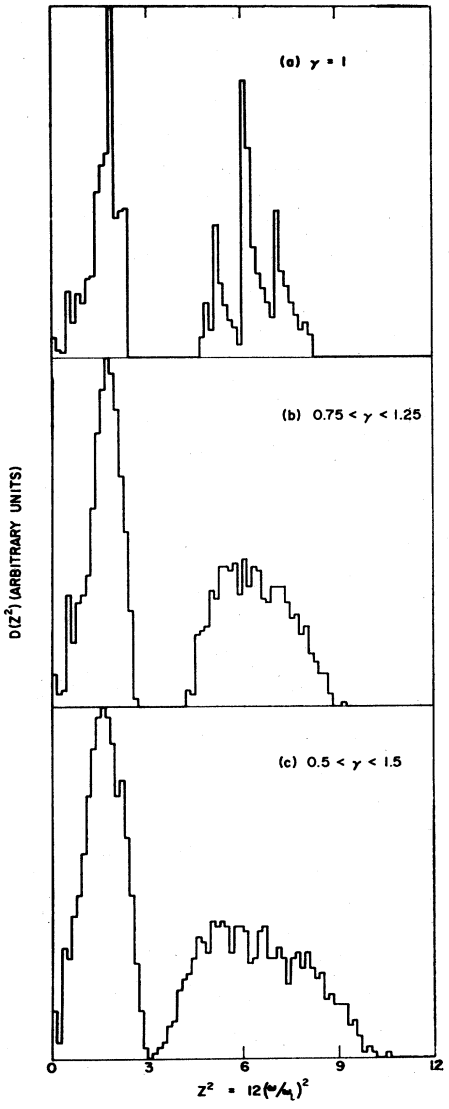

FIG. 162. Normal mode frequency distributions for ordered diatomic simple-cubic lattices ($6 \times 6 \times 40$ NaCl structure), in which one component has a mass $\frac{3}{2}$ the other. Central and noncentral force constants γ are chosen at random uniformly over the intervals specified. From Payton and Visscher (1968).

In addition to the modes described above for the continuous structure, the authors find some more-localized modes connected with broken bonds, which always occur at the surface of the model. These broken bonds can be inserted in the interior, for example, to simulate radiation-damaged silica. Modes observed near 900 cm^{-1} have been assigned to such broken bond locations (Bell and Dean, 1968). No optical matrix elements have been calculated for these SiO_2 models, so that only very rough comparisons can be made between the calculated density of states and the observed spectra.

Recently Alben *et al.* (1974) have calculated the density of vibrational modes and the infrared and Raman spectra of amorphous silicon and germanium. They adopt a finite cell of randomly positioned atoms, subject to the constraint of tetrahedral nearest-neighbor coordination, but possessing a substantial number of fivefold rings of bonds. Bonds through a surface of the cell are reconnected by periodic boundary conditions to the far side with the constraint that the bond must be completed to an allowed tetrahedral site and must not be greatly distorted. The rms variation of one specific

61-atom model is 12.5° in angular bond distortion. Figure 164 shows a comparison of their calculated results for two similar models of amorphous silicon. One model contained 61 atoms in the cubic cell, and the other 62 atoms. Diamond structure crystalline silicon would contain 64 atoms in this same cell. Note that neither the infrared absorption nor the Raman scattering is related to the density of states in a very direct way (see Fig. 164). Reasonable agreement between theory and experiment is found for major features in the spectra. In addition Alben *et al.* are able to deduce some general conclusions concerning the parameters which control the appearance of major bands in amorphous systems.

C. Infrared and Raman spectra of several systems

1. Chalcogenide glasses

Many chalcogen compounds form bulk glass samples on cooling from the melt. The structures are thought to differ widely, however, exhibiting one-dimensional correlations (chains) such as in a-Se (amorphous Se) (Lucovsky *et al.*, 1967) or two-dimensional correlations (layered structures) as in a-As_2Se_3. (See Taylor *et al.* and Lucovsky in Stuke and Brenig (1974) for opposing arguments on the two-dimensional or one-dimensional nature of a-As_2Se_3). By way of contrast, a-Ge and a-Si with their pronounced preference for tetrahedral bonding form three-dimensional networks. As discussed in the introduction to this Section, the structure may not be unique in some cases but depends on the method of preparation (Rechtin and Averback, 1973).

As_2Se_3 and As_2S_3 can be prepared in amorphous or crystalline form. Felty *et al.* (1967) have made an infrared reflectivity study of the strongest modes in a mixture of these two compounds in the amorphous form. The reststrahlen bands show two-mode behavior (Sec. IX) as a function of composition. The modes are quite broad, even the pure end compounds showing much more breadth than the pure crystalline forms. Taylor *et al.* (1970) have made a much more detailed infrared study of amorphous As_2Se_3 as well as dielectric loss measurements in the microwave range. They find three reststrahlen bands at 102, 156, and 237 cm^{-1}. These bands have frequencies within 10% of the frequencies of the strongest modes seen in the $E \parallel a$-axis spectrum in the crystalline form of As_2Se_3 measured by Zallen *et al.* (1971). Taylor *et al.* (1974) suggest that this correspondence supports a two-dimensional bonding model. Lucovsky (1974) has taken a different viewpoint of the structural interpretation of the optical spectra. He adopts a molecular model approach (zero-dimensional correlations) for the high-frequency modes in the chalcogenide glasses in which the internal vibrations of the AsS_3 molecule, for example, would explain the three reststrahlen bands in this material. Mitchell *et al.*, (1972) have found that the line shape of the strong phonon modes cannot be fit by the Lorentzian line shape which is commonly used for crystalline materials. A good fit is obtained by using a Gaussian distribution of Lorentzian line shapes. The width of the distribution is

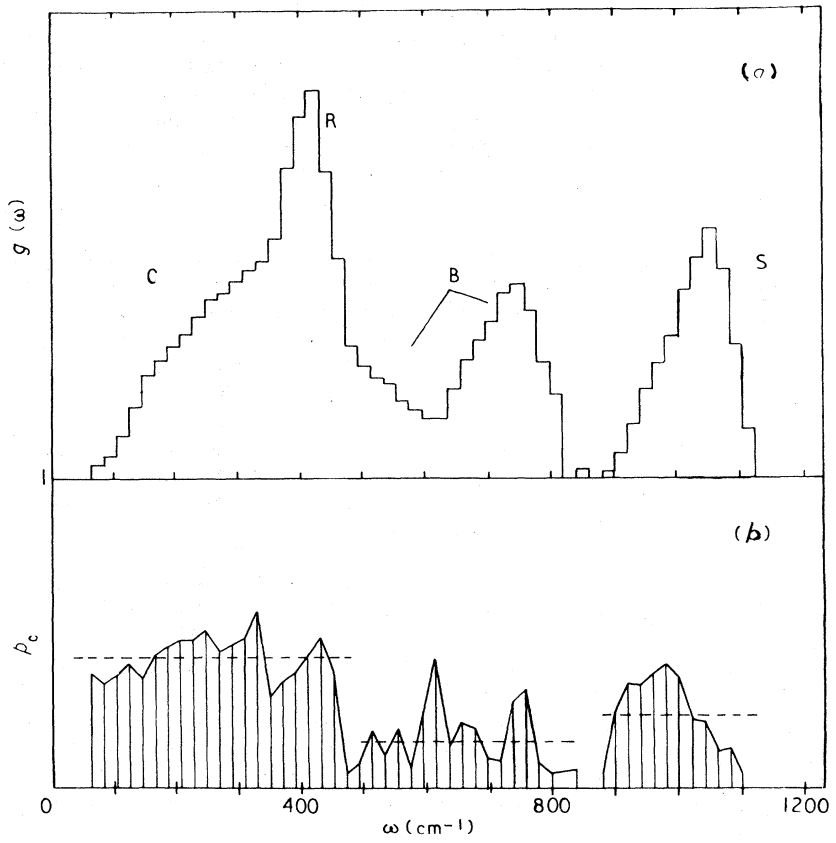

FIG. 163. Vibrational frequency spectra (a) and participation ratio (b) for vitreous SiO_2. These diagrams refer to a model with the fixed-end boundary condition. The assignments "R," "B," "S," etc. correspond to the types of atomic motion (bond-rocking, bond-bending, bond-stretching, etc.). The participation ratio p_c varies from 0 to 1 as indicated, while the vertical scale on the frequency spectrum is arbitrary. From Bell, Dean, and Hibbens-Butler (1970).

about 20 cm^{-1} for each of the modes. The authors feel that this type of statistical distribution is consistent with the disordered structure.

Figure 165 shows the conductivity as a function of frequency for As_2Se_3 from 0.1 cm^{-1} together with the spectra of several other amorphous solids. The mechanism of the loss at frequencies below the obvious phonon peaks in Fig. 165 remains unclear. At frequencies below about 10^6Hz As_2Se_3 shows a conductivity which depends approximately linearly on frequency (Taylor *et al.*, 1970; Owen and Robertson, 1970). Owen and Robertson (1970) suggested that this is evidence for hopping conduction by mobile carriers. As Fig. 165 shows, at microwave frequencies many amorphous solids show an ω^2 frequency dependence for the conductivity σ' (Note: $\sigma'(\text{mho/cm}) = (1/120\pi)n\alpha = \nu\epsilon''/60$, where n = index of refraction, and ν = frequency in cm^{-1}.) Strom *et al.* (1974) and Taylor *et al.* (1974) relate the magnitude of this ω^2 absorption to the T^3 (Debye-like) part of the specific heat in these materials. Since there is a good correlation, this result suggests that the low-frequency absorption comes from a disorder-induced coupling to Debye modes. In addition, the coupling coefficient M is frequency independent in the expression

$$\sigma'(\omega) = Mg(\omega) \ldots \text{Debye modes.} \qquad (10.1)$$

This same type of expression is obtained by Elliott for the band mode absorption in the one-defect case when there are no resonant mode enhancements (Elliott, 1966), but has not been derived in any convincing manner for the amorphous case. Fritzsche (1974) has pointed out the wide applicability of the power law $\sigma'(\omega) \sim \omega^s$, where

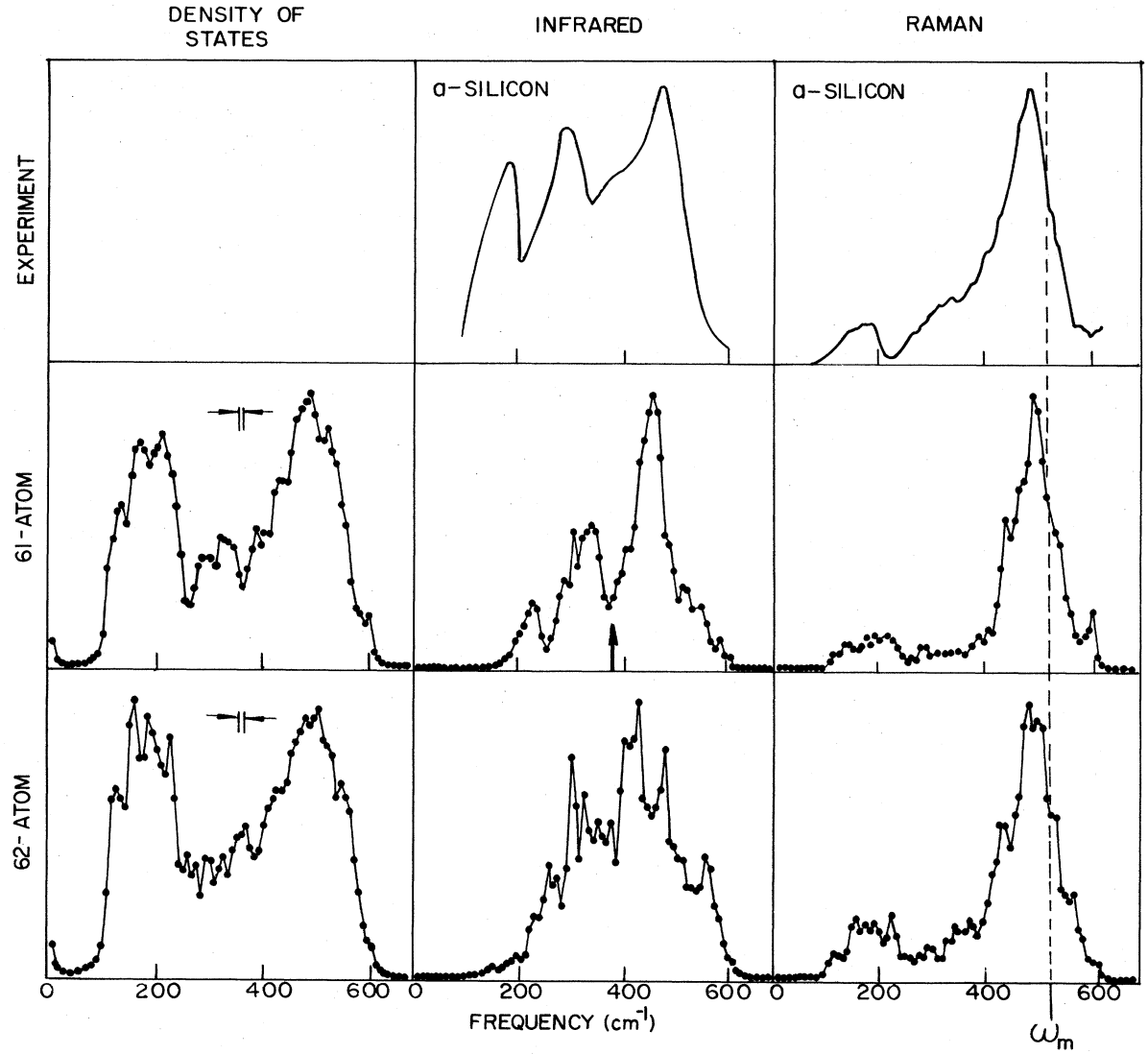

FIG. 164. Theoretical results for density of states, infrared absorption, and Raman scattering for 61- and 62-atom periodic models compared with the experimental data on amorphous silicon. The position of the maximum frequency mode for the crystalline diamond form (the Raman-active TO mode) is indicated by the dashed line on the Raman graphs; the position of the density of states minimum near the center of spectrum for the diamond form with the force constants used in these calculations is indicated by the arrow at 380 cm^{-1}. Spectra are formed by adding weighted Lorentzian contributions from the calculated $\vec{q} = 0$ modes and are normalized to the same maximum value. From Alben *et al.* (1974).

s ranges from less than one to two for a diversity of amorphous compounds. Mott and Davis (1971) give a derivation of $\sigma(\omega) \sim \omega^2$ for a model consisting of random potential wells which lead to localized states. They also discuss other power law behavior and the temperature dependence of σ'. It must be concluded that most of the arguments relating spectra to structure are extremely speculative at present. Much more work on harmonic models like those used by Alben *et al.* (1974) is needed. In addition it will be necessary to model anharmonic motion and tunneling motion within various structures to correlate the low frequency spectra with structure.

Finally, it is interesting to note the preservation of the optic mode peaks in the 100–400 cm^{-1} range when a glass softens and then enters the liquid phase. Taylor *et al.* (1971) have measured the infrared transmission of As_2Se_3 and $Tl_2SeAs_2Te_3$ glasses in the temperature range 300° to 675 °K. Both glasses show well-defined absorption peaks which change very little on passing through the glass transition temperature T_g and into the liquid phase. The $Tl_2SeAs_2Te_3$ glass showed an abrupt loss of mode structure about 120 °K above Tg. The authors estimate that As_2Se_3 would have shown a similar loss of mode structure at a temperature $T_s \approx 725$ °K. The observed mode structure is taken as evidence that a layer-type coordination is retained in the liquid phase but then abruptly lost above a well-defined temperature T_s.

2. Amorphous semiconductors

Figure 166(a) shows a Raman spectrum of amorphous silicon at room temperature and low temperature. Once the temperature-dependent Stoke's factor $n+1$ has been removed (see Table II.2), the two spectra are almost identical, showing that each spectrum arises from the same one-phonon processes. Simple models (one-defect) of infrared absorption in disordered systems give a spectrum proportional to the density of states $g(\omega)$ as long as there is no enhancement due to resonant modes (Elliott, 1966). For the Raman spectrum Smith *et al.* (1971) have used an expression suggested by Shuker and Gammon (1970) for amorphous silicon. These latter authors use

$$I(\omega) \propto (n+1)g(\omega)/\omega, \tag{10.2}$$

where I is the scattered intensity, and $(n+1)$ the Stoke's factor. Smith *et al.* plot $\omega I/(n+1)$ so that if Eq. (10.2) holds, their data should reflect the density of states $g(\omega)$. Comparison is made in Fig. 166(b) of this reduced data with the density of states of crystalline silicon broadened in a very specific but *ad hoc* manner. There are some correspondences between major features in parts (a) and (b) of the figure, though an extra factor of ω in (10.2) would obviously put the two major peaks in better agreement when comparing the theory and experiment. It should be stressed that there is no fundamental reason to expect simple forms like (10.2) to hold over the entire frequency range of Fig. 166, or even within one band of modes. At low frequencies (below 100 cm^{-1} in silicon), where the Debye approximation should hold, theoretical models

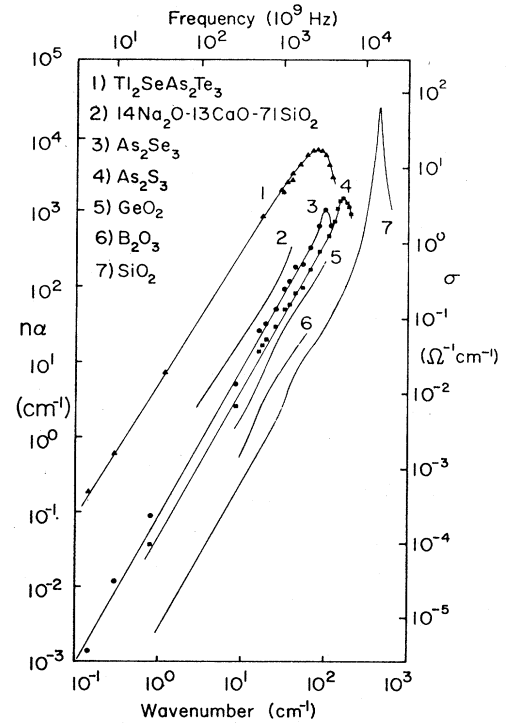

FIG. 165. Room temperature conductivity versus frequency of selected amorphous materials. From Strom *et al.* (1974).

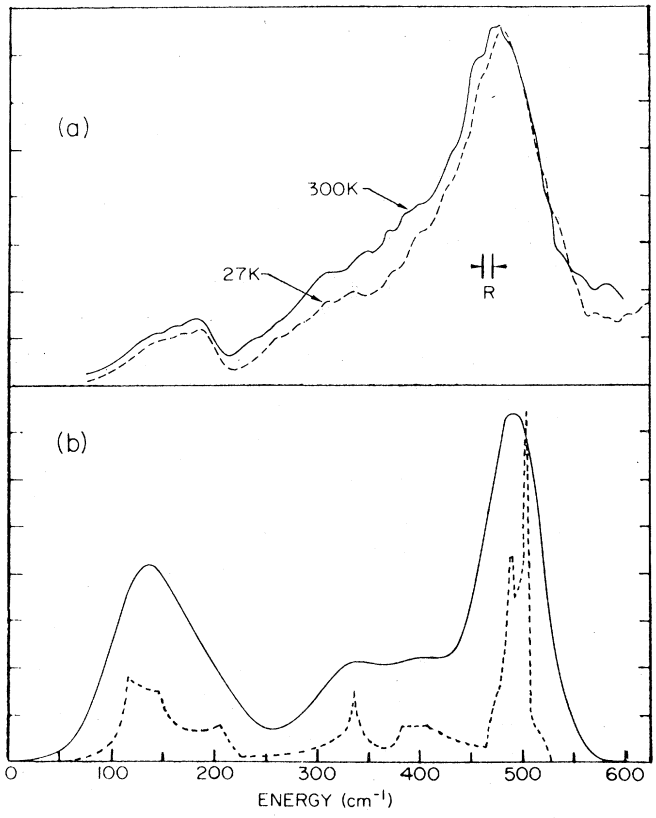

FIG. 166. (a) Raman spectra of amorphous Si at 27 and 300 °K reduced by $[n(\omega, T)+1]/\omega$. Resolution is indicated by R. (b) Single-phonon density of states of crystalline Si; dashed line is the density of modes $g(\omega)$, and the solid line is obtained by broadening $g(\omega)$. From Smith *et al.* (1971).

are not in agreement on the expected form for the optical spectra (see R. J. Bell, 1972). King *et al.* (1974) have measured the heat capacity of amorphous germanium between 2° and 30 °K. The measurements show a Debye-like [$g(\omega) \propto \omega^2$] density of phonon states at low energies similar to crystalline germanium but with all frequencies reduced by 16%. These measurements do not go low enough in temperature, however, to uncover the anomalous linear terms discussed in Sec. X.D.

Lannin (1973) has made a careful study of the two independent polarization components of the Raman scattering in amorphous silicon. In the range below 67 cm^{-1} he finds that $I(\omega) \propto \omega^2$. If we insert the Stoke's factor and assume the Debye density of states, this result is

$$I(\omega) \propto \omega(n+1)g(\omega) \quad \text{(low frequency modes)} \qquad (10.3)$$

in contrast to (10.2) above. Equation (10.3) may be obtained from (10.2) if we insert a mode coupling parameter (matrix element) which is constant in (10.2) but proportional to ω^2 for low-frequency modes. Such a dependence has been suggested by Whalley and Bertie (1966). Recently, Alben *et al.* (1974) have given a review of optical, electron tunneling, electron energy loss, and neutron spectra of amorphous silicon and germanium. These authors have carried out model calculations of $g(\omega)$, $I(\omega)$, and infrared absorption for random network structures, microcrystalline structures, and polymorph structures. The infrared activity is expressed as a sum of the differences in bond extension about an atom. Three independent Raman polarizabilities are set up which also depend on local bond compression and extension. Figure 164 shows the calculated spectra for two random network models. These models compare favorably with experiment, while the microcrystalline models give a much poorer comparison. The authors note that the calculated density of states is close to that of the crystalline solid. This result is shown to depend on the importance of the nearest-neighbor central forces, which are essentially preserved in passing from the crystal to the amorphous form in these materials. They conclude that the broad features of the density of states and the variation with frequency of the optical matrix elements can be rather well explained in terms of the short-range order. Approaches which start from perfect crystal results and then smear out the spectra to approximate the amorphous phase [cf. Fig. 166(b)] are therefore in some difficulty. Joannopoulos and Cohen (1973), in a study of the electronic transitions in amorphous silicon and germanium, agree that modifications or smearing of pure crystal results cannot yield the correct density of states. They find, however, that short-range parameters (bond angles, etc.) must contain significant disorder to explain major features of the electronic band structure of amorphous silicon and germanium.

3. Ammonium bromide and ammonium chloride

The ammonium halide crystals all show an order–disorder transition as a function of temperature. At low temperatures they are ordered; however, on heating they pass through a lambda transition and become disordered. The disorder is of a particularly simple nature, encouraging hope for some understanding of the vibrations in these systems using a perturbation approach. These materials are not amorphous in the usual sense, but are characterized by a special type of disorder on one sublattice. From one point of view these materials are similar to an AB_xC_{1-x} type mixed crystal. The mixing is not of different species with different mass, but of one species with two kinds of orientation resulting in two kinds of force constants. In the disordered phase the halide ion maintains a regular approximately simple cubic array, while the ammonium ion is disordered, being able to take one of two orientations within the cube. The idea of a perturbation approach comes form the observation that the internal modes of vibration of the ammonium molecule lie above 1000 cm^{-1}, while the modes of vibration involving relative ammonium-halide motions lie at about 300 cm^{-1} and below. This fact, together with the form of the structure, shows that any one ammonium molecule vibrates fairly independently of its neighbors and thus should only weakly feel the effects of the ordering. Wang and Fleury (1969) have studied the Raman spectra of NH_4Br. They note that two sharp modes near 60 cm^{-1} persist in the disordered phase. These authors present arguments suggesting that the enlarged Brillouin zone in the disordered phase still feels the effects of the smaller zone which exists at lower temperatures. This causes an activation of a zone boundary phonon mode. Schumaker and Garland (1970) have made an infrared absorption study of one of the internal vibrations of the ammonium molecule. They are able to make correlations of the strength of this mode with a long-range order parameter which changes with temperature. Figure 167 shows the Raman spectra taken by Wright and Wang (1973) also in the region of the internal ammonium molecule vibrations. The order–disorder transition is 235 °K. As the sample is cooled, a rather strong broad mode near 1400 cm^{-1} begins to sharpen and become quite asymmetric as the ordered phase is approached. This mode persists into the ordered phase and a new, much sharper, mode grows at 1420 cm^{-1}. According to the authors' analysis, the 1400 cm^{-1} mode is Raman forbidden at low temperatures in the ordered phase. This mode therefore serves as a probe of the local site symmetry, and its integrated strength can be used as a measure of the evolution of order below the lambda transition. From the figure we note that the order evolves rather gradually, with considerable disorder remaining present 30° to 60 °K below the ordering temperature.

Fritz (1973) has studied the low-frequency Raman spectrum of NH_4Cl in its disordered phase. The author's viewpoint is that since there is only one allowed lattice vibration which is optically active in the ordered phase, any new features which appear in the disordered phase must reflect the activation of lattice vibrations throughout the zone. Since the disorder is a small perturbation, the actual phonon frequencies are considered to be those of the ordered phase which have been measured separately by neutron scattering. Fritz merely compares the observed Raman peaks in the 50–400 cm^{-1} range with a list of critical point frequencies taken from previous theoretical and experimental work on the ordered phase. The agreement is good

once the critical point frequencies are corrected for the difference in temperatures between the two sets of data. This approach has intuitive appeal when the disorder is weak, as in the ammonium halides. It would be useful here to correlate the temperature dependence of some order parameter measured by x-ray methods with the temperature dependence of the low-frequency spectral intensities. A positive correlation would provide a stronger experimental basis for the method proposed by Fritz.

Loveluck and Sokoloff (1973) have developed a theory of systems with substitutional disorder and applied it to NH_4Cl. By assuming that the force constants which depend on the orientation of the ammonium molecule are weak, they are able to draw some conclusions about the form of the spectrum in NH_4Cl. These authors use the ratio of the order-dependent force constant to an order-independent force constant as an expansion parameter in the theory. For small values of this expansion parameter they obtain expressions for the Raman scattering and infrared absorption. By making certain assumptions they are able to show that the Raman spectrum consists of two terms in the disordered phase. One term contains the features of the $\vec{q} \simeq 0$ spectrum of the ordered lattice, while the other depends directly on the density of states of the ordered lattice throughout the zone. Since the $\vec{q} = 0$ features appear directly in this theory, there is no need to postulate a remnant short-range order in the disordered phase as some experimentors have suggested when analyzing their data. The authors make some comparisons with measured spectra and suggest that it would be useful to be able to subtract experimentally the density of states type features from the measured spectrum, in order to separate the two types of terms and thus fix some of the parameters which enter their theory.

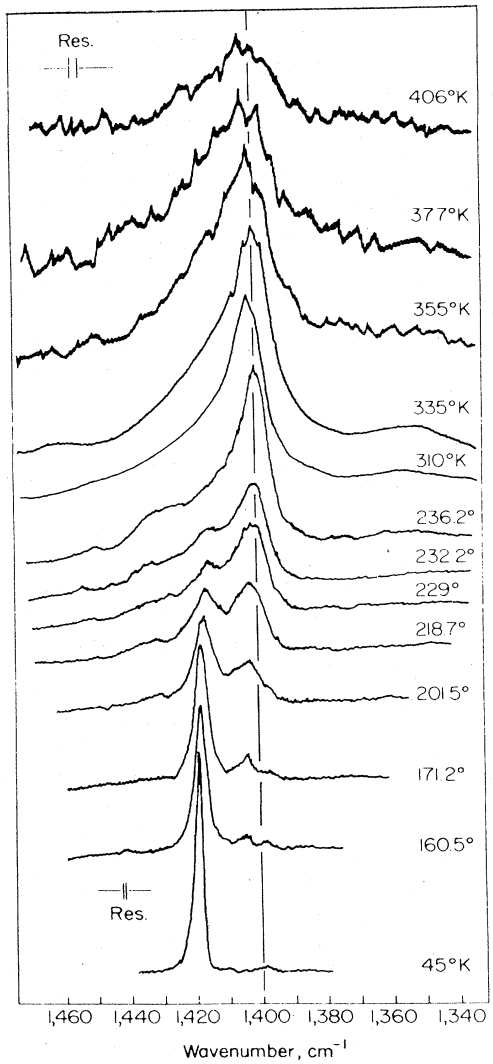

FIG. 167. Raman spectra for the internal bending mode, ν_4, region at various temperatures in Phases II and III obtained in the $a(ca)b(=b(cb)a)$ scattering configuration. From Wright and Wang (1973).

D. Low-frequency modes in amorphous solids

There are several kinds of indirect experimental evidence that anomalous low-frequency modes occur in some amorphous materials. Flubacher *et al.* (1959) have fit the heat capacity of fused quartz very carefully over a moderately wide temperature range above 2.5 °K. They find they must use the usual Debye form plus three Einstein oscillators located at 9, 22, and 40 cm^{-1}. Such low-frequency modes are not observed in optical spectra of crystalline quartz. Strakna (1961) has analyzed the ultrasonic absorption in fused quartz before and after fast neutron irradiation. He postulates a distribution of barrier heights for oxygen motion ranging in energy from 0–1000 cm^{-1}. This distribution has considerable weight below 300 cm^{-1}. These modes are quite different from the usual Debye modes of a solid. More recently Zeller and Pohl (1971), Lasjaunias *et al.* (1972), and Stephens (1973) have measured the specific heat of several amorphous systems including fused quartz below 2 °K. The results show a large non-Debye-like contribution which varies as T. This is interpreted as anomalous modes whose density can be specified in the energy range 0.2 to 4 cm^{-1}. Using Brillouin scattering, Love (1973) and Pohl *et al.* (1974) have established that there are regular well-behaved transverse and longitudinal thermal phonons at 0.5 and 0.78 cm^{-1} in addition to the anomalous modes. We discuss this very-low-frequency region later.

Turning to optical studies, we discuss first the region above 20 cm^{-1}. The low-frequency peak in the spectrum shown in Fig. 161 has been investigated using polarized Raman scattering. Hass (1970) and Stolen (1970) have carefully checked the temperature dependence of the peak near 40 cm^{-1}. Figure 168 shows the results of Stolen at 300° and 14 °K. The work of Hass and of Stolen establishes the important result that the broad band between approximately 20 and 200 cm^{-1} is a one-phonon loss spectrum. The two curves in Fig. 168 are different only because of the Stoke's factor $n+1$ being different for the two temperatures shown. Stolen goes on to show that the room temperature Raman spectrum and the infrared absorption plotted as $\alpha(\omega)/\omega^2$ have the same shape in the range 20–100 cm^{-1}. He finds the same result for

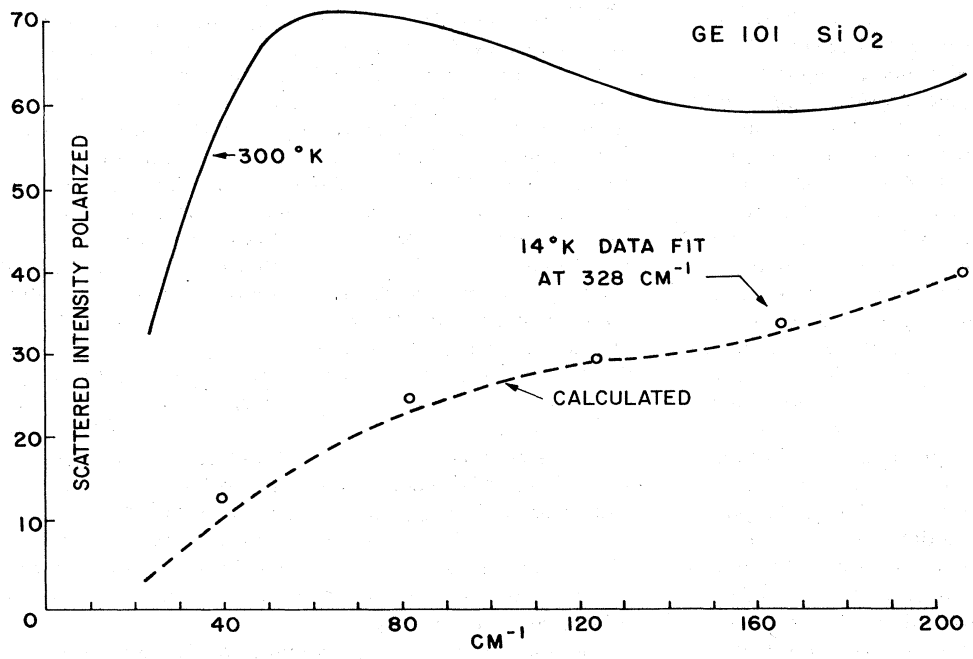

FIG. 168. Comparison of measured 14 °K Raman scattering intensity in vitreous SiO_2 with the dashed curve calculated using the room temperature intensity. From Stolen (1970).

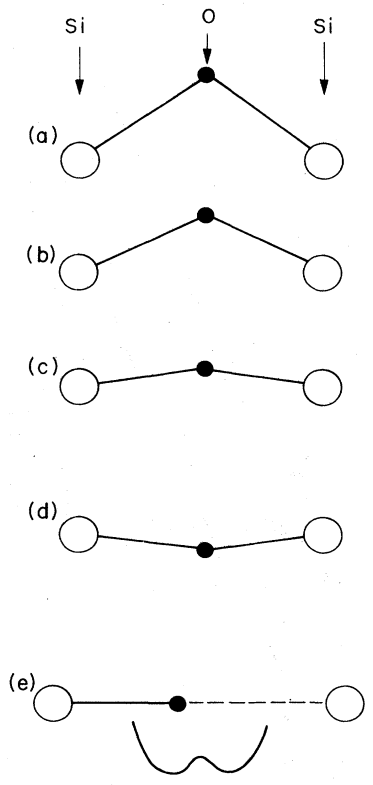

FIG. 169. Possible silicon-oxygen-silicon bond configurations in fused quartz. For oxygen motion in the vertical direction, configurations (a) through (c) will have progressively lower frequencies. Tunneling or thermal hopping may occur between configurations (c) and (d). (e) shows a stretched Si—Si distance with the oxygen bonding to the left Si atom. Harmonic motion may occur about this position as well as tunneling or hopping over the barrier to the right-hand Si.

glassy GeO_2 and B_2O_3.

At this point we digress on possible models for the low-frequency optical absorption. Figure 169 shows a small part of the silica structure. In parts (a)–(d) of the figure an oxygen atom is shown with various possible Si–O–Si bond angles. To make a specific model we consider oxygen motion in the plane of the figure in the vertical direction. If the Si–O bond has a stretching but no bending restoring force, then as we progress from (a) to (c) in the figure, the frequency of the oxygen mode will decrease. For this rather unrealistic model with no bending restoring force, a point of instability is reached when the bond angle is 180°, yielding a zero-frequency mode. Since the configurations shown in part (a)–(c) of the figure occur at random throughout the silica network (cf. Fig. 160), the modes we are describing would be localized modes. Such grossly strained bonds may be characteristic of oxide glasses but not of amorphous germanium and silicon. The strong tendency of the Group IV elements to form tetrahedral bonds would explain this difference. Such speculation must still be tested by a study of the very-low-temperature specific heat of amorphous germanium.

An estimate may be made of the number of local modes participating in the broad band, which is peaked near 40 cm^{-1}. In crystalline quartz the dimensionless strength of the 1050 cm^{-1} mode is $S = 0.67$ (see Table II.2). This mode is known to have predominantly oxygen motion connected with it. If the force constant associated with this mode is now reduced to move it down to the 40 cm^{-1} region, its strength would increase to approximately $S = 500$. Since the integrated absorption of the broad band near 40 cm^{-1} yields a dimensionless strength of $S = 0.05$, we find by this argument that only 1 in 10^4 oxygen atoms have the weakened force constant which gives modes in this low-frequency region. That is, configurations shown schematically in Fig. 169(c) are

rather rare occurrences in the fused quartz structure.

Figure 169(e) shows a different model of Si–O–Si bonding in fused quartz. This is the model suggested by Strakna to explain the ultrasonic absorption. It is best described as a broken-bond model. In some regions of the fused quartz structure neighboring silicon atoms are too far apart for the regular Si–O–Si bridge form. In this situation Strakna suggests the oxygen remains bound to one of the silicons, leaving the dangling bond shown schematically by the dashed line in the figure. Since the single oxygen bond can actually involve either of the nearest silicon atoms, this suggests that the oxygen resides in a double-well potential. Such a double-well model is not unique to the stretched Si–O–Si bond but can also occur, for example, for the two configurations shown in parts (c) and (d) of the figure. That is, under the influence of thermal excitations, the system may jump from configuration (c) to configuration (d). If we consider thermal hopping over the top of the potential hump in either two-well model, we obtain the well-known Debye expression for the dielectric constant. To produce the broad absorption peak observed in fused quartz we would have to postulate a distribution of potential wells with different barriers between the two positions. For the Debye model with thermal excitations over the barrier the relaxation time is exponentially dependent on temperature, and the strength of the absorption goes as $1/T$. This model appears to be ruled out, therefore, by the lack of temperature dependence in the infrared absorption.

We return now to the harmonic oscillator description of the absorption in the 20 to 100 cm^{-1} frequency region in a-SiO_2. Recent work by Stolen (1970) and Stolen *et al.* (1970) shows the broad absorption discussed previously which peaks near 40 cm^{-1} when the data is plotted as α/ω^2. Figure 170 shows the low-frequency edge of this absorption. The strong peak centered at 40 cm^{-1} has little or no temperature dependence, as mentioned above. If we regard this peak as arising from a distribution of localized oxygen oscillators as shown in Fig. 169, we may draw some conclusions concerning the distribution of these oscillators. Since the absorption is low, we are in a region where the absorption coefficient α is proportional to $\omega \mathrm{Im}[\epsilon]$ (see Table II.2). If we take each of the local modes to be fairly narrow on the scale of this broad mode, then the spread of modes is caused by a distribution of force constants, since all the masses are the same. In this situation the distribution of modes in frequency is given simply by the absorption coefficient itself. That is, $g(\omega) \propto \alpha(\omega)$. The data of Fig. 170 would then imply $g(\omega) \propto \omega^2$ for silica and plastic in the 10 to 40 cm^{-1} range. This result is parallel to the discussion leading up to Eq. (10.1). If, however, the spread of modes is caused by a distribution of masses, which we might picture as clusters of various sizes joined by a relatively small number of bonds to the host structure, then $g(\omega) \propto \alpha/\omega^2$. The infrared data alone cannot decide between these models. We have already noted that for the first type of situation, where each oscillator has the same mass (and we assume the same effective charge), approximately 10^{-4} of the oxygen atoms in the silica structure participate in the low-frequency band.

Stolen's finding that the infrared and Raman spectra are nearly identical when compared in a suitable fashion puts some additional restrictions on models which will fit the absorption data. The simplest model of Raman scattering consists of postulating one nonlinear bond connecting the vibrating atom with the electronic charge cloud which provides the high-frequency electronic polarizability (Barker and Loudon, 1972). If we use a model like that shown in the upper part of Fig. 169, then it seems reasonable that each oscillating unit would probably have the same nonlinear bond describing the coupling of the electronic and ionic motions. Using this model, we find that the Raman spectrum will have the same shape as α/ω^2 derived from the infrared spectrum, as long as the Raman spectrum is measured at high temperatures (i.e., in the classical limit). This is the result that Stolen has established for the broad 40 cm^{-1} band in fused quartz. If the local vibrating units have a distribution of masses and of effective charges, then $\alpha\omega^{2/3}$ (or some similar weighted function of α depending on the model) has the same form as the Raman spectrum. At least in fused silica this latter result appears not to apply.

The specific heat measurements on fused quartz,

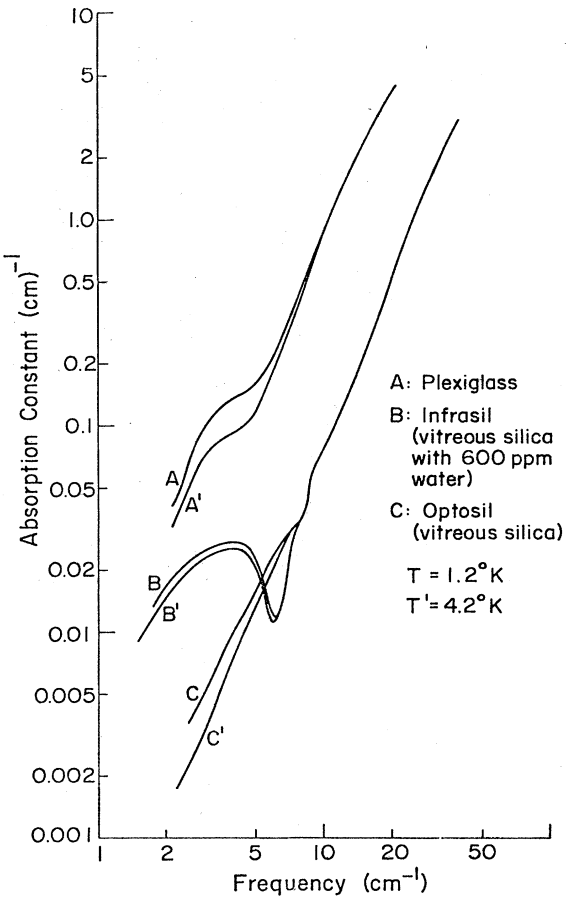

FIG. 170. Absorption in vitreous silica and plexiglass at low temperatures. Note the features near 3 cm^{-1} which show little temperature dependence. The low-frequency end of the curve C shows quite strong temperature dependence. After Mon and Sievers (1975).

glasses, and other amorphous systems at temperatures well below 1 °K have been discussed above. These measurements suggest that some extremely low-lying levels (below 20 cm^{-1}) must exist in amorphous systems The specific heat varies linearly with T and only at higher temperatures is controlled by the standard T^3 term which arises from acoustic band phonons characteristic of the Debye model (Zeller and Pohl, 1971; Stephens, 1973). Anderson *et al.* (1972) and independently Phillips (1972) have explained the anomalous low-temperature thermal properties by postulating a double-well situation for a set of atoms in the glass system. A broad distribution of potential barriers and of energy differences between the two minima is to be expected in an amorphous system. If the distribution of the energy differences is smooth on the scale of k_BT (10^{-5} to 10^{-3} eV) and if the potential barrier separating the wells permits tunneling so that thermal equilibration can occur in an acceptable time span t (10^{-10} sec $< t < 10^3$ sec), then the entropy and the specific heat are proportional to T. The authors point out that only a small fraction of the atomic units within the lattice will have acceptable energy separations and barrier heights to contribute to the low-temperature specific heat.

Golding *et al.* (1973) and Hunklinger *et al.* (1973) have measured the phonon attenuation in fused quartz at temperatures below 1 °K and at frequencies in the 1 GHz region. The strong nonlinearities which are observed are taken as evidence for the tunneling states mentioned above. Castle *et al.* (1963), in studying relaxation of electron spin resonance at defect centers in quartz, suggest that there are modes in the 1-5 cm^{-1} frequency region near a Si–O vacancy which relax the neighboring paramagnetic Si ion. Taylor and Rubinstein (1974) have noted evidence for very-low-frequency modes in chalcogenide glasses from spin lattice relaxation. The interesting specific heat, ultrasonic attenuation, and ESR measurements suggest that there may be a region of very-temperature-dependent absorption well below 20 cm^{-1} in fused quartz and other amorphous solids. Figure 170 shows prominent features near 3 cm^{-1} in two solids which may be associated with the low-lying levels. These peaks show little temperature dependence (see figure), which is a rather unexpected result for tunneling modes; however, the curves C, C' show a strong temperature dependence, which may indicate the onset of tunneling modes at energies below 2 cm^{-1}. Recently Winterling (1975) has measured Raman scattering in silica down to 4 cm^{-1} and finds excess temperature-dependent intensity which may be related to the tunneling modes. Amrhein and Heil (1971) have measured losses in glasses and polymers in the microwave region which show significant temperature dependence. It is evident that there is much insight to be gained by performing additional low-frequency optical experiments on glassy systems. The intriguing similarity of the low-temperature specific heat in many widely different amorphous systems, as well as the wide divergence of many experimental results from the corresponding crystalline cases, shows this to be an area which should lead to an improved basic understanding of disordered systems.

ACKNOWLEDGMENTS

The authors are indebted to many colleagues who have given suggestions and criticism during the preparation of this review. We are particularly indebted to Professor W. G. Spitzer and the Physics Department at the University of Southern California, and to Professor A. A. Maradudin and the Physics Department at the University of California (Irvine) for hospitality and helpful suggestions and advice during sabbatical visits by the authors when parts of the review were written.

REFERENCES

Aannestad, P. A., and E. M. Purcell, 1973, in *Annual Review of Astronomy and Astrophysics*, edited by L. Goldberg (Annual Reviews, Palo Alto) Vol. 11, p. 309.

Alben, R., D. Weaire, J. E. Smith, Jr., and M. H. Brodsky, 1974, to be published.

Alderman, D. W., and R. M. Cotts, 1970, Phys. Rev. B **1**, 2870.

Alexander, R. W., 1968, Ph.D. Thesis, Cornell University; Materials Science Center Report No. 932.

Alexander, R. W., and A. J. Sievers, 1967, in *Optical Properties of Ions in Crystals*, edited by H. M. Crosswhite and H. W. Moos (Interscience, New York).

Alexander, R. W., A. E. Hughes, and A. J. Sievers, 1970, Phys. Rev. B **1**, 1563.

Allen, J. W., 1970, J. Phys. C **3**, L48.

Allen, S. J., 1966, J. Chem. Phys. **44**, 394.

Amrhein, E. M., and H. Heil, 1971, J. Phys. Chem. Solids **32**, 1925.

Anderson, P. W., B. I. Halperin, and C. M. Varma, 1972, Phil. Mag. **25**, 1.

Andrews, A. M., H. W. Korb, N. Holonyak, Jr., C. B. Duke, and G. G. Kleiman, 1972, Phys. Rev. B **5**, 2273.

Angress, J. F., T. Arai, A. R. Goodwin, and S. D. Smith, 1964, in *Physics of Semiconductors: Proceedings of the 7th International Conference*, edited by M. Hulin (Dunad, Paris), p. 1115.

Angress, J. F., A. R. Goodwin, and S. D. Smith, 1965, Proc. R. Soc. Lond. A**287**, 64.

Angress, J. F., A. R. Goodwin, and S. D. Smith, 1968, Proc. R. Soc. Lond. A**308**, 111.

Avarmaa, R., 1968, Izv. Akad. Nauk Est. SSR, Sev. Tekhn. i Fiz. Mat. Nauk **17**, 78.

Avarmaa, R., and L. Rebane, 1969, Phys. Status Solidi **35**, 107.

Baars, J., and F. Sorger, 1972, Solid State Commun. **10**, 875.

Babloyantz, A., 1959, Mol. Phys. **2**, 39.

Bagley, B. G., 1974, in *Amorphous and Liquid Semiconductors*, edited by J. Tauc (Plenum, New York), p. 1.

Balkanski, M., 1971, editor, *Light Scattering in Solids* (Flammarion, Paris).

Balkanski, M., R. Beserman, and J. M. Besson, 1966, Solid State Commun. **4**, 201.

Balkanski, M., and W. Nazarewicz, 1966, J. Phys. Chem. Solids **27**, 671.

Balkanski, M., and R. Beserman, 1968, in *Proceedings of the IX International Conference on the Physics of Semiconductors*, Moscow, 1968 (Nauka, Leningrad), p. 1042.

Barker, Jr., A. S., 1967, in *Ferroelectricity*, edited by E. F. Weller (Elsevier Publ. Co., Amsterdam), p. 213.

Barker, Jr., A. S., 1968a, Phys. Rev. **165**, 917.

Barker, Jr., A. S., 1968b, in *Localized Excitations in Solids*, edited by R. F. Wallis (Plenum, New York), p. 581.

Barker, Jr., A. S., 1970, in *Far Infrared Properties of Solids*, edited by S. S. Mitra and S. Nudelman (Plenum, New York), Chp. 10.

Barker, Jr., A. S., 1973, Phys. Rev. B **7**, 2507.

Barker, A. S., and R. Berman, 1974, "Lattice Vibrational Studies of the solubility of oxygen and other impurities in GaP," unpublished.

Barker, A. S., R. Berman, and H. W. Verleur, 1973, J. Phys. Chem. Solids **34**, 123.

Barker, Jr., A. S., J. A. Ditzenberger, and H. J. Guggenheim, 1968, Phys. Rev. **175**, 1180.

Barker, Jr., A. S., and R. Loudon, 1972, Rev. Mod. Phys. **44**, 18.

Barker, Jr., A. S., and H. W. Verleur, 1967, Solid State Commun. **5**, 695.

Barker, Jr., A. S., and W. M. Yim, "Reflectivity studies of mixed III–V+II–VI Crystals," unpublished.

Barnes, A. J., 1973, in *Vibrational Spectroscopy of Trapped Species*, edited by H. E. Hallam (Wiley, London), p. 133.

Barnes, A. J., J. B. Davis, H. E. Hallam, and G. F. Scrimshaw, 1969, Chem. Commun., **19**, 1089.

Barnes, A. J., H. E. Hallam, and G. F. Scrimshaw, 1969, Trans. Faraday Soc. **65**, 3159.

Barrett, C. S., and L. Meyer, 1965, J. Chem. Phys. **43**, 3502.

Barrett, C. S., L. Meyer, and J. Wasserman, 1966, J. Chem. Phys. **44**, 998.

Barth, W., and B. Fritz, 1967, Phys. Status Solidi **19**, 515.

Barthel, C., X. Gerbaux, and A. Hadni, 1970, Spectrochim. Acta A**26**, 1183.

Bass, A. M., and H. P. Broida, 1960, editors, *Formation and Trapping of Free Radicals* (Academic, New York).

Batchelder, D. N., M. F. Collins, B. C. G. Haywood, and G. R. Sidney, 1970, J. Phys. C: Solid State Phys. **3**, 249.

Batt, J. A., F. C. Douglass, and F. S. Galasso, 1969, Am. Ceramic Soc. Bull. **48**, 622.

Bäuerle, D., 1973, *Springer Tracts in Modern Physics* (Springer, Berlin) Vol. **68**, p. 77.

Bäuerle, D., and B. Fritz, 1967, Phys. Status Solidi **24**, 207.

Bäuerle, D., and B. Fritz, 1968, Phys. Status Solidi **29**, 639.

Bäuerle, D., and B. Fritz, 1968, Solid State Commun. **6**, 453;

Bäuerle, D., and R. Hübner, 1970, Phys. Rev. 2B, 4252.

Bauman, F. C., and R. O. Pohl, 1965, Phys. Rev. **140**, A1030.

Bauman, F. C., J. P. Harrison, R. O. Pohl, and D. W. Seward, 1967, Phys. Rev. **159**, 691.

Becker, C. R., 1971, Solid State Commun. **9**, 13.

Becker, C. R., and T. P. Martin, 1972, Phys. Rev. B **5**, 1604.

Bell, R. J., 1972, Rep. Prog. Phys. **35**, 1315.

Bell, R. J., and P. Dean, 1966, Nature **212**, 1354.

Bell, R. J., and P. Dean, 1968, in *Localized Excitations in Solids*, edited by R. F. Wallis (Plenum, New York), p. 124.

Bell, R. J., P. Dean, and D. C. Hibbens-Butler, 1970, J. Phys C **3**, 2111.

Bellomonte, L., and M. H. L. Pryce, 1968, in *Localized Excitations in Solids*, edited by R. F. Wallis (Plenum, New York), p. 203.

Benedek, G., 1967, Solid State Commun. **5**, 101.

Benedek, G., 1970, Phys. Status Solidi **42**, 389.

Benedek, G., and A. A. Maradudin, 1968, J. Phys. Chem. Solids **29**, 423.

Benedek, G., and E. Mulazzi, 1969, Phys. Rev. **179**, 906.

Benedek, G., and G. F. Nardelli, 1967a, Phys. Rev. **154**, 872.

Benedek, G., and G. F. Nardelli, 1967b, Phys. Rev. **155**, 1004.

Benedek, G., and G. F. Nardelli, 1968a, J. Chem. Phys. **48**, 5242.

Benedek, G., and G. F. Nardelli, 1968b, Phys. Rev. **167**, 837.

Beyeler, H. U., 1974a, J. Chem. Phys. **60**, 4123.

Beyeler, H. U., 1974b, Phys. Rev. B **10**, 2614.

Bilz, H., 1969, in *Optical Properties of Solids*, edited by S. Nudelman and S. S. Mitra (Plenum, New York), Chap. 12.

Bilz, H., D. Strauch, and B. Fritz, 1966, J. Phys. Rad. Suppl. **27**, C2-3.

Bootz, B., W. von der Osten, and N. Uhle, 1974, Phys. Status Solidi (b) **66**, 169.

Born, M., and K. Huang, 1954, *Dynamical Theory of Crystal Lattices* (Clarendon, Oxford).

Bosomworth, D. R., 1967, Solid State Commun. **5**, 681.

Bowers, M. T., and W. H. Flygare, 1966, J. Chem. Phys. **44**, 1389.

Bowers, M. T., G. I. Kerley, and W. H. Flygare, 1966, J. Chem. Phys. **45**, 3399.

Brafman, O., 1972, Solid State Commun. **11**, 447.

Brafman, O., I. F. Chang, G. Lengyel, S. S. Mitra, and E. Carnal, Jr., 1968, in *Localized Excitations in Solids*, edited by R. F. Wallis (Plenum, New York).

Bratoz, S., J. Rios, and Y. Guissana, 1970, J. Chem. Phys. **52**, 439.

Bridges, F., 1972, Phys. Rev. B **8**, 3321.

Briscoe, C. V., and C. F. Squire, 1957, Phys. Rev. **106**, 1175.

Brockhouse, B. N., 1964, in *Phonons and Phonon Interactions*, edited by T. A. Bak (Benjamin, New York), p. 221.

Brodsky, M. H., and G. Lucovsky, 1968, Phys. Rev. Lett. **21**, 990.

Brodsky, M. H., G. Lucovsky, M. F. Chen, and T. S. Plaskett, 1970, Phys. Rev. B **2**, 3303.

Bron, W. E., 1965, Phys. Rev. **140**, A2005.

Bron, W. E., 1969, Phys. Rev. **185**, 1163.

Bron, W. E., and W. R. Heller, 1964, Phys. Rev. **136**, A1433.

Brunel, L. C., and M. Peyron, 1966, Compt. Rend. **262**, 1297.

Brya, W. J., 1973, Solid State Commun. **12**, 253.

Buchanan, M., and E. J. Woll, 1969, Can. J. Phys. **47**, 121.

Buchanan, M., W. Bauhofer, and T. P. Martin, 1974, Phys. Rev. B **10**, 4358.

Buchenauer, C. J., D. B. Fitchen, and J. B. Page, 1969, in *Light Scattering Spectra of Solids*, edited by G. B. Wright (Springer, New York), p. 521.

Burgiel, J. C., H. Meyer, and P. L. Richards, 1965, J. Chem. Phys. **43**, 4291.

Busse, G., W. Prettl, and L. Genzel, 1968, Phys. Lett. **27A**, 438.

Busse, G., 1972, Ph.D. Thesis, Universität Freidburg i. Br. (unpublished).

Busse, G., and G. Haider, 1970, Optics Commun. **2**, 45.

Buyers, W. J. L., and R. A. Cowley, 1968, *Neutron Inelastic Scattering* (IAEA, Vienna), Vol. 1.

Cabana, A., G. B. Savitsky, and D. F. Hornig, 1963, J. Chem. Phys. **39**, 2942.

Cabana, A., A. Anderson, and R. Savoie, 1965, J. Chem. Phys. **42**, 1122.

Caldwell, R. F., and M. V. Klein, 1967, Phys. Rev. **158**, 861.

Callender, R., and P. S. Pershan, 1970, Phys. Rev. A **2**, 672.

Carter, D. L., M. A. Kinch, and D. D. Buss, 1971, in *Physics of Semimetals and Narrow Gap Semiconductors*, edited by D. L. Carter and R. J. Bate (Pergamon, Oxford), p. 275.

Castle, J. G., D. W. Feldman, P. G. Klemens, and R. A. Weeks, 1963, Phys. Rev. **130**, 577.

Catalano, E., and D. E. Milligan, 1959, J. Chem. Phys. **30**, 45.

Cerdeira, F., T. A. Fjeldly, and M. Cardona, 1974, Phys. Rev. B **9**, 4344.

Chambers, D. N., and R. C. Newman, 1969, Phys. Status Solidi **35**, 685.

Chan, S. I., T. R. Borgers, J. W. Russel, H. L. Strauss, and W. D. Gwinn, 1966, J. Chem. Phys. **44**, 1103.

Chang, I. F., and S. S. Mitra, 1968, Phys. Rev. **172**, 924.

Chang, I. F., and S. S. Mitra, 1970, Phys. Rev. B **2**, 1215.

Chang, I. F., and S. S. Mitra, 1971, Adv. Phys. **20**, 359.

Chang, R. K., B. Lacina, and P. S. Pershan, 1966, Phys. Rev. Lett. **17**, 755.

Chapman, R. A., and W. G. Hutchinson, 1967, Phys. Rev. Lett. **18**, 443.

Chase, L. L., D. Kühner, and W. E. Bron, 1973, Phys. Rev. B **7**, 3892.

Chen, Y. S., W. Shockley, and G. L. Pearson, 1966, Phys. Rev. **151**, 648.

Chrenko, R. M., R. S. McDonald, and E. M. Pell, 1965, Phys. Rev. A **138**, 1775.

Clayman, B. P., 1969, Ph. D. Thesis, Cornell University, MSC Report No. 1026 (unpublished).

Clayman, B. P., 1971, Phys. Rev. B **3**, 2813.

Clayman, B. P., I. G. Nolt, and A. J. Sievers, 1969, Solid State Commun. **7**, 7.

Clayman, B. P., R. D. Kirby, and A. J. Sievers, 1971, Phys. Rev. B **3**, 1351.

Claytor, R. N., and B. J. Marshall, 1960, Phys. Rev. **120**, 332.

Cochran, W., S. J. Fray, F. A. Johnson, J. E. Quarrington, and N. Williams, 1961, J. Appl. Phys. Suppl. **32**, 2102.

Cosand, A. E., 1971, J. Appl. Phys. **42**, 5230.

Cosand, A. E., and W. G. Spitzer, 1971, J. Appl. Phys. **42**, 5241.

Cowley, E. R., and R. A. Cowley, 1965, Proc. R. Soc. Lond. A**287**, 259.

Cowley, R. A., 1966, in *Phonons*, edited by R. W. H. Stevenson (Plenum, New York), Chap. 7.

Cowley, R. A., W. Cochran, B. N. Brockhouse, and A. D. B. Woods, 1963, Phys. Rev. **131**, 1030.

Cundill, M. A., and W. F. Sherman, 1968, Phys. Rev. **168**, 1007.

Cundy, H. M., 1938, Proc. R. Soc. Lond. A**164**, 420.

Daniels, W. B., G. Shirane, B. C. Frazer, H. Umebayashi, and J. A. Leake, 1967, Phys. Rev. Lett. **18**, 548.

Davies, P. R., 1969, Disc. Faraday Soc. **48**, 181.

Dawber, P. G., and R. J. Elliott, 1963a, Proc. R. Soc. Lond. **273**, 222.

Dawber, P. G., and R. J. Elliott, 1963b, Proc. Phys. Soc. **81**, 453.

Dean, P., 1967, J. Inst. Maths. Applics. **3**, 98.

Dean, P. J., 1971, Phys. Rev. B **4**, 2596.

Dean, P. J., D. D. Manchon, Jr., and J. J. Hopfield, 1970, Phys. Rev. Lett. **25**, 1027.

Decius, J. C., J. L. Jacobson, W. F. Sherman, and G. R. Wilkinson, 1965, J. Chem. Phys. **43**, 2180.

DeRemigis, J., and H. L. Welsh, 1970, Can. J. Phys. **48**, 1622.

DeRemigis, J., H. L. Welsh, R. Bruno, and D. W. Taylor, 1971, Can. J. Phys. **49**, 3201.

de Souza, M., A. G. Góngora, M. Aegerter, and F. Lüty, 1970, Phys. Rev. Lett. **25**, 1426.

Deutsch, T. F., 1973, J. Phys. Chem. Solids **34**, 2091.

Devine, S. D., and R. C. Newman, 1970, J. Phys. Chem. Solids **31**, 685.

Devonshire, A. F., 1936, Proc. R. Soc. Lond. A**153**, 601.

Dienes, G. J., R. D. Hatcher, R. Smoluchowski, and W. D. Wilson, 1966, Phys. Rev. Lett. **16**, 25.

Dolling, G., 1963, *Inelastic Scattering of Neutrons in Solids and Liquids* (IAEA, Vienna), Vol. II, p. 37.

Dolling, G., and J. L. T. Waugh, 1965, in *Lattice Dynamics*, edited by R. F. Wallis (Pergamon, London), p. 19.

Dolling, G., and R. A. Cowley, 1966, Proc. Phys. Soc. **88**, 463.

Dolling, G., R. A. Cowley, C. Schittenhelm, and I. M. Thorsen, 1966, Phys. Rev. **147**, 577.

Dolling, G., H. G. Smith, R. M. Nicklow, P. R. Vijayaraghaven, and M. K. Wilkinson, 1968, Phys. Rev. **168**, 970.

Dötsch, H., 1969, Phys. Status Solidi **31**, 649.

Dötsch, H., W. Gebhardt, and C. Martius, 1965, Solid State Commun. **3**, 297.

Dötsch, H., and S. S. Mitra, 1969, Phys. Rev. **178**, 1492.

Dreybrodt, W., and K. Fussgaenger, 1966, Phys. Status Solidi **18**, 133.

Dreyfus, R. W., 1969, Solid State Commun. **7**, 827.

Dürr, U., and D. Bäuerle, 1970, Z. Phys. **233**, 94.

Dyson, F., 1953, Phys. Rev. **92**, 1331.

Egger, H. A., M. Gsanger, E. Luscher, and B. Dorner, 1968, Phys. Lett. **28A**, 433.

Elliott, R. J., 1966, in *Phonons*, edited by R. W. H. Stevenson (Plenum, New York), Chap. 14.

Elliott, R. J., W. Hayes, G. D. Jones, H. F. MacDonald, and C. P. Sennett, 1965, Proc. R. Soc. Lond. A**289**, 1.

Elliott, R. J., and P. Pfeuty, 1967, J. Phys. Chem. Solids **28**, 1789.

Elliott, R. J., and D. W. Taylor, 1967, Proc. R. Soc. Lond. A**296**, 161.

Elliott, R. J., J. A. Krumhansl, and P. L. Leath, 1974, Rev. Mod. Phys. **46**, 465.
Evans, A. R., and D. B. Fitchen, 1970, Phys. Rev. B **2**, 1074.
Evans, D., and R. Richards, 1954, Proc. R. Soc. Lond. A**223**, 238.
Eynthave, R. K., and J. van der Elsken, 1969, J. Phys. Rev. Lett. **23**, 1455.
Feldman, D. W., M. Ashkin, and J. H. Parker, Jr., 1966, Phys. Rev. Lett. **17**, 1209.
Felty, E. J., G. Lucovsky, and M. B. Myers, 1967, Solid State Commun. **5**, 555.
Fertel, J. H., and C. H. Perry, 1969, Phys. Rev. **184**, 874.
Fieschi, R., G. F. Nardelli, and N. Terzi, 1964, Phys. Lett. **12**, 290.
Fieschi, R., G. F. Nardelli, and N. Terzi, 1965, Phys. Rev. **138**, A203.
Finkham, E., and J. Tauc, 1973, Phys. Rev. Lett. **31**, 890.
Fiory, A. T., 1971, Phys. Rev. B **4**, 614.
Flubacher, P. A., J. Leadbetter, J. A. Morrison, and B. P. Stoicheff, 1959, J. Phys. Chem. Solids **12**, 53.
Flygare, W. H., 1963, J. Chem. Phys. **39**, 2263.
Frayer, F. H., and G. E. Ewing, 1967, J. Chem. Phys. **46**, 1994.
Frayer, F. H., and G. E. Ewing, 1968, J. Chem. Phys. **48**, 781.
Friedmann, H., 1962, Adv. Chem. Phys. **4**, 225.
Friedmann, H., and S. Kimel, 1963, J. Chem. Phys. **42**, 2552.
Friedmann, H., and S. Kimel, 1965, J. Chem. Phys. **43**, 3925.
Friedmann, H., and S. Kimel, 1967, J. Chem. Phys. **47**, 3589.
Fritz, B., 1962, J. Phys. Chem. Solids **23**, 375.
Fritz, B., 1964, in *Lattice Dynamics*, edited by R. F. Wallis (Pergamon, London).
Fritz, B., 1965, J. Phys. Chem. Solids, Suppl. 1, 485.
Fritz, B., 1968a, in *Localized Excitations in Solids*, edited by R. F. Wallis, (Plenum, New York), p. 480.
Fritz, B., 1968b, in *Localized Excitations in Solids*, edited by R. F. Wallis (Plenum, New York), p. 496.
Fritz, B., U. Gross, and D. Bäuerle, 1965, Phys. Status Solidi **11**, 231.
Fritz, B., J. Gerlach, and U. Gross, 1968, in *Localized Excitations in Solids*, edited by R. F. Wallis (Plenum, New York), p. 504.
Fritz, I. J., 1973, Solid State Commun. **12**, 271.
Fritzsche, H., 1974, in *Amorphous and Liquid Semiconductors*, edited by J. Tauc (Plenum, New York), Chap. 5.
Fuller, C. S., 1959, in *Semiconductors*, edited by N. B. Hannay (Reinhold, New York), p. 192.
Galt, J. K., 1948, Phys. Rev. **73**, 1460.
Ganguly, B. N., R. D. Kirby, M. V. Klein, and G. P. Montgomery, 1972, Phys. Rev. Lett. **28**, 307.
Gaur, S. P., J. F. Vetelino, and S. S. Mitra, 1971, J. Phys. Chem. Solids **32**, 2737.
Gebhardt, W., 1967, Phys. Rev. **159**, 726.
Gebhardt, W., and K. Maier, 1965, Phys. Status Solidi **8**, 303.
Geick, R., and J. Hassler, 1969, Phys. Status Solidi **33**, 689.
Genzel, L., 1969, in *Optical Properties of Solids*, edited by S. Nudelman and S. S. Mitra (Plenum, New York), Chap. 15.
Genzel, L., K. F. Renk, and R. Weber, 1965, Phys. Status Solidi **12**, 639.
Genzel, L., W. Prettl, and E. Siep, 1969, Optics Commun. **1**, 28.
Gerbaux, X., C. Barthel, A. Hadni, and M. M. Pradhan, 1973, Spectrochim. Acta **29**A, 1695.
Gethins, T., 1970, Can. J. Phys. **48**, 580.
Gethins, T., T. Timusk, and E. Woll, 1967, Phys. Rev. **157**, 744.
Gielisse, P. J., J. N. Plendl, L. C. Mansur, R. Marshal, S. S. Mitra, R. Mykolajewycz, and A. Smakula, 1965, J. Appl. Phys. **36**, 2446.
Glasel, J. A., 1960, J. Chem. Phys. **33**, 252.
Gnädinger, R., 1953, J. Chem. Phys. **21**, 323.
Golding, B., J. E. Graebner, B. I. Halperin, and R. J. Schuty, 1973, Phys. Rev. Lett. **30**, 223.
Goldstein, E., 1896, Zeits. f. Instrumentkunde **16**, 211.
Gomez, M., 1968, Ph. D. Thesis, Cornell University, MSC Report No. 910 (unpublished).
Gomez, M., S. P. Bowen, and J. A. Krumhansl, 1967, Phys. Rev. **153**, 1009.
Gorska, M., and W. Nazarewicz, 1974, Phys. Status Solidi (b) **65**, 193.
Grey, N. R., and L. A. K. Staveley, 1963, Mol. Phys. **7**, 83.
Grigorovici, R., 1974, in *Amorphous and Liquid Semiconductors*, edited by J. Tauc (Plenum, New York), p. 45.
Grindlay, J., and R. Howard, 1965, in *Proceedings of the International Conference on Lattice Dynamics*, edited by R. F. Wallis (Pergamon, Oxford), p. 129.
Haas, M., 1967, *Semiconductors and Semimetals*, edited by R. K. Willardson and A. C. Beer (Academic, New York), Vol. 3.
Hadni, A., 1967, *Essentials of Modern Physics Applied to the Study of the Infrared* (Pergamon, Oxford), p. 562.
Hägg, G., 1935, J. Chem. Phys. **3**, 42.
Hallam, H. E., 1973, in *Vibrational Spectroscopy of Trapped Species*, edited by H. E. Hallam (Wiley, London), p. 67.
Hallam, H. E., and G. F. Scrimshaw, 1973, in *Vibrational Spectroscopy of Trapped Species*, edited by H. E. Hallam (Wiley, London), p. 11.
Halperin, B. I., 1968, Adv. Chem. Phys. **13**, 123.
Harada, H., and S. Narita, 1971, J. Phys. Soc. Japan **30**, 1628.
Hardy, J. R., 1962, Phil. Mag. Series 8, **7**, 315.
Haridasan, T. M., R. K. Gupta, and W. Ludwig, 1973, Solid State Commun. **12**, 1205.
Harley, R. T., J. B. Page, and C. T. Walker, 1969, Phys. Rev. Lett. **23**, 922.
Harley, R. T., J. B. Page, and C. T. Walker, 1971, Phys. Rev. B **3**, 1365.
Harrington, J. A., R. T. Harley, and C. T. Walker, 1970, Solid State Commun. **8**, 407.
Harrington, J. A., and C. T. Walker, 1971, Phys. Status Solidi **43**, 619.
Harrison, J. P., G. Lombardo, and P. P. Peressini, 1968, J. Phys. Chem. Solids **29**, 557.
Harrison, J. P., P. P. Peressini, and R. O. Pohl, 1968, Phys. Rev. **171**, 1037.
Hartmann, W. M., and R. Elliott, 1967, Proc. Phys. Soc. **91**, 187.
Hass, M., 1970, J. Phys. Chem. Solids **31**, 415.
Hass, M., H. B. Rosenstock, and R. E. McGill, 1969, Solid State Commun. **7**, 1.
Hattori, T., K. Ehara, A. Mitsuishi, S. Sakuragi, and H. Kanzaki, 1973, Solid State Commun. **12**, 545.
Havighurst, R. J., E. Mack, and F. C. Blake, 1925, J. Am. Chem. Soc. **47**, 29.
Hayes, W., 1965, Phys. Rev. **138**, A1227.
Hayes, W., and H. F. MacDonald, 1967, Proc. R. Soc. Lond. A**297**, 503.
Hayes, W., H. F. MacDonald, and C. T. Sennett, 1969, J. Phys. C **2**, 2402.
Hayes, W., and A. R. L. Spray, 1969, J. Phys. C **2**, 1129.
Hayes, W., M. C. K. Wiltshire, and P. J. Dean, 1970, J. Phys. C **3**, 1762.
Hayes, W., M. C. K. Wiltshire, R. Berhman, and P. R. W. Hudson, 1973, J. Phys. C **6**, 1157.
Henry, G. H., and C. P. Slichter, 1968, in *Physics of Color Centers*, edited by W. B. Fowler (Academic, New York), p. 351.
Herendeen, R. A., and R. H. Silsbee, 1969, Phys. Rev. **188**, 645.
Hermann, T. S., 1969, Appl. Spectrosc. **23**, 461.

Herzberg, G., 1964, *Molecular Spectra and Molecular Structure I and II* (Van Nostrand, New York).

Hetzler, M. C., and D. Walton, 1970, Phys. Rev. Lett. **24**, 505.

Hetzler, M. C., and D. Walton, 1973a, Phys. Rev. B **8**, 4801.

Hetzler, M. C., and D. Walton, 1973b, Phys. Rev. B **8**, 4812.

Hexter, R. M., and D. A. Dows, 1956, J. Chem. Phys. **25**, 504.

Hilsch, R., and R. W. Pohl, 1933, Nachr. Akad. Wiss. Göttingen, II Math.-Physik. K1 **46**, 322.

Hilsch, R., and R. W. Pohl, 1936, Gött. Nachr. Math. Phys. Neue Folge **2**, 139.

Hilsch, R., and R. W. Pohl, 1938, Trans. Faraday Soc. **34**, 883.

Hopkins, H. P., R. F. Curl, and K. S. Pitzer, 1968, J. Chem. Phys. **48**, 2959.

Hori, J., 1968, *Spectral Properties of Disordered Chains and Lattices* (Pergamon, Oxford).

Horton, G. K., and J. W. Leech, 1963, Proc. Phys. Soc., **82**, 816.

Hughes, A. E., 1968, Phys. Rev. **173**, 860.

Hughes, A. E., 1968, Solid State Commun. **6**, 61.

Hughes, A. E., 1970, private communication.

Hunklinger, S., W. Arnold, and S. Stein, 1973, Phys. Lett. **45A**, 311.

Hurrell, J. P., S. P. S. Porto, T. C. Damen, and S. Mascarenhas, 1968, Phys. Lett. **26A**, 194.

Ikezawa, M., and K. Nasu, 1973, J. Phys. Soc. Japan **34**, 1563.

Ilegems, M., and G. L. Pearson, 1970, Phys. Rev. B **1**, 1576.

Ipatova, I. P., and A. A. Klotchichin, 1966, Sov. Phys.—JETP **23**, 1068.

Irwin, D. M., and R. M. Cotts, 1971, Phys. Rev. B **4**, 235.

Ishigama, M., C. R. Becker, T. P. Martin, and W. Prettl, 1972, Phys. Status Solidi **54**, K81.

Ivanov, M. A., M. A. Krivoglaz, D. N. Mirlin, and I. I. Reshina, 1966, Sov. Phys.-Solid State **8**, 150.

Jain, S. C., and H. K. Sehgal, 1970, Phys. Lett. **31A**, 209.

Jaswal, S. S., 1972, Phys. Lett. **42A**, 309.

Jaswal, S. S., and J. R. Hardy, 1968, Phys. Rev. **171**, 1090.

Jaswal, S. S., and D. J. Montgomery, 1964, Phys. Rev. **135**, A1257.

Joannopoulos, J. D., and M. L. Cohen, 1973, Solid State Commun. **13**, 1115.

Johnson, F. A., 1965, in *Progress in Semiconductors*, edited by A. F. Gibson and R. F. Burgess (Temple Press, London), Vol. 9, p. 179.

Johnson, F. A., and R. Loudon, 1966, Proc. R. Soc. A**281**, 274.

Jones, G. D., and R. A. Satten, 1966, Phys. Rev. **147**, 566.

Jones, G. D., S. Yalsiv, S. Peled, and A. Rosenwacks, 1968, in *Localized Excitations in Solids*, edited by R. F. Wallis (Plenum, New York), p. 512.

Jones, G. O., and M. Woodfine, 1965, Proc. Phys. Soc. **86**, 101.

Kahan, A. M., 1973, Ph.D. Thesis, Cornell University, MSC Report No. 1906 (unpublished).

Kahan, A. M., and A. J. Sievers, 1971, Phys. Lett. **37A**, 203.

Kahan, A. M., M. Patterson, and A. J. Sievers, 1975, "Far Infrared Properties of Lattice Resonant Modes: 6. Hydrostatic Pressure Measurements."

Kaiser, R., and W. Möller, 1969, Phys. Lett. **28A**, 619.

Kamitakahara, W. A., and B. N. Brockhouse, 1972, in *Neutron Inelastic Scattering* (IAEA, Vienna), p. 73.

Kaplyanskii, A. A., 1964, Opt. Spektrosk. **16**, 602 [Opt. Spectrosc. **16**, 329 (1964)].

Kapphan, S., 1970, Ph.D. Thesis, University of Utah (unpublished).

Kapphan, S., and F. Lüty, 1968, Solid State Commun. **6**, 907.

Kapphan, S., and F. Lüty, 1972, Phys. Rev. B **6**, 1537.

Karo, A. M., and J. R. Hardy, 1963, Phys. Rev. **129**, 2024.

Katz, B., A. Rowland, O. Schnepp, 1967, J. Chem. Phys. **46**, 1926.

Keeler, G. J., and D. N. Batchelder, 1972, J. Phys. C **5**, 3264.

Kekelidze, N. P., G. P. Kekelidze, and Z. D. Makharadze, 1973, J. Phys. Chem. Solids **34**, 2117.

Keyser, L. F., and G. W. Robinson, 1966, J. Chem. Phys. **44**, 3225.

King, C. N., W. A. Phillips, and J. P. deNeufrille, 1974, Phys. Rev. Lett. **32**, 538.

Kirby, R. D., 1969, Ph.D. Thesis, Cornell University, Materials Science Center Report No. 1122 (unpublished).

Kirby, R. D., 1971, Phys. Rev. B **4**, 3557.

Kirby, R. D., A. E. Hughes, and A. J. Sievers, 1970, Phys. Rev. B **2**, 481.

Kirby, R. D., I. G. Nolt, R. W. Alexander, and A. J. Sievers, 1968, Phys. Rev. **168**, 1057.

Kirby, R. D., and A. J. Sievers, 1968, Solid State Commun. **6**, 613.

Kittel, C., 1958, *Elementary Statistical Physics* (Wiley, New York), Sec. 44.

Kittel, C., 1966, in *Phonons*, edited by R. W. H. Stevenson (Plenum, New York), Chap. 1.

Kittel, C., 1968, *Introduction to Solid State Physics* (Wiley, New York), Chap. 5.

Kivelson, D., and T. Keyes, 1972, J. Chem. Phys. **57**, 4599.

Klein, M. V., 1968, in *Physics of Color Centers*, edited by B. Fowler, (Academic, New York), Chap. 7.

Klein, M. V., and H. F. MacDonald, 1968, Phys. Rev. Lett. **20**, 1031.

Kleinman, D. A., 1964, Phys. Rev. **134**, 423.

Kressel, H., 1968, J. Appl. Phys. **39**, 2006.

Kriegler, R. J., and H. L. Welsh, 1968, Can. Phys. **46**, 1181.

Kruger, F., O. Reinkober, and E. Koch-Holm, 1928, Ann. Phys. (Leipz.) **85**, 110.

Krumhansl, J. A., 1968, in *Localized Excitations in Solids*, edited by R. F. Wallis (Plenum, New York), p. 17.

Krumhansl, J. A., 1969, in *Tunneling Phenomena in Solids*, edited by E. Burstein and S. Lundqvist (Plenum, New York), p. 551.

Krumhansl, J. A., and J. A. D. Matthew, 1968, Phys. Rev. **166**, 856.

Kuhn, U., and F. Lüty, 1965, Solid State Commun. **4**, 31.

Kühner, D., and M. Wagner, 1968, Z. Phys. **207**, 111.

Kühner, D., and M. Wagner, 1970, Phys. Status Solidi **40**, 517.

Kühner, D. H., H. V. Lauer, and W. E. Bron, 1972, Phys. Rev. **513**, 4112.

Kunitomi, N., Y. Tsunoda, and Y. Hirai, 1973, Solid State Commun. **13**, 495.

Lacina, W. B., and P. S. Pershan, 1970, Phys. Rev. B **1**, 1765.

Lakatos, A., and H. S. Sack, 1966, Solid State Commun. **4**, 315.

Lannin, J. S., 1973, Solid State Commun. **12**, 947.

Lannin, J. S., 1975, "Raman Scattering in $B_{1-x}Sb_x$ Alloys," unpublished.

Larson, T. R., and R. H. Silsbee, 1972, Phys. Rev. B **5**, 778.

Lasjaunias, J. C., R. Maynard, and D. Thoulouze, 1972, Solid State Commun. **10**, 215.

Lax, M., and D. F. Nelson, 1971, Phys. Rev. B **4**, 3694.

Leadbetter, A. J., 1968, Phys. Chem. of Glasses **9**, 1.

Leake, J. A., W. B. Daniels, J. Skalyo, B. C. Frazer, and G. Shirane, 1969, Phys. Rev. **181**, 1251.

Leigh, R. S., and B. Szigeti, 1967, Phys. Rev. Lett. **19**, 566.

Leigh, R. S., and B. Szigeti, 1968, in *Localized Excitations in Solids*, edited by R. F. Wallis (Plenum, New York), p. 159.

Lennard-Jones, T., and A. Devonshire, 1937, Proc. R. Soc. Lond. A**163**, 53.

Lennard-Jones, T., and A. Devonshire, 1938, Proc. R. Soc. Lond. A**165**, 1.

Leung, P. C., L. H. Skolnik, W. P. Allred, and W. G. Spitzer, 1972, J. Appl. Phys. **43**, 4096.

Levy, M., O. Lorimor, and W. G. Spitzer, 1968, J. Appl. Phys. **39**, 1914.
Levy, M. E., and W. G. Spitzer, 1973, J. Phys. C **6**, 3223.
Lewis, J. T., A. Lehoczky, and C. V. Briscoe, 1967, Phys. Rev. **161**, 877.
Lightowlers, E. C., 1972, J. Elect. Matls. **1**, 39.
Logan, R. A., J. M. Rowell, and F. A. Trumbore, 1964, Phys. Rev. **136**, 1751.
Lombardo, G., and R. O. Pohl, 1965, Phys. Rev. Lett. **15**, 291.
Lombardo, G., and R. O. Pohl, 1966, Bull. Am. Phys. Soc. **11**, 212.
Lombardo, G., 1971, Ph.D. Thesis, Cornell University (unpublished).
Lorimor, O. G., W. G. Spitzer, and M. Waldner, 1966, J. Appl. Phys. **37**, 2509.
Lorimor, O. G., and W. G. Spitzer, 1966, J. Appl. Phys. **37**, 3687.
Lorimor, O. G., and W. G. Spitzer, 1967a, J. Appl. Phys. **38**, 2713.
Lorimor, O. G., and W. G. Spitzer, 1967b, J. Appl. Phys. **38**, 3008.
Love, W. F., 1973, Phys. Rev. Lett. **31**, 822.
Loveluck, J. M., and J. B. Sokoloff, 1973, J. Phys. Chem. Solids **34**, 869.
Lubberts, G., 1971, Phys. Rev. B **3**, 1965.
Lucovsky, G., 1974, in *Amorphous and Liquid Semiconductors*, edited by J. Stuke and W. Brenig (Taylor and Francis, London), Vol. 2, p. 1099.
Lucovsky, G., E. Lind, and E. A. Davis, 1967, in *Proceedings of the International Conference on II-VI Semiconducting Compounds*, edited by D. G. Thomas (Benjamin, New York), p. 1150.
Lucovsky, G., A. Mooradian, W. Taylor, G. B. Wright, and R. C. Keezer, 1967, Solid State Commun. **5**, 113.
Lucovsky, G., M. H. Brodsky, and E. Burstein, 1968, in *Localized Excitations in Solids*, edited by R. F. Wallis (Plenum, New York).
Lucovsky, G., M. H. Brodsky, and E. Burstein, 1970, Phys. Rev. B **2**, 3295.
Lucovsky, G., and M. F. Chen, 1970, Solid State Commun. **8**, 1397.
Lucovsky, G., M. H. Brodsky, M. F. Chen, R. J. Chicotka, and A. T. Ward, 1971, Phys. Rev. B **4**, 1945.
Lucovsky, G., R. D. Burnham, A. S. Alimonda, and H. A. Six, 1974, in *Proceedings of the 12th International Conference on Semiconductors*, edited by M. Pilkuhn (Teubner, Stuttgart).
Ludwig, W., 1967, in *Springer Tracts in Modern Physics*, edited by G. Hohler (Springer, Berlin), Vol. 43.
Lüty, F., 1974a, Phys. Rev. B **10**, 3667.
Lüty, F., 1974b, Phys. Rev. B **10**, 3677.
Lüty, F., 1974c, J. Phys. (Paris) C **9**, 49.
Lytle, C. D., and A. J. Sievers, 1965, Bull. Am. Phys. Soc. **10**, 616.
MacDonald, H. F., M. V. Klein, and T. P. Martin, 1969, Phys. Rev. **177**, 1292.
MacDonald, R. A., 1966, Phys. Rev. **150**, 597.
MacPherson, R. W., and T. Timusk, 1970, Can. J. Phys. **48**, 2176.
Manabe, A., A. Mitsuiski, H. Komiya, and S. Ibuki, 1973, Solid State Commun. **12**, 337.
Mann, D. E., N. Acquista, and D. White, 1966, J. Chem. Phys. **44**, 3225.
Mannheim, P. D., and H. Friedmann, 1970, Phys. Status Solidi **39**, 409.
Maradudin, A. A., 1963, in *Astrophysics and the Many Body Problem;* 1962 Brandeis Lectures (Benjamin, New York), Vol. 2.
Maradudin, A. A., 1965, Rep. Prog. Phys. **28**, 331.
Maradudin, A. A., 1966a, in *Solid State Physics*, edited by F. Seitz and D. Turnbull (Academic, New York), Vol. 18, p. 273.
Maradudin, A. A., 1966b, in *Solid State Physics*, edited by F. Seitz and D. Turnbull (Academic, New York), Vol. 19, p. 1.
Maradudin, A. A., E. W. Montroll, and G. H. Weiss, 1963, in *Theory of Lattice Dynamics in the Harmonic Approximation*, edited by F. Seitz and D. Turnbull (Academic, New York).
Maradudin, A. A., E. W. Montroll, and G. H. Weiss, 1963, in *Solid State Physics*, edited by F. Seitz and D. Turnbull (Academic, New York), Supplement 3.
Maradudin, A. A., E. W. Montroll, C. H. Weiss, and I. P. Ipotova, 1971, in *Solid State Physics*, edited by H. Ehrenreich, F. Seitz, and D. Turnbull (Academic, New York), Supplement 3, 2nd edition.
Markov, Yu. F., and N. B. Reshetnyak, 1972, Sov. Phys.-Solid State **14**, 37.
Martin, T. P., 1967, Phys. Rev. **160**, 686.
Martin, T. P., 1971, J. Phys. C **4**, 2269.
Maslakowez, I., 1928, Z. Phys. **51**, 696.
Mason, M. G., W. G. Von Holle, and D. W. Robinson, 1971, J. Chem. Phys. **54**, 3491.
Matossi, F., 1950, J. Chem. Phys. **19**, 161.
Matsuda, H., 1967, Prog. Theor. Phys. **38**, 512.
Matthew, J. A. D., 1965, Solid State Commun. **3**, 365; and MSC Report No. 373, Cornell University (unpublished).
Mazur, P., E. W. Montroll, and R. B. Potts, 1956, J. Wash. Acad. Sci. **46**, 2.
McCumber, D. E., and M. D. Sturge, 1963, J. Appl. Phys. **34**, 1682.
McCumber, D. E., 1964, Phys. Rev. **133**, A163.
McKean, D. C., 1973, in *Vibrational Spectroscopy of Trapped Species*, edited by H. E. Hallam (Wiley, London), p. 355.
Metselaar, R., and J. van der Elsken, 1968, Phys. Rev. **165**, 359.
Meyer, H., and T. A. Scott, 1959, J. Phys. Chem. Solids **11**, 215.
Minkiewiez, V. J., T. A. Kitchens, F. P. Lipschultz, R. Nathams, and G. S. Shirane, 1968, Phys. Rev. **174**, 267.
Mirlin, D. N., and I. I. Reshina, 1964, Sov. Phys.-Solid State **6**, 2454.
Mirlin, D. N., and I. I. Reshina, 1966, Sov. Phys.-Solid State **8**, 116.
Mitani, Y., and S. Takeno, 1965, Prog. Theor. Phys. (Kyoto) **33**, 779.
Mitchell, D. L., S. G. Bishop, and P. C. Taylor, 1972, J. Noncryst. Solids **8**, 231.
Mitra, S. S., and Y. Brada, 1965, Phys. Lett. **17**, 19.
Mitra, S. S., and R. S. Singh, 1966, Phys. Rev. Lett. **16**, 694.
Mitsiushi, A., and H. Yoshinaga, 1962, Prog. Theor. Phys. (Kyoto) Suppl. **23**, 241.
Mitsiushi, A., 1965, U. S.-Japan Seminar on Far Infrared Spectroscopy, Columbus, Ohio, (unpublished).
Möller, W., and R. Kaiser, 1970, Z. Naturforsch. A **25**, 1024.
Möller, W., R. Kaiser, and H. Bilz, 1970a, Phys. Lett. **31A**, 309.
Möller, W., R. Kaiser, and H. Bilz, 1970b, Phys. Lett. **32A**, 171.
Möller, W., and R. Kaiser, 1972, Phys. Status Solidi **50b**, 155.
Mon, J., and A. J. Sievers, 1975, "Absorption Spectra of Glasses in the Far Infrared," to be published.
Montgomery, D. J., and J. R. Hardy, 1965, in *Lattice Dynamics*, edited by R. F. Wallis (Pergamon, Oxford), p. 491.
Montgomery, D. J., and J. R. Hardy, 1965, J. Phys. Chem. Solids, Suppl. **1**, 491.
Montgomery, G. P., and R. D. Kirby, 1971, in *Light Scattering in Solids*, edited by M. Balkanski (Flammarion, Paris).
Montgomery, G. P., W. R. Fenner, M. V. Klein, and T. Timusk, 1972, Phys. Rev. **5**, 3343.

Montgomery, G. P., M. V. Klein, B. N. Ganguly, and R. F. Wood, 1972, Phys. Rev. B **6**, 4047.
Mooradian, A., and T. C. Harman, 1971, in *Physics of Semimetals and Narrow Gap Semiconductors*, edited by D. L. Carter and R. T. Bate (Pergamon, Oxford), p. 297.
Moss, T. S., 1959, *Optical Properties of Semiconductors* (Butterworth, London).
Mott, N. F., and E. A. Davis, 1971, *Electronic Processes in Noncrystalline Materials* (Clarendon, Oxford).
Murahashi, T., T. Koda, Y. Oka, and T. Kushida, 1973, Solid State Commun. **13**, 307.
Nair, I. R., and C. T. Walker, 1971, Phys. Rev. B **3**, 3446.
Nair, I. R., and C. T. Walker, 1973, Phys. Rev. B **7**, 2740.
Nakashima, T., T. Fukumoto, and A. Mitsiushi, 1971, J. Phys. Soc. Japan **30**, 1508.
Nakashima, S., T. Fukumoto, A. Mitsiushi, and K. Itoh, 1973, J. Phys. Soc. Japan **35**, 1437.
Nakashima, S., H. Mishima, and H. Tai, 1974, J. Phys. Chem. Solids **35**, 531.
Narayanamurti, V., 1964, Phys. Rev. Lett. **13**, 693.
Narayanamurti, V., W. D. Seward, and R. O. Pohl, 1966, Phys. Rev. **148**, 481.
Narayanamurti, V., and R. O. Pohl, 1970, Rev. Mod. Phys. **42**, 201.
Nassau, K., 1971, Applied Solid State Science **2**, 174.
Newman, R. C., 1969, Adv. Phys. **18**, 545.
Newman, R. C., *Infrared Studies of Crystal Defects*, 1974 (Taylor and Francis, London).
Newman, R. C., and J. B. Willis, 1965, J. Phys. Chem. Solids **26**, 373.
Newman, R. C., and R. S. Smith, 1968, in *Localized Excitations in Solids*, edited by R. F. Wallis (Plenum, New York), p. 177.
Nijboer, B. R. A., and F. W. DeWette, 1965, Phys. Lett. **18**, 256.
Nolt, I. G., 1967, Ph.D. Thesis, Cornell University, Materials Science Center Report No. 765.
Nolt, I. G., R. A. Westwig, R. W. Alexander, and A. J. Sievers, 1967, Phys. Rev. **157**, 730.
Nolt, I. G., and A. J. Sievers, 1968, Phys. Rev. **174**, 1004.
Norman, I., and G. Porter, 1954, Nature, **174**, 508.
Norwood, M. H., and C. V. Briscoe, 1958, Phys. Rev. **112**, 45.
Obriot, J., P. Marteau, and B. Vodar, 1970, Spectrochim. Acta A **26**, 2051.
Oswald, F., 1959, Z. Naturforsch. **14**, 374.
Owen, A. E., and J. M. Robertson, 1970, J. Noncrystalline Solids **2**, 40.
Page, J. B., 1974, Phys. Rev. B **10**, 719 (1974).
Page, J. B., and B. G. Dick, 1967, Phys. Rev. **163**, 910.
Page, J. B., and D. Strauch, 1967, Phys. Status Solidi, **24**, 469.
Palin, D. E., and H. M. Powell, 1947, J. Chem. Soc. 208.
Pandey, G. K., 1968, J. Chem. Phys., **49**, 1555.
Pandey, G. K., D. K. Shukla, and A. Pandey, 1973, J. Phys. C **6**, 3514.
Pandey, G. K., D. K. Shukla, and A. Pandey, 1974, J. Phys. C **7**, 1242.
Parrish, J. F., C. H. Perry, O. Brafman, I. F. Chang, and S. S. Mitra, 1967, in *II-VI Semiconducting Compounds*, edited by D. G. Thomas (Benjamin, New York).
Parsonage, N. G., and L. A. K. Staveley, 1959, Mol. Phys. **2**, 212.
Parsonage, N. G., and L. A. K. Staveley, 1960, Mol. Phys. **3**, 59.
Patterson, M., 1973, M. S. Thesis, Cornell University, Materials Science Center Report No. 2016.
Pauling, L., 1930, Phys. Rev. **36**, 430.
Payton, D. N., and W. M. Visscher, 1968, Phys. Rev. **175**, 1201.
Peascoe, J. G., and M. V. Klein, 1973, J. Chem. Phys. **59**, 2394.
Peascoe, J. G., W. R. Fenner, and M. V. Klein, 1974, J. Chem. Phys. **60**, 4208.
Peressini, P. P., J. P. Harrison, and R. O. Pohl, 1969, Phys. Rev. **180**, 926.
Perry, C. H., and N. E. Tornberg, 1969, Phys. Rev. **183**, 595.
Pfeuty, P., 1968, in *Localized Excitations in Solids*, edited by R. F. Wallis (Plenum, New York), p. 193.
Phillips, W. A., 1972, J. Low Temp. Phys. **7**, 351.
Picus, G., E. Burstein, B. W. Henvis, and M. Hass, 1959, J. Phys. Chem. Solids **8**, 282.
Pohl, R. O., 1968, in *Localized Excitations in Solids*, edited by R. F. Wallis (Plenum, New York), p. 434.
Pohl, R. O., W. F. Love, and R. B. Stephens, 1974, in *Amorphous and Liquid Semiconductors*, edited by J. Stuke and W. Brenig (Taylor and Francis, London), Vol. 2, p. 1121.
Postmus, C., J. R. Ferraro, and S. S. Mitra, 1968, Phys. Rev. **174**, 983.
Prettl, W., and E. Siep, 1971, Phys. Status Solidi **44**, 759.
Price, W. C., and G. R. Wilkinson, December 1960, Final Tech. Report No. 2, U. S. Army Cont. DA–91–591 EUC–130801–4201–60 (R and D260), U. S. Army, through European Research Office.
Queisser, H. J., 1966, J. Appl. Phys. **37**, 2909.
Quigley, R. J., and T. P. Das, 1967, Phys. Rev. **164**, 1185.
Quigley, R. J., and T. P. Das, 1969, Phys. Rev. **177**, 1340.
Ram, P. N., and B. K. Agrawal, 1972, Solid State Commun. **10**, 1111.
Rebane, L. A., and P. M. Saari, 1971, Sov. Phys.-Solid State **12**, 1547.
Rechtin, M. D., and B. L. Averbach, 1973, Solid State Commun. **13**, 491.
Redington, R. L., and D. E. Milligan, 1962, J. Chem. Phys. **37**, 2162.
Redington, R. L., and D. E. Milligan, 1963, J. Chem. Phys. **39**, 1276.
Reiss, H., and C. S. Fuller, 1956, J. Metals **8**, 276.
Renk, K. F., 1965, Phys. Lett. **14**, 281.
Renucci, M. A., J. B. Renucci, and M. Cardona, 1971, in *Light Scattering in Solids*, edited by M. Balkanski (Flammarion, Paris) p. 326.
Reynolds, D. C., C. W. Litton, and T. C. Collins, 1971, Phys. Rev. B **4**, 1868.
Robertson, R., J. J. Fox, and A. E. Martin, 1934, Phil. Trans. R. Soc. Lond. **A232**, 463.
Robinson, D. W., 1963, J. Chem. Phys. **39**, 3430.
Robinson, D. W., and W. G. VonHolle, 1966, J. Chem. Phys. **44**, 410.
Robinson, G. W., and M. McCarthy, 1959, J. Chem. Phys. **30**, 999.
Rolfe, J., M. Ikezawa, and T. Timusk, 1973, Phys. Rev. B **7**, 3913.
Rollefson, R. J., 1972, Phys. Rev. B **5**, 3235.
Rosenbaum, R. L., C. K. Chau, and M. V. Klein, 1969, Phys. Rev. **186**, 852.
Rowell, J. M., W. L. McMillan, and P. W. Anderson, 1965, Phys. Rev. Lett. **14**, 633.
Sack, H. S., and M. C. Moriarty, 1965, Solid State Commun. **3**, 93.
Schäfer, G., 1960, J. Phys. Chem. Solids **12**, 233.
Schawlow, A. L., A. H. Piksis, and S. Sugano, 1961, Phys. Rev. **122**, 1469.
Schoen, L. J., D. E. Mann, C. Knobler, and D. White, 1962, J. Chem. Phys. **37**, 1146.
Schröder, U., 1966, Solid State Commun. **4**, 347.
Schumaker, N. F., and C. W. Garland, 1970, J. Chem. Phys. **53**, 392.
Scott, J. F., and S. P. S. Porto, 1967, Phys. Rev. **161**, 903.

Sennett, C. T., D. R. Bosomworth, W. Hayes, and A. R. L. Spray, 1969, J. Phys. C **2**, 1137.
Seward, W. D., and V. Narayanamurti, 1966, Phys. Rev. **148**, 463.
Shamu, R. E., W. M. Hartmann, and E. L. Yasaitis, 1968, Phys. Rev. **170**, 822.
Sherman, W. F., and G. R. Wilkinson, 1973, in *Vibrational Spectroscopy of Trapped Species*, edited by H. E. Hallam (Wiley, London), p. 245.
Shotts, W. J., 1973, Ph.D. Thesis, Cornell University, Materials Science Center Report No. 2063.
Shotts, W. J., and A. J. Sievers, 1973, Phys. Lett. **44A**, 307.
Shotts, W. J., and A. J. Sievers, 1974, Phys. Rev. B **10**, 4495.
Shuker, R., and R. W. Gammon, 1970, Phys. Rev. Lett. **25**, 222.
Sievers, A. J., 1964, Phys. Rev. Lett. **13**, 310.
Sievers, A. J., 1965, in *Low Temperature Physics*, edited by J. Daunt, D. Edwards, F. Milford, and M. Yaqub (Plenum, New York), Part B, p. 1170.
Sievers, A. J., 1966, "Resonant Modes in Magnetic Crystals," unpublished.
Sievers, A. J., 1968, in *Localized Excitations in Solids*, edited by R. F. Wallis (Plenum, New York), p. 27.
Sievers, A. J., 1969, in *Elementary Excitations in Solids*, edited by A. A. Maradudin and G. F. Nardelli (Plenum, New York), p. 193.
Sievers, A. J., 1971, in *Far Infrared Spectroscopy*, edited by K. D. Möller and W. G. Rothschild (Wiley-Interscience, New York), p. 525.
Sievers, A. J., 1973, in *Proceedings of the Conference on In Situ Composites*, National Academy of Sciences, NMAB 308–III, p. 129.
Sievers, A. J., and C. D. Lytle, 1965, Phys. Lett. **14**, 271.
Sievers, A. J., A. A. Maradudin, and S. S. Jaswal, 1965, Phys. Rev. **138**, A272.
Sievers, A. J., and R. L. Pompi, 1967, Solid State Commun. **5**, 963.
Sievers, A. J., and S. Takeno, 1965, Phys. Rev. **140**, 1030.
Silsbee, R. H., and D. B. Fitchen, 1964, Rev. Mod. Phys. **36**, 432.
Skolnik, L. H., W. P. Allred, and W. G. Spitzer, 1971, J. Phys. Chem. Solids **32**, 1.
Skolnik, L. H., W. G. Spitzer, A. Kahen, F. Euler, and R. G. Hunsperger, 1972, J. Appl. Phys. **43**, 2146.
Smith, Jr., J. E., M. H. Brodsky, B. L. Crowder, and M. I. Nathan, 1971, Phys. Rev. Lett. **26**, 642.
Smoluchowski, R., 1969, Colloque Ampere XV (North-Holland, Amsterdam), p. 120.
Sparks, M., and L. J. Sham, 1973, Phys. Rev. B **8**, 3037.
Spitzer, W. G., 1971, in *Festkörperprobleme XI*, edited by O. Madelung (Pergamon, London), p. 1–44.
Spitzer, W. G., and W. Allred, 1968, J. Appl. Phys. **39**, 4999.
Spitzer, W. G., W. Allred, S. E. Blum, and R. J. Chicotka, 1969b, J. Appl. Phys. **40**, 2589.
Spitzer, W. G., A. Kahan, and I. Bouthillette, 1969a, J. Appl. Phys. **40**, 3398.
Spitzer, W. G., and M. Waldner, 1965b, J. Appl. Phys. **36**, 2450.
Spitzer, W. G., and M. Waldner, 1965a, Phys. Rev. Lett. **14**, 223.
Stephens, R. B., 1973, Phys. Rev. B **8**, 2896.
Stolen, R. H., 1970, Phys. Chem. Glasses **11**, 83.
Stolen, R. H., J. T. Krause, and C. R. Kurkjian, 1970, Disc. Faraday Soc. **50**, 103.
Strahm, N. D., and A. L. McWhorter, 1969, in *Light Scattering in Solids*, edited by G. B. Wright (Springer, New York).
Strakna, R. E., 1961, Phys. Rev. **123**, 2020.
Strauch, D., 1969, Phys. Status Solidi **33**, 397.
Striefler, M. E., and S. S. Jaswal, 1969a, J. Phys. Chem. Solids **30**, 827.
Striefler, M. E., and S. S. Jaswal, 1969b, Phys. Rev. **185**, 1194.
Strom, U., J. R. Hendrickson, R. J. Wagner, and P. C. Taylor, 1974, Solid State Commun. **15**, 1871.
Stuke, J., and W. Brenig, editors, 1974, *Amorphous and Liquid Semiconductors* (Taylor and Francis, London), Vols. 1 and 2. (See also earlier conference proceedings in this series with the same title.)
Subashier, A. V., 1970, Sov. Phys.-Solid State **11**, 2871.
Takeno, S., and A. J. Sievers, 1965, Phys. Rev. Lett. **15**, 1020.
Talwar, D. N., and B. K. Agrawal, 1975, Phys. Rev. B.
Tauc, J., 1974, in *Amorphous and Liquid Semiconductors*, edited by J. Tauc (Plenum, New York), p. 159.
Taylor, D. W., 1973, Solid State Commun. **13**, 117.
Taylor, P. C., S. G. Bishop, and D. L. Mitchell, 1970, Solid State Commun. **8**, 1783.
Taylor, P. C., S. G. Bishop, and D. L. Mitchell, 1971, Phys. Rev. Lett. **27**, 414.
Taylor, P. C., S. G. Bishop, D. L. Mitchell, and D. Treacy, 1974, in *Amorphous and Liquid Semiconductors*, edited by J. Stuke and W. Brenig (Taylor and Francis, London), Vol. 2, p. 1267.
Taylor, P. C., and M. Rubinstein, 1974, in *Amorphous and Liquid Semiconductors*, edited by J. Stuke and W. Brenig (Taylor and Francis, London), Vol. 2, p. 1161.
Taylor, P. C., U. Strom, J. R. Hendrickson, and M. Rubinstein, 1974, in *Proceedings of the XII International Conference on the Physics of Semiconductors*, to be published.
Templeton, T. L., 1973, Ph.D. Thesis, Simon Fraser University (unpublished).
Templeton, T. L., and B. P. Clayman, 1971, Solid State Commun. **9**, 697.
Templeton, T. L., and B. P. Clayman, 1972, Phys. Rev. B **6**, 4004.
Timmesfeld, K. H., 1968, Phys. Status Solidi **30**, 73.
Timusk, T., and M. Buchanan, 1967, Phys. Rev. **164**, 345.
Timusk, T., and M. V. Klein, 1966, Phys. Rev. **141**, 664.
Timusk, T., and W. Staude, 1964, Phys. Rev. Lett. **13**, 373.
Tinkham, M., 1964, *Group Theory and Quantum Mechanics* (McGraw-Hill, New York).
Title, R. S., 1969, J. Appl. Phys. **40**, 4902.
Tobin, M. C. and T. Baak, 1968, J. Opt. Soc. Am. **58**, 1459.
Tsvetov, V., W. Allred, and W. G. Spitzer, 1967, Appl. Phys. Lett. **10**, 326.
Tsvetov, V., W. Allred, and W. G. Spitzer, 1968, in *Localized Excitations in Solids*, edited by R. F. Wallis (Plenum, New York), p. 185.
Turrell, G., 1972, *Infrared and Raman Spectra of Crystals* (Academic, New York), p. 304.
van der Waals, J. H., 1956, Trans. Faraday Soc. **52**, 184.
van der Waals, J. H., and J. C. Platteeuw, 1956, Recl. Trav. Chim. Pays-Bas **75**, 912.
van der Waals, J. H., and J. C. Platteeuw, 1959, Adv. Chem. Phys. **2**, 1.
Van Hove, L., 1953, Phys. Rev. **89**, 1189.
Vavilov, V. S., V. S. Vinogradov, L. K. Vodopyanov, and B. S. Umarov, 1971, in *Light Scattering in Solids*, edited by M. Balkanski (Flammarion, Paris), p. 338.
Vegard, L., 1921, Z. Phys. **5**, 17.
Verleur, H. W., 1966, Ph.D. Thesis, New York University (unpublished).
Verleur, H. W., and A. S. Barker, Jr., 1966, Phys. Rev. **149**, 715.
Verleur, H. W., and A. S. Barker, Jr., 1967a, Phys. Rev. **155**, 750.
Verleur, H. W., and A. S. Barker, Jr., 1967b, Phys. Rev. **164**, 1169.
Verstegen, J., M. P. H. Goldring, S. Kimel, and B. Katz, 1966, J. Chem. Phys. 44, 3216.

Vinogradov, E. A., L. K. Vodopyanov, and G. S. Oleinik, 1973, Sov. Phys.–Solid State **15**, 322.
Vodopyanov, L. K., E. A. Vinogradov, A. M. Blinov, and V. A. Rukavishnikov, 1972, Sov. Phys.–Solid State **14**, 219.
VonHolle, W. G., and D. W. Robinson, 1970, J. Chem. Phys. **53**, 3768.
Wagner, M., and W. E. Bron, 1965, Phys. Rev. **139**, A223.
Wakabayashi, W., R. M. Nicklow, and H. G. Smith, 1971, Phys. Rev. B **4**, 2558.
Wakamura, K., T. Arai, S. Onari, K. Kudo, and T. Takahashi, 1973, J. Phys. Soc. Japan **35**, 1430.
Waldner, M., M. A. Hiller, and W. G. Spitzer, 1965, Phys. Rev. A **140**, 172.
Wang, C. H., and P. A. Fleury, 1969, in *Light Scattering Spectra of Solids*, edited by G. B. Wright (Springer, New York), Sec. H.
Ward, R. W., and B. P. Clayman, 1974a, Phys. Rev. B **9**, 4455.
Ward, R. W., and B. P. Clayman, 1974b, Can. J. Phys. **52**, 1492; 1502.
Ward, R. W., B. P. Clayman, and S. S. Jaswal, 1974, Solid State Commun. **14**, 1335.
Ward, R. W., B. P. Clayman, and T. Timusk, 1975, Can. J. Phys. **53**, 424.
Ward, R. W., and T. Timusk, 1972, Phys. Rev. B **5**, 2351.
Watkins, G. D., 1972, *Radiation Damage and Defects in Semiconductors* (Institute of Physics, London), p. 228.
Weber, R., 1964, Phys. Lett. **12**, 311.
Weber, R., and P. Nette, 1966, Phys. Lett. **20**, 493.
Weber, R., and F. Siebert, 1968, Z. Phys. **213**, 273.
Wedding, B., and M. V. Klein, 1969, Phys. Rev. **177**, 1274.
Weeks, J. D., J. C. Tully, and L. C. Kimerling, 1975, to be published.
Westwig, R. A., 1967, M. S. Thesis, Cornell University, Materials Science Center Report No. 629.
Whalley, E., and J. E. Bertie, 1966, J. Chem. Phys. **46**, 1264.
Whittle, E., D. A. Dows, and G. C. Pimentel, 1954, J. Chem. Phys. **44**, 2361.
Wilson, E. B., J. C. Decius, and P. C. Cross, 1955, *Molecular Vibrations* (McGraw-Hill, New York), p. 162.
Wilson, W. D., R. D. Hatcher, G. J. Dienes, and R. Smoluchowski, 1967, Phys. Rev. **161**, 888.
Wilson, W. D., R. D. Hatcher, R. Smoluchowski, and G. J. Dienes, 1969, Phys. Rev. **184**, 844.
Winterling, G., 1975, Phys. Rev. B.
Wolfram, G., S. S. Jaswal, and T. P. Sharma, 1972, Phys. Rev. Lett. **29**, 160.
Woll, E. J., T. Gethins, and T. Timusk, 1968, Can. J. Phys. **46**, 2263.
Woods, A. D. B., W. Cochran, B. N. Brockhouse, 1960, Phys. Rev. **119**, 980.
Woods, A. D. B., B. N. Brockhouse, R. A. Cowley, and W. Cochran, 1963, Phys. Rev. **131**, 1025.
Worlock, J. M., and S. P. S. Porto, 1965, Phys. Rev. Lett. **15**, 697.
Wright, G. B., 1969, editor, *Light Scattering Spectra of Solids* (Springer, New York).
Wright, R. B., and C. H. Wang, 1973, J. Phys. Chem. Solids **34**, 787.
Xinh, N. X., 1966, Solid State Commun. **4**, 9.
Xinh, N. X., 1967, Phys. Rev. **163**, 896.
Yarnell, J. L., J. L. Warren, R. G. Wenzel, and P. J. Dean, 1968, in *Neutron Inelastic Scattering* (IAEA, Vienna), Vol. 1, p. 301.
Yim, W. M., J. P. Dismukes, and H. Kressel, 1970, RCA Review **31**, 662.
Zachariasen, W. H., 1932, J. Am. Chem. Soc. **54**, 3841.
Zachariasen, W. H., 1935, J. Chem. Phys. **3**, 162.
Zallen, R., M. L. Slade, and A. T. Ward, 1971, Phys. Rev. B **3**, 4257.
Zeller, R. C., and R. O. Pohl, 1971, Phys. Rev. B **4**, 2029.
Zitter, R. N., and P. C. Watson, 1974, Phys. Rev. B **10**, 607.